



THE INDIVIDUAL MICROBE: SINGLE-CELL ANALYSIS AND AGENT-BASED MODELLING

EDITED BY: Johan H. J. Leveau, Ferdi L. Hellweger, Jan-Ulrich Kreft,
Clara Prats and Weiwen Zhang
PUBLISHED IN: Frontiers in Microbiology



frontiers

Frontiers Copyright Statement

© Copyright 2007-2019 Frontiers Media SA. All rights reserved.

All content included on this site, such as text, graphics, logos, button icons, images, video/audio clips, downloads, data compilations and software, is the property of or is licensed to Frontiers Media SA ("Frontiers") or its licensees and/or subcontractors. The copyright in the text of individual articles is the property of their respective authors, subject to a license granted to Frontiers.

The compilation of articles constituting this e-book, wherever published, as well as the compilation of all other content on this site, is the exclusive property of Frontiers. For the conditions for downloading and copying of e-books from Frontiers' website, please see the Terms for Website Use. If purchasing Frontiers e-books from other websites or sources, the conditions of the website concerned apply.

Images and graphics not forming part of user-contributed materials may not be downloaded or copied without permission.

Individual articles may be downloaded and reproduced in accordance with the principles of the CC-BY licence subject to any copyright or other notices. They may not be re-sold as an e-book.

As author or other contributor you grant a CC-BY licence to others to reproduce your articles, including any graphics and third-party materials supplied by you, in accordance with the Conditions for Website Use and subject to any copyright notices which you include in connection with your articles and materials.

All copyright, and all rights therein, are protected by national and international copyright laws.

The above represents a summary only. For the full conditions see the Conditions for Authors and the Conditions for Website Use.

ISSN 1664-8714

ISBN 978-2-88945-749-6

DOI 10.3389/978-2-88945-749-6

About Frontiers

Frontiers is more than just an open-access publisher of scholarly articles: it is a pioneering approach to the world of academia, radically improving the way scholarly research is managed. The grand vision of Frontiers is a world where all people have an equal opportunity to seek, share and generate knowledge. Frontiers provides immediate and permanent online open access to all its publications, but this alone is not enough to realize our grand goals.

Frontiers Journal Series

The Frontiers Journal Series is a multi-tier and interdisciplinary set of open-access, online journals, promising a paradigm shift from the current review, selection and dissemination processes in academic publishing. All Frontiers journals are driven by researchers for researchers; therefore, they constitute a service to the scholarly community. At the same time, the Frontiers Journal Series operates on a revolutionary invention, the tiered publishing system, initially addressing specific communities of scholars, and gradually climbing up to broader public understanding, thus serving the interests of the lay society, too.

Dedication to Quality

Each Frontiers article is a landmark of the highest quality, thanks to genuinely collaborative interactions between authors and review editors, who include some of the world's best academicians. Research must be certified by peers before entering a stream of knowledge that may eventually reach the public - and shape society; therefore, Frontiers only applies the most rigorous and unbiased reviews.

Frontiers revolutionizes research publishing by freely delivering the most outstanding research, evaluated with no bias from both the academic and social point of view. By applying the most advanced information technologies, Frontiers is catapulting scholarly publishing into a new generation.

What are Frontiers Research Topics?

Frontiers Research Topics are very popular trademarks of the Frontiers Journals Series: they are collections of at least ten articles, all centered on a particular subject. With their unique mix of varied contributions from Original Research to Review Articles, Frontiers Research Topics unify the most influential researchers, the latest key findings and historical advances in a hot research area! Find out more on how to host your own Frontiers Research Topic or contribute to one as an author by contacting the Frontiers Editorial Office: researchtopics@frontiersin.org

THE INDIVIDUAL MICROBE: SINGLE-CELL ANALYSIS AND AGENT-BASED MODELLING

Topic Editors:

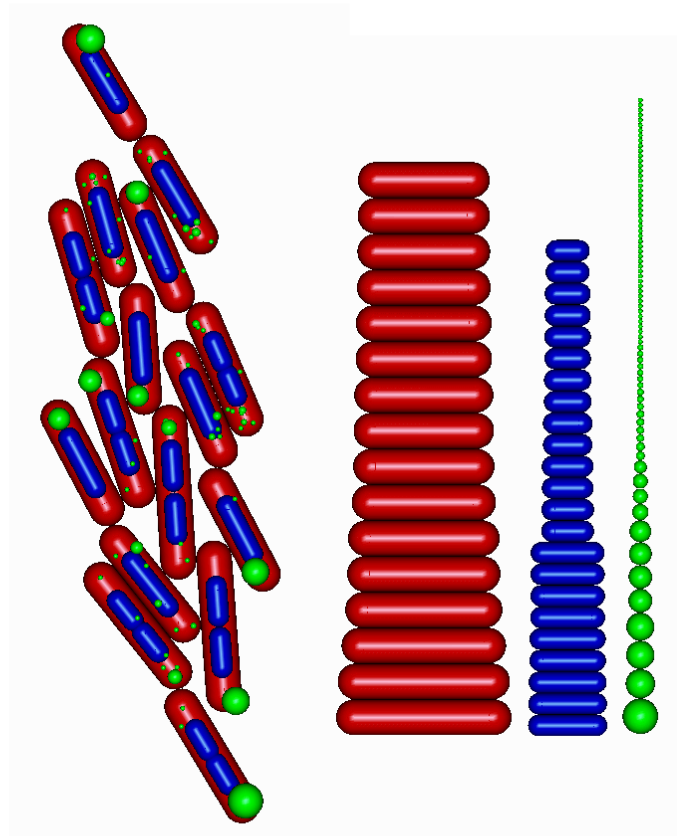
Johan H. J. Leveau, University of California, Davis, United States

Ferdi L. Hellweger, Technical University of Berlin, Germany

Jan-Ulrich Kreft, University of Birmingham, United Kingdom

Clara Prats, Universitat Politècnica de Catalunya - BarcelonaTech, Spain

Weiwen Zhang, Tianjin University, China



The above image was inspired by the artwork of Ursus Wehrli ("The Art of Tidying Up", <http://www.kunstaufraeumen.ch>). Johan Leveau first related this concept to microbiology in his keynote address to the 2013 Congress of European Microbiologists (FEMS) in Leipzig, Germany. This picture is from a model of aging in bacteria (Koleva and Hellweger 2015, <https://doi.org/10.1016/j.ecolmodel.2015.01.024>) and displays cells (red), nucleoids (blue) and damaged protein aggregates (green).

Image: Ferdi Hellweger.

Cover image: Perception7/Shutterstock.com

Recent technological advances in single-cell microbiology, using flow cytometry, microfluidics, x-ray fluorescence microprobes, and single-cell-omics, allow for the observation of individuals within populations. Simultaneously, individual-based models (or more generally agent-based models) allow for individual microbes to be simulated. Bridging these techniques forms the foundation of individual-based ecology of microbes (μ IBE). μ IBE has elucidated genetic and phenotypic heterogeneity that has important consequences for a number of human interests, including antibiotic or biocide resistance, the productivity and stability of industrial fermentations, the efficacy of food preservatives, and the potential of pathogens to cause disease. Individual-based models can help us to understand how these sets of traits of individual microbes influence the above. This eBook compiles all publications from a recent Research Topic in Frontiers in Microbiology. It features recent research where individual observational and/or modelling techniques are applied to gain unique insights into the ecology of microorganisms.

The Research Topic “The Individual Microbe: Single-Cell Analysis and Agent-Based Modelling” arose from the 2016 @ASM conference of the same name hosted by the American Society for Microbiology at its headquarters in Washington, D.C. We are grateful to ASM for funding and hosting this conference.

Citation: Leveau, J. H. J., Hellweger, F. L., Kreft, J.-U., Prats, C., Zhang, W., eds. (2019). The Individual Microbe: Single-Cell Analysis and Agent-Based Modelling. Lausanne: Frontiers Media. doi: 10.3389/978-2-88945-749-6

Table of Contents

06 Editorial: The Individual Microbe: Single-Cell Analysis and Agent-Based Modelling

Johan H. J. Leveau, Ferdi L. Hellweger, Jan-Ulrich Kreft, Clara Prats and Weiwen Zhang

CHAPTER I

NEW TECHNIQUES

09 Mass Cytometry for Detection of Silver at the Bacterial Single Cell Level

Yuting Guo, Sabine Baumgart, Hans-Joachim Stärk, Hauke Harms and Susann Müller

18 Vibrational Spectroscopy for Imaging Single Microbial Cells in Complex Biological Samples

Jesse P. Harrison and David Berry

25 Tools for Genomic and Transcriptomic Analysis of Microbes at Single-Cell Level

Zixi Chen, Lei Chen and Weiwen Zhang

37 A Microfluidics and Agent-Based Modeling Framework for Investigating Spatial Organization in Bacterial Colonies: The Case of *Pseudomonas Aeruginosa* and H1-Type VI Secretion Interactions

Jared L. Wilmoth, Peter W. Doak, Andrea Timm, Michelle Halsted, John D. Anderson, Marta Ginovart, Clara Prats, Xavier Portell, Scott T. Retterer and Miguel Fuentes-Cabrera

48 Stochastic Individual-Based Modeling of Bacterial Growth and Division Using Flow Cytometry

Miriam R. García, José A. Vázquez, Isabel G. Teixeira and Antonio A. Alonso

60 Corrigendum: Stochastic Individual-Based Modeling of Bacterial Growth and Division Using Flow Cytometry

Miriam R. García, José A. Vázquez, Isabel G. Teixeira and Antonio A. Alonso

61 Digital Image Analysis of Yeast Single Cells Growing in Two Different Oxygen Concentrations to Analyze the Population Growth and to Assist Individual-Based Modeling

Marta Ginovart, Rosa Carbó, Mónica Blanco and Xavier Portell

CHAPTER II

NEW DISCOVERIES

82 Heterogeneity in Pure Microbial Systems: Experimental Measurements and Modeling

Rebeca González-Cabaleiro, Anca M. Mitchell, Wendy Smith, Anil Wipat and Irina D. Ofițeru

90 Heterogeneity Between and Within Strains of *Lactobacillus brevis* Exposed to Beer Compounds

Yu Zhao, Susanne Knøchel and Henrik Siegmundfeldt

- 103** *Repetitive Short-Term Stimuli Imposed in Poor Mixing Zones Induce Long-Term Adaptation of E. coli Cultures in Large-Scale Bioreactors: Experimental Evidence and Mathematical Model*
Alexander Nieß, Michael Löffler, Joana D. Simen and Ralf Takors
- 112** *Simulation of Escherichia coli Dynamics in Biofilms and Submerged Colonies With an Individual-Based Model Including Metabolic Network Information*
Ignace L. M. M. Tack, Philippe Nimmegeers, Simen Akkermans, Ihab Hashem and Jan F. M. Van Impe
- 126** *Analysis of abrB Expression During the Infectious Cycle of Bacillus thuringiensis Reveals Population Heterogeneity*
Samia Ben Rejeb, Didier Lereclus and Leyla Slamti
- 137** *Phenotypic Heterogeneity in Attachment of Marine Bacteria Toward Antifouling Copolymers Unraveled by AFM*
Sofiane El-Kirat-Chatel, Aurore Puymege, The H. Duong, Perrine Van Overtvelt, Christine Bressy, Lénaïk Belec, Yves F. Dufrêne and Maëlle Molmeret

CHAPTER III

NEW IDEAS

- 149** *Extracellular Polymeric Substance Production and Aggregated Bacteria Colonization Influence the Competition of Microbes in Biofilms*
Pahala G. Jayathilake, Saikat Jana, Steve Rushton, David Swailes, Ben Bridgens, Tom Curtis and Jinju Chen

REVIEW

- 163** *From Genes to Ecosystems in Microbiology: Modeling Approaches and the Importance of Individuality*
Jan-Ulrich Kreft, Caroline M. Plugge, Clara Prats, Johan H. J. Leveau, Weiwen Zhang and Ferdi L. Hellweger



Editorial: The Individual Microbe: Single-Cell Analysis and Agent-Based Modelling

Johan H. J. Leveau^{1*}, Ferdi L. Hellweger², Jan-Ulrich Kreft³, Clara Prats⁴ and Weiwen Zhang⁵

¹ Department of Plant Pathology, University of California, Davis, Davis, CA, United States, ² Water Quality Engineering, Technical University of Berlin, Berlin, Germany, ³ Centre for Computational Biology & Institute of Microbiology and Infection & School of Biosciences, University of Birmingham, Birmingham, United Kingdom, ⁴ Department of Physics, School of Agricultural Engineering of Barcelona, Universitat Politècnica de Catalunya–BarcelonaTech, Castelldefels, Spain, ⁵ Laboratory of Synthetic Microbiology, Key Laboratory of Systems Bioengineering (Ministry of Education), School of Chemical Engineering and Technology, Tianjin University, Tianjin, China

Keywords: individual microbe, single-cell analysis, individual-based ecology, agent-based modeling, research topic

Editorial on the Research Topic

The Individual Microbe: Single-Cell Analysis and Agent-Based Modelling

The field of microbial individual-based ecology, or μ IBE (Kreft et al., 2013), is grounded in the notion that to truly understand the interactions of microorganisms with their biotic and abiotic environment, one cannot ignore the scales at which such interactions occur. The collection and interpretation of data along these scales (from very small spatial dimensions to very large population sizes) remains a major challenge. Embracing the idea that “progress in science depends on new techniques, new discoveries, and new ideas, probably in that order” (Brenner, 2002), we introduce here a collection of 14 articles authored by 65 leading experts on the topic of “The Individual Microbe” (<https://www.frontiersin.org/research-topics/5193>). We frame these articles in a narrative that explores the progress made on techniques that extract and process information from individual microbes (IMs) and their environment, how that information allows the discovery and prediction of novel single-cell behaviors, and how those discoveries might generate new ideas about the outcomes and impacts of microscopic activity at macroscopic levels.

NEW TECHNIQUES

Techniques of importance to μ IBE fall into one of two categories that we refer to here as “wet” and “dry.” Both types allow the observation and interrogation of IMs and their surroundings, but wet techniques do so of “real” IMs (i.e., bacteria, yeast, fungi, protists, etcetera) in a laboratory or field setting, while dry techniques involve virtual IMs (or “agents”) in computer-simulated environments (Kreft et al.). For wet approaches, much of the recently reported progress relates to increased compatibility with other methods that interrogate the same IM for multiple attributes or experiences, or at increasingly finer spatial or temporal resolution and/or with higher throughput. Some examples are highlighted here. While flow cytometry is a very useful high-throughput interrogation technique, it is incompatible with single-cell interrogation methods that are not fluorochromogenic. Guo et al. describe a variation of flow cytometry called “mass cytometry” where fluorochromes are replaced with heavy metal ions and which allowed the researchers to establish a direct link between the uptake of (antibacterial) silver and cell viability at the single-cell

OPEN ACCESS

Edited by:

George Tsiamis,
University of Patras, Greece

Reviewed by:

Matthias Hess,
University of California, Davis,
United States

*Correspondence:

Johan H. J. Leveau
jleveau@ucdavis.edu

Specialty section:

This article was submitted to
Systems Microbiology,
a section of the journal
Frontiers in Microbiology

Received: 12 September 2018

Accepted: 02 November 2018

Published: 21 November 2018

Citation:

Leveau JHJ, Hellweger FL, Kreft J-U,
Prats C and Zhang W (2018) Editorial:
The Individual Microbe: Single-Cell
Analysis and Agent-Based Modelling.
Front. Microbiol. 9:2825.
doi: 10.3389/fmicb.2018.02825

level. Harrison and Berry compare applications of vibrational microspectroscopy (a combination of spectroscopy and microscopy) for chemical imaging of microbial cells and their surroundings at high resolution and high throughput. The compatibility of Raman and Fourier-transform infrared imaging with other methods such as fluorescent *in situ* hybridization, stable-isotope probing, secondary ion mass spectrometry, and X-ray computed tomography makes it possible to extract local environmental context for the behavior or location of IMs. Such context can help with the interpretation of heterogeneity among a population of IMs as inherent to the IMs or in response to environmental heterogeneity (see below). Chen et al. review tools for DNA- and RNA-based single-cell analysis, which range from low and medium resolution (DAPI staining of chromosomal DNA to count IMs and transcriptional fusions to a reporter such as *gfp* to monitor expression of a single gene of interest, respectively) to high resolution (whole-genome or whole-transcriptome sequencing of single cells). Tools like the latter are still relatively new and face formidable technical challenges. Yet, they offer great hope not only for assessing single-cell variation in DNA and RNA content, but also for unlocking nucleotide-based information from hard-to-culture microorganisms.

As for dry μ IBE techniques (i.e., agent-based modeling approaches), key advances often allow handling larger numbers of IMs per time unit, more attributes per IM, or including IMs representing multiple taxa or guilds. Such advances may be achieved by increasing computing power (for example Wilmoth et al.) or by structuring models more efficiently for faster (re-)calculations of location, perception, and response of IMs. Sometimes, the bottleneck for model progress is the lack of experimental data. For example, Garcia et al. measured cell volumes of exponentially growing bacterial cells using flow cytometry, and were able to derive parameters for a stochastic model of cell elongation and division to predict bacterial population growth. Similarly, Ginovart et al. used digital image analysis to determine yeast growth under different oxygen concentrations and to parameterize individual behavior into an agent-based model for the interpretation of population-level measurements. Often, agent-based models are improved by introducing additional layers of complexity, for example by modeling the behavior and interactions of IMs as a function of the behavior and interactions of cellular components within each IM (Kreft et al.).

NEW DISCOVERIES

One major discovery in recent years is the existence and extent of heterogeneity among IMs. González-Cabaleiro et al. explore the magnitudes, sources and consequences of such heterogeneity, in particular as it pertains to bioprocess industries and design, where such heterogeneity has macroscopic consequences. Zhao et al. demonstrated this for IMs in clonal populations of the beer-spoilage bacterium *Lactobacillus brevis*. While all cells in populations of hop-sensitive strains were classified as dead after exposure to (antimicrobial) hops, a small fraction of cells in populations of hop-tolerant strains was alive and responsible for

the tolerant phenotype. This type of heterogeneity is referred to as intrinsic, i.e., inherent to the IM, as opposed to extrinsic heterogeneity. An example of the latter is Nieß et al. who showed that long mixing times in large-scale bioreactors cause spatial variation in nutrient availability, which in turn triggered heterogeneity in the starvation response among microbes in the reactor. Intrinsic and extrinsic heterogeneity are often coupled. For example, Tack et al. combined an individual-based modeling framework with a metabolic simulation of the bacterium *Escherichia coli* to show that local differences in bacterial activity (i.e., oxygen consumption) lead to local differences in responses of those bacteria (i.e., secretion of weak acid products) generating local differences in environmental conditions (i.e., pH). Oftentimes, heterogeneity among IMs in their natural environment is observed, but its intrinsic or extrinsic nature is not well-understood. Ben Rejeb et al. used GFP-based bioreporters to show significant variation in gene expression among individual cells of a *Bacillus thuringiensis* population during infection of the host insect species *Galleria mellonella*. But is this heterogeneity due to the variation in the IM's experience of different microenvironments inside the insect (is it extrinsic heterogeneity?), or does it represent intrinsic heterogeneity, where variation in gene expression is hardwired into the *B. thuringiensis* way of life, representing what is known as programmed heterogeneity (Kreft et al.)?

Especially exciting (and challenging) are new discoveries that follow from observations of IMs and that defy or generate expectations. An example is El-Kirat-Chatel et al. who used atomic force microscopy to quantify the surface adhesion of bacteria at the single cell level. Surprisingly, their measurements did not correlate well with the adhesion forces measured at the population level. Do such unexpected observations expose fundamental flaws in our ability to scale microbial behaviors? How about agent-based models that accurately describe and validate one type of lab-observed IM behavior, but then also predict another type of behavior, one that has never been seen before, but that if experimentally confirmed would challenge existing theories and/or generate new ideas about the biology and ecology of IMs?

NEW IDEAS

When asked about the field of biology, the philosopher Rudolf Carnap offered a definition (Carnap, 1938) that referred to “the behavior of individual organisms and groups of organisms within their environment.” This distinction between individual and group is, in a nutshell, the big idea behind μ IBE. As a discipline, microbiology has long relied on population-based measurements, with little regard for the fact that life at the microscale is different from life as humans experience it (Dusenbery, 2011). Different rules apply at that scale, many of which are not intuitive and involve laws of small forces, large numbers, and unexpected probabilities. In reference to the latter, Jayatilake et al. used an agent-based model of 2-dimensional bacterial biofilm formation to test outcomes of single-cell variation in the ability to produce extracellular polymeric substances and to engage in quorum sensing. The

study showed that chance played a key role in the outcome of the simulations, as the structure of the biofilm was partly determined by the initial random colonization of bacteria on the surface. For experimentalists, chance is difficult to accept as a driving force behind outcomes. Moreover, chance events at the micrometer scale are hard to control for when most experimental techniques do not allow high-resolution manipulation of single cells or their immediate environment. This frustration is in part what underlies many recent improvements in wet μ IBE technology that deal with the construction of experimental arenas where such micro-manipulation is possible (for example, microfluidic setups like the one used by Wilmoth et al.).

And so, Brenner's postulate (Brenner, 2002) certainly rings true for the field of μ IBE, where progress crucially depends on new techniques, both wet and dry, not only to allow new discoveries about the existence and extent of heterogeneity between IMs, but also in pursuit of testing the idea that such heterogeneity matters.

REFERENCES

- Brenner, S. (2002). Detective Rummage investigates. *Scientist* 16:15.
- Carnap, R. (1938). "Logical foundations of the unity of science," in *International Encyclopedia of Unified Science, Vol. I, Part 1*, eds O. Neurath, R. Carnap, and C.W. Morris (Chicago, IL: University of Chicago Press), 42–62.
- Dusenbery, D. B. (2011). *Living at Micro Scale: the Unexpected Physics of Being Small*. Harvard, IL: Harvard University Press.
- Kreft, J.-U., Plugge, C. M., Grimm, V., Prats, C., Leveau, J. H. J., Banitz, T., et al. (2013). Mighty small: observing and modeling individual microbes becomes big science. *Proc. Natl. Acad. Sci. U.S.A.* 110, 18027–18028. doi: 10.1073/pnas.1317472110

AUTHOR CONTRIBUTIONS

FH, J-UK, CP, and WZ wrote summaries of the papers published on this Research Topic. JL wrote the first draft of the manuscript, which was read and revised by the other authors. All authors approved the submitted version.

ACKNOWLEDGMENTS

This Research Topic grew out of an @ASM conference entitled The individual microbe: Single-cell analysis and agent-based modeling, which was held at the headquarters of the American Society of Microbiology (ASM) in Washington, DC, March 18–20, 2016. The authors thank ASM for conference support and @ASM participants for their thoughtful contributions to the topic of the individual microbe. JL would like to acknowledge funding from USDA-NIFA award number 2014-67017-21695.

Conflict of Interest Statement: The authors declare that the research was conducted in the absence of any commercial or financial relationships that could be construed as a potential conflict of interest.

Copyright © 2018 Leveau, Hellweger, Kreft, Prats and Zhang. This is an open-access article distributed under the terms of the Creative Commons Attribution License (CC BY). The use, distribution or reproduction in other forums is permitted, provided the original author(s) and the copyright owner(s) are credited and that the original publication in this journal is cited, in accordance with accepted academic practice. No use, distribution or reproduction is permitted which does not comply with these terms.



Mass Cytometry for Detection of Silver at the Bacterial Single Cell Level

Yuting Guo¹, Sabine Baumgart², Hans-Joachim Stärk³, Hauke Harms¹ and Susann Müller^{1*}

¹ Department of Environmental Microbiology, Helmholtz Centre for Environmental Research, Leipzig, Germany, ² Department of Immune Monitoring, German Rheumatism Research Centre, An-Institute of the Leibniz Association, Berlin, Germany,

³ Department of Analytical Chemistry, Helmholtz Centre for Environmental Research, Leipzig, Germany

OPEN ACCESS

Edited by:

Clara Prats,
Universitat Politècnica de Catalunya,
Spain

Reviewed by:

Dimitris Tsaltas,
Cyprus University of Technology,
Cyprus
Ping Zeng,
Chinese Research Academy
of Environmental Sciences, China

*Correspondence:

Susann Müller
susann.mueller@ufz.de

Specialty section:

This article was submitted to
Systems Microbiology,
a section of the journal
Frontiers in Microbiology

Received: 28 April 2017

Accepted: 30 June 2017

Published: 17 July 2017

Citation:

Guo Y, Baumgart S, Stärk H-J,
Harms H and Müller S (2017) Mass
Cytometry for Detection of Silver
at the Bacterial Single Cell Level.
Front. Microbiol. 8:1326.
doi: 10.3389/fmicb.2017.01326

Background: Mass cytometry (Cytometry by Time of Flight, CyTOF) allows single-cell characterization on the basis of specific metal-based cell markers. In addition, other metals in the mass range such as silver can be detected per cell. Bacteria are known to be sensible to silver and a protocol was developed to measure both the number of affected cells per population and the quantities of silver per cell.

Methods: For mass cytometry ruthenium red was used as a marker for all cells of a population while parallel application of cisplatin discriminated live from dead cells. Silver quantities per cell and frequencies of silver containing cells in a population were measured by mass cytometry. In addition, live/dead subpopulations were analyzed by flow cytometry and distinguished by cell sorting based on ruthenium red and propidium iodide double staining. Verification of the cells' silver load was performed on the bulk level by using ICP-MS in combination with cell sorting. The protocol was developed by conveying both, fast and non-growing *Pseudomonas putida* cells as test organisms.

Results: A workflow for labeling bacteria in order to be analyzed by mass cytometry was developed. Three different parameters were tested: ruthenium red provided counts for all bacterial cells in a population while consecutively applied cisplatin marked the frequency of dead cells. Apparent population heterogeneity was detected by different frequencies of silver containing cells. Silver quantities per cell were also well measurable. Generally, AgNP-10 treatment caused higher frequencies of dead cells, higher frequencies of silver containing cells and higher per-cell silver quantities. Due to an assumed chemical equilibrium of free and bound silver ions live and dead cells were associated with silver in equal quantities and this preferably during exponential growth. With ICP-MS up to 1.5 fg silver per bacterial cell were detected.

Conclusion: An effective mass cytometry protocol was developed for the detection and quantification of silver in single bacterial cells of different physiological states. The silver quantities were generally heterogeneously distributed among cells in a population, the degree of which was dependent on micro-environmental conditions and on silver applied either in ion or nanoparticle-aggregated form.

Keywords: mass cytometry, metal-based cell marker, silver quantification in single cells, silver distribution, bacterial heterogeneity, silver nanoparticles

INTRODUCTION

Increasing use of antimicrobial commercial products amended with silver nanoparticles (AgNP) has caused concerns, and extensive study was directed on AgNP toxicity of causing generation of reactive oxygen species (Choi and Hu, 2008; Franci et al., 2015), cell growth inhibition (Ivask et al., 2014), or cell viability loss (Guo et al., 2017). The characterization of AgNP physicochemical behavior with the focus on their dissolution, aggregation, and transformation in biological environments became increasingly important (Fabrega et al., 2011). As a result of these efforts recent studies suggested that dissolved silver ions can be held responsible for the antimicrobial qualities of AgNP (Xiu et al., 2012). We confirmed these findings in an own study but revealed an additional particle effect supposedly caused by fast formation of huge AgNP-aggregates of about 500 nm in cell solutions and suggested their contribution to higher cell death ratios (Guo et al., 2017). The attachment of AgNP-aggregates to single bacterial cells was identified by TEM and SEM-EDX (Guo et al., 2017). Aside from TEM and SEM-EDX, other techniques have been used to visualize and identify metals in single human cells, e.g., AFM, SXFM (Cerchiaro et al., 2013). However, these microscopy techniques have limitations including random sample detection, and lack of quantitative information regarding cellular interactions with nanoparticles. Flow cytometry has been reported to characterize single cells in microbial populations with high-throughput by means of light scatter and fluorescent dyes (Müller and Nebe-von-Caron, 2010). Cellular AgNP uptake was conveyed by this method via changes of side scatter characteristics but only for eukaryotic cells (Lankoff et al., 2012; Zucker et al., 2013; Zhao and Ibuki, 2015). For bacterial cells side scatter did not reveal any AgNP uptake (for sizes of 10 and 30 nm; Guo et al., 2017). Instead, ICP-MS has been operated widely to quantify the contents of silver ions in bacterial cells (Swathy et al., 2014; Wakshlak et al., 2015). It is a destructive technique where entire cell suspensions are digested and injected which prevents differentiation of silver-affected cells from unaffected ones. The ICP-MS obtained average value from a highly heterogeneous cell population disregards cell subsets and diverse phenotypes that may be relevant to reveal causality of cell reaction and toxicity in response to silver.

A growing interest in single-cell analysis can be recognized and numerous analytical methods have been developed or improved. One of those technologies is mass cytometry, which couples mass spectrometry with single-cell analysis and was introduced as Cytometry by Time of Flight (CyTOF) (Bendall et al., 2011; Chang et al., 2017). CyTOF offers numerous potential advantages over fluorescence-based flow cytometry, e.g., overcoming the challenge of spectral overlap intrinsic to fluorescent dyes by using rare-earth-metal stable isotopes with little signal overlap. In addition, more than 35 simultaneously measured cellular parameters compared to 10 markers in fluorescence-based flow cytometry can be measured (Bjornson et al., 2013; Chattopadhyay et al., 2014). To date this promising technique is mainly used for human cells as an effective tool for drug development or improvement of therapeutic programs

ranging from infectious disease to cancer (Bendall et al., 2011; Gavasso et al., 2016; Robinson and Mao, 2016; Baca et al., 2017; Baumgart et al., 2017). Also other inorganic nanoparticles have been labiles (Vancaeyzeele et al., 2007; Lin et al., 2014; Tong et al., 2016; Schulz et al., 2017) but were in the focus of biodistribution experiments (Yang et al., 2017). Limited studies have been reported on microbial cells (Leipold et al., 2011; Miyashita et al., 2014), where, e.g., a combination of a metal-based membrane stain and lectins, conjugated to lanthanide-chelating polymers, was used to differentiate *Escherichia coli* cells based on their cell surface polysaccharides.

In this study, we tested the mass cytometry technology for discrimination of live/dead cell states and simultaneous quantification of silver in single bacterial cells. An earlier study (Guo et al., 2017) revealed random attachment of huge up to 500-nm-AgNP-aggregates to a limited number of cells in a population after few minutes treatment of cells with 10- and 30-nm AgNP at environmental relevant concentrations. A relation between viability states and increased quantities of silver ions in cells by those AgNP-aggregates was suggested. Because flow cytometry does not allow direct detection of these two events simultaneously, a mass cytometry workflow was developed for the purpose. Such data may be especially useful to link cell states and features with cell fate and thus to contribute to the development of models that implement immanent characteristics of an individual cell and its individual capacity to notice random, selective, and perhaps lethal influences from the environment.

MATERIALS AND METHODS

Materials

Silver nitrate (AgNO₃) (99.9%) and ruthenium red (RR) was purchased from Sigma-Aldrich (United States). AgNPs were provided by nanoComposix (United States) as aqueous suspensions [citrate coated, mass concentration (Ag) 0.02 mg/mL] of the size 10 nm (9.4 ± 1.7 nm, AgNP-10). Cis-Platinum (II) diamine dichloride (cisPt) was purchased from Enzo Life Sciences GmbH (Lörrach, Germany). Nitric acid (HNO₃) was purchased from Merck (Germany). M12 medium and PBS compositions were shown in Supplementary Table S1. For washing purposes 18.2 MΩ-cm water (MilliQ, Germany) was used.

Bacterial Cultivation

Pseudomonas putida KT2440 was obtained from the German Collection of Microorganisms and Cell Cultures (DSMZ, Germany). Bacterial standard-growth was performed in M12 medium on a rotary shaker at 30°C and 170 rpm. The growth was monitored by optical density at $\lambda = 600$ nm (Spectra max Plus 384 photometer, Molecular Devices, Sunnyvale, CA, United States).

Bacterial Cultivation under Silver Treatment

An overnight pre-culture of *P. putida* KT2440 was incubated in M12 medium with an initial OD₆₀₀ of 0.09 and grown

for 72 h (30°C, 170 rpm). Either AgNP-10 (1.29 mg/L) or AgNO₃ (0.19 mg/L) were implemented in the cultivations and chosen concentrations referred to the determined EC₅₀ values from an earlier publication (Guo et al., 2017). Cultivations without silver treatment served as silver-ion negative control while application of AgNO₃ served as silver-ion positive control. Cells were harvested at 0, 12, 48, and 72 h and treated separately according to the mass cytometry staining protocol (see below).

Determination of Cell Number

To analyze bacteria on the single cell level at the mass cytometer, a concentration of 5.0×10^5 cells/mL was required for each injection. Therefore, a fast and accurate cell counting method was required and for this a range of linear relationship between cell counts and OD₆₀₀ was exploited. Cell counts were determined by a flow cytometer (Becton, Dickinson and Company, Franklin Lakes, NJ, United States) together with a calibrated suspension of microsphere standard (6.0 µm diameter microspheres at a concentration of 10⁸ beads/mL in Milli-Q water containing 2 mM sodium azide, L34856, Thermo Fisher Scientific, Germany) for accurate cell count measurements. OD₆₀₀ was analyzed by a spectrophotometer. All measurements were done in replicates and shown in Supplementary Figure S1.

All Cell Indicator for Mass Cytometry

To optimize RR staining for *P. putida* KT2440 populations, a stock solution of 1.3 mM of RR in PBS was prepared and stored at 4°C. Before use the solution was ultra-sonicated (Ultrasonic bath, Merck Eurolab, Darmstadt, Germany) for 10 min. 10⁸ cells were treated with different concentrations of RR (0 to 0.33 µM) for 30 and 60 min. The final staining protocol requires 0.13 µM RR/10⁸ cells/200 µL PBS and a staining time of 30 min at room temperature (RT). Details of staining optimization were shown in Supplementary Figure S2A.

Dead Cell Indicator for Mass Cytometry

To optimize cisPt staining for *P. putida* KT2440 populations, a stock solution of 25 mM of cisPt in dimethyl sulfoxide (Sigma-Aldrich, United States) was prepared and stored at −20°C. 10⁸ cells were stained with different concentrations of cisPt (0 to 20 µM) and treated for 1, 5, 10, 30 min. The final staining protocol requires 5 µM cisPt/10⁸ cells/1 mL PBS and a staining time of 10 min at RT. Details of staining optimization and calibration curves generated on the basis of RR and cisPt measurements were shown in Supplementary Figures S2B,C.

Dead Cell Indicator for Flow Cytometry

The fluorescent dye propidium iodide (PI) was used as dead cell indicator for *P. putida* KT2440. Staining optimization and calibration were published (Guo et al., 2017). The final protocol requires 2 µM PI/10⁸ cells/1 mL PBS and a staining time of 2 min. For quantification of PI stained dead cells (PI+dead) of RR labeled *P. putida* KT2440, cells were double stained with RR (0.13 µM, 30 min), followed by PI (2 µM, 2 min) and analyzed by flow cytometry at log scale.

Workflow for Analysis of Bacterial Cells at the Mass Cytometer

Harvested cells were diluted to 10⁸ cells/1 mL PBS and centrifuged at 3200 × g for 10 min. The pelleted cells were re-suspended in cisPt solution (5 µM, 10 min, RT). Subsequently, the cisPt stained dead cells (cisPt+dead) were washed (3200 × g, 10 min) twice with 3 and 1 mL PBS, respectively, to remove unbound cisPt. Finally, cells were stained with RR (0.13 µM, 30 min, RT), washed twice (3200 × g, 10 min) with 1 mL water to remove salts and unbound RR. For mass cytometry measurement the cell concentration was adjusted to 5.0×10^5 cells/mL in Milli-Q water. Four element calibration beads (Fluidigm, United States) were added 1:10 v/v before acquisition for later normalization (Finck et al., 2013).

Mass Cytometry

The CyTOF instrument (Fluidigm Corp, South Francisco, CA, United States) was tuned, calibrated, and cleaned on the daily base according to the manufacturer's advice. Aqueous bacterial cell suspensions were acquired on a CyTOF instrument version 1 upgraded to the control software of v6.0.626 with a flow rate of 45 µL/min. Argon gas 5.0 was used to generate the plasma and for nebulizing the cell suspension. About 1.5×10^5 cells per sample were subsequently loaded onto a 450 µL sample loop and measured in a dual instrument mode with noise reduction turned on, a cell length range from 1 to 75 and with 'on the fly' processing. The initial raw data were processed into standard FCS file format, randomized and normalized by Software Helios version 6.5.358 (Fluidigm Corp, South San Francisco, CA, United States). Data analysis was performed with FlowJo (version 10) (TreeStar, Ashland, OR, United States). Monitoring was done by analyzing natural abundance isotopes of ruthenium (¹⁰²Ru and ¹⁰⁴Ru), platinum (¹⁹⁵Pt) and silver (¹⁰⁷Ag and ¹⁰⁹Ag, 51.8 and 48.2%, respectively). Silver was measured in ionic form and resulting data were related to the ¹⁰⁷Ag isotope.

Flow Cytometry and Cell Sorting

Cytometric measurements were performed with a BD Influx v7 Sorter USB, (Becton, Dickinson and Company, Franklin Lakes, NJ, United States) equipped with a blue 488-nm Sapphire OPS laser (400 mW, Coherent, Santa Clara, CA, United States). The 488-nm laser light was used for the analysis of the forward scatter (FSC, 488/10), the side scatter (SSC, 488/10, trigger signal), and the PI induced red fluorescence (616/23). The fluidic system was run at 33 psi using a 70-µm nozzle. The sheath fluid consisted of 0.5 × FACSFlow buffer (BD). For the optical calibration of the cytometer in the linear range, 1-µm blue fluorescent FluoSpheres (Molecular Probes, F-8815, Eugene, OR, United States) and 2-µm yellow-green fluorescent FluoSpheres (Thermo Fisher Scientific, F8827, Waltham, MA, United States) were used. For calibration in the log range, 0.5-µm UV Fluoresbrite Microspheres (Polysciences, 18339, Warrington, PA, United States) were applied. Sorting of PI unstained live (PI−live) and PI stained dead (PI+dead) cells into plastic tubes was performed at an event rate of 5.000/sec which corresponded to a sort rate of 700–1.500 cells/sec. The sort mode was 1.0 Drop Pure. To obtain

sufficient cell amounts for the following mass cytometry and ICP-MS measurements, up to 3.0×10^6 cells were sorted for either PI–live or PI+dead cells. After sorting cells were pre-processed before CyTOF or ICP-MS analysis: sorted cells were transferred from plastic tubes into glass tubes and centrifuged at $3200 \times g$ for 10 min, supernatant was removed and the cell pellets were stored at -20°C . Before mass cytometry measurements, cell pellets were washed once with 1 mL Milli-Q water by re-suspension in 1 mL Milli-Q water for injection.

ICP-MS Analysis

For bulk ICP-MS analysis, the sorted PI–live and PI+dead cell pellets were digested by addition of 50 μL HNO_3 (60%, ultrapure) for a period of 15 min. Subsequently the solution was suspended in Milli-Q water dispensed with rhodium (^{103}Rh) as internal standard [$c(\text{Rh}) = 0.75 \text{ ng/mL}$] to a 1 mL solution. The solution was measured with an Inductively Coupled Plasma Mass Spectrometer (ICP-MS, Element XR, Thermo, Germany) equipped with a micro-concentric nebulizer (Micromist-100, Glass Expansion, Australia) consuming 135 μL sample per minute. Silver was measured and quantified in ionic form related to the ^{109}Ag isotope.

RESULTS AND DISCUSSION

Bacterial Labeling for Mass Cytometry Analysis

Cytometry by Time of Flight technology substitutes isotopes of transition elements and lanthanides for fluorescent dyes. The cells are directed into a narrow flow to be screened one by one and vaporized. Elements of the cells are atomized, ionized, and subsequently analyzed by a time-of-flight mass spectrometer. The measured signal of natural abundance isotopes of the rare-earth-metals ruthenium and platinum per cell from applied RR and cisPt provided the number of labeled cells and the isotopes' quantity per cell. RR is a cationic reagent and has been widely used to locate acidic polysaccharide-like material (Fletcher and Floodgate, 1973; Fassel and Edmiston, 1999; Waller et al., 2004) and to visualize numerous ultra-structural details in and outside of cells (Lingens et al., 1985; Chatterjee et al., 2010; Perfumo et al., 2014). Because RR is easy to operate by addressing all cells in a population directly without pre-treatment (instead of, e.g., fixation, necessary for flow cytometric measurements; Günther et al., 2008) and its atomic mass is within the detectable mass range of mass cytometers, RR was used as an all cell indicator for the CyTOF workflow. However, the metal was not used in this context for bacteria before. The second dye used in this study, cisPt, is a readily available platinum based chemotherapeutic agent and reacts with protein nucleophiles, with which it can form covalent platinum–sulfur or sulfhydryl bonds (Fienberg et al., 2012). cisPt enters cells with compromised cell membranes, where it non-specifically labels total cellular protein. The reagent can thus be used to discriminate live from dead cells which is well practiced for human cells (Bjornson et al., 2013; Nair et al., 2015). However, applications on bacteria haven't been tested yet to our knowledge.

In our study, the Gram-negative bacterium *P. putida* KT2440 was used as a test organism to establish a protocol for RR and cisPt staining in order to detect all cells in a population and to differentiate live from dead cells. The RR stained bacteria were well detectable by the CyTOF and entirely identified within a cell gate plotted via the two most natural abundance ruthenium isotopes $^{102}\text{Ru}/^{104}\text{Ru}$. Protein binding cisPt was used as second cell marker for dead cells and identified by the ^{195}Pt isotope. For this combined marker group optimized staining conditions were tested with regard to dye concentrations and times of incubation and the trade-off between highest intensity and shortest staining time was chosen for the final workflow (**Figure 1A** and Supplementary Figure S2B). To verify the reliability of the cisPt marker different ratios of live and dead cells (70% ethanol treated, 20 min, RT) were prepared and measured at CyTOF. In parallel the same ratios were analyzed by using the fluorescent marker PI (binding on nucleic acids) for dead cells and flow cytometry. While flow cytometry mirrored the precise ratios, CyTOF gave lower dead cell counts (Supplementary Figure S2C). Up to now the dye was only applied to cell-wall-free cells such as human cells effectively (Majonis et al., 2011; Fienberg et al., 2012). Bacterial cells, however, have rigid cell walls, subsistent also in dead cells, forming a barrier which must be overcome by cisPt. It can be assumed that the limitation in the quantitative detection of dead cells in a population may be caused by this boundary. Nevertheless, despite the determination of dead cell numbers by cisPt in a population of *P. putida* KT2440 was lower in comparison to PI staining (Supplementary Figure S2C: $k_{\text{cisPt}} = 0.45$, $k_{\text{PI}} = 0.98$), the stable isotopes' calibration of RR and cisPt proved to be useful cell markers. Standard-grown *P. putida* KT2440 cells (48 h) were represented in typical 2D-plots for RR staining (**Figure 1B**). The number of dead cells was 2.7% (Q2) measured by cisPt and mass cytometry (**Figure 1C**), and 4.1% (R2) measured by PI and flow cytometry (**Figure 1D**).

Detection of Silver of Single Cells of *P. putida*

Pseudomonas putida KT2440 is known to react on various silver concentrations by changes in growth rates and live/dead cell ratios. The toxicity of silver was recently assumed to be caused by the ions only (Xiu et al., 2012; Gao et al., 2017; Juganson et al., 2017) but we detected an additional particle-related effect (Guo et al., 2017). We assumed that the typical fast aggregation of AgNPs to huge complexes in a nature-like environment within 30 min (Guo et al., 2017) might contribute to a further increase of dead cell counts due to their random attachment to bacterial cell surfaces and their thereby steady release of additional silver ions into those cells.

Thus, mass cytometry was involved in this study to clarify if the treatment of bacteria with either silver ions or AgNP (1) generates different frequencies of cells that contain silver which may cause different live/dead cell ratios and (2) produces disparate quantities of silver per cell suggesting that populations exposed to AgNP might contain cells with a higher silver load. To answer these questions *P. putida* KT2440 cells were treated with the respective EC_{50} concentrations of 1.29 mg/L for AgNP-10

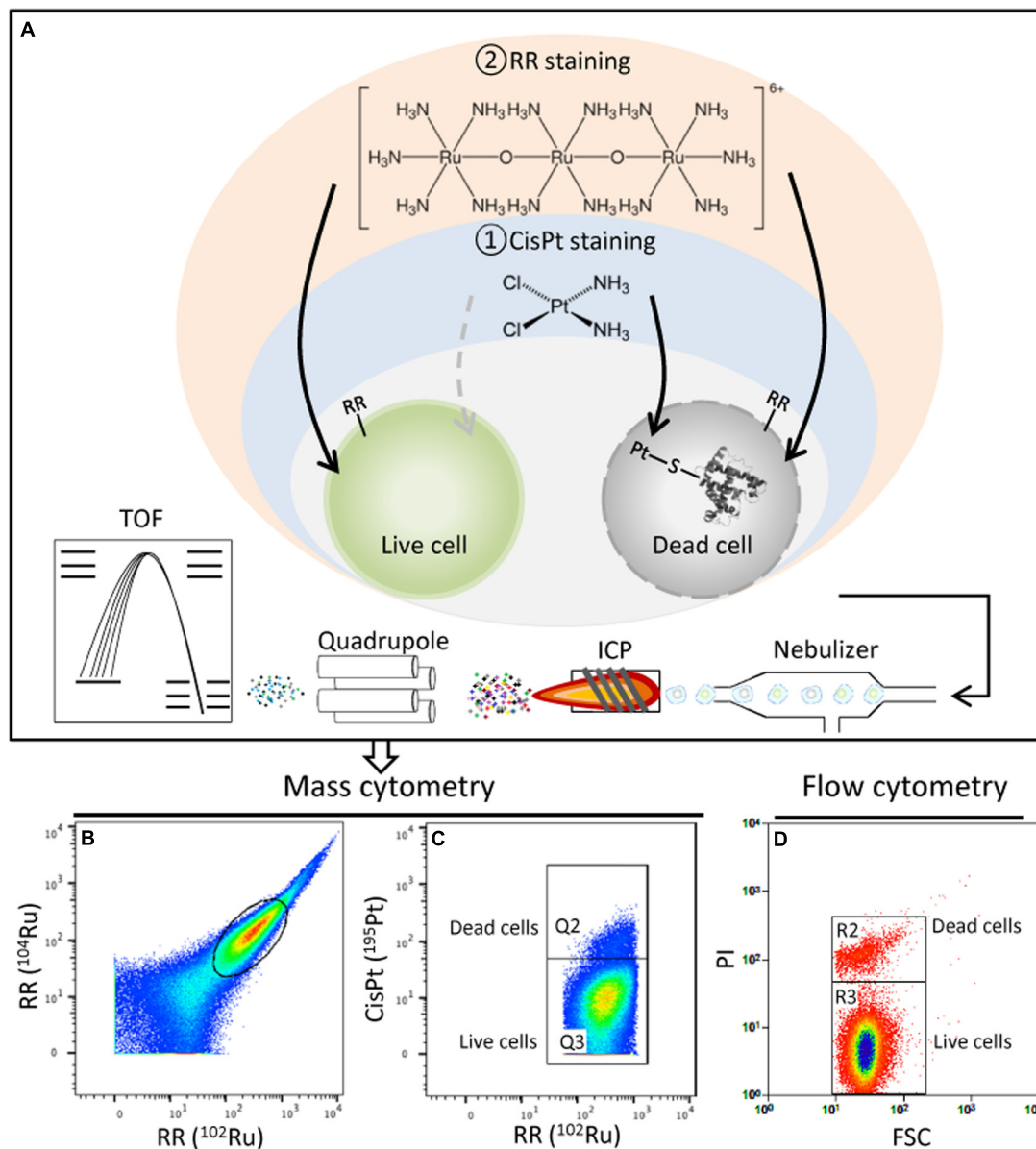
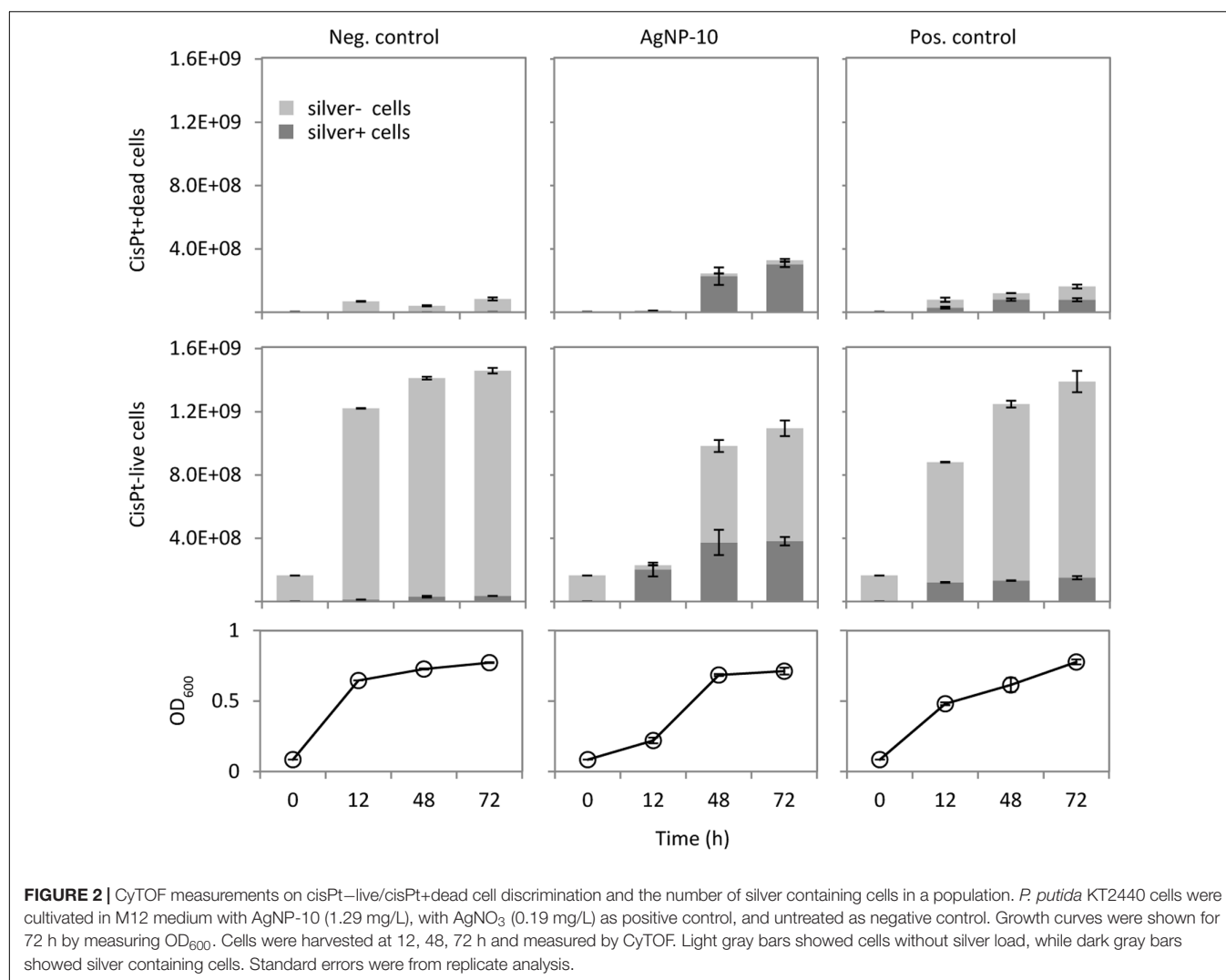


FIGURE 1 | (A) CyTOF workflow for bacteria. Cells were first stained by cisPt for live/dead discrimination, followed by RR staining as an overall bacterial cell indicator. After washing, cells were subjected to the mass cytometer as a stream of single cells. In the plasma region elements of the cells are atomized and ionized. Ions of high-mass elements (i.e., ruthenium, platinum, and silver) enter selectively the TOF chamber and are separated according to their mass before detection. **(B)** CyTOF analysis of standard-grown and harvested *P. putida* KT2440 (48 h). CyTOF plots marked all events based on $^{102}\text{Ru}/^{104}\text{Ru}$ signal. **(C)** Dead cisPt+ (Q2) cells are distinguished from live cisPt- (Q3) cells. **(D)** Dead (R2) and live (R3) cells are distinguished by PI staining and flow cytometry.

and 0.19 mg/L for AgNO_3 as the positive control. As determined before, the released ion concentrations were nearly similar because cell-free AgNP-10 dissolution kinetic curves inferred 0.08 mg/L silver ions released from AgNP-10 (1.29 mg/L) in comparison to 0.12 mg/L silver ions from AgNO_3 (0.19 mg/L) over a time period of 72 h (Guo et al., 2017). Standard-grown *P. putida* KT2440 without silver treatment served as the negative control. The growth curves (Figure 2, bottom) showed a delayed lag-phase for the AgNP-10 treated bacteria and a slower growth rate ($\mu = 0.14/\text{h}$) for the AgNO_3 positive control in comparison

to the negative control ($\mu = 0.18/\text{h}$). CyTOF technology was used to mark all bacterial cells of those populations and to distinguish live from dead cells. The additional measured silver signal was used to determine the frequency of silver containing cells as well as the quantities of silver per cell via the intensity of the mass cytometric signal for silver (IAG).

After 72 h and in comparison to the negative control AgNP-10 treatment caused an increase of cisPt+dead cells by a factor of about 4 while the AgNO_3 positive control showed a factor of 2 (Figure 2), indicating that the particles caused higher



frequencies of dead cells. Further, the frequency of cells that contain silver (Figure 2, dark gray bars) was also higher for the AgNP-10 treatment in comparison to the positive control while cells of the untreated negative control were nearly not loaded with silver (Figure 2). After 72 h AgNP-10 treatment 92% of cisPt+dead cells and 35% of cisPt–live cells were loaded with silver. Instead, the AgNO₃ positive control revealed 48% silver containing cells of the cisPt+dead and only 11% of the cisPt–live cells (Figure 2). The data show that AgNP-10 treatment caused the highest frequencies of dead cells in comparison to both controls after 72 h, and that almost all of the dead cells were loaded with silver. At the beginning of the exponential phase (12 h) where cells thrived at merely low numbers, live cells were still predominant but silver was loaded to any cell independent of its viability state. At longer exposure time the high frequency of silver loaded dead cells was almost consistent between 48 and 72 h. A similar tendency was observed within the larger fraction of surviving silver containing cells, indicating that the absorbed silver (ions) do not cause immediate cell death.

We also determined silver quantities per cell by measuring their IAg values which were different between AgNO₃ positive control and AgNP-10 treated cells (Table 1). Overall, AgNP-10 treatment led to much higher silver quantities per cell in comparison to the positive control. Our data also suggest that the AgNP-aggregates, formed asap from AgNP-10, were not present at all or at least in their entirety due to the stringent washing procedures before CyTOF measurement otherwise we would expect an elevated silver signal in the 1D-plot of the silver channel (Supplementary Figure S3). But the silver ions released earlier by AgNP-aggregates and then bound by the cells were obviously responsible for the higher silver contents in AgNP-10 treated cells. In addition, for AgNP-10 treated cells we found nearly identical IAg values for both cisPt–live and cisPt+dead cells when cells grew exponentially (12 h: 18.3 ± 0.6 vs. 17.1 ± 1.1 , Table 1) which was different for early and late stationary cells where the IAg values were higher for the cisPt+dead cells (e.g., for 72 h: 1.6 ± 0.1 vs. 10.3 ± 0.6). For AgNO₃ treated cells the IAg values per cell were generally much lower and increased finally to only 3.0 ± 0.3 after 72 h for cisPt+dead cells. Thus, silver

TABLE 1 | The silver quantities per cell via the intensity of the mass cytometric signal for silver (IAg).

Time (h)	Treatment	IAg	
		cispt–live cells	cispt+dead cells
12	Pos. control	0.5 ± 0.0	0.9 ± 0.1
	AgNP-10	18.3 ± 0.6	17.1 ± 1.1
48	Pos. control	0.3 ± 0.0	3.4 ± 0.3
	AgNP-10	2.1 ± 0.0	11.0 ± 0.5
72	Pos. control	0.3 ± 0.0	3.0 ± 0.3
	AgNP-10	1.6 ± 0.1	10.3 ± 0.6

P. putida KT2440 cells were cultivated in M12 medium with AgNP-10 (1.29 mg/L) and with AgNO₃ (0.19 mg/L) as positive control for 72 h. Cells were harvested at 12, 48, 72 h and measured by CyTOF. Median values for intensities of ¹⁰⁷Ag (IAg) in cisPt–live and cisPt+dead cells were shown. Examples of CyTOF plots were in Supplementary Figure S3.

quantities per cell were higher under AgNP-10 treatment with the highest IAg values determined for cells from exponential phase independent if they were dead or alive.

The data of both the calculated frequencies in cell numbers and the silver quantities per cell follow the same trend. AgNP-10 treatment cause higher frequencies of dead cells, higher frequencies of silver affected cells and higher per-cell silver quantities whereby live and dead cells load silver in equal quantities and this preferably during exponential growth.

Independent from this, the population showed heterogeneous cell states with respect to silver quantities which might simply be caused by chemical equilibria of available free silver ions. Although we were not able to distinguish a silver signal related to cell-attached AgNP-aggregates or to distinguish aggregate-dissolved silver ions from free silver ions with CyTOF technology we assume that by a fast process an equilibrium is established and leads to the silver ions' equal distribution among cells. When the equilibrium changes in favor of the cells, because of increasing cell numbers during growth, these mostly new live cells were found free of silver. This observation was made also with AgNO₃ treated cells. It can also be assumed that a continuous uptake of silver ions by the cells may influence the equilibrium between AgNP-aggregate bound and unbound silver ions in the medium and cause further dissolution of silver ions from the aggregates (Yue et al., 2017).

The equal silver quantities in both live and dead exponential grown cells were verified by sorting identical numbers (3×10^6 cells each) of PI unstained/PI stained cells, from which an aliquot of cells of each sample were injected into the mass cytometer and 10^6 cells of each sample was used for ICP-MS measurements. As before, the cells were treated by AgNP-10 at EC₅₀ dosage of 1.29 mg/L. From CyTOF analysis we found analogous silver quantities per cell among PI–live and PI+dead cells with IAg = 21.6 and IAg = 17.9, respectively. The equal silver quantities per cell were by tendency confirmed by the ICP-MS results with 1.5 fg and 1.1 fg silver per PI–live and PI+dead cells, respectively. Overall, the equal silver quantity distribution among live and dead cells suggested that random AgNP-aggregate attachment is not only affecting and toxic to an appended cell but also to every other cell in its vicinity.

CONCLUSION

The primary objective of this study was to establish a mass cytometry method for the analysis of bacteria exemplary taking the Gram-negative bacterium *P. putida* KT2440. Our data show that by using RR, mass cytometry is able to detect all bacteria in a population, and that, by combining RR with cisPt, the method differentiates live from dead bacterial cells. The panel was extended by including natural abundance silver isotopes in order to measure the silver level in a single bacterial cell.

In Guo et al. (2017), PI uptake was correlated with silver-cell toxicity. This proof, however, was indirect. Now, mass cytometry was not only able to confirm the data of the earlier study by a direct measurement of silver per cell but provided further findings. AgNP-10 treatment caused a two times higher number of dead cells in comparison to AgNO₃ treatment after 72 h cultivation and three times higher numbers of cells with silver load. The per-cell silver quantities were also higher in AgNP-10 treated cells. Therefore, mass cytometry clearly supported the earlier discussion of a particle effect in addition to the toxicity of silver ions. The origin of this additional silver can be assumed to come from the AgNP-aggregates. In addition, the heterogenic distribution of silver ions was verified but seems to be independent on live/dead cell states but rather on existing chemical equilibria in the environmental vicinity. Thus, the action of the silver is clearly dependent on complex effects. Prediction of toxicant behavior to cells in natural environments will be even more complex due to the presence of further affecting parameters and can probably only be predicted when models implement equilibria of chemical components and their bioavailability and adjoin such data with the heterogeneous state or feature of single cells.

AUTHOR CONTRIBUTIONS

YG designed and conducted the experiments, evaluated the data and wrote the paper. SB analyzed samples for mass cytometry, helped to evaluate the data, and contributed to writing. H-JS analyzed samples for ICP-MS, helped to evaluate the data, and contributed to writing. HH contributed to writing. SM designed the experiments, evaluated the data and wrote the paper.

ACKNOWLEDGMENTS

This work was supported by the Graduate School “Leipzig School of Natural Sciences-Building with Molecules and Nano-objects (BuildMoNa)”, funded by the European Social Fund (ESF, project number R313H044), the European Regional Development Funds (EFRE – Europe funds Saxony, 100192205), and the German Federal Ministry of Education and Research (BMBF) within the framework of the Med research and funding concept (sysINFLAME, grant # 01ZX1306B). We thank Thomas Hübschmann for advice and bacterial flow cytometric

measurements at Flow Cytometry Group in Helmholtz Centre for Environmental Research (Leipzig, Germany). We also thank Toralf Kaiser for cell counts measuring at Flow Cytometry Core Facility in German Rheumatism Research Center (Berlin, Germany).

REFERENCES

- Baca, Q., Cosma, A., Nolan, G., and Gaudilliere, B. (2017). The road ahead: implementing mass cytometry in clinical studies, one cell at a time: editorial. *Cytometry B Clin. Cytom.* 92, 10–11. doi: 10.1002/cyto.b.21497
- Baumgart, S., Peddinghaus, A., Schulte-Wrede, U., Mei, H. E., and Grützkau, A. (2017). OMIP-034: comprehensive immune phenotyping of human peripheral leukocytes by mass cytometry for monitoring immunomodulatory therapies. *Cytometry A* 91, 34–38. doi: 10.1002/cyto.a.22894
- Bendall, S. C., Simonds, E. F., Qiu, P., El-ad, D. A., Krutzik, P. O., Finck, R., et al. (2011). Single-cell mass cytometry of differential immune and drug responses across a human hematopoietic continuum. *Science* 332, 687–696. doi: 10.1126/science.1198704
- Bjornson, Z. B., Nolan, G. P., and Fantl, W. J. (2013). Single-cell mass cytometry for analysis of immune system functional states. *Curr. Opin. Immunol.* 25, 484–494. doi: 10.1016/j.coi.2013.07.004
- Cerchiaro, G., Manieri, T. M., and Bertuchi, F. R. (2013). Analytical methods for copper, zinc and iron quantification in mammalian cells. *Metallomics* 5, 1336–1345. doi: 10.1039/c3mt00136a
- Chang, Q., Ornatsky, O. I., Siddiqui, I., Loboda, A., Baranov, V. I., and Hedley, D. W. (2017). Imaging mass cytometry. *Cytometry A* 91, 160–169. doi: 10.1002/cyto.a.23053
- Chatterjee, A., Carpentieri, A., Ratner, D. M., Bullitt, E., Costello, C. E., Robbins, P. W., et al. (2010). Giardia cyst wall protein 1 is a lectin that binds to curled fibrils of the GalNAc homopolymer. *PLoS Pathog.* 6:e1001059. doi: 10.1371/journal.ppat.1001059
- Chattopadhyay, P. K., Gierahn, T. M., Roederer, M., and Love, J. C. (2014). Single-cell technologies for monitoring immune systems. *Nat. Immunol.* 15, 128–135. doi: 10.1038/ni.2796
- Choi, O., and Hu, Z. (2008). Size dependent and reactive oxygen species related nanosilver toxicity to nitrifying bacteria. *Environ. Sci. Technol.* 42, 4583–4588. doi: 10.1021/es703238h
- Fabrega, J., Luoma, S. N., Tyler, C. R., Galloway, T. S., and Lead, J. R. (2011). Silver nanoparticles: behaviour and effects in the aquatic environment. *Environ. Int.* 37, 517–531. doi: 10.1016/j.envint.2010.10.012
- Fassel, T. A., and Edmiston, C. E. Jr. (1999). Ruthenium red and the bacterial glycocalyx. *Biotech. Histochem.* 74, 194–212. doi: 10.3109/10520299909047974
- Fienberg, H. G., Simonds, E. F., Fantl, W. J., Nolan, G. P., and Bodenmiller, B. (2012). A platinum-based covalent viability reagent for single-cell mass cytometry. *Cytometry A* 81A, 467–475. doi: 10.1002/cyto.a.22067
- Finck, R., Simonds, E. F., Jager, A., Krishnaswamy, S., Sachs, K., Fantl, W., et al. (2013). Normalization of mass cytometry data with bead standards. *Cytometry A* 83A, 483–494. doi: 10.1002/cyto.a.22271
- Fletcher, M., and Floodgate, G. D. (1973). An electron-microscopic demonstration of an acidic polysaccharide involved in the adhesion of a marine bacterium to solid surfaces. *Microbiology* 74, 325–334. doi: 10.1099/00221287-74-2-325
- Franci, G., Falanga, A., Galdiero, S., Palomba, L., Rai, M., Morelli, G., et al. (2015). Silver nanoparticles as potential antibacterial agents. *Molecules* 20, 8856–8874. doi: 10.3390/molecules20058856
- Gavasso, S., Gullaksen, S.-E., Skavland, J., and Gjertsen, B. T. (2016). Single-cell proteomics: potential implications for cancer diagnostics. *Expert Rev. Mol. Diagn.* 16, 579–589. doi: 10.1586/14737159.2016.1156531
- Giao, N. T., Limpiyakorn, T., Kunapongkiti, P., Thuptimang, P., and Siripattanakul-Ratpukdi, S. (2017). Influence of silver nanoparticles and liberated silver ions on nitrifying sludge: ammonia oxidation inhibitory kinetics and mechanism. *Environ. Sci. Pollut. Res.* 24, 9229–9240. doi: 10.1007/s11356-017-8561-0
- Günther, S., Hübschmann, T., Rudolf, M., Eschenhagen, M., Röske, I., Harms, H., et al. (2008). Fixation procedures for flow cytometric analysis of environmental bacteria. *J. Microbiol. Methods* 75, 127–134. doi: 10.1016/j.mimet.2008.05.017
- Guo, Y., Stärk, H. J., Hause, G., Schmidt, M., Harms, H., Wick, L. Y., et al. (2017). Heterogenic response of prokaryotes toward silver nanoparticles and ions is facilitated by phenotypes and attachment of silver aggregates to cell surfaces. *Cytometry A* doi: 10.1002/cyto.a.23055 [Epub ahead of print].
- Ivask, A., ElBadawy, A., Kaweeteerawat, C., Boren, D., Fischer, H., Ji, Z., et al. (2014). Toxicity mechanisms in *Escherichia coli* vary for silver nanoparticles and differ from ionic silver. *ACS Nano* 8, 374–386. doi: 10.1021/nn4044047
- Juganson, K., Mortimer, M., Ivask, A., Pucciarelli, S., Miceli, C., Orupöld, K., et al. (2017). Mechanisms of toxic action of silver nanoparticles in the protozoan *Tetrahymena thermophila*: from gene expression to phenotypic events. *Environ. Pollut.* 225, 481–489. doi: 10.1016/j.envpol.2017.03.013
- Lankoff, A., Sandberg, W. J., Wegierek-Ciuk, A., Lisowska, H., Refsnes, M., Sartowska, B., et al. (2012). The effect of agglomeration state of silver and titanium dioxide nanoparticles on cellular response of HepG2, A549 and THP-1 cells. *Toxicol. Lett.* 208, 197–213. doi: 10.1016/j.toxlet.2011.11.006
- Leipold, M. D., Ornatsky, O., Baranov, V., Whitfield, C., and Nitz, M. (2011). Development of mass cytometry methods for bacterial discrimination. *Anal. Biochem.* 419, 1–8. doi: 10.1016/j.ab.2011.07.035
- Lin, W., Hou, Y., Lu, Y., Abdelrahman, A. I., Cao, P., Zhao, G., et al. (2014). A high-sensitivity lanthanide nanoparticle reporter for mass cytometry: tests on microgels as a proxy for cells. *Langmuir* 30, 3142–3153. doi: 10.1021/la403627p
- Lingens, F., Blecher, R., Blecher, H., Blobel, F., Eberspächer, J., Fröhner, C., et al. (1985). *Phenyllobacterium immobile* gen. nov., sp. nov., a gram-negative bacterium that degrades the herbicide chloridazon. *Int. J. Syst. Evol. Microbiol.* 35, 26–39. doi: 10.1099/00207713-35-1-26
- Majonis, D., Ornatsky, O., Kinach, R., and Winnik, M. A. (2011). Curious results with palladium- and platinum-carrying polymers in mass cytometry bioassays and an unexpected application as a dead cell stain. *Biomacromolecules* 12, 3997–4010. doi: 10.1021/bm201011t
- Miyashita, S., Groombridge, A. S., Fujii, S., Minoda, A., Takatsu, A., Hioki, A., et al. (2014). Highly efficient single-cell analysis of microbial cells by time-resolved inductively coupled plasma mass spectrometry. *J. Anal. At. Spectrom.* 29, 1598–1606. doi: 10.1039/C4JA00040D
- Müller, S., and Nebe-von-Caron, G. (2010). Functional single-cell analyses: flow cytometry and cell sorting of microbial populations and communities. *FEMS Microbiol. Rev.* 34, 554–587. doi: 10.1111/j.1574-6976.2010.00214.x
- Nair, N., Mei, H. E., Chen, S.-Y., Hale, M., Nolan, G. P., Maecker, H. T., et al. (2015). Mass cytometry as a platform for the discovery of cellular biomarkers to guide effective rheumatic disease therapy. *Arthritis Res. Ther.* 17, 127. doi: 10.1186/s13075-015-0644-z
- Perfumo, A., Elsaesser, A., Littmann, S., Foster, R. A., Kuypers, M. M. M., Cockell, C. S., et al. (2014). Epifluorescence, SEM, TEM and nanoSIMS image analysis of the cold phenotype of *Clostridium psychrophilum* at subzero temperatures. *FEMS Microbiol. Ecol.* 90, 869–882. doi: 10.1111/1574-6941.12443
- Robinson, W. H., and Mao, R. (2016). Biomarkers to guide clinical therapeutics in rheumatology? *Curr. Opin. Rheumatol.* 28, 168–175. doi: 10.1097/BOR.0000000000000250
- Schulz, A. R., Stanislawski, S., Baumgart, S., Grützkau, A., and Mei, H. E. (2017). Silver nanoparticles for the detection of cell surface antigens in mass cytometry. *Cytometry A* 91, 25–33. doi: 10.1002/cyto.a.22904
- Swathy, J. R., Sankar, M. U., Chaudhary, A., Aigal, S., Anshup, and Pradeep, T. (2014). Antimicrobial silver: an unprecedented anion effect. *Sci. Rep.* 4:7161. doi: 10.1038/srep07161
- Tong, L., Lu, E., Pichaandi, J., Zhao, G., and Winnik, M. A. (2016). Synthesis of uniform NaLnF₄ (Ln: Sm to Ho) nanoparticles for mass cytometry. *J. Phys. Chem. C* 120, 6269–6280. doi: 10.1021/acs.jpcc.6b00570
- Vancaeyzele, C., Ornatsky, O., Baranov, V., Shen, L., Abdelrahman, A., and Winnik, M. A. (2007). Lanthanide-containing polymer nanoparticles for

SUPPLEMENTARY MATERIAL

The Supplementary Material for this article can be found online at: <http://journal.frontiersin.org/article/10.3389/fmicb.2017.01326/full#supplementary-material>

- biological tagging applications: nonspecific endocytosis and cell adhesion. *J. Am. Chem. Soc.* 129, 13653–13660. doi: 10.1021/ja073970w
- Wakshlak, R. B.-K., Pedahzur, R., and Avnir, D. (2015). Antibacterial activity of silver-killed bacteria: the “zombies” effect. *Sci. Rep.* 5:9555. doi: 10.1038/srep09555
- Waller, L. N., Fox, N., Fox, K. F., Fox, A., and Price, R. L. (2004). Ruthenium red staining for ultrastructural visualization of a glycoprotein layer surrounding the spore of *Bacillus anthracis* and *Bacillus subtilis*. *J. Microbiol. Methods* 58, 23–30. doi: 10.1016/j.mimet.2004.02.012
- Xiu, Z., Zhang, Q., Puppala, H. L., Colvin, V. L., and Alvarez, P. J. J. (2012). Negligible particle-specific antibacterial activity of silver nanoparticles. *Nano Lett.* 12, 4271–4275. doi: 10.1021/nl301934w
- Yang, Y.-S. S., Atukorale, P. U., Moynihan, K. D., Bekdemir, A., Rakhra, K., Tang, L., et al. (2017). High-throughput quantitation of inorganic nanoparticle biodistribution at the single-cell level using mass cytometry. *Nat. Commun.* 8:14069. doi: 10.1038/ncomms14069
- Yue, Y., Li, X., Sigg, L., Suter, M. J.-F., Pillai, S., Behra, R., et al. (2017). Interaction of silver nanoparticles with algae and fish cells: a side by side comparison. *J. Nanobiotechnol.* 15:16. doi: 10.1186/s12951-017-0254-9
- Zhao, X., and Ibuki, Y. (2015). Evaluating the toxicity of silver nanoparticles by detecting phosphorylation of histone H3 in combination with flow cytometry side-scattered light. *Environ. Sci. Technol.* 49, 5003–5012. doi: 10.1021/acs.est.5b00542
- Zucker, R. M., Daniel, K. M., Massaro, E. J., Karafas, S. J., Degn, L. L., and Boyes, W. K. (2013). Detection of silver nanoparticles in cells by flow cytometry using light scatter and far-red fluorescence. *Cytometry A* 83, 962–972. doi: 10.1002/cyto.a.22342

Conflict of Interest Statement: The authors declare that the research was conducted in the absence of any commercial or financial relationships that could be construed as a potential conflict of interest.

Copyright © 2017 Guo, Baumgart, Stärk, Harms and Müller. This is an open-access article distributed under the terms of the Creative Commons Attribution License (CC BY). The use, distribution or reproduction in other forums is permitted, provided the original author(s) or licensor are credited and that the original publication in this journal is cited, in accordance with accepted academic practice. No use, distribution or reproduction is permitted which does not comply with these terms.



Vibrational Spectroscopy for Imaging Single Microbial Cells in Complex Biological Samples

Jesse P. Harrison and David Berry*

Division of Microbial Ecology, Department of Microbiology and Ecosystem Science, Research Network "Chemistry Meets Microbiology", University of Vienna, Vienna, Austria

OPEN ACCESS

Edited by:

Clara Prats,
Universitat Politècnica de Catalunya,
Spain

Reviewed by:

Steven Singer,
Lawrence Berkeley National
Laboratory, USA
Anne-Kristin Kaster,
Leibniz Institute DSMZ-German
Collection of Microorganisms and Cell
Cultures, Germany

*Correspondence:

David Berry
berry@microbial-ecology.net

Specialty section:

This article was submitted to
Systems Microbiology,
a section of the journal
Frontiers in Microbiology

Received: 20 February 2017

Accepted: 31 March 2017

Published: 13 April 2017

Citation:

Harrison JP and Berry D (2017)
Vibrational Spectroscopy for Imaging
Single Microbial Cells in Complex
Biological Samples.
Front. Microbiol. 8:675.
doi: 10.3389/fmicb.2017.00675

Vibrational spectroscopy is increasingly used for the rapid and non-destructive imaging of environmental and medical samples. Both Raman and Fourier-transform infrared (FT-IR) imaging have been applied to obtain detailed information on the chemical composition of biological materials, ranging from single microbial cells to tissues. Due to its compatibility with methods such as stable isotope labeling for the monitoring of cellular activities, vibrational spectroscopy also holds considerable power as a tool in microbial ecology. Chemical imaging of undisturbed biological systems (such as live cells in their native habitats) presents unique challenges due to the physical and chemical complexity of the samples, potential for spectral interference, and frequent need for real-time measurements. This Mini Review provides a critical synthesis of recent applications of Raman and FT-IR spectroscopy for characterizing complex biological samples, with a focus on developments in single-cell imaging. We also discuss how new spectroscopic methods could be used to overcome current limitations of single-cell analyses. Given the inherent complementarity of Raman and FT-IR spectroscopic methods, we discuss how combining these approaches could enable us to obtain new insights into biological activities either *in situ* or under conditions that simulate selected properties of the natural environment.

Keywords: imaging, isotope labeling, single-cell analysis, vibrational spectroscopy

INTRODUCTION

Natural habitats are often physically and chemically complex, which has far-reaching consequences for the spatial distribution of microbial taxa and the processes they mediate (Resat et al., 2012; Vos et al., 2013; Pande et al., 2016; Ratzke and Gore, 2016). Because controlled laboratory experiments rarely capture the heterogeneity present within natural environments, our knowledge of microbial activities is often based on indirect observation. To address this source of uncertainty, there is a need for methods that facilitate the *in situ* profiling of microorganisms and their activities in complex environments. A full understanding of these topics also requires an ability to study these processes at the level of single cells (Fike et al., 2008; Resat et al., 2012; Roose et al., 2016). Due to its ability to rapidly and non-destructively probe the physiology and activities of microorganisms, vibrational (Raman and FT-IR) microspectroscopy (a combination of microscopy and spectroscopy) shows considerable promise in this respect (Escoriza et al., 2006; Wagner, 2009; Lu et al., 2011). In particular, Raman and infrared imaging have emerged as useful methods for the spatially resolved analysis of biological samples. In this Mini Review, we highlight recent

studies that have used these techniques to image single microbial cells within spatially and chemically complex environments. These include pure cultures incubated in contact with physical substrata, multi-species assemblages within their native habitats, as well as other challenging sample types. State-of-the-art approaches for spectral imaging are critically evaluated in order to identify guidelines for future applications of single-cell analyses in microbial ecology.

RAMAN IMAGING

While several types of Raman spectroscopic instrumentation and analytical approaches have been developed, each of these relies on measuring the scattering of monochromatic light as it interacts with a sample. Most photons are elastically scattered and possess the same energy as the incident light beam (also termed Rayleigh scattering). However, a small fraction is inelastically scattered, involving a decrease or an increase in energy compared with the excitation wavelength (Stokes and anti-Stokes Raman scattering, respectively). By providing information on vibrational and other low-frequency transitions in a molecule, both types of inelastically scattered light can be used to determine and differentiate between the chemical composition of solids, liquids and gases. For a more detailed introduction to this technique (as well as infrared spectroscopy), the reader is referred to Skoog et al. (2007) and Lu et al. (2011). Recent advances in the design of high-speed Raman imaging instrumentation have been summarized by Ando et al. (2016). Moreover, developments concerning techniques including surface- and tip-enhanced Raman scattering (SERS and TERS), as well as resonance Raman and coherent anti-Stokes Raman spectroscopy (CARS), are discussed in several reviews (Opilik et al., 2013; Camp and Cicerone, 2015; Cicerone, 2016; Kano et al., 2016).

Two features that make Raman microspectroscopy an ideal technique for single-cell analyses include its direct compatibility with aqueous samples (due to water exhibiting only weak Raman scattering) and its high spatial resolution (Skoog et al., 2007). While a resolution of $\sim 1 \mu\text{m}$ is possible using conventional Raman instrumentation, measurements at the nanometer scale are achievable by TERS (Mariani et al., 2010; Opilik et al., 2013; Rusciano et al., 2014). Raman measurements are also well-suited for analyzing motile cells using optical tweezers, as well as monitoring microbial activities by stable isotope probing (SIP) (Chan et al., 2004; Wagner, 2009; Huang et al., 2010; Berry et al., 2015; Wang et al., 2016). Although the real-time Raman imaging of microorganisms remains non-trivial due to issues including background autofluorescence (Polisetti et al., 2016) and weak signal intensities (partly due to a need for low laser excitation power to avoid photodamage), significant progress in this field has already been made. For example, Li et al. (2012) used resonance Raman imaging combined with ^{13}C labeling to identify cells that fixed carbon dioxide in culture and in field-collected seawater samples. By reducing spectral acquisition times to milliseconds, resonance Raman spectroscopy – a method in which the excitation wavelength matches the electronic transition of a selected molecule – was key to enabling the

rapid imaging of these samples. It is also possible to visualize selected strains and their locations within habitats including human endothelial cells (Große et al., 2015), macrophages (Silge et al., 2015) and other environments, even when the taxa of interest are present at low abundances (Kalasinsky et al., 2007). Through combining imaging of *Staphylococcus aureus* cells with a multivariate classification model [based on principal component analysis (PCA) and linear discriminant analysis (LDA)], Große et al. (2015) were further able to detect small differences in the spectral profiles that allowed the authors to discern between intra- and extracellular cells, due to shifts in the physiological state of the bacteria that occur upon host invasion.

In addition, resonance Raman and SERS have been used to directly image rhizosphere bacteria (*Pantoea* sp. YR343) on *Arabidopsis thaliana* root surfaces (Polisetti et al., 2016). This is of interest because Raman-based investigations of plant-microbial interactions are often challenging or impossible due to the strong autofluorescence originating from plant materials. In the study by Polisetti et al. (2016), background interference from the roots was reduced by aging them for 5–15 days. Similar to Große et al. (2015), PCA was used to discriminate bacterial spectra from spectra of other materials. Moreover, using SERS allowed the authors to circumvent the need for a photo-bleaching step which is often employed for the analysis of pigmented cells using conventional Raman instrumentation, but which can result in the degradation of cell components and metabolites that are of importance to understanding bacterially mediated processes in the rhizosphere (Polisetti et al., 2016). Taken together, the studies highlighted above illustrate how advanced Raman imaging techniques and multivariate analyses can be used to generate new insights into the distribution and activities of microorganisms within diverse environments, including systems which have previously been difficult to visualize and where the ability to differentiate between cells and other materials is dependent on detecting minor differences in spectral features. By removing the need for sample treatment steps that are likely to introduce analytical biases, such as sample photo-bleaching prior to the collection of Raman spectra (Polisetti et al., 2016), these techniques can also provide increasingly accurate information on metabolic processes occurring at multiple levels of biological organization (from individual cells to communities).

While a limited number of studies have been published on Raman imaging of microbial strains or uncultured cells within their native environments, new instrumentation is likely to lead to an expansion of this field by enabling reduced spectral acquisition times without a loss of signal intensity (Opilik et al., 2013; Ando et al., 2016; Kano et al., 2016). In addition, combining this approach with well-established methods in microbial ecology (including fluorescence *in situ* hybridization) (Wang et al., 2016) as well as newer techniques such as bioorthogonal chemical imaging (Berry et al., 2015; Wei et al., 2016) and Raman microfluidics (Chrimes et al., 2013) are likely to find increasing use in the analysis of microbiological samples. Several sample types which have not yet been subjected to Raman imaging have already been characterized using single-point measurements, and therefore represent promising targets for future research. For example, while the Raman-based detection of meningitis-causing

pathogens in human cerebrospinal fluid has been achieved (Harz et al., 2009), spatially resolved imaging of such samples could facilitate the development of improved diagnostic tests. One imaging modality that is particularly promising from a microbiological perspective, but which is yet to find widespread use in the field of microbial ecology, is CARS (Krafft et al., 2009; Camp and Cicerone, 2015; Cicerone, 2016). This technique can enable the acquisition of Raman spectra at a rate that is approximately 100 times faster than conventional Raman analyses, making it highly suitable for the real-time imaging of biological samples (Cicerone, 2016). CARS has already been used for the rapid profiling of microorganisms at the subcellular level (Okuno et al., 2010; Yue and Cheng, 2016), and a single study has also employed it to image bacteria within complex matrices including milk and urine (Hong et al., 2016). Another technique which has found surprisingly limited use in the field of microbial ecology is TERS (Mariani et al., 2010; Opilik et al., 2013; Rusciano et al., 2014). However, since this method enables Raman measurements at sub-micron spatial scales, it could be used to analyze microorganisms that are under the conventional size detection limit of $\sim 1 \mu\text{m}$, as well as viral particles present within diverse environmental matrices. Indeed, TERS has already been used for the analysis and classification of viral strains (Hermann et al., 2011; Olschewski et al., 2015).

FT-IR IMAGING

While Raman spectroscopy relies on irradiating a sample with a monochromatic laser beam, Fourier-transform infrared (FT-IR) spectroscopy is based on measuring the absorption

of polychromatic infrared light. The functional groups in a given molecule are identified according to their vibrational modes at different IR frequencies (for detailed information, see Skoog et al., 2007). Raman analyses depend on a shift in the polarizability of a molecule, whereas FT-IR measurements depend on changes in the dipole moment. Indeed, Raman-active vibrational modes often exhibit weak IR signals and vice versa (with symmetric and asymmetric moieties producing strong Raman and IR spectral bands, respectively), and the two methods provide complementary information on the molecular composition of microbial cells (Lu et al., 2011; Ojeda and Dittrich, 2012; Tang et al., 2013; Wang et al., 2016). Infrared imaging could, therefore, provide insights into microbial physiology in samples that are difficult to analyze using Raman spectroscopy alone. Indeed, high-speed imaging of large (centimeter-scale) sample areas can be achieved using a focal plane array (FPA) detector that enables the simultaneous acquisition of tens of thousands of IR spectra (Dorling and Baker, 2013). Studies employing FPA-based FT-IR analysis are common in biomedical science and have, for example, involved chemical imaging of tissues (Kastyak-Ibrahim et al., 2012; Miller et al., 2013) and cancer cells (Kuimova et al., 2009). Chemical mapping by reflectance FT-IR microspectroscopy has also been used to characterize bacteria on opaque steel surfaces, without a need for destructive sampling (Ojeda et al., 2009). In comparison with Raman analyses, however, few studies have used FT-IR microspectroscopy to investigate single microbial cells within their native environments, potentially due to the coarse spatial resolution ($\sim 10 \mu\text{m}$) of conventional FT-IR measurements and water being a strong absorber of IR radiation. Even so, several ways to overcome these challenges have been developed. For

TABLE 1 | Experimental goals associated with the Raman and FT-IR imaging of single microbial cells in complex biological samples.

Goal	Recommended technique	Notes	Reference
Analysis of motile cells and/or cell sorting	Raman microspectroscopy	Optical tweezers can be used to trap or move individual cells	Huang et al., 2010; Berry et al., 2015
Detection of cells on autofluorescent and opaque surfaces	Both	Autofluorescence does not interfere with IR measurements; Raman measurements possible using resonance Raman, SERS, sample photobleaching or aging	Ojeda et al., 2009; Polisetti et al., 2016
Addressing other sources of background interference	Both	Water is a strong IR absorber; using microfluidics or an ATR accessory can reduce signal interference	Kuimova et al., 2009; Birarda et al., 2016; Lougherback et al., 2016
Stable isotope probing	Both	Approaches currently better-established for Raman analyses	Wang et al., 2016
Imaging of large (cm-scale) surface areas	FT-IR microspectroscopy	FPA detectors readily available for FT-IR instruments; Raman instrumentation also available, but not as widely accessible	Kuimova et al., 2009; Kastyak-Ibrahim et al., 2012; Miller et al., 2013; Ando et al., 2016
Localization of cells in 3D space	Raman microspectroscopy	Imaging of z-stacks possible using confocal Raman measurements	Große et al., 2015; Silge et al., 2015
High-resolution (including subcellular) measurements	Both	Raman analyses (e.g., TERS) better-established; also possible using FT-IR but requires specialist equipment or access to synchrotron beamline	Mariani et al., 2010; Opilik et al., 2013; Saulou et al., 2013; Rusciano et al., 2014; Findlay et al., 2015
Label-free discrimination between individual strains or taxa	FT-IR microspectroscopy	FT-IR analyses can outperform Raman spectroscopy in terms of spectral quality and reproducibility	AlMasoud et al., 2016; Muhamadali et al., 2016

Recommendations for analytical techniques are provided for meeting each goal.

example, synchrotron radiation sources have enabled FT-IR measurements at the micron scale (Nasse et al., 2011; Jamme et al., 2013; Saulou et al., 2013) and combining this approach with microfluidics can reduce background interference from water by making it possible to culture cells within a thin layer of fluid (Holman et al., 2009; Loutharback et al., 2015, 2016; Birarda et al., 2016).

While synchrotron-FT-IR analyses require dedicated facilities, advances in the development of high-magnification optics have made it possible to perform FPA-based infrared imaging at a spatial resolution comparable with Raman instruments, even without access to a synchrotron beamline (Findlay et al., 2015). Analyses of cells in aqueous suspensions are additionally possible using attenuated total reflectance (ATR)-FT-IR imaging (Kuimova et al., 2009). Where required, techniques for nano-scale infrared imaging have been developed (Reddy et al., 2013; Centrone, 2015; Amenabar et al., 2017) and even relatively thick aqueous samples can be analyzed by quantum cascade laser-based IR microspectroscopy (Haase et al., 2016). Crucially for the *in situ* analysis of microbial activities, there is evidence that FT-IR spectroscopy is compatible with SIP and can be used to track the cellular uptake of stable-isotope-labeled carbon (^{13}C) and nitrogen (^{15}N) compounds (Muhamadali et al., 2015). FT-IR microspectroscopy can detect differences in the spectra

of water and heavy water (D_2O), due to absorbance peaks corresponding to O–H and O–D bending modes occurring at different wavenumber regions (Miller et al., 2013). While we are unaware of studies that have combined D_2O labeling with FT-IR spectroscopy to monitor the activities of individual microbial cells, this has recently been achieved using Raman spectroscopy (Berry et al., 2015), and it is likely that both methods can be used to identify actively metabolizing cells within their native habitats.

Further to the studies discussed above, Muhamadali et al. (2016) evaluated the applicability of three vibrational spectroscopy techniques (FT-IR, conventional Raman and SERS) for differentiating between several clinically relevant taxa including *Escherichia coli*, *Pseudomonas* spp., *Bacillus* spp. and *Enterococcus faecium*. Of these techniques, infrared spectroscopy was found to provide the most consistent results for the entire sample set (in terms of spectral quality and reproducibility), which led the authors to suggest that FT-IR analyses could be particularly useful for characterizing mixed cultures (also see Wenning et al., 2005). Indeed, FT-IR microspectroscopy has already been used to quantify compare the abundances of bacteria and archaea within subsurface aquifer samples, based on domain-specific $\text{CH}_3\text{:CH}_2$ absorbance ratios (Igisu et al., 2012). In comparison with Raman spectroscopy, there is evidence to suggest that FT-IR analyses can additionally give a higher degree

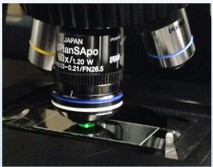

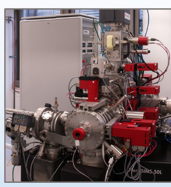
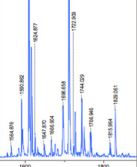

					
Technique	Raman and FT-IR microspectroscopy	Synchrotron UV microspectroscopy	(Nano-)SIMS	MALDI-ToF-MS	X-ray CT
Application	μm -scale analysis of molecular composition; compatible with SIP	μm -scale analysis of molecular composition; suitable for autofluorescent materials; UV Raman also possible	High-resolution elemental/ isotopic quantification; analysis of small molecules; compatible with SIP	Analysis of molecular composition (including large molecules); microbial identification	Visualization of habitat 3D structure and connectivity
Previously used to image single microbial cells?	Yes <i>Raman has also been used to analyze cells within complex environmental matrices</i>	No <i>Has been used for human tissue analysis</i>	Yes <i>NanoSIMS has additionally been combined with Raman microspectroscopy</i>	No <i>Has been used to image bacterial colonies</i>	No <i>Can be combined with single-cell imaging</i>

FIGURE 1 | Techniques which have or could be utilized for the *in situ* imaging of single microbial cells within physically and chemically complex environments. Previously demonstrated applications of each approach are discussed in the main text. FT-IR, Fourier-transform infrared; SIP, stable isotope probing; UV, ultraviolet; (Nano-)SIMS, nanoscale secondary ion mass spectrometry; MALDI-ToF-MS, matrix-assisted laser desorption/ionization mass spectrometry; CT, computed tomography.

of confidence when there is a need to discriminate between strains belonging to the same species (69 and 89% strain-level prediction accuracies for Raman and FT-IR, respectively, based on chemometric analysis; AlMasoud et al., 2016). Given these results, we anticipate infrared imaging to become an increasingly common technique in the field of microbial ecology, particularly when there is a need for quantitatively analyzing multi-species assemblages and/or in-depth physiological profiling of selected isolates.

RECOMMENDATIONS AND OUTLOOK

The spectroscopic imaging of microbial cells in physically and chemically complex samples involves diverse analytical challenges. While addressing these will often require sample-specific optimization steps (such as identifying an appropriate laser wavelength; Edwards et al., 2003; Chan et al., 2004; Jorge Villar et al., 2005), many of them could be overcome by carefully selecting between Raman- and FT-IR-based measurements or a combination of both. Based on the case studies discussed in this Mini Review, it is possible to identify several general guidelines for achieving this (Table 1). The suggestions provided in Table 1 additionally highlight the promising role that live-cell FT-IR imaging could play in environmental microbiological research, further to Raman measurements which have traditionally been more common in this field. The future development of vibrational spectroscopy instrumentation and analytical methods may serve to further enhance the cross-compatibility of Raman and FT-IR techniques (e.g., via improved access to advanced Raman imaging equipment and validation of new protocols for FT-IR-SIP).

Additionally to considering the benefits and pitfalls inherent to Raman vs. FT-IR measurements, experiments focusing on the imaging of single cells in complex habitats can be expected to profit from combining these techniques with other analytical approaches (Figure 1). Synchrotron-FT-IR microspectroscopy has been paired with synchrotron ultraviolet microspectroscopy and time-of-flight-secondary ion mass spectrometry (ToF-SIMS) for the analysis of human liver tissue, with each technique yielding unique information on the chemical composition of the sample (Petit et al., 2010). Raman microspectroscopy has been combined with nanoscale secondary ion mass spectrometry (NanoSIMS) to quantify the bacterial uptake of deuterium during heavy water labeling experiments (Berry et al., 2015). Moreover, matrix-assisted laser desorption/ionization time-of-flight mass spectrometry (MALDI-ToF-MS) is compatible with microbiological analyses and Raman imaging (Bocklitz et al., 2013; Pande et al., 2016; Stasulli and Shank, 2016). Although

it has not yet been applied for the imaging of cells within complex environments such as soils, MALDI-ToF-MS been used to characterize individual bacterial colonies (Pande et al., 2016; Stasulli and Shank, 2016). Promisingly, the technique can be used for strain identification (Singhal et al., 2015) and a method for single-cell MALDI analyses has also been developed (Xiong et al., 2016). Vibrational spectroscopic imaging of microbial cells could be further combined with techniques that provide information on the 3D structure of the surrounding environment. X-ray computed tomography, for example, has been used to visualize roots within undisturbed soil (Mooney et al., 2012). The technique has also been used to produce micron-scale 3D representations of soil pore space (Nunan et al., 2006).

One of the most important challenges involved in the spectral imaging of microorganisms within their native habitats, regardless of the techniques involved, concerns the ability to successfully discriminate between cells and other materials. Additionally, an ability to discern between diverse taxa is required to understand the distribution and activities of microbial cells at the community level. To facilitate research into these topics, we strongly recommend that databases including relevant reference spectra are made available as part of future publications. We also note that using Raman and/or FT-IR spectroscopy alone for the reliable identification of microbial taxa often remains challenging (see FT-IR imaging), and that result using these methods may need to be verified using additional methods. For example, Raman-activated cell sorting has recently been combined with single-cell genomics to identify members of a novel cyanobacterial order within seawater samples (Song et al., 2017). Ultimately, the approaches discussed in this Mini Review could enable us to significantly improve our knowledge of microbial community assembly and the contribution of interspecies interactions to key ecosystem processes, including the cycling of carbon within soils, sediments and other spatially structured habitats.

AUTHOR CONTRIBUTIONS

All authors listed, have made substantial, direct and intellectual contribution to the work, and approved it for publication.

ACKNOWLEDGMENT

This work was supported by the U.S. Department of Energy (Grant No. BER DE-SC0013887) and the European Research Council (Starting Grant 741623 FunKeyGut).

REFERENCES

- AlMasoud, N., Xu, Y., Ellis, D. I., Rooney, P., Turton, J. F., and Goodacre, R. (2016). Rapid discrimination of *Enterococcus faecium* strains using phenotypic analytical techniques. *Anal. Methods* 8, 7603–7613. doi: 10.1039/C6AY02326F
- Amenabar, I., Poly, S., Goikoetxea, M., Nuansing, W., Lasch, P., and Hillenbrand, R. (2017). Hyperspectral infrared nanoimaging of organic samples based on Fourier transform infrared nanospectroscopy. *Nat. Commun.* 8:14402. doi: 10.1038/ncomms14402
- Ando, J., Palonpon, A. F., Sodeoka, M., and Fujita, K. (2016). High-speed Raman imaging of cellular processes. *Curr. Opin. Chem. Biol.* 33, 16–24. doi: 10.1016/j.cbpa.2016.04.005
- Berry, D., Mader, E., Lee, T. K., Woebken, D., Wang, Y., and Zhu, D. (2015). Tracking heavy water (D₂O) incorporation for identifying and sorting active

- microbial cells. *Proc. Natl. Acad. Sci. U.S.A.* 112, E194–E203. doi: 10.1073/pnas.1420406112
- Birarda, G., Ravasio, A., Suryana, M., Maniam, S., Holman, H.-Y. N., and Greci, G. (2016). IR-Live: fabrication of a low-cost plastic microfluidic device for infrared spectromicroscopy of living cells. *Lab Chip* 16, 1644–1651. doi: 10.1039/c5lc01460c
- Bocklitz, T. W., Crecelius, A. C., Matthäus, C., Tarcea, N., von Eggeling, F., Schmitt, M., et al. (2013). Deeper understanding of biological tissue: quantitative correlation of MALDI-ToF and Raman imaging. *Anal. Chem.* 85, 10829–10834. doi: 10.1021/ac402175c
- Camp, C. H. Jr., and Cicerone, M. T. (2015). Chemically sensitive bioimaging with coherent Raman scattering. *Nat. Photonics* 9, 295–305. doi: 10.1038/nphoton.2015.60
- Centrone, A. (2015). Infrared imaging and spectroscopy beyond the diffraction limit. *Annu. Rev. Anal. Chem.* 8, 101–126. doi: 10.1146/annurev-anchem-071114-040435
- Chan, J. W., Esposito, A. P., Talley, C. E., Hollars, C. W., Lane, S. M., and Huser, T. (2004). Reagentless identification of single bacterial spores in aqueous solution by confocal laser tweezers Raman spectroscopy. *Anal. Chem.* 76, 599–603. doi: 10.1021/ac0350155
- Chrimes, A. F., Khoshmanesh, K., Stoddart, P. R., Mitchell, A., and Kalantar-zadeh, K. (2013). Microfluidics and Raman microscopy: current applications and future challenges. *Chem. Soc. Rev.* 42, 5880–5906. doi: 10.1039/c3cs35515b
- Cicerone, M. (2016). Molecular imaging with CARS micro-spectroscopy. *Curr. Opin. Chem. Biol.* 33, 179–185. doi: 10.1016/j.cbpa.2016.05.010
- Dorling, K. M., and Baker, M. J. (2013). Rapid FTIR chemical imaging: highlighting FPA detectors. *Trends Biotechnol.* 31, 437–438. doi: 10.1016/j.tibtech.2013.05.008
- Edwards, H. G. M., Newton, E. M., Wynn-Williams, D. D., Dickensheets, D., Schoen, C., and Crowder, C. (2003). Laser wavelength selection for Raman spectroscopy of microbial pigments *in situ* in Antarctic desert ecosystem analogues of former habitats on Mars. *Int. J. Astrobiol.* 1, 333–348. doi: 10.1017/S147355040300123X
- Escoriza, M. F., Vanbriesen, J. M., Stewart, S., and Maier, J. (2006). Studying bacterial metabolic states using Raman spectroscopy. *Appl. Spectrosc.* 60, 971–976. doi: 10.1366/000370206778397290
- Fike, D. A., Gammon, C. L., Ziebis, W., and Orphan, V. J. (2008). Micron-scale mapping of sulfur cycling across the oxycline of a cyanobacterial mat: a paired nanoSIMS and CARD-FISH approach. *ISME J.* 2, 749–759. doi: 10.1038/ismej.2008.39
- Findlay, C. R., Wiens, R., Rak, M., Sedlmair, J., Hirschmugl, C. J., Morrison, J., et al. (2015). Rapid biddiagnostic *ex vivo* imaging at 1 μ m pixel resolution with thermal source FTIR FPA. *Analyst* 140, 2493–2503. doi: 10.1039/c4an01982b
- Große, C., Bergner, N., Dellith, J., Heller, R., Bauer, M., Mellmann, A., et al. (2015). Label-free imaging and spectroscopic analysis of intracellular bacterial infections. *Anal. Chem.* 87, 2137–2142. doi: 10.1021/ac503316s
- Haase, K., Kröger-Lui, N., Pucci, A., Schönhals, A., and Petrich, W. (2016). Advancements in quantum cascade laser-based infrared microscopy of aqueous media. *Analyst* 187, 119–134. doi: 10.1039/c5fd00177c
- Harz, M., Kiehntopf, M., Stöckel, S., Rösch, P., Straube, E., Deufel, T., et al. (2009). Direct analysis of clinical relevant single bacterial cells from cerebrospinal fluid during bacterial meningitis by means of micro-Raman spectroscopy. *J. Biophotonics* 2, 70–80. doi: 10.1002/jbjo.200810068
- Hermann, P., Hermelink, A., Lausch, V., Holland, G., Möller, L., Bannert, N., et al. (2011). Evaluation of tip-enhanced Raman spectroscopy for characterizing different virus strains. *Analyst* 136, 1148–1152. doi: 10.1039/c0an00531b
- Holman, H. Y., Miles, R., Hao, Z., Wozel, E., Anderson, L. M., and Yang, H. (2009). Real-time chemical imaging of bacterial activity in biofilms using open-channel microfluidics and synchrotron FTIR spectromicroscopy. *Anal. Chem.* 81, 8564–8570. doi: 10.1021/ac9015424
- Hong, W., Liao, C.-S., Zhao, H., Younis, W., Zhang, Y., Seleem, M. N., et al. (2016). *In situ* detection of a single bacterium in complex environment by hyperspectral CARS imaging. *ChemistrySelect* 3, 513–517. doi: 10.1002/slct.201600166
- Huang, W. E., Li, M., Jarvis, R. M., Goodacre, R., and Banwart, S. A. (2010). Shining light on the microbial world: the application of Raman microspectroscopy. *Adv. Appl. Microbiol.* 70, 153–186. doi: 10.1016/S0065-2164(10)70005-8
- Igisu, M., Takai, K., Ueno, Y., Nishizawa, M., Nunoura, T., Hirai, M., et al. (2012). Domain-level identification and quantification of relative prokaryotic cell abundance in microbial communities by micro-FTIR spectroscopy. *Environ. Microbiol. Rep.* 4, 42–49. doi: 10.1111/j.1758-2229.2011.00277.x
- Jamme, F., Vindigni, J.-D., Méchin, V., Cherif, T., Chardot, T., and Froissard, M. (2013). Single cell synchrotron FT-IR microspectroscopy reveals a link between neutral lipid and storage carbohydrate fluxes in *S. cerevisiae*. *PLoS ONE* 8:e74421. doi: 10.1371/journal.pone.0074421
- Jorge Villar, S. E., Edwards, H. G. M., and Worland, M. R. (2005). Comparative evaluation of Raman spectroscopy at different wavelengths for extremophile exemplars. *Orig. Life Evol. Biosph.* 35, 489–506. doi: 10.1007/s11084-005-3528-4
- Kalasinsky, K. S., Hadfield, T., Shea, A. A., Kalasinsky, V. F., Nelson, M. P., Neiss, J., et al. (2007). Raman chemical imaging spectroscopy reagentless detection and identification of pathogens: signature development and evaluation. *Anal. Chem.* 79, 2658–2673. doi: 10.1021/ac0700575
- Kano, H., Segawa, H., Okuno, M., Leproux, P., and Couderc, V. (2016). Hyperspectral coherent Raman imaging – principle, theory, instrumentation, and applications to life sciences. *J. Raman Spectrosc.* 47, 116–123. doi: 10.1002/jrs.4853
- Kastyak-Ibrahim, M. Z., Nasse, M. J., Rak, M., Hirschmugl, C., Del Bigio, M. R., Albensi, B. C., et al. (2012). Biochemical label-free tissue imaging with subcellular-resolution synchrotron FTIR with focal plane array detector. *Neuroimage* 60, 376–383. doi: 10.1016/j.neuroimage.2011.11.069
- Krafft, C., Dietzek, B., and Popp, J. (2009). Raman and CARS microspectroscopy of cells and tissues. *Analyst* 134, 1046–1057. doi: 10.1039/b822354h
- Kuimova, M. K., Chan, K. L. A., and Kazarian, S. G. (2009). Chemical imaging of live cancer cells in the natural aqueous environment. *Appl. Spectrosc.* 63, 164–171. doi: 10.1366/000370209787391969
- Li, M., Canniffe, D. P., Jackson, P. J., Davison, P. A., FitzGerald, S., Dickman, M. J., et al. (2012). Rapid resonance Raman microspectroscopy to probe carbon fixation by single cells in microbial communities. *ISME J.* 6, 875–885. doi: 10.1038/ismej.2011.150
- Loutherback, K., Chen, L., and Holman, H.-Y. N. (2015). Open-channel microfluidic membrane device for long-term FT-IR spectromicroscopy of live adherent cells. *Anal. Chem.* 87, 4601–4606. doi: 10.1021/acs.analchem.5b00524
- Loutherback, K., Giovanni, B., Liang, C., and Holman, H.-Y. (2016). Microfluidic approaches to synchrotron radiation-based Fourier transform infrared (SR-FTIR) spectral microscopy of living biosystems. *Protein Pept. Lett.* 23, 273–282. doi: 10.2174/0929866523666160106154035
- Lu, X., Al-Qadiri, H. M., Lin, M., and Rasco, B. A. (2011). Application of mid-infrared and Raman spectroscopy to the study of bacteria. *Food Bioprocess Technol.* 4, 919–935. doi: 10.1007/s11947-011-0516-8
- Mariani, M. M., Day, P. J. R., and Deckert, V. (2010). Applications of modern micro-Raman spectroscopy for cell analyses. *Integr. Biol.* 2, 94–101. doi: 10.1039/b920572a
- Miller, L. M., Bourassa, M. W., and Smith, R. J. (2013). FTIR spectroscopic imaging of protein aggregation in living cells. *BBA Biomembranes* 1828, 2339–2346. doi: 10.1016/j.bbamem.2013.01.014
- Mooney, S. J., Pridmore, T. P., Helliwell, J., and Bennett, M. J. (2012). Developing X-ray computed tomography to non-invasively image 3-D root systems architecture in soil. *Plant Soil* 352, 1–22. doi: 10.1007/s11104-011-1039-9
- Muhamadali, H., Chisanga, M., Subaihi, A., and Goodacre, M. (2015). Combining Raman and FT-IR spectroscopy with quantitative isotopic labeling for differentiation of *E. coli* cells at community and single cell levels. *Anal. Chem.* 87, 4578–4586. doi: 10.1021/acs.analchem.5b00892
- Muhamadali, H., Subaihi, A., Mohammadtaheri, M., Xu, Y., Ellis, D. I., Ramanathan, R., et al. (2016). Rapid, accurate, and comparative differentiation of clinically and industrially relevant microorganisms via multiple vibrational spectroscopic fingerprinting. *Analyst* 141, 5127–5136. doi: 10.1039/c6an00883f
- Nasse, M. J., Walsh, M. J., Mattson, E. C., Reininger, R., Kajdacsy-Balla, A., Macias, V., et al. (2011). High-resolution Fourier-transform infrared chemical imaging with multiple synchrotron beams. *Nat. Methods* 8, 413–416. doi: 10.1038/nmeth.1585
- Nunan, N., Ritz, K., Rivers, M., Feeney, D. S., and Young, I. M. (2006). Investigating microbial micro-habitat structure using X-ray computed tomography. *Geoderma* 133, 398–407. doi: 10.1016/j.geoderma.2005.08.004
- Ojeda, J. J., and Dittrich, M. (2012). “Fourier transform infrared spectroscopy for molecular analysis of microbial cells,” in *Microbial Systems Biology: Methods*

- and *Protocols (Methods in Molecular Biology)*, Vol. 881, ed. A. Navid (Berlin: Springer), 187–211.
- Ojeda, J. J., Romero-González, M. E., and Banwart, S. A. (2009). Analysis of bacteria on steel surfaces using reflectance micro-Fourier transform infrared spectroscopy. *Anal. Chem.* 81, 6467–6473. doi: 10.1021/ac900841c
- Okuno, M., Kano, H., Leproux, P., Couderc, V., Day, J. P. R., Bonn, M., et al. (2010). Quantitative CARS molecular fingerprinting of single living cells with the use of the maximum entropy method. *Angew. Chem. Int. Ed. Engl.* 49, 6773–6777. doi: 10.1002/anie.201001560
- Olschewski, K., Kämmer, E., Stöckel, S., Bocklitz, T., Deckert-Gaudig, T., Zell, R., et al. (2015). A manual and an automatic TERS based virus discrimination. *Nanoscale* 7, 4545–4552. doi: 10.1039/c4nr07033j
- Opilik, L., Schmid, T., and Zenobi, R. (2013). Modern Raman imaging: vibrational spectroscopy on the micrometer and nanometer scales. *Annu. Rev. Anal. Chem.* 6, 379–398. doi: 10.1146/annurev-anchem-062012-092646
- Pande, S., Kaftan, F., Lang, S., Svatoš, A., Germerodt, S., and Kost, C. (2016). Privatization of cooperative benefits stabilizes mutualistic cross-feeding interactions in spatially structured environments. *ISME J.* 10, 1413–1423. doi: 10.1038/ismej.2015.212
- Petit, V. W., Réfrégiers, M., Guettier, C., Jamme, F., Sebanayakam, K., Brunelle, A., et al. (2010). Multimodal spectroscopy combining time-of-flight-secondary ion mass spectrometry, synchrotron-FT-IR, and synchrotron-UV microspectroscopies on the same tissue section. *Anal. Chem.* 82, 3963–3968. doi: 10.1021/ac100581y
- Polisetti, S., Bible, A. N., Morrell-Falvey, J. L., and Bohn, P. W. (2016). Raman chemical imaging of the rhizosphere bacterium *Pantoea* sp. YR343 and its co-culture with *Arabidopsis thaliana*. *Analyst* 141, 2175–2182. doi: 10.1039/c6an00080k
- Ratzke, C., and Gore, J. (2016). Self-organized patchiness facilitates survival in a cooperatively growing *Bacillus subtilis* population. *Nat. Microbiol.* 1, 16022. doi: 10.1038/nmicrobiol.2016.22
- Reddy, R. K., Walsh, M. J., Schulmerich, M. V., Carney, P. S., and Bhargava, R. (2013). High-definition infrared spectroscopic imaging. *Appl. Spectrosc.* 67, 93–105. doi: 10.1366/11-06568
- Resat, H., Bailey, V., McCue, L. A., and Konopka, A. (2012). Modeling microbial dynamics in heterogeneous environments: growth on soil carbon sources. *Microb. Ecol.* 63, 883–897. doi: 10.1007/s00248-011-9965-x
- Roose, T., Keyes, S. D., Daly, K. R., Carminati, A., Otten, W., Vetterlein, D., et al. (2016). Challenges in imaging and predictive modeling of rhizosphere processes. *Plant Soil* 407, 9–38. doi: 10.1007/s11104-016-2872-7
- Rusciano, G., Zito, G., Istatico, R., Sirec, T., Ricca, E., Bailo, E., et al. (2014). Nanoscale chemical imaging of *Bacillus subtilis* spores by combining tip-enhanced Raman scattering and advanced statistical tools. *ACS Nano* 8, 12300–12309. doi: 10.1021/nn504595k
- Saulou, C., Jamme, F., Girbal, L., Maranges, C., Fourquaux, L., Coccain-Bousquet, M., et al. (2013). Synchrotron FTIR microspectroscopy of *Escherichia coli* at single-cell scale under silver-induced stress conditions. *Anal. Bioanal. Chem.* 405, 2685–2697. doi: 10.1007/s00216-013-6725-4
- Silge, A., Abdou, E., Schneider, K., Meisel, S., Bocklitz, T., Lu-Walther, H. W., et al. (2015). Shedding light on host niches: label-free *in situ* detection of *Mycobacterium gordonae* via carotenoids in macrophages by Raman microspectroscopy. *Cell. Microbiol.* 17, 832–842. doi: 10.1111/cmi.12404
- Singhal, N., Kumar, M., Kanaujia, P. K., and Virdi, J. S. (2015). MALDI-TOF mass spectrometry: an emerging technology for microbial identification and diagnosis. *Front. Microbiol.* 6:791. doi: 10.3389/fmicb.2015.00791
- Skoog, D. A., Holler, F. J., and Crouch, S. R. (2007). *Principles of Instrumental Analysis*, 6th Edn. Belmont: Thomson Brooks / Cole.
- Song, Y., Kaster, A.-K., Vollmers, J., Song, Y., Davison, P. A., Frentrup, M., et al. (2017). Single-cell genomics based on Raman sorting reveals novel carotenoid-containing bacteria in the Red Sea. *Microb. Biotechnol.* 10, 125–137. doi: 10.1111/1751-7915.12420
- Stasulli, N. M., and Shank, E. A. (2016). Profiling the metabolic signals involved in chemical communication between microbes using imaging mass spectrometry. *FEMS Microbiol. Rev.* 40, 807–813. doi: 10.1093/femsre/fuw032
- Tang, M., McEwen, G. D., Wu, Y., Miller, C. D., and Zhou, A. (2013). Characterization and analysis of mycobacteria and Gram-negative bacteria and co-culture mixtures by Raman microspectroscopy, FTIR, and atomic force microscopy. *Anal. Bioanal. Chem.* 405, 1577–1591. doi: 10.1007/s00216-012-6556-8
- Vos, M., Wolf, A. B., Jennings, S. J., and Kowalchuk, G. A. (2013). Micro-scale determinants of bacterial diversity in soil. *FEMS Microbiol. Rev.* 37, 936–954. doi: 10.1111/1574-6976.12023
- Wagner, M. (2009). Single-cell ecophysiology of microbes as revealed by Raman microspectroscopy or secondary ion mass spectrometry imaging. *Annu. Rev. Microbiol.* 63, 411–429. doi: 10.1146/annurev.micro.091208.073233
- Wang, Y., Huang, W. E., Cui, L., and Wagner, M. (2016). Single cell stable isotope probing in microbiology using Raman microspectroscopy. *Curr. Opin. Biotechnol.* 41, 34–42. doi: 10.1016/j.copbio.2016.04.018
- Wei, L., Hu, F., Chen, Z., Shen, Y., Zhang, L., and Min, W. (2016). Live-cell bioorthogonal chemical imaging: stimulated Raman scattering microscopy of vibrational probes. *Acc. Chem. Res.* 49, 1494–1502. doi: 10.1021/acs.accounts.6b00210
- Wenning, M., Theilmann, V., and Scherer, S. (2005). Rapid analysis of two food-borne microbial communities at the species level by Fourier-transform infrared microspectroscopy. *Environ. Microbiol.* 8, 848–857. doi: 10.1111/j.1462-2920.2005.00971.x
- Xiong, C., Zhou, X., He, Q., Huang, X., Wang, J., Peng, W.-P., et al. (2016). Development of visible-wavelength MALDI cell mass spectrometry for high-efficiency single-cell analysis. *Anal. Chem.* 88, 11913–11918. doi: 10.1021/acs.analchem.6b03789
- Yue, S., and Cheng, J.-X. (2016). Deciphering single cell metabolism by coherent Raman scattering microscopy. *Curr. Opin. Chem. Biol.* 33, 46–57. doi: 10.1016/j.cbpa.2016.05.016

Conflict of Interest Statement: The authors declare that the research was conducted in the absence of any commercial or financial relationships that could be construed as a potential conflict of interest.

Copyright © 2017 Harrison and Berry. This is an open-access article distributed under the terms of the Creative Commons Attribution License (CC BY). The use, distribution or reproduction in other forums is permitted, provided the original author(s) or licensor are credited and that the original publication in this journal is cited, in accordance with accepted academic practice. No use, distribution or reproduction is permitted which does not comply with these terms.



Tools for Genomic and Transcriptomic Analysis of Microbes at Single-Cell Level

Zixi Chen^{1,2,3}, Lei Chen^{1,2,3*} and Weiwen Zhang^{1,2,3,4}

¹ Laboratory of Synthetic Microbiology, School of Chemical Engineering and Technology, Tianjin University, Tianjin, China,

² Key Laboratory of Systems Bioengineering (Ministry of Education), Tianjin University, Tianjin, China, ³ SynBio Research Platform, Collaborative Innovation Center of Chemical Science and Engineering, Tianjin, China, ⁴ Center for Biosafety Research and Strategy, Tianjin University, Tianjin, China

OPEN ACCESS

Edited by:

Dimitris G. Hatzinikolaou,
National and Kapodistrian University
of Athens, Greece

Reviewed by:

Anne-Kristin Kaster,
Karlsruhe Institute of Technology,
Germany
Gwenael Piganeau,
FR3724 Observatoire Océanologique
de Banyuls sur Mer (OOB), France

*Correspondence:

Lei Chen
lchen@tju.edu.cn

Specialty section:

This article was submitted to
Systems Microbiology,
a section of the journal
Frontiers in Microbiology

Received: 25 April 2017

Accepted: 06 September 2017

Published: 20 September 2017

Citation:

Chen Z, Chen L and Zhang W (2017)
Tools for Genomic and Transcriptomic
Analysis of Microbes at Single-Cell
Level. *Front. Microbiol.* 8:1831.
doi: 10.3389/fmicb.2017.01831

Microbiologists traditionally study population rather than individual cells, as it is generally assumed that the status of individual cells will be similar to that observed in the population. However, the recent studies have shown that the individual behavior of each single cell could be quite different from that of the whole population, suggesting the importance of extending traditional microbiology studies to single-cell level. With recent technological advances, such as flow cytometry, next-generation sequencing (NGS), and microspectroscopy, single-cell microbiology has greatly enhanced the understanding of individuality and heterogeneity of microbes in many biological systems. Notably, the application of multiple 'omics' in single-cell analysis has shed light on how individual cells perceive, respond, and adapt to the environment, how heterogeneity arises under external stress and finally determines the fate of the whole population, and how microbes survive under natural conditions. As single-cell analysis involves no axenic cultivation of target microorganism, it has also been demonstrated as a valuable tool for dissecting the microbial 'dark matter.' In this review, current state-of-the-art tools and methods for genomic and transcriptomic analysis of microbes at single-cell level were critically summarized, including single-cell isolation methods and experimental strategies of single-cell analysis with NGS. In addition, perspectives on the future trends of technology development in the field of single-cell analysis was also presented.

Keywords: single-cell analysis, microbes, heterogeneity, genomics, transcriptomics, next-generation sequencing

INTRODUCTION

Microbiologists usually study microorganisms by deciphering their physiology, internal interactions, and even genetic information. Traditionally, these studies are all carried out at the population level, typically using millions to billions of cells for analysis in bulk, and assuming the status of individual cells is similar to that observed in the population. Although these results are, no

Abbreviations: CNV, copy-number variation; D-DOP-PCR, displacement DOP-PCR; DOP-PCR, degenerate oligonucleotide-primed PCR; FACS, fluorescence-activated cell sorting; FluidFM, fluidic force microscope; IPS-PCR, interspersed repetitive sequence PCR; ISH, *in situ* hybridization; IVT, *in vitro* transcription; LA-PCR, linker-adapter or ligation-anchored PCR; LIANTI, linear amplification via transposon insertion; MALBAC, multiple annealing and looping-based amplification cycles; MDA, multiple displacement amplification; NGS, next-generation sequencing; PDMS, polydimethylsiloxane; PEP-PCR, preamplification PCR; poly(A), polyadenylated; RNA-seq, RNA sequencing; SMRT, single molecule real-time; SNV, single nucleotide variant; SPIA, single primer isothermal amplification; tSMS, true single molecule sequencing; UMIs, unique molecular identifiers; WGA, whole genomic amplification.

doubt, informative, they often neglect any heterogeneity that is possibly present in the population. Meanwhile, the recent studies have shown that cell-to-cell heterogeneity at both cellular and molecular levels in isogenic population could be an order of magnitude greater than previously thought (Lidstrom and Meldrum, 2003), suggesting the importance of extending traditional microbiology studies to the single-cell level. It is now increasingly accepted that conclusions based on conventional average molecular or phenotypic measurements of a population could be biased, as the patterns of distinct sub-populations cannot be revealed (Wang et al., 2015).

Heterogeneities could result from either phenotypic difference between isogenic cells or genetic diversity at population level (Davis and Isberg, 2016). Mechanisms responsible for the cell-to-cell variation could be classified into four categories: stochastic gene expression, phenotypic plasticity, genotypic plasticity, and reversible genotypic variation (Roberfroid et al., 2016). While stochastic gene expression and phenotypic plasticity only lead to phenotypic differences, genotypic plasticity and reversible genotypic variation could introduce heterogeneity to an isogenic population at the genetic level. Stochastic gene expression widely exists in both prokaryotic and eukaryotic populations and is not exclusively driven by genomic information. Noise is one of the mechanisms of stochastic variability, which could be independent of environmental signals. This variation, either triggered by intrinsic or extrinsic noise, is usually unimodal. However, a unimodal noisiness of gene expression may trigger a bimodal behavior of downstream gene expression, leading to bimodality and bistability in a population (Dubnau and Losick, 2006; Veening et al., 2008). As different subpopulations co-exist, some individual cells may express genes that allow them to survive stresses prior to environmental changes. By using this mechanism, microbes could ensure that some individuals will survive under harsh conditions (Veening et al., 2008). Phenotypic plasticity is a kind of environmental-driven viability and could make it possible for cells to adapt to the fluctuations in the environment (Viney and Reece, 2013). An example is that in heterogeneous environmental conditions such as biofilm, isogenic cells could differentiate into various phenotypes and form several sub-populations for adapting to their local environmental conditions (van Gestel et al., 2015). Genotypic plasticity usually occurs in populations subjected to the experimental evolution. Driven by clonal evolution, clonal cells could evolve and finally result in genotypic diversification (Korona et al., 1994; Rainey and Travisano, 1998). Various mechanisms of genotypic diversification, such as clonal interference (Barrick and Lenski, 2013), niche construction, and niche partitioning (Barrick and Lenski, 2009), have been reported for both well-mixed and spatially structured environments (Roberfroid et al., 2016). As the final cause of variation, reversible genotypic variations are driven by random site-specific recombination, gene conversion, or epigenetic modification, leading to phase variations that play important roles in the virulence of some pathogens, and causing increased heterogeneity in the population (Davis and Isberg, 2016; Roberfroid et al., 2016).

Another major shortage of traditional microbiology approaches is the dependence on establishing laboratory culture for studying targeted microbes. Meanwhile, it is well-known that so far only a small number of microbial species in the biosphere could be cultivated successfully in the laboratory, leaving a great deal of microbial information untouched (Cardenas and Tiedje, 2008; Rinke et al., 2013). The hidden information, also known as microbial 'dark matter,' has drawn great interests recently and provides potential solutions for several critical issues, such as new drugs and antibiotics discovery (Ling et al., 2015), toxic chemicals degradation (Jiang et al., 2016), understanding pathogen virulence and disease mechanisms (Omsland et al., 2009), and revealing the human microbiome (Browne et al., 2016). Although obtaining axenic culture from natural isolates remains important, it is usually labor-intensive (Connon and Giovannoni, 2002), having a low success rate, and might be biased (Wu et al., 2009). In addition, comparing with the axenic cultures in the laboratory, microorganisms usually live in a more complex and barren environment in nature, making it unable to present the original state of microorganisms in the laboratory (Stewart, 2012). In recent years, many attempts have been employed for analyzing the microbe without axenic culture. For example, metagenomics and metatranscriptomics have been widely used for studying microbial community (Venter et al., 2004; Tringe et al., 2005; Mason et al., 2012, 2014; Meng et al., 2014). However, metagenomics and metatranscriptomics are not well-suited to reveal unambiguous information about the organization of discovered genes within genomes, evolutionary histories of specific organisms, and *in situ* interactions among organisms (Yoon et al., 2011; Stepanauskas, 2012). Genomic information, such as genome rearrangements, gene insertions, duplications and loss, is hard to obtain from metagenomic analysis since the assembled results could be mosaics of DNA from cells sharing high-homology regions but vary in genome-wide similarity (Stepanauskas, 2012).

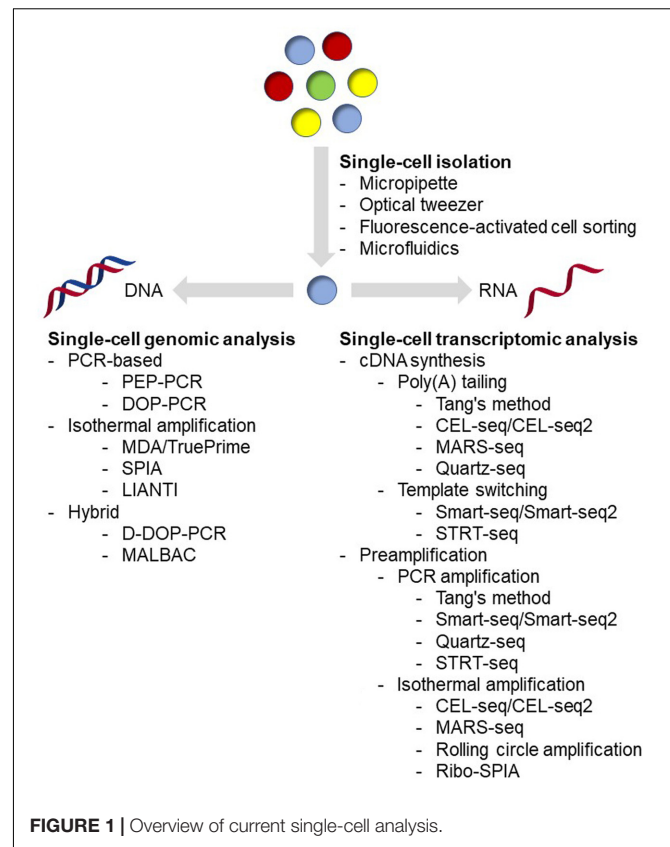
Single-cell analysis can be effective for addressing these issues and providing better and in-depth understanding of the status of microbial cells. As it starts from only one cell, single-cell analysis could reveal information about individual cell without laboratory cultivation. With the help of high-throughput sequencing, it is possible to obtain functional genomics information of each single cell in its natural environment, so that its original genetic and functional status in a complex community can be revealed globally, quantitatively, and absolutely. Several reports using single-cell analysis have successfully revealed information like coexisting subpopulations, organismal interactions, and new metabolic pathways from uncultivated samples, which could hardly be obtained by traditional approaches (Marcy et al., 2007b; Hess et al., 2011; Siegl et al., 2011; Yoon et al., 2011; Martinez-Garcia et al., 2012a; Kashtan et al., 2014). In recent years, significant progress has been made to apply metagenomics and metatranscriptomics approaches to reveal the genetic information and gene expression patterns of cells in a population, and uncover microbial species and gene diversity in a community (Bowler et al., 2009). However, as metagenomics and metatranscriptomics could not reveal the information such as repetitive regions or strain heterogeneity comprehensively

in a complex population, single-cell-based analysis has been proposed as a valuable supplement to the efficient identification of novel microbial species and the accurate interpretation of the metagenomics and metatranscriptomics results (Massana et al., 2014; Vannier et al., 2016; Ji et al., 2017). In this review, we summarize current state-of-the-art tools and methods for genomic and transcriptomic analysis of microbes at single-cell level, including single-cell isolation methods and experimental strategies of single-cell analysis with NGS, and provide some perspectives on the future trends of technology development in single-cell analysis field.

TOOLS FOR SINGLE-CELL ISOLATION

Single-cell isolation is the very first step in the single-cell analysis process (Figure 1). The major challenge of this step is: how to isolate cells of interest accurately in a high-throughput manner and without causing any genetic or physiological change to the target cells. Basically, methods being applied for microbial single-cell isolation could be classified as two principal approaches: micromanipulation and random encapsulation (Blainey, 2013). Micromanipulation methods, including micropipette and optical tweezer approaches, are carried out under high-resolution microscope. These methods offer a great confidence that every single cell can be observed, captured and delivered to the next step. Traditional micropipette method could be easily applied in any laboratory on an inverted microscope with mechanical liquid handling. Although very labor-consuming and low-throughput, approximately in the order of 50 cells/h and person (Picelli, 2016), it is the first choice if only a small number of cells are required for the next step analysis (Qi et al., 2014, 2016; Wang et al., 2015). In addition, commercial robotic manipulation system for automated single-cell selection has also been developed and applied for microbial single-cell analysis (Anis et al., 2008; Merza et al., 2009; Gao et al., 2011; Banerjee et al., 2014), making it possible for relatively high-throughput single-cell isolation. Optical tweezer approaches are implemented by tightly focusing a laser beam for trapping cells in solution (Ashkin et al., 1986, 1987; Ashkin and Dziedzic, 1987). Usually, by using near-infrared wavelengths of light, cells could be easily handled without any harm (Neuman et al., 1999; Ericsson et al., 2000). This method has been successfully applied in many microbial isolation experiments, including filamentous bacteria (Pamp et al., 2012) and even virus (Ashkin and Dziedzic, 1987). More detailed reviews of this method have been published recently (Moffitt et al., 2008; Hashemi Shabestari et al., 2017), interested readers could refer to these articles.

Flow cytometry and microfluidic device are the most widely used random encapsulation approaches in recent years. Flow cytometry and FACS have a much higher throughput, and have been demonstrated as an effective platform for single-cell analysis in microbial cells (Raghunathan et al., 2005; Stepanauskas and Sieracki, 2007; Woyke et al., 2009; Swan et al., 2011; Martinez-Garcia et al., 2012b; Field et al., 2015). Although FACS is fundamentally based on random encapsulation, flow cytometers can monitor several parameters of individuals, which means



single cells can be sorted according to their size, morphology, spontaneous fluorescence, fluorescence-labeled antibodies and staining dyes simultaneously, making it possible to sort even rare cell types. In addition, it is easy to sort single cells directly into 96- and 384-well plates using commercial instruments, which means single-cell analysis workflow could be entirely performed using automated liquid handling robots. However, cells are typically subjected to physical stresses during the sorting, such as fluidic pressure, laser beam, electrostatic charges, voltage fields, and collisions with container surfaces, which could significantly affect the cell physiology and even the recovery rate during the cultivation (Marie et al., 2017). In the case when the sorted cells are used for gene expression or transcriptome analysis, proper RNA protectant needs to be added (Qi et al., 2014, 2016; Wang et al., 2015); while in the case when the sorted cells are used for clonal cultivation, extra efforts to carefully optimize the cultivation conditions are necessary in order to maximize the success rates (Marie et al., 2017). Under the conception of 'Lab-on-a-chip,' microfluidic devices have become the most popular method for single-cell isolation. With these devices, researchers could integrate single-cell analysis process from cell isolation to sequencing library preparation in only a coin-sized microchip, which could be either purchased from commercial manufacturers or designed and fabricated using materials such as PDMS in the laboratory. Combining with detection technologies, such as fluorescence spectroscopy (Wolff et al., 2003) or raman spectroscopy (Song et al., 2016), microfluidic devices

could perform specific sorting while encapsulating cells with reagents for cell lysis and sequencing library preparation at nanoliter volume with high-throughput (Klein et al., 2015). Comparing with traditional tube-based reactions, microfluidic devices require few manual liquid handling, leading to a significant decrease in contamination and less variations among samples (de Bourcy et al., 2014). Notably, less contamination with nanoliter reaction volume means a higher concentration of substrates, resulting in better uniformity amplification (Fu et al., 2015; Leung et al., 2016). In addition, comparing with other methods, microfluidic devices cause less physical stresses to cells, leading to more accurate physiological analysis and high success rates of further cultivation analysis (Jiang et al., 2016; Kim et al., 2017; Song et al., 2017; Zhang et al., 2017). In general, both flow cytometry and microfluidic devices could provide high-throughput and accurate single-cell sorting. Flow cytometers could monitor multiple parameters and are capable for rare cell detection and sorting, but are usually expensive and require skilled operators. Before sorting, it is also necessary to prepare a sterile system for flow cytometers to prevent contamination. By contrast, microfluidic devices can be designed and made in the laboratory. They can be disposable in order to minimize contamination, and are easy to operate. Besides single-cell sorting, microfluidic devices could offer integrative single-cell analysis including cell culture and tracking (Yu et al., 2017), digital PCR (Ottesen et al., 2006), and sequencing library preparation (Hosokawa et al., 2017; Lan et al., 2017). With several advantages mentioned above, in recent years, microfluidic devices tended to be used as an analytic platform rather than just an isolation method for single-cell analysis (Marshall et al., 2012; Zhang et al., 2015, 2017; Jiang et al., 2016; Haliburton et al., 2017; Hosokawa et al., 2017; Kim et al., 2017; Lan et al., 2017; Shahi et al., 2017; Song et al., 2017). Several detailed reviews have been published recently on microfluidic devices (Wen et al., 2016; Caen et al., 2017; Prakadan et al., 2017; Xi et al., 2017), and interested readers could refer to these articles.

TOOLS FOR GENOMIC ANALYSIS AT SINGLE-CELL LEVEL

A single microbial cell usually contains picogram to femtogram level of genomic DNA (Kim et al., 2017). Sequencing technologies, up to now, are still unable to sequence such a low amount of nucleic acids directly without any amplification. Therefore, researches have been applying WGA methods since 1990 (Lichter et al., 1990). However, as amplification is conducted using DNA polymerases, the amplified products could contain genetic information of the original cell as well as some artifacts, such as genome fragment loss, amplification bias, mutations, and chimeras. Over the past 20 years, WGA methods have been optimized with substantial progress, including less contamination and better amplification performance (Blainey, 2013). In general, amplification methods could be classified into three categories: pure PCR-based amplification, isothermal amplification, and hybrid methods (Gawad et al., 2016).

Pure PCR-based WGA methods are the primary methods at early stage in the single-cell genomic analysis. Early approaches with specific primers, such as linker-adapter (also known as ligation-anchored) PCR (LA-PCR) (Troutt et al., 1992; Klein et al., 1999) and IRS-PCR (Lengauer et al., 1990; Lichter et al., 1990), require ligation reaction or prior knowledge of the target sequence. Later, methods with random primers, including primer extension pre-amplification PCR (PEP-PCR) (Hubert et al., 1992) and DOP-PCR (Telenius et al., 1992) were introduced. As the most representative method in this category, DOP-PCR typically contains two stages, with the first facilitating random primer extension on the template genome DNA and the second favoring amplicon replication with specific primer (Telenius et al., 1992).

The second category of WGA is isothermal amplification, which was first reported in Dean et al. (2001); Zhang et al. (2001) and has been demonstrated as a powerful tool in microbial single-cell genomic analysis, especially with MDA (Lasken, 2012). Unlike PCR-based methods, isothermal amplification methods use polymerases with strong strand displacement activity, such as ϕ 29 polymerase, and 6-mer 3'-protected random primers for isothermal extension (Dean et al., 2001; Zhang et al., 2001). During extension, polymerase creates and displaces synthesized products from single-stranded DNA template, and the displaced DNA is the template for further priming and synthesis (Dean et al., 2001; Zhang et al., 2001). Compared with PCR-based methods, MDA shows higher genome coverage, lower error rates and much longer extension length over 10,000 nt (Blanco et al., 1989; de Bourcy et al., 2014). However, the loci amplified first are typically found to be overrepresented, indicating non-uniformity of MDA (de Bourcy et al., 2014). Recently, a novel primer-free method called TruePrime was reported and has been successfully used for the amplification of genomic DNA from single human HEK293 cells (Picher et al., 2016). In this method, an enzyme called *Tth*PrimPol, which has a wide range of template specificity, serves as primase for ϕ 29 polymerase mediated MDA. During the reaction, *Tth*PrimPol binds to the denatured DNA and synthesizes short DNA primers. The DNA primers are recognized and extended by ϕ 29 polymerase. Then, *Tth*PrimPol catalyzes new rounds of priming on the elongated single-strand DNA, followed by further rounds of strand-displacement synthesis and resulting in exponential amplification (Picher et al., 2016). Another isothermal amplification method, called SPIA, could achieve linear amplification under isothermal conditions by using a specific DNA/RNA hybrid primer, together with RNase H and a strand-displacing DNA polymerase (Kurn et al., 2005). In SPIA method, strand-displacement only occurs at the DNA/RNA hybrid primer site of the amplicons, preventing the exponential amplification in MDA. Recently, a new method called LIANTI was reported (Chen et al., 2017). As an isothermal amplification method, this approach depends on RNA polymerase but not DNA polymerase for linear amplification. In this method, genomic DNA from a single cell was fragmented and tagged by Tn5 transposon with a T7 promoter, then linear amplified with T7 RNA polymerase, and finally converted to DNA by reverse transcription for further library preparation (Chen et al., 2017).

Two similar hybrid methods, displacement DOP-PCR (D-DOP-PCR, also known as PicoPLEX or GenomePlex)

(Langmore, 2002) and MALBAC (Lu et al., 2012; Zong et al., 2012), were recently developed to overcome the low coverage of PCR-based methods and the non-uniformity of MDA. These two methods both use isothermal amplification followed by PCR amplification, but different primers for extension. D-DOP-PCR uses degenerated primers in the first step adding an anchor sequence with isothermal amplification and then using PCR amplification for the second step (Langmore, 2002). MALBAC, however, uses a random primer with a designed anchor which could promote looping of the isothermal amplification products to prevent further amplification before the second PCR step, suggesting a more uniform amplification (Lu et al., 2012; Zong et al., 2012).

In practice, isothermal and hybrid methods are currently the most commonly used approaches, as they show better performance comparing with pure PCR-based methods. Several groups have compared these methods using both microbial and mammalian cells (Chen et al., 2014; de Bourcy et al., 2014; Deleye et al., 2015; Hou et al., 2015; Ning et al., 2015). These reports have drawn similar conclusions that MDA has significantly higher genome coverage breadth and lower false-positive rates, while hybrid methods demonstrate better coverage uniformity (Chen et al., 2014; de Bourcy et al., 2014; Deleye et al., 2015; Hou et al., 2015; Ning et al., 2015). For example, one report showed that MDA has better coverage breadth than MALBAC (84% vs. 52%), resulting in higher detection rates of SNVs (88% vs. 52%) in human cells (Hou et al., 2015). Another report showed that hybrid methods has better coverage uniformity than MDA, suggesting that hybrid methods have better performance than MDA in detecting CNVs (Ning et al., 2015). In the report, the researchers also found that MALBAC tended to over-amplify genomic regions with a high-GC content (Ning et al., 2015). The average GC content of amplified DNA using GenomePlex (41.6%) was very close to the reference genome (41.9%), while the average GC contents of amplified DNA regions by MDA and MALBAC were 43.4 and 46.6%, respectively (Ning et al., 2015). However, after a GC-correction, the correlation of read abundance between MALBAC and bulk-cell samples ($R^2 = 0.53$) was nearly the same as GenomePlex ($R^2 = 0.56$), while MDA gave a very poor correlation ($R^2 = 0.02$) (Ning et al., 2015). The TruePrime method was reported to have better coverage uniformity than the primer-based MDA, leading to an improved CNV detection accuracy, thus an advantage over the traditional primer-based MDA protocol (Picher et al., 2016). In addition, by using human genomic DNA as input, TruePrime could amplify as low as 1 fg DNA, which is about 100-fold more sensitive than the primer-based MDA (Picher et al., 2016). This superior sensitivity could be very valuable for microbial single-cell genomic analysis, as most microbes are much smaller and contain less DNA than eukaryotic cells. Notably, the most recent LIANTI method exhibited significantly improved amplification uniformity and genome coverage over the previous methods on all scales, and was capable for both high accuracy of CNV detection and low SNV false-positive rate (Chen et al., 2017). As new invented approaches, both TruePrime and LIANTI have the potential but still need more evaluation to demonstrate their performance on microbial single-cell genomic analysis. In conclusion, there

is no clear winner in performance between MDA and hybrid methods yet, and researchers should choose methods depending on the metric of their interest (Gawad et al., 2016). As microbial single-cell analysis usually focuses on elucidating the genomic information of the microbial 'dark matter,' genome coverage is the key to be concerned. Therefore, MDA method has been far more widely used for microbial single-cell analysis rather than the others.

Besides amplification methods, previous reports also found that by using microfluidic devices, microbial single-cell analysis could obtain a better performance comparing with the traditional tube-based approach (de Bourcy et al., 2014). With higher mapping ratio and better repeatability, microfluidic devices could also reduce the contamination especially from the experiment operator (de Bourcy et al., 2014). Recently, two groups independently reported high-throughput microbial single-cell analysis protocols based on self-designed microfluidic devices (Hosokawa et al., 2017; Lan et al., 2017). These two protocols shared some similarities in single microbe encapsulation and lysis protocols. However, one protocol involved sorting the positive amplification droplets and re-amplification of the DNA for further analysis by NGS and qPCR (Hosokawa et al., 2017), while the other protocol used a strategy of labeling DNA fragments from the same cell with a barcode, and then pooling and sequencing of the barcoded fragments of all cells (Lan et al., 2017). These protocols could provide reliable pipelines for analyzing 10s of 1000s of single microbial cells within a couple of hours with a comparable performance to the conventional techniques. In conclusion, with further improvements on both amplification methods and microfluidic devices, microbial single-cell genomic analysis will be more efficient, reliable, and convenient in the near future.

TOOLS FOR TRANSCRIPTOMIC ANALYSIS AT SINGLE-CELL LEVEL

Prior to whole-genome transcriptomic analysis, relative quantification methodologies have been developed to measure expression of small number of genes at single-cell level. For example, methods using fluorescent reporter proteins coupling with high-throughput data acquisition approaches such as flow cytometry have been widely applied for detecting gene expression heterogeneities within the microbial population (Taniguchi et al., 2010; Roberfroid et al., 2016). In addition, methods using RT-qPCR for detecting gene expression in single cells have also been reported and successfully applied to several types of microbes for heterogeneity analysis (Gao et al., 2011; Shi et al., 2013; Qi et al., 2014, 2016; Wang et al., 2015; Thompson et al., 2017; Turkarslan et al., 2017). However, these methods could only reveal gene expression patterns of a very limited number of genes, while not able to uncover global information in a cell. Moreover, application of such approaches typically requires genetic engineering tools and genomic information of the target microorganisms, limiting the application to only model organisms.

Global transcriptomic analysis could circumvent the above drawbacks and even possible for unknown species without genome information using *de novo* NGS approach. Compared to genomic analysis, transcriptomic analysis for microbes at single-cell level is much more challenging for several reasons. First, microbial cells usually contain picogram to femtogram level RNA molecules (de Bekker et al., 2011; Kang et al., 2011; Wang et al., 2015), while mammalian cells could have up to nanogram level RNA molecules (Picelli, 2016). Besides the low-RNA content, RNA molecules of prokaryotic cells are less stable than DNA and could be degraded by ribonucleases that are widely existing and hard to be deactivated. Moreover, rRNA and tRNA molecules usually represent over 90% of total RNA, but offer limited biological information and should be excluded in the amplification process, as most researches focus on mRNA and other rare molecules. With a complicated cell wall, harsher conditions are typically required to lyse a microbial cell, which may lead to damage or loss of RNA, and accuracy and efficiency of the downstream transcriptomic analysis (Khan and Yadav, 2004; Hall et al., 2013; Heera et al., 2015; He et al., 2016). More importantly, unlike genomic analysis, in which the methods for mammalian cells could be also readily applied to prokaryotic microbes, not all methods for mammalian single-cell transcriptomic analysis could be used to microbes. This is simply because of the structure differences of mRNA molecules between eukaryotic and prokaryotic cells. Currently, most of the mammalian single-cell transcriptomic analysis approaches use oligo(dT) primers in the first cDNA synthesis step. This is based on the 3' poly(A) structure of mRNA molecules from eukaryotic cells, which makes them easier to be enriched from rRNA and tRNA. However, mRNA molecules from prokaryotic cells usually lack the poly(A) tail, and require random primers for cDNA synthesis. By using random primers, both rRNA and tRNA will also be included in the resulting transcriptome library, thus being sequenced together, leading to a low coverage of the target mRNA. In addition, application of random primers for cDNA synthesis causes losses of 3' sequence information, as they are usually unable to obtain the full-length transcripts. Hence, so far only a few reports on prokaryotic single-cell transcriptomic analysis have been reported (Kang et al., 2011, 2015; Wang et al., 2015). Even for eukaryotic microbes that could be analyzed with well-developed approaches for mammalian cells, only one report analyzing single-cell transcriptomics of neighboring

hyphae of *Aspergillus niger* was reported (de Bekker et al., 2011). Concerning this circumstance, we summarized below all the state-of-the-art tools in single-cell transcriptomic analysis and discussed possibilities for their microbial applications, especially for prokaryotic microorganisms.

To our knowledge, the earliest study of single-cell transcriptomics was reported in Eberwine et al. (1992). In this work, mRNA molecules from single-living neurons were reverse transcribed to cDNA using oligo(dT)-T7 primer. Then, the synthesized double-stranded cDNA molecules with T7 promoter were used as templates for IVT with T7 RNA polymerase for producing amplified RNA. Next, the amplified RNA molecules were used as templates for the second turn of reverse transcription. After this process, over a million-fold amplification of the original RNA was achieved. Although this report only used ISH for accessing gene expression, it reveals the possibility about analyzing gene expression at a single-cell level. Based on the concept of this study, several studies have successfully analyzed the whole transcriptome of single mammalian cells (Morris et al., 2011; Hashimshony et al., 2012, 2016; Jaitin et al., 2014).

In the past decade, several new approaches were developed, leading to a tremendous progress in mammalian single-cell RNA-seq (Tang et al., 2009, 2010; Islam et al., 2011, 2012; Goetz and Trimarchi, 2012; Hashimshony et al., 2012, 2016; Picelli et al., 2013, 2014; Sasagawa et al., 2013; Jaitin et al., 2014; Soumillon et al., 2014; Fan H.C. et al., 2015; Klein et al., 2015; Macosko et al., 2015). The most widely used single-cell RNA-seq methods are characterized in **Table 1**. As these methods have been well reviewed in several excellent articles (Saliba et al., 2014; Chen et al., 2015; Kolodziejczyk et al., 2015; Picelli, 2016), we will focus only on some newly developed methods here. Among the methods listed in **Table 1**, Smart-seq/Smart-seq2 and Quartz-seq use a method called 'template switch' for the second strand cDNA synthesis, generating full-length double-stranded cDNA comparing with the others (Goetz and Trimarchi, 2012; Picelli et al., 2013, 2014; Sasagawa et al., 2013). Smart-seq, CEL-seq2 and STRT-seq are compatible with Fluidigm C1 Single-Cell Auto Prep system, which is an automated platform and captured using integrated fluidic circuits (Ziegenhain et al., 2017). For amplification types, Tang's method, Smart-seq/Smart-seq2, Quartz-seq, and STRT-seq are all based on PCR amplification, while CEL-seq/CEL-seq2 and MARS-seq are based on IVT.

TABLE 1 | Characteristics of several widely used single-cell RNA-seq methods.

Name	Transcript coverage	Position bias	Strand specificity	UMI compatible	Key reference
Tang's method	Nearly full-length	Strongly 3'	No	No	Tang et al., 2009, 2010
Quartz-seq	Full-length	Weakly 3'	No	No	Sasagawa et al., 2013
Smart-seq/Smart-seq2	Full-length	Weakly 3'	No	No	Goetz and Trimarchi, 2012; Picelli et al., 2013, 2014
STRT-seq	5' only	5' only	Yes	Yes	Islam et al., 2011, 2012
CEL-seq/CEL-seq2	3' only	3' only	Yes	Yes	Hashimshony et al., 2012, 2016
MARS-seq	3' only	3' only	Yes	Yes	Jaitin et al., 2014
SCR-seq	3' only	3' only	Yes	Yes	Soumillon et al., 2014
Drop-seq/InDrop	3' only	3' only	Yes	Yes	Klein et al., 2015; Macosko et al., 2015
Cyto-seq	Pre-defined genes only	3' only	Yes	Yes	Fan H.C. et al., 2015

The advantage of IVT is that the amplification efficiency is sequence independent. However, as it requires a second time of reverse transcription, there is 3' coverage bias of the sequencing results (Kolodziejczyk et al., 2015). When choosing an appropriate single-cell RNA-seq method, transcript coverage, strand specificity, position bias, and UMI compatibility should be concerned depending on the purpose of the research (Table 1). For example, full-length RNA-seq methods such as Smart-seq/Smart-Seq2, and Quartz-seq could sequence the transcripts in their entirety, and thus are suggested for *de novo* sequencing and the detection of SNPs and mutations. However, these methods are not compatible with strand-specific protocol and UMI. Methods such as STRT-seq, CEL-seq/CEL-seq2, MARS-seq, and Drop-seq are all compatible with strand-specific protocol and UMI, although they tend to be 5' or 3' end biased. While UMI approach in single-cell sequencing could reduce amplification noise and provide more accurate expression quantification, strand-specific sequencing could provide more information for antisense transcript discovery, genome annotation, and expression profiling. In conclusion, current single-cell RNA-seq methods are still facing a trade-off between coverage and uniformity (Picelli, 2016). Notably, none of these methods has been evaluated in eukaryotic microbes, suggesting further optimization and development are needed for microbial cells. Recently, a systematic evaluation of six prominent single-cell RNA-seq methods has been reported (Ziegenhain et al., 2017), and the results indicated that Smart-seq2 had the best coverage because of its full-length synthesis ability. However, as Smart-seq2 is incompatible with UMIs, all methods using UMIs have less amplification noise. In addition, power simulations showed that Drop-seq is more cost-efficient for analyzing a large number of cells, while Smart-seq2, MARS-seq, and SCRB-seq are more efficient with the analysis of a small number of cells (Ziegenhain et al., 2017).

Besides the above methods, several new methods have also been developed recently. Some of them have already been utilized for single-cell RNA-seq in prokaryotic cells (Kang et al., 2011, 2015; Wang et al., 2015). The first case of single-cell microbial transcriptomic analysis, to our knowledge, was reported in Kang et al. (2011). In this report, transcriptome of single bacterium *Burkholderia thailandensis* was analyzed using microarray through amplification of RNA molecules by rolling circle amplification. In this report, bacterial cells were first lysed with Triton X-100 and lysozyme, and then the lysate was used for direct cDNA synthesis with random primers. After genomic DNA degradation, single-stranded cDNA molecules were self-ligated and then used as the template for multiply primed rolling circle amplification using ϕ 29 polymerase with random primers. The result showed low fold-change bias and only less than 6% drop-outs with no contamination. In addition, this method also preferred an optional rRNA/tRNA elimination step for deep sequencing. By using 5'-phosphate-dependent exonuclease, rRNA and tRNA molecules, which have the 5'-phosphate structure, will be specifically degraded, leaving the mRNA molecules which lacking the 5'-phosphate structure for the next cDNA synthesis step. This is also the only report we could find, which has successfully depleted

rRNA from single microbial cells, indicating the requirements for further innovation of other effective rRNA depletion and mRNA enrichment methods for microbes. Later in the same year, another approach using Ribo-SPIA method, that is, derived from SPIA method for amplification, has successfully been employed to analyze transcriptomics of neighboring hyphae of the eukaryotic fungus *A. niger* using microarray (de Bekker et al., 2011). In this article, total RNA from different 5 hyphal tips were isolated using a column based kit and amplified using the WT-Ovation One-Direct RNA Amplification System (Nugen) with both oligo(dT) and random primers. Microarray analysis resulted in a present call for 4–7% of the *A. niger* genes, of which 12% showed heterogeneous RNA levels, indicating the feasibility of using this method for microbial transcriptomic analysis. In another study with prokaryotic cells, Wang et al. (2015) successfully conducted single-cell RNA-seq in single cyanobacterium *Synechocystis* sp. PCC 6803 cells with Ribo-SPIA method. To determine the heterogeneity upon environmental stress, this method was applied to *Synechocystis* single cells at 24 and 72 h after nitrogen starvation treatment. With up to 98% of all putative *Synechocystis* genes identified in single cells, a possible increasing gene-expression heterogeneity from 24 to 72 h after nitrogen starvation stress was also found, indicating the method could achieve good identification of the transcripts in single bacterial cells (Wang et al., 2015). More recently, a technology for targeted depletion of abundant transcripts was developed by Nugen (Armour et al., 2015). Unlike the exonuclease-based depletion method that Kang et al. (2011) reported, this method depleted the unwanted sequences after cDNA synthesis using probes that target unwanted sequences. However, the information of the unwanted sequences is required, making it impossible for *de novo* single-cell RNA-seq. SUPeR-seq (Fan X. et al., 2015) is another method to sequence both polyadenylated and non-polyadenylated RNAs, suggesting its possible application to prokaryotic microbes. This method shares some similarities to Tang's method (Tang et al., 2009, 2010), but used a primer containing an anchor sequence (AnchorX), 15-mer dT sequence and 6-mer random sequence for simultaneous detection of both polyadenylated and non-polyadenylated RNA molecules and synthesizing the first strand cDNA. After poly(A) tailing for the first strand cDNA, a primer containing another anchor sequence (AnchorY) and 24-mer dT sequence was used for second strand cDNA synthesis, and then the double-stranded cDNA molecules were amplified by PCR using AnchorX and AnchorY primers. With this approach, the researchers discovered 2891 circRNAs in mouse preimplantation embryos. Like other methods using random primers, rRNA could not be excluded with this method. However, this method provides another possible method for single-cell RNA-seq in prokaryotic microbes, especially with the rRNA depletion methods mentioned above.

FUTURE PERSPECTIVES

Current genomic and transcriptomic analysis of single microbial cells share several similar challenges. Cell lysis is a major challenge for single-cell analysis. As microbes typically contain

complicated structure of cell walls, appropriate lysis strategies need to be chosen carefully without damaging the DNA/RNA inside. In addition, in the case if the lysate is directly used for amplification without purification, the lysis condition should also be carefully optimized to minimize the influence of lysis related reagents to the downstream reactions. Alternatively, a method called FluidFM might be a promising approach for DNA/RNA isolation from microbial cells, as it used a ‘nanosyringe’ to extract cytoplasmic and nucleoplasmic fractions from single live cells rather than lysis the cell (Meister et al., 2009; Guillaume-Gentil et al., 2016). Contamination is another key challenge in single-cell analysis. As low-input and high-fold amplification are required for sequencing, single-cell analysis is very sensitive to contamination, either from the laboratory environment or reagents and instruments used for sample preparation. Several approaches have been applied to minimize contamination, including reducing the reaction volume of lysis and amplification reaction to nanoliter scale in a sealed, disposable microfluidic device (Marcy et al., 2007a,b), using UV exposure to inactivate contaminants in reagents (Zhang et al., 2006; Woyke et al., 2011), and disposable plasticware produced from virgin materials (Blainey and Quake, 2011). Another challenge for microbial single-cell analysis is the ultra-low nuclei acids content in a single microbial cell. Current microbial single-cell sequencing methods were all modified from those developed for mammalian cells, as they contain more nuclei acids. While using these methods in microbial cells, nuclei acids template could be a 1000-fold less than using a mammalian cell. With a much lower concentration of templates, the amplification process could be more sensitive to any contamination and non-specific amplification. In addition, less input may also challenge the sensitivity of the polymerase used for the amplification process (Picher et al., 2016). Using microfluidic devices for amplification could significantly solve these problems (de Bourcy et al., 2014). Moreover, the low input also influences the uniformity of the amplification. Even for single-cell analysis of mammalian cells, the amplification uniformity is still not comparable with that at the bulk-cell level. Therefore, the sequencing depth could be a critical factor to ensure good genome coverage, especially for unculturable microbes with unknown genome sizes.

Current single-cell sequencing methods all require amplification of DNA/RNA from a single cell for NGS

sequencing, which will inevitably introduce bias and loss. Recently, new sequencing platforms such as true single molecule sequencing (tSMS, Helicos, now SeqLL), SMRT sequencing (PacBio), and nanopore sequencing (Oxford Nanopore) could sequence DNA/RNA molecules at single-molecule level and prove to be possible to sequence DNA/RNA molecules directly from bulk-cells without pre-amplification (Ozsolak et al., 2009; Ozsolak and Milos, 2011; Coupland et al., 2012; Ayub et al., 2013). Although directly sequencing a single cell without pre-amplification is still challenging, further innovation of these new technologies and sequencing platforms could eventually make it possible for single-cell analysis without any amplification.

CONCLUSION

As a rapidly growing field, single-cell analysis plays a significant role in extending our understanding of microorganisms by revealing how individual cells perceive, respond and adapt to the environment, and determine the fate of the whole population. The key drivers of new technology for single-cell analysis will be advancement in throughput, integration of isolation and amplification, and integrated analysis with multiple ‘omics.’ Even with many challenges still ahead, we believe that this field will receive a tremendous boost with progress of several related fields, such as microfluidic devices and new sequencing platforms.

AUTHOR CONTRIBUTIONS

WZ envisioned this project. ZC, LC, and WZ wrote the manuscript. All authors have read and agreed on the manuscript.

ACKNOWLEDGMENTS

The research was supported by grants from the Natural Science Foundation of China (NSFC) (Nos. 31470217, 91751102, and 21621004), National Basic Research Program of China (National ‘973’ program, project No. 2014CB745101), and the Tianjin Municipal Science and Technology Commission (No. 15JCZDJC32500).

REFERENCES

- Anis, Y. H., Holl, M. R., and Meldrum, D. R. (2008). “Automated vision-based selection and placement of single cells in microwell array formats,” in *IEEE International Conference on Automation Science and Engineering*, Xian. doi: 10.1109/COASE.2008.4626575
- Armour, C., Amorese, D., Li, B., and Kurn, N. (2015). Compositions and methods for negative selection of non-desired nucleic acid sequences. U.S. Patent No 20150299767. Washington, DC: U.S. Patent and Trademark Office.
- Ashkin, A., and Dziedzic, J. M. (1987). Optical trapping and manipulation of viruses and bacteria. *Science* 235, 1517–1520. doi: 10.1126/science.3547653
- Ashkin, A., Dziedzic, J. M., Bjorkholm, J. E., and Chu, S. (1986). Observation of a single-beam gradient force optical trap for dielectric particles. *Opt. Lett.* 11:288. doi: 10.1364/OL.11.000288
- Ashkin, A., Dziedzic, J. M., and Yamane, T. (1987). Optical trapping and manipulation of single cells using infrared laser beams. *Nature* 330, 769–771. doi: 10.1038/330769a0
- Ayub, M., Hardwick, S. W., Luisi, B. F., and Bayley, H. (2013). Nanopore-based identification of individual nucleotides for direct RNA sequencing. *Nano Lett.* 13, 6144–6150. doi: 10.1021/nl403469r
- Banerjee, S., Wang, W., and Gutschmidt, S. (2014). “Design and analysis of actuated microneedles for robotic manipulation,” in *ASME International Mechanical Engineering Congress and Exposition*, Montreal, QC, 8–13. doi: 10.1115/imece2014-39308
- Barrick, J. E., and Lenski, R. E. (2009). Genome-wide mutational diversity in an evolving population of *Escherichia coli*. *Cold Spring Harb. Symp. Quant. Biol.* 74, 119–129. doi: 10.1101/sqb.2009.74.018
- Barrick, J. E., and Lenski, R. E. (2013). Genome dynamics during experimental evolution. *Nat. Rev. Genet.* 14, 827–839. doi: 10.1038/nrg3564

- Blainey, P. C. (2013). The future is now: single-cell genomics of bacteria and archaea. *FEMS Microbiol. Rev.* 37, 407–427. doi: 10.1111/1574-6976.12015
- Blainey, P. C., and Quake, S. R. (2011). Digital MDA for enumeration of total nucleic acid contamination. *Nucleic Acids Res.* 39, e19. doi: 10.1093/nar/gkq1074
- Blanco, L., Bernad, A., Lazaro, J. M., Martin, G., Garmendia, C., and Salas, M. (1989). Highly efficient DNA synthesis by the phage phi 29 DNA polymerase. Symmetrical mode of DNA replication. *J. Biol. Chem.* 264, 8935–8940.
- Bowler, C., Karl, D. M., and Colwell, R. R. (2009). Microbial oceanography in a sea of opportunity. *Nature* 459, 180–184. doi: 10.1038/nature08056
- Browne, H. P., Forster, S. C., Anonye, B. O., Kumar, N., Neville, B. A., Stares, M. D., et al. (2016). Culturing of 'unculturable' human microbiota reveals novel taxa and extensive sporulation. *Nature* 533, 543–546. doi: 10.1038/nature17645
- Caen, O., Lu, H., Nizard, P., and Taly, V. (2017). Microfluidics as a strategic player to decipher single-cell omics? *Trends Biotechnol.* 35, 713–727. doi: 10.1016/j.tibtech.2017.05.004
- Cardenas, E., and Tiedje, J. M. (2008). New tools for discovering and characterizing microbial diversity. *Curr. Opin. Biotechnol.* 19, 544–549. doi: 10.1016/j.copbio.2008.10.010
- Chen, C., Xing, D., Tan, L., Li, H., Zhou, G., Huang, L., et al. (2017). Single-cell whole-genome analyses by Linear Amplification via Transposon Insertion (LIANTI). *Science* 356, 189–194. doi: 10.1126/science.aak9787
- Chen, K., Dong, X., and Wu, J. (2015). "The application of single-cell sequencing in dynamic transcriptomes," in *Single Cell Sequencing and Systems Immunology*, ed. X. Wang (Dordrecht: Springer), 41–63. doi: 10.1007/978-94-017-9753-5_4
- Chen, M., Song, P., Zou, D., Hu, X., Zhao, S., Gao, S., et al. (2014). Comparison of multiple displacement amplification (MDA) and multiple annealing and looping-based amplification cycles (MALBAC) in single-cell sequencing. *PLOS ONE* 9:e114520. doi: 10.1371/journal.pone.0114520
- Connon, S. A., and Giovannoni, S. J. (2002). High-throughput methods for culturing microorganisms in very-low-nutrient media yield diverse new marine isolates. *Appl. Environ. Microbiol.* 68, 3878–3885. doi: 10.1128/AEM.68.8.3878-3885.2002
- Coupland, P., Chandra, T., Quail, M., Reik, W., and Sverdlow, H. (2012). Direct sequencing of small genomes on the Pacific Biosciences RS without library preparation. *Biotechniques* 53, 365–372. doi: 10.2144/000113962
- Davis, K. M., and Isberg, R. R. (2016). Defining heterogeneity within bacterial populations via single cell approaches. *Bioessays* 38, 782–790. doi: 10.1002/bies.201500121
- de Bekker, C., Bruning, O., Jonker, M. J., Breit, T. M., and Wosten, H. A. (2011). Single cell transcriptomics of neighboring hyphae of *Aspergillus niger*. *Genome Biol.* 12:R71. doi: 10.1186/gb-2011-12-8-r71
- de Bourcy, C. F., De Vlaminc, I., Kanbar, J. N., Wang, J., Gawad, C., and Quake, S. R. (2014). A quantitative comparison of single-cell whole genome amplification methods. *PLOS ONE* 9:e105585. doi: 10.1371/journal.pone.0105585
- Dean, F. B., Nelson, J. R., Giesler, T. L., and Lasken, R. S. (2001). Rapid amplification of plasmid and phage DNA using Phi 29 DNA polymerase and multiply-primed rolling circle amplification. *Genome Res.* 11, 1095–1099. doi: 10.1101/gr.180501
- Deleye, L., De Coninck, D., Christodoulou, C., Sante, T., Dheedene, A., Heindryckx, B., et al. (2015). Whole genome amplification with SurePlex results in better copy number alteration detection using sequencing data compared to the MALBAC method. *Sci. Rep.* 5:11711. doi: 10.1038/srep11711
- Dubnau, D., and Losick, R. (2006). Bistability in bacteria. *Mol. Microbiol.* 61, 564–572. doi: 10.1111/j.1365-2958.2006.05249.x
- Eberwine, J., Yeh, H., Miyashiro, K., Cao, Y., Nair, S., Finnell, R., et al. (1992). Analysis of gene expression in single live neurons. *Proc. Natl. Acad. Sci. U.S.A.* 89, 3010–3014. doi: 10.1073/pnas.89.7.3010
- Ericsson, M., Hanstorp, D., Hagberg, P., Enger, J., and Nystrom, T. (2000). Sorting out bacterial viability with optical tweezers. *J. Bacteriol.* 182, 5551–5555. doi: 10.1128/jb.182.19.5551-5555.2000
- Fan, H. C., Fu, G. K., and Fodor, S. P. (2015). Expression profiling. Combinatorial labeling of single cells for gene expression cytometry. *Science* 347:1258367. doi: 10.1126/science.1258367
- Fan, X., Zhang, X., Wu, X., Guo, H., Hu, Y., Tang, F., et al. (2015). Single-cell RNA-seq transcriptome analysis of linear and circular RNAs in mouse preimplantation embryos. *Genome Biol.* 16, 148. doi: 10.1186/s13059-015-0706-1
- Field, E. K., Sczyrba, A., Lyman, A. E., Harris, C. C., Woyke, T., Stepanauskas, R., et al. (2015). Genomic insights into the uncultivated marine Zetaproteobacteria at Loihi Seamount. *ISME J.* 9, 857–870. doi: 10.1038/ismej.2014.183
- Fu, Y., Li, C., Lu, S., Zhou, W., Tang, F., Xie, X. S., et al. (2015). Uniform and accurate single-cell sequencing based on emulsion whole-genome amplification. *Proc. Natl. Acad. Sci. U.S.A.* 112, 11923–11928. doi: 10.1073/pnas.1513988112
- Gao, W., Zhang, W., and Meldrum, D. R. (2011). RT-qPCR based quantitative analysis of gene expression in single bacterial cells. *J. Microbiol. Methods* 85, 221–227. doi: 10.1016/j.mimet.2011.03.008
- Gawad, C., Koh, W., and Quake, S. R. (2016). Single-cell genome sequencing: current state of the science. *Nat. Rev. Genet.* 17, 175–188. doi: 10.1038/nrg.2015.16
- Goetz, J. J., and Trimarchi, J. M. (2012). Transcriptome sequencing of single cells with Smart-Seq. *Nat. Biotechnol.* 30, 763–765. doi: 10.1038/nbt.2325
- Guillaume-Gentil, O., Grindberg, R. V., Kooger, R., Dorwling-Carter, L., Martinez, V., Ossola, D., et al. (2016). Tunable single-cell extraction for molecular analyses. *Cell* 166, 506–516. doi: 10.1016/j.cell.2016.06.025
- Haliburton, J. R., Shao, W., Deutschbauer, A., Arkin, A., and Abate, A. R. (2017). Genetic interaction mapping with microfluidic-based single cell sequencing. *PLOS ONE* 12:e0171302. doi: 10.1371/journal.pone.0171302
- Hall, E. W., Kim, S., Appadoo, V., and Zare, R. N. (2013). Lysis of a single cyanobacterium for whole genome amplification. *Micromachines* 4, 321–332. doi: 10.3390/mi4030321
- Hashemi Shabestari, M., Meijering, A. E., Roos, W. H., Wuite, G. J., and Peterman, E. J. (2017). Recent advances in biological single-molecule applications of optical tweezers and fluorescence microscopy. *Methods Enzymol.* 582, 85–119. doi: 10.1016/bs.mie.2016.09.047
- Hashimshony, T., Senderovich, N., Avital, G., Klochendler, A., de Leeuw, Y., Anavy, L., et al. (2016). CEL-Seq2: sensitive highly-multiplexed single-cell RNA-seq. *Genome Biol.* 17, 77. doi: 10.1186/s13059-016-0938-8
- Hashimshony, T., Wagner, F., Sher, N., and Yanai, I. (2012). CEL-Seq: single-cell RNA-Seq by multiplexed linear amplification. *Cell Rep.* 2, 666–673. doi: 10.1016/j.celrep.2012.08.003
- He, J., Du, S., Tan, X., Arefin, A., and Han, C. S. (2016). Improved lysis of single bacterial cells by a modified alkaline-thermal shock procedure. *Biotechniques* 60, 129–135. doi: 10.2144/000114389
- Heera, R., Sivachandran, P., Chinni, S. V., Mason, J., Croft, L., Ravichandran, M., et al. (2015). Efficient extraction of small and large RNAs in bacteria for excellent total RNA sequencing and comprehensive transcriptome analysis. *BMC Res. Notes* 8:754. doi: 10.1186/s13104-015-1726-3
- Hess, M., Sczyrba, A., Egan, R., Kim, T. W., Chokhawala, H., Schroth, G., et al. (2011). Metagenomic discovery of biomass-degrading genes and genomes from cow rumen. *Science* 331, 463–467. doi: 10.1126/science.1200387
- Hosokawa, M., Nishikawa, Y., Kogawa, M., and Takeyama, H. (2017). Massively parallel whole genome amplification for single-cell sequencing using droplet microfluidics. *Sci. Rep.* 7, 5199. doi: 10.1038/s41598-017-05436-4
- Hou, Y., Wu, K., Shi, X., Li, F., Song, L., Wu, H., et al. (2015). Comparison of variations detection between whole-genome amplification methods used in single-cell resequencing. *Gigascience* 4, 37. doi: 10.1186/s13742-015-0068-3
- Hubert, R., Weber, J. L., Schmitt, K., Zhang, L., and Arnheim, N. (1992). A new source of polymorphic DNA markers for sperm typing: analysis of microsatellite repeats in single cells. *Am. J. Hum. Genet.* 51, 985–991.
- Islam, S., Kjallquist, U., Moliner, A., Zajac, P., Fan, J. B., Lonnerberg, P., et al. (2011). Characterization of the single-cell transcriptional landscape by highly multiplex RNA-seq. *Genome Res.* 21, 1160–1167. doi: 10.1101/gr.110882.110
- Islam, S., Kjallquist, U., Moliner, A., Zajac, P., Fan, J. B., Lonnerberg, P., et al. (2012). Highly multiplexed and strand-specific single-cell RNA 5' end sequencing. *Nat. Protoc.* 7, 813–828. doi: 10.1038/nprot.2012.022
- Jaitin, D. A., Kenigsberg, E., Keren-Shaul, H., Elefant, N., Paul, F., Zaretsky, I., et al. (2014). Massively parallel single-cell RNA-seq for marker-free decomposition of tissues into cell types. *Science* 343, 776–779. doi: 10.1126/science.1247651
- Ji, P., Zhang, Y., Wang, J., and Zhao, F. (2017). MetaSort untangles metagenome assembly by reducing microbial community complexity. *Nat. Commun.* 8:14306. doi: 10.1038/ncomms14306

- Jiang, C. Y., Dong, L., Zhao, J. K., Hu, X., Shen, C., Qiao, Y., et al. (2016). High throughput single-cell cultivation on microfluidic streak plates. *Appl. Environ. Microbiol.* 82, 2210–2218. doi: 10.1128/AEM.03588-15
- Kang, Y., McMillan, I., Norris, M. H., and Hoang, T. T. (2015). Single prokaryotic cell isolation and total transcript amplification protocol for transcriptomic analysis. *Nat. Protoc.* 10, 974–984. doi: 10.1038/nprot.2015.058
- Kang, Y., Norris, M. H., Zarzycki-Siek, J., Nierman, W. C., Donachie, S. P., and Hoang, T. T. (2011). Transcript amplification from single bacterium for transcriptome analysis. *Genome Res.* 21, 925–935. doi: 10.1101/gr.116103.110
- Kashtan, N., Roggensack, S. E., Rodrigue, S., Thompson, J. W., Biller, S. J., Coe, A., et al. (2014). Single-cell genomics reveals hundreds of coexisting subpopulations in wild *Prochlorococcus*. *Science* 344, 416–420. doi: 10.1126/science.1248575
- Khan, I. U. H., and Yadav, J. S. (2004). Development of a single-tube, cell lysis-based, genus-specific PCR method for rapid identification of Mycobacteria: optimization of cell lysis, PCR primers and conditions, and restriction pattern analysis. *J. Clin. Microbiol.* 42, 453–457. doi: 10.1128/jcm.42.1.453-457.2004
- Kim, S., De Jonghe, J., Kulesa, A. B., Feldman, D., Vatanen, T., Bhattacharyya, R. P., et al. (2017). High-throughput automated microfluidic sample preparation for accurate microbial genomics. *Nat. Commun.* 8:13919. doi: 10.1038/ncomms13919
- Klein, A. M., Mazutis, L., Akartuna, I., Tallapragada, N., Veres, A., Li, V., et al. (2015). Droplet barcoding for single-cell transcriptomics applied to embryonic stem cells. *Cell* 161, 1187–1201. doi: 10.1016/j.cell.2015.04.044
- Klein, C. A., Schmidt-Kittler, O., Schardt, J. A., Pantel, K., Speicher, M. R., and Riethmüller, G. (1999). Comparative genomic hybridization, loss of heterozygosity, and DNA sequence analysis of single cells. *Proc. Natl. Acad. Sci. U.S.A.* 96, 4494–4499. doi: 10.1073/pnas.96.8.4494
- Kolodziejczyk, A. A., Kim, J. K., Svensson, V., Marioni, J. C., and Teichmann, S. A. (2015). The technology and biology of single-cell RNA sequencing. *Mol. Cell* 58, 610–620. doi: 10.1016/j.molcel.2015.04.005
- Korona, R., Nakatsu, C. H., Forney, L. J., and Lenski, R. E. (1994). Evidence for multiple adaptive peaks from populations of bacteria evolving in a structured habitat. *Proc. Natl. Acad. Sci. U.S.A.* 91, 9037–9041. doi: 10.1073/pnas.91.19.9037
- Kurn, N., Chen, P., Heath, J. D., Kopf-Sill, A., Stephens, K. M., and Wang, S. (2005). Novel isothermal, linear nucleic acid amplification systems for highly multiplexed applications. *Clin. Chem.* 51, 1973–1981. doi: 10.1373/clinchem.2005.053694
- Lan, F., Demaree, B., Ahmed, N., and Abate, A. R. (2017). Single-cell genome sequencing at ultra-high-throughput with microfluidic droplet barcoding. *Nat. Biotechnol.* 35, 640–646. doi: 10.1038/nbt.3880
- Langmore, J. P. (2002). Rubicon Genomics, Inc. *Pharmacogenomics* 3, 557–560. doi: 10.1517/14622416.3.4.557
- Lasken, R. S. (2012). Genomic sequencing of uncultured microorganisms from single cells. *Nat. Rev. Microbiol.* 10, 631–640. doi: 10.1038/nrmicro2857
- Lengauer, C., Riethman, H., and Cremer, T. (1990). Painting of human chromosomes with probes generated from hybrid cell lines by PCR with Alu and L1 primers. *Hum. Genet.* 86, 1–6. doi: 10.1007/BF00205163
- Leung, K., Klaus, A., Lin, B. K., Laks, E., Biele, J., Lai, D., et al. (2016). Robust high-performance nanoliter-volume single-cell multiple displacement amplification on planar substrates. *Proc. Natl. Acad. Sci. U.S.A.* 113, 8484–8489. doi: 10.1073/pnas.1520964113
- Lichter, P., Ledbetter, S. A., Ledbetter, D. H., and Ward, D. C. (1990). Fluorescence *in situ* hybridization with Alu and L1 polymerase chain reaction probes for rapid characterization of human chromosomes in hybrid cell lines. *Proc. Natl. Acad. Sci. U.S.A.* 87, 6634–6638. doi: 10.1073/pnas.87.17.6634
- Lidstrom, M. E., and Meldrum, D. R. (2003). Life-on-a-chip. *Nat. Rev. Microbiol.* 1, 158–164. doi: 10.1038/nrmicro755
- Ling, L. L., Schneider, T., Peoples, A. J., Spoering, A. L., Engels, I., Conlon, B. P., et al. (2015). A new antibiotic kills pathogens without detectable resistance. *Nature* 517, 455–459. doi: 10.1038/nature14098
- Lu, S., Zong, C., Fan, W., Yang, M., Li, J., Chapman, A. R., et al. (2012). Probing meiotic recombination and aneuploidy of single sperm cells by whole-genome sequencing. *Science* 338, 1627–1630. doi: 10.1126/science.1229112
- Macosko, E. Z., Basu, A., Satija, R., Nemesh, J., Shekhar, K., Goldman, M., et al. (2015). Highly parallel genome-wide expression profiling of individual cells using nanoliter droplets. *Cell* 161, 1202–1214. doi: 10.1016/j.cell.2015.05.002
- Marcy, Y., Ishoe, T., Lasken, R. S., Stockwell, T. B., Walenz, B. P., Halpern, A. L., et al. (2007a). Nanoliter reactors improve multiple displacement amplification of genomes from single cells. *PLOS Genet.* 3:1702–1708. doi: 10.1371/journal.pgen.0030155
- Marcy, Y., Ouerney, C., Bik, E. M., Losekann, T., Ivanova, N., Martin, H. G., et al. (2007b). Dissecting biological “dark matter” with single-cell genetic analysis of rare and uncultivated TM7 microbes from the human mouth. *Proc. Natl. Acad. Sci. U.S.A.* 104, 11889–11894. doi: 10.1073/pnas.0704662104
- Marie, D., Le Gall, F., Edern, R., Gourvil, P., and Vaultot, D. (2017). Improvement of phytoplankton culture isolation using single cell sorting by flow cytometry. *J. Phycol.* 53, 271–282. doi: 10.1111/jpy.12495
- Marshall, I. P., Blainey, P. C., Spormann, A. M., and Quake, S. R. (2012). A single-cell genome for *Thiovulum* sp. *Appl. Environ. Microbiol.* 78, 8555–8563. doi: 10.1128/AEM.02314-12
- Martinez-Garcia, M., Brazel, D. M., Swan, B. K., Arnosti, C., Chain, P. S., Reitenga, K. G., et al. (2012a). Capturing single cell genomes of active polysaccharide degraders: an unexpected contribution of Verrucomicrobia. *PLOS ONE* 7:e35314. doi: 10.1371/journal.pone.0035314
- Martinez-Garcia, M., Swan, B. K., Poulton, N. J., Gomez, M. L., Masland, D., Sieracki, M. E., et al. (2012b). High-throughput single-cell sequencing identifies photoheterotrophs and chemoautotrophs in freshwater bacterioplankton. *ISME J.* 6, 113–123. doi: 10.1038/ismej.2011.84
- Mason, O. U., Hazen, T. C., Borglin, S., Chain, P. S., Dubinsky, E. A., Fortney, J. L., et al. (2012). Metagenome, metatranscriptome and single-cell sequencing reveal microbial response to Deepwater Horizon oil spill. *ISME J.* 6, 1715–1727. doi: 10.1038/ismej.2012.59
- Mason, O. U., Scott, N. M., Gonzalez, A., Robbins-Pianka, A., Baelum, J., Kimbrel, J., et al. (2014). Metagenomics reveals sediment microbial community response to Deepwater Horizon oil spill. *ISME J.* 8, 1464–1475. doi: 10.1038/ismej.2013.254
- Massana, R., del Campo, J., Sieracki, M. E., Audic, S., and Logares, R. (2014). Exploring the uncultured microeukaryote majority in the oceans: reevaluation of ribogroups within stramenopiles. *ISME J.* 8, 854–866. doi: 10.1038/ismej.2013.204
- Meister, A., Gabi, M., Behr, P., Studer, P., Voros, J., Niedermann, P., et al. (2009). FluidFM: combining atomic force microscopy and nanofluidics in a universal liquid delivery system for single cell applications and beyond. *Nano Lett.* 9, 2501–2507. doi: 10.1021/nl901384x
- Meng, J., Xu, J., Qin, D., He, Y., Xiao, X., and Wang, F. (2014). Genetic and functional properties of uncultivated MCG archaea assessed by metagenome and gene expression analyses. *ISME J.* 8, 650–659. doi: 10.1038/ismej.2013.174
- Merza, S. A., Posner, J. D., Anis, Y. H., Young, A. C., Johnson, R. H., and Meldrum, D. R. (2009). “Microfluidic device for transport and observation of single cells,” in *ASME 2009 International Mechanical Engineering Congress and Exposition*, New York City, NY. doi: 10.1115/IMECE2009-13019
- Moffitt, J. R., Chemla, Y. R., Smith, S. B., and Bustamante, C. (2008). Recent advances in optical tweezers. *Annu. Rev. Biochem.* 77, 205–228. doi: 10.1146/annurev.biochem.77.043007.090225
- Morris, J., Singh, J. M., and Eberwine, J. H. (2011). Transcriptome analysis of single cells. *J. Vis. Exp.* 2011:e2634. doi: 10.3791/2634
- Neuman, K. C., Chadd, E. H., Liou, G. F., Bergman, K., and Block, S. M. (1999). Characterization of photodamage to *Escherichia coli* in optical traps. *Biophys. J.* 77, 2856–2863. doi: 10.1016/S0006-3495(99)77117-1
- Ning, L., Li, Z., Wang, G., Hu, W., Hou, Q., Tong, Y., et al. (2015). Quantitative assessment of single-cell whole genome amplification methods for detecting copy number variation using hippocampal neurons. *Sci. Rep.* 5:11415. doi: 10.1038/srep11415
- Omsland, A., Cockrell, D. C., Howe, D., Fischer, E. R., Virtaneva, K., Sturdevant, D. E., et al. (2009). Host cell-free growth of the Q fever bacterium *Coxiella burnetii*. *Proc. Natl. Acad. Sci. U.S.A.* 106, 4430–4434. doi: 10.1073/pnas.0812074106
- Ottesen, E. A., Hong, J. W., Quake, S. R., and Leadbetter, J. R. (2006). Microfluidic digital PCR enables multigene analysis of individual environmental bacteria. *Science* 314, 1464–1467. doi: 10.1126/science.1131370
- Ozsolak, F., and Milos, P. M. (2011). Single-molecule direct RNA sequencing without cDNA synthesis. *Wiley Interdiscip. Rev. RNA* 2, 565–570. doi: 10.1002/wrna.84

- Ozsolak, F., Platt, A. R., Jones, D. R., Reifenger, J. G., Sass, L. E., McInerney, P., et al. (2009). Direct RNA sequencing. *Nature* 461, 814–818. doi: 10.1038/nature08390
- Pamp, S. J., Harrington, E. D., Quake, S. R., Relman, D. A., and Blainey, P. C. (2012). Single-cell sequencing provides clues about the host interactions of segmented filamentous bacteria (SFB). *Genome Res.* 22, 1107–1119. doi: 10.1101/gr.131482.111
- Picelli, S. (2016). Single-cell RNA-sequencing: the future of genome biology is now. *RNA Biol.* 14, 637–650. doi: 10.1080/15476286.2016.1201618
- Picelli, S., Bjorklund, A. K., Faridani, O. R., Sagasser, S., Winberg, G., and Sandberg, R. (2013). Smart-seq2 for sensitive full-length transcriptome profiling in single cells. *Nat. Methods* 10, 1096–1098. doi: 10.1038/nmeth.2639
- Picelli, S., Faridani, O. R., Bjorklund, A. K., Winberg, G., Sagasser, S., and Sandberg, R. (2014). Full-length RNA-seq from single cells using Smart-seq2. *Nat. Protoc.* 9, 171–181. doi: 10.1038/nprot.2014.006
- Picher, A. J., Budeus, B., Wafzig, O., Kruger, C., Garcia-Gomez, S., Martinez-Jimenez, M. I., et al. (2016). TruePrime is a novel method for whole-genome amplification from single cells based on *Tth*PrimPol. *Nat. Commun.* 7:13296. doi: 10.1038/ncomms13296
- Prakadan, S. M., Shalek, A. K., and Weitz, D. A. (2017). Scaling by shrinking: empowering single-cell 'omics' with microfluidic devices. *Nat. Rev. Genet.* 18, 345–361. doi: 10.1038/nrg.2017.15
- Qi, Z., Pei, G., Chen, L., and Zhang, W. (2014). Single-cell analysis reveals gene-expression heterogeneity in syntrophic dual-culture of *Desulfovibrio vulgaris* with *Methanosarcina barkeri*. *Sci. Rep.* 4:7478. doi: 10.1038/srep07478
- Qi, Z. H., Chen, L., and Zhang, W. W. (2016). Comparison of transcriptional heterogeneity of eight genes between batch *Desulfovibrio vulgaris* biofilm and planktonic culture at a single-cell level. *Front. Microbiol.* 7:597. doi: 10.3389/fmicb.2016.00597
- Raghunathan, A., Ferguson, H. R. Jr., Bornarth, C. J., Song, W., Driscoll, M., and Lasken, R. S. (2005). Genomic DNA amplification from a single bacterium. *Appl. Environ. Microbiol.* 71, 3342–3347. doi: 10.1128/AEM.71.6.3342-3347.2005
- Rainey, P. B., and Travisano, M. (1998). Adaptive radiation in a heterogeneous environment. *Nature* 394, 69–72. doi: 10.1038/27900
- Rinke, C., Schwiertek, P., Sczyrba, A., Ivanova, N. N., Anderson, I. J., Cheng, J. F., et al. (2013). Insights into the phylogeny and coding potential of microbial dark matter. *Nature* 499, 431–437. doi: 10.1038/nature12352
- Roberfroid, S., Vanderleyden, J., and Steenackers, H. (2016). Gene expression variability in clonal populations: causes and consequences. *Crit. Rev. Microbiol.* 42, 969–984. doi: 10.3109/1040841X.2015.1122571
- Saliba, A. E., Westermann, A. J., Gorski, S. A., and Vogel, J. (2014). Single-cell RNA-seq: advances and future challenges. *Nucleic Acids Res.* 42, 8845–8860. doi: 10.1093/nar/gku555
- Sasagawa, Y., Nikaido, I., Hayashi, T., Danno, H., Uno, K. D., Imai, T., et al. (2013). Quartz-Seq: a highly reproducible and sensitive single-cell RNA sequencing method, reveals non-genetic gene-expression heterogeneity. *Genome Biol.* 14:R31. doi: 10.1186/gb-2013-14-4-r31
- Shahi, P., Kim, S. C., Haliburton, J. R., Gartner, Z. J., and Abate, A. R. (2017). Abseq: ultrahigh-throughput single cell protein profiling with droplet microfluidic barcoding. *Sci. Rep.* 7:44447. doi: 10.1038/srep44447
- Shi, X., Gao, W., Chao, S. H., Zhang, W., and Meldrum, D. R. (2013). Monitoring the single-cell stress response of the diatom *Thalassiosira pseudonana* by quantitative real-time reverse transcription-PCR. *Appl. Environ. Microbiol.* 79, 1850–1858. doi: 10.1128/AEM.03399-12
- Siegl, A., Kamke, J., Hochmuth, T., Piel, J., Richter, M., Liang, C., et al. (2011). Single-cell genomics reveals the lifestyle of Poribacteria, a candidate phylum symbiotically associated with marine sponges. *ISME J.* 5, 61–70. doi: 10.1038/ismej.2010.95
- Song, Y., Kaster, A. K., Vollmers, J., Song, Y., Davison, P. A., Frentrup, M., et al. (2017). Single-cell genomics based on Raman sorting reveals novel carotenoid-containing bacteria in the Red Sea. *Microb. Biotechnol.* 10, 125–137. doi: 10.1111/1751-7915.12420
- Song, Y., Yin, H., and Huang, W. E. (2016). Raman activated cell sorting. *Curr. Opin. Chem. Biol.* 33, 1–8. doi: 10.1016/j.cbpa.2016.04.002
- Soumillon, M., Cacchiarelli, D., Semrau, S., van Oudenaarden, A., and Mikkelsen, T. S. (2014). Characterization of directed differentiation by high-throughput single-cell RNA-Seq. *bioRxiv*. doi: 10.1101/003236
- Stepanaukas, R. (2012). Single cell genomics: an individual look at microbes. *Curr. Opin. Microbiol.* 15, 613–620. doi: 10.1016/j.mib.2012.09.001
- Stepanaukas, R., and Sieracki, M. E. (2007). Matching phylogeny and metabolism in the uncultured marine bacteria, one cell at a time. *Proc. Natl. Acad. Sci. U.S.A.* 104, 9052–9057. doi: 10.1073/pnas.0700496104
- Stewart, E. J. (2012). Growing unculturable bacteria. *J. Bacteriol.* 194, 4151–4160. doi: 10.1128/JB.00345-12
- Swan, B. K., Martinez-Garcia, M., Preston, C. M., Sczyrba, A., Woyke, T., Lamy, D., et al. (2011). Potential for chemolithoautotrophy among ubiquitous bacteria lineages in the dark ocean. *Science* 333, 1296–1300. doi: 10.1126/science.1203690
- Tang, F., Barbacioru, C., Nordman, E., Li, B., Xu, N., Bashkurov, V. I., et al. (2010). RNA-Seq analysis to capture the transcriptome landscape of a single cell. *Nat. Protoc.* 5, 516–535. doi: 10.1038/nprot.2009.236
- Tang, F., Barbacioru, C., Wang, Y., Nordman, E., Lee, C., Xu, N., et al. (2009). mRNA-Seq whole-transcriptome analysis of a single cell. *Nat. Methods* 6, 377–382. doi: 10.1038/nmeth.1315
- Taniguchi, Y., Choi, P. J., Li, G. W., Chen, H., Babu, M., Hearn, J., et al. (2010). Quantifying *E. coli* proteome and transcriptome with single-molecule sensitivity in single cells. *Science* 329, 533–538. doi: 10.1126/science.1188308
- Telenius, H., Carter, N. P., Bebb, C. E., Nordenskjold, M., Ponder, B. A., and Tunnacliffe, A. (1992). Degenerate oligonucleotide-primed PCR: general amplification of target DNA by a single degenerate primer. *Genomics* 13, 718–725. doi: 10.1016/0888-7543(92)90147-K
- Thompson, A. W., Turkarslan, S., Arens, C. E., Lopez Garcia de Lomana, A., Raman, A. V., Stahl, D. A., et al. (2017). Robustness of a model microbial community emerges from population structure among single cells of a clonal population. *Environ. Microbiol.* 19, 3059–3069. doi: 10.1111/1462-2920.13764
- Tringe, S. G., von Mering, C., Kobayashi, A., Salamov, A. A., Chen, K., Chang, H. W., et al. (2005). Comparative metagenomics of microbial communities. *Science* 308, 554–557. doi: 10.1126/science.1107851
- Trout, A. B., McHeyzer-Williams, M. G., Pulendran, B., and Nossal, G. J. (1992). Ligation-anchored PCR: a simple amplification technique with single-sided specificity. *Proc. Natl. Acad. Sci. U.S.A.* 89, 9823–9825. doi: 10.1073/pnas.89.20.9823
- Turkarslan, S., Raman, A. V., Thompson, A. W., Arens, C. E., Gillespie, M. A., von Netzer, F., et al. (2017). Mechanism for microbial population collapse in a fluctuating resource environment. *Mol. Syst. Biol.* 13, 919. doi: 10.15252/msb.20167058
- van Gestel, J., Vlamakis, H., and Kolter, R. (2015). Division of labor in biofilms: the ecology of cell differentiation. *Microbiol. Spectr.* 3:MB-0002-2014. doi: 10.1128/microbiolspec.MB-0002-2014
- Vannier, T., Leconte, J., Seeleuthner, Y., Mondy, S., Pelletier, E., Aury, J. M., et al. (2016). Survey of the green picoalga *Bathycoccus* genomes in the global ocean. *Sci. Rep.* 6:37900. doi: 10.1038/srep37900
- Veening, J. W., Smits, W. K., and Kuipers, O. P. (2008). Bistability, epigenetics, and bet-hedging in bacteria. *Annu. Rev. Microbiol.* 62, 193–210. doi: 10.1146/annurev.micro.62.081307.163002
- Venter, J. C., Remington, K., Heidelberg, J. F., Halpern, A. L., Rusch, D., Eisen, J. A., et al. (2004). Environmental genome shotgun sequencing of the Sargasso Sea. *Science* 304, 66–74. doi: 10.1126/science.1093857
- Viney, M., and Reece, S. E. (2013). Adaptive noise. *Proc. Biol. Sci.* 280:20131104. doi: 10.1098/rspb.2013.1104
- Wang, J., Chen, L., Chen, Z., and Zhang, W. (2015). RNA-seq based transcriptomic analysis of single bacterial cells. *Integr. Biol. (Camb)* 7, 1466–1476. doi: 10.1039/c5ib00191a
- Wen, N., Zhao, Z., Fan, B., Chen, D., Men, D., Wang, J., et al. (2016). Development of droplet microfluidics enabling high-throughput single-cell analysis. *Molecules* 21:881. doi: 10.3390/molecules21070881
- Wolff, A., Perch-Nielsen, I. R., Larsen, U. D., Friis, P., Goranovic, G., Poulsen, C. R., et al. (2003). Integrating advanced functionality in a microfabricated high-throughput fluorescent-activated cell sorter. *Lab Chip* 3, 22–27. doi: 10.1039/b209333b
- Woyke, T., Sczyrba, A., Lee, J., Rinke, C., Tighe, D., Clingenpeel, S., et al. (2011). Decontamination of MDA reagents for single cell whole genome amplification. *PLOS ONE* 6:e26161. doi: 10.1371/journal.pone.0026161

- Woyke, T., Xie, G., Copeland, A., Gonzalez, J. M., Han, C., Kiss, H., et al. (2009). Assembling the marine metagenome, one cell at a time. *PLOS ONE* 4:e5299. doi: 10.1371/journal.pone.0005299
- Wu, D., Hugenholtz, P., Mavromatis, K., Pukall, R., Dalin, E., Ivanova, N. N., et al. (2009). A phylogeny-driven genomic encyclopaedia of Bacteria and Archaea. *Nature* 462, 1056–1060. doi: 10.1038/nature08656
- Xi, H. D., Zheng, H., Guo, W., Ganan-Calvo, A. M., Ai, Y., Tsao, C. W., et al. (2017). Active droplet sorting in microfluidics: a review. *Lab Chip* 17, 751–771. doi: 10.1039/c6lc01435f
- Yoon, H. S., Price, D. C., Stepanauskas, R., Rajah, V. D., Sieracki, M. E., Wilson, W. H., et al. (2011). Single-cell genomics reveals organismal interactions in uncultivated marine protists. *Science* 332, 714–717. doi: 10.1126/science.1203163
- Yu, F. B., Willis, L., Chau, R. M., Zambon, A., Horowitz, M., Bhaya, D., et al. (2017). Long-term microfluidic tracking of coccoid cyanobacterial cells reveals robust control of division timing. *BMC Biol.* 15:11. doi: 10.1186/s12915-016-0344-4
- Zhang, D. Y., Brandwein, M., Hsuih, T., and Li, H. B. (2001). Ramification amplification: a novel isothermal DNA amplification method. *Mol. Diagn.* 6, 141–150. doi: 10.1054/modi.2001.25323
- Zhang, K., Martiny, A. C., Reppas, N. B., Barry, K. W., Malek, J., Chisholm, S. W., et al. (2006). Sequencing genomes from single cells by polymerase cloning. *Nat. Biotechnol.* 24, 680–686. doi: 10.1038/nbt1214
- Zhang, Q., Wang, T., Zhou, Q., Zhang, P., Gong, Y., Gou, H., et al. (2017). Development of a facile droplet-based single-cell isolation platform for cultivation and genomic analysis in microorganisms. *Sci. Rep.* 7:41192. doi: 10.1038/srep41192
- Zhang, Q., Zhang, P., Gou, H., Mou, C., Huang, W. E., Yang, M., et al. (2015). Towards high-throughput microfluidic Raman-activated cell sorting. *Analyst* 140, 6163–6174. doi: 10.1039/c5an01074h
- Ziegenhain, C., Vieth, B., Parekh, S., Reinus, B., Guillaumet-Adkins, A., Smets, M., et al. (2017). Comparative analysis of single-cell RNA sequencing methods. *Mol. Cell* 65, 631–643.e4. doi: 10.1016/j.molcel.2017.01.023
- Zong, C., Lu, S., Chapman, A. R., and Xie, X. S. (2012). Genome-wide detection of single-nucleotide and copy-number variations of a single human cell. *Science* 338, 1622–1626. doi: 10.1126/science.1229164

Conflict of Interest Statement: The authors declare that the research was conducted in the absence of any commercial or financial relationships that could be construed as a potential conflict of interest.

Copyright © 2017 Chen, Chen and Zhang. This is an open-access article distributed under the terms of the Creative Commons Attribution License (CC BY). The use, distribution or reproduction in other forums is permitted, provided the original author(s) or licensor are credited and that the original publication in this journal is cited, in accordance with accepted academic practice. No use, distribution or reproduction is permitted which does not comply with these terms.



A Microfluidics and Agent-Based Modeling Framework for Investigating Spatial Organization in Bacterial Colonies: The Case of *Pseudomonas Aeruginosa* and H1-Type VI Secretion Interactions

Jared L. Wilmoth¹, Peter W. Doak², Andrea Timm¹, Michelle Halsted³, John D. Anderson³, Marta Ginovart⁴, Clara Prats⁵, Xavier Portell⁶, Scott T. Retterer^{1,2*} and Miguel Fuentes-Cabrera^{2,7*}

OPEN ACCESS

Edited by:

Dimitris G. Hatzinikolaou,
National and Kapodistrian University
of Athens, Greece

Reviewed by:

Thibault Géry Sana,
Stanford University, United States
Nuno F. Azevedo,
Universidade do Porto, Portugal

*Correspondence:

Miguel Fuentes-Cabrera
fuentescabma@ornl.gov
Scott T. Retterer
rettererst@ornl.gov

Specialty section:

This article was submitted to
Systems Microbiology,
a section of the journal
Frontiers in Microbiology

Received: 18 August 2017

Accepted: 09 January 2018

Published: 06 February 2018

Citation:

Wilmoth JL, Doak PW, Timm A,
Halsted M, Anderson JD, Ginovart M,
Prats C, Portell X, Retterer ST and
Fuentes-Cabrera M (2018) A
Microfluidics and Agent-Based
Modeling Framework for Investigating
Spatial Organization in Bacterial
Colonies: The Case of *Pseudomonas*
Aeruginosa and H1-Type VI Secretion
Interactions. *Front. Microbiol.* 9:33.
doi: 10.3389/fmicb.2018.00033

The factors leading to changes in the organization of microbial assemblages at fine spatial scales are not well characterized or understood. However, they are expected to guide the succession of community development and function toward specific outcomes that could impact human health and the environment. In this study, we put forward a combined experimental and agent-based modeling framework and use it to interpret unique spatial organization patterns of H1-Type VI secretion system (T6SS) mutants of *P. aeruginosa* under spatial confinement. We find that key parameters, such as T6SS-mediated cell contact and lysis, spatial localization, relative species abundance, cell density and local concentrations of growth substrates and metabolites are influenced by spatial confinement. The model, written in the accessible programming language NetLogo, can be adapted to a variety of biological systems of interest and used to simulate experiments across a broad parameter space. It was implemented and run in a high-throughput mode by deploying it across multiple CPUs, with each simulation representing an individual well within a high-throughput microwell array experimental platform. The microfluidics and agent-based modeling framework we present in this paper provides an effective means by which to connect experimental studies in microbiology to model development. The work demonstrates progress in coupling experimental results to simulation while also highlighting potential sources of discrepancies between real-world experiments and idealized models.

Keywords: agent-based modeling, *Pseudomonas aeruginosa*, Type VI secretion, silicon microwell arrays, microbial succession, microbial organization, spatial confinement

INTRODUCTION

Spatial organization has a strong influence on the development and dynamics of biological systems (Kreft et al., 1998; Lardon et al., 2011; Halsted et al., 2016; Hansen et al., 2016; McNally et al., 2017; Timm et al., 2017). The factors leading to changes in organization of multicellular assemblages at fine spatial scales are not well characterized or understood, however, they are expected to guide the succession of community development and function toward specific outcomes (Liu et al., 2009; Cline and Zak, 2015; Dini-Andreote et al., 2015). The organization of distinct microbial populations can be shaped by physical and chemical processes, and affect important activities such as antibiotic resistance, efficient energy conversion, C and N cycling and quorum sensing (Ginovart et al., 2005; Gras et al., 2010, 2011b; Sahari et al., 2014; Wang and Ma, 2014; Koonin and Wolf, 2015; Biteen et al., 2016). Microbe-microbe interactions can also depend on direct and indirect competition for resources between different community members (Kreft, 2004; Hellweger et al., 2008; Borenstein et al., 2015; McNally et al., 2017). The microscale/local transport of essential microbe-derived metabolites and cell-to-cell competition are likely to be strongly influenced by spatial confinement and individual cell behavior in the environment (Lardon et al., 2011; Pintelon et al., 2012; Vogel et al., 2015; McNally et al., 2017). Consequently, investigating the complexity of these processes and emergence of unique behaviors requires the combination of experimental and computational tools that can be used to explore the impact of spatial organization, while correlating individual microbial behavior and interactions to specific outcomes (Dini-Andreote et al., 2015; Zhu et al., 2015; Hansen et al., 2016).

Cells can compete directly with surrounding species through physical contact, and in more specialized cases, are capable of transferring toxic effector proteins to susceptible cells. The Type VI secretion system (T6SS) is an important example of such a pathway, being responsible for the assembly of a pilus apparatus that can be used to contact neighboring cells and potentially induce cell death (Hood et al., 2010; Chou et al., 2012; LeRoux et al., 2012). Hood et al. (2010) showed that the H1-T6SS of *Pseudomonas aeruginosa* is required to direct the injection of toxins from T6SS active cells (T6SS+) into T6SS-susceptible cells (T6SS-) that lack immunity. Other important secretion systems such as H2- and H3-T6SS in *P. aeruginosa* direct toxins preferentially to eukaryotic cells. However, because the H1-T6SS toxin is preferentially directed toward other bacteria, it is particularly well suited for studies of contact-mediated interactions between neighboring and competing prokaryotes (Mougous et al., 2006; Sana et al., 2016, 2017). T6SS interactions in mixed microbial populations also play an important role in the regulation of more complex biological processes and microbial community dynamics (Russell et al., 2014; Verster et al., 2017). For instance, the T6SS interactions occurring amongst commensal bacteria in the mammalian gut microbiome have been shown to modulate community composition and interactions, as well as provide a mechanism for defending commensal bacteria from invading pathogens (Hecht et al., 2016). Furthermore, these T6SS interactions are highly active and

prevalent, where $> 10^9$ T6SS firing events (i.e., predicted pilus injections) $\text{min}^{-1} \text{g}^{-1}$ colonic contents can occur and nearly 25% of human gut microbiota have been shown to encode a T6SS pathway (Wexler et al., 2016; Sana et al., 2017).

Using two-member communities as a model system of T6SS interactions in the laboratory, Borenstein et al. (2015) demonstrated that established colonies of T6SS- *Escherichia coli* could survive contact with T6SS+ *Vibrio cholerae*. Agent-based modeling (ABM) simulations further showed that T6SS- cells could survive T6SS+ attack when placed in situations of nutrient limitation and relatively slow growth rates, and could even outcompete the T6SS+ cells, as long as T6SS- cells were able to establish microcolonies within the mixed community (Borenstein et al., 2015). These results demonstrate the importance of spatial confinement and local organization on cell growth and survival. Thus, competition between neighboring microbial cells and spatial confinement are expected to drive changes in cell assemblage and organization (Borenstein et al., 2015; Halsted et al., 2016; Hansen et al., 2016).

Numerous advances in our understanding of cell-to-cell behavior and interactions at fine spatial scales have stemmed from the use and development of nano/micro-fabricated platforms (Wang et al., 2013; Yamazaki et al., 2014; Swennenhuis et al., 2015; Xue et al., 2015; Hansen et al., 2016; Zhang et al., 2016; Timm et al., 2017; Yeh et al., 2017). Timm et al. (2017) used a microwell array platform to study the contact-mediated T6SS interactions of *P. aeruginosa*. The microwell array platform enabled high-resolution and high-throughput imaging of mixed T6SS+ and T6SS- cells growing under spatial confinement within microwells, with well diameters ranging from 20 to 100 μm and 5 μm depth. Interpreting the results of these cell-to-cell interactions with simplified analytical models of overall growth within each well becomes challenging and potentially unreliable when trying to capture the complex interactions reflected by spatial organization of microorganisms within the microwells. Alternatively, ABM simulations can capture how changes at the level of individual microbial interactions lead to changes observed at the community and microcolony levels. In conjunction with laboratory experiments ABM simulations can be used to infer and test important growth parameters that impact spatial organization within colonies (Borenstein et al., 2015).

In this study, we have developed an ABM model around experimental data obtained from a microwell array platform. We use the model to interpret spatial organization patterns of *P. aeruginosa* mutants growing under spatial confinement. The novelty of our approach relies on the high throughput nature of both the experiment and ABM simulations, which allows investigating how the initial ratio of community member abundances, initial growth location and T6SS interactions affect spatial organization during growth. The model is written in the language NetLogo (Wilensky(1999), NetLogo, <http://ccl.northwestern.edu/netlogo/>; Center for Connected Learning and Computer-Based Modeling, Northwestern University, Evanston, IL) and is linked to a computational framework that permits submitting many calculations in parallel for different initial parameters, where each combination of parameters can be

conceptualized to represent a micro-environment of interest. The ABM model has been deployed in the Compute and Data Environment for Science, CADES (<http://cades.ornl.gov/>), which also stores the relevant experimental data used during fitting routines. We find that key parameters, such as spatial constraints, local concentrations of growth substrates/metabolites and associated rate constants alter the impact of *P. aeruginosa* Type VI secretion activity on the spatial organization of cells in confined environments.

MATERIALS AND METHODS

Bacterial Cell Culture

Two *P. aeruginosa* PAO1 mutants were modeled during growth simulations to investigate the effects of Type VI secretion on cell organization. Cultures included a Δ retS mutant that constitutively expresses GFP and the toxic effector proteins associated with Type VI secretion, and a Δ retS/ Δ tse/il-6 deletion mutant that constitutively expresses m-Cherry and is susceptible to Type VI secretion interactions (i.e., injection of toxic effector proteins) (Timm et al., 2017). Cell culture conditions for growth experiments followed Hood et al. (2010) and Timm et al. (2017).

Microwell Fabrication

Fabrication of Si microwells followed the methods outlined in (Hansen et al., 2016). Briefly, a 1 μ m parylene film was deposited on a 4 inch diameter silicon wafer with a silicon dioxide coating. An adhesion promoter and positive photoresist were spun onto the wafer with a spin coater, followed by 1 min of baking on a hot plate at 115°C. The substrate was exposed to UV light using a contact mask aligner, baked on a hot plate for an additional minute at 115°C, then developed. The parylene exposed in the patterned photoresist was etched with O₂ plasma in a Reactive Ion Etch (RIE), and was followed by a Bosch process to etch into the silicon to form microwells. Residual photoresist was removed by etching with O₂ plasma. The final well depth was 5 μ m. The layout of the microwell platform can be found in Hansen et al. (2016). It contains arrays of microwells ranging in size from 5 to 50 μ m in diameter, in increments of 5 microns, along with wells that are 100 μ m in diameter. Twelve arrays of each size, including four replicates of three different well spacing, are included in each array. Individual microwell-array chips were sectioned from the Si wafers and subsequently used for growth experiments with *P. aeruginosa* mutants.

Microwell Culture Experiments and Image Analysis

The cell-seeding, growth, imaging and image analysis methods used in this study correspond to those described in Timm et al. (2017). Timm et al. (2017) provides a detailed step-by-step description of those protocols along with online video content displaying those techniques. Representative data, as well as the image collection and correction procedures, are provided there. Specifically, we provide additional analysis of a more comprehensive data set and describe the development of a new ABM framework that helps explain some of the unresolved

questions reported by Timm et al. (2017). Briefly, cells of *P. aeruginosa* were mixed in a 1:2 ratio (GFP:m-Cherry) suspended in growth media and incubated on bovine serum albumin (BSA)-functionalized microwell chips in a humid environment for 1 h (Timm et al., 2017). The number of cells that attach within any given well is dependent on the number of cells present in solution and the time allowed for the cells to attach. Not all of the cells will attach inside a microwell during a 1 h interval. Some cells remain in suspension or attach outside of the wells on the parylene cover. Following 1 h incubation the solution is removed and the parylene is peeled, leaving behind only cells that were attached inside the wells. The entire microwell array is then sealed under a nutrient agarose layer and grown in a live cell chamber on an automated microscope stage. Details of fluorescence microscopy used to measure growth are given in Timm et al. (2017). Images were collected every 30 min over a 24 h period, and were then processed and analyzed using ImageJ and Matlab software (Timm et al., 2017). Data presented here is taken from images collected from multiple chips imaged during experiments performed on different days. Experimental data for co-culture experiments represents analysis from 63 (20 μ m), 35 (25 μ m), 49 (30 μ m), 16 (35 μ m), 16 (40 μ m), 16 (45 μ m), 16 (50 μ m), and 4 (100 μ m) wells. Mono-culture experiments were performed as controls, with equivalent numbers of wells examined for T6SS+ and T6SS− only cultures at each well size. Representative images taken from a single 100 μ m diameter well are shown in **Figure 1A**. Growth curves were established by measuring total fluorescence from both GFP and m-Cherry expressing mutants over time in each well and corrected for background fluorescence (Timm et al., 2017).

Analysis of Experimental Imaging Data

A multi-stage fitting was performed on both the ABM population curves and time series fluorescence data corresponding to the experimental population curves of T6SS+ and T6SS− in each well. Using a derivative zero crossing algorithm, the growth period of each fluorescence series was separated from the decay stage (**Figure 2**). The data from the cell growth period was then fit to the logistic function, Equation 1, using the least squares Trust Region Reflective algorithm implemented in the Python scipy 0.19.0 library:

$$\frac{a}{1 + e^{\frac{4\mu}{a}(\tau - t)} + 2} + a_0 \quad (1)$$

where a_0 is the initial fluorescence intensity, which reflects the number of living cells present inside the well at the beginning of the experiment. In this form, a is the maximum intensity, μ is the maximum growth rate and τ is the lag time. The analysis presented in this paper deals exclusively with observations of the growth phase. The parameters a , μ and τ for each well were collected and a and μ scaled as shown in (Eq. 2) to represent per unit intensity values; the scaled a' , μ' , and τ were then plotted vs. the initial ratio T6SS+:T6SS− for each well size and a linear fit was performed. The slope of each line, i.e., a'/ratio , μ'/ratio and τ/ratio , for each well was then plotted vs. all the well sizes.

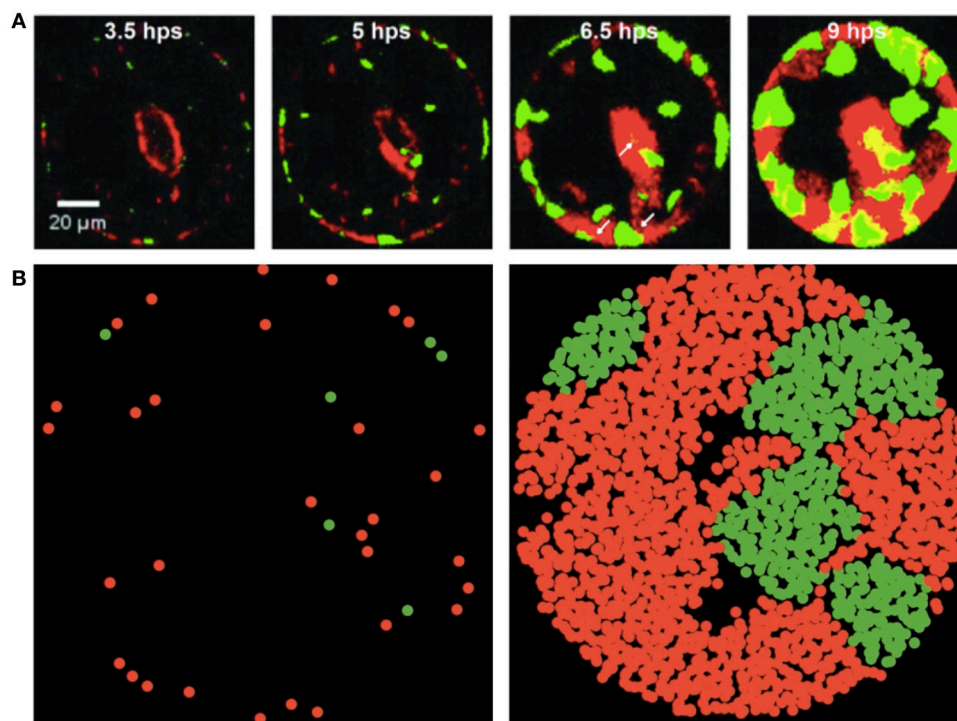


FIGURE 1 | Experimental and simulated images of *P. aeruginosa* T6SS+ and – mutants during growth in microwells (green and red fluorescence, respectively). **(A)** Mutants shown during growth in 100 μm well and images collected with a fluorescence microscope at 3.5, 5, 6.5 and 9 h post seeding (hps). Scale bar is 20 μm. Experimental images are those presented in Figure 6 of Timm et al. (2017) and reproduced here with permission. Further analytical details of how the images were acquired can be found in Timm et al. (2017). **(B)** Early and late stages of simulated growth using the agent-based model (left to right).

$$\begin{aligned} a' &= \frac{a}{a_0} \\ \mu' &= \frac{\mu}{a_0} \end{aligned} \quad (2)$$

ABM Development and Simulations

The model is described following the protocol ODD (Overview—Design Concepts—Details) that was initially established by Grimm et al. (2006) and later revised and updated by Grimm et al. (2010). This protocol was specifically developed in order to provide a standard way to describe ABMs, so that both the basic features and the details of the models could be correctly communicated to the scientific community. In the following, we provide a concise description of our particular ABM (see full details in the Supplementary text and **Supplementary Figure 1** flowchart).

The basic principles of the bacterial model and protocol system developed here are taken from the INDISIM model (Ginovart et al., 2002; Gras and Ginovart, 2006; Gras et al., 2011a; Granda et al., 2016). The basic entities of our model represent bacterial cells of the two *P. aeruginosa* mutants, including the $\Delta retS$ mutant (T6SS+) and the $\Delta retS/\Delta tse/i1-6$ deletion mutant (T6SS–) that is susceptible to Type VI secretion (Hood et al., 2010), and spatially confined areas (or grids) of a two-dimensional circular well that represents the growth

environment on the microwell array chip used for laboratory experiments. The bacterial cells are defined by several individual variables and parameters: bacterial species (T6SS+ or T6SS–), mass, mass to initiate the division process, energy, and viability. Spatial grid variables contain the local content of a carbon (C) source, together with the x-y spatial coordinates. Global variables account for the global balance of bacteria (in terms of number and biomass for each of the two mutants of *P. aeruginosa*) and nutrient source, as well as the emerging bacterial and biomass mean growth rates, and the bacterial biomass distributions. The model can simulate a population of up to 10^5 bacterial cells in spatial grid domain. This is a qualitative version of the model as it currently uses values that are given in relative units.

It is assumed that bacteria are able to respond to and detect the nutrient concentration in the space in which they are located. Both T6SS+ and T6SS– bacteria are modeled to consume resources at the same rate. The nutrient consumption is adjusted according to its local availability and the uptake is driven by the local concentration of available C. Cell movement and reproduction may also be driven by the occupation of the surrounding growth space. The mutants interact by direct cell-to-cell contact via the Type VI secretion system and, in this case, a T6SS+ can kill a contacted T6SS– cell. Additionally, indirect interaction can occur through the competition for available C and for the occupation of space. Stochasticity is introduced through setting initial individual locations at random by using a Gaussian

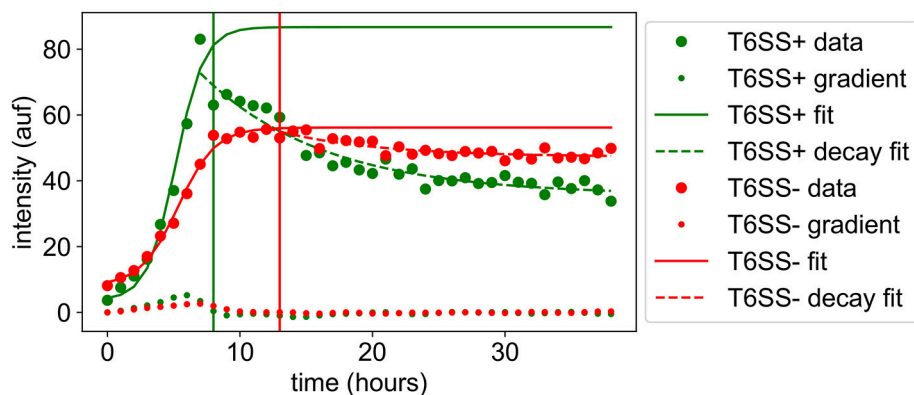


FIGURE 2 | Growth trajectories of *P. aeruginosa* T6SS+ and – mutants during growth in microwells (green and red lines, respectively). Experimental data from 30 μm wells are shown as closed circles. Solid lines show the logistic fit to the growth phase. Dotted lines show the fit of an exponential to the decay phase. The gradient zero crossing used as the division between the growth and decay phases is shown by a vertical line in the plot. Vertical y-axis values represent the relative microbial population (pop) abundances based on corrected fluorescence intensities and horizontal x-axis values represent time in hours. The notation auf stands for arbitrary units of fluorescence intensity.

distribution around an expected mean value (initial individual mass, mass to start the reproduction cycle, viability time and cell lysis when optimal conditions for cellular maintenance are not met). Random variation is applied to individuals within grid spaces to deal with the initiation of the reproduction cycle in each bacterium and with the change in location of cells. For instance, the model permits assigning a probability of initial growth at the edge of the well, a behavior that, as it will be discussed later, is observed experimentally. Moreover, in the predation process by T6SS+ cells, randomness is considered in the identification of a neighboring T6SS– cell. This randomness accounts for the uncertainty in these processes and reflects the high variety of mechanisms that underlie the variability observed in real systems. In order to avoid privileged first-acting bacteria in the model, the order of the bacteria to perform simulated actions is chosen randomly at each time step.

Overall, the execution of the model consists of four main parts: (1) initialization of the system, where the initial population of T6SS+ and T6SS– mutants are defined and distributed according to the user's input parameters, the spatial cells are set up with the corresponding initial amount of nutrient, and global variables are formally evaluated for the first time; (2) the core of the simulation, with the main loop where all the individual actions and environmental processes take place iteratively until the end of the simulation; (3) the output of results at the end of each time step, both graphical representation and numerical evaluation, as well as a final external text file with the simulation outcome for further analysis; (4) analysis of the results and comparison to experimental data.

The population curves obtained with the ABM model were fit using Equation 1 and scaled as in Equation 2, and the resultant parameters a' , μ' , τ plotted vs. the initial T6SS+:T6SS– ratio, similarly to what it was done with the experimental parameters. The ABM model, however, contains many input values that define a very large parameter space, where different results are obtained by using a different set of input values. In this paper, we

have chosen to inspect a range of input values in order to examine how the level of aggressiveness of T6SS+ cells affect the outcomes of the simulations. Specifically, for each well and T6SS+:T6SS– initial ratio, 100 simulations were run, each corresponding to the same set of input values. To mimic the experimental conditions better, T6SS+ and T6SS– cells were initially constrained to areas corresponding to the well dimensions, and the bacteria were added in initial ratios and densities corresponding to those observed in the experimental wells of the same size.

RESULTS

Previously, Timm et al. (2017) demonstrated that the GFP ΔretS mutant T6SS+ and the m-Cherry $\Delta\text{retS}/\Delta\text{tse}/\text{i1-6}$ deletion mutant T6SS– that is susceptible to Type VI secretion, formed discrete microcolony assemblages during co-growth in microwells. Observed well populations were heterogeneous (Figure 1A) with distinct assemblages of individual species forming across the wells. Instances of T6SS– microcolony formation were unexpected based on the hypothesis that T6SS+ cells would dominate each well environment due to their directed injection of toxic effector proteins into susceptible cells. In the present study, we used ABM simulations (Figure 1B) to examine how spatial confinement and Type VI secretion can lead to growth conditions that allow the formation of microcolony assemblages and enable susceptible T6SS– cells to persist.

In Figure 3, we show how the experimental values for a' , μ' , τ change with the initial T6SS+:T6SS– seeding ratio for both types of cells in 30 μm diameter wells. Although the initial ratio of cells in the solution used to seed the wells is 1:2, natural variability in the number of cells of each type that seed into the wells provides initial ratios ranging between nearly 0 (all T6SS–) to 3:1 (3 times more T6SS+ than T6SS–). For both types of cells, τ is practically independent of the initial ratio, whereas a' and μ' for T6SS+ linearly decrease as the T6SS+:T6SS– ratio increases. Likewise,

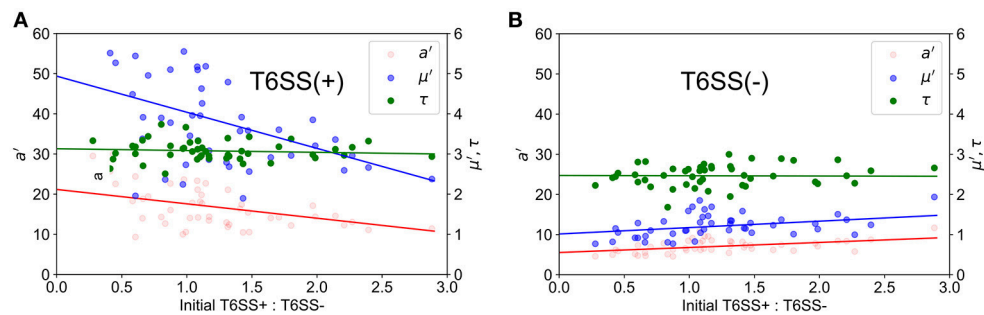


FIGURE 3 | Experimental growth parameters vs. initial relative ratios of mutants. a' (red), μ' (blue) and τ (green) variables refer to maximum corrected fluorescence intensity (i.e., maximum relative cell abundance), maximum rate in change of fluorescence intensity (i.e., relative growth rate) and lag time to start of growth, respectively. Closed circles indicate corrected experimental data and lines represent regression trends. **(A)** T6SS+ growth parameters as a function of initial relative ratios of mutants when both mutants are grown together. **(B)** T6SS- growth parameters as a function of initial relative ratios of mutants when both mutants are grown together.

μ' and a' values decrease as cultures have an increasing number of T6SS- cells compared to T6SS+. For both T6SS- and T6SS+ the maximum number of cells per initial number of cells (a'), as well as the maximum rate of increase per initial numbers of cells (μ'), decreases as the corresponding cell type is initially present in excess. As seen in **Figure 4**, for each 30 μm well, the initial density is relatively constant, independent of the initial T6SS+:T6SS- ratio. Cells are, for the most part, segregated into domains that contain either T6SS + or - cells. The latter is observed both in experiment and simulations (**Figures 1A,B**, respectively), though some overlap can be seen within the experimental images (**Figure 1A**, yellow region). We speculate that larger clusters or colonies of cells will grow more slowly on a per cell basis because of nutrient limitations that may occur at the center of those microcolonies relative to growth at the edges. Thus, even though the overall density within the wells is the same, local microcolony size may influence the maximum growth rate per initial number of cells (μ') and maximum number of cells per initial number of cells (a'). A more detailed image analysis strategy that allows quantitative description of microcolony size and patchiness within wells throughout these experiments is warranted and under development.

During growth on the experimental microwell platform, both T6SS + and - cells showed a general preference for seeding at the well edges regardless of well size (Timm et al., 2017). During ABM-simulated growth in a circular well with preferential seeding at the boundaries, microcolony formation qualitatively mirrors the experimental results of Timm et al. (2017) (**Figure 1**) though, again, a more quantitative analysis of microcolony size and patchiness within wells is needed to make a direct comparison. In the simulations, the cell placement is biased so that there is a higher probability of cells beginning the simulation at the edges of a well. Cells seeded near the edge of wells, in both the experiments and the simulations, propagate toward the interior because of confinement imposed by the well edge. Based on the contact mediated pathogenesis associated with T6SS interactions, we expect that subsequent cell-to-cell interactions would help maintain bacterial domain segregation and minimize co-localization.

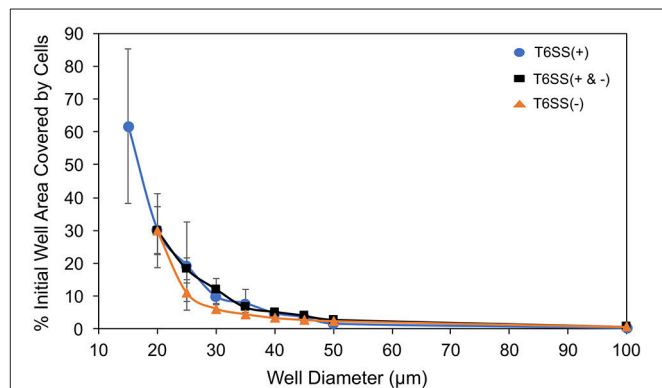
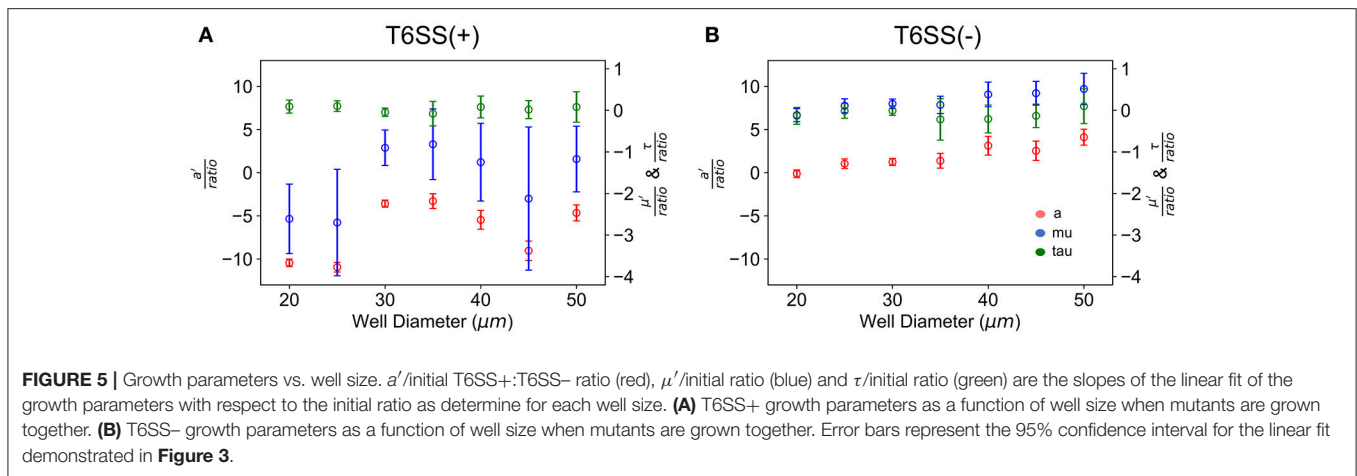


FIGURE 4 | Well area (%) covered by initially seeded cells vs. well size. T6SS+ mutant only data (blue circle), combined mutant data (black square) and T6SS- mutant only data (orange triangle). The expected ratio of T6SS(+):(-) was 1:2. Error bars represent standard deviations around the mean value.

In **Figure 5** we have plotted the slope of the straight lines, i.e., a'/ratio , μ'/ratio and τ/ratio , for each well size vs. the well diameter. In the case of T6SS+ cells, the slope of these lines shows more variation than that seen for T6SS- cells. The reason for this remains unclear and may result from T6SS+ cells growing outside the wells and outside the analytical region of interest (see **Supplementary Movie 1**). Also, fluctuations in GFP expression or loss of GFP intensity may contribute to this variation across experiments. For T6SS- cells, the sensitivity (slope, μ'/ratio and a'/ratio) of maximum growth rate per initial number of T6SS-cells and maximum number of cells per initial number of cells, increases slightly with well diameter. **Figure 4** shows that the initial seeded cell density per well on the experimental platform decreased as a function of increasing well diameter between 15 and 100 μm . One might expect that at lower cell densities, the sensitivity to initial ratio of T6SS+ to T6SS- cells would decrease because lower densities should correspond to fewer T6SS+ to T6SS- interactions. However, if increasing microcolony size is suspected



to cause reductions in μ' and a' , as described above, larger wells could facilitate formation of these larger domains by (i) allowing unimpeded growth of microcolonies and (ii) increasing the possibility for the seeding of larger microbial aggregates or flocs from solution. Again, more detailed image analysis techniques should facilitate future investigations using the array platform.

Using the ABM model, we performed a similar study of microcolony formation in a population of T6SS+ and T6SS- cells, where the aggressiveness of the former was changed from high to moderate to low. For simulating the experimental conditions closely, we computed the experimental distribution of T6SS+:T6SS- initial ratios and densities and used similar initial values in the simulations. The results of the simulations are shown in **Figure 6** for a well size of 30 μm , where we have plotted a' , μ' and τ for initial T6SS+:T6SS- ratios that resemble those obtained experimentally. When the aggressiveness was 1 (i.e., each contact occurring between a T6SS+ and a T6SS- cell results in the death of a T6SS- cell), the behavior of a' , μ' and τ for T6SS+ resembles that seen experimentally (compare **Figure 6A** to **Figure 3A**). The opposite is true for T6SS- cells (**Figure 6B** vs. **Figure 3B**), and the results indicate that the fewer T6SS- there are present, the more poorly T6SS- cells grow. The trend seen in **Figure 6B** for T6SS- cells can be explained as follows: while T6SS+ cells are not affected by their own aggressiveness, T6SS- cells are, and although it is theoretically advantageous for T6SS- cells to have relatively fewer neighboring T6SS- competitors, this advantage is offset by a high rate of lysis caused by the highly aggressive T6SS+ cells. Lowering the aggressiveness of T6SS+ from 100 to 10% does not significantly change the behavior of a' , μ' and τ for both T6SS+ and T6SS- mutants (**Figures 6C,D**). However, if the aggressiveness is lowered to 1% (**Figures 6E,F**), then a' and μ' of T6SS- cells follow the same trend as in the experiment (**Figure 3B**). At this low killing rate, however, the growth rate of T6SS+ cells decreases (compare **Figure 6E** to **Figure 3A**). Specifically, as the aggressiveness of T6SS+ cells is reduced, the linear fit of a' intersects the y-axis at a lower point. Thus, at lower abundances and lower levels of aggressiveness, T6SS+ cells can no longer effectively compete with T6SS- cells.

DISCUSSION

The T6SS of *P. aeruginosa* is an important biological model for understanding how cell-to-cell contact directs the succession and organization of microbial communities (Robinson et al., 2009; Hood et al., 2010; Sarris and Scoulica, 2011; LeRoux et al., 2012; Das et al., 2013). As mentioned in the introduction, T6SS interactions play a significant role in the regulation of microbiomes, which has important implications for biomedical and pathogen research, particularly for understanding mammalian gut microbiomes, and also environmental biogeochemistry relevant to native microbial interactions with plants and soil. However, the factors leading to changes in organization of microbial cells at fine spatial scales, driven by T6SS interactions, are not well characterized or understood. Recent laboratory investigations and ABM simulations indicated that established T6SS- colonies of *Escherichia coli* could persist during cell-to-cell interactions with *Vibrio cholerae* T6SS+ cells (Borenstein et al., 2015). The results of Timm et al. (2017) further suggested that spatial confinement, as well as T6SS activity between growing effector and susceptible *P. aeruginosa* mutants, could potentially direct cell organization in micro-colonies and affect the survival of susceptible cells. In the present study, building upon additional analysis of the complete dataset of Timm et al. (2017), and in combination with ABM simulations, we provide supporting evidence that both spatial confinement and T6SS activity can lead to changes in the organization and persistence of *P. aeruginosa*.

We found that discrete zones of clearing occurred around T6SS- cell assemblages during co-growth with T6SS+ cells in ABM simulations (**Figure 1**; see also **Supplementary Movie 2**). This cell-to-cell organization of T6SS- cells, surrounded by a zone of clearing, is consistent with T6SS-induced cell lysis at the boundary between both *P. aeruginosa* mutants (Hood et al., 2010; Borenstein et al., 2015). This zone of clearing provides a mechanism of *P. aeruginosa* cellular organization, as previously observed in Si-based microwell arrays (Timm et al., 2017). We speculate that during growth of both mutant strains, these buffer zones can occur randomly during growth, perhaps forming

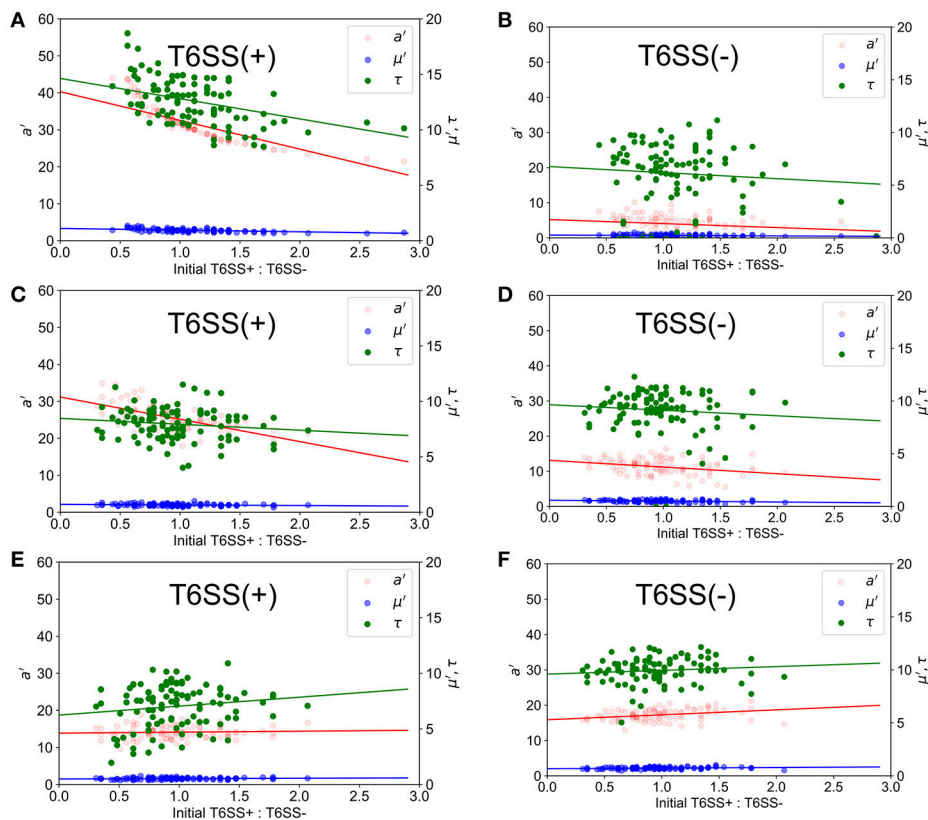


FIGURE 6 | Simulated growth parameters vs. initial relative ratios of mutants. a' (red), μ' (blue) and τ (green) variables refer to maximum corrected fluorescence intensity (i.e., maximum relative cell abundance), maximum rate in change of fluorescence intensity (i.e., relative growth rate) and lag time to start of growth, respectively. Closed circles indicate ABM data and lines represent regression trends. (Left) T6SS+ growth parameters as a function of initial relative ratios of mutants when both mutants are grown together. (Right) T6SS- growth parameters as a function of initial relative ratios of mutants when both mutants are grown together. Aggressiveness of the T6SS+ in an immediate kill mode was set to a probability of kill on attack of 1.0 (A,B), 0.1 (C,D), and 0.01 (E,F).

safe-pockets for susceptible cells to continue growing, and can become more defined as microcolonies of both species expand and interact at their outer boundaries. Fitting of the complete experimental dataset indicated that starting at the apparent peak in cell growth for both strains, a general decay in T6SS+ GFP signal intensities began, while T6SS- m-Cherry intensities subsequently remained more persistent over time (Figure 2). Borenstein et al. (2015) demonstrated that more-established microcolonies of T6SS-susceptible cells can potentially survive T6SS attack, which helps explain the persistence of susceptible *P. aeruginosa* mutants as deduced from the fluorescence intensities taken from our experimental data. We also observed that T6SS+ cells could outgrow a well once the interior of the well cavity had become nearly filled by growing cells (Supplementary Movie 1); this may explain, to some extent, the sharp decay phase generally observed for T6SS+ GFP intensities (Figure 2).

We found that the initial seeded cell density per well on the experimental platform decreased as a function of increasing well diameter between 15 and 100 μm (Figure 4), but cell density did not have an apparent effect on cell organization during different growth simulations, which is consistent with the results of Timm et al. (2017) that demonstrated microcolony formation

across all well sizes between 20 and 100 μm diameters. The correlation between initial cell density after seeding and well size likely reflects the preparation of the experimental microwell platform. For instance, following the experimental cell seeding step (Timm et al., 2017): (1) slight drying of the aqueous culture media before contact with the nutrient agarose cover; (2) difficulty rinsing cells from smaller diameter wells during the final water rinse step; or (3) a larger side-wall to floor area ratio per well could have affected initial cell densities such that smaller wells were more densely packed than larger wells, particularly at well edge boundaries. However, qualitatively, we found that spatial organization into distinct T6SS mutant assemblages during experimental and simulated growth was not strongly influenced by cell density or close packing. Future quantitative analysis of assemblage size and spacing for different well sizes may reveal a more defined mechanism. Densely packed cell assemblages have been shown in previous studies to follow similar biological-phase separation where distinct microcolony formation is favored regardless of cell-to-cell density in spatially confined environments (Tolker-Nielsen and Molin, 2000; Berk et al., 2011; Borenstein et al., 2015; Cutler et al., 2015; McNally et al., 2017).

We generally found the impact of well size to be negligible for the size ranges explored in experiments, see **Figures 5A,B**. Well size did not have a significant impact on overall growth rates per initial cell number or maximum growth rate per initial cell number. This was unexpected. Indeed, in well diameters $<25\ \mu\text{m}$, competition for resources and cell-to-cell interactions would have been expected to suppress T6SS $-$ growth. Reductions in spatial confinement within larger wells would, in principle, allow T6SS $-$ cells to grow more efficiently with increasing well diameters, reducing the likelihood of encountering T6SS $+$ because of the lower seeding densities and more available area. In wells of $45\ \mu\text{m}$ diameter and greater, at much lower initial densities (**Figure 4**), the individual T6SS $-$ colonies may have had the potential to develop with less competition and become more established before interacting with the more aggressive mutant strain. In this case, the perimeter of T6SS $-$ interactions around a colony would be overshadowed by the more established interior of each mutant colony. In other words, with larger wells above 40 microns, T6SS-killing should have become secondary to the size of mutant colonies by the time they interact at their edges. Clearly, a more systematic study of micro-colony size and distribution is needed to understand these results. The behavior of T6SS $+$ cells across well sizes displays variation in the data that makes it difficult to draw specific conclusions about T6SS $+$ growth as a function of well size.

Finally, average a' , μ' and τ for each well size vs. the entire well size distribution were also calculated, see **Figure 7**; the results obtained in a mixed population of T6SS $+$ and T6SS $-$ cells were compared to those obtained in control experiments

comprising only one cell type. As seen in **Figure 7D**, for the control experiments, the average a' , μ' and τ of T6SS $-$ cells are practically insensitive to the well size, whereas the same data for T6SS $+$, **Figure 7C**, shows variation and an increase at larger well sizes. In mixed populations, the data for T6SS $-$ cells shows a similar trend, **Figure 7B**, although the error bars are larger, illustrating the interactions with T6SS $+$ cells. The data for T6SS $+$ cells, **Figure 7A**, shows even larger error bars, which is surprising because these cells should not be negatively impacted by the presence of T6SS $-$ strains. As mentioned above, inspection of the data reveals that on some occasions T6SS $+$ cells can outgrow/leave the well boundaries (**Supplementary Movie 1**). We believe this is one of the primary reasons for the large variation observed in **Figures 7A,B**. Consequently, whether or not T6SS $+$ cells outgrow or escape the wells should also affect the growth of T6SS $-$ cells remaining within the same wells.

In this study we have developed an experimental-ABM framework that can be used to interpret unique spatial-organization patterns of *P. aeruginosa* cells growing under spatial confinement. The ABM model developed here, although qualitative, is capable of showing microcolony formation regardless of initial density, or whether the bacteria prefer to begin growth at the well edges, which is consistent with other recent studies that have examined different microbial species under T6SS interactions. Our model was also capable of reproducing the behavior of a' , μ' and τ of T6SS $+$ cells for a particular well size, and the same was true for T6SS $-$ cells once the aggressiveness level of T6SS $+$ cells was lowered. As such, this model can be used to extract

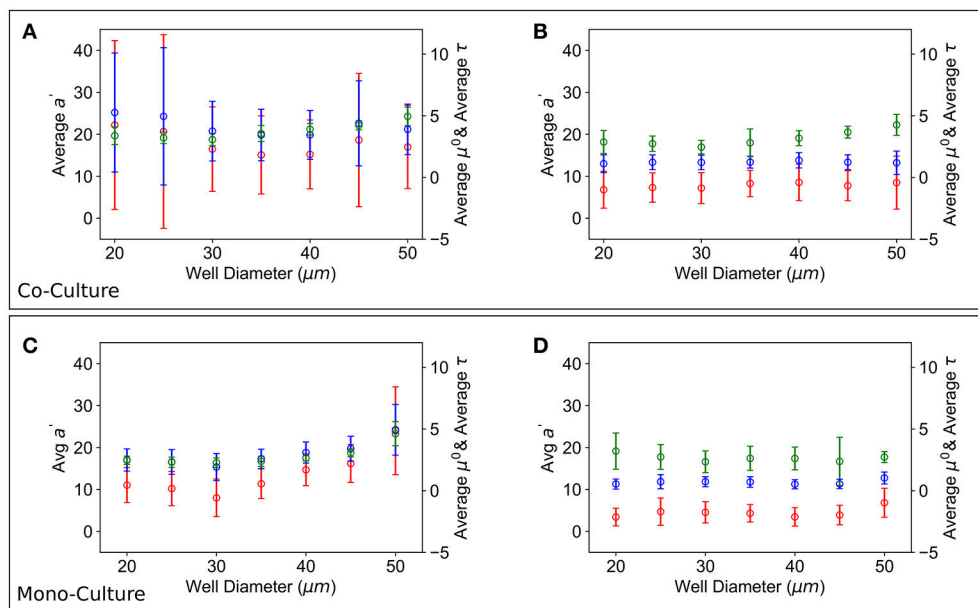


FIGURE 7 | Growth parameters vs. well size. Average a' (red), μ' (blue) and τ (green) growth parameters over all the T6SS $+$:T6SS $-$ initial ratios across wells of different size. **(A)** T6SS $+$ average growth parameters as a function of well size when mutants are grown together. **(B)** T6SS $-$ average growth parameters as a function of well size when mutants are grown together. Error bars represent the 95% confidence interval for the linear fit demonstrated in **Figure 3**. **(C,D)** Panels show equivalent parameters in monoculture.

information regarding aggressiveness levels, amount of available resources, and rate of consumption of nutrients, as well as how all these variables affect the growth of the bacterial colony. Yet, there are some uncertainties that the current model does not take into account. Future work will focus on optimizing the model by identifying the most essential growth parameters and developing a more quantitative description of variables used for running the simulations. Further, the ABM model is capable of investigating 5000 wells in 30 min, and in connection with the microfluidic platform, constitutes a powerful framework to connect microbiological experiments to ABM simulations, while improving the ABM models to more accurately reproduce the experimental observations. Finally, this new microfluidic-ABM framework could be used in the future to predict the types of microcolonies that are likely to develop when different microbial species are mixed, which is expected to advance our understanding of microbial ecology at fine spatial scales, as well as mechanistically describe how microbial succession occurs in nature and shapes environments of interest.

AUTHOR CONTRIBUTIONS

All authors were involved in the writing and proofing of the manuscript. JW, AT, MH, and SR were responsible for the design, execution and interpretation of the experimental platform and ABM results. PD, JDA, MG, CP, XP, and MF-C were responsible for implementing the ABM model, doing the simulations and interpreting the results.

REFERENCES

- Berk, V., Fong, N., Dempsey, G., Develioglou, O., Zhuang, X. W., Yildiz, F., et al. (2011). Superresolution imaging of intact microbial communities reveals molecular architecture of biofilm development and bacterial organization. *Biophys. J.* 100, 617–617. doi: 10.1016/j.bpj.2010.12.3552
- Biteen, J. S., Blainey, P. C., Cardon, Z. G., Chun, M., Church, G. M., Dorrestein, P. C., et al. (2016). Tools for the microbiome: nano and beyond. *ACS Nano* 10, 6–37. doi: 10.1021/acsnano.5b07826
- Borenstein, D. B., Ringel, P., Basler, M., and Wingreen, N. S. (2015). Established microbial colonies can survive type vi secretion assault. *PLoS Comput. Biol.* 11:e1004520. doi: 10.1371/journal.pcbi.1004520
- Chou, S., Bui, N. K., Russell, A. B., Lexa, K. W., Gardiner, T. E., LeRoux, M., et al. (2012). Structure of a peptidoglycan amidase effector targeted to gram-negative bacteria by the type vi secretion system. *Cell Rep.* 1, 656–664. doi: 10.1016/j.celrep.2012.05.016
- Cline, L. C., and Zak, D. R. (2015). Soil microbial communities are shaped by plant-driven changes in resource availability during secondary succession. *Ecology* 96, 3374–3385. doi: 10.1890/15-0184.1
- Cutler, N. A., Chaput, D. L., Oliver, A. E., and Viles, H. A. (2015). The spatial organization and microbial community structure of an epilithic biofilm. *FEMS Microbiol. Ecol.* 91:fiu027. doi: 10.1093/femsec/fiu027
- Das, C., Dutta, A., Rajasingh, H., and Mande, S. S. (2013). Understanding the sequential activation of type iii and type vi secretion systems in salmonella typhimurium using boolean modeling. *Gut Pathog.* 5, 28. doi: 10.1186/1757-4749-5-28
- Dini-Andreote, F., Stegen, J. C., Van Elsas, J. D., and Salles, J. F. (2015). Disentangling mechanisms that mediate the balance between stochastic and deterministic processes in microbial succession. *Proc. Natl. Acad. Sci. U. S. A.* 112, E1326–E1332. doi: 10.1073/pnas.1414261112
- Genovart, M., Lopez, D., and Gras, A. (2005). Individual-based modelling of microbial activity to study mineralization of c and n and nitrification process in soil. *Nonlinear Anal. Real* 6, 773–795. doi: 10.1016/j.nonrwa.2004.12.005
- Genovart, M., López, D., and Valls, J. (2002). INDISIM, an individual-based discrete simulation model to study bacterial cultures. *J. Theor. Biol.* 214, 305–319. doi: 10.1006/jtbi.2001.2466
- Granda, P. A., Gras, A., Genovart, M., and Moulton, V. (2016). INDISIM-Paracoccus, an individual-based and thermodynamic model for a denitrifying bacterium. *J. Theor. Biol.* 403, 45–58. doi: 10.1016/j.jtbi.2016.05.017
- Gras, A., Cañadas, J. C., and Genovart, M. (2011a). “INDISIM-SOM: An individual-based simulator on a website for experimenting with and investigating diverse dynamics of carbon and nitrogen in mineral soils,” in *Microorganisms in Industry and Environment: From Scientific and Industrial Research to Consumer Products*, ed A. Mendez-Vilas (Singapore; Hackensack, NJ; London: World Scientific Publishing Co. Pte. Ltd.), 167–171.
- Gras, A., and Genovart, M. (2006). “INDISIM-SOM, an individual-based model to study short-term evolutions of carbon and nitrogen pools related to microbial activity in soil organic matter,” in *Oral communication in the European Conference on Modelling and Simulation - ECMS 2006 Bonn-Rhein-Sieg*, eds W. Borutzky, A. Orsoni, R. Zobel, and K. Al-Begain (Germany: Key Technologies in Academia and Industry), 554–559.
- Gras, A., Genovart, M., Portell, X., and Baveye, P. C. (2010). Individual-based modeling of carbon and nitrogen dynamics in soils: parameterization and sensitivity analysis of abiotic components. *Soil Sci.* 175, 363–374. doi: 10.1097/SS.0b013e3181eda507
- Gras, A., Genovart, M., Valls, J., and Baveye, P. C. (2011b). Individual-based modelling of carbon and nitrogen dynamics in soils: parameterization and sensitivity analysis of microbial components. *Ecol. Model.* 222, 1998–2010. doi: 10.1016/j.ecolmodel.2011.03.009

ACKNOWLEDGMENTS

Microwell arrays were fabricated and characterized, including aspects of computational simulations, at the Center for Nanophase Materials Sciences User Facilities Division, Office of Basic Energy Sciences, U.S. Department of Energy. Financial support for this work was provided through the Oak Ridge National Laboratory Director's Research and Development Fund. JDA research was supported in part by an appointment to the Higher Education Research Experiences Program at Oak Ridge National Laboratory, administered by ORAU through the U.S. Department of Energy Oak Ridge Institute for Science and Education. The authors would also like to thank the J. Mougous Laboratory (University of Washington, Seattle, WA) for the supply of *P. aeruginosa* strains used in these studies. The authors would like to thank the computational and storage resources provided via the Compute and Data Environment for Sciences, CADES, at the Oak Ridge National Laboratory.

SUPPLEMENTARY MATERIAL

The Supplementary Material for this article can be found online at: <https://www.frontiersin.org/articles/10.3389/fmicb.2018.00033/full#supplementary-material>

Supplementary Figure 1 | Flow chart of the bacterial ABM model designed and implemented in the NetLogo platform.

Supplementary Movie 1 | Co-growth of T6SS+ and T6SS- in the micro-fluidics device.

Supplementary Movie 2 | ABM simulation of T6SS+ and T6SS- cells co-growth.

- Grimm, V., Berger, U., Bastiansen, F., Eliassen, S., Ginot, V., Giske, J., et al. (2006). A standard protocol for describing individual-based and agent-based models. *Ecol. Model.* 198, 115–126. doi: 10.1016/j.ecolmodel.2006.04.023
- Grimm, V., Berger, U., Deangelis, D. L., Polhill, J. G., Giske, J., and Railsback, S. F. (2010). The odd protocol a review and first update. *Ecol. Model.* 221, 2760–2768. doi: 10.1016/j.ecolmodel.2010.08.019
- Halsted, M., Wilmoth, J. L., Briggs, P. A., Hansen, R. R., Briggs, D. P., Timm, A. C., et al. (2016). Development of transparent microwell arrays for optical monitoring and dissection of microbial communities. *J. Vac. Sci. Technol. B.* 34:06K103. doi: 10.1116/1.4962739
- Hansen, R. H., Timm, A. C., Timm, C. M., Bible, A. N., Morrell-Falvey, J. L., Pelletier, D. A., et al. (2016). Stochastic assembly of bacteria in microwell arrays reveals the importance of confinement in community development. *PLoS ONE* 11:e0155080. doi: 10.1371/journal.pone.0155080
- Hecht, A. L., Casterline, B. W., Earley, Z. M., Goo, Y. A., Goodlett, D. R., and Wardenburg, J. (2016). Strain competition restricts colonization of an enteric pathogen and prevents colitis. *EMBO Rep.* 17, 1281–1291. doi: 10.15252/embr.201642282
- Hellweger, F. L., Kravchuk, E. S., Novotny, V., and Gladyshev, M. I. (2008). Agent-based modeling of the complex life cycle of a cyanobacterium (anabaena) in a shallow reservoir. *Limnol. Oceanogr.* 53, 1227–1241. doi: 10.4319/lo.2008.53.4.1227
- Hood, R. D., Singh, P., Hsu, F. S., Güvener, T., Carl, M. A., Trinidad, R. R. S., et al. (2010). A type vi secretion system of *Pseudomonas aeruginosa* targets, a toxin to bacteria. *Cell Host Microbe* 7, 25–37. doi: 10.1016/j.chom.2009.12.007
- Koonin, E. V., and Wolf, Y. I. (2015). Evolution of the crisper-cas adaptive immunity systems in prokaryotes: models and observations on virus-host coevolution. *Mol. Biosyst.* 11, 20–27. doi: 10.1039/C4MB00438H
- Kreft, J. U. (2004). Biofilms promote altruism. *Microbiol. Sgm* 150, 2751–2760. doi: 10.1099/mic.0.26829-0
- Kreft, J. U., Booth, G., and Wimpenny, J. W. (1998). Bacsim, a simulator for individual-based modelling of bacterial colony growth. *Microbiol. U. K.* 144, 3275–3287. doi: 10.1099/00221287-144-12-3275
- Lardon, L. A., Merkey, B. V., Martins, S., Dötsch, A., Picioreanu, C., Kreft, J. U., et al. (2011). Idynamics: next-generation individual-based modelling of biofilms. *Environ. Microbiol.* 13, 2416–2434. doi: 10.1111/j.1462-2920.2011.02414.x
- LeRoux, M., De Leon, J. A., Kuwada, N. J., Russell, A. B., Pinto-Santini, D., Hood, R. D., et al. (2012). Quantitative single-cell characterization of bacterial interactions reveals type vi secretion is a double-edged sword. *Proc. Natl. Acad. Sci. U. S. A.* 109, 19804–19809. doi: 10.1073/pnas.1213963109
- Liu, W., Kim, H. J., Lucchetta, E. M., Du, W., and Ismagilov, R. F. (2009). Isolation, incubation, and parallel functional testing and identification by fish of rare microbial single-copy cells from multi-species mixtures using the combination of chemistore and stochastic confinement. *Lab. Chip* 9, 2153–2162. doi: 10.1039/b904958d
- McNally, L., Bernardy, E., Thomas, J., Kalziki, A., Pentz, J., Brown, S. P., et al. (2017). Killing by type vi secretion drives genetic phase separation and correlates with increased cooperation. *Nat Comm* 8:14371. doi: 10.1038/ncomms14371
- Mougous, J. D., Cuff, M. E., Raunser, S., Shen, A., Zhou, M., Gifford, C. A., et al. (2006). A virulence locus of *Pseudomonas aeruginosa* encodes a protein secretion apparatus. *Science* 312, 1526–1530. doi: 10.1126/science.1128393
- Pintelon, T. R., Picioreanu, C., Loosdrecht, M. C., and Johns, M. L. (2012). The effect of biofilm permeability on bio-clogging of porous media. *Biotechnol. Bioeng.* 109, 1031–1042. doi: 10.1002/bit.24381
- Robinson, J. B., Telepnev, M. V., Zudina, I. V., Bouyer, D., Monteneri, J. A., Bearden, S. W., et al. (2009). Evaluation of a yersinia pestis mutant impaired in a thermoregulated type vi-like secretion system in flea, macrophage and murine models. *Microb. Pathog.* 47, 243–251. doi: 10.1016/j.micpath.2009.08.005
- Russell, A. B., Wexler, A. G., Harding, B. N., Whitney, J. C., Bohn, A. J., Goo, Y. A., et al. (2014). A type vi secretion-related pathway in bacteroidetes mediates interbacterial antagonism. *Cell Host Microbe* 16, 227–236. doi: 10.1016/j.chom.2014.07.007
- Sahari, A., Traore, M. A., Stevens, A. M., Scharf, B. E., and Behkam, B. (2014). Toward development of an autonomous network of bacteria-based delivery systems (bacteriabots): spatiotemporally high-throughput characterization of bacterial quorum-sensing response. *Anal. Chem.* 86, 11489–11493. doi: 10.1021/ac5021003
- Sana, T. G., Berni, B., and Bleves, S. (2016). The t6ss of *Pseudomonas aeruginosa* strain pa01 and their effectors: beyond bacterial-cell targeting. *Front. Cell. Infect. Microbiol.* 6:61. doi: 10.3389/fcimb.2016.00061
- Sana, T. G., Lugo, K. A., and Monack, D. M. (2017). T6ss: the bacterial “fight club” in the host gut. *PLoS Pathog.* 13:e1006325. doi: 10.1371/journal.ppat.1006325
- Sarris, P. F., and Scoulica, E. V. (2011). *Pseudomonas entomophila* and *Pseudomonas mendocina*: potential models for studying the bacterial type vi secretion system. *Infect. Genet. Evol.* 11, 1352–1360. doi: 10.1016/j.meegid.2011.04.029
- Swennenhuis, J. F., Tibbe, A. G. J., Stevens, M., Katika, M. R., Van Dalum, J., Tong, H. D., et al. (2015). Self-seeding microwell chip for the isolation and characterization of single cells. *Lab Chip* 15, 3039–3046. doi: 10.1039/C5LC00304K
- Timm, A. C., Halsted, M. C., Wilmoth, J. L., and Retterer, S. T. (2017). Assembly and tracking of microbial community development within a microwell array platform. *J. Vis. Exp.* 6:e55701. doi: 10.3791/55701
- Tolker-Nielsen, T., and Molin, S. (2000). Spatial organization of microbial biofilm communities. *Microb. Ecol.* 40, 75–84. doi: 10.1007/s002480000057
- Verster, A. J., Ross, B. D., Radey, M. C., Bao, Y., Goodman, A. L., Mougous, J. D., et al. (2017). The landscape of type vi secretion across human gut microbiomes reveals its role in community composition. *Cell Host & Microbe* 22, 411.e4–419.e4. doi: 10.1016/j.chom.2017.08.010
- Vogel, L. E., Makowski, D., Garnier, P., Vieuble-Gonod, L., Coquet, Y., Raynaud, X., et al. (2015). Modeling the effect of soil meso- and macropores topology on the biodegradation of a soluble carbon substrate. *Adv. Water Resour.* 83, 123–136. doi: 10.1016/j.advwatres.2015.05.020
- Wang, X. L., Gou, X., Chen, S. X., Yan, X., and Sun, D. (2013). Cell manipulation tool with combined microwell array and optical tweezers for cell isolation and deposition. *J. Micromech. Microeng.* 23:075006. doi: 10.1088/0960-1317/23/7/075006
- Wang, Y., and Ma, S. (2014). Small molecules modulating ahl-based quorum sensing to attenuate bacteria virulence and biofilms as promising antimicrobial drugs. *Curr. Med. Chem.* 21, 296–311. doi: 10.2174/09298673113206660294
- Wexler, A. G., Bao, Y., Whitney, J. C., Bobay, L. M., Xavier, J. B., Schofield, W. B., et al. (2016). Human symbionts inject and neutralize antibacterial toxins to persist in the gut. *Proc. Natl. Acad. Sci. U.S.A.* 113, 3639–3644. doi: 10.1073/pnas.1525637113
- Xue, N., Bleris, L., and Lee, J. B. (2015). One-step fabrication of three-dimensional polydimethylsiloxane peel-off microwell array for cell trapping. *J. Micro. Nanolith. Mem.* 14:014503. doi: 10.1117/1.JMM.14.1.014503
- Yamazaki, H., Gotou, S., Ito, K., Kohashi, S., Goto, Y., Yoshiura, Y., et al. (2014). Micropatterned culture of hepg2 spheroids using microwell chip with honeycomb-patterned polymer film. *J. Biosci. Bioeng.* 118, 455–460. doi: 10.1016/j.jbiosc.2014.03.006
- Yeh, S. I., Hau, C. C., Huang, C. J., Chang, H. C., Hsu, C. H., and Yang, J. T. (2017). Development of a simple static microwell array with uniform cell seeding and a chemical concentration gradient. *Microfluid. Nanofluid.* 21: 80. doi: 10.1007/s10404-017-1921-8
- Zhang, P., Zhang, J., Bian, S., Chen, Z., Hu, Y., Hu, R., et al. (2016). High-throughput superhydrophobic microwell arrays for investigating multifactorial stem cell niches. *Lab Chip* 16, 2996–3006. doi: 10.1039/C6LC00331A
- Zhu, L., Jin, J., Lin, H. Z., Gao, K. T., and Xu, X. Y. (2015). Succession of microbial community and enhanced mechanism of a zvi-based anaerobic granular sludge process treating chloronitrobenzenes wastewater. *J. Hazard. Mater.* 285, 157–166. doi: 10.1016/j.jhazmat.2014.11.029

Conflict of Interest Statement: The authors declare that the research was conducted in the absence of any commercial or financial relationships that could be construed as a potential conflict of interest.

Copyright © 2018 Wilmoth, Doak, Timm, Halsted, Anderson, Ginovart, Prats, Portell, Retterer and Fuentes-Cabrera. This is an open-access article distributed under the terms of the Creative Commons Attribution License (CC BY). The use, distribution or reproduction in other forums is permitted, provided the original author(s) and the copyright owner are credited and that the original publication in this journal is cited, in accordance with accepted academic practice. No use, distribution or reproduction is permitted which does not comply with these terms.



Stochastic Individual-Based Modeling of Bacterial Growth and Division Using Flow Cytometry

Miriam R. García^{1*}, José A. Vázquez², Isabel G. Teixeira^{3†} and Antonio A. Alonso^{1*}

¹ Bioprocess Engineering Group, Marine Research Institute-Spanish National Research Council (IIM-CSIC), Vigo, Spain,

² Group of Recycling and Valorisation of Waste Materials, Marine Research Institute-Spanish National Research Council

(IIM-CSIC), Vigo, Spain, ³ Oceanology, Marine Research Institute-Spanish National Research Council (IIM-CSIC), Vigo, Spain

OPEN ACCESS

Edited by:

Ferdi L. Hellweger,
Northeastern University, United States

Reviewed by:

Musashi Takenaka,
Kobe University, Japan
Chaitanya A. Athale,
Indian Institute of Science Education
and Research (IISER) Pune, India
Jean-Christophe Augustin,
École Nationale Vétérinaire d'Alfort,
France

*Correspondence:

Miriam R. García
miriamr@iim.csic.es
Antonio A. Alonso
antonio@iim.csic.es

† Present Address:

Isabel G. Teixeira,
CESAM & Biology Department,
University of Aveiro, Aveiro, Portugal

Specialty section:

This article was submitted to
Systems Microbiology,
a section of the journal
Frontiers in Microbiology

Received: 11 July 2017

Accepted: 15 December 2017

Published: 05 January 2018

Citation:

García MR, Vázquez JA, Teixeira IG
and Alonso AA (2018) Stochastic
Individual-Based Modeling of Bacterial
Growth and Division Using Flow
Cytometry. *Front. Microbiol.* 8:2626.
doi: 10.3389/fmicb.2017.02626

A realistic description of the variability in bacterial growth and division is critical to produce reliable predictions of safety risks along the food chain. Individual-based modeling of bacteria provides the theoretical framework to deal with this variability, but it requires information about the individual behavior of bacteria inside populations. In this work, we overcome this problem by estimating the individual behavior of bacteria from population statistics obtained with flow cytometry. For this objective, a stochastic individual-based modeling framework is defined based on standard assumptions during division and exponential growth. The unknown single-cell parameters required for running the individual-based modeling simulations, such as cell size growth rate, are estimated from the flow cytometry data. Instead of using directly the individual-based model, we make use of a modified Fokker-Plank equation. This only equation simulates the population statistics in function of the unknown single-cell parameters. We test the validity of the approach by modeling the growth and division of *Pediococcus acidilactici* within the exponential phase. Estimations reveal the statistics of cell growth and division using only data from flow cytometry at a given time. From the relationship between the mother and daughter volumes, we also predict that *P. acidilactici* divide into two successive parallel planes.

Keywords: individual-based modeling, stochastic modeling, cell cycle, bacterial growth and division, modified Fokker-Planck equation, flow cytometry, coccoid bacteria, predictive microbiology

1. INTRODUCTION

Population- and individual-based modeling are usually presented as incompatible approaches, although both describe the same system at different levels (Fahse et al., 1998; Wilson, 1998).

Traditionally, deterministic population-based models have been the underlying method behind predictive microbiology (Baranyi and Roberts, 1995). These models have been successfully applied to, for example, monitoring of food spoilage and microbial safety (Koutsoumanis and Nychas, 2000; Ross et al., 2000), smart sensing of food quality (García et al., 2015, 2017), Quantitative Microbial Risk Assessment (Cassin et al., 1998; Membré and Lambert, 2008), and design and control of food processes (Simpson et al., 1993; Alonso et al., 2013).

Over the last 15 years, stochastic individual-based modeling emerged as a promising tool to produce realistic estimations of safety risks along the food chain by describing the variability of

single-cell behavior and small populations (Ferrer et al., 2009; Augustin et al., 2015; Koutsoumanis and Aspridou, 2017). Often, contamination of food starts with a small number of bacteria that adapt and proliferate on a given food matrix. At low cell concentrations, standard deterministic population models fail to predict the variability of the bacterial population. This is so because, at low initial cell numbers, heterogeneity between individuals and its influence on the division times become relevant and have a net influence on the population. Consequently, the behavior of individual cells cannot be neglected when assessing possible health risks along the food chain, either during storage or during distribution.

There are still many challenges in individual-based modeling, including the lack of information about single-cell behavior inside a population. The emergence of individual-based modeling was possible thanks to two main factors: (1) the increase of computer processing power and (2) the availability of single-cell measurements using new techniques such as the “mother machine” microfluidic device (Wang et al., 2010). However, the information from single-cell measurements is limited in those techniques where cells have to be isolated from the population. That was illustrated for example by Gangan and Athale (2017), who showed the difference in single-cell growth in a “mother machine” or in a population.

In this work, we hypothesize that population statistics of cell volume encode information about single-cell growth and division that can be used for individual-based modeling. For this purpose, we derive a modified Fokker-Planck Equation (forward Kolmogorov equation) describing the population volume distribution. The underlying idea is similar to that in Alonso et al. (2014) who derived a backward Kolmogorov equation to estimate single-cell growth using time-to-division distributions. We should remark that not only our approach is different, but it extends the previous theory to consider not only single-cell growth but also single-cell division. This allows us to simulate the individual-based modeling of bacterial growth and division.

In the first part of the work, we will test theoretically how population statistics obey a modified Fokker-Planck equation that encodes single-cell information. The equivalent individual-based modeling approach is derived in parallel to check consistency. Both models simulate single-cell growth and division assuming that cell volumes grow exponentially and cells divide following the sizer principle, i.e., division occurs at a critical volume (Métris et al., 2005; Alonso et al., 2014; Robert et al., 2014). Whereas, exponential growth of cell volume is a standard principle in bacterial physiology (Fishov et al., 1995), the main trigger of bacterial division is still a matter of controversy (Taheri-Araghi et al., 2015). There are three major paradigms: the sizer, timer, and adder principle depending on whether division is triggered by a certain volume, time, or after growing a given volume. As in most predictive microbiology studies (Métris et al., 2005; Alonso et al., 2014), we focus on fully adapted cells (medium growth is kept constant and measurements are within the exponential phase) and the sizer principle remains the reasonable assumption.

Once the theory is established, we combine the modified Fokker-Planck equation with flow cytometry data to find the single-cell behavior of *Pediococcus acidilactici* within the exponential phase. The food industry is interested in this species for several reasons, including its probiotic attributes (Planas et al., 2004; Standen et al., 2015), its ability to valorize food wastes (Vázquez et al., 2011; Banwo et al., 2013; Scatassa et al., 2015), and its ability to produce a very potent and broad-spectrum bacteriocin (pediocin SA-1) with high capacities as food biopreservative (Ray, 1992; Anastasiadou et al., 2008; Vázquez and Murado, 2008). *P. acidilactici* has been also selected for being coccoid cells with interest in the food industry. This shape makes easier to find correlations between side scatter and volume, and differ from the well-studied *Escherichia coli* (model of rod-shaped cells). We should stress that cell volume, membrane area and diameter scale similarly when the cell is rod-shaped, although that is not the case for round cells. For such reason, along this work we consider the term size as equivalent to volume, but not bacterial diameter or membrane area.

2. MATERIALS AND METHODS

This work combines theory with experimental data and requires three types of methodologies to (1) develop models at the single-cell and population level, (2) acquire data with flow cytometry and optical density, and (3) determine the best parameters to reconcile the theory with the experimental results.

2.1. Modeling at Single-Cell and Population Levels

2.1.1. Individual-Based Modeling of Single-Cell Bacterial Growth and Division

We tested different alternatives with stochastic or deterministic division and growth, that are specific cases of the general individual-based modeling approach we describe in this section.

The model assumes that the growth of the logarithm of the single-cell volume is subject to a stochastic fluctuation δW characterized by a Wiener process (Alonso et al., 2014):

$$\delta X^i = \mu \delta t + \xi \delta W \quad \text{with} \quad X^i = \ln(V^i) \quad (1a)$$

where X^i represents the volume of cell i (V^i) in a logarithmic scale, μ represents the growth rate within the exponential phase and ξ is the intensity of the stochastic fluctuation. For the case of deterministic division $\xi = 0$ and cell volumes grow exponentially.

The division was modeled by adding a new cell to the population and resizing mother and newborn cell to the daughter size. The division event is triggered when the size of one or more cells is greater than a continuous random variable X_m with statistics defined by the probability density function (pdf) of mother sizes ($f_{X_m}(x)$):

$$\text{If } X^i \geq X_m \sim f_{X_m}(x), \quad X^{n+1} \rightarrow X^i - \ln(2) \quad (1b)$$

$$X^i \rightarrow X^i - \ln(2) \quad (1c)$$

where n is the number of cells in the population, i runs from 1 to n and the daughter volume is half the mother volume ($v_d = v_m/2$).

We tested different probability density functions to describe the statistics of cell division, i.e., for the probability density function of mother sizes $f_{X_m}(x)$. The probability showing the best agreement with the data suggests that the volume of the mothers V_m is a random variable following a log-normal distribution (Koch, 1966; Amir, 2014):

$$f_{X_m}(x) = \mathcal{N}(x_m, \sigma^2) \quad \text{with} \quad x_m = \ln(v_m) \quad (1d)$$

For simulating the deterministic division, σ was set to zero so that the normal distribution turns into Dirac delta function centered at the logarithm of the mother size x_m .

Simulations were initialized with a single cell ($X^1 = x_d = \ln(v_d)$) and run for a given time horizon where a given cell and its offspring grow following (1a) and divide according to the rule in (1b). We selected the Euler-Maruyama algorithm to solve the stochastic differential equations for its simplicity as compared with other numerical methods (Higham, 2001). The bins of all the histograms to represent the population statistics were determined using the Freedman-Diaconis rule (Freedman and Diaconis, 1981). For convenience, simulations of population dynamics from the proposed single-cell stochastic model were performed on a cluster composed of 12 processing nodes (openSUSE 11.0 Linux with 23.5 GB of RAM) and 160 processors in total, using the SGE task manager to distribute the calculations among them.

2.1.2. Population Modeling Using the Modified Fokker-Planck Equation

The statistic of the cell sizes in the population is formally described by a probability density function (pdf) $p(t, x)$ that depends on size x and time t . For the sake of clarity, we keep previous subsection notation: v and x denote size in terms of volume and natural logarithm of the volume, respectively. Subindexes d and m denote daughter and mother respectively, whereas f_{X_d} and f_{X_m} are the corresponding pdfs for sizes. As before, growth rate and fluctuation intensity are denoted by μ and ξ , respectively. The function $p(t, x)$ is the solution of the following modified Fokker-Planck equation:

$$\frac{\partial p(t, x)}{\partial t} = \underbrace{\frac{\xi^2}{2} \frac{\partial^2 p(t, x)}{\partial x^2} - \mu \frac{\partial p(t, x)}{\partial x}}_{\text{cell growth} = \frac{\partial J(t, x)}{\partial x}} + \underbrace{2f_{X_d}(x)Z - f_{X_m}(x)Z}_{\text{division}} - \underbrace{p(t, x)Z}_{\text{normalization}} \quad (2a)$$

being

$$Z = \int_{\underline{x}}^{\bar{x}} F_m(x) \frac{\partial J(t, x)}{\partial x} dx \quad (2b)$$

$$p(t, \underline{x}) = p(t, \bar{x}) = 0 \quad \forall t \quad \text{boundary conditions} \quad (2c)$$

$$p(0, x) = \delta(x - x_d) \quad \forall x \quad \text{initial conditions} \quad (2d)$$

where $f_{X_d}(x) = \mathcal{N}(x_d, \sigma^2)$ is the pdf of daughter sizes, $f_{X_m}(x) = \mathcal{N}(x_m, \sigma^2)$ the pdf of mother sizes and F_{X_m} its cumulative distribution function. The model is valid only for large domains $x \in [\underline{x}, \bar{x}]$ where no cell sizes are close to their (minimum and maximum) boundaries.

Without the terms of division and normalization, Equation (2a) is the classical Fokker-Planck equation of the stochastic

differential Equation (1a). It explains how the change in the distribution of volumes depends on a diffusion term which is proportional to the square of the fluctuation plus a convective term proportional to the cell growth rate (Gardiner, 2004; Alonso et al., 2014). To account for division, we have added two terms proportional to the pdfs of daughter and mother volumes. Normalization is required for $p(t, x)$ to be a pdf. This is performed via the last term in the right hand side.

Simulations were performed using the finite difference discretization scheme in <http://www.matmol.org/> (Vande Wouwer et al., 2014) for the x domain. For all cases, the discretization scheme consisted of 501 elements. That was considered enough to approximate the equation since further refinements resulted in negligible improvements in the accuracy of the results. First derivatives were calculated using an upwind 5 points in the stencil and second derivatives with centred 5 points in the stencil. Due to the hard non-linearity at division, not only is a refined mesh in x required, but also a stiff time integrator. Ode15s in Matlab (Shampine and Reichelt, 1997) was selected for time integration of the resulted set of ordinary differential equations after the spatial discretization.

2.2. Data Acquisition and Analysis

2.2.1. Microbiological Methods

Pediococcus acidilactici NRRL B-5627 was kindly provided by the Northern Regional Research Laboratory (Peoria, IL, USA). Stock cultures of bacterium were stored at -80°C in MRS commercial medium (Pronadisa, Hispanlab S.A., Spain) with 25% glycerol. The inoculum to study the growth dynamics of *P. acidilactici* was prepared as follows:

1. One hundred and fifty milliliters of cellular suspension from the cryotube was transferred to 5 mL of MRS fresh medium and then incubated at 30°C in an orbital shaker at 200 rpm for 16 h.
2. From the obtained culture, 1 mL was added to an Erlenmeyer flask with 150 mL of MRS fresh medium and fermented at $30^\circ\text{C}/200\text{ rpm}$ for 22 h.
3. From the previous cultivation, serial 10-fold dilutions were prepared in peptone-buffered solutions, and 0.1 mL samples were plated (MRS agar medium) in triplicate and incubated at 30°C for 48 h.

Five individual colonies from plates were isolated and transferred to 5 Erlenmeyer flasks with 200 mL of MRS fresh medium and cultivated at $30^\circ\text{C}/200\text{ rpm}$. Samples from flasks were taken each hour up to 17 h (except at 12 and 16 h). All samples were separated in two aliquots, one of them was prepared for cytometer evaluation following the indications described in the next section. The other aliquot was centrifuged at 4,000 g for 15 min and the sediment washed twice and re-suspended in distilled water at an appropriate dilution to measure the optical density at 700 nm. The dry weight was estimated from a calibration curve ($G(\text{g/L}) = -0.008 + 0.342A_{700} + 0.028A_{700}^2$).

The percentage of viable cells smaller than certain diameters was calculated during the exponential phase. The cultures at 8 h were filtered, under sterile conditions, through 1.2 and $1\text{ }\mu\text{m}$ glass microfiber filters (Filter-Lab, Filtros Anioia S.A., Barcelona,

Spain). Thus, in these filtered solutions and in the final unfiltered culture (control), viable cells (colony forming units per mL) were quantified by count on MRS-agar plate as it was mentioned in the previous paragraph.

2.2.2. Flow Cytometer Data Acquisition

The abundance and size of *P. acidilactici* were determined with a BD FACSCalibur flow cytometer (BD Biosciences, San José, CA, USA) equipped with a laser emitting at 488 nm. Bacteria samples were fixed with a P+G solution (1 % paraformaldehyde + 0.05 % glutaraldehyde) at 10 % final concentration for 15 min in the dark. Then, samples were quickly frozen in liquid nitrogen and stored at -80°C . Prior to analysis, bacteria were stained with SybrGreen I DNA dye (5 mM final concentration) and diluted adequately. Bacteria were detected in the flow cytometer by their signature in a plot of Side Scatter (SSC) vs. FL1 (green fluorescence). All the reagents and chemicals were purchased from Sigma-Aldrich S.A. (St. Louis, MO, USA).

2.2.3. Estimation of *P. acidilactici* Population Growth

The logistic equation was used to fit the population growth data (Zwietering et al., 1990; Peleg and Shetty, 1997). Biomass and number of cells were obtained respectively by dry weight and cytometry of *P. acidilactici*:

$$G = \frac{G_m}{1 + \exp[2 + \mu^p(\lambda - t)]} \quad (3)$$

where G is the *P. acidilactici* growth as biomass or cells (g L^{-1} or cells mL^{-1}). G_m represents the maximum growth or plateau phase (g L^{-1} or cells mL^{-1}), λ is the lag phase (h), t denotes the time of culture (h) and $\mu^p = \frac{4\mu_m^p}{G_m}$ is the specific growth rate of the population (h^{-1}) with μ_m^p being the maximum specific growth rate ($\text{g L}^{-1} \text{h}^{-1}$ or cells $\text{mL}^{-1} \text{h}^{-1}$).

Non-linear least-squares method (quasi-Newton) was applied for growth data modeling. Confidence intervals from the parametric estimates (Student's t -test) and consistency of mathematical models (Fisher's F -test) and residual analysis (Durbin-Watson test) were evaluated by "SolverAid" macro (Levie's Excelsaneous website: <http://www.bowdoin.edu/~rdelevie/excelsaneous>)

2.3. Model Calibration

Reliable single-cell parameters of *P. acidilactici* are unknown and were estimated by minimizing the distance between the modified Fokker-Planck Equations (2a–2d) and the data from the flow cytometry. The unknown parameters are the growth rate μ , the fluctuation intensity ξ , the statistics of the mother distribution (x_d and σ) and the parameter relating mother and daughter sizes ω . The estimated parameters were used to simulate single-cell dynamics based on the individual-based modeling approach (1a–1d).

The method of least squares was used to define the distance between the model and the data. Essentially, it aims at minimizing the differences between the stationary distribution of sizes calculated with (2a–2d) and the stationary distribution estimated from the data. The experimental distribution was

obtained using different replicates at one given time using histograms with a number of bins given by the Freedman-Diaconis rule. For noisy data, optimization could lead to a multimodal problem, i.e., it has several sub-optimal solutions (Vilas et al., 2017). To assure convergence to the global solution in a reasonable time, the global optimizer Enhanced Scatter Search (eSS) was employed (Egea et al., 2009).

3. RESULTS AND DISCUSSION

3.1. Population Statistics of Single-Cell Growth and Division Obey a Modified Fokker-Planck Equation

3.1.1. Deterministic Growth and Division

We first simulate the individual-based modeling of deterministic growth and division. We assume that cell volumes grow exponentially and cells divide following the sizer principle, i.e., division occurs at a critical volume (Métris et al., 2005; Alonso et al., 2014; Robert et al., 2014). The adder model is more realistic while cells are adapting to the growth media (lag phase), but it becomes a sizer when, as in our case, cells are fully adapted within the exponential phase (see Figure 1B in Sauls et al., 2016). It should be noted that considering an adder model would complicate considerably the derivation of the equivalent Fokker-Planck equation without altering the final results.

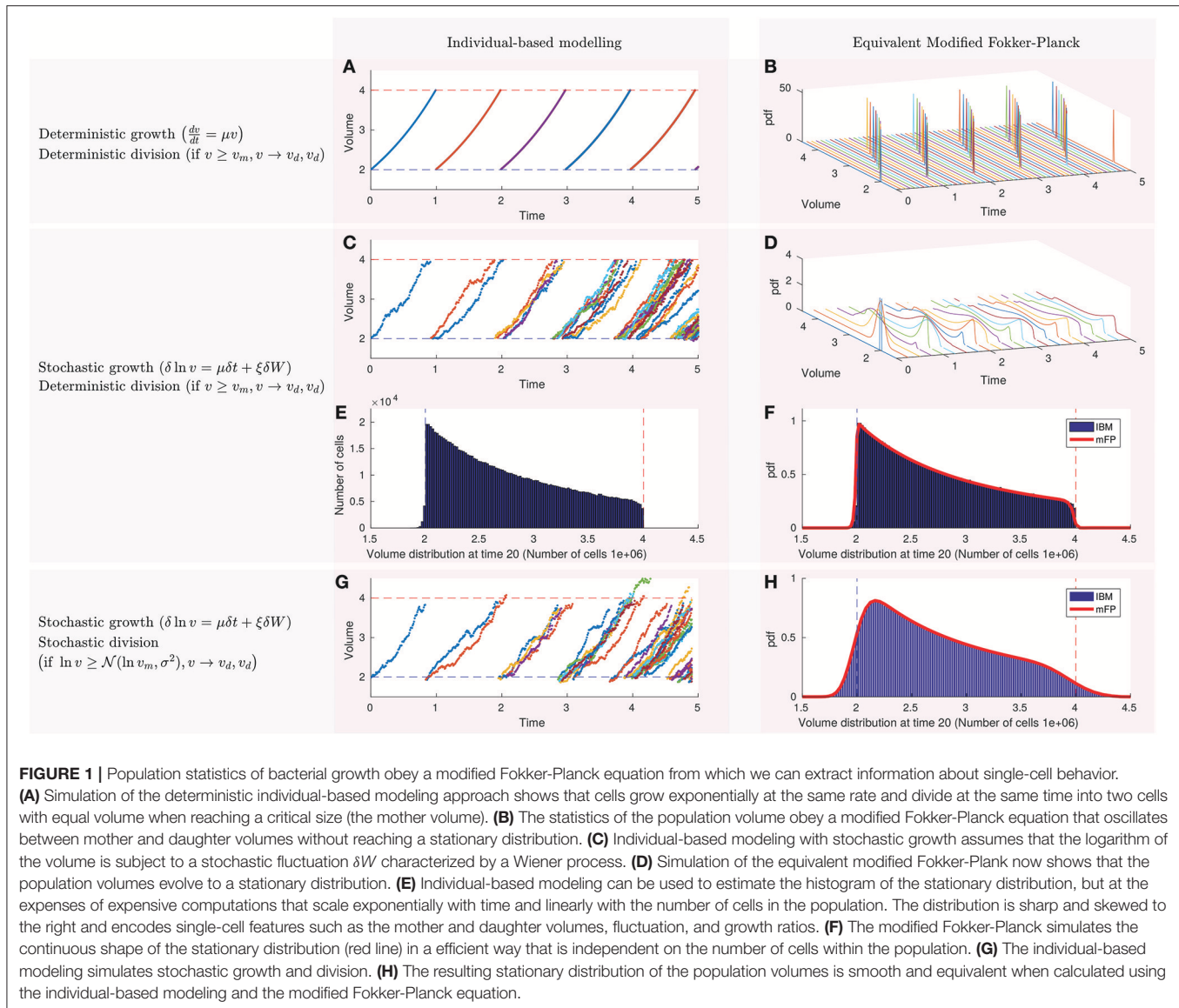
Figure 1A shows the simulations of the deterministic single-cell dynamics. All the cells have the same volume because they grow and divide at the same velocity and time. For this example only 3 parameters are required: the daughter volume (v_d) and the mother volume ($v_m = 4$), depicted in dashed blue and red lines, and the single-cell growth rate $\mu = 0.7$. At time 0 there is only one cell that grows until reaching the critical volume of division (or mother volume). This cell divides into two cells of half their volumes (daughter volume). Therefore, at time 1 there are two cells that cannot be distinguished in the figure because their dynamics overlap. The process is repeated until reaching a population of 32 cells at time 5.

The dynamics of the population volume distribution obey a modified Fokker-Planck equation that, as shown in Figure 1B, consists of a pulse that oscillates between the daughter and mother volumes. Each color line represents the distribution at a different time and are simulated using the partial derivative Equation (2a) with stochastic parameters set to zero ($\xi = 0$ and $\sigma = 0$) and the single-cell parameters in Figure 1A ($v_d = 2$, $v_m = 4$, $\mu = 0.7$).

This model with deterministic growth and division is invalid since the population statistics fluctuates instead of evolving to a stationary distribution. Fishov et al. (1995) explained how balanced exponential growth implies steady-state growth and stationary frequency distribution of the various components that constitute the cell. In words by Painter and Marr (1968) "the distribution of each intensive random variable is time-invariant."

3.1.2. Stochastic Growth and Deterministic Division

Single-cell measurements of bacteria suggest that growth is a stochastic process (see for example Figure 1A in Deforet et al.,



2015 for *Pseudomonas aeruginosa*). Alonso et al. (2014) proposed an individual-based modeling approach reproducing such single-cell dynamics. They assumed that the logarithm of the volume is subject to a stochastic fluctuation δW characterized by a Wiener process following Equation (1a). We use the same assumption to model stochastic growth. **Figure 1C** shows simulations of the single-cell dynamics with stochastic growth and deterministic division. After the first division (time = 0.9) the dynamics of the two daughter volumes differ and the same happens with division times.

We confirm how simulations of the population statistics with stochastic growth now evolve to a stationary distribution (**Figure 1D**) as predicted by (Fishov et al., 1995). At time 0 the distribution is a Dirac delta function that spreads and moves between mother and daughter volumes. The rate of spread depends on the intensity of the fluctuation ξ whereas the velocity

of the moving pulse is determined by the growth parameter μ . Single-cell parameters are as in previous section ($v_d = 2, v_m = 4, \mu = 0.7$) except for the fluctuation that it is now $\xi = 0.1$.

The stationary distribution can be calculated either using a large number of single-cell simulations (1a–1d) or solving the modified Fokker-Planck equation (2a–2d). We plot in **Figure 1E** the histogram for a population of $1e6$ cells using the individual-based modeling approach. The mode of the histogram coincides with the daughter volume whereas the end of the histogram is the mother volume. The shape depends on the growth rate μ and the fluctuation ξ . Normalizing the area of this histogram we obtain the blue probability density function in **Figure 1F**. The modified Fokker-Planck equation, on the other hand, calculates directly the probability density function (red line). Both approaches coincide as shown in **Figure 1F**.

Results with stochastic growth and deterministic division evolve to a stationary distribution, but sharper than observed experimentally. In fact, the distribution of *E. coli* is commonly approximated for some authors by a smooth log-normal distribution (Kaya and Koser, 2009; Athale and Chaudhari, 2011). In addition, the end of the distribution (the mother volume) is not exactly the double of the mode (the daughter volume) in experiments.

3.1.3. Stochastic Growth and Division

A great amount of works in the literature assumes stochastic division and focus on the distribution of mother or daughter sizes (Amir, 2014; Taheri-Araghi, 2015; Taheri-Araghi et al., 2015; Sauls et al., 2016). Some works measure symmetric distributions close to a normal distribution (Sauls et al., 2016), whereas others assumed asymmetric distributions. That is the case of Koch (1966) and Amir (2014) who concluded that the daughter volume distribution is log-normal.

We extended our model considering that cells divide stochastically with a certain probability, either normal (Sauls et al., 2016) or log-normal (Amir, 2014). In other words, we moved from a strict sizer model to a sizer model with stochastic division. For the simulations in **Figure 1G** we assumed log-normal division. Now cells may divide before or after reaching the volume of 4 (red dashed line). As the model was implemented in the logarithm of the volume X , the log-normal stochastic division in the logarithm becomes a normal probability with mean $\nu_m = 4$ and a standard deviation that we assumed to be $\sigma = 0.1$. The remaining parameters are kept as in the previous section ($\nu_d = 2$, $\nu_m = 4$, $\mu = 0.7$, $\xi = 0.1$).

As shown in **Figure 1H**, results from the individual-based modeling coincide with the modified Fokker-Planck also for stochastic growth and division.

We should note how it is critical to assume stochastic growth and division to obtain realistic and smooth stationary distributions where the mode is larger than the daughter volume (ν_d).

3.1.4. Comparison of Individual-Based Modeling and Population Modeling with the Modified Fokker-Planck Equation

Individual-based modeling is a bottom-up approach providing valuable information at the single-cell level, but it requires parameters that cannot be easily measured (Ferrer et al., 2009; Augustin et al., 2015). The modified Fokker-Planck equation here presented focuses on population statistics that can be measured by flow cytometry. Comparisons between this equation and the experimental data are sufficient to estimate single-cell parameters that can be used for individual-based modeling.

The modified Fokker-Planck equation directly provides the evolution of the volume distribution without the need of predefining a probability density function. When populations are not large enough, the histograms calculated with individual-based modeling are too poor to extract relevant statistics. It is then usually preferred to assume a certain family of probability density functions. The precision of the modified Fokker-Planck equation, however, depends only on the discretization method

to solve the partial differential equation, and works for large and small populations whenever the assumptions of the Wiener process are satisfied (Gardiner, 2004).

In addition, individual-based modeling is characterized by requiring long computational times which make its use prohibitive in applications that demand many model evaluations (An et al., 2017), such as parameter estimation. The computation time of individual-based modeling grows exponentially with time, whereas the growth is linear for the equivalent modified Fokker-Planck equation. Note that the individual-based modeling approach requires one equation per cell. As cells grow exponentially, computation time scales linearly with the number of cells and exponentially with time. The modified Fokker-Planck equation, however, is a unique partial differential equation (PDE). Its computation time will depend on the degree of discretization and the simulation time. For the examples in **Figure 1**, computational times (2–6 s) are similar until time 15 (population of less than 3×10^4 cells) for both approaches. However from this time the modified Fokker-Planck equation becomes more efficient in orders of magnitude.

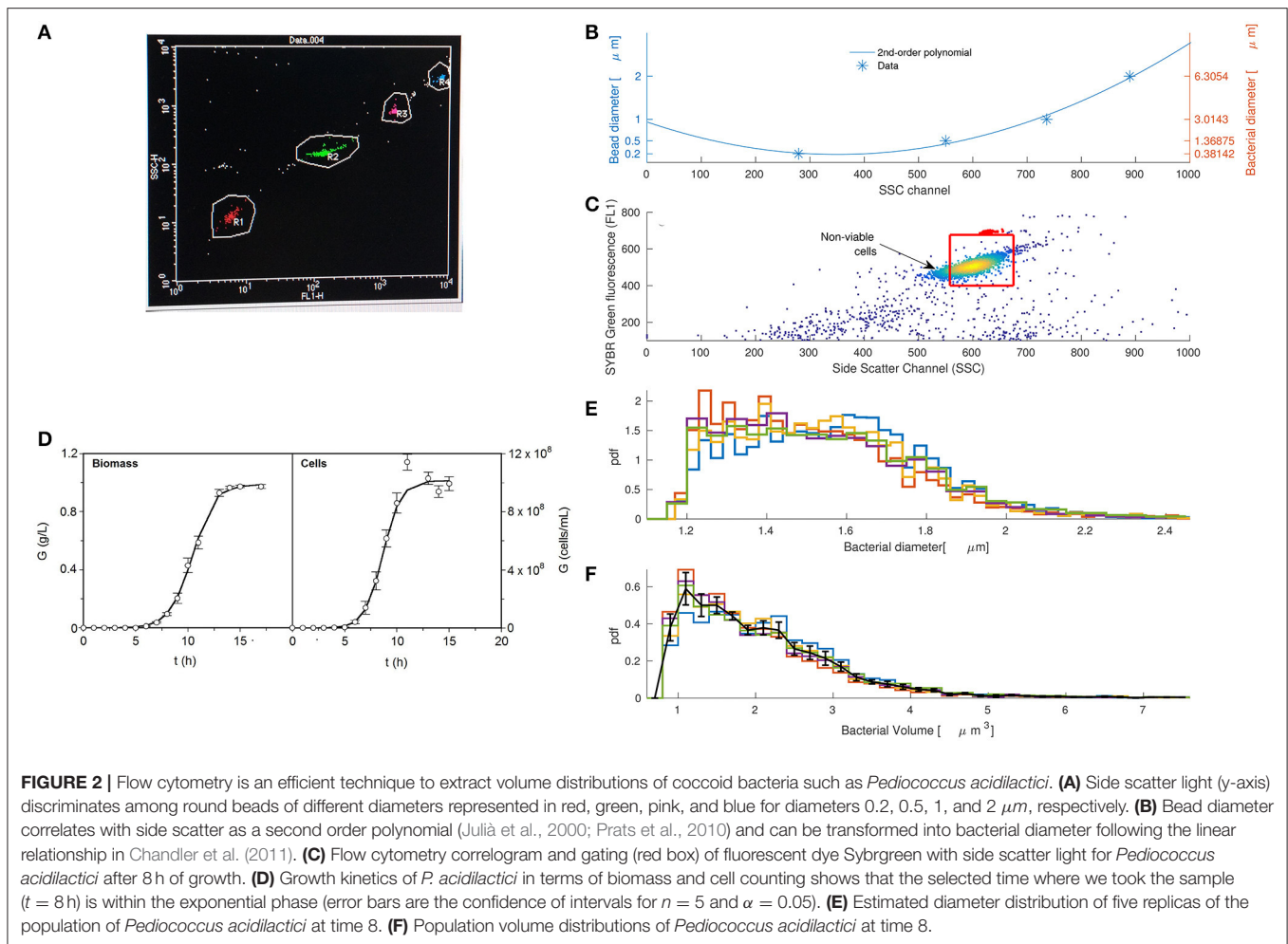
Moreover, the partial differential equation for stochastic growth has a diffusion term allowing efficient simulations using the appropriate techniques. Classical discretization methods transform the partial differential equation into a large number of ordinary differential equations. When the original equation is diffusive, a number of methods are at hand to take advantage of this property and significantly reduce the number of ordinary differential equations, thus reducing computational times (Trefethen, 2000; García et al., 2008).

3.2. Flow Cytometry Allows Estimation of Volume Distributions for *P. acidilactici*

Flow cytometry is the standard technique for fast acquisition of population statistics. It is commonly employed to estimate different mammalian cell characteristics such as cell size using forward scattered light. This technique is also useful for bacteria, but as their diameters are close to the light wavelength (488 nm or 0.5 μm), side scattered light has better resolution and is preferred. **Figure 2A** shows how side scattered light (y-axis) discriminates among different bead diameters. Events in red, green, pink and blue correspond with beads of diameters 0.2, 0.5, 1, 2 μm , respectively. Sizes smaller than 0.2 μm were below the detection limit of the device.

Estimation of bacterial diameters from side scattered light requires two steps: (1) to find the correlation between the bead diameter and side scattered light and (2) to transform the bead diameters to bacterial diameters. **Figure 2B** shows that the bead diameter is a second order polynomial of side scatter (Julià et al., 2000; Prats et al., 2010). However, bacteria and polystyrene beads have different refractive indexes. To correct the differences in the refractive index we make use of the linear relationship in Chandler et al. (2011). The figure shows in the right y-axis the final relationship between bacterial diameter (d) and side scatter (SSC), outlined in the following expression:

$$d = a(p_1 \text{SSC}^2 + p_2 \text{SSC} + p_3) + b \quad (4)$$



where SSC is the side scatter channel, $a = 3.2911$ and $b = -0.2769$ are the parameters provided in Chandler et al. (2011) to correct the differences in the refractive index and $p = [p_1, p_2, p_3] = [6.13 \times 10^{-6}, -0.0043, 0.94]$ the estimated parameters of the second-order polynomial.

We acquired and processed side scatter data of *P. acidilactici* at one sampling time after 8 h of growth. **Figure 2C** shows the flow cytometry correlogram of Sybrgreen fluorescence and side scatter for one of the replicates. Red points indicate beads used to count the number of events.

The red box defines the gating where viable cells lie. We used two sources of information to define the gating: Sybrgreen fluorescence and experiments counting viable cells at different diameters. Sybrgreen was helpful to determine those events with too low DNA material to be consistent with a viable cell (upper and lower horizontal lines of red box). They probably represent either dead cells from the lag phase that have lost some of their DNA material, or free DNA detected as an event. Only with this gating, most diameters were between 1 and 2.5 μm as reported in the literature (Holt, 1994). However, the first calibrations of the model suggested that smaller cells were not able to divide. We passed cells through a 1.2 μm filter and found that only about 2%

of the cells were viable. Consequently, we did not consider cells smaller than 1.2 μm (left vertical line of the red box).

In order to assume that the selected sampling time ($t = 8$ h) was within the exponential phase of growth, we estimated growth kinetics in terms of biomass and cell counting. **Figure 2D** shows the experimental curves with the standard sigmoid growth pattern for lactic acid bacteria. Both cases are described by the logistic equation (3) ($R^2 = 0.993$ – 0.999). p -values from Fisher's F -test show consistency and robustness of the logistic to appropriately describe these profiles (**Table 1**). It is noted that no autocorrelation was observed in the fittings (data not shown). All parameters were statistically significant (t-Student test). The production of biomass was 25–30% lower as compared to previous cultures (Vázquez and Murado, 2008) which may be due to the minimum inocula employed in the present study. Typically, inocula used for the production of bacteriocins from lactic acid bacteria including *P. acidilactici* are much more populated, reaching values of 10^5 – 10^7 cfu/mL and longer productive periods (Vázquez et al., 2008).

Five data replicates at $t = 8$ h and the relationship in (4) were combined to estimate the volume distribution of *P. acidilactici*. **Figure 2E** shows the bacterial diameter distribution of different

replicates at time 8 h calculated from relationship (4). Volume distributions in **Figure 2F** are calculated by applying the volume equation of a sphere to the diameter histograms. Error bars show the mean and standard deviation of the histogram values for the five replicates. The distribution is smooth and skewed to the right, as expected from the modeling analysis in section 3.1. A similar behavior was observed in volume distributions of *E. coli* growing inside a population (Gangan and Athale, 2017).

3.3. The Modified Fokker-Planck Equation Is Combined with Flow Cytometry Data to Find the Single-Cell Behavior of *P. acidilactici*

The volume distributions of the *P. acidilactici* at time 8 h provide enough information to find the single-cell parameters of the modified Fokker-Planck equation. The problem consists in finding the best set of parameters of the modified Fokker-Planck equation that represents the experimental volume distributions by solving a least square problem.

Preliminary computations demonstrated the inability of the model in (2a–2d) to reproduce the data, suggesting that the

volume of each daughter is approximately one-fourth of the mother volume, i.e., $v_d = (1/4)v_m$. This hypothesis contradicts the principle of binary fission and had to be rejected because, if a mother gives two cells of this size, total volume would be destroyed and not conserved during division. This would imply that the specific growth rate of the population μ^P differs from the growth rate of the single-cell volumes μ , contradicting common observations in rod-shaped bacteria (Taheri-Araghi et al., 2015; Harris and Theriot, 2016). We could devise that this hypothesis, however, may be plausible in coccoid cells since cell volume, membrane area, and diameter scale differently. In fact, assuming that cells are spheres, simple calculations indicate that membrane area, instead of volume, is conserved if $v_d = (1/4)v_m$. However, it is well-known that coccoid bacteria create membrane (septal growth) before division (Pinho et al., 2013; Monteiro et al., 2015), suggesting again, that volume is conserved.

It resulted that the data pointed out to another mechanism to explain the daughter volumes: *P. acidilactici*, like *Pediococcus pentosaceus* and other coccoid cells (Zhou et al., 2010; Pinho et al., 2013; Monteiro et al., 2015), have two planes of division (Turner et al., 2010). That means that cells undergo two consecutive divisions and, at the time-scales of interest, one mother divides into four daughters with fourth of the mother volume. Hence we derive the individual-based and population-based modeling approaches considering two planes of division (see Appendix).

Figure 3A compares experimental data with both models at the population and single-cell levels considering two planes of division. **Table 2** shows the single-cell parameters used in the simulations. The three elements exhibit the same steady-state volume distribution. The black line represents the experimental data (see also **Figure 2F**) and the red line and histogram are the solutions of the modified Fokker-Planck distribution and individual-based modeling, respectively.

All the estimated parameters are within the selected bounds (see **Table 2**) except for the standard deviation of the distribution of mother volumes (σ). Probably, this parameter tries to

TABLE 1 | Summary of the parameter values obtained from the fittings of *P. acidilactici* growths (biomass and cells production) to the logistic Equation (3).

Parameters	Biomass	Cells
G_m	$0.990 \pm 0.021 \text{ g L}^{-1}$	$(10.14 \pm 0.72) \times 10^8 \text{ cells mL}^{-1}$
μ^P	$0.904 \pm 0.021 \text{ h}^{-1}$	$1.163 \pm 0.394 \text{ h}^{-1}$
λ	$8.23 \pm 0.18 \text{ h}$	$6.72 \pm 0.61 \text{ h}$
μ_m^P	$0.224 \pm 0.018 \text{ g L}^{-1} \text{ h}^{-1}$	$(2.95 \pm 0.93) \times 10^8 \text{ cells mL}^{-1} \text{ h}^{-1}$
R^2	0.999	0.993
p -values	<0.0001	<0.0001

Statistical parameters R^2 and p -values are also shown.

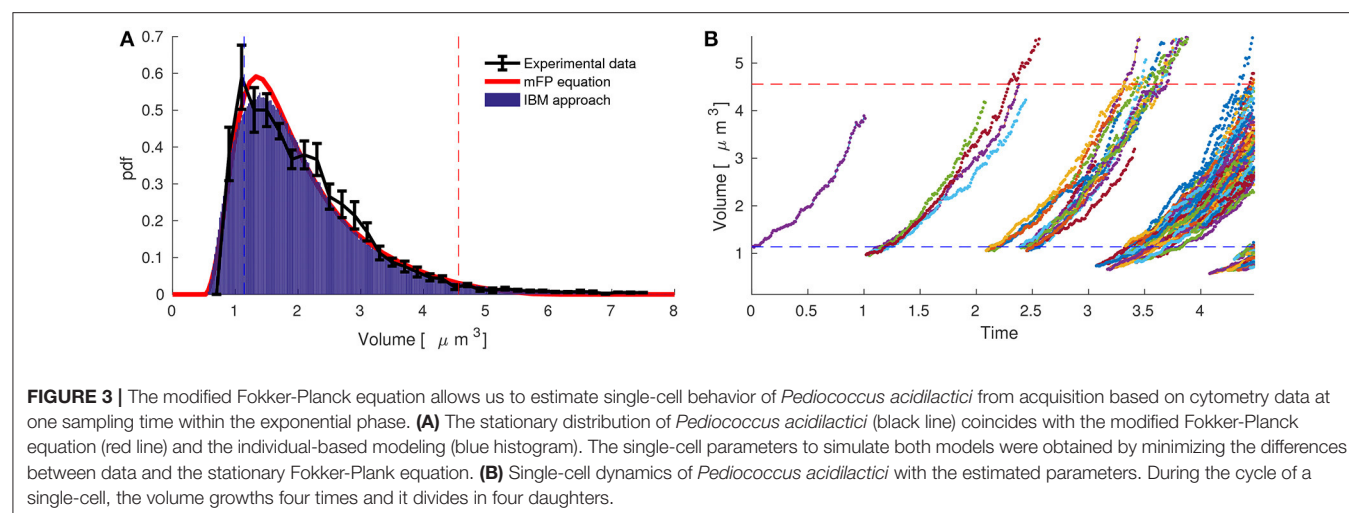


TABLE 2 | Bounds and estimations of the best set of parameters of the modified Fokker-Planck equation to reproduce the experimental volume stationary distribution of *P. acidilactici*.

θ	θ_{\min}	θ_{\max}
$v_m = 4.5574$	1	9
$\mu = 1.1619$	0.7	1.5
$\xi = 0.13439$	0.075	0.2
$\sigma = 0.3$	0	0.3

We assume that bacteria have 2 division planes and therefore one mother produces four daughters of 1/4 of the mother's volume. Upper bound on the standard deviation of the statistics of division σ was considered 0.3 to avoid overlapping between distribution of mother sizes and daughter sizes.

accommodate the errors for assuming that the mother divides into four perfectly round daughters. For coccoid cells with two planes of division, there is a short transition where cells are not completely round (Pinho et al., 2013; Monteiro et al., 2015). For the time-scales here considered this is a simplification that seems appropriate. Moreover, we have tried to reduce this bound resulting in similar estimations but with worse fit. For all these reasons we have considered an upper bound for the standard deviation of the mother distribution sufficiently small to avoid relevant overlapping between the mother and the daughter distributions. In this way, we force a scenario where the probability of having daughter volumes greater than mother volumes is low. Note that a standard deviation of 0.3 is reasonable attending to other mother distributions in the literature (Amir, 2014).

We also validate the results confirming that the specific growth rate of the population, μ^p in (3), coincides with the growth rate of the cell volume, μ in (A1a) and (A2a). Both population and volume should increase by one-fourth in one cell cycle. The specific growth rate of the population was estimated using the growth curves of *P. acidilactici* in **Figure 2D**. The calculated specific growth rate (1.1619 h^{-1}) is similar to the rate using cell counting with cytometry ($1.163 \pm 0.394 \text{ h}^{-1}$) and larger than the rate estimated from the biomass growth curve ($0.904 \pm 0.021 \text{ h}^{-1}$).

Individual-based modeling of *P. acidilactici* can now be implemented using the estimated single-cell parameters in **Table 2**. **Figure 3B** depicts the simulations starting with one cell at the mean of the daughter volumes ($v_d = v_m/4 = 1.14$). We observe how the fluctuations, dependent on ξ , resembles experimental single-cell dynamics in the literature (Deforet et al., 2015). In order to obtain such simulations, it is critical to consider that during division one mother gives four daughters, volume is conserved and that volumes grow four-fold during a cell-cycle.

4. CONCLUDING REMARKS

In this work, we have developed a modified Fokker-Planck equation describing the statistics of a population from

their single-cell parameters. The model is based on the assumptions that cell volumes grow exponentially and cells divide following the sizer principle. We have tested and numerically compared the modified Fokker-Planck with its equivalent individual-based modeling approach. Simulations resulted critical to understand several observed phenomena during the exponential phase of growth of bacteria, including the necessity of considering stochasticity to obtain a distribution of volumes that is time-invariant and similar to experimental observations.

The modified Fokker-Planck equation is also a powerful tool to estimate the behavior of single-cells inside populations. Instead of requiring single-cell measurements, we make use of flow cytometry to find the volume distribution of a population of *P. acidilactici* within the exponential phase. The combination of the modified Fokker-Planck equation with data provides information about the growth rate and stochasticity of the single-cell volume, as well as the statistics of the mother and daughter volumes. For a good correspondence between model and data, it is fundamental to assume that the *P. acidilactici* have two planes of division and its volume and population numbers grow by a fourth during a cell cycle.

The proposed methods allow efficient analysis of flow cytometry data to find single-cell behavior. In fact, they pave the way for studying cell heterogeneity in numerous applications in food microbiology, such as in quantitative risk assessment and prediction of shelf life.

AUTHOR CONTRIBUTIONS

MG and AA: designed the theoretical study, developed the methodology, and drafted the manuscript; JV: designed the experimental study and analyzed the data; IT: collected the data in the flow cytometry; MG: conducted the modeling experiments. All authors approved the final version of the manuscript.

FUNDING

The authors acknowledge financial support from the Spanish Government (MINECO) and the European Regional Development Fund (ERDF) through the projects "RESISTANCE" (DPI2014-54085-JIN) and "IMPROWINE" (AGL2015-67504-C3-2-R) and from the Spanish Council for Scientific Research (CSIC) for the project PIE 201230E042. We also acknowledge funds received from the Axencia Galega de Investigación (GAIN).

ACKNOWLEDGMENTS

We thank J. I. Molina for helping to program cytometry codes and Dr J. M. Freire (PosDoctoral Researcher at Pasteur Institute) for sharing with us his expertise in flow cytometry.

REFERENCES

- Alonso, A. A., Arias-Méndez, A., Balsa-Canto, E., García, M. R., Molina, J. I., Vilas, C., et al. (2013). Real time optimization for quality control of batch thermal sterilization of prepackaged foods. *Food Control* 32, 392–403. doi: 10.1016/j.foodcont.2013.01.002
- Alonso, A. A., Molina, I., and Theodoropoulos, C. (2014). Modeling bacterial population growth from stochastic single cell dynamics. *Appl. Environ. Microbiol.* 80, 5241–5253. doi: 10.1128/AEM.01423-14
- Amir, A. (2014). Cell size regulation in bacteria. *Phys. Rev. Lett.* 112:208102. doi: 10.1103/PhysRevLett.112.208102
- An, G., Fitzpatrick, B. G., Christley, S., Federico, P., Kanarek, A., Neilan, R. M., et al. (2017). Optimization and control of agent-based models in biology: a perspective. *Bull. Math. Biol.* 79, 63–87. doi: 10.1007/s11538-016-0225-6
- Anastasiadou, S., Papagianni, M., Filiouis, G., Ambrosiadis, I., and Koidis, P. (2008). Pediocin SA-1, an antimicrobial peptide from *Pediococcus acidilactici* NRRL B5627: production conditions, purification and characterization. *Bioresour. Technol.* 99, 5384–5390. doi: 10.1016/j.biortech.2007.11.015
- Athale, C. A., and Chaudhari, H. (2011). Population length variability and nucleoid numbers in *Escherichia coli*. *Bioinformatics* 27, 2944–2948. doi: 10.1093/bioinformatics/btr501
- Augustin, J. C., Ferrier, R., Hezard, B., Lintz, A., and Stahl, V. (2015). Comparison of individual-based modeling and population approaches for prediction of foodborne pathogens growth. *Food Microbiol.* 45, 205–215. doi: 10.1016/j.fm.2014.04.006
- Banwo, K., Sanni, A., and Tan, H. (2013). Technological properties and probiotic potential of *Enterococcus faecium* strains isolated from cow milk. *J. Appl. Microbiol.* 114, 229–241. doi: 10.1111/jam.12031
- Baranyi, J., and Roberts, T. A. (1995). Mathematics of predictive food microbiology. *Int. J. Food Microbiol.* 26, 199–218. doi: 10.1016/0168-1605(94)00121-L
- Cassin, M. H., Lammerding, A. M., Todd, E. C. D., Ross, W., and McColl, R. S. (1998). Quantitative risk assessment for *Escherichia coli* O157:H7 in ground beef hamburgers. *Int. J. Food Microbiol.* 41, 21–44. doi: 10.1016/S0168-1605(98)00028-2
- Chandler, W. L., Yeung, W., and Tait, J. F. (2011). A new microparticle size calibration standard for use in measuring smaller microparticles using a new flow cytometer. *J. Thromb. Haemost.* 9, 1216–1224. doi: 10.1111/j.1538-7836.2011.04283.x
- Deforet, M., van Ditmarsch, D., and Xavier, J. B. (2015). Cell-size homeostasis and the incremental rule in a bacterial pathogen. *Biophys. J.* 109, 521–528. doi: 10.1016/j.bpj.2015.07.002
- Egea, J. A., Vazquez, E., Banga, J. R., and Martín, R. (2009). Improved scatter search for the global optimization of computationally expensive dynamic models. *J. Glob. Optim.* 43, 175–190. doi: 10.1007/s10898-007-9172-y
- Fahse, L., Wissel, C., and Grimm, V. (1998). Reconciling classical and individual-based approaches in theoretical population ecology: a protocol for extracting population parameters from individual-based models. *Am. Nat.* 152, 838–52. doi: 10.1086/286212
- Ferrer, J., Prats, C., López, D., and Vives-Rego, J. (2009). Mathematical modelling methodologies in predictive food microbiology: a SWOT analysis. *Int. J. Food Microbiol.* 134, 2–8. doi: 10.1016/j.ijfoodmicro.2009.01.016
- Fishov, I., Zaritsky, A., and Grover, N. B. (1995). On microbial states of growth. *Mol. Microbiol.* 15, 789–794.
- Freedman, D., and Diaconis, P. (1981). On the histogram as a density estimator: L 2 theory. *Z. Wahrscheinlichkeitstheor. Verw. Geb.* 57, 453–476. doi: 10.1007/BF01025868
- Gangan, M. S., and Athale, C. A. (2017). Threshold effect of growth rate on population variability of *Escherichia coli* cell lengths. *R. Soc. Open Sci.* 4:160417. doi: 10.1098/rsos.160417
- García, M. R., Cabo, M. L., Herrera, J. R., Ramilo-Fernández, G., Alonso, A. A., and Balsa-Canto, E. (2017). Smart sensor to predict retail fresh fish quality under ice storage. *J. Food Eng.* 197, 87–97. doi: 10.1016/j.jfoodeng.2016.11.006
- García, M. R., Vilas, C., Banga, J. R., and Alonso, A. A. (2008). Exponential observers for distributed tubular (bio)reactors. *AIChE J.* 54, 2943–2956. doi: 10.1002/aic.11571
- García, M. R., Vilas, C., Herrera, J. R., Bernárdez, M., Balsa-Canto, E., and Alonso, A. A. (2015). Quality and shelf-life prediction for retail fresh hake (*Merluccius merluccius*). *Int. J. Food Microbiol.* 208, 65–74. doi: 10.1016/j.ijfoodmicro.2015.05.012
- Gardiner, C. (2004). *Handbook of Stochastic Methods: For Physics, Chemistry & the Natural Sciences*. Berlin: Springer.
- Harris, L. K., and Theriot, J. A. (2016). Relative rates of surface and volume synthesis set bacterial cell size. *Cell* 165, 1479–1492. doi: 10.1016/j.cell.2016.05.045
- Higham, D. J. (2001). An algorithmic introduction to numerical simulation of stochastic differential equations. *SIAM Rev.* 43, 525–546. doi: 10.1137/S0036144500378302
- Holt, J. G. (1994). *Bergey's Manual of Determinative Bacteriology*, 9th Edn. Baltimore, MD: Williams & Wilkins.
- Julià, O., Comas, J., and Vives-Rego, J. (2000). Second-order functions are the simplest correlations between flow cytometric light scatter and bacterial diameter. *J. Microbiol. Methods* 40, 57–61. doi: 10.1016/S0167-7012(99)00132-3
- Kaya, T., and Koser, H. (2009). Characterization of hydrodynamic surface interactions of *Escherichia coli* cell bodies in shear flow. *Phys. Rev. Lett.* 103:138103. doi: 10.1103/PhysRevLett.103.138103
- Koch, A. L. (1966). Distribution of cell size in growing cultures of bacteria and the applicability of the collins-richmond principle. *J. Gen. Microbiol.* 45, 409–417. doi: 10.1099/00221287-45-3-409
- Koutsoumanis, K., and Nychas, G.-J. E. (2000). Application of a systematic experimental procedure to develop a microbial model for rapid fish shelf life predictions. *Int. J. Food Microbiol.* 60, 171–184. doi: 10.1016/S0168-1605(00)00309-3
- Koutsoumanis, K. P., and Aspidou, Z. (2017). Individual cell heterogeneity in predictive food microbiology: challenges in predicting a “noisy” world. *Int. J. Food Microbiol.* 240, 3–10. doi: 10.1016/j.ijfoodmicro.2016.06.021
- Membré, J. M., and Lambert, R. J. W. (2008). Application of predictive modelling techniques in industry: from food design up to risk assessment. *Int. J. Food Microbiol.* 128, 10–15. doi: 10.1016/j.ijfoodmicro.2008.07.006
- Métris, A., Le Marc, Y., Elfving, A., Ballagi, A., and Baranyi, J. (2005). Modelling the variability of lag times and the first generation times of single cells of *E. coli*. *Food Microbiol.* 100, 13–19. doi: 10.1016/j.ijfoodmicro.2004.10.004
- Monteiro, J. M., Fernandes, P. B., Vaz, F., Pereira, A. R., Tavares, A. C., Ferreira, M. T., et al. (2015). Cell shape dynamics during the staphylococcal cell cycle. *Nat. Commun.* 6:8055. doi: 10.1038/ncomms9055
- Painter, P. R., and Marr, A. G. (1968). Mathematics of microbial populations. *Annu. Rev. Microbiol.* 22, 519–548. doi: 10.1146/annurev.mi.22.100168.002511
- Peleg, M., and Shetty, K. (1997). Modeling microbial populations with the original and modified versions of the continuous and discrete logistic equations. *Crit. Rev. Food Sci. Nutr.* 37, 471–490. doi: 10.1080/10408399709527785
- Pinho, M. G., Kjos, M., and Veening, J. (2013). How to get (a)round: mechanisms controlling growth and division of coccoid bacteria. *Nat. Rev. Microbiol.* 11, 601–614. doi: 10.1038/nrmicro3088
- Planas, M., Vázquez, J., Marqués, J., Pérez-Lomba, R., González, M., and Murado, M. (2004). Enhancement of rotifer (*Brachionus plicatilis*) growth by using terrestrial lactic acid bacteria. *Aquaculture* 240, 313–329. doi: 10.1016/j.aquaculture.2004.07.016
- Prats, C., Ferrer, J., López, D., Giró, A., and Vives-Rego, J. (2010). On the evolution of cell size distribution during bacterial growth cycle: experimental observations and individual-based model simulations. *Afr. J. Microbiol. Res.* 4, 400–407.
- Ray, B. (1992). “Bacteriocins of starter culture bacteria as food biopreservatives: an overview,” in *Food Biopreservatives of Microbial Origin*, eds B. Ray and M. A. Daeschel (Boca Raton, FL: CRC Press), 177–205.
- Robert, L., Hoffmann, M., Krell, N., Aymerich, S., Robert, J., and Doumic, M. (2014). Division in *Escherichia coli* is triggered by a size-sensing rather than a timing mechanism. *BMC Biol.* 12:17. doi: 10.1186/1741-7007-12-17
- Ross, T., Dalgaard, P., and Tienungoon, S. (2000). Predictive modelling of the growth and survival of *Listeria* in fishery products. *Int. J. Food Microbiol.* 62, 231–245. doi: 10.1016/S0168-1605(00)00340-8
- Sauls, J. T., Li, D., and Jun, S. (2016). Adder and a coarse-grained approach to cell size homeostasis in bacteria. *Curr. Opin. Cell Biol.* 38, 38–44. doi: 10.1016/j.cceb.2016.02.004
- Scatassa, M. L., Gaglio, R., Macaluso, G., Francesca, N., Randazzo, W., Cardamone, C., et al. (2015). Transfer, composition and technological characterization of the

- lactic acid bacterial populations of the wooden vats used to produce traditional stretched cheeses. *Food Microbiol.* 52, 31–41. doi: 10.1016/j.fm.2015.06.008
- Shampine, L. F., and Reichelt, M. W. (1997). The MATLAB ODE suite. *SIAM J. Sci. Comput.* 18, 1–22. doi: 10.1137/S1064827594276424
- Simpson, R., Almonacid-Merino, S. F., and Torres, J. A. (1993). Mathematical models and logic for the computer control of batch retorts: Conduction-heated foods. *J. Food Eng.* 20, 283–295. doi: 10.1016/0260-8774(93)90069-V
- Standen, B. T., Rodiles, A., Peggs, D. L., Davies, S. J., Santos, G. A., and Merrifield, D. L. (2015). Modulation of the intestinal microbiota and morphology of tilapia, *Oreochromis niloticus*, following the application of a multi-species probiotic. *Appl. Microbiol. Biotechnol.* 99, 8403–8417. doi: 10.1007/s00253-015-6702-2
- Taheri-Araghi, S. (2015). Self-consistent examination of Donachie's constant initiation size at the single-cell level. *Front. Microbiol.* 6:1349. doi: 10.3389/fmicb.2015.01349
- Taheri-Araghi, S., Bradde, S., Sauls, J. T., Hill, N. S., Levin, P. A., Paulsson, J., et al. (2015). Cell-size control and homeostasis in bacteria. *Curr. Biol.* 25, 385–391. doi: 10.1016/j.cub.2014.12.009
- Trefethen, L. N. (2000). *Spectral Methods in MATLAB*. Philadelphia, PA: Society for Industrial and Applied Mathematics.
- Turner, R. D., Ratcliffe, E. C., Wheeler, R., Golestanian, R., Hobbs, J. K., and Foster, S. J. (2010). Peptidoglycan architecture can specify division planes in *Staphylococcus aureus*. *Nat. Commun.* 1, 1–9. doi: 10.1038/ncomms1025
- Vande Wouwer, A., Saucez, P., and Vilas, C. (2014). *Simulation of ODE/PDE Models with MATLAB®, OCTAVE and SCILAB. Scientific and Engineering Applications*. Cham: Springer International Publishing.
- Vázquez, J., Docasal, S., Prieto, M., González, M., and Murado, M. (2008). Growth and metabolic features of lactic acid bacteria in media with hydrolysed fish viscera. An approach to bio-silage of fishing by-products. *Bioresour. Technol.* 99, 6246–6257. doi: 10.1016/j.biortech.2007.12.006
- Vázquez, J. A., and Murado, M. A. (2008). Mathematical tools for objective comparison of microbial cultures. Application to evaluation of 15 peptones for lactic acid bacteria productions. *Biochem. Eng. J.* 39, 276–287. doi: 10.1016/j.bej.2007.09.012
- Vázquez, J. A., Nogueira, M., Durán, A., Prieto, M. A., Rodríguez-Amado, I., Rial, D., et al. (2011). Preparation of marine silage of swordfish, ray and shark visceral waste by lactic acid bacteria. *J. Food Eng.* 103, 442–448. doi: 10.1016/j.jfoodeng.2010.11.014
- Vilas, C., Arias-Méndez, A., García, M. R., Alonso, A. A., and Balsa-Canto, E. (2017). Towards predictive food process models: a protocol for parameter estimation. *Crit. Rev. Food Sci. Nutr.* doi: 10.1080/10408398.2016.1186591. [Epub ahead of print].
- Wang, P., Robert, L., Pelletier, J., Dang, W. L., Taddei, F., Wright, A., et al. (2010). Robust growth of *Escherichia coli*. *Curr. Biol.* 20, 1099–1103. doi: 10.1016/j.cub.2010.04.045
- Wilson, W. G. (1998). Resolving discrepancies between deterministic population models and individual-based simulations. *Am. Nat.* 151, 116–134.
- Zhou, J., Ellis, A. V., Voelcker, N. H., Zambon, A., Horowitz, M., Bhaya, D., et al. (2010). Recent developments in PDMS surface modification for microfluidic devices. *Electrophoresis* 31, 2–16. doi: 10.1002/elps.200900475
- Zwietering, M. H., Jongenburger, I., Rombouts, F. M., and van 't Riet, K. (1990). Modeling of the bacterial growth curve. *Appl. Environ. Microbiol.* 56, 1875–1881.

Conflict of Interest Statement: The authors declare that the research was conducted in the absence of any commercial or financial relationships that could be construed as a potential conflict of interest.

Copyright © 2018 García, Vázquez, Teixeira and Alonso. This is an open-access article distributed under the terms of the Creative Commons Attribution License (CC BY). The use, distribution or reproduction in other forums is permitted, provided the original author(s) or licensor are credited and that the original publication in this journal is cited, in accordance with accepted academic practice. No use, distribution or reproduction is permitted which does not comply with these terms.

APPENDIX

The individual-based modeling equations assuming 2 planes of division lead to:

$$\delta X^i = \mu \delta t + \xi \delta W \quad \text{with} \quad X^i = \ln(V^i) \quad (\text{A1a})$$

$$\text{If } X^i \geq X_m \sim f_{X_m}(x), \quad X^{n+1} \rightarrow X^i - \ln(4) \quad (\text{A1b})$$

$$X^{n+2} \rightarrow X^i - \ln(4) \quad (\text{A1c})$$

$$X^{n+3} \rightarrow X^i - \ln(4) \quad (\text{A1d})$$

$$X^i \rightarrow X^i - \ln(4) \quad (\text{A1e})$$

and the equivalent modified Fokker-Planck equation now reads:

$$\frac{\partial p(t, x)}{\partial t} = \underbrace{\frac{\xi^2}{2} \frac{\partial^2 p(t, x)}{\partial x^2} - \mu \frac{\partial p(t, x)}{\partial x}}_{\text{cell growth} = \frac{\partial J(t, x)}{\partial x}} + \underbrace{4f_{X_d}(x)Z - f_{X_m}(x)Z}_{\text{division}} - \underbrace{3p(t, x)Z}_{\text{normalization}} \quad \text{being} \quad (\text{A2a})$$

$$Z = \int_{\underline{x}}^{\bar{x}} F_m(x) \frac{\partial J(t, x)}{\partial x} dx \quad (\text{A2b})$$

$$p(t, \underline{x}) = p(t, \bar{x}) = 0 \quad \forall t \quad \text{boundary conditions} \quad (\text{A2c})$$

$$p(0, x) = \delta(x - x_d) \quad \forall x \quad \text{initial conditions} \quad (\text{A2d})$$



Corrigendum: Stochastic Individual-Based Modeling of Bacterial Growth and Division Using Flow Cytometry

Miriam R. García^{1*}, José A. Vázquez², Isabel G. Teixeira³ and Antonio A. Alonso^{1*}

¹ Bioprocess Engineering Group, Marine Research Institute-Spanish National Research Council (IIM-CSIC), Vigo, Spain,

² Group of Recycling and Valorisation of Waste Materials, Marine Research Institute-Spanish National Research Council (IIM-CSIC), Vigo, Spain, ³ Oceanology, Marine Research Institute-Spanish National Research Council (IIM-CSIC), Vigo, Spain

Keywords: individual-based modeling, stochastic modeling, cell cycle, bacterial growth and division, modified Fokker-Planck equation, flow cytometry, coccoid bacteria, predictive microbiology

A corrigendum on

Stochastic Individual-Based Modeling of Bacterial Growth and Division Using Flow Cytometry by García, M. R., Vázquez, J. A., Teixeira, I. G., and Alonso, A. A. (2018). *Front. Microbiol.* 8:2626. doi: 10.3389/fmicb.2017.02626

OPEN ACCESS

Edited and reviewed by:

Ferd L. Hellweger,
Technische Universität Berlin,
Germany

*Correspondence:

Miriam R. García
miriamr@iim.csic.es
Antonio A. Alonso
antonio@iim.csic.es

Specialty section:

This article was submitted to
Systems Microbiology,
a section of the journal
Frontiers in Microbiology

Received: 20 February 2018

Accepted: 19 March 2018

Published: 28 March 2018

Citation:

García MR, Vázquez JA, Teixeira IG
and Alonso AA (2018) Corrigendum:
Stochastic Individual-Based Modeling
of Bacterial Growth and Division Using
Flow Cytometry.
Front. Microbiol. 9:633.
doi: 10.3389/fmicb.2018.00633

1. There was a mistake in the writing of the cell growth term in Equation (2a) as published. The correct version appears below.

$$\frac{\partial p(t, x)}{\partial t} = \underbrace{\frac{\xi^2}{2} \frac{\partial^2 p(t, x)}{\partial x^2} - \mu \frac{\partial p(t, x)}{\partial x}}_{\text{cell growth} = \frac{\partial J(t, x)}{\partial x}} + \underbrace{2f_{X_d}(x)Z - f_{X_m}(x)Z}_{\text{division}} - \underbrace{p(t, x)Z}_{\text{normalization}} \quad (1)$$

2. The same mistake is repeated in equation (A2a). The correct version appears below.

$$\frac{\partial p(t, x)}{\partial t} = \underbrace{\frac{\xi^2}{2} \frac{\partial^2 p(t, x)}{\partial x^2} - \mu \frac{\partial p(t, x)}{\partial x}}_{\text{cell growth} = \frac{\partial J(t, x)}{\partial x}} + \underbrace{4f_{X_d}(x)Z - f_{X_m}(x)Z}_{\text{division}} - \underbrace{3p(t, x)Z}_{\text{normalization}} \quad \text{being} \quad (2)$$

The authors apologize for these mistakes. This error does not change the scientific conclusions of the article in any way.

The original article has been updated.

Conflict of Interest Statement: The authors declare that the research was conducted in the absence of any commercial or financial relationships that could be construed as a potential conflict of interest.

Copyright © 2018 García, Vázquez, Teixeira and Alonso. This is an open-access article distributed under the terms of the Creative Commons Attribution License (CC BY). The use, distribution or reproduction in other forums is permitted, provided the original author(s) and the copyright owner are credited and that the original publication in this journal is cited, in accordance with accepted academic practice. No use, distribution or reproduction is permitted which does not comply with these terms.



Digital Image Analysis of Yeast Single Cells Growing in Two Different Oxygen Concentrations to Analyze the Population Growth and to Assist Individual-Based Modeling

Marta Ginovart^{1*}, Rosa Carbó², Mónica Blanco¹ and Xavier Portell³

¹ Department of Mathematics, Universitat Politècnica de Catalunya, Barcelona, Spain, ² Department of Agri-Food Engineering and Biotechnology, Universitat Politècnica de Catalunya, Barcelona, Spain, ³ Cranfield Soil and Agrifood Institute, Cranfield University, Bedfordshire, United Kingdom

OPEN ACCESS

Edited by:

Ferdi L. Hellweger,
Northeastern University, United States

Reviewed by:

Marco Vanoni,
Università degli studi di Milano
Bicocca, Italy

José Manuel Guzmán,
Consejo Superior de Investigaciones
Científicas (CSIC), Spain

*Correspondence:

Marta Ginovart
marta.ginovart@upc.edu

Specialty section:

This article was submitted to
Systems Microbiology,
a section of the journal
Frontiers in Microbiology

Received: 29 June 2017

Accepted: 15 December 2017

Published: 04 January 2018

Citation:

Ginovart M, Carbó R, Blanco M and
Portell X (2018) Digital Image Analysis
of Yeast Single Cells Growing in Two
Different Oxygen Concentrations to
Analyze the Population Growth and to
Assist Individual-Based Modeling.
Front. Microbiol. 8:2628.
doi: 10.3389/fmicb.2017.02628

Nowadays control of the growth of *Saccharomyces* to obtain biomass or cellular wall components is crucial for specific industrial applications. The general aim of this contribution is to deal with experimental data obtained from yeast cells and from yeast cultures to attempt the integration of the two levels of information, individual and population, to progress in the control of yeast biotechnological processes by means of the overall analysis of this set of experimental data, and to assist in the improvement of an individual-based model, namely, INDISIM-Saccha. Populations of *S. cerevisiae* growing in liquid batch culture, in aerobic and microaerophilic conditions, were studied. A set of digital images was taken during the population growth, and a protocol for the treatment and analyses of the images obtained was established. The piecewise linear model of Buchanan was adjusted to the temporal evolutions of the yeast populations to determine the kinetic parameters and changes of growth phases. In parallel, for all the yeast cells analyzed, values of direct morphological parameters, such as area, perimeter, major diameter, minor diameter, and derived ones, such as circularity and elongation, were obtained. Graphical and numerical methods from descriptive statistics were applied to these data to characterize the growth phases and the budding state of the yeast cells in both experimental conditions, and inferential statistical methods were used to compare the diverse groups of data achieved. Oxidative metabolism of yeast in a medium with oxygen available and low initial sugar concentration can be taken into account in order to obtain a greater number of cells or larger cells. Morphological parameters were analyzed statistically to identify which were the most useful for the discrimination of the different states, according to budding and/or growth phase, in aerobic and microaerophilic conditions. The use of the experimental data for subsequent modeling work was then discussed and compared to simulation results generated with INDISIM-Saccha, which allowed us to advance in the development of this yeast model, and illustrated the utility of data at different levels of observation and the needs and logic behind the development of a microbial individual-based model.

Keywords: *Saccharomyces cerevisiae*, morphometry, image analysis, aerobic, microaerophilic, Buchanan model, individual-based model, INDISIM-Saccha

INTRODUCTION

Saccharomyces cerevisiae, known as brewer's yeast or bread yeast, is one of the yeasts with the greatest economic and social impact. *Saccharomyces cerevisiae* is a facultative anaerobic yeast and a Crabtree-positive yeast. In the presence of oxygen and low glucose concentration (e.g., below 10 g/L) it usually uses oxidative metabolism, but ferments in higher glucose concentrations (e.g., above 10 g/L) regardless of oxygen concentration. Alcoholic fermentation is the most widely used in several industrial processes. When the conditions of the environment vary *S. cerevisiae* must adapt to the environmental changes being forced to pass in a short period of time from aerobic conditions to microaerophilic and anaerobic conditions at the end, changing the type of metabolism depending on the concentration of oxygen present in its neighborhood.

There is an increasing interest in yeasts because of the potentiality of whole cells. For some biotechnological applications, it is very important to obtain large amounts of yeast biomass (rather than ethanol, as happens in other types of applications). In order to obtain greater numbers of cells or larger cells with more cellular components usable in diverse industries, *Saccharomyces* must grow in a medium with oxygen available and low initial sugar concentration, to avoid the Crabtree effect. The yeast obtained is utilized as starter in fermented beverage industries, or as probiotic yeast with health benefit, and it is also used to obtain cellular components such as proteins and polysaccharides (e.g., glucans), which are of great value as functional ingredients in the food industry (Arevalo-Villena et al., 2017).

Like all microorganisms, *S. cerevisiae* has defined growth phases that characterize the temporal evolution of population size in a batch culture: adaptation or latency phase (lag phase), exponential or logarithmic phase (log phase), stationary phase, and death phase. The determination of the different growth phases of a culture can assist in the understanding of the changes experienced by microbial population and single microorganisms. Studies about yeast life-history traits involved in the adaptation to different environments are indispensable. Carrying capacity (maximum size of the population that can be supported upon the available resources), reproduction rate or intrinsic growth rate, and cell size are three life-history traits affected by the medium. For instance, understanding the causes of the variability and correlations of life-history traits in a yeast batch culture requires the analysis of the rate of resource uptake, which depends both on the amount of resources in the environment and on the activity of enzymes involved in the uptake (Spor et al., 2008); in that work, these three life-history traits were strongly affected by the glucose content in the culture medium, with obvious trade-offs between carrying capacity and growth rate, and between growth rate and cell size.

Morphometry, a branch of morphology that refers to quantitative analysis of form (size and shape), can be applied to unicellular microorganisms. In the case of *S. cerevisiae*, spheroidal cells, ellipsoidal cells, and sometimes cylindrical cells can be observed. The components of size and shape are obtained from a set of quantitative variables such as length, width,

height, angles, etc. that can be analyzed statistically in order to summarize the changes undergone in the object of study, that is, the microbial cell (Bookstein, 1997). The morphometric analysis consists of three fundamental stages: image processing, acquisition of variables, and statistical analysis (Toro et al., 2010). It should be noted that the growth rate, mutation, and environmental conditions affect the size and shape of the yeast. For instance, when *S. cerevisiae* grows in anaerobic conditions, cells are generally smaller than cells grown under aerobic conditions (Liesche et al., 2015). In addition, the morphology of the cells is closely related to their physiological state and their status in the cell cycle (Coelho et al., 2004). The relevance of cell size measurements to study the response of yeast cells submitted to various stresses has also been shown (Tibayrenc et al., 2010; Portell et al., 2011).

Modeling, from its broadest definition, is a very necessary tool to represent, analyze and discuss issues related to biological systems. The classical mathematical modeling based on continuous functions, derivable functions, differential equations, optimization methods, function adjustments, together with statistical modeling are by far the most widely used methodologies. Computational models are an interesting alternative to these methodologies and they are a modeling approach that is gaining pace to investigate microbial systems. Among them, the agent-based models or individual-based models (IBMs) are becoming more frequently used (Gorochowski, 2016; Hellweger et al., 2016; Jayathilake et al., 2017). In order to investigate a microbial system the above mentioned tools or methodologies are necessary, and can complement one another, providing additional information that benefits the overall modeling task. The diverse sets of experimental data, from macroscopy or population-level and from microscopic or individual-level, proceeding from the system itself, enhance the different modeling methodologies, since they provide the opportunity to deal with different types of observations of the same system.

Microbial IBMs are computational models that explicitly simulate autonomous living entities. Traditionally, they have not been deemed necessary to deal with microbial liquid cultures, usually assumed to be performed by axenic populations under perfectly homogeneous media; however, even clonal populations show biological heterogeneity in the individual behavior (González-Cabaleiro et al., 2017). Microbes (individuals) are treated as unique and discrete entities which have at least two independent properties plus their position in the medium. Rules are applied to define the individuals and the behavior of the medium; hence, the descriptor rule-based approach fits the methodology. The behavior of the population, of all existing individuals at any given time, emerges from the cumulative behavior of biotic interactions (among individuals) and abiotic interactions (between individuals and surrounding medium), which are interactions at individual-level. At the same time, the system-level dynamics constrain the behavior of the individuals. IBMs facilitate the understanding and formulation of the connection between individual microbes and properties at population level (e.g. heterogeneity, diversity, structure), as well as the interactions of microbes within the population

and with their changing environment. INDISIM-YEAST is a microbial IBM that simulates a generic budding yeast, and it was used to assess the methodology for the investigation of this microbial population (Ginovart et al., 2007, 2011a,b). After that, a quantitative IBM which was focused on the fermentative (anaerobic) growth of the yeast *S. cerevisiae* was designed and termed INDISIM-*Saccha* (Portell et al., 2014). However, the fact that this model incorporated a fermentative (anaerobic) yeast metabolism limited its applicability for the study of some interesting biotechnological processes. Thus INDISIM-*Saccha* was extended and adapted to take into account the aerobic growth of *S. cerevisiae*, obtaining only some preliminary results at a population level, but not those results corresponding to an individual level of observation (Portell, 2014).

Microbial IBMs in general (Hellweger et al., 2016), and in particular INDISIM-*Saccha* (Portell et al., 2014) construct a virtual representation of a real system, which allows the characterization of the cells by means of their size, shape, and biomass. Thus, this type of model is capable of dealing with ideas that configure certain purposes of biotechnological applications using these individuals (their biomass and/or cellular wall components), facilitating the investigation of the system by modeling individual actions or behaviors directly linked with metabolic pathways, reproduction and viability, limited or stimulated by the local environmental conditions where the microbe is located. This representation of a microbial system allows the inclusion of diverse life-history traits involved in the adaptation of yeast to its environment, for instance, at population level, the reproduction rate estimated by the intrinsic growth rate or the carrying capacity (maximum size of population supported by the available resources), and, at the same time, at individual level, the cell size related to lifespan. Aging in the mother cell by means of an asymmetry and replicative lifespan and aging in the population by means of nutrient availability and chronological lifespan of the individual yeast cells (Cipollina et al., 2007; Carmona-Gutierrez and Büttner, 2014) are taken into account in the INDISIM-*Saccha* model. These different forms of yeast aging enable the control of population dynamics.

The need to connect experimentalists and modelers in general, and in particular, the combination of microbial IBMs and experimentation has recently been advocated as microbial individual-based ecology (Kreft et al., 2013; Hellweger et al., 2016). Microbial IBMs use data provided by individual-based observations but the integration of these data into the formulation and implementation of these models is not a direct task. A gap between modelers and experimentalists does really exist and efforts to bring together and encourage cooperation between both communities is indispensable (Hellweger, 2017; Succurro et al., 2017). Providing clear evidence of the utility of the experimental data for, and the needs and logic behind the IBMs can be a valuable and straightforward way of filling the stated gap.

The aims of this work are: (i) to obtain and analyze the results of the different morphometric parameters from the digital image analysis of yeast cells growing in two initial oxygen conditions (aerobic and microaerophilic cultures); (ii) to analyze the kinetic parameters of the population growth in order to detect the transition among lag, log, and stationary phases; (iii)

to identify and connect the individual yeast states and population growth phases using individual-based and population-based experimental observations; (iv) to detect in both concentrations of oxygen the population growth phases with either larger cells or greater number of cells; (v) to explore and critically assess the data analysis developed in the improvement of the parameterization and calibration of INDISIM-*Saccha*, carrying out the testing of some model predictions, both at a population level and single-cell level.

MATERIALS AND METHODS

Experimental Data

The experimental study was carried out using the *Saccharomyces cerevisiae* (LALVIN DV10, LALLEMAND Australia), a yeast strain with remarkable biotechnological characteristics. The medium used in the aerobic growth tests was composed of 10 g/L glucose, 3 g/L yeast extract, and 3 g/L of casein peptone. In microaerophilic conditions, the medium was supplemented with 0.5 g/L sodium thioglycolate and 0.001 g/L resazurin which acted by lowering the redox potential of the medium and redox indicator respectively. The media pH was adjusted to 3.5 with orthophosphoric acid. In aerobic conditions the inocula were cultured in 250 mL cotton-plugged flasks with 100 mL of the same media used in the experimental cultures. In microaerophilic conditions the inocula were cultured in 50 mL tubes completely filled with the described media. The inocula were incubated at 27°C and stirred magnetically for 72 h. The cultures for the experimental data were cultivated in a 1,000 mL flask, with 600 mL of the same fresh medium, inoculated with 0.1 mL of the preculture and also incubated at 27°C using a magnetic stirrer (300 r.p.m.) for approximately 30 h.

The experiments were performed with five replicates. Every 90 min a sample was extracted from four flasks to be analyzed, reserving the fifth flask for measuring the dissolved oxygen. Viable population, dissolved oxygen and glucose concentration were determined regularly throughout the 30 h of the study. Ethanol concentration was determined at 18 h and at the end of the study. Colony forming units were determined by using the pour plate method. Glucose concentration was measured by high-performance liquid chromatography equipped with RI detector (HPLC; Bekman). Ethanol concentration was determined with a Hewlett Packard 5890 Series II GC equipped with flame ionization detection using nitrogen as carrier gas. Initial dissolved oxygen concentration was determined with an oxygen electrode (OxyGuard, Handy Polarix).

Acquisition of Digital Images

Images were taken using a Nikon Eclipse LV100 microscope equipped with a digital camera Nikon Infinity 1 Tv lens C-0.45x mounting an objective Nikon Lu Plan Fuer 50x/0.08° (numerical aperture). After calibration, the software Perfect Image v7.7 was used to obtain the images. The pixel size found was 0.0975 µm. Cell preparations were obtained every 90 min for the four replicates of the aerobic and microaerophilic conditions, producing three images per preparation. Samples were not sonicated before being processed (see also Supplementary

Material). When necessary, the cell suspension was diluted in sterile saline solution and homogenized using a Vortex mixer. **Figure 1** shows an example of the images obtained.

Digital Image Analysis

ImageJ is an open source image processing program for multidimensional image data with a focus on scientific imaging in the public domain (<http://rsb.info.nih.gov/ij/index.html>). Fiji is a distribution of ImageJ that focuses on biological-image analysis (<http://fiji.sc/Fiji>). To analyze all digital images obtained a protocol was designed and performed using the open source image processing package Fiji (Schindelin et al., 2012). The 32 B color images were transformed to binary files following the steps summarized in **Figure 2**. A blurred copy of the image was subtracted from the original image in order to decrease the noise coming from the background and the resulting 32 B color image was saved as an 8 B greyscale image. The image contrast was enhanced using the options “Saturated pixels” and “Normalize” from the “Enhance Contrast” tool. After segmentation using the option “Auto Threshold” from the “Adjust” menu of Fiji, the image was saved as a 1B black and white image. Four more steps were then applied to the binary image to obtain separated yeast cells: automatic object closing, hole filling, object separation, and manual object closing (Pertusa, 2010).

Each of the cells studied was analyzed individually to verify that the ImageJ program had complied with the criteria previously established in the protocol of the digital image analysis to separate the objects correctly. In order to identify the budded cells in the image analysis, in the case of pairs of cells, it was considered that the buds were those cells which were smaller than

the one to which they were adhered. However, when a couple of cells were of similar sizes they were digitally processed as separate cells. Thus, from direct visual inspection of the images collected, the budding state (yes or not) of each one of the cells was

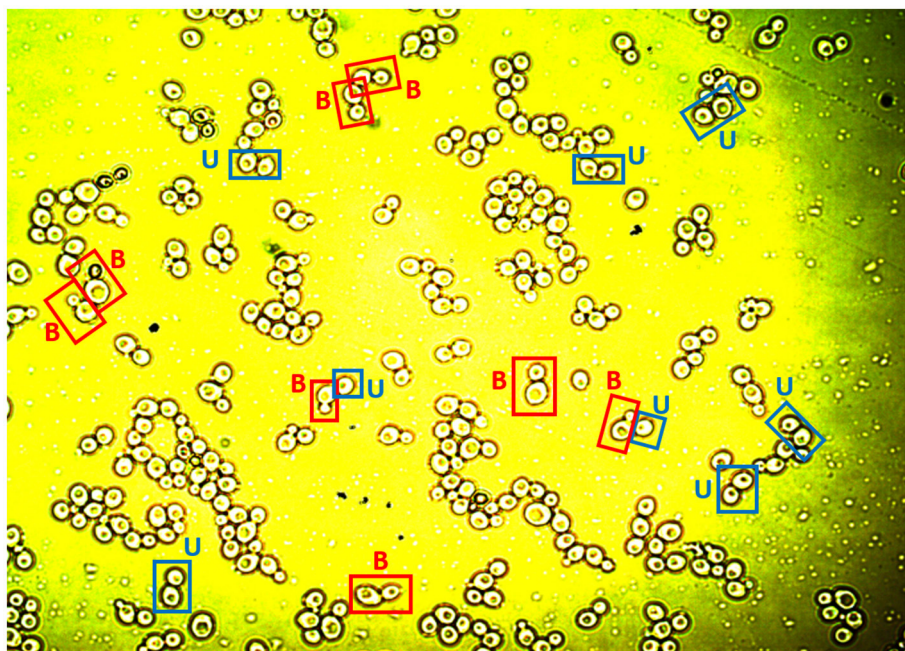
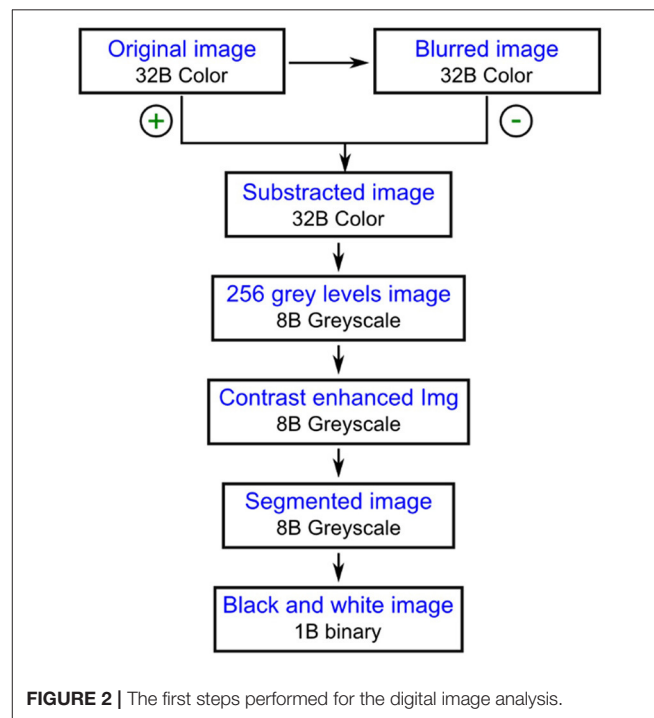


FIGURE 1 | An image showing yeast cells available for analysis. The labels “B” and “U” exemplify cells classified as budded cells (B) or unbudded cells (U) after the analysis of the image (see text).

manually recorded (as would have been done with the help of a microscope). **Figure 1** shows some examples of the classification applied to the yeast cells as budded cells and unbudded cells.

Imaged objects (yeast cells) were characterized by measuring direct and derived morphological parameters. Direct morphological parameters studied were: the area (A), the perimeter (P), the major diameter (D_{MAX}), and the minor diameter (D_{MIN}). The derived morphological parameters computed and studied were circularity and elongation (or aspect ratio). The circularity (C) is a measure of the agreement of the shape of the object to a perfect circle ($C = 1$) that takes into account the area and perimeter of a cell, and can be computed as follows:

$$C = 4 \pi \frac{A}{P^2} \quad (1)$$

The aspect ratio (AR) is the quotient between the major diameter and minor diameter of the ellipse fitting inside the object surface:

$$AR = \frac{D_{MAX}}{D_{MIN}} \quad (2)$$

and it can also be regarded as a common measure of elongation (E) because values moving away from 1 indicate an increasingly elongated shape.

A macro was implemented in the ImageJ program to carry out the analysis of all the images in the most automatic way possible (fix the scale, introduce fixed values of some parameters, improve image contrast, etc.), obtaining better defined cells with no dirty spots or background noise around them. After performing several tests to adjust the threshold, three macros were created with three different methods for the “Auto Threshold” option included in Fiji. The most frequently used method was “Default,” although depending on the image, the options “Intermodes” or “Yen” were applied since they better defined the cells, with clearly delimited borders and less noise. However, once a macro was executed, to evaluate whether a manual intervention was necessary in this process, it was verified that: (i) all the analyzed objects were considered as cells of interest, since the program did not distinguish a yeast cell from other objects (such as air bubbles or suspended particles); (ii) the budded cells remained attached; and (iii) the correct execution of the closures of the edges of the cells was made.

Analysis of Data at Both the Microbial Population Level and the Individual Level of Yeast Cells

In a microbial system there are macroscopic observations that inform about the temporal evolution of the population, and microscopic observations that provide information on the specific characteristics of the cells making up this population. In this study both type of observations were accomplished and the investigation of the system was carried out by combining and comparing results on kinetic parameters of adjusted continuous dynamic models at the population level (macroscopic observations), and on models related to the distributions of individual properties of the elements that configure this

population (microscopic observations). Thus, for the analysis of the data two different methodologies were applied according to the typology of the observations. In the first stage of the process, the modeling of the growth of the microbial population with the estimated kinetic parameters that characterized the temporal evolution was used. In the second stage of the modeling process, the individual variables (area, perimeter, minor diameter, major diameter, circularity and elongation) of the cells forming these populations were studied by means of the evolutions of their distributions. At this stage, the information obtained in the first stage of the population analysis was taken into account.

Both numerical summaries (descriptive statistics) and graphical summaries (boxplots, histograms, and scatterplots) were performed to synthesize and provide information for the two growth conditions (aerobic and microaerophilic). Possible association between pairs of variables were tested using the Chi-square test of independence.

From the temporal evolutions of number of yeast cells, the fitting of the three phase linear model known as Buchanan model (Buchanan et al., 1997) was carried out. It is a simple but good enough model for the purposes of this work, since it allowed us to estimate the kinetic parameters involved in the definition of the three main phases that characterize a typical curve of microbial growth in a closed liquid culture: lag phase, log phase, and stationary phase. In the Buchanan model, the three phases are described as follows:

$$P(t) = \begin{cases} P_0 & \text{for } t \leq t_{lag} \\ P_0 + \mu (t - t_{lag}) & \text{for } t_{lag} \leq t \leq t_{max} \\ P_{max} & \text{for } t \geq t_{max} \end{cases} \quad (3)$$

where: $P(t)$ is the base 10 logarithm of population density at time t (Log cfu/mL); P_0 is the base 10 logarithm of the initial population density (Log cfu/mL); P_{max} is the base 10 logarithm of the maximum population density maintained by the environment or the carrying capacity of the system (Log cfu/mL); t is the elapsed time (h); t_{lag} is the time at which the adaptation phase ends (h); t_{max} is the time in which the maximum population density is reached (h); and μ is the specific growth rate of the culture (Log cfu/mL h⁻¹). The model describes the evolution of the population providing a mathematical method for the adjustment of growth curves with a good approximation to the way in which microbiologists have traditionally estimated the kinetic parameters of growth. The piecewise linear model of Buchanan was fitted to the experimental data with the `nlsMicrobio` package (Baty and Delignette-Muller, 2014) of the statistical program R (R Core Team, 2013). Point estimations of all the kinetic parameters involved in the definition of this model were obtained, identifying and characterizing the three growth phases, lag, log, and stationary, for each of the eight temporal evolutions available (four replicates for the two growth conditions).

To assess the influence of the medium conditions on the growth kinetic parameters obtained, the Student's t -test was used to compare the two means (independent samples for aerobic

vs. microaerophilic), assuming or not equal standard deviations depending on the result of the Bonett test (for the comparison of variances).

In order to analyze the morphologic data acquired from the individual yeast cells, graphical and numerical summaries of the direct morphologic variables (area, perimeter, minor diameter and major diameter) were obtained, as well as of the variables derived from them (circularity and elongation). Data were grouped first by sampling times and growth conditions (aerobic or microaerophilic). Furthermore, the fact that each yeast cell belonged to one of the three different phases identified with the Buchanan model (for each replicate) contributed to the interpretation and comparative analysis of the results.

Contingency tables were used to study the independence between cell classification variables by considering the growth medium, the growth phase and the state of the cellular cycle (budded cell or unbudded cell). Scatterplots and linear correlation coefficients aided in the examination of linear and nonlinear relationships between the different variables. The analysis of variance (ANOVA) was applied to compare the means of the variables studied for the different groups determined by growth conditions, growth phase and bud state, followed by the corresponding separation of means. Nevertheless, because these data had unequal variances between groups the Welch's ANOVA test was run and subsequently Games-Howell method was used to compare all pairs of groups.

Discriminant analysis, a multivariate technique to classify observations into two or more groups from a data set with known groups (the training set), was applied to the data set of the four replicates taken together. It also helped to investigate how variables (predictors) contributed to group separation and to place individuals into defined groups (response). This can be used to develop rules for classifying other data sets for which group membership is not known. Linear discriminant analysis, one of the most commonly used techniques, assumes multivariate normality of the variables measured within each group and equal variances and covariances within each group. Using this model, linear discriminant analysis creates variables (discriminant functions) that are combinations of the original variables, which discriminate maximally between groups, and a quadratic analysis is used instead when the assumption of equal variances and covariances for all groups is not adequate (Sparks et al., 1999).

The program Minitab® 17 (2010) and the significance level 5% were used in the statistical analyses.

INDISIM-Saccha: An Individual-Based Model of the Yeast *Saccharomyces cerevisiae*

The original INDISIM-Saccha model focused on the fermentative growth of *S. cerevisiae* and was introduced to the scientific community by the work of Portell et al. (2014), which was accompanied with Supplementary Material online, with a detailed description of INDISIM-Saccha and some significant aspects of the process used for the parameterization of this model. Here an overview of the modeling methodology used

in the present work is shown. INDISIM-Saccha was developed to analyze the dynamics of *S. cerevisiae* in anaerobic batch cultures evolving in a non-stirred liquid medium with glucose as a main carbon source and organic and inorganic nitrogen sources. Global simulation scheduling consisted of initialization of the simulated system with the entrance of the input data, establishment of the initial configuration of the population, initial setting of the space, and the time step loop (which is repeated until the end of the defined time steps) including the random order of the individuals' acting order, the individual actions loop, the actions over the medium, and the output of variables. At each time step and at the individual actions loop, the existing yeast cells carry out, sequentially, the following set of actions: (i) random motion, (ii) uptake of the three substrates, namely, glucose, organic nitrogen and ammonium (controlled by the internal carbon to nitrogen ratio of the yeast cell) using size-based uptake submodel, (iii) metabolism with maintenance requirements, creation of carbon reserves, new mass synthesis, and release of substances, (iv) reproduction of mother cells and daughter cells, with a budding phase and an unbudded phase, and (v) lifespan (both chronological and replicative lifespan are considered).

INDISIM-Saccha assumes that the cellular cycle involves two differentiated phases. Phase 1, or unbudded phase, covers most of Gap1 phase (G1) and a very small fraction of synthesis phase (S) in the traditional division of the cell cycle; while Phase 2, or budding phase, covers a small fraction of G1, most of S and all of Gap2 phase (G2) and mitosis phase (M) (see Prats et al., 2010; Ginovart et al., 2011a,b, and references therein). Conceptually, the model assumes that in the unbudded phase the yeast cell is getting ready for budding and that change to the budding phase takes place only when the cell: (i) has attained a minimum cellular mass, defined by the parameter m_C , the critical or minimum mass; and (ii) has achieved a minimum growth of its mass, which is related to the model parameter Δm_{B1} . Within the model, two conditions must be satisfied for the releasing of the bud, and the subsequent change to the unbudded phase. These are: (i) a minimum growth of mass, which is related to the parameter Δm_{B2} ; and (ii) a minimum time interval, which is related to the parameter Δt_2 .

For further comprehension of the model the reader is referred to the published work Portell et al. (2014).

Adaptation of INDISIM-Saccha to Tackle Aerobic Conditions

The model was extended to deal with the analysis of dynamics of *S. cerevisiae* batch cultures evolving into a stirred aerobic liquid medium with glucose as a main C source, organic and inorganic N sources. This adaptation required the implementation of the following new features: (i) introduction of oxygen as a metabolic substrate for the yeast; (ii) utilization of aerobic or anaerobic catabolic pathways according to the local level of oxygen; and (iii) control of an individual lag time for the adaptation of the inoculum to new environmental conditions. When possible, model parameter values were taken following the work of Portell et al. (2014), but the new parameters had to be parameterized anew to guarantee a reasonably good reproduction of some

experimental macroscopic results of the culture such as glucose, ethanol and cell density at the first stage of the iterative modeling process (Portell, 2014).

In INDISIM-*Saccha* a yeast cell is defined by a set of variables: the three Cartesian coordinates identifying its position in the domain; $M(t)$, its structural mass (CN_{MIC}-pmol); $B(t)$, its genealogical age (bud scars); $Ph(t)$, the reproduction phase in the cellular cycle in which the cell is currently (unbudded or budding phase); $M_{Start}(t)$, its “Start mass” (CN_{MIC}-pmol), the mass required to change from the unbudded to the budding phase; $M_{inc}(t)$, the increased mass (CN_{MIC}-pmol) since the cell entered to the budding phase; $T_{inc}(t)$, time spent into the current reproduction phase (time steps); $R_{GLU}(t)$, the amount of C stored in the cell as reserve carbohydrates or in the model as a glucose polymers (glucose-pmol); $R_{CN}(t)$, the amount of organic N stored in the cell as a reserve (CN-pmol); $C_{GLU}^n(t)$, amount of non-metabolized glucose inside the cell (glucose-pmol); and, $D(t)$ the mortality index to evaluate cell viability. The values of these variables of all individual cells are stored internally and if required, can be used to generate individual based and global-based simulated observations. The environment simulates a liquid medium enclosed in a cube whose faces do not allow neither the ingress nor the egress of either organic or inorganic elements, with the exception of molecular oxygen that can be, or not, inflow to the system to maintain aerobic conditions. Four substrates can be taken up by the yeast cells: glucose (GLU), organic N (CN), ammonium (NH₄), and molecular oxygen (O₂), and ethanol and CO₂ can be produced. The reproduction submodel of INDISIM-*Saccha* assumes that for a budded cell, the mass of the bud (M_{Inc}) and the mass of the mother cell ($M - M_{Inc}$) to be spherical. Therefore, it is possible to compute the radius of the mother (R_m) and the bud mass (R_b).

The metabolism submodel of this extended INDISIM-*Saccha* version considers the respiratory catabolic pathway (glycolysis and Krebs cycle) as the first option in achieving metabolic energy. Nevertheless, it is assumed that the cell can also use the fermentative catabolic pathway (glycolysis and alcoholic fermentation) once the uptaken O₂ is depleted (or locally found at a very low level). This enables to control the level of O₂ to fix growth conditions. Such an assumption allows the model to be used in aerobic growth conditions with low glucose content media, i.e., growth conditions not promoting a noticeable Crabtree effect.

An extra effort needs to be done in order to improve the parameterization of this new version INDISIM-*Saccha* able to tackle yeast growth with oxygen in the medium. The parameterization and calibration of the model will benefit from the individual-level data obtained with the digital image analysis protocol developed in the present work. A new output module was created so that the INDISIM-*Saccha* model could mimic the experimental output obtained in the present contribution. The stated module stored the reproduction phase (budded cell or unbudded cell), that is, the values of R_m , and R_b of all the existing yeast cells at the requested sampling times. It is worth noticing that displaying the outputs in this way it is possible to simulate most of the morphologic measures obtained experimentally in this contribution.

RESULTS

Image Analysis of the Yeast Cells

Table 1 displays the number of cells analyzed in each experimental replicate for each sampling time for the two growth conditions, aerobic and microaerophilic.

Before performing the statistical analysis of the obtained results it was necessary to debug the data set and eliminate some very extreme outliers.

Examples of data achieved with the digital image analyses are shown in Figure 3. The sets of boxplots presented are useful for assessing and comparing sample distributions. They display the temporal evolutions of 50% of central data with the location of means and medians of the samples for each time corresponding to direct (area, perimeter, major and minor diameter) and derived (circularity and elongation) morphologic parameters studied for two of the eight replicates, one performed in aerobic conditions and the other in microaerophilic conditions. From the boxplots it is clear that the majority of the distributions are far from Gaussian distributions. These variables change their values, tendencies and variabilities along the temporal evolutions studied, and the values for the two growth conditions differ depending on the ranges used for those representations. These comments can be generalized to the rest of the experimental replicates with all variables (data not shown).

TABLE 1 | Number of cells analyzed for the different sampling times and for the four replicates (R1, R2, R3, and R4) under aerobic (A) and microaerophilic (M) conditions.

Time (h)	AR1	AR2	AR3	AR4	ATotal	Time (h)	MR1	MR2	MR3	MR4	MTotal
4.50	40	26	32	35	133	1.50	18	13	10	15	56
6.00	32	31	36	24	123	3.00	11	9	16	0	36
7.50	47	80	45	107	279	4.50	16	11	15	12	54
9.00	67	82	56	59	264	6.00	15	15	13	21	64
12.00	39	34	31	51	155	7.50	22	13	21	16	72
13.50	43	49	35	40	167	9.00	17	17	23	21	78
15.00	35	77	69	12	193	10.50	15	17	24	18	74
16.50	58	41	38	77	214	11.75	19	23	18	25	85
18.00	62	142	138	80	422	12.25	9	9	7	14	39
19.50	207	121	150	202	680	13.50	16	15	16	14	61
21.00	152	127	106	185	570	15.00	17	25	40	24	106
22.50	269	197	154	163	783	16.00	17	30	28	33	108
24.00	254	156	69	171	650	16.50	43	32	26	26	127
25.50	162	172	132	204	670	19.50	29	48	42	35	154
27.00	128	276	245	127	776	21.00	60	31	35	36	162
35.00	104	73	96	215	488	22.50	27	33	38	35	133
36.50	102	78	181	97	458	24.25	52	48	24	33	157
47.75	183	161	183	142	669	25.75	64	80	23	20	187
	1,984	1,923	1,796	1,991	7,694	27.25	22	64	36	44	166
						28.75	7	17	43	68	135
						30.25	71	77	56	59	263
							567	627	554	569	2,317

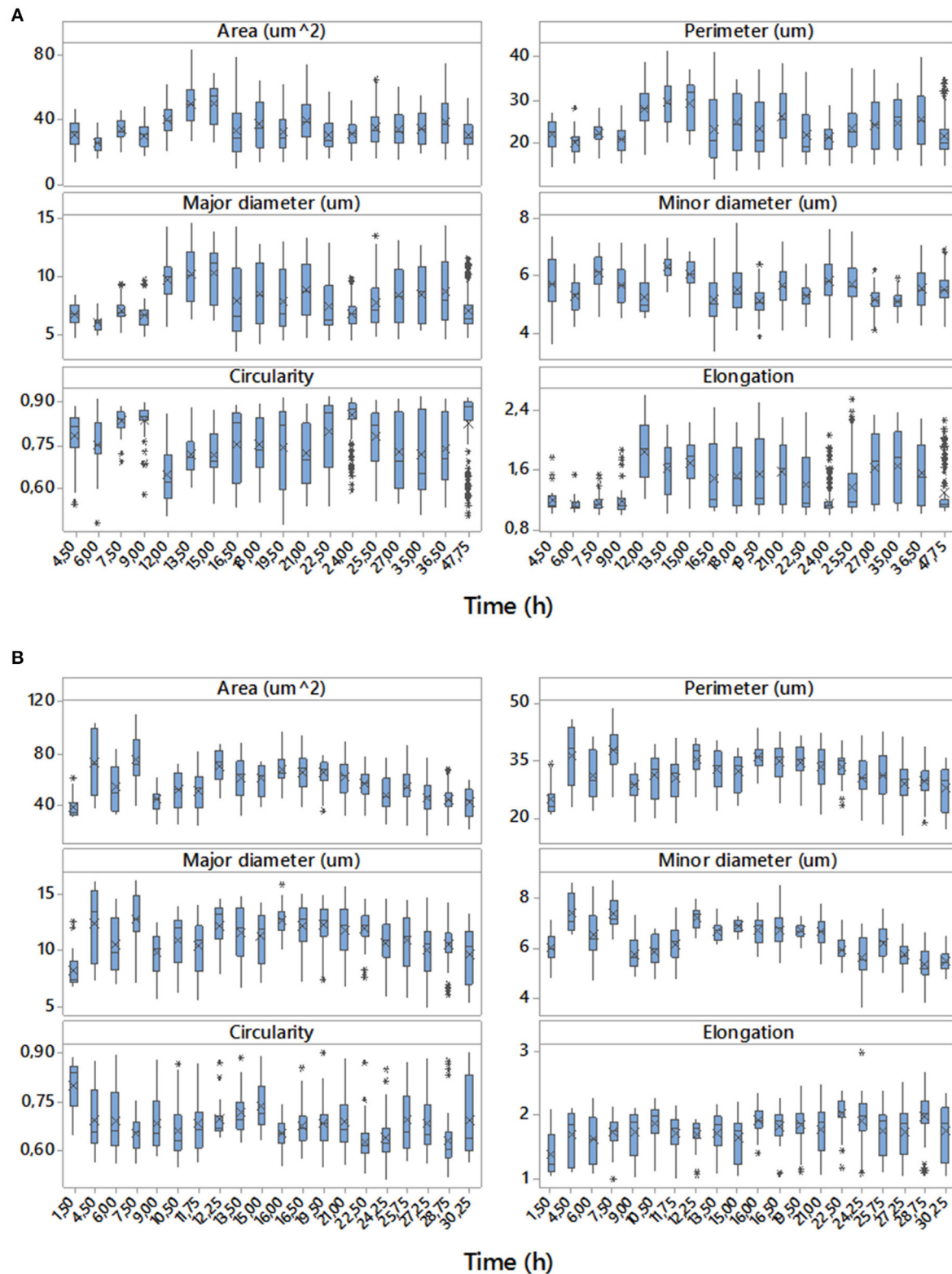


FIGURE 3 | Temporal evolutions of boxplots for the data of the set of variables studied corresponding to replicate 1 with aerobic conditions **(A)** and replicate 4 with microaerophilic conditions **(B)**. On the boxplots, a line is drawn across the box at the median. Asterisks denote outliers (data that were more than 1.5 times the interquartile range above or below the box), and the “x” symbol represents the mean.

Population Kinetic Parameters

Before fitting the Buchanan model the data were transformed using the base-10 (common) logarithm. The visual inspection of the adjusted piecewise linear model, together with the information generated by the `nlsmicrobio` package of the statistical program R, confirmed that for the eight replicates the quality of the fitting was very good. **Figure 4** shows two examples of this type of adjusted model, one with aerobic conditions and the other with microaerophilic conditions, in which the estimates of the parameters involved are also displayed.

Once the parameters of the Buchanan model for each of the experimental replicates were estimated (**Table 2**), the transition time between the end of the log phase and the beginning of the stationary phase ($t_{\text{Exp-Stat}}$) could be calculated by replacing the corresponding values of the estimates in the mathematical expression of the piecewise linear model. Furthermore, from this information the duration of the log phase for each replicate was estimated as the difference between the time of the entrance in the stationary phase and the duration of the adaptation or output of the lag phase. Taking into account the information in **Table 2** each of the objects identified as a yeast cell with the digital analysis performed was labeled to indicate to which population growth phase they belonged. From the estimates of the kinetic parameters obtained by the fitting of the Buchanan model (**Table 2**), the temporal evolutions of the eight replicates were characterized.

In order to compare the kinetic parameters in the two growth conditions the Student's *t*-test for independent samples was applied. It can be concluded that the maximum growth rates for both conditions were significantly different ($p = 0.016$), with a greater growth rate in aerobic conditions. The means of the times in which the change from log phase to stationary phase took place were also significantly different ($p < 0.001$), with a greater time for microaerophilic conditions. Regarding the duration of the log phase, significant differences were also observed between the two growth conditions ($p < 0.001$), and, in particular, this duration was greater for the microaerophilic case. For the rest of parameters studied (initial population, final population and duration of the lag phase) it was concluded that the differences were non-significant at 5% (p -values were equal to 0.259, 0.747, and 0.086, respectively). Therefore, the evenness of mean values for these parameters in the two growth conditions was maintained.

Descriptive Analysis of the Distributions of the Morphologic Parameters of Yeast Cells Throughout the Different Phases of Population Growth

Considering that sampling of images was carried out during the population growth, and using the estimations of the kinetic parameters obtained previously with the Buchanan model, it was possible to locate each of the sampling times for each of the eight replicates (4 aerobic and 4 microaerophilic) to one specific population growth phase (lag, log, or stationary). Once the data

sets debugged, the graphical representation and characterization of the distributions for the different morphologic variables according to the sampling times were conducted for each of the replicates of the two growth conditions tested, were conducted (data not shown). Since no noteworthy differences were detected between the behaviors observed for the four replicates in each of the two growth conditions, the data of the four replicates for each time sampling for both conditions were combined and analyzed for both conditions. Hence, changes in the central trends of distributions according to the growth phase, changes in variability or range of distributions, as well as changes in the form of distributions, were much better appreciated and more evident. **Figure 5** and Figures S2.1–S2.4 of the Supplementary Material illustrate this type of information obtained from the individual analysis of the cells.

Figure 5 shows the variable area of cells. In aerobic conditions the areas range from 20 to 70 μm^2 and that the distribution of the percentages vary according to the phase of growth in which the population is. Mainly in the lag phase (sampling times at 4.5, 6, and 7.5 h), but also in the stationary phase (sample times greater than 20 h), there is a higher percentage of cells of areas smaller than 45 μm^2 . However, during the log phase there is an increase in the percentage of cells with a larger area (greater than 45 μm^2), some of them even reaching up to 75 μm^2 . In general, the areas followed approximately normal (Gaussian) distributions, with the exception of the end of log phase and beginning of the stationary phase that presented bimodal distributions. In these distributions, the smaller areas showed the highest frequencies. In microaerophilic conditions most of the areas range of values from 20 to 80 μm^2 and even, in some cases, reach values of 95 μm^2 in the first samples, which correspond to the lag phase, yet with lower percentages. Shape and central tendency of the distributions of the areas change slightly according to the growth phase. During the lag phase (sampling times less than 9 h) and stationary phase (samples corresponding to times beyond 27 h), the highest percentages correspond to values of low and medium areas ($<55 \mu\text{m}^2$). In the log phase, the distribution of the cell areas shifts toward intermediate and high values (60–80 μm^2). The distributions of areas in the lag and log phases are, for the most part, rectangular distributions, but at the end of the log phase and in the stationary phase the distribution tends to be about normal. The values of the areas may be associated with the growth phase, and the differences are better appreciated in aerobic rather than in microaerophilic conditions. In general, it is also observed that the cells in the lag phase and stationary phase are smaller than those in the log phase. The temporal distributions of the cell perimeters (**Figure S2.1** in Supplementary Material) display in general similar behaviors to those observed with the cell areas (**Figure 5**). **Figure S2.2** in Supplementary Material presents histograms of the major diameter and minor diameter of the cells. The temporal evolutions of the variables estimating shape, namely, elongation (or aspect ratio) and circularity, are displayed, respectively, in **Figures S2.3, S2.4**, which can be found in the Supplementary Material.

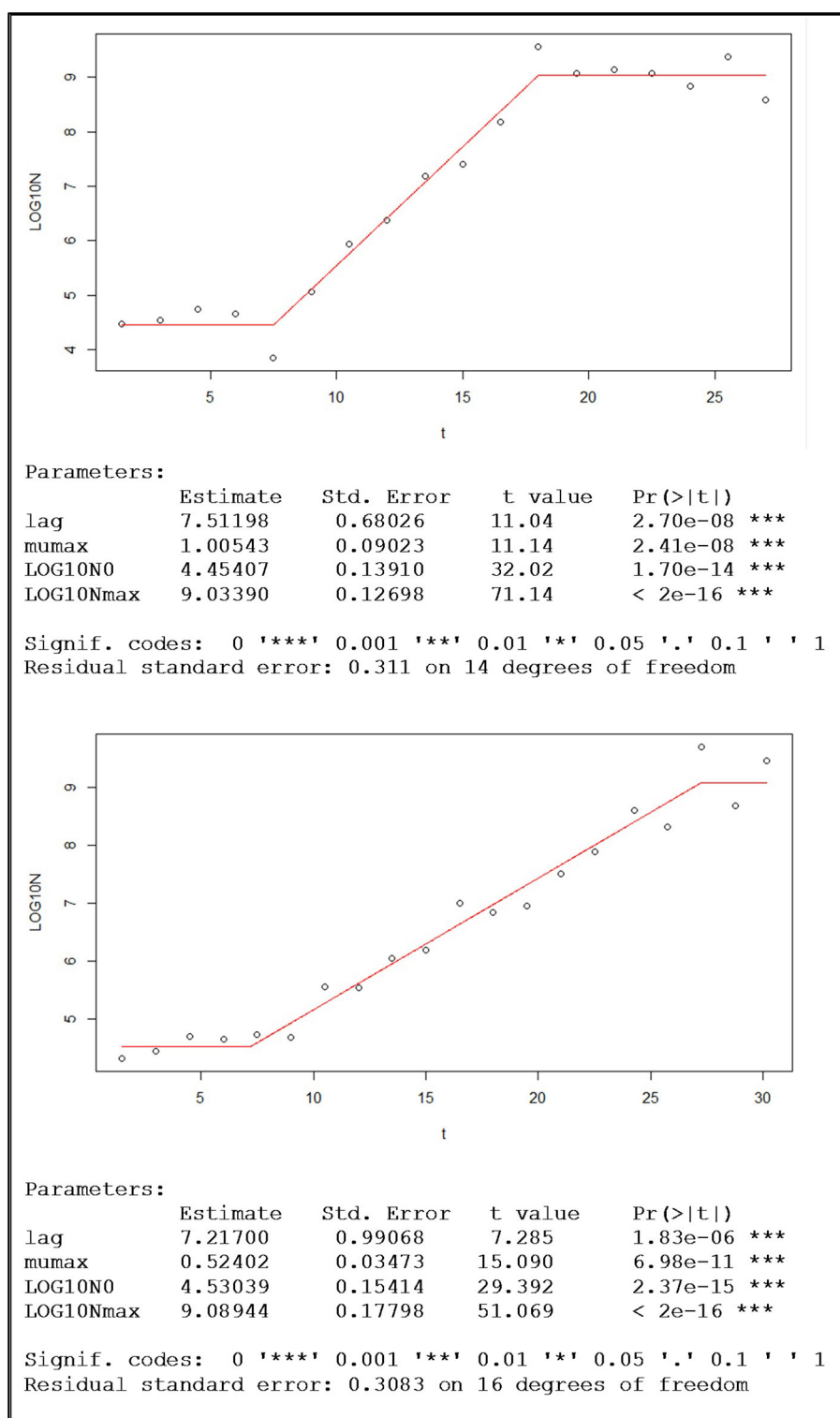


FIGURE 4 | Examples of population growth, with the data of one replicate under aerobic conditions (top) and the other under microaerophilic conditions (bottom), fitted to the Buchanan's piecewise linear model and the sets of corresponding kinetic parameter estimations provided by the nlsMicrobio package of R, from the formula: $\text{LOG10N} \sim \text{LOG10N0} + (t \geq \text{lag}) * (t \leq (\text{lag} + (\text{LOG10Nmax} - \text{LOG10N0}) * \log(10)/\text{mumax})) * \text{mumax} * (t - \text{lag})/\log(10) + (t \geq \text{lag}) * (t > (\text{lag} + (\text{LOG10Nmax} - \text{LOG10N0}) * \log(10)/\text{mumax})) * (\text{LOG10Nmax} - \text{LOG10N0})$, where lag corresponds to time at which the change from lag phase to log phase occurs, the duration of the lag phase (h); mumax is the maximum rate of growth (Log cfu/mL h⁻¹); LOG10N0 is the logarithm of the initial population (Log cfu/mL); and LOG10Nmax is the logarithm of the maximum population (Log cfu/mL).

TABLE 2 | Summary of the kinetic parameters for the replicates of the aerobic conditions and the microaerophilic conditions with: $t_{\text{Lag-Exp}}$, duration time of the lag phase or time at which the change from lag phase to log phase occurs (h); μ_{max} , maximum growth rate ($\log \text{cfu/mL h}^{-1}$); $\log_{10}(\text{N}_0)$, logarithm of the initial population ($\log \text{cfu/mL}$); $\log_{10}(\text{N}_{\text{max}})$, logarithm of the maximum population ($\log \text{cfu/mL}$), and $t_{\text{Exp-Stat}}$, time in which the change from log phase to stationary phase occurs.

Parameters	Aerobic conditions					Microaerophilic conditions				
	R1	R2	R3	R4	Mean \pm StDev	R1	R2	R3	R4	Mean \pm StDev
$t_{\text{Lag-Exp}}$	6.31	8.63	7.51	7.37	7.46 ± 0.95	6.79	7.95	7.22	7.14	7.28 ± 0.49
μ_{max}	0.80	0.95	1.01	0.74	0.88 ± 0.13	0.54	0.60	0.52	0.55	0.55 ± 0.03
$\log_{10}(\text{N}_0)$	4.62	4.90	4.45	4.70	4.67 ± 0.19	4.48	4.60	4.53	4.59	4.55 ± 0.06
$\log_{10}(\text{N}_{\text{max}})$	8.97	9.14	9.03	8.86	9.00 ± 0.12	9.16	9.19	9.09	9.57	9.25 ± 0.22
$t_{\text{Exp-Stat}}$	18.83	18.89	18.00	20.34	19.02 ± 0.97	26.58	25.61	27.25	28.03	26.48 ± 0.82

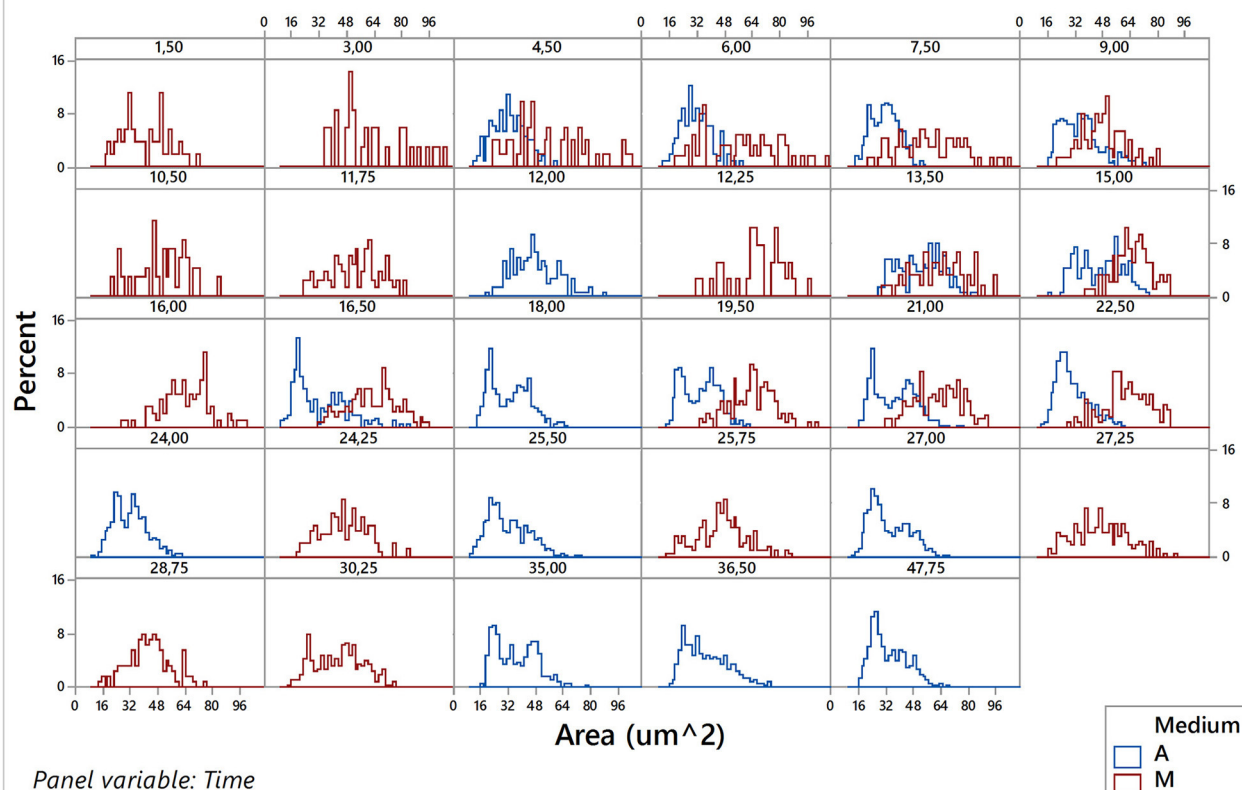


FIGURE 5 | Histograms of the area variable for the pooled data of the four replicates under aerobic conditions (A) and of the four replicates under microaerophilic conditions (M) corresponding to different sampling times.

Relationships between Morphologic Variables of Yeast Cells and Phases of Population Growth According to the State in the Reproduction Cycle

It is evident that the studied variables of shape and size are considerably affected by the state of the cellular reproduction cycle. Taking into account the direct visual inspection of the images collected and the manual data recorded on the budding state of each of the cells, the dichotomous variable budding (Yes/No) was incorporated to the analysis.

Chi-square test for independence was used to assess the relationship between the two categorical variables (budding, growth phase) from the contingency table or cross tabulation of the pooled data (the two growth conditions together). As was expected, there was a strong evidence of association between the two variables ($p < 0.001$). For the 582 cells belonging to the lag phase only 184 were budded cells (31.6 %) and for the 5881 cells belonging to the stationary phase only 2719 were in the budding phase (46.2%), while in the log phase from the 3144 cells controlled, 2221 cells were in the budding phase (70.6%).

In order to analyze the association of these two variables, and to characterize their distributions, the raw data were split according to the budding phase, and the subsequent distributions were studied again. This separation of the data affected the shape, location and variability of the morphologic distributions in a very remarkable way. After having introduced the variable budding in the analysis, the distributions became much more regular and symmetric, approaching Gaussian distributions. The analysis of variance (ANOVA) was used to compare the means between the different subgroups obtained from the combination of these three factors (growth conditions, growth phase and budding reproduction). As the assumption of equal variances between groups was violated, Welch's one-way ANOVA test was performed. Once it was concluded that the means of subgroups were significantly different for all the variables (all p -values < 0.001), then the Games-Howell test was used to compare differences between all pairs of groups. **Table 3** provides a numerical summary of the variables according to these three factors studied.

For instance, regarding the area variable, **Figure 6** displays a set of histograms corresponding to different sampling times, presenting the budded and unbudded cells separately for each of the two growth conditions.

Table 3 shows that for each phase, the mean of the areas of the unbudded cells in microaerophilic conditions were greater than those in aerobic conditions, and the same applies for the budded cells. In general, the means of the areas of budded cells were higher than those of unbudded cells, although not always significantly different. In relation to the means of the areas according to the growth phase, the budded cells in microaerophilic growth did not present significant differences between lag and log phases, nor when comparing the unbudded cells. Nevertheless, in aerobic conditions there were significant differences between the means of areas for lag and log phases in both cases (budded and unbudded cells). In the stationary

phase for budded and unbudded cells and in both growth conditions, the means of the areas were reduced, although not always with significant differences. The highest values for the mean of the area were achieved by budded yeast growing in microaerophilic conditions during the lag and log phases with values of 65.6 and 60.7 μm^2 (not significantly different). The means of the perimeters behaved similarly to the means of the areas. About the variability of the area distributions, the biggest coefficient of variation (35.5%) was for the unbudded cells grown in microaerophilic conditions that were in the lag phase (followed by those cells that were in the stationary phase, with a value of 29.5%), while the smallest coefficient of variation of the area distributions (21.1%) was for the budded cells grown in aerobic conditions that were in the stationary phase. The group of budded cells grown in microaerophilic conditions in the log phase had a small coefficient of variation (23%).

Regarding the three growth phases, the means of the minor diameters in aerobic conditions behaved differently from those in microaerophilic conditions (**Table 3**). The mean of the minor diameters of the unbudded cells under aerobic conditions in the lag phase was higher than those in the log and stationary phases. The latter two means showed no significant differences between them. The means of the lag and log phases behaved similarly in both growth conditions. Regarding the major diameters, the means followed the same pattern in the three growth phases. The means of unbudded cells in aerobic conditions showed the lowest values, while the highest values corresponded to the budded cells in microaerophilic conditions in lag and log phases. Unbudded cells in microaerophilic conditions, and budded cells in aerobic conditions showed significant differences according to growth phases. The means of the major diameters of the lag phase were higher than the means of the log and stationary phases, except in the case of budded cells under aerobic conditions. In microaerophilic conditions the means of budded cells in the

TABLE 3 | Number of yeast cells (N), means (\pm standard deviations) of the groups formed with the combinations of the three factors (growth condition, population growth phase, individual state in the reproductive cycle) with the grouping mean information using the Games-Howell Method (95% confidence).

Conditions-Phase-Budding	N	Area (μm^2)	Perimeter (μm)	Minor diameter (μm)	Major diameter (μm)	Elongation	Circularity
A-lag-N	303	29.65 \pm 7.98 g	21.46 \pm 3.21 f g	5.70 \pm 0.84 e	6.50 \pm 0.91 g	1.15 \pm 0.09 d	0.80 \pm 0.07 d
A-lag-Y	61	39.24 \pm 9.05 d	26.04 \pm 3.61 d	5.79 \pm 0.77 d e	8.58 \pm 1.40 d	1.50 \pm 0.27 c	0.72 \pm 0.06 e
A-log-N	760	26.44 \pm 7.71 h	19.62 \pm 3.06 h	5.40 \pm 0.77 f	6.12 \pm 1.00 h	1.14 \pm 0.10 d	0.85 \pm 0.04 a b
A-log-Y	953	46.34 \pm 11.82 c	29.58 \pm 4.01 c	5.59 \pm 0.73 e	10.45 \pm 1.71 c	1.88 \pm 0.29 b	0.66 \pm 0.07 f
A-stat-N	3,027	26.25 \pm 6.54 h	19.48 \pm 2.61 h	5.39 \pm 0.67 f	6.12 \pm 0.85 h	1.14 \pm 0.10 a	0.86 \pm 0.04 a
A-stat-Y	2,276	43.20 \pm 9.12 d	29.25 \pm 3.63 c	5.32 \pm 0.59 f	10.28 \pm 1.49 c	1.95 \pm 0.28 d	0.63 \pm 0.06 h
M-lag-N	95	38.93 \pm 13.82 d e	24.20 \pm 4.86 d e	6.35 \pm 1.04 a b c	7.66 \pm 1.78 e	1.21 \pm 0.25 d	0.82 \pm 0.07 c d
M-lag-Y	123	65.58 \pm 19.10 a	35.27 \pm 5.47 a	6.72 \pm 0.97 a	12.24 \pm 2.19 a	1.83 \pm 0.28 b	0.65 \pm 0.06 f g
M-log-N	163	33.93 \pm 8.29 e f	22.41 \pm 3.00 e f	6.12 \pm 0.80 c d	6.96 \pm 0.93 f	1.14 \pm 0.10 d	0.84 \pm 0.04 b c
M-log-Y	1,268	60.67 \pm 13.93 a	34.05 \pm 4.34 a	6.35 \pm 0.76 a b	12.05 \pm 0.74 a	1.91 \pm 0.25 b	0.65 \pm 0.06 f g
M-stat-N	135	30.69 \pm 9.06 f g	21.16 \pm 3.40 g	5.75 \pm 0.88 e	6.66 \pm 1.05 f g	1.16 \pm 0.11 d	0.85 \pm 0.04 a b c
M-stat-Y	443	48.90 \pm 13.05 b	30.95 \pm 4.60 b	5.59 \pm 0.80 e	10.99 \pm 1.81 b	1.98 \pm 0.29 a	0.63 \pm 0.06 g h

Where: M, microaerophilic condition; A, aerobic condition; lag, adaptation phase; log, exponential phase; stat, stationary phase; Y, budded cells; N, unbudded cells. Means that do not share a letter are significantly different.

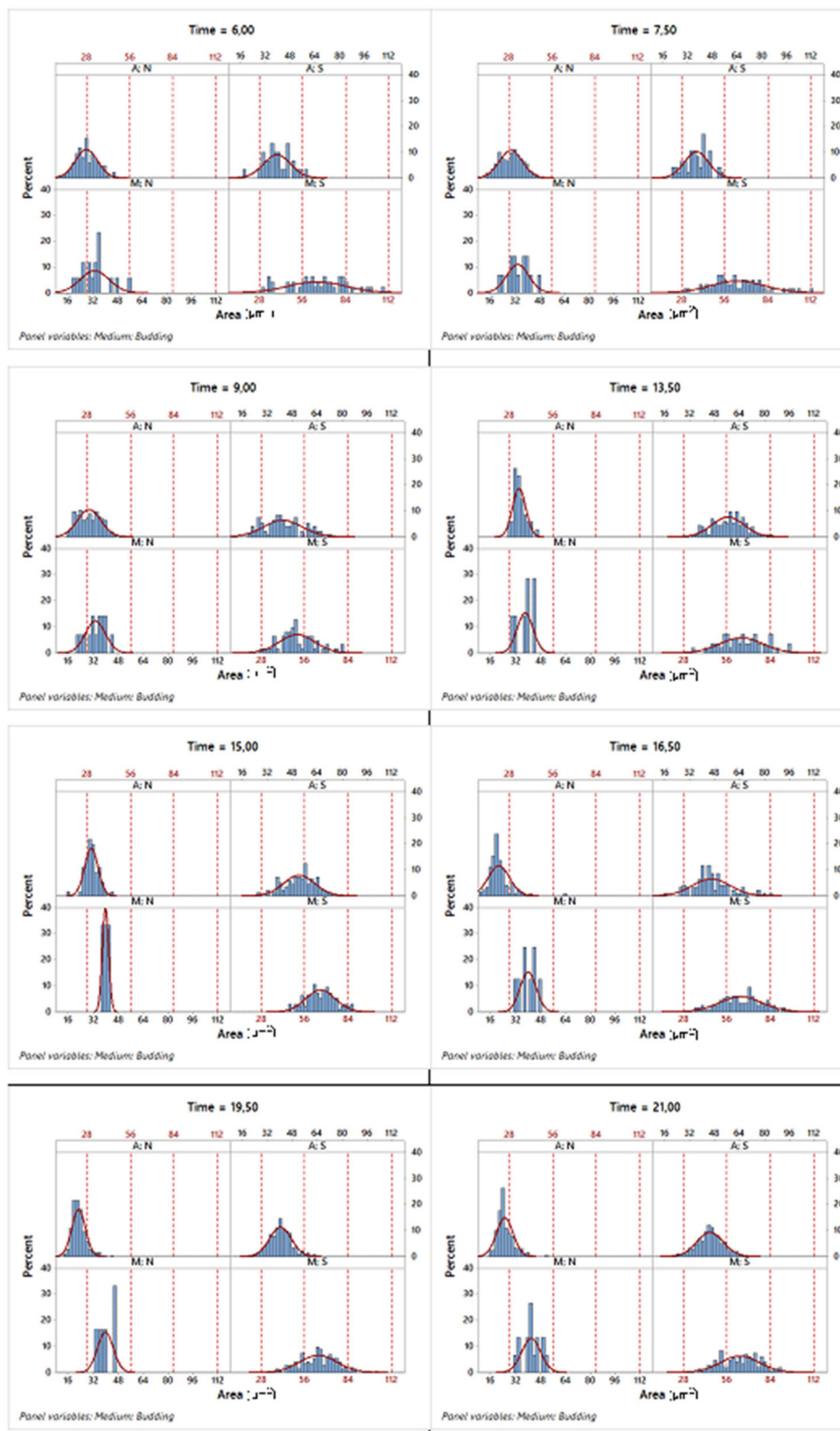


FIGURE 6 | Histograms of the corresponding area variable in different sampling times where the data were split according to the two growth conditions and state in the reproduction process. A, aerobic conditions; M, microaerophilic conditions; S, budded cells and; N, unbudded cells.

lag and log phases were significantly different from that in the stationary phase.

From direct visual inspection, a set of 5124 budded cells was gathered, with a mean elongation value of 1.92 and a coefficient of variation of 14.6%. Considering the data of the two growth conditions together, the 95% confidence interval of the mean elongation was (1.91, 1.93). The median of this data set was 1.95, and the 50% of the central values for elongation of budded cells ranged between 1.76 and 2.12. However, the means of elongation corresponding to the different phases of growth were 1.72, 1.90, and 1.95 for the lag, log and stationary phases respectively, with their corresponding 95% confidence intervals (1.68, 1.77), (1.89, 1.91), and (1.94, 1.96) respectively. No significant differences were observed for unbudded cells, regardless of the growth phase or the growth conditions, obtaining the smallest values. Under microaerophilic conditions the elongation had always higher values than under aerobic conditions. Taking into account the budded cells, for the log and stationary phases no significant differences were detected between both growth conditions, while for the lag phase the elongation means were significantly different. The mean elongation of the lag phase and budded cells in aerobic growth was much lower than the rest of budded cells with a value of 1.5 (Table 3).

In both growth conditions, the means of the circularity values of the unbudded cells were higher than those of the budded cells, and significantly different, with values clearly far from 1 (Table 3). Considering the unbudded cells, the highest value observed was 0.86 and the smallest was 0.80 corresponding to cells in the stationary phase and in the lag phase for aerobic growth conditions. In microaerophilic growth and unbudded cells there were no significant differences of the means of circularity according to the growth phases. The means of the circularity of the budded cells were different depending on the growth phase in aerobic conditions. The differences for this variable in function of the phases were smaller in microaerophilic growth than in aerobic growth.

Discriminant Analysis in Aerobic and Microaerophilic Conditions

All the variables can be considered to be approximately normally distributed within each group, except circularity and elongation. Therefore, these two variables were excluded from the analysis. Since equal variances could not be assumed, a quadratic discriminant function was used, and there was no need to jackknife or cross-validate the results because the data set was sufficiently large (Sparks et al., 1999).

First, the data set of the cells was used in an attempt to discriminate between the two growth conditions (aerobic, microaerophilic) on the basis of their morphometry (area, perimeter, major diameter, minor diameter). The overall percentages of the cells that could be correctly allocated to aerobic and microaerophilic conditions were: area (78.5%), perimeter (70.2%), major diameter (69.0%), and minor diameter (73.8%), with partial percentages of correct classification in each group ranging from 60.9 to 82.1%. If allocations to growth conditions were completely at random one would expect

50% correct allocation. When two predictors were combined, the percentages were slightly improved. In particular, it was worth considering the combinations: area-perimeter (80.4%) and major-minor diameters (76.5%), because the former is connected with circularity, and the latter with elongation. The four-predictor combination was disregarded due to collinearity. Since the morphometric predictors showed a strong potential to discriminate between growth conditions, discriminant analysis to classify cells according to phase (lag, log, stationary) and to budding (Yes-No) is discussed below for each growth condition separately. The results are displayed in Table 4. It should be remembered that if allocation to groups budding and phase were completely at random, one would expect a 50% and a 33.3% correct allocation, respectively. From Table 4 it is clear that in both growth conditions, all the predictors, except minor diameter, showed a high potential to classify cells into groups according to their budding condition. The main differences in the discriminant power were detected when allocating cells to their growth phase. In microaerophilic conditions all predictors presented overall percentages much larger than 33.3%. However, the partial percentage of cells in lag phase correctly classified fell far below 33.3%, except for predictors minor diameter, and the combination major-minor diameters, with all the partial percentages in each phase above 33.3%. On the contrary, in aerobic conditions the overall percentages did not achieve 33.3%, except for the minor diameter. Nevertheless, even in this case not all groups were well classified. A more detailed analysis revealed that cells in stationary phase were not correctly classified, in general. To achieve a better discrimination in aerobic conditions, phase and budding were merged into a new group phase-budding, with six categories. Hence, if cells were allocated at random, one would expect a 16.67% correct allocation. The overall percentages improved in general: area (46.3%), perimeter (48.7%), major diameter (48.0%), minor diameter (24.9%), area-perimeter (53.4%), major-minor diameters (54.9%). It is worth

TABLE 4 | Quadratic discriminant analysis of morphometric predictors, showing allocation of cells to groups (phase, budding), in aerobic and microaerophilic conditions.

Percentages correct (overall)	Predictors	Group	
		Phase	Budding
Aerobic	Area	18.4	85.0
	Perimeter	18.2	92.0
	Major diameter	18.2	94.7
	Minor diameter	57.9	50.4
	Area-Perimeter	33.1	95.3
	Major diameter-Minor diameter	28.0	97.0
Microaerophilic	Area	56.0	79.6
	Perimeter	59.5	89.1
	Major diameter	57.2	91.3
	Minor diameter	52.4	62.8
	Area-perimeter	52.8	94.1
	Major diameter-Minor diameter	57.0	94.4

pointing out that only for major diameter and area-perimeter all the groups showed partial percentages above 16.67%.

Simulations with the Individual-Based Model INDISIM-Saccha

The IBM INDISIM-Saccha was extended by the incorporation of an oxygen-using metabolic alternative (see section Adaptation of INDISIM-Saccha to Tackle Aerobic Conditions). The preliminary simulation results aimed to test whether the adapted model was also capable of tackling experimental cultures with oxygen available, combining outputs at population level and at individual level in order to take full advantage of the experimental data recently achieved and previously analyzed.

Experimental results were compared with simulation results at population level by means of the number of cells in the population growing in aerobic conditions and in microaerophilic conditions as **Figures 7A, 8A** respectively show. Nevertheless, with the study performed on the experimental distributions of the individual characteristics of yeast cells offered new options and challenges to be explored. A preliminary exploration of the outputs at individual level related with the mass of the yeast cells was carried out. Distributions of areas and volumes for budded and unbudded cells were recorded (see section INDISIM-Saccha: An Individual-Based Model of the Yeast *Saccharomyces cerevisiae*). A direct comparison can be drawn between simulation and experimental data. The simulated size distributions corresponding to the 7.0 and 16.5 h for aerobic conditions are shown in **Figure 7B**. Similarly, for microaerophilic conditions the simulated size distributions obtained at the sampling times 9.0 and 25.5 h are shown in **Figure 8B**. As can be seen, the area distributions from the simulated population followed unimodal distributions that change during time. Comparing the simulated distributions to their experimental equivalents a number of remarks can be made. First, simulated distributions during the lag phase (results not shown) did not change while changes were evident in the distributions of areas, perimeters, minor and major diameters, as well as in the derived morphologic variables (elongation and circularity) as **Figure 5** and Figures S2.1–S2.2 display. Second, simulated both budded and unbudded cells were smaller than those observed experimentally, and the amplitude of the distributions found experimentally was greater; and, in addition, the simulated distributions were well formed (**Figures 7B, 8B**).

Several sets of simulations were carried out modifying the values of the parameters of the reproduction submodel. When these values increased, both mean cell sizes and amplitude of the simulated distributions of budded and unbudded cells increased and became closer to the experimental values. However, there was a fundamental difference between the experimental and the simulation sampling procedures that partially explained the discrepancies observed. The fact that a small allcot of the experimental procedure was being measured against the whole simulated population suggested that the sampling effect had to be accounted for also in the simulations. Consequently, samples of the virtual system were also generated in order to represent the simulated size distributions. **Figures 7C, 8C** show these improved simulation results. Nevertheless, focusing on the glucose, ethanol and cell number temporal evolutions, the

agreement between experimental and simulated values became poorer (results not shown).

DISCUSSION

A collection of digital images of *S. cerevisiae* cells growing in two different initial concentrations of oxygen was processed to perform subsequently the statistical analysis of a set of morphologic parameters. A working protocol was established for the treatment of digital images of yeast cells using the free program ImageJ-Fiji, adjusting the parameters when necessary and designing different macros to automate the procedure. It turned out that the automation of the image analysis was not always the most suitable method, nor did it guarantee the thorough analysis of all the cells. Therefore, an individualized and manual review of all the analyzed cells was carried out, including the supervision of the corresponding morphologic parameters and the budding state with the visual inspection.

Concerning the type of model selected for the population growth, the Buchanan model proved to be very appropriate to fit the data analyzed, since in all the microbial cultures the different growth phases could be clearly identified (adaptation-lag, exponential-log, and stationary). The temporal experimental evolutions of yeast populations for the aerobic and microaerophilic conditions were well characterized from the estimations of the parameters provided by the fitting to the Buchanan model and from derived calculations. All the kinetic population parameters obtained from the model (durations of the lag and log phases, maximum growth rate, final population or carrying capacity, times of change from the log to the stationary phase) are of great microbiological interest for specific applications in biotechnology. However, it is necessary to point out that the values for the kinetic parameters also depend on the adjusted model (Buchanan et al., 1997; López et al., 2004; Griffiths et al., 2016). This fact should be taken into account when comparing experimental results with simulated results, as well as when referring to published results.

The production of starter cultures, a remarkable biotechnological application, using a batch process with a respiratory metabolism in microaerophilic conditions, according to the results obtained, allows the log phase to be extended, thus obtaining fully active and ready cells to be used as starters for a longer period of time. Therefore, the achievement of a long-term log phase of a population is positive for the industry. Starter populations that are in stationary phase suffer from a delay in their metabolic activity in the adaptation phase and in longer fermentative processes (Ekberg et al., 2013). In addition, in the stationary phase there is an aging of the population and a reduction of viable cells as a consequence of lack of nutrients. When the situation persists it causes the damage cell accumulating and cell death (Carmona-Gutierrez and Büttner, 2014).

Likewise, the population level parameters assisted to the interpretation of the morphologic parameter distributions of the yeast cells collected from the analysis of the digital images during the successive population growth phases. According to the purpose of the yeast cultivation, the study of growth conditions advantageous for the attainment of either a high number of yeast

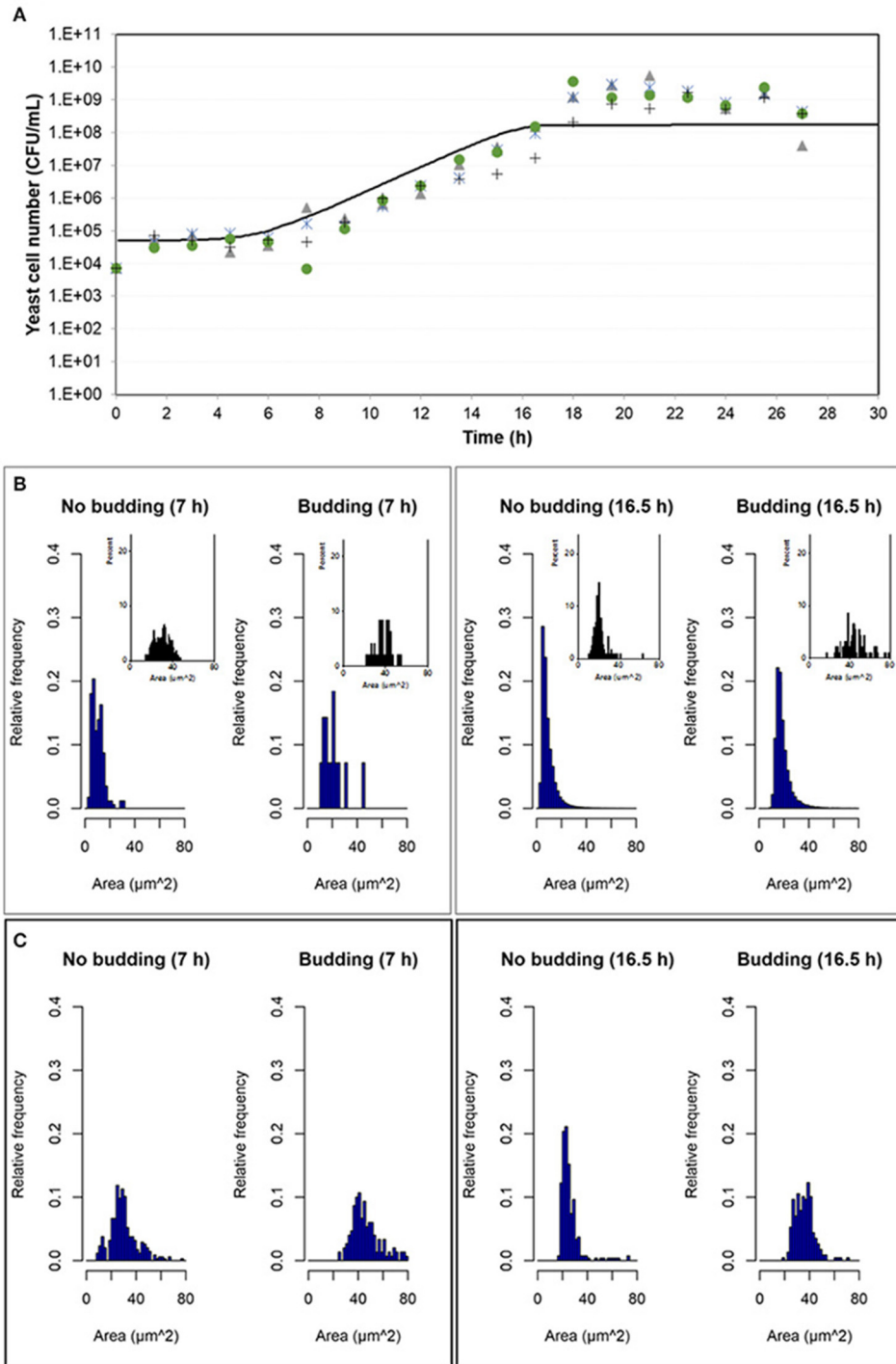


FIGURE 7 | Outputs obtained in aerobic conditions. **(A)** Temporal evolution of the experimental data of the four replicates of the population growth (different symbols) with a simulation performed with INDISIM-Saccha (continuous line). **(B)** Distributions of the areas of the yeast cells that make up the virtual system (*in silico* population) at different sampling times with the data split according to the state in the reproduction process: S, budded cells and N, unbudded cells. Notice that the representation of the corresponding experimental results by means of small plots have been included in the same area of the simulated plots to facilitate the comparison. **(C)** Size distributions that were obtained by changing the value of the standard variability of the minimum reproduction mass (σ_{mC} , from 0.15 to 0.25), the minimum growth required for the cell to start the budding process (Δm_{B1} , from 0.5 to 2.0), and the minimum growth required for the bud to detach itself from the mother cell (Δm_{B2} , from 1.0 to 9.0) and its standard deviation (σ_{mB2} , from 0.25 to 0.02), while keeping the rest of the parameter values used in the simulation displayed in **(A,B)**. In addition, the size distributions in **(C)** were produced by randomly sampling 500 individuals from the simulated yeast population to better mimic the procedure used to produce the experimental distributions.

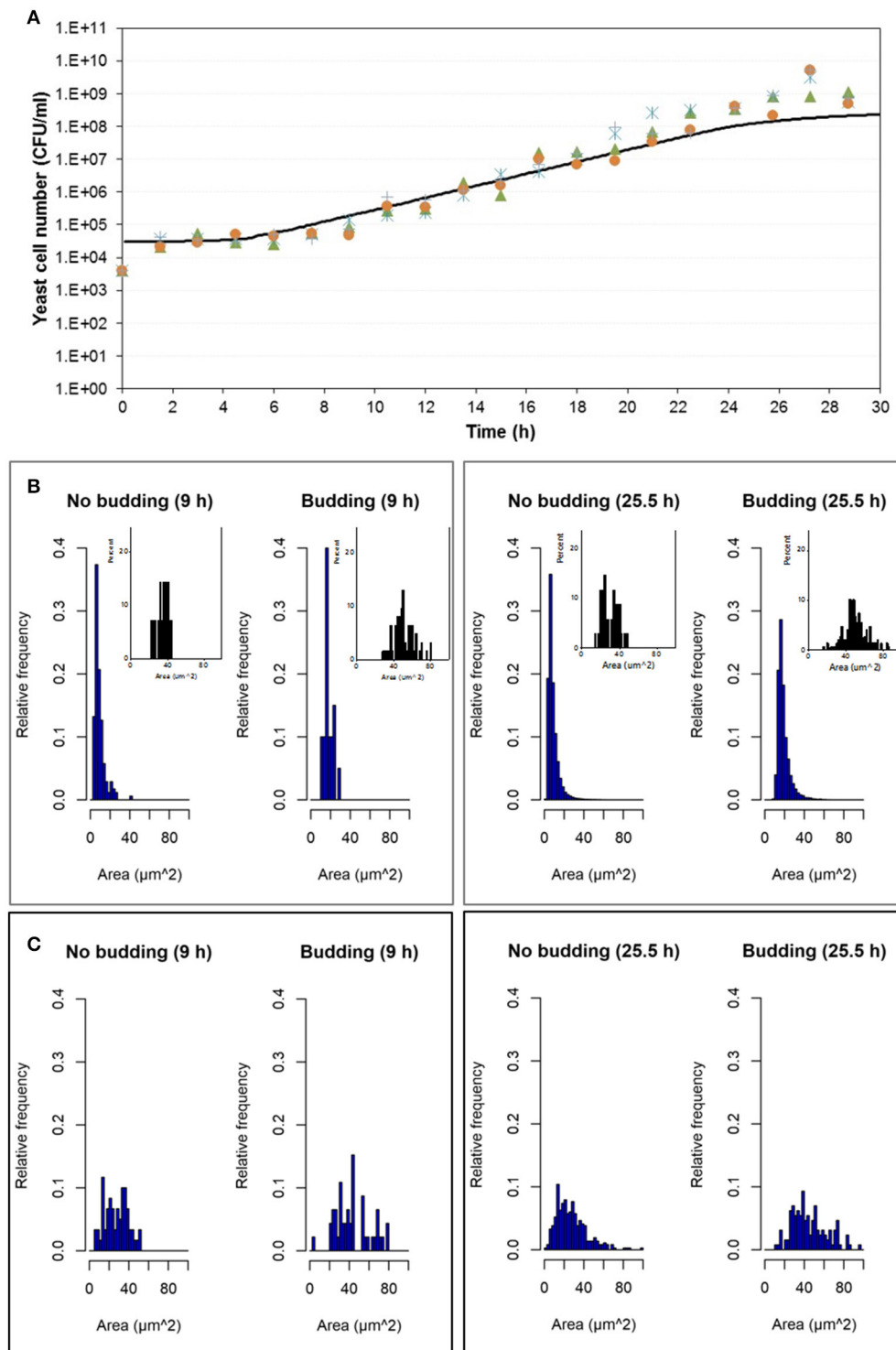


FIGURE 8 | Outputs obtained in microaerophilic conditions. **(A)** Temporal evolution of the experimental data of the four replicates of the population growth (different symbols) with a simulation performed with INDISIM-Saccha (continuous line). **(B)** Distributions of the areas of the yeast cells that make up the virtual system (*in silico* population) at different sampling times with the data split according to the state in the reproduction process: S, budded cells and N, unbudded cells. Notice that the representation of the corresponding experimental results by means of small plots have been included in the same area of the simulated plots to facilitate the comparison. **(C)** Size distributions that were obtained by changing the value of the minimum reproduction mass (m_C , from 5 to 15), of its standard variability (σ_{mC} , from 0.15 to 0.5), the minimum growth required for the bud to detach itself from the mother cell (Δm_{B2} , from 1.0 to 25.0) and of its standard deviation (σ_{mB2} , from 0.25 to 0.75) while keeping the rest of the parameter values used in the simulation displayed in **(A,B)**. In addition, the size distributions in **(C)** were produced by randomly sampling 500 individuals from the simulated yeast population to better mimic the procedure used to produce the experimental distributions.

cells or larger cells is noteworthy. For both the kinetic parameters of the population growth and the distributions of the individual variables of size and shape of the cells, it was shown that there were important differences between the two growth conditions tested. This reinforces the idea that a microbial system should be analyzed from different perspectives (population - individual) in order to make the most of the available information in any modeling process. This two-fold analysis is indispensable and much more relevant in any iterative process of parameterization and calibration of IBMs. It has also been established that the individual information obtained experimentally should be coupled with that obtained at the population level for the same system since, for slightly different levels of oxygen significant differences in population parameters were detected, as well as in the distributions of individual variables of the yeast cells that made up those populations.

In both aerobic and microaerophilic growth conditions, the numerical summaries of central tendency and variability obtained for the area, perimeter, major and minor diameters, elongation and circularity of the yeast cells were studied together with their respective distributions, which were not always normally distributed. Analysis and comparison of the distributions of these morphometric variables allowed to connect them with the three main microbial growth phases (log, lag, and stationary). These distributions reflected the changes between population growth phases in both growth conditions, and in a more relevant way for the aerobic growth, probably due to a faster growth and greater differentiation between phases.

The distributions of the size variables such as area and perimeter presented similar evolutions. The results obtained showed that cells growing in microaerophilic conditions presented larger areas than those growing under aerobic conditions. There were wider ranges for the distributions of the budded cells than for those corresponding to the unbudded cells. In general, the greatest cellular sizes occurred in the log phase, in both oxygen conditions, in keeping with other studies (Powell et al., 2003; Dungrawala et al., 2012), although in certain conditions their values get closer to those achieved in the lag phase.

The values of the major diameters, and to a lesser extent, those of the minor diameters, reproduce again the evolution of the cell size in the different growth phases, as observed in the variables area and perimeter. As the log phase progressed, the percentage of cells with a larger diameter increased, although percentages of smaller cells (new cells) were also maintained. The bimodal distributions in the log phase of all size parameters (except for the minor diameter) indicated the presence of two groups of cells differentiated by sizes that could be related to mother cells and daughter cells, the latter not having yet reached critical size to bud. The increasing percentage of small cells detected in the stationary phase has been described in several studies (Aragon et al., 2008; Svenkrtova et al., 2016) and may be related to glucose depletion. But it may also be connected with the presence of cells that in the stationary phase could give rise to quiescent cells (Li et al., 2013; Carbó et al., 2015). Cells in microaerophilic growth did not present the two size-differentiated subpopulations at the end of the log phase and at the onset of the stationary

phase, although a wide range of cell sizes could be observed, probably due to the slower and asynchronous growth. In general, they were larger than in aerobic growth at all phases. The small reduction of the initial oxygen concentration in the medium, such as the one proposed in this study, led to larger *Saccharomyces* cells. This could mean an improvement in the industrial production of cells for dietary supplements or cellular derivatives, such as glucans used in the bakery industry, or for their bioactive properties in the pharmaceutical products (Freimund et al., 2003). Under microaerophilic conditions larger cells were obtained and foreseeably with greater concentration of some cell components (although for some type of components this should be checked, in general it is true for cellular wall components such as glucans as they, β 1-6 and β 1-3 glucans, which constitute about 55–65% of the wall dry weight of the cell wall, Klis et al., 2002) It is worth bearing this result in mind if the purpose is to produce cells to extract cell metabolites. Besides, the populations grown in microaerophilic conditions were more homogeneous than those grown in aerobic conditions. On the other hand, a similar cellular concentration (biomass) was obtained in both growth conditions, but in aerobic conditions this concentration was achieved from 8 to 10 h before that in microaerophilic conditions, which indicates a higher yield in the aerobic case. Nevertheless, the consumption of glucose was superior in aerobic conditions, which makes it more expensive to obtain biomass in industry [the glucose in aerobic growth was exhausted at 18 h, just at the beginning of the stationary phase, whereas at the beginning of the stationary phase of the microaerophilic growth, there were still 6.68 g/L of glucose (data not shown)].

Differences in shape were also detected (see Figures S2.3, S2.4 of the Supplementary Material). Cells in microaerophilic growth presented mainly cylindrical or more elongated shape, whereas those in the aerobic conditions were mostly oval or elliptic. The elongation and circularity variables provided information on the deformation of the cells. Coelho et al. (2004) proposed an elongation value of 1.5 for *S. cerevisiae*. Although this reference value must be calculated for each microorganism growing under specific conditions, it held for the yeast cells in this study, in both growth conditions, hence allowing the discrimination between budded and unbudded cells. Differences in elongation values depending on the growth phase could be in agreement with the changes of the cell size for the different growth phases. Regarding the circularity, it was more difficult to establish a value that allowed to discriminate so clearly the budded cells from the unbudded cells, since apparently it depended on the growth phase. The discriminant analysis supported that, in both growth conditions, size assisted in classifying cells according to their budding state. However, while in microaerophilic conditions size could accurately allocate cells to their growth phase, in aerobic conditions only the combination of growth phase with budding state granted an adequate discrimination.

Both oxygen concentrations studied affected the growth rate, cell size and to a lesser degree, the number of viable cells of *Saccharomyces* obtained at the end of the study. There is a trade-off between the growth rate and the cellular size similar to that shown by Spor et al. (2008) when studying the influence of

different concentrations of glucose. It was observed that with a higher concentration of oxygen dissolved in the medium, a higher growth rate was detected, while cell sizes were smaller; but, conversely, with lower initial oxygen concentration, a lower growth rate appeared while cell sizes were greater. There was no trade-off between the growth rate and the final viable population achieved unlike the results shown in the work of Spor et al. (2008); a higher initial oxygen concentration resulted in a greater growth rate and a greater number of cells achieved in less time (while more time was required to achieve the same final number of cells with a little less initial oxygen). Probably this behavior is due to the fact that the two initial oxygen concentrations considered in this study did not constitute a stress factor.

Key aspects that should be further developed to move microbial community modeling toward greater predictive power have recently been revised (e.g., Song et al., 2014). In many cases, in a microbial context, it is not yet understood how individual cells should be programmed, manipulated or cultivated to ensure the emergence of the required collective behavior. IBMs, together with a suitable experimental work, makes it easier to tackle these issues, offering a framework in which to simulate such systems.

The number of studies on IBMs addressing bacterial populations greatly exceeds those dealing with yeast populations (Hellweger and Bucci, 2009). However, there are, to our knowledge, a few microbial IBMs that have been used to tackle diverse questions related to yeast such as the work of Hellweger et al. (2014) who investigated the hypothesis of a fitness benefit of age-correlated stress resistance of yeast, or the work of Momeni et al. (2013) who examined how through partner fidelity feedback heterotypic cooperation between yeasts may be protected against cheaters. Studies performed with INDISIM-YEAST and INDISIM-*Saccha* focused on the qualitative behavior and on the patterns and tendencies of variables connected with the yeast system and their effect on the growth phases of the population, specifically on the duration of the lag phase (Ginovart et al., 2007, 2011a,b) and on the fermentative (anaerobic) growth (Portell et al., 2014) respectively. Based on individual actions and parameters for individual yeast cells rather than fitting the model to data, these IBMs could predict the measured compounds profiles as well as biomass and genealogical age distributions. With the current experimental information gathered and from the examination of the distributions of sizes and shapes of individual yeast throughout the different phases of population growth, a quantitative study was carried out in order to improve the parameterization and calibration of the new aerobic version of INDISIM-*Saccha*. The individual-level observation of size is an important parameter involved in the uptake submodel, which takes into account the available nutrient at a microscale patch and the probability of it encountering and entering the yeast through the cellular membrane. Likewise, the review of the budding reproduction submodel could be performed since it allowed not only to distinguish mother yeast cells from daughter yeast cells, but also to control the budding process, that is, the times and masses for the separations of the buds from the cells. Besides, the consideration of the cellular membrane of the individual yeast (which is related with its size and geometry) in the uptake submodel has effect on the amount of nutrients that the cell uses.

The uptake submodel, which assumes that a yeast cell translocates low molecular weight compounds dissolved in water through its cell membrane, could be revisited in light of these findings about sizes and shapes of yeast cells. Such a revision would not be possible without the availability of hands-on experimentation as the one presented in this contribution.

There are several models that allow for mathematical descriptions of distributed cell properties within microbial populations, and cell size is usually chosen as a model variable to study yeast populations due to its tight coupling to cell growth and division, which in the case of this microorganism is asymmetric (e.g., Hatzis and Porro, 2006; Lencastre Fernandes et al., 2013). Nevertheless, an IBM grants the representation of biological actions for a microorganism and its integration into the structure of the model, and thereby cell size is indirectly involved in the individual behavior rules. In consequence, the available resources achieved by the virtual cell are shared between maintenance, creation of new biomass (size growth) and reproduction (increasing the size of the bud during the budding phase), which mostly determines the distribution of sizes that the model provides. Moreover, the distinction between timers and sizes, two classical concepts for G1 control, was investigated in yeast cells, and it turned out that size-independent noise (presumably molecular noise) is the leading source of variability in the duration of G1 (Di Talia et al., 2007). Thus, a deterministic size control model would seem insufficient, being then appropriate to incorporate certain stochasticity at individual cell level to achieve virtual representations of yeast populations when mass distributions and dynamics are explored. This reinforces the idea that stochastic IBMs, such as INDISIM-*Saccha*, are necessary tools to integrate both biological and environmental heterogeneity to improve the process design and scale up of microbial processes (González-Cabaleiro et al., 2017).

In the INDISIM-*Saccha* model, yeast cells experienced an individual lag time, that is, a period in which they were internally adapting in order to be able to undergo cellular growth. In the simulation, the size of the cells undergoing the lag phase did not change since the model assumed they were suffering the internal changes required to start growing. Such behavior was chosen for the sake of simplicity but there exist other conceptualizations that can be regarded as plausible in the literature (Prats et al., 2008, 2010). The behavior observed in the simulations does not seem to agree completely with the experimental findings. Although at the population level and during the adaptation phase no movement of the total number of cells was perceived, at individual level, as **Figure 5** and Figures S2.1–S2.4 showed, changes were evident in the distributions of areas, perimeters, minor and major diameters, as well as in the derived morphologic variables (elongation and circularity). This seems to suggest that the submodel describing the lag time of the individual cells should be reviewed in such a way that would allow for more variability and changes in the temporal evolution of the distribution of the individual areas, and, eventually, validated against the tendencies observed in the present contribution.

The development of a calibration procedure incorporating cell size distribution at strategic time points during the different growth phases will help reach a better agreement between both

kinds of data (experimental and simulated). It should be pointed out that the digital analysis procedure that we have developed lets sorting the size of budded and unbudded yeast. To our knowledge this approach has not been used so far, yet it offers some interesting characteristics that render it suitable for a calibration step. In particular, it allows to isolate more efficiently the effect of changes on the model parameters of the reproduction submodel so they can be detected more easily. For instance, in relation to the second simulation result (**Figure 7C**) from the first simulation result (**Figure 7B**) of the size distributions, fine tuning a model parameter, mainly controlling the size of the bud before detaching it from the mother cell (i.e., Δm_{B2}), will affect exclusively the distribution of the budded cells, but not the distribution of the unbudded yeasts. Other parameters, such as the critical mass before starting the budding phase (Δm_{B1}), will have an impact on the distribution of both budded and unbudded yeast cells.

The comparison between the individual-level information, obtained from the digital analysis procedure, and the simulation outputs of a calibrated IBM of the yeast *S. cerevisiae* is a valuable approach to test the accuracy of the process undergone. Although this does not invalidate the usefulness of the calibrated model for particular goals, the model obviously is not able to capture a number of important aspects of the real system. From now on, and with the current experimental information accomplished, a quantitative study can be carried out in order to improve the calibration of the new INDISIM-*Saccha* from the particular examination of distributions of sizes and shapes of individual yeast throughout the different phases of population growth.

This type of study on microorganisms is essential to ponder and develop methodologies for calibration processes of models to tackle different levels of observation of the system under consideration. Making IBMs simultaneously reproduce patterns observed at both the individual and population level will make these IBMs structurally realistic so that they can deliver independent, testable predictions (Kreft et al., 2013; Hellweger et al., 2016). The tasks to

complete this experimental-modeling-experimental iterative process require a close relationship and extra effort to connect both experimentalists and modelers, this approach being exemplified by the model INDISIM-*Saccha*. Neither of the two levels of observation (population and individual) in the process of parameterization and calibration can be neglected, although this requires an extra effort for modelers and an increment in the complexity of the models (Hellweger, 2017).

The combination of individual-level knowledge, gathered from the digital images processed, with population-level information, drawn from primary growth models and the estimation of kinetic parameters, proves to be crucial in understanding the biological processes connecting different experimental observations. The design, parameterization, calibration and validation of a microbial IBMs can certainly benefit from this 2-fold approach. At the same time, the exploration of different strategies to study a specific microbial population enhances the research process, providing in turn the opportunity to address new objectives in the *in vitro* and *in silico* representations of microbial systems and a more profound understanding of community dynamics.

AUTHOR CONTRIBUTIONS

All authors were involved in the writing and proofing of the manuscript. RC, XP, and MG were responsible for the design, execution and interpretation of the experimental results. MB and MG were responsible for the statistical analysis of the experimental data. XP and MG were responsible for the modeling and simulation. All authors have read and approved the final manuscript.

SUPPLEMENTARY MATERIAL

The Supplementary Material for this article can be found online at: <https://www.frontiersin.org/articles/10.3389/fmicb.2017.02628/full#supplementary-material>

REFERENCES

- Aragon, A. D., Rodríguez, A. L., Meirilles, O., Roy, S., Davidson, G. S., Tapia, P. H., et al. (2008). Characterization of differentiated quiescent and nonquiescent cells in yeasts stationary-phase cultures. *Mol. Biol. Cell* 19, 1271–1280. doi: 10.1091/mbc.E07-07-0666
- Arevalo-Villena, M., Briones-Perez, A., Corbo, M. R., Sinigaglia, M., and Bevilacqua, A. (2017). Biotechnological application of yeasts in food science: starter cultures, probiotics and enzyme production. *J. Appl. Microbiol.* 123, 1360–1372. doi: 10.1111/jam.13548
- Baty, F., and Delignette-Muller, M.-L. (2014). *nlsMicrobio: Data Sets and Nonlinear Regression Models Dedicated to Predictive Microbiology*. R package version 0.0-1. Available online at: <https://CRAN.R-project.org/package=nlsMicrobio> (Accessed May 2, 2016).
- Bookstein, F. L. (1997). *Morphometric Tools for Landmark Data: Geometry and Biology*. Cambridge: Cambridge University Press.
- Buchanan, R. L., Whiting, R. C., and Damert, W. C. (1997). When is simple good enough: a comparison of the Gompertz, Baranyi, and three phase linear models for fitting bacterial growth curves. *Food Microbiol.* 14, 313–326. doi: 10.1006/fmic.1997.0125
- Carbó, R., Ginovart, M., Carta, A., Portell, X., and del Valle, L. J. (2015). Effect of aerobic and microaerophilic culture in the growth dynamics of *Saccharomyces cerevisiae* and in training of quiescent and non-quiescent subpopulations. *Arch. Microbiol.* 197, 991–999. doi: 10.1007/s00203-015-1136-x
- Carmona-Gutierrez, D., and Büttner, S. (2014). The many ways to age for a single yeast cell. *Yeast* 31, 289–298. doi: 10.1002/yea.3020
- Cipollina, C., Vai, M., Porro, D., and Hatzis, C. (2007). Towards understanding of the complex structure of growing yeast populations. *J. Biotech.* 128, 393–402. doi: 10.1016/j.jbiotec.2006.10.012
- Coelho, M. A., Belo, I., Pinheiro, R., Amaral, A. L., Mota, M., Coutinho, J. A., et al. (2004). Effect of hyperbaric stress on yeast morphology: study by automated image analysis. *Appl. Microbiol. Biotech.* 66, 318–324. doi: 10.1007/s00253-004-1648-9
- Di Talia, S., Skotheim, J. M., Bean, J. M., Siggia, E. D., and Cross, F. R. (2007). The effects of molecular noise and size control on variability in the budding yeast cell cycle. *Nature* 448, 947–951. doi: 10.1038/nature06072
- Dungrawala, H., Hua, J., Wright, J., Abraham, L., Kasemsri, T., McDowell, A., et al. (2012). Identification of new cell size control genes *S. cerevisiae*. *Cell Div.* 7:24. doi: 10.1186/1747-1028-7-24
- Eikberg, J., Rautio, J., Mattinen, L., Vidgren, V., Londesborough, J., and Gibson, B. R. (2013). Adaptive evolution of the lager brewing yeast *Saccharomyces pastorianus* for improved growth under hyperosmotic conditions and its

- influence on fermentation performance. *FEMS Yeast Res.* 13, 335–349. doi: 10.1111/1567-1364.12038
- Freimund, S., Sauter, M., Käppeli, O., and Dutler, H. (2003). A new non-degrading isolation process for 1,3- β -glucan of high purity from baker's yeast *Saccharomyces cerevisiae*. *Carbohydr. Polym.* 54, 159–171. doi: 10.1016/S0144-8617(03)00162-0
- Ginovart, M., Prats, C., Portell, X., and Silbert, M. (2011a). Analysis of the effect of inoculum characteristics on the first stages of a growing yeast population in beer fermentations by means of an Individual-based Model. *J. Ind. Microbiol. Biotechnol.* 38, 153–165. doi: 10.1007/s10295-010-0840-4
- Ginovart, M., Prats, C., Portell, X., and Silbert, M. (2011b). Exploring the lag phase and growth initiation of a yeast culture by means of an Individual-based Model. *Food Microbiol.* 28, 810–817. doi: 10.1016/j.fm.2010.05.004
- Ginovart, M., Xifré, J., López, D., and Silbert, M. (2007). "INDISIM-YEAST, an individual-based model to study yeast population in batch cultures," in *Communicating Current Research and Educational Topics and Trends in Applied Microbiology, Microbiology Book Series Vol. 1*, ed A. Méndez-Vilas (Badajoz: Formatex), 401–409.
- González-Cabaleiro, R., Mitchell, A. M., Smith, W., Wipat, A., and Ofiteru, I. D. (2017). Heterogeneity in pure microbial systems: experimental measurements and modeling. *Front. Microbiol.* 8:1813. doi: 10.3389/fmicb.2017.01813
- Gorochowski, T. (2016). Agent-based modelling in synthetic biology. *Essays Biochem* 60, 325–336. doi: 10.1042/EBC20160037
- Griffiths, G. A., Suprinya, T., and Shantae, W. (2016). Storage of hybrid rough ric – Consideration of microbial growth kinetics and prediction models. *J. Stored Prod. Res.* 69, 235–244. doi: 10.1016/j.jspr.2016.09.003
- Hatzis, C., and Porro, D. (2006). Morphologically-structured models of growing budding yeast populations. *J. Biotechnol.* 124, 420–438. doi: 10.1016/j.jbiotec.2006.01.011
- Hellweger, F. L. (2017). 75 years since Monod: it is time to increase the complexity of our predictive ecosystem models (opinion). *Ecol. Model.* 346, 77–87. doi: 10.1016/j.ecolmodel.2016.12.001
- Hellweger, F. L., and Bucci, V. (2009). A bunch of tiny individuals-Individual-based modeling for microbes. *Ecol. Model.* 220, 8–22. doi: 10.1016/j.ecolmodel.2008.09.004
- Hellweger, F. L., Clegg, R. J., Clark, J. R., Plugge, C. M., and Kreft, J. U. (2016). Advancing microbial sciences by individual-based modelling. *Nat. Rev. Microbiol.* 14, 461–471. doi: 10.1038/nrmicro.2016.62
- Hellweger, F. L., Fredrick, N. D., and Berges, J. A. (2014). Age-correlated stress resistance improves fitness of yeast: support from agent-based simulations. *BMC Syst. Biol.* 8:18. doi: 10.1186/1752-0509-8-18
- Jayathilake, P. G., Gupta, P., Li, B., Madsen, C., Oyebamiji, O., González-Cabaleiro, R., et al. (2017). A mechanistic individual-based model of microbial communities. *PLoS ONE* 12:e0181965. doi: 10.1371/journal.pone.0181965
- Klis, F. M., Mol, P., Hellingwerf, K., and Brul, S. (2002). Dynamics of cell wall structure in *Saccharomyces cerevisiae*. *FEMS Microbiol. Rev.* 26, 239–256. doi: 10.1111/j.1574-6976.2002.tb00613.x
- Kreft, J. U., Plugge, C. M., Grimm, V., Prats, C., Leveau, J. H., Banitz, T. (2013). Mighty small: observing and modeling individual microbes becomes big science. *Proc. Natl. Acad. Sci. U.S.A.* 110, 18027–18028. doi: 10.1073/pnas.1317472110
- Lencastre Fernandes, R., Carlquist, M., Lundin, L., Heins, A. L., Dutta, A., Sørensen, S. J., et al. (2013). Cell mass and cell cycle dynamics of an asynchronous budding yeast population: experimental observations, flow cytometry data analysis, and multi-scale modeling. *Biotech. Bioeng.* 110, 812–826. doi: 10.1002/bit.24749
- Li, L., Miles, S., Melville, Z., Prasad, A., Bradley, G., and Breeden, L. L. (2013). Key events during the transition from rapid growth to quiescence in budding yeast require posttranscriptional regulators. *Mol. Biol. Cell* 24, 3697–3709. doi: 10.1091/mbc.E13-05-0241
- Liesche, J., Marek, M., and Günther-Pomorski, T. (2015). Cell wall staining with Trypan blue enables quantitative analysis of morphological changes in yeast cells. *Front. Microbiol.* 6:107. doi: 10.3389/fmicb.2015.00107
- López, S., Prieto, M., Dijkstra, J., Dhanoa, M. S., and France, J. (2004). Statistical evaluation of mathematical models for microbial growth. *Int. J. Food Microbiol.* 96, 289–300. doi: 10.1016/j.ijfoodmicro.2004.03.026
- Minitab 17 Statistical Software (2010). [Computer software]. State College, PA: Minitab, Inc. (www.minitab.com)
- Momeni, B., Waite, A. J., and Shou, W. (2013). Spatial self-organization favors heterotypic cooperation over cheating. *eLife* 2:e00960. doi: 10.7554/eLife.00960
- Pertusa, J. F. (2010). *Técnicas de Análisis de Imagen: Aplicaciones en Biología*, 2nd Edn. Valencia: Universitat de València.
- Portell, X. (2014). *Individual-Based Observations and Individual-Based Simulations to Study Saccharomyces cerevisiae Cultures*. Dissertation Thesis, Universitat Politècnica de Catalunya, Barcelona.
- Portell, X., Ginovart, M., Carbó, R., and Vives-Rego, J. (2011). Differences in stationary-phase cells of a commercial *Saccharomyces cerevisiae* wine yeast grown in aerobic and microaerophilic batch cultures assessed by electric particle analysis, light diffraction and flow cytometry. *J. Ind. Microbiol. Biotechnol.* 38, 141–151. doi: 10.1007/s10295-010-0839-x
- Portell, X., Gras, A., and Ginovart, M. (2014). INDISIM-Saccha, an individual-based model to tackle *Saccharomyces cerevisiae* fermentations. *Ecol. Model.* 279, 12–23. doi: 10.1016/j.ecolmodel.2014.02.007
- Powell, C. D., Quain, D. E., and Smart, K. A. (2003). Chitin scar breaks in aged *Saccharomyces cerevisiae*. *Microbiology* 149, 3129–3137. doi: 10.1099/mic.0.25940-0
- Prats, C., Ferrer, J., López, D., Giró, A., and Vives-Rego, J. (2010). On the evolution of cell size distribution during bacterial growth cycle: experimental observations and individual-based model simulations. *Afr. J. Microbiol. Res.* 4, 400–407.
- Prats, C., Giro, A., Ferrer, J., López, D., and Vives-Rego, J. (2008). Analysis and IbM simulation of the stages in bacterial lag phase: basis for an updated definition. *J. Theor. Biol.* 252, 56–68. doi: 10.1016/j.jtbi.2008.01.019
- R Core Team (2013). *R: A Language and Environment for Statistical Computing*. Vienna: R Foundation for Statistical Computing. Available online at: <http://www.R-project.org/>
- Schindelin, J., Arganda-Carreras, I., Frise, E., Kaynig, V., Longair, M., Pietzsch, T., et al. (2012). Fiji: an open-source platform for biological-image analysis. *Nat. methods* 9, 676–682. doi: 10.1038/nmeth.2019
- Song, H. S., Cannon, W., Beliaev, A., and Konopka, A. (2014). Mathematical modeling of microbial community dynamics: a methodological review. *Processes* 2, 711–752. doi: 10.3390/pr2040711
- Sparks, T. H., Scott, W. A., and Clarke, R. T. (1999). Traditional multivariate techniques: potential for use in ecotoxicology. *Environ. Toxicol. Chem.* 18, 128–137. doi: 10.1002/etc.5620180206
- Spor, A., Wang, S., Dillmann, C., de Vienne, D., and Sicard, D. (2008). "Ant" and "Grasshopper" Life-History Strategies in *Saccharomyces cerevisiae*. *PLoS ONE* 3:e1579. doi: 10.1371/journal.pone.0001579
- Succurro, A., Moejes, F. W., and Ebenhöf, O. (2017). A diverse community to study communities: integration of experiments and mathematical models to study microbial consortia. *J. Bacteriol.* 199, e00865-16. doi: 10.1128/JB.00865-16
- Svenkrtova, A., Belicova, L., Volejnikova, A., Sigler, K., Jazwinski, S. M., and Pichova, A. (2016). Stratification of yeast cells during chronological aging by size points to the role of trehalose in cell vitality. *Biogerontology* 17, 395–408. doi: 10.1007/s10522-015-9625-5
- Tibayrenc, P., Preziosi-Belloya, L., Roger, J. M., and Ghommidha, C. (2010). Assessing yeast viability from cell size measurements? *J. Biotech.* 149, 74–80. doi: 10.1016/j.jbiotec.2010.06.019
- Toro, I. M. V., Manriquez, S. G., and Suazo, G. I. (2010). Morfometría geométrica y el estudio de las formas biológicas: de la morfología descriptiva a la morfometría cuantitativa. *Int. J. Morphol.* 28, 977–990. doi: 10.4067/S0717-95022010000400001

Conflict of Interest Statement: The authors declare that the research was conducted in the absence of any commercial or financial relationships that could be construed as a potential conflict of interest.

Copyright © 2018 Ginovart, Carbó, Blanco and Portell. This is an open-access article distributed under the terms of the Creative Commons Attribution License (CC BY). The use, distribution or reproduction in other forums is permitted, provided the original author(s) or licensor are credited and that the original publication in this journal is cited, in accordance with accepted academic practice. No use, distribution or reproduction is permitted which does not comply with these terms.



Heterogeneity in Pure Microbial Systems: Experimental Measurements and Modeling

Rebeca González-Cabaleiro^{1†}, Anca M. Mitchell^{1†}, Wendy Smith², Anil Wipat² and Irina D. Ofițeru^{1*}

¹ School of Engineering, Chemical Engineering, Newcastle University, Newcastle upon Tyne, United Kingdom,

² Interdisciplinary Computing and Complex BioSystems (ICOS), School of Computing, Newcastle University, Newcastle upon Tyne, United Kingdom

OPEN ACCESS

Edited by:

Clara Prats,
Universitat Politècnica de Catalunya,
Spain

Reviewed by:

Xavier Portell,
Cranfield University, United Kingdom
Susann Müller,
Helmholtz-Zentrum für
Umweltforschung (UFZ), Germany

*Correspondence:

Irina D. Ofițeru
dana.ofiteru@ncl.ac.uk

[†]These authors have contributed
equally to this work.

Specialty section:

This article was submitted to
Systems Microbiology,
a section of the journal
Frontiers in Microbiology

Received: 29 June 2017

Accepted: 05 September 2017

Published: 20 September 2017

Citation:

González-Cabaleiro R, Mitchell AM,
Smith W, Wipat A and Ofițeru ID
(2017) Heterogeneity in Pure
Microbial Systems: Experimental
Measurements and Modeling.
Front. Microbiol. 8:1813.
doi: 10.3389/fmicb.2017.01813

Cellular heterogeneity influences bioprocess performance in ways that until date are not completely elucidated. In order to account for this phenomenon in the design and operation of bioprocesses, reliable analytical and mathematical descriptions are required. We present an overview of the single cell analysis, and the mathematical modeling frameworks that have potential to be used in bioprocess control and optimization, in particular for microbial processes. In order to be suitable for bioprocess monitoring, experimental methods need to be high throughput and to require relatively short processing time. One such method used successfully under dynamic conditions is flow cytometry. Population balance and individual based models are suitable modeling options, the latter one having in particular a good potential to integrate the various data collected through experimentation. This will be highly beneficial for appropriate process design and scale up as a more rigorous approach may prevent *a priori* unwanted performance losses. It will also help progressing synthetic biology applications to industrial scale.

Keywords: population heterogeneity, single cell analysis, flow cytometry, population balance models, individual based models

INTRODUCTION

Microbial populations developing in seemingly homogenous environments have been historically considered as formed by identical individuals. In reality no two cells in a pure culture are alike, even if they are derived from single clonal colonies (Ackermann, 2015). This phenomenon is of fundamental importance in biotechnological fermentations as the yields obtained will be lower if the cells are not in the same optimal productive state (Fernandes et al., 2011).

In bioprocess industries the bioreactors, and in particular the stirred tanks, are the central production units. The performance of any bioreactor is the emergent property of the activity and interactions at the single cell level and therefore, variations at this level can profoundly affect the dynamics and productivity of the process. Fluctuations that affect cell metabolism in industrial fermentations are estimated to generate losses of 30% or above (Lara et al., 2006; Takors, 2012). Moreover, sometimes recombinant protein production processes fail completely for reasons which are not fully understood but can be related to heterogeneity in the microbial population (Rosano and Ceccarelli, 2014).

The effect of cell individuality when using bacteria for obtaining useful products has been emphasized recently in several publications (Li and You, 2013; Wyre and Overton, 2014a,b; Chen et al., 2015). Nevertheless, the true impact of microbial population heterogeneity on bioprocesses remains unknown (Delvigne and Goffin, 2014) and therefore it is not systematically considered in design. This is partially due to the fact that experimental biological data obtained with traditional methods represents population average information (Pasotti and Zucca, 2014) which means that the performance of individuals is masked (Ackermann and Schreiber, 2015). Another potential reason is the relatively limited options for monitoring the heterogeneity under dynamic conditions. There are suggestions that minor subpopulations will not have significant influence on the whole population function (Lidstrom and Konopka, 2010), but more recent work emphasizes that non-genetic variation plays an important role in the overall biosynthetic performance of a bioprocess (Xiao et al., 2016).

Ultimately, industry needs to be able to engineer heterogeneity to obtain better yields and more robust processes. This requires both quantitative evaluation of the change of individual cells in time and of their interaction with the environment (Bley, 2011; Sauer and Mattanovich, 2012). Furthermore, this information needs to be included in mathematical frameworks used for design and control in order to have a realistic representation of the bioprocesses and to improve their performance.

In this mini-review we present an overview of the experimental methods used for characterizing the cell to cell variation in bacterial cultures and the corresponding mathematical tools for modeling them (see **Figure 1**), with a focus on the appropriate ones for fermentation processes.

SOURCES OF CELL HETEROGENEITY

The sources of heterogeneity in clonal microbial populations are biological (intrinsic) or environmental (extrinsic), or both. Whereas the intrinsic heterogeneity is generated by factors as cell cycle states, age distribution or the stochasticity of gene expression and metabolic reactions, the source for the extrinsic heterogeneity are the fluctuations in the environment. Therefore the latter represents a physiological response to stress (Lidstrom and Konopka, 2010; Ryall et al., 2012) and a survival strategy developed over evolutionary times (Booth, 2002; Sumner and Avery, 2002). This is the real challenge in the scaling-up of bioprocesses as poor mixing and heat transfer limitations generate concentration gradients which further influence the cells physiology.

A proposed way to overcome extrinsic heterogeneity and obtain similar performance in large scale reactors compared with laboratory reactors is to use strains specifically engineered to withstand certain environmental variability (Löffler et al., 2016). However, some investigations, both by modeling (Lavric and Graham, 2010) and experimental studies (Chi Fru et al., 2011; Oñifler et al., 2012) suggest that bacterial populations display constant heterogeneity in apparently steady growth and habitat

conditions, questioning the very existence of truly homogenous cultures (Grote et al., 2015).

EXPERIMENTAL METHODS

The first step in single cell analysis is the isolation and/or immobilization of individuals from cell suspension. The experimental methods employed for this include serial dilutions (the traditional method), physical trapping (mechanical, hydrodynamic or dielectrophoretic), flow suspension [e.g., flow cytometry and in particular fluorescence-activated cell sorting (Winson and Davey, 2000)] and micromanipulation [mechanical or with optical tweezers (Landry et al., 2013)]. Between these techniques, the use of trapping of single cells in lab-on-a-chip microfluidic devices is expanding.

Once the isolation is achieved, single cell heterogeneity can be assessed. Bioprocess monitoring requires high throughput methods which allow rapid and highly parallel experimentation, with relative fast processing time. In general, the methods for single cell analysis were primarily developed for basic research and not all of them are adapted to be used for fermentation processes (Geiler-Samerotte et al., 2013). At the same time, some micro tools for isolation and interrogation of single cells developed for mammalian cells need further refinement when dealing with smaller microbial cells (Love et al., 2013).

The experimental methods for monitoring and assessing single cell heterogeneity can be classified as: (i) biophysical characterization; (ii) gene expression; (iii) protein analysis; and (iv) metabolite analysis. Several detailed reviews exist on single cell heterogeneity analysis (Brehm-Stecher and Johnson, 2004; Amantonico et al., 2010; Fernandes et al., 2011; Lecault et al., 2012; Shi et al., 2015; Vasdekis et al., 2015). We are presenting a general overview, emphasizing the ones appropriate for microbial population under dynamic process conditions.

Biophysical characterization gives information on the cell size, mass, volume, internal structure, and mechanical properties. Optical microscopy is widely used, being the simplest and quickest method but with low throughput. A high throughput method which provides information on cell size is flow cytometry. The composition of the individual cells can be obtained by Raman spectroscopy, a label free optical method that has been used for bioprocess investigation (Huang et al., 2004).

Gene expression methods (e.g., RT-qPCR, RNA-seq, FISH) give information on the expression state of a certain gene and protein synthesis dynamics. However, if a method involves lysis of cells, the dynamics of the gene expression in bioprocesses cannot be followed. An alternative is to use reporter systems (e.g., green fluorescent protein and its variants) that can be monitored with fluorescent time-lapse microscopy (Young et al., 2012). The limitation in this case is that production cultures usually do not contain fluorescent protein as marker and therefore this method is less suitable for monitoring fermentation processes.

Protein analysis at the single cell level can, in theory, provide information on protein abundance, protein secretion, or protein/protein interaction. Flow cytometry is the most commonly used method for measuring the protein content (Wu

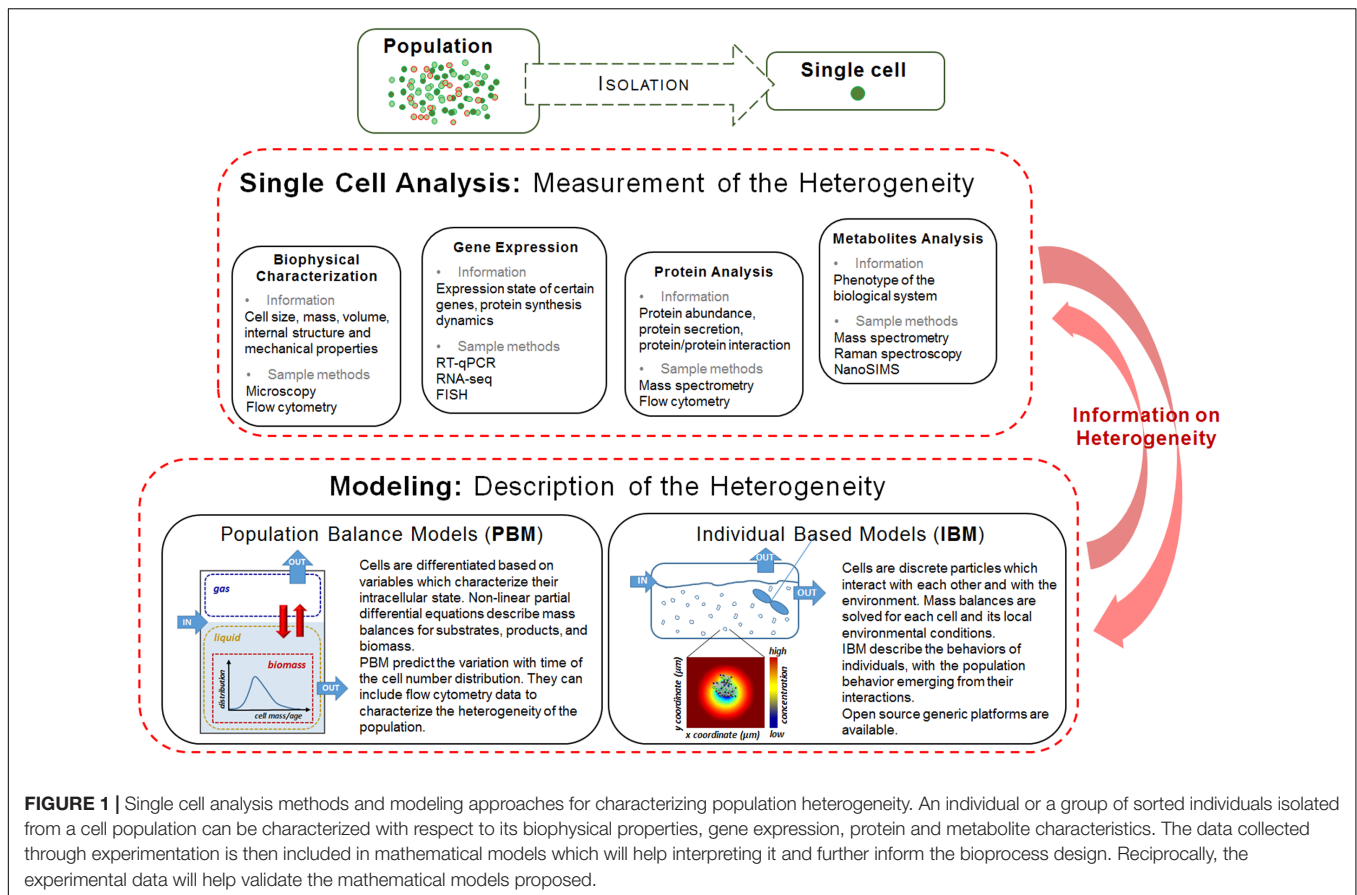


FIGURE 1 | Single cell analysis methods and modeling approaches for characterizing population heterogeneity. An individual or a group of sorted individuals isolated from a cell population can be characterized with respect to its biophysical properties, gene expression, protein and metabolite characteristics. The data collected through experimentation is then included in mathematical models which will help interpreting it and further inform the bioprocess design. Reciprocally, the experimental data will help validate the mathematical models proposed.

and Singh, 2012). Mass spectrometry has a high sensitivity and offers high quantity of information, from simultaneous identification of proteins to their posttranslational modifications. A workflow for sorted subpopulations, involving flow cytometry and mass spectrometry, was reported by Jahn et al. (2013). Nevertheless, there are still significant limitations due to the complexity of the proteome, the small amount of protein and the various types of measurement to be performed.

Metabolites analysis (intracellular and extracellular) is an indirect measurement of the phenotype of the biological system. The small size of the microbial cell and the minute quantity of metabolites make their detection at the single cell level very challenging. Methods used successfully in proof-of-concept experiments are Raman microspectroscopy, secondary ion mass spectrometry (SIMS) and Fourier transform infrared spectroscopy (Heinemann and Zenobi, 2011; Armitage et al., 2013; Rubakhin et al., 2013). Coupling a microfluidic unit to a mass spectrometer has the highest potential to deliver relevant data. NanoSIMS is a powerful tool for revealing element distribution in nanometer-scale resolution (Musat et al., 2012; Gao et al., 2016). However, the single cell metabolite analysis is considered to still be in its early stages.

From the reviewed methods, flow cytometry is the most suitable, relatively fast and user-friendly for measuring phenotypic single cell heterogeneity in bioprocesses and

under dynamic conditions (Want et al., 2009; Muller and Nebe-von-Caron, 2010; Ambriz-Aviña et al., 2014; Delvigne and Goffin, 2014; Baert et al., 2016). Flow cytometry measures the distribution of a large variety of cellular parameters across a cell population by analyzing the light scattering and fluorescent signals of stained cells which flow in front of a powerful light source (e.g., a laser beam). Individual cells can be segregated based on their size, shape, intracellular properties, membrane potential, and variation in fluorescent signal. Because the large number of cells (tens of thousands) measured in a short processing time, flow cytometry offers statistically significant results and provides a quantitative measurement of heterogeneity in the sample, having the potential to identifying rare cell types (Shapiro, 2000; Davey and Winson, 2003). Recently, in combination with supervised machine learning techniques, flow cytometry was used also for single cell identification of populations in synthetic bacterial communities (Rubbens et al., 2017).

Nevertheless, the challenge of the high throughput methods is the amount of data generated, which requires rigorous quality control, together with sophisticated bioinformatics and statistics. Therefore, although automated flow-cytometry was expected to be implemented for real-time quality programs in factories (Hewitt et al., 1999; Díaz et al., 2010), to date single cell characterization is not routinely used in-process (Royle et al., 2013).

A complementary way to evaluate the microbial phenotypic heterogeneity under realistic bioprocess conditions is by employing scale down single cell micro-cultivation devices in which large scale reactors conditions are mimicked. Single cells in lab-on-a-chip microfluidic devices allow parallelization and high throughput experiments (Grünberger et al., 2014; Dusny and Schmid, 2015; Rosenthal et al., 2015; Oliveira et al., 2016), contributing to large-scale bioprocess improvement (Grünberger et al., 2012; Ladner et al., 2017). Sorting of different subpopulations of cells in order to understand the physiological responses in fluctuating microenvironments was also performed by microarray analysis (Hewitt et al., 2007).

MODELING OPTIONS FOR HETEROGENEOUS POPULATIONS

There is currently a gap between the new methods for single cell analysis and the availability of mathematical models which can integrate the data collected. But models are essential in the design and control of bioprocesses. Use of the complex information obtained by investigations of cells at genomic, transcriptomic, proteomic, and metabolomic level to predict bioprocesses is challenging and requires multidisciplinary analysis and significant computational efforts (Zhang et al., 2010).

The traditional classification of the mathematical models for cell populations is in unsegregated/segregated and unstructured/structured. The least complex is a model unstructured and unsegregated, which considers a homogenous population represented by an average unstructured cell, while the most complex is a model structured and segregated, which considers a heterogeneous population of structured cells (Song et al., 2014). The behavior of an average cell is representative only for a synchronous population (Noack et al., 2008), but for a heterogeneous population the model needs to include at least the segregation in the biophase.

Since their initial development, single cell models were seen as a promise for connecting the macroscopic bioreactor with the microscopic one, the cell (Shuler, 1999). Integrated multi-omics predictive models can inform biological discovery but their application is in its infancy (Brink et al., 2016; Kim et al., 2016). Some authors have attempted models which involve a laborious theoretical development to account for different sources of heterogeneity (Stamatakis and Zygorakis, 2010), though the same authors acknowledge them as being far too complex to lend themselves for practical application (Fredrickson and Mantzaris, 2002). Therefore, so far, the distributed properties measured within cell population are not integrated in a single modeling framework appropriate to be used in design, optimization and control of bioprocesses (Henson, 2003; Müller et al., 2010; Fernandes et al., 2011).

Here, we are presenting two options for modeling heterogeneity: population balance models (PBM) and individual based models (IBM). Both modeling approaches describe the variation in the population, but, while the PBM consider each fraction of the population as a continuous phase, in IBM the cells are discrete particles.

Population Balance Models

In PBM cells are differentiated based on variables which characterize their intracellular state. Most commonly these variables are cell age or/and cell mass. The mass balances for substrates, biomass, and products are represented by non-linear and partial differential equations which have as independent variables time and the internal state of the cells. The different phases during the cell life cycle can be represented. The results obtained with PBM will predict the time variation of the cell number distribution, as resulted from growth and division.

Multidimensional PBM can be developed based on flow cytometry data (Fernandes et al., 2013; Ramkrishna and Singh, 2014). Biological heterogeneity in bioreactors was modeled by coupling a population balance model with a biokinetic model (Morchain et al., 2013) and later with a hydrodynamic model (Pigou and Morchain, 2015). One important limitation of PBM is that they are computationally demanding if they are represented more than one single internal state of the cells and this limits on line applications (Royle et al., 2013).

Individual Based Models

In IBM the cells are discrete particles which interact with each other and with the environment. Microbial characteristics are described at single cell level. This allows the study of the system behavior as a result of the properties and performance of the individual components (Railsback and Grimm, 2012). However, it is not always possible to simulate all the individual cells of the system due to computing constraints and choices need to be made about the type of agents used (a cell or a cluster of cells or superindividual) and the level of detail for each of them.

In the last two decades IBM have gained popularity in microbiology (Ferrer et al., 2008; Schuler et al., 2011; Hellweger et al., 2016) due to rapid advancement in computational technologies and the development of specialized software. Open source generic platforms are now available (e.g., Sklar, 2007; Lardon et al., 2011; Rudge et al., 2012; Coakley et al., 2016). However, due to their complex structure IBM require more computing skills than other modeling approaches.

Both PBM and IBM approaches can be used for multispecies fermentation and can take into account the environmental heterogeneity in bioreactors (see *Coupling the scales*). However, PBM models explicitly the behavior of the population and can include only limited cell properties. They are also more restricted in representing stochastic processes as problems of closure may arise (Ramkrishna and Mahoney, 2002). Instead, IBM models the behavior of individuals, each having its own properties, with the population behavior emerging from their interactions. Therefore, it has a higher potential to integrate the detailed data generated with single cell analysis. At the same time, IBM offers a better representation of the stochastic processes, being able to describe the average fluctuations and not only the average behavior in a population.

Coupling the Scales

The solution for PBM and IBM involve a numerical method using discrete time steps. In biological processes there is a wide range of

relevant timescales, varying from nanoseconds to hours. The use of time steps in solving the mathematical models means that all the transformations which have a timescale smaller than the time step chosen for the numerical solution will only be approximated. Their influence on the state variables may then results as non-realistically high. Therefore, it is important to understand the effect of the approximations on the final output of the model and how it affects its predictive capabilities (Gameiro et al., 2016).

For a complete mathematical representation of the bioprocess, suitable to be used in scale-up and design applications, a two-way coupling between mass transfer, hydrodynamics, and biology is required (Wang et al., 2015; Morchain, 2017). These interactions are important as extracellular micro-heterogeneities may amplify the intracellular ones and place an upper limit on productivity and bioprocess reliability (Vasdekis et al., 2015). Local environmental conditions generated by flow streams affect the microbial metabolism and can be described by computational fluid dynamics (CFD). The Euler-Lagrange method represents the appropriate option for studying the impact of substrate gradients on the microbial metabolism in conjunction with the hydrodynamics (Lapin et al., 2004; Liu et al., 2016; Haringa et al., 2017; Kuschel et al., 2017). However, because of the high number of individual cells involved in a fermentation, it is not feasible to directly couple IBM with CFD at the large scale. One useful approach is using statistical emulators (metamodels), which extract the significant information from microscale and are computationally much faster (Wilkinson, 2009; Conti and O'Hagan, 2010). The advantage of an emulator over using a continuous model is that the former will not select *a priori* the information to be transmitted across scales but it will be based on a detailed mechanistic single cell model, representing therefore a simplified simulation strategy to calibrate multi-scale models. This approach was recently implemented by Oyebamiji et al. (2017) as an attempt to scale up a microbial system.

CONCLUSION

In industrial setups there is a tradeoff between cellular growth and process robustness (Carlquist et al., 2012). Understanding and controlling cell heterogeneity at the single cell level will generate more robust and efficient bioprocesses, as, for example, it has been proven that it is not the highest biomass concentration, but higher proportion of viable cells which gives the best productivity

(Want et al., 2009). Insights into bioprocesses at single cell level are expected to contribute also to the development of more accurate mathematical models that can be applied to the prediction and control of fermentative processes (Zhang et al., 2015). This will be highly beneficial as appropriate process and bioreactor design, able to prevent *a priori* unwanted performance losses, is still missing (Takors, 2012) and scaling up has a high degree of empiricism (Brognaux et al., 2013). IBM have the potential to integrate protein measurements with genomics, transcriptomics and metabolomics, and to predict the dynamics of the system across scales and in different environments (Hellweger et al., 2016), giving a better evaluation of the overall system performance.

This is relevant also for synthetic biology, a rapidly growing field which is limited by the lack of understanding on complex fluctuations in physiology and fitness of overall microbial populations (Cardinale and Arkin, 2012). Therefore connecting the single cell dynamics and heterogeneity of cell population with the bioreactor performance is a strategically important objective that is vital to the translation of systems and synthetic biology into an industrial reality.

AUTHOR CONTRIBUTIONS

All authors contributed to the writing of the manuscript. IO carried out the initial literature review and wrote the initial draft. RG-C provided insight relating to the mathematical modeling. AM and WS provided expertise relating the experimental methods. AW provided over-all guidance of the work and editing of the text.

FUNDING

AM acknowledges the support of the EPSRC DTA scholarship. RG-C, AW, and IO acknowledge the support of the EPSRC Frontier Grant "Simulation of open engineered biological systems," led by Newcastle University, ref EP/K038648. WS and AW acknowledge the support of the EPSRC Grant "Synthetic Portabolomics: Leading the way at the crossroads of the Digital and the Bio Economies," ref EP/R003629/1. No new data were created during this study.

REFERENCES

- Ackermann, M. (2015). A functional perspective on phenotypic heterogeneity in microorganisms. *Nat. Rev. Microbiol.* 13, 497–508. doi: 10.1038/nrmicro3491
- Ackermann, M., and Schreiber, F. (2015). A growing focus on bacterial individuality. *Environ. Microbiol.* 17, 2193–2195. doi: 10.1111/1462-2920.12877
- Amantonico, A., Urban, P. L., and Zenobi, R. (2010). Analytical techniques for single-cell metabolomics: state of the art and trends. *Anal. Bioanal. Chem.* 398, 2493–2504. doi: 10.1007/s00216-010-3850-1
- Ambriz-Aviña, V., Contreras-Garduño, J. A., and Pedraza-Reyes, M. (2014). Applications of flow cytometry to characterize bacterial physiological responses. *Biomed Res. Int.* 2014:461941. doi: 10.1155/2014/461941
- Armitage, E. G., Kotze, H. L., and Lockyer, N. P. (2013). Imaging of metabolites using secondary ion mass spectrometry. *Metabolomics* 9, S102–S109. doi: 10.1007/s11306-012-0477-6
- Baert, J., Delepierre, A., Telek, S., Fickers, P., Toye, D., Delamotte, A., et al. (2016). Microbial population heterogeneity versus bioreactor heterogeneity: evaluation of Redox Sensor Green as an exogenous metabolic biosensor. *Eng. Life Sci.* 16, 643–651. doi: 10.1002/elsc.201500149
- Bley, T. (2011). From single cells to microbial population dynamics: modelling in biotechnology based on measurements of individual cells. *Adv. Biochem. Eng. Biotechnol.* 124, 211–227. doi: 10.1007/10_2010_79
- Booth, I. R. (2002). Stress and the single cell: intrapopulation diversity is a mechanism to ensure survival upon exposure to stress. *Int. J. Food Microbiol.* 78, 19–30. doi: 10.1016/S0168-1605(02)00239-8

- Brehm-Stecher, B. F., and Johnson, E. A. (2004). Single-cell microbiology: tools, technologies, and applications. *Microbiol. Mol. Biol. Rev.* 68, 538–559. doi: 10.1128/MMBR.68.3.538-559.2004
- Brink, B. G., Seidel, A., Kleinbolting, N., Nattkemper, T. W., and Albaum, S. P. (2016). Omics fusion - a platform for integrative analysis of omics data. *J. Integr. Bioinform.* 13:296. doi: 10.2390/biecoll-jib-2016-296
- Brognaux, A., Thonart, P., Delvigne, F., Neubauer, P., Twizere, J. C., Francis, F., et al. (2013). Direct and indirect use of GFP whole cell biosensors for the assessment of bioprocess performances: design of milliliter scale-down bioreactors. *Biotechnol. Prog.* 29, 48–59. doi: 10.1002/btpr.1660
- Cardinale, S., and Arkin, A. P. (2012). Contextualizing context for synthetic biology - identifying causes of failure of synthetic biological systems. *Biotechnol. J.* 7, 856–866. doi: 10.1002/biot.201200085
- Carlquist, M., Fernandes, R. L., Helmark, S., Heins A-L, Lundin, L., Sørensen, S. J., et al. (2012). Physiological heterogeneities in microbial populations and implications for physical stress tolerance. *Microb. Cell Fact.* 11:94. doi: 10.1186/1475-2859-11-94
- Chen, Y., Kim, J. K., Hirning, A. J., Josić, K., and Bennett, M. R. (2015). Emergent genetic oscillations in a synthetic microbial consortium. *Science* 349, 986–989. doi: 10.1126/science.aaa3794
- Chi Fru, E., Ofițeru, I. D., Lavric, V., and Graham, D. W. (2011). Non-linear population dynamics in chemostats associated with live-dead cell cycling in *Escherichia coli* strain K12-MG1655. *Appl. Microbiol. Biotechnol.* 89, 791–798. doi: 10.1007/s00253-010-2895-6
- Coakley, S., Richmond, P., Gheorghe, M., Chin, S., Worth, D., Holcombe, M., et al. (2016). Large-scale simulations with FLAME, in *Intelligent Agents in Data-intensive Computing*, eds J. Kołodziej, L. Correia, and J. Manuel Molina (Cham: Springer International Publishing), 123–142. doi: 10.1007/978-3-319-23742-8_6
- Conti, S., and O'Hagan, A. (2010). Bayesian emulation of complex multi-output and dynamic computer models. *Int. J. Stat. Plan. Inference* 140, 640–651. doi: 10.1016/j.jspi.2009.08.006
- Davey, H. M., and Winson, M. K. (2003). Using flow cytometry to quantify microbial heterogeneity. *Curr. Issues Mol. Biol.* 5, 9–15.
- Delvigne, F., and Goffin, P. (2014). Microbial heterogeneity affects bioprocess robustness: dynamic single-cell analysis contributes to understanding of microbial populations. *Biotechnol. J.* 9, 61–72. doi: 10.1002/biot.201300119
- Díaz, M., Herrero, M., García, L. A., and Quirós, C. (2010). Application of flow cytometry to industrial microbial bioprocesses. *Biochem. Eng. J.* 48, 385–407. doi: 10.1111/1751-7915.12018
- Dusny, C., and Schmid, A. (2015). Microfluidic single-cell analysis links boundary environments and individual microbial phenotypes. *Environ. Microbiol.* 17, 1839–1856. doi: 10.1111/1462-2920.12667
- Fernandes, R. L., Carlquist, M., Lundin, L., Heins, A. L., Dutta, A., Sørensen, S. J., et al. (2013). Cell mass and cell cycle dynamics of an asynchronous budding yeast population: experimental observations, flow cytometry data analysis, and multi-scale modeling. *Biotechnol. Bioeng.* 110, 812–826. doi: 10.1002/bit.24749
- Fernandes, R. L., Nierychlo, M., Lundin, L., Pedersen, A. E., Puentes Tellez, P. E., Dutta, A., et al. (2011). Experimental methods and modeling techniques for description of cell population heterogeneity. *Biotechnol. Adv.* 29, 575–599. doi: 10.1016/j.biotechadv.2011.03.007
- Ferrer, J., Prats, C., and López, D. (2008). Individual-based modelling: an essential tool for microbiology. *J. Biol. Phys.* 34, 19–37. doi: 10.1007/s10867-008-9082-3
- Fredrickson, A. G., and Mantzaris, N. V. (2002). A new set of population balance equations for microbial and cell cultures. *Chem. Eng. Sci.* 57, 2265–2278. doi: 10.1016/S0009-2509(02)00116-1
- Gameiro, D., Pérez-Pérez, M., Pérez-Rodríguez, G., Monteiro, G., Azevedo, N. F., and Lourenço, A. (2016). Computational resources and strategies to construct single-molecule metabolic models of microbial cells. *Brief. Bioinform.* 17, 863–876. doi: 10.1093/bib/bbv096
- Gao, D. W., Huang, X. L., and Tao, Y. (2016). A critical review of NanoSIMS in analysis of microbial metabolic activities at single-cell level. *Crit. Rev. Biotechnol.* 36, 884–890. doi: 10.3109/07388551.2015.1057550
- Geiler-Samerotte, K. A., Bauer, C. R., Li, S., Ziv, N., Gresham, D., and Siegal, M. L. (2013). The details in the distributions: why and how to study phenotypic variability. *Curr. Opin. Biotechnol.* 24, 752–759. doi: 10.1016/j.copbio.2013.03.010
- Grote, J., Krysiak, D., and Streit, W. R. (2015). Phenotypic heterogeneity, a phenomenon that may explain why quorum sensing does not always result in truly homogenous cell behavior. *Appl. Environ. Microbiol.* 81, 5280–5289. doi: 10.1128/AEM.00900-15
- Grünberger, A., Paczia, N., Probst, C., Schendzielorz, G., Eggeling, L., Noack, S., et al. (2012). A disposable picolitre bioreactor for cultivation and investigation of industrially relevant bacteria on the single cell level. *Lab Chip* 12, 2060–2068. doi: 10.1039/c2lc40156h
- Grünberger, A., Wiechert, W., and Kohlheyer, D. (2014). Single-cell microfluidics: opportunity for bioprocess development. *Curr. Opin. Biotechnol.* 29, 15–23. doi: 10.1016/j.copbio.2014.02.008
- Haringa, C., Noorman, H. J., and Mudde, R. F. (2017). Lagrangian modeling of hydrodynamic-kinetic interactions in (bio)chemical reactors: practical implementation and setup guidelines. *Chem. Eng. Sci.* 157, 159–168. doi: 10.1016/j.ces.2016.07.031
- Heinemann, M., and Zenobi, R. (2011). Single cell metabolomics. *Curr. Opin. Biotechnol.* 22, 26–31. doi: 10.1016/j.copbio.2010.09.008
- Hellweger, F. L., Clegg, R. J., Clark, J. R., Plugge, C. M., and Kreft, J. U. (2016). Advancing microbial sciences by individual-based modelling. *Nat. Rev. Microbiol.* 14, 461–471. doi: 10.1038/nrmicro.2016.62
- Henson, M. A. (2003). Dynamic modeling of microbial cell populations. *Curr. Opin. Biotechnol.* 14, 460–467. doi: 10.1016/S0958-1669(03)00104-6
- Hewitt, C. J., Caron, G. N. V., Nienow, A. W., and McFarlane, C. M. (1999). The use of multi-parameter flow cytometry to compare the physiological response of *Escherichia coli* W3110 to glucose limitation during batch, fed-batch and continuous culture cultivations. *J. Biotechnol.* 75, 251–264. doi: 10.1016/S0168-1656(99)00168-6
- Hewitt, C. J., Onyeaka, H., Lewis, G., Taylor, I. W., and Nienow, A. W. (2007). A comparison of high cell density fed-batch fermentations involving both induced and non-induced recombinant *Escherichia coli* under well-mixed small-scale and simulated poorly mixed large-scale conditions. *Biotechnol. Bioeng.* 96, 495–505. doi: 10.1002/bit.21127
- Huang, W. E., Griffiths, R. I., Thompson, I. P., Bailey, M. J., and Whiteley, A. S. (2004). Raman microscopic analysis of single microbial cells. *Anal. Chem.* 76, 4452–4458. doi: 10.1021/ac049753k
- Jahn, M., Seifert, J., von Bergen, M., Schmid, A., Bühler, B., and Müller, S. (2013). Subpopulation-proteomics in prokaryotic populations. *Curr. Opin. Biotechnol.* 24, 79–87. doi: 10.1016/j.copbio.2012.10.017
- Kim, M., Rai, N., Zorraqino, V., and Tagkopoulou, I. (2016). Multi-omics integration accurately predicts cellular state in unexplored conditions for *Escherichia coli*. *Nat. Commun.* 7:13090. doi: 10.1038/ncomms13090
- Kuschel, M., Siebler, F., and Takors, R. (2017). Lagrangian trajectories to predict the formation of population heterogeneity in large-scale bioreactors. *Bioengineering* 4:27. doi: 10.3390/bioengineering4020027
- Ladner, T., Grünberger, A., Probst, C., Kohlheyer, D., Büchs, J., and Delvigne, F. (2017). “Application of mini- and micro-bioreactors for microbial bioprocesses,” in *Current Developments in Biotechnology and Bioengineering*, eds C. Larroche, M. Á. Sanromán, G. Du and A. Pandey (Amsterdam: Elsevier), 433–461.
- Landry, Z. C., Giovanonni, S. J., Quake, S. R., and Blainey, P. C. (2013). Optofluidic cell selection from complex microbial communities for single-genome analysis. *Methods Enzymol.* 531, 61–90. doi: 10.1016/B978-0-12-407863-5.00004-6
- Lapin, A., Müller, D., and Reuss, M. (2004). Dynamic behavior of microbial populations in stirred bioreactors simulated with Euler-Lagrange methods: traveling along the lifelines of single cells. *Ind. Eng. Chem. Res.* 43, 4647–4656. doi: 10.1021/ie030786k
- Lara, A. R., Galindo, E., Ramírez, O. T., and Palomares, L. A. (2006). Living with heterogeneities in bioreactors. *Mol. Biotechnol.* 34, 355–381. doi: 10.1385/MB:34:3:355
- Lardon, L. A., Merkey, B. V., Martins, S., Dotsch, A., Picioreanu, C., Kreft, J. U., et al. (2011). iDynoMiCS: next-generation individual-based modelling of biofilms. *Environ. Microbiol.* 13, 2416–2434. doi: 10.1111/j.1462-2920.2011.02414.x
- Lavric, V., and Graham, D. W. (2010). Birth, growth and death as structuring operators in bacterial population dynamics. *J. Theor. Biol.* 264, 45–54. doi: 10.1016/j.jtbi.2010.01.020

- Lecault, V., White, A. K., Singhal, A., and Hansen, C. L. (2012). Microfluidic single cell analysis: from promise to practice. *Curr. Opin. Chem. Biol.* 16, 381–390. doi: 10.1016/j.cbpa.2012.03.022
- Li, B., and You, L. (2013). Predictive power of cell-to-cell variability. *Quant. Biol.* 1, 131–139. doi: 10.1007/s40484-013-0013-3
- Lidstrom, M. E., and Konopka, M. C. (2010). The role of physiological heterogeneity in microbial population behavior. *Nat. Chem. Biol.* 6, 705–712. doi: 10.1038/nchembio.436
- Liu, Y., Wang, Z.-J., Xia, J.-Y., Haringa, C., Liu, Y.-P., Chu, J. et al. (2016). Application of Euler-Lagrange CFD for quantitative evaluating the effect of shear force on *Carthamus tinctorius* L. cell in a stirred tank bioreactor. *Biochem. Eng. J.* 114, 209–217. doi: 10.1016/j.bej.2016.07.006
- Löffler, M., Simen, J. D., Jäger, G., Schäferhoff, K., Freund, A., and Takors, R. (2016). Engineering *E. coli* for large-scale production – strategies considering ATP expenses and transcriptional responses. *Metab. Eng.* 38, 73–85. doi: 10.1016/j.ymben.2016.06.008
- Love, K. R., Bagh, S., Choi, J., and Love, J. C. (2013). Microtools for single-cell analysis in biopharmaceutical development and manufacturing. *Trends Biotechnol.* 31, 280–286. doi: 10.1016/j.tibtech.2013.03.001
- Morchain, J. (2017). “Numerical tools for scaling up bioreactors,” in *Current Developments in Biotechnology and Bioengineering: Bioprocesses, Bioreactors and Controls*, eds M. Á. Sanromán, G. Du, and A. Pandey (Toronto, ON: Elsevier), 495–523. doi: 10.1016/B978-0-444-63663-8.00017-3
- Morchain, J., Gabelle, J. C., and Cockx, A. (2013). Coupling of biokinetic and population balance models to account for biological heterogeneity in bioreactors. *Aiche J.* 59, 369–379. doi: 10.1002/aic.13820
- Müller, S., Harms, H., and Bley, T. (2010). Origin and analysis of microbial population heterogeneity in bioprocesses. *Curr. Opin. Biotechnol.* 21, 100–113. doi: 10.1016/j.copbio.2010.01.002
- Muller, S., and Nebe-von-Caron, G. (2010). Functional single-cell analyses: flow cytometry and cell sorting of microbial populations and communities. *FEMS Microbiol. Rev.* 34, 554–587. doi: 10.1111/j.1574-6976.2010.00214.x
- Musat, N., Foster, R., Vagner, T., Adam, B., and Kuypers, M. M. M. (2012). Detecting metabolic activities in single cells, with emphasis on nanoSIMS. *FEMS Microbiol. Rev.* 36, 486–511. doi: 10.1111/j.1574-6976.2011.00303.x
- Noack, S., Kloden, W., and Bley, T. (2008). Modeling synchronous growth of bacterial populations in phased cultivation. *Bioprocess Biosyst. Eng.* 31, 435–443. doi: 10.1007/s00449-007-0180-6
- Oñte, I. D., Ferdeş, M., Knapp, C. W., Graham, D. W., and Lavric, V. (2012). Conditional confined oscillatory dynamics of *Escherichia coli* strain K12-MG1655 in chemostat systems. *Appl. Microbiol. Biotechnol.* 94, 185–192. doi: 10.1007/s00253-011-3697-1
- Oliveira, A. F., Pessoa, A., Bastos, R. G., and de la Torre, L. G. (2016). Microfluidic tools toward industrial biotechnology. *Biotechnol. Prog.* 32, 1372–1389. doi: 10.1002/btpr.2350
- Oyebamiji, O. K., Wilkinson, D. J., Jayatilake, P. G., Curtis, T. P., Rushton, S. P., Li, B., et al. (2017). Gaussian process emulation of an individual-based model simulation of microbial communities. *J. Comput. Sci.* 22, 69–84. doi: 10.1016/j.jocs.2017.08.006
- Pasotti, L., and Zucca, S. (2014). Advances and computational tools towards predictable design in biological engineering. *Comput. Math. Methods Med.* 2014:369681. doi: 10.1155/2014/369681
- Pigou, M., and Morchain, J. (2015). Investigating the interactions between physical and biological heterogeneities in bioreactors using compartment, population balance and metabolic models. *Chem. Eng. Sci.* 126, 267–282. doi: 10.1016/j.ces.2014.11.035
- Railsback, S. F., and Grimm, V. (2012). *Agent-based and Individual-based Modeling: A Practical Introduction*. Princeton, NJ: Princeton University Press.
- Ramkrishna, D., and Mahoney, A. W. (2002). Population balance modeling. Promise for the future. *Chem. Eng. Sci.* 57, 595–606. doi: 10.1016/S0009-2509(01)00386-4
- Ramkrishna, D., and Singh, M. R. (2014). Population balance modeling: current status and future prospects. *Annu. Rev. Chem. Biomol. Eng.* 5, 123–146. doi: 10.1146/annurev-chembioeng-060713-040241
- Rosano, G. L., and Ceccarelli, E. A. (2014). Recombinant protein expression in *Escherichia coli*: advances and challenges. *Front. Microbiol.* 5:172. doi: 10.3389/fmicb.2014.00172
- Rosenthal, K., Falke, F., Frick, O., Dusny, C., and Schmid, A. (2015). An inert continuous microreactor for the isolation and analysis of a single microbial cell. *Micromachines* 6, 1836–1855. doi: 10.3390/mi6121459
- Royle, K. E., del Val, I. J., and Kontoravdi, C. (2013). Integration of models and experimentation to optimise the production of potential biotherapeutics. *Drug Discov. Today* 18, 1250–1255. doi: 10.1016/j.drudis.2013.07.002
- Rubakhin, S. S., Lanni, E. J., and Sweedler, J. V. (2013). Progress toward single cell metabolomics. *Curr. Opin. Biotechnol.* 24, 95–104. doi: 10.1016/j.copbio.2012.10.021
- Rubbens, P., Props, R., Boon, N., and Waegeman, W. (2017). Flow cytometric single-cell identification of populations in synthetic bacterial communities. *PLOS ONE* 12:e0169754. doi: 10.1371/journal.pone.0169754
- Rudge, T. J., Steiner, P. J., Phillips, A., and Haseloff, J. (2012). Computational modeling of synthetic microbial biofilms. *ACS Synth. Biol.* 1, 345–352. doi: 10.1021/sb300031n
- Ryall, B., Eydallin, G., and Ferenci, T. (2012). Culture history and population heterogeneity as determinants of bacterial adaptation: the adaptomics of a single environmental transition. *Microbiol. Mol. Biol. Rev.* 76, 597–625. doi: 10.1128/MMBR.05028-11
- Sauer, M., and Mattanovich, D. (2012). Construction of microbial cell factories for industrial bioprocesses. *J. Chem. Technol. Biotechnol.* 87, 445–450. doi: 10.1002/jctb.3711
- Schuler, A. J., Majed, N., Bucci, V., Hellweger, F. L., Tu, Y., and Gu, A. Z. (2011). Is the whole the sum of its parts? Agent-based modelling of wastewater treatment systems. *Water Sci. Technol.* 63, 1590–1598. doi: 10.2166/wst.2011.218
- Shapiro, H. H. (2000). Microbial analysis at the single-cell level: tasks and techniques. *J. Microbiol. Methods* 42, 3–16. doi: 10.1016/S0167-7012(00)00167-6
- Shi, X., Gao, W. M., Wang, J. X., Chao, S. H., Zhang, W. W., and Meldrum, D. R. (2015). Measuring gene expression in single bacterial cells: recent advances in methods and micro-devices. *Crit. Rev. Biotechnol.* 35, 448–460. doi: 10.3109/07388551.2014.899556
- Shuler, M. L. (1999). Single-cell models: promise and limitations. *J. Biotechnol.* 71, 225–228. doi: 10.1016/S0168-1656(99)00024-3
- Sklar, E. (2007). Software review: NetLogo, a multi-agent simulation environment. *Artif. Life* 13, 303–311. doi: 10.1162/artl.2007.13.3.303
- Song, H.-S., Cannon, W., Beliaev, A., and Konopka, A. (2014). Mathematical modeling of microbial community dynamics: a methodological review. *Processes* 2, 711–752. doi: 10.3390/pr2040711
- Stamatakis, M., and Zygorakis, K. (2010). A mathematical and computational approach for integrating the major sources of cell population heterogeneity. *J. Theor. Biol.* 266, 41–61. doi: 10.1016/j.jtbi.2010.06.002
- Sumner, E. R., and Avery, S. V. (2002). Phenotypic heterogeneity: differential stress resistance among individual cells of the yeast *Saccharomyces cerevisiae*. *Microbiology* 148, 345–351. doi: 10.1099/00221287-148-2-345
- Takors, R. (2012). Scale-up of microbial processes: impacts, tools and open questions. *J. Biotechnol.* 160, 3–9. doi: 10.1016/j.jbiotec.2011.12.010
- Vasdekis, A. E., Silverman, A. M., and Stephanopoulos, G. (2015). Origins of cell-to-cell bioprocessing diversity and implications of the extracellular environment revealed at the single-cell level. *Sci. Rep.* 5:17689. doi: 10.1038/srep17689
- Wang, G., Tang, W. J., Xia, J. Y., Chu, J., Noorman, H., and van Gulik, W. M. (2015). Integration of microbial kinetics and fluid dynamics toward model-driven scale-up of industrial bioprocesses. *Eng. Life Sci.* 15, 20–29. doi: 10.1002/elsc.201400172
- Want, A., Thomas, O. R. T., Kara, B., Liddell, J., and Hewitt, C. J. (2009). Studies related to antibody fragment (fab) production in *Escherichia coli* W3110 fed-batch fermentation processes using multiparameter flow cytometry. *Cytometry A* 75, 148–154. doi: 10.1002/cyto.a.20683
- Wilkinson, D. J. (2009). Stochastic modelling for quantitative description of heterogeneous biological systems. *Nat. Rev. Genet.* 10, 122–133. doi: 10.1038/nrg2509
- Winson, M. K., and Davey, H. M. (2000). Flow cytometric analysis of microorganisms. *Methods* 21, 231–240. doi: 10.1006/meth.2000.1003
- Wu, M. Y., and Singh, A. K. (2012). Single-cell protein analysis. *Curr. Opin. Biotechnol.* 23, 83–88. doi: 10.1016/j.copbio.2011.11.023

- Wyre, C., and Overton, T. (2014a). Flow cytometric analysis of *E. coli* on agar plates: implications for recombinant protein production. *Biotechnol. Lett.* 36, 1485–1494. doi: 10.1007/s10529-014-1511-8
- Wyre, C., and Overton, T. (2014b). Use of a stress-minimisation paradigm in high cell density fed-batch *Escherichia coli* fermentations to optimise recombinant protein production. *J. Ind. Microbiol. Biotechnol.* 41, 1391–1404. doi: 10.1007/s10295-014-1489-1
- Xiao, Y., Bowen, C. H., Liu, D., and Zhang, F. (2016). Exploiting nongenetic cell-to-cell variation for enhanced biosynthesis. *Nat. Chem. Biol.* 12, 339–344. doi: 10.1038/nchembio.2046
- Young, J. W., Locke, J. C. W., Altinok, A., Rosenfeld, N., Bacarian, T., Swain, P. S., et al. (2012). Measuring single-cell gene expression dynamics in bacteria using fluorescence time-lapse microscopy. *Nat. Protoc.* 7, 80–88. doi: 10.1038/nprot.2011.432
- Zhang, H., Cui, X. L., Bi, J. X., Dai, S., and Ye, H. T. (2015). Single-cell analysis for bioprocessing. *Eng. Life Sci.* 15, 582–592. doi: 10.1002/elsc.201400155
- Zhang, W. W., Li, F., and Nie, L. (2010). Integrating multiple ‘omics’ analysis for microbial biology: application and methodologies. *Microbiology* 156, 287–301. doi: 10.1099/mic.0.034793-0
- Conflict of Interest Statement:** The authors declare that the research was conducted in the absence of any commercial or financial relationships that could be construed as a potential conflict of interest.

Copyright © 2017 González-Cabaleiro, Mitchell, Smith, Wipat and Ofițeru. This is an open-access article distributed under the terms of the Creative Commons Attribution License (CC BY). The use, distribution or reproduction in other forums is permitted, provided the original author(s) or licensor are credited and that the original publication in this journal is cited, in accordance with accepted academic practice. No use, distribution or reproduction is permitted which does not comply with these terms.



Heterogeneity between and within Strains of *Lactobacillus brevis* Exposed to Beer Compounds

Yu Zhao, Susanne Knøchel and Henrik Siegumfeldt*

Microbiology and Fermentation, Department of Food Science, Faculty of Science, University of Copenhagen, Frederiksberg, Denmark

OPEN ACCESS

Edited by:

Clara Prats,
Polytechnic University of Catalonia,
Spain

Reviewed by:

Steven Singer,
Lawrence Berkeley National
Laboratory, USA
Dimitris Tsaltas,
Cyprus University of Technology,
Cyprus

*Correspondence:

Henrik Siegumfeldt
siegum@food.ku.dk

Specialty section:

This article was submitted to
Systems Microbiology,
a section of the journal
Frontiers in Microbiology

Received: 01 October 2016

Accepted: 3 February 2017

Published: 14 February 2017

Citation:

Zhao Y, Knøchel S and
Siegumfeldt H (2017) Heterogeneity
between and within Strains
of *Lactobacillus brevis* Exposed
to Beer Compounds.
Front. Microbiol. 8:239.
doi: 10.3389/fmicb.2017.00239

This study attempted to investigate the physiological response of six *Lactobacillus brevis* strains to hop stress, with and without the addition of Mn^{2+} or ethanol. Based on the use of different fluorescent probes, cell viability and intracellular pH (pHi) were assessed by fluorescence microscopy combined with flow cytometry, at the single cell level. The combined approach was faster than the traditional colony based method, but also provided additional information about population heterogeneity with regard to membrane damage and cell size reduction, when exposed to hop compounds. Different physiological subpopulations were detected under hop stress in both hop tolerant and sensitive strains. A large proportion of cells were killed in all the tested strains, but a small subpopulation from the hop tolerant strains eventually recovered as revealed by pHi measurements. Furthermore, a short term protection against hop compounds was obtained for both hop tolerant and sensitive strains, by addition of high concentration of Mn^{2+} . Addition of ethanol in combination with hop compounds caused an additional short term increase in damaged subpopulation, but the subsequent growth suggested that the presence of ethanol provides a slight cross resistance toward hop compounds.

Keywords: *Lactobacillus brevis*, hop compounds, manganese, ethanol, fluorescence microscopy, flow cytometry, heterogeneity

INTRODUCTION

Beer represents a hostile environment for most microorganisms due to the presence of hop compounds, low pH, ethanol and carbon dioxide as well as the limited amount of oxygen and nutrients (Sakamoto and Konings, 2003; Suzuki, 2011). Nevertheless, some bacteria are still able to spoil beer. *Lactobacillus brevis* is the predominant spoilage organism, and has therefore been studied extensively (Yansanjav et al., 2004; Behr et al., 2007; Suzuki, 2011; Bergsveinson et al., 2015; Schurr et al., 2015a).

Hop compounds are an essential part of beer brewing. Besides imparting a bitter flavor, hop compounds (mainly iso- α -acids) are antimicrobial, and tolerance toward hop is therefore a prerequisite for beer spoilage bacteria (Suzuki, 2011). There are two antibacterial modes of hop compounds. They can act as mobile-carrier ionophores, which cause a decrease in intracellular pH (Simpson, 1993). The minimum inhibitory concentration (MIC) of *trans*-iso- α -acids decrease with pH and increase with concentration of divalent cations, particularly Mn^{2+} (Simpson, 1993). An additional mode of action with hop that influence on transmembrane redox reactions in the

presence of Mn^{2+} gradients, was recently demonstrated (Behr and Vogel, 2010). Interestingly,

Haakensen et al. (2009) investigated a wide selection of *Lactobacilli* and *Pediococcus* isolates and found that the addition of ethanol to hop agar plates caused a decreased growth of some isolates, while ethanol protected other isolates against hop compounds.

The traditional method of studying susceptibility of microorganisms, e.g., *Lactobacillus* and *Pediococcus* species toward hop compounds has been used to assess the growth of an isogenic population (Simpson, 1993; Fernandez and Simpson, 1995; Haakensen et al., 2009). However, these culture-based method require extended incubations and some strains even exhibit viable but non-culturable characteristics in traditional laboratory media like the de Man Rogosa Sharpe (MRS) medium (Suzuki et al., 2008). In addition, recent studies showed that even cells from an isogenic population exhibit heterogeneous gene expression and differ in physiological parameters such as growth rate and resistance to stress (Strovas et al., 2007; Ryssel et al., 2013; Zhao et al., 2014). Several studies have also shown that under stress conditions, a minor robust subpopulation can subsequently dominate the overall population (Balaban et al., 2004; Lidstrom and Konopka, 2010; Ambriz-Avina et al., 2014). Therefore, single cell analysis can provide additional insights into microbial behavior under stress from hop compounds.

Fluorescence microscopy (FM) and/or flow cytometry (FCM) have been successfully used for determination of cell population heterogeneity, including live, dead, or intermediate subpopulations (Guldfeldt and Arneborg, 1998; Barbesti et al., 2000; Ambriz-Avina et al., 2014; Stiefel et al., 2015). These observations include morphological changes like cell size and clumping, as well as physiological changes in membrane permeability, intracellular pH and membrane potential at a single cell level (Davey and Kell, 1996; Garcia-Betancur et al., 2012). Morphological information is readily available from microscopy, while a very large number of individual cells can be analyzed by FCM. Hence, the combined methods of FM and FCM can deliver a combination of qualitative and quantitative information that will provide a comprehensive description of subpopulations and even individual cells.

To the best of our knowledge, the response of *L. brevis* toward hop compounds is still not well described at the single cell level. Therefore, the aim of this study was to analyze how individual cells from six different isogenic strains respond to hop compounds by FM and FCM. Furthermore, an interaction with Mn^{2+} or ethanol under hop stress was investigated, in order to further elucidate mechanisms involved in hop tolerance.

MATERIALS AND METHODS

Media and Chemicals

Two different MRS media were used throughout the study. Normal MRS medium (MRS_{5.6}, Merck), which was prepared according to the instructions from the supplier. An acidified MRS medium (MRS_{4.3}), where pH was lowered to 4.3 using hydrochloric acid. The final concentration of hop compounds

TABLE 1 | Organisms used in this study.

Abbreviation	Organisms	Source
JK09	<i>Lactobacillus brevis</i> JK09	Danish craft beer
JK09-- ^a	<i>Lactobacillus brevis</i> JK09--	Plasmid cured JK09
HF01	<i>Lactobacillus brevis</i> HF01	Danish craft beer
A	<i>Lactobacillus brevis</i> A	Danish craft beer
G430 ^b	<i>Lactobacillus brevis</i> G430	Czech beer
Q	<i>Lactobacillus brevis</i> Q	Danish craft beer

^aPlasmid cured variant JK09-- was derived by subculturing JK09 in MRS_{5.6} containing the plasmid curing agent novobiocin. The plasmid curing was confirmed by the absence of selected plasmid-borne hop tolerant related genes by PCR (results not shown).

^b*L. brevis* G430 was kindly provided by Dr. J. J. Leisner (Department of Veterinary Disease Biology, University of Copenhagen).

(iso- α -acids) in stress experiments was 55.2 μ M unless otherwise indicated, which was obtained by addition of a stock solution of 30% (w/w) iso- α -acids in an aqueous solution of potassium (Hopsteiner, New York, NY, USA). Sodium acetate buffer (50.0 mM, pH 4.3, with 0.1 M glucose) was used for experiments where growth was not wanted. A final concentration of either 2.9 μ M manganese (corresponding to levels in pilsner lager beer) (Behr and Vogel, 2009) or 265.0 μ M manganese (as in MRS), was obtained by addition of a 26.5 mM $MnSO_4$ stock solution to sodium acetate buffer.

Bacteria Strains and Culture Condition

A total of six *L. brevis* strains isolated from beer were included in the present study (Table 1). A preculture was started by inoculating 10 mL MRS_{5.6} from a frozen stock culture, and incubated at 30°C overnight. The preculture was subcultured into fresh MRS_{5.6} (inoculation concentration 1%) at 30°C. After 16 h, optical density (OD₆₀₀) of each strain was adjusted with fresh MRS_{5.6} to 1.0, corresponding to approximately 5×10^8 CFU/mL.

Determination of Growth Activity of *L. brevis*

Hundred microliter standardized culture was inoculated into 10 mL of the following media MRS_{5.6} (control), MRS_{5.6} with hop compounds (MRS_{5.6+H}), MRS_{4.3} and MRS_{4.3} with hop compounds (MRS_{4.3+H}), separately. The growth curves were assessed in 96-wells microplates by measuring OD₆₀₀ for every 12 h using a VarioskanTM Flash (Thermo Fisher Scientific Oy, Finland) until 168 h. Each well of a microplate was added 200 μ L suspension. Microplates were sealed with parafilm (Sigma-Aldrich) to minimize loss of volume and incubated at 30°C until measurement. For each strain, the average OD₆₀₀ value was calculated from 16 wells.

Fluorescent Staining

To investigate viability in individual cells, cells were stained with SYTO 13 (Molecular Probes, Thermo Fisher scientific) and Propidium Iodide (PI, Molecular Probes, Thermo Fisher scientific). 1 mL of an overnight culture was incubated with SYTO 13 (final concentration 10.0 μ M) and PI (final concentration 15.0 μ M) simultaneously at 30°C for 30 min in the

dark. The suspensions were subsequently diluted 20 times to an approximate concentration of 10^7 cells/mL with saline solution (NaCl, 0.9%, w/w). All dual stained cell suspensions were kept on ice until further analysis.

For pH_i measurement, cells were stained with 5(6)-Carboxy-2,7-dichlorofluorescein diacetate succinimidyl ester (CDCFDA-SE, 3.9 mM, Molecular Probes, Thermo Fisher scientific). The CDCFDA-SE staining procedure used in this study was modified from Shabala et al. (2006). Briefly, 1 mL standardized culture was harvested by centrifugation ($10,000 \times g$, 5 min), and the pellet was re-suspended in 980 μ L phosphate buffered saline (PBS, 50.0 mM, pH 7.4) with 10 μ L 1.0 M glucose and 10 μ L CDCFDA-SE. The cell suspension was incubated at 30°C in the dark for 30 min.

Sample Preparation for Viability Assessments and Cell Size Comparisons

A standardized culture (200 μ L) was inoculated in 20 mL MRS_{4.3} and MRS_{4.3+H}, separately, and incubated at 30°C. A 1 mL sample was taken every 6 h until 48 h and then every 24 h until 96 h. Cells were centrifuged at $10,000 \times g$ for 5 min and the pellets were re-suspended in 0.5 mL saline solution and stained with SYTO13/PI as described above. Subsequently, samples were analyzed by FM and/or FCM. For FCM, a positive control (fresh overnight culture, live cells) was stained with SYTO 13 and a negative control (dead cells) was stained with PI. For the negative control, preliminary results using 70% ethanol to kill all the cells, but this method caused cell aggregation in FCM analysis. Therefore, a combination of 552 μ M hop compounds and 20% ethanol (v/v) was used to obtain a fully permeabilized population of single cells, where almost 100% cells were stained with PI, which was confirmed by FM.

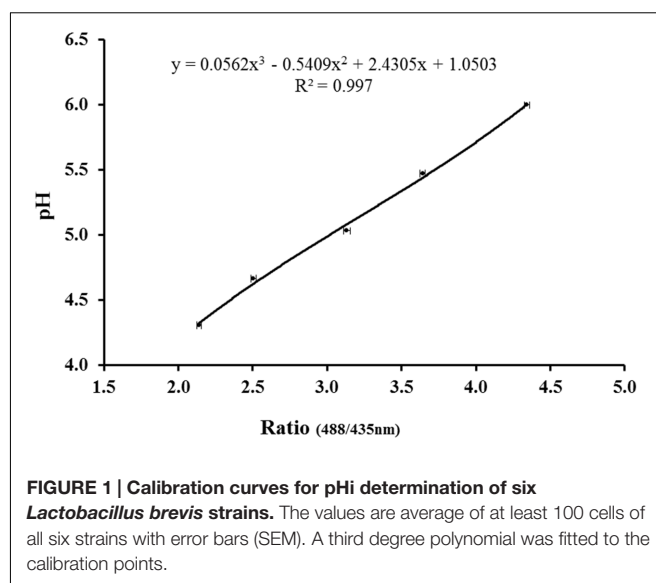
Sample Preparation for pH_i Measurement

Cells from overnight culture were stained with CDCFDA-SE, centrifuged at $10,000 \times g$ for 5 min and the pellet was re-suspended in 1 mL sodium acetate buffer. Subsequently, the suspension was divided into two tubes, centrifuged at $10,000 \times g$ for 5 min and re-suspended into 500 μ L sodium acetate buffer with and without hop compounds. Images were acquired after 1, 12, and 24 h by FM. Samples were kept at 30°C in the dark until image acquisition.

To construct a calibration curve for pH_i, stained cells were exposed to 70% ethanol for 30 min to achieve fully permeabilized cells. Aliquots of permeabilized cells were then re-suspended in sodium acetate buffer with pH 4.3, 4.7, 5.0, 5.5, and 6.0. Since all six strains exhibited similar ratio values at a given pH, it was decided to construct one standard curve. The average ratio of at least 100 cells for each pH value was plotted against the Ratio (488/435 nm), and the standard error of the mean (SEM) was calculated (Figure 1).

Manganese Addition

1.5-mL standardized culture was centrifuged at $10,000 \times g$ for 5 min and re-suspended in 1.5 mL of acetate buffer. For viability



assessment, the suspension was divided into three tubes, followed by centrifugation ($10,000 \times g$, 5 min), and the pellets were re-suspended in acetate buffer with hop compounds, acetate buffer with hop and 2.9 μ M manganese, as well as acetate buffer with hop and 265.0 μ M manganese, respectively. Cell suspensions were incubated at 30°C for 2.5 h, stained with SYTO 13/PI for 0.5 h, and analyzed by FCM. For pH_i measurement, the suspension was first stained with CDCFDA-SE, then divided into three tubes, centrifuged at $10,000 \times g$ for 5 min and the pellets were re-suspended in the three solutions described above. Cell suspensions were incubated at 30°C for 3 h before being analyzed by FM.

Ethanol Addition

OD₆₀₀ of all strains were measured in MRS_{4.3} and MRS_{4.3+H} with and without addition of ethanol (4.6%, v/v), according to the method described above. For viability assessment, 2 mL standardized culture was centrifuged at $10,000 \times g$ for 5 min and the pellet was re-suspended in 2 mL acetate buffer. The suspension was divided into four tubes, followed by centrifugation ($10,000 \times g$, 5 min) and the pellets were re-suspended in acetate buffer with and without hop compounds and ethanol. Cell suspensions were incubated at 30°C for 2.5 h, stained with SYTO 13/PI for 0.5 h, and then analyzed by FCM.

Fluorescence Microscopy and Data Analysis

For viability assessment, a 63 \times Plan-Apochromat, N.A 1.4 (Zeiss) was used. The green fluorescence (SYTO 13) was recorded by excitation of 470–490 nm and emission of 515–565 nm. The red fluorescence (PI) was recorded by excitation of 515–565 nm and emission of 610–680 nm.

For pH_i measurement, the method was the same as previously described (Shabala et al., 2006). Briefly, the two excitation wavelengths were 435 and 488 nm, and emission was collected by a 515–565 nm bandpass filter. Images were acquired by

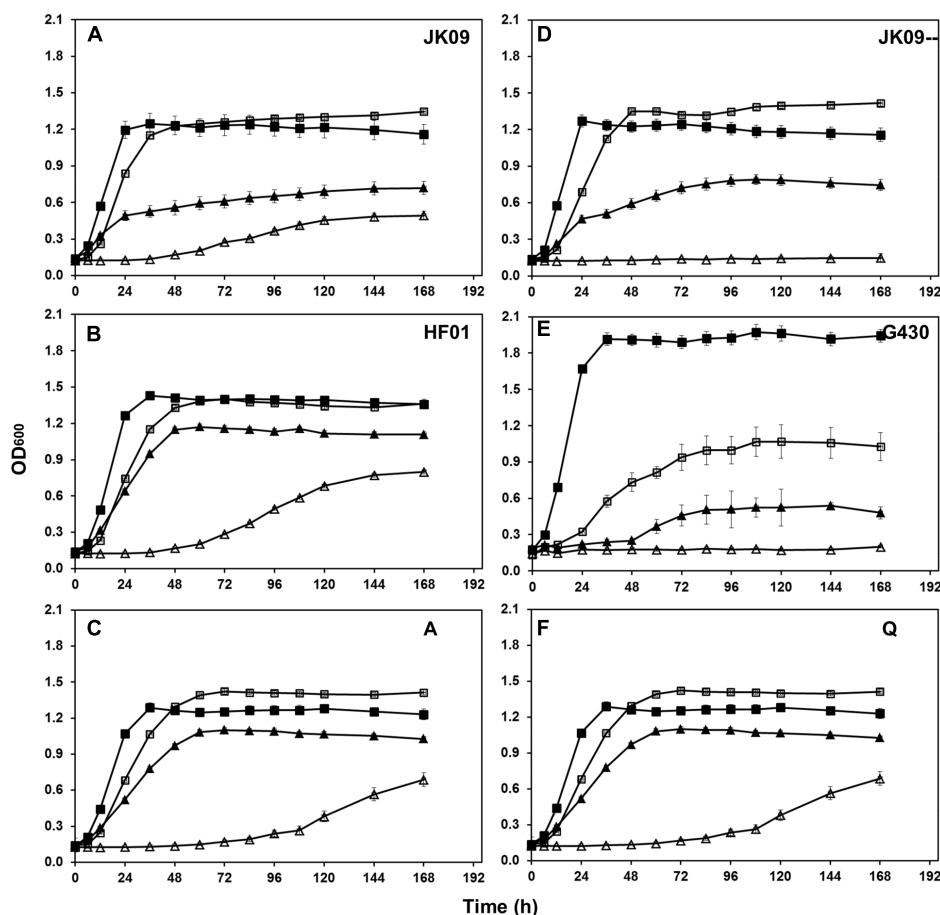


FIGURE 2 | Growth curves of *L. brevis* exposed to hop compounds in MRS adjusted to different pH values. Cells were cultured at 30°C in MRS_{5.6} (control, ■), MRS_{5.6}+H (▲), MRS_{4.3} (□), MRS_{4.3}+H (△). (A–F) JK09, HF01, A, JK09--, G430 and Q. The values are the means of OD₆₀₀ of 16 wells in 96-wells microplate, and the error bars indicate the standard deviation.

using the Metamorph 7 software (Universal imaging Corp., West Chester, PA, USA) and analyzed with the free image analysis software ImageJ [version 1.48; National Institutes of Health (NIH), Bethesda, MD, USA¹].

Flow Cytometry and Data Analysis

Samples were counted and analyzed by a BD FACS Jazz Cell Sorter with a 488 nm argon ion laser. Green fluorescence emitted from SYTO 13 stained cells was collected with bandpass filter 530 ± 20 nm, whereas the red fluorescence emitted from PI stained cells was collected with bandpass filter 692 ± 20 nm. Events were collected by triggering on the side scatter channel. A 1 mL cell suspension was added into a plastic tube and 100,000 events per sample were recorded. Data were collected and stored in BD FACS Software sorter software (BD Biosciences, USA). The collected data were analyzed with the FlowJo_V10 (Tree Star, Inc. USA). For subpopulation assessments, four quadrants were defined clockwise starting from the top-left one as Q1, Q2, Q3,

and Q4 on the dot plot images. For cell size comparisons, the histogram of the forward scatter channel (FSC) was used.

Data Analysis

When growth experiments were performed in several replicates, the average and the standard deviation were calculated. In the FCM experiments, 100,000 cells were analyzed to obtain a large sample, and the proportions of subpopulations were generated by FlowJo_V10 software. In the intracellular pH experiments, the calibration curve from section “Sample Preparation for pH_i Measurement” was used to calculate the pH_i. Subsequently, the average of at least 20 individual cells was calculated, and the individual cells were manually ascribed to predefined pH_i intervals.

RESULTS

Growth Behavior of *L. brevis* Strains

Growth curves of six strains were obtained under normal conditions, under low pH stress, under hop compounds stress

¹<http://imagej.nih.gov/ij/>

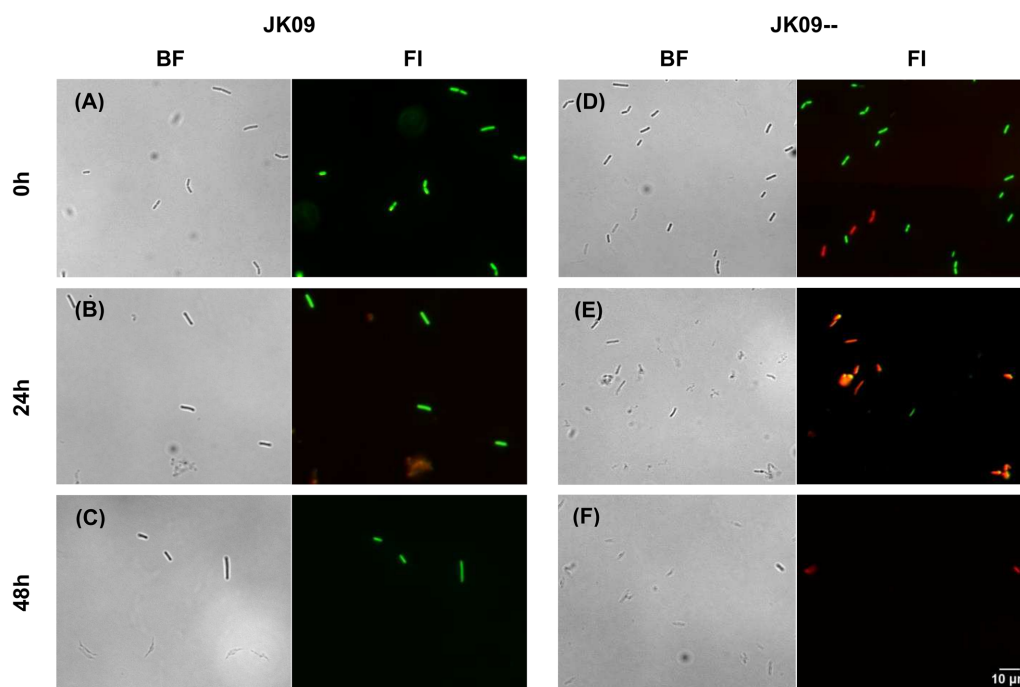


FIGURE 3 | Cells of JK09 (A–C) and JK09-- (D–F) exposed to hop compounds in MRS_{4.3} after 0, 24, and 48 h, stained with SYTO 13 and PI and analyzed by fluorescence microscopy (FM). BF, bright-field; FI, fluorescent image. For fluorescent images, cells stained with SYTO 13 are labeled green, while cells stained with PI are labeled red.

as well as under the combined stress condition (Figure 2). All six isolates grew well in normal MRS_{5.6}, with G430 reaching the highest OD₆₀₀ (Figure 2E). In MRS_{4.3}, five strains had a slightly prolonged lag phase, but with the same growth rate and the same final OD₆₀₀. Only G430 was significantly inhibited by the low pH alone (Figure 2E). In contrast, all the bacteria exhibited poor growth under hop stress. The combined stress was even more inhibitory. In MRS_{4.3+H}, JK09--, G430 and Q were so inhibited that they did not produce any change in optical density during the experiment (168 h), and these strains were consequently designated as hop sensitive strains. JK09, HF01 and A were comparatively tolerant to hop compounds in MRS_{4.3+H}, and these strains were designated as hop tolerant strains. However, the lag phase and growth rate of the hop tolerant strains were dramatically affected, particularly for strain A. As the antibacterial effect of hop compounds was mostly pronounced at pH 4.3, a typical pH for beer, pH 4.3 was used for further investigations.

Viability Assessment of *L. brevis* Cells by FM Analysis

Viable cells could easily be distinguished from membrane damaged cells by dual-staining with SYTO 13 (green fluorescence) and PI (red fluorescence) using FM. At the beginning of the experiment ($T = 0$ h), most cells of both JK09 and JK09-- showed bright green fluorescence (Figures 3A,D). After incubation in MRS_{4.3+H} for 24 h, fuzzy, weak red fluorescent clusters of cells could be observed for both strains,

and some cells even appeared unstained (Figures 3B,E). But most fluorescent cells of JK09 were labeled green (Figure 2B) while most cells of JK09-- were red (Figure 3E). After 48 h, the same pattern could be observed with the exception that most of the clusters were not stained with any fluorescent dye (Figures 3C,F).

Viability Assessment and Cell Size Comparison of *L. brevis* Cells by FM Analysis

In order to investigate the viability of *L. brevis* under hop compounds stress at a single cell level, stained cells were additionally analyzed with flow cytometer. Four different quadrants were recognized, which represents cells in different physiological states. Quadrant 1 (Q1) is the subpopulation of viable cells with intact membranes that only stained with SYTO 13, Q2 represents an intermediate subpopulation which corresponds to viable cells but with damaged membranes, Q3 describes the subpopulation of dead cells, which stained strongly with PI, Q4 consists of weakly stained cells after hop treatment (Figure 4A).

The proportion of viable cells for all the strains without hop compounds treatment were above 90% until 72 h followed by a small reduction after 96 h (results not shown). The hop compounds caused an obvious reduction in viable cells in the first 24 h in all strains, especially for the sensitive strains (Figures 4 and 5). The viable proportions of JK09, HF01, and A dropped to 48, 35, and 20%, respectively, after 24 h

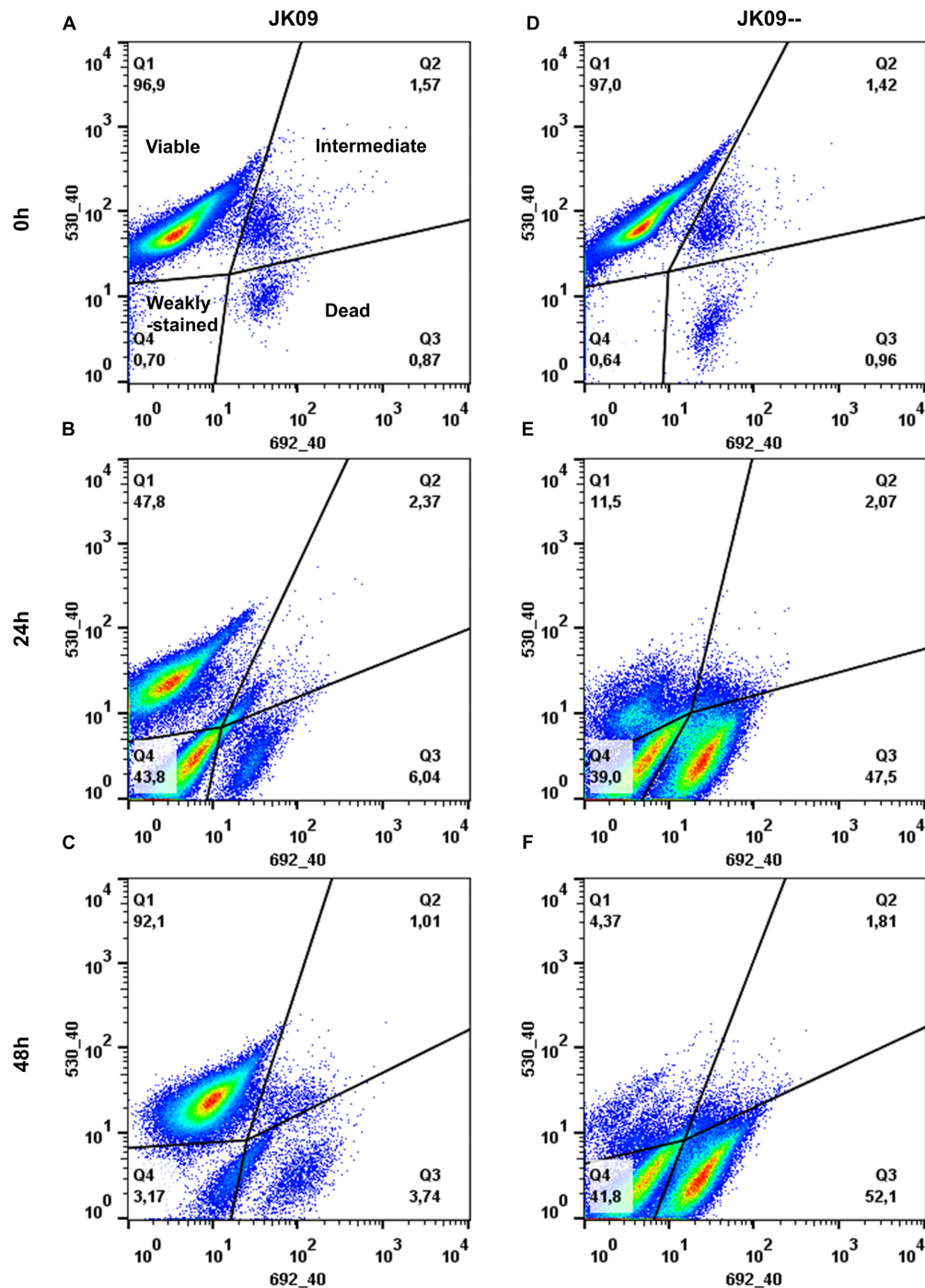
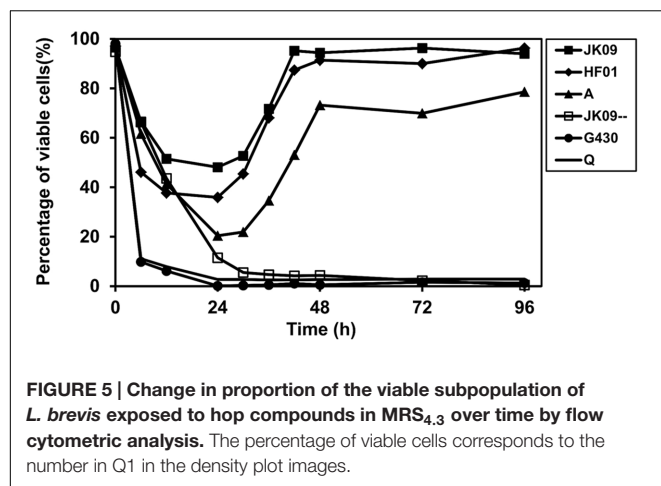


FIGURE 4 | Density plot images of JK09 (A–C) and JK09-- (D–F) exposed to hop compounds in MRS_{4.3} after 0, 24, and 48 h, analyzed by flow cytometry (FCM). The SYTO 13 signal was recorded in the green channel (530_40), the PI signal was recorded in the red channel (692_40). Events in different quadrants corresponds to different populations: viable cells (Q1), intermediate population with damaged membranes (Q2), dead cells (Q3) and weakly stained cells (Q4), the number in each quadrants represents the relative percentage of each population.

exposure (Figures 4B and 5; Supplementary Figure S1), most of the cells were situated in Q3 and/or Q4 instead (Figure 4B; Supplementary Figure S1). However, the proportion of viable cells of these three strains increased markedly during the next

24 h, where the viable proportion of JK09 and HF01 reached the same level as in the control experiments after 48 h (Figures 4C and 5; Supplementary Figure S1). On the contrary, the proportion of viable cells in the hop sensitive strains JK09--, G430 and Q



continued to decrease after 24 h, and there were almost no viable cells detected after 48 h (Figures 4E,F and 5; Supplementary Figure S1). The proportion of viable cells did not change from 48 to 96 h for any of the strains (Figure 5).

The histogram of the FSC from the FCM analysis reveals the distribution of cell sizes after 48 h (Figure 6). Some of the strains revealed a homogenous distribution of cell sizes in the control experiments, e.g., JK09 and Q (Figures 6A,F), where other strains exhibited a more heterogeneous distribution, e.g., HF01 and JK09-- (Figures 6B,D). The histogram of hop stressed cells shifted toward lower values for all the strains, which indicates that the average cell size was reduced, compared to the control cells, and this tendency was more pronounced for the three sensitive strains.

Dynamic Change in Intracellular pH of *L. brevis* Cells

Changes in the intracellular pH during 24 h of hop stress in acetate buffer (pH 4.3) were determined by fluorescence microscopy. For clarity, three subpopulations were created according to the pH points of the calibration curve. Cells with $4.3 \leq \text{pHi} < 4.7$ have a small or absent ΔpH , which correspond to the population of damaged or dead cells, cells with $4.7 \leq \text{pHi} < 5.0$ have a small but noticeable ΔpH , and represent the intermediate population, whereas cells with $\text{pHi} \geq 5.0$ have a large ΔpH and are regarded as viable cells.

After 1 h, the average pHi of all six strains in acetate buffer without hop compounds was 5.3 ± 0.1 , with all of the individual cells exhibiting a $\text{pHi} \geq 5.0$ (Figure 7A). The only exception was JK09--, which had a minor percentage (10%) in the intermediate population. There was a slight reduction in average pHi for all strains over time, but G430 showed the biggest pHi reduction. Under hop stress for 1 h, a sharp drop in pHi was observed for all six strains, where all cells reached the detection limit of pH 4.3 (Figure 7B). During the following 23 h, JK09, HF01, A as well as JK09-- had an obvious increase in pHi. For HF01, the average pHi value after 24 h reached 5.0, and with 55% of the individual cells exhibiting a $\text{pHi} \geq 5.0$. On the other hand, the average pHi value for Q and G430 was fluctuating around 4.3, with almost all cells in

the damaged/dead subpopulation ($4.3 \leq \text{pHi} < 4.7$) throughout the experiment.

Protective Effect of Mn^{2+} on *L. brevis* Cells

The impact of manganese on the viability of *L. brevis* was tested in acetate buffer with hop compounds using FCM (Figure 8A). After 3 h of exposure to hop compounds, the number of viable cells in acetate buffer without manganese was decreased. There is no clear trend that separated the hop tolerant strains from the hop sensitive strains. After supplementation with the level of Mn^{2+} found in pilsner lager beer ($2.9 \mu\text{M Mn}^{2+}$), there was a tiny increase in the viable and/or intermediate populations of all strains except JK09--. When Mn^{2+} addition was increased to the level found in MRS ($265.0 \mu\text{M}$), the percentage of viable cells increased significantly in all strains with the largest relative change in strain Q.

As shown in Figure 8B, the pHi of all six strains after 3 h exposure was around 4.3, the same value as after 1 h exposure (Figure 7B). $2.9 \mu\text{M Mn}^{2+}$ had limited effect on pHi for most of the strains except JK09, where 40% shifted to the intermediate population. At high level of Mn^{2+} ($265.0 \mu\text{M}$), a very significant increase in the average pHi was observed in all strains, with 100% individual cells exhibiting a $\text{pHi} \geq 4.7$, except in JK09--, where 55% individual cells had $\text{pHi} < 4.7$.

Effect of Ethanol on *L. brevis* Cells

Ethanol (4.6% v/v) inhibited the growth of both hop tolerant strain HF01 and hop sensitive strain Q, as demonstrated by the OD₆₀₀ values after 96 h incubation (Figure 9A). This reduction was less pronounced than the effect of hop addition, but the combined addition of hop and ethanol did not show any additional reduction in OD₆₀₀. In fact, the hop tolerant strain grew faster in the combined addition than hop alone, with the largest difference in OD₆₀₀ at 96 h (Figure 9A). This phenomenon was also observed in the other two hop tolerant strains (results not shown). The two strains, HF01 and Q, were subsequently analyzed by FCM, and the damaged subpopulations after 3 h showed that the combination of hop and ethanol at this stage was more lethal than hop alone (Figure 9B).

DISCUSSION

Initially, the growth potential of *L. brevis* strains exposed to various combinations of pH, and hop compounds was determined on the population level. Low pH in beer did not by itself inhibit the growth of most of the tested *L. brevis*. However, the low pH had a pronounced influence on the inhibitory effect of hop compounds, and this combination was further explored. The hop tolerant strains JK09, HF01 and A were able to grow slowly during exposure to hop compounds at pH 4.3 (Figures 2A–C), but from the growth curves, it is not possible to distinguish whether all cells in the population exhibit a similar response, or whether there are subpopulations that differ in their response to hop compounds.

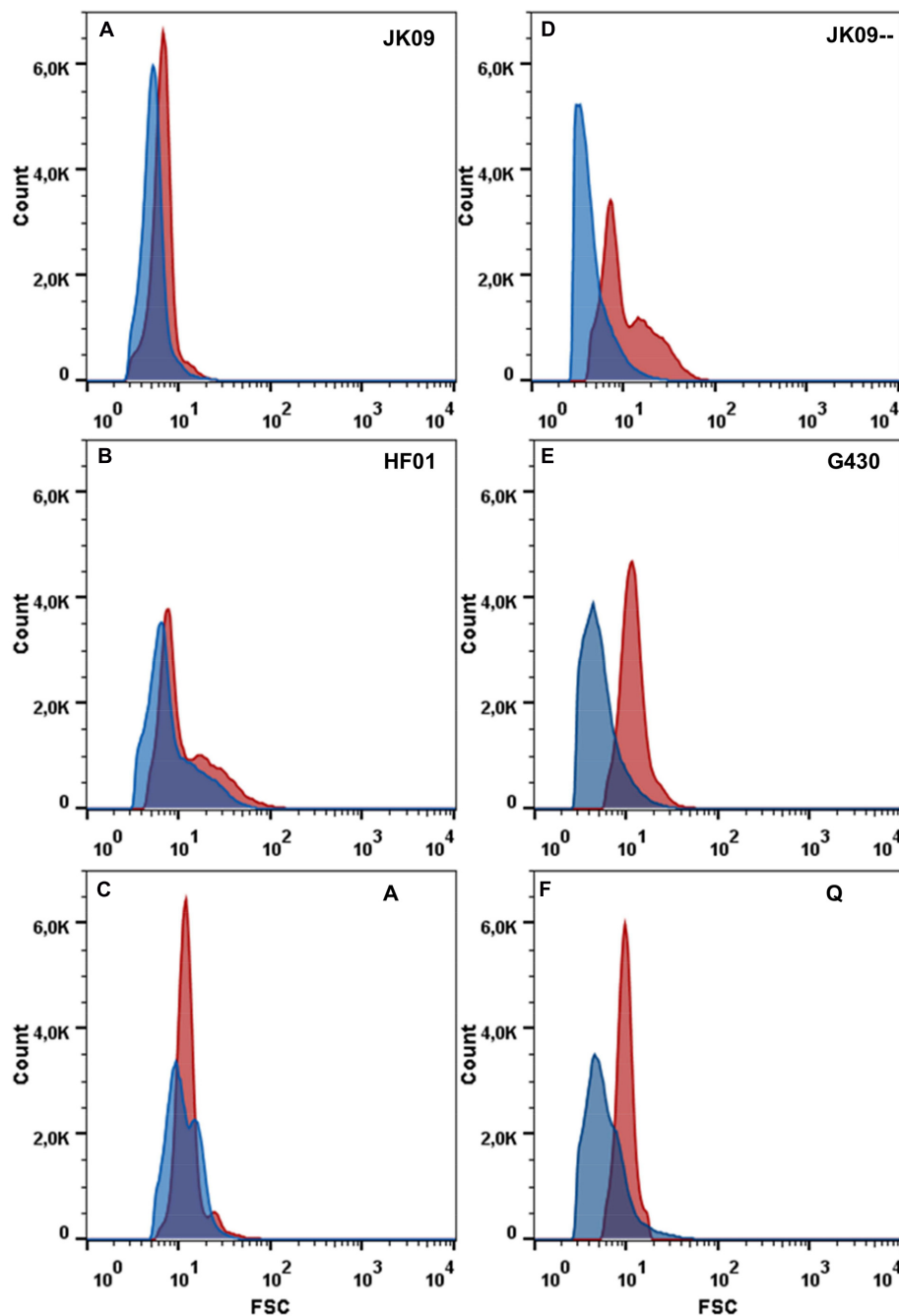


FIGURE 6 | Cell size distribution of *L. brevis* in MRS_{4.3} after 48 h incubation determined by the forward scatter channel (FSC) from FCM. (A–F) JK09, HF01, A, JK09--, G430 and Q. The red histogram corresponds to cells incubated without hop compounds, while the blue histogram corresponds to cells incubated with hop compounds.

To answer these questions, we investigated the dynamic physiological response of *L. brevis* cells to hop compounds at a single cell level using FM and FCM. A clear difference in the proportions of subpopulations between hop tolerant and sensitive strains was observed with both techniques. A small but significant subpopulation of the hop tolerant strains exhibited only green fluorescence, while almost 100% of fluorescent cells

of the sensitive strains were labeled red after 24 h (Figures 3–5; Supplementary Figure S1). This indicates that hop compounds causes membrane damage in most cells. Moreover, unstained cells or weakly stained cells could be found after 24 h as well (Figures 3 and 4). The reason is still unclear, but ‘ghost cells,’ which has intact cell structures but without nucleic acids, have been reported previously (Booyens and Thantsha, 2014; Léonard

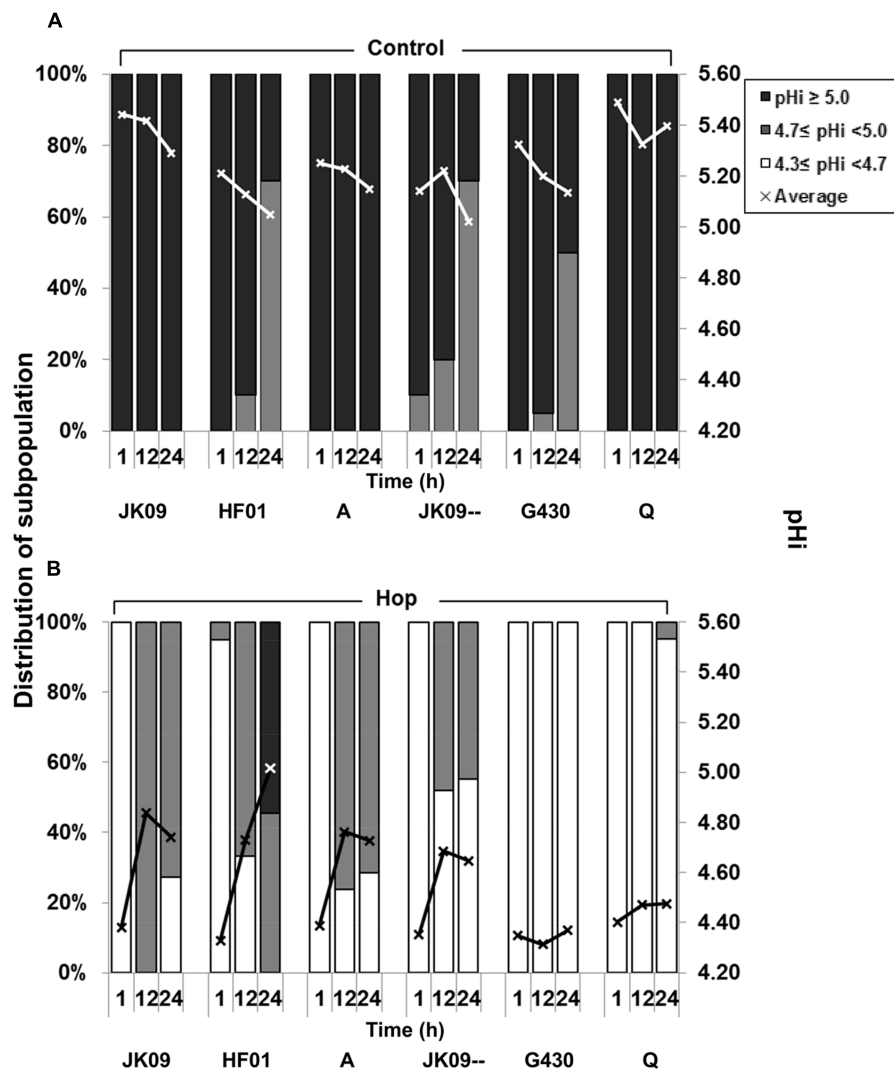


FIGURE 7 | Distribution of subpopulations of *L. brevis* according to the pH of individual cells. In sodium acetate buffer (A) and in sodium acetate buffer with hop compounds (B) after 1, 12, and 24 h, analyzed by FM. The average pH value is based on at least 20 individual cells, and the cells were attributed to different subpopulations according to the pH points of the calibration curve.

et al., 2016). It is conceivable that hop compounds caused such severe damage to the cells that DNA was lost, and consequently the cells were weakly stained.

The hop tolerant strains exhibited a pronounced heterogeneity at the single cell level, which must be a phenotypic variation, as the population is genetically homogeneous. In addition, the growth curves of the tolerant strains exhibited a longer lag phase when exposed to hop compounds (Figure 2), which may be partly explained by the reduction of viable cells, and partly by the lower growth rate that was observed. Within the three tolerant strains, the reduction in viable cells was most pronounced in strain A (Figure 5), which also had the longest lag phase (Figure 2C). This suggests that the reduction in viable cells had a large influence on the observed lag phase. Furthermore, the viable population of the hop tolerant

strains increased gradually during the next 24 h (Figure 5), which could be explained by the growth of the surviving cells.

Additional morphological information was obtained from the combined analysis. When grown in MRS_{4.3+H} for 48 h, the individual cells retained their rod shape (Figure 3), but there was a small reduction in the cell size of hop tolerant strains, compared to grow in MRS_{4.3} (Figure 6). This result is in agreement with previous results where *L. brevis* and *L. lindneri* cells appeared as smaller rods when grown in degassed beer compared to growth in MRS (Suzuki, 2011). The hop sensitive strains were much smaller after exposure to hop, probably because they have not divided (Figure 6).

Intracellular pH is another parameter to assess stress response (Yansanjav et al., 2004; Smigic et al., 2009; Schurr et al., 2015b).

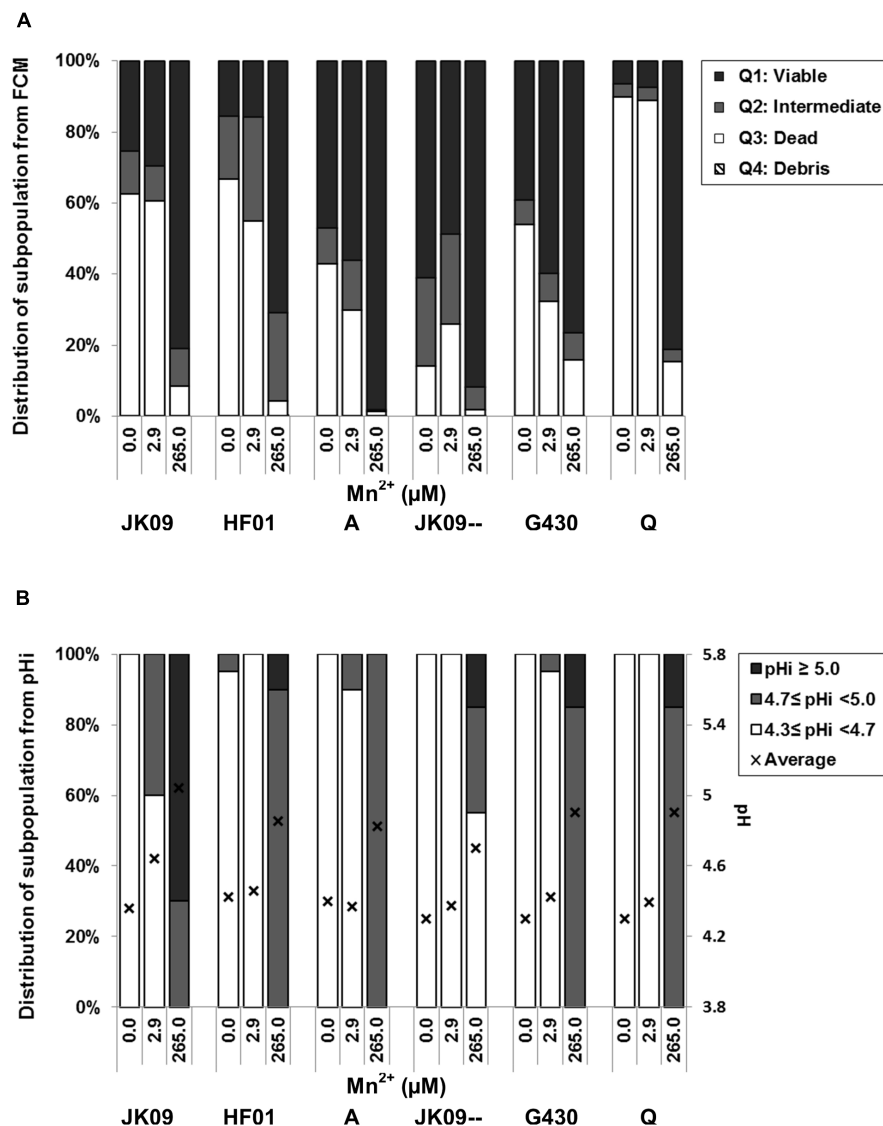


FIGURE 8 | Distribution of subpopulations of *L. brevis* according to the addition of manganese. Effects of different concentrations of Mn²⁺ on viability (A) and pHi (B) of *L. brevis* after exposure to hop compounds in acetate buffer for 3 h. The distribution in (A) corresponds to the number in each quadrant of the density plot images. The average of pHi values in (B) is based on at least 20 individual cells and the cells were attributed to different subpopulations according to the pH points of the calibration curve.

As cell division after staining with CDCFDA-SE will reduce the intensity of cell fluorescence, we decided to test the pHi in sodium acetate buffer, with the same pH, acetate and glucose as MRS_{4.3}, but without additional nutrients. This enabled an assessment of recovery with 24 h without cell division. Since most of the tested strains were only slightly affected by the exposure to pH 4.3 (Figure 2), the pHi values in pure acetate buffer provided information about the basic pH regulation in an acidic environment. The average pHi of all strains was around 5.3 at $T = 1$ h, with a small decline in the following hours (Figure 7A), but this was probably due to a slight acidification of the media (down to pH 4.1) caused by lactic acid production. This is comparable to previous reports that

lactic acid bacteria was able to maintain a constant Δ pH of approximately 1.0 (Hutkins and Nannen, 1993). Moreover, G430 had the biggest pHi decrease among the six strains (Figure 7A) which corresponds well with the observed acid sensitivity (Figure 2E).

Simpson (1993) observed that hop tolerant strains can maintain a higher intracellular pH than sensitive strains. On the other hand, Behr et al. (2006) found that the pHi of a hop-adapted strain also decreased strongly after exposure to hop compounds in acetate buffer for 40 min. In this study, the pHi of all tested strains dropped to pH 4.3 in 1 h (Figure 7B), indicating that the initial drop in pHi following exposure to hop compounds is unavoidable. It is a consequence of the

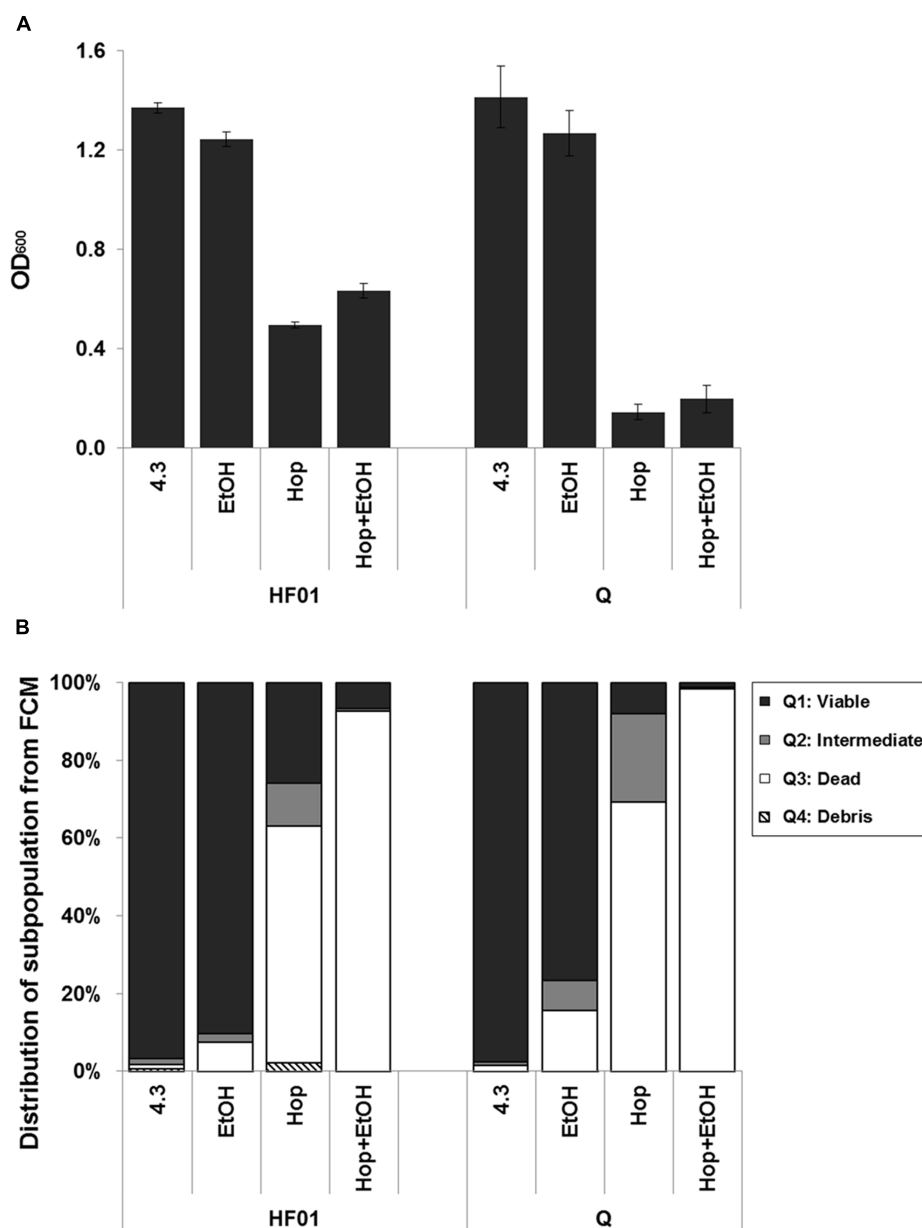


FIGURE 9 | Effect of ethanol in combination with hop compounds. The growth experiments of HF01 and Q were performed in MRS 4.3 with and without addition of hop compounds and ethanol, and the OD₆₀₀ values were measured after 96 h incubation (A). The subpopulations of HF01 and Q were analyzed after exposure to acetate buffer with and without addition of hop compounds and ethanol for 3 h (B).

protonophoric effects of the hop compounds, but may also be influenced by the reduction in cell size (Figure 6), which can increase the intracellular concentration of protons (Vindeløv and Arneborg, 2002). However, we found that the pH_i of some individual cells of the hop tolerant strains increased after 12 h (Figure 7B). This was also observed in the plasmid cured strain JK09⁻, but not in the two other sensitive strains. This may be due to the overexpression of membrane-bound ATPase, which pumps protons from the cytoplasm (Sakamoto et al., 2002). Although JK09⁻ was sensitive to hop compounds

in the growth experiments (Figure 2D), this strain exhibited a similar recovery in the pH_i experiment as the wild type JK09 (Figure 7B). This suggests that part of this recovery mechanism can be chromosomal and therefore present in both JK09 and JK09⁻. This underlines that the mechanism behind hop tolerance is multifactorial, and in this case, partly related to the plasmid borne resistance genes, but also to a certain degree to chromosomal genes. The heterogeneity in the pH_i regulation further emphasizes that only a proportion of the cells can withstand the stress from hop compounds.

Previous studies have shown that the MIC of hop compounds increased with an increased addition of Mn^{2+} (Simpson, 1993), and the growth of *L. brevis* could be accelerated by high concentrations of Mn^{2+} (Behr, 2008). We therefore investigated the effect of Mn^{2+} on the viability and intracellular pH by FCM and FM. The viable proportion was slightly increased for most strains by low amounts of Mn^{2+} , while it was greatly enhanced for all strains by higher amounts of Mn^{2+} (Figure 8A). It has been reported that lipoteichoic acids from the cell wall provides a reservoir of divalent cation such as Mn^{2+} . This is very close to the plasma membrane, and therefore the divalent cation probably interact with the negatively charged head groups of phospholipids and decrease the membrane fluidity (Asai et al., 2000; Behr, 2008). It is conceivable that this can reduce the intrusion of hop compounds into cells, and thereby reduce the toxicity of hop compounds. It also has been demonstrated that hop compounds form Mn^{2+} -hop compounds complexes inside the cell (Simpson and Hughes, 1993; Behr and Vogel, 2010), so another possibility is that they form complexes outside the cells if there is sufficient Mn^{2+} , and these complexes cannot efficiently penetrate the cytoplasmic membrane. Furthermore, the high concentration of Mn^{2+} is equivalent to MRS, and it is surprising that the physiological response from the FCM experiments with high Mn^{2+} suggest a protective effect against hop after 3 h (Figure 8A), but this protection does not correlate with the observed growth, where only the hop tolerant strains grew (Figure 2). This indicates a difference between short term and long term effects. In addition, without Mn^{2+} addition, some of the sensitive strains exhibited higher survival than some of the hop tolerant strains after 3 h exposure (Figure 8A). This mechanism requires further investigation, but we hypothesize that it may be related to manganese transporters.

The pH_i reduction was less pronounced when hop compounds was added together with high amount of Mn^{2+} (Figure 7B), which indicates that the protonophoric effect of hop compounds is much decreased, at least in the short term. These results are similar to the FCM experiments (Figure 8A), and suggest that extracellular Mn^{2+} provides some degree of short term protection against hop, but the results from growth experiments (Figure 2) and pH_i measurement (Figure 7) demonstrate that manganese protection is only part of the explanation behind hop tolerance, which must include several other factors as suggested previously (Behr et al., 2006; Bergsveinson et al., 2015).

The combination of hop and ethanol resulted in a larger damaged subpopulation after 3 h than each treatment alone (Figure 9B). This suggests that ethanol increases the membrane permeability (Barker and Park, 2001), facilitating the immediate intrusion of hop compounds and injury. In contrast, when following the optical density of the investigated strains over time, the hop tolerant strains grew faster and to slightly higher levels when ethanol and hop was present compared to hop alone (Figure 9A). This may seem surprising, but supports a previous observation made on solid hop-gradient agar plates, where a higher tolerance toward hop in the presence of ethanol was observed in a number of beer spoilage strains (Haakensen et al., 2009). Changes in membrane fluidity may be involved, as it has been demonstrated that the membrane fluidity decreases when

L. brevis cells are grown at low pH and even more upon the addition of hop compounds (Behr et al., 2006). Furthermore, Da Silveira et al. (2003) observed that even though the membranes of *Oenococcus oeni* become more fluid and leaky with increasing concentrations of ethanol, intact cells are able to adapt and reduce their membrane fluidity. We therefore assume that, although the combination of ethanol and hop is more lethal, the few individual cells that survive and grow will adapt to the ethanol in the medium, and the consequent reduction in membrane fluidity has the side effect of protecting cells against hop compounds. This phenomenon highlights that in order to predict beer spoilage potential, it is not sufficient to look only at the immediate physiological response, but also the cell division of the small subpopulation of robust cells.

CONCLUSION

The results from FM combined with FCM provide important information about the variation in the response of different *L. brevis* strains. Our results show that hop compounds caused membrane damage, intracellular pH decrease, and cell size reduction in *L. brevis* cells. Upon hop exposure at low pH, only a small subpopulation within the hop tolerant strains maintained membrane integrity. It is only these cells that eventually upregulate the pH_i and contribute to the subsequent growth. Furthermore, a high amount of Mn^{2+} provides a short term protection as it increased the viability and the pH_i of *L. brevis* cells exposed to hop compounds. In the tested strains, a combination of ethanol and hop compounds caused increased immediate damage to the overall population, while the surviving subpopulation exhibited slightly better growth indicating a level of cross-protection. Overall, the combination of FM and FCM enables us to obtain a better understanding of the physiological response of *L. brevis* cells exposed to a beer-like environment. Additionally, FCM has the potential to become a rapid quality control method in breweries, even though this requires further optimization of the equipment.

AUTHOR CONTRIBUTIONS

YZ, HS, and SK conceived and designed the study. YZ ran the experiments and the data analysis. All authors contributed to the writing of the manuscript.

ACKNOWLEDGMENTS

The authors are grateful to China Scholarship Council for financial support of Yu Zhao. We would like to thank Sine N. Haxgart for obtaining the plasmid cured strain.

SUPPLEMENTARY MATERIAL

The Supplementary Material for this article can be found online at: <http://journal.frontiersin.org/article/10.3389/fmicb.2017.00239/full#supplementary-material>

REFERENCES

- Ambriz-Avina, V., Contreras-Garduno, J. A., and Pedraza-Reyes, M. (2014). Applications of flow cytometry to characterize bacterial physiological responses. *Biomed. Res. Int.* 2014:461941. doi: 10.1155/2014/461941
- Asai, Y., Sano, Y., Kikuchi, K., Iwamoto, K., and Watanabe, S. (2000). The effect of divalent cations on the membrane properties and pharmacokinetics in rat of the lipid A analogue E5531. *J. Pharm. Pharmacol.* 52, 39–45. doi: 10.1211/0022357001773661
- Balaban, N. Q., Merrin, J., Chait, R., Kowalik, L., and Leibler, S. (2004). Bacterial persistence as a phenotypic switch. *Science* 305, 1622–1625. doi: 10.1126/science.1099390
- Barbesti, S., Citterio, S., Labra, M., Baroni, M. D., Neri, M. G., and Sgorbati, S. (2000). Two and three-color fluorescence flow cytometric analysis of immunoidentified viable bacteria. *Cytometry* 40, 214–218. doi: 10.1002/1097-0320(20000701)40:3<214::AID-CYTO6>3.0.CO;2-M
- Barker, C., and Park, S. F. (2001). Sensitization of *Listeria monocytogenes* low pH, organic acids, and osmotic stress by ethanol. *Appl. Environ. Microbiol.* 67, 1594–1600. doi: 10.1128/aem.67.4.1594-1600.2001
- Behr, J. (2008). *Mechanisms of Hop Inhibition, Tolerance and Adaptation in Lactobacillus brevis*. Ph.D. thesis, Technical University of Munich, Munich.
- Behr, J., Ganzle, M. G., and Vogel, R. F. (2006). Characterization of a highly hop-resistant *Lactobacillus brevis* strain lacking hop transport. *Appl. Environ. Microbiol.* 72, 6483–6492. doi: 10.1128/aem.00668-666
- Behr, J., Israel, L., Gänzle, M. G., and Vogel, R. F. (2007). Proteomic approach for characterization of hop-inducible proteins in *Lactobacillus brevis*. *Appl. Environ. Microbiol.* 73, 3300–3306. doi: 10.1128/AEM.00124-07
- Behr, J., and Vogel, R. F. (2009). Mechanisms of hop inhibition: hop ionophores. *J. Agric. Food Chem.* 57, 6074–6081. doi: 10.1021/jf900847y
- Behr, J., and Vogel, R. F. (2010). Mechanisms of hop inhibition include the transmembrane redox reaction. *Appl. Environ. Microbiol.* 76, 142–149. doi: 10.1128/aem.01693-1699
- Bergsveinson, J., Baecker, N., Pittet, V., and Ziola, B. (2015). Role of plasmids in *Lactobacillus brevis* BSO 464 hop tolerance and beer spoilage. *Appl. Environ. Microbiol.* 81, 1234–1241. doi: 10.1128/aem.02870-2814
- Booyens, J., and Thantsha, M. S. (2014). Fourier transform infra-red spectroscopy and flow cytometric assessment of the antibacterial mechanism of action of aqueous extract of garlic (*Allium sativum*) against selected probiotic *Bifidobacterium* strains. *BMC Complement. Altern. Med.* 14:289. doi: 10.1186/1472-6882-14-289
- Da Silva, M. G., Golovina, E. A., Hoekstra, F. A., Rombouts, F. M., and Abee, T. (2003). Membrane fluidity adjustments in ethanol-stressed *Oenococcus oeni* cells. *Appl. Environ. Microbiol.* 69, 5826–5832. doi: 10.1128/AEM.69.10.5826-5832.2003
- Davey, H. M., and Kell, D. B. (1996). Flow cytometry and cell sorting of heterogeneous microbial populations: the importance of single-cell analyses. *Microbiol. Rev.* 60, 641–696.
- Fernandez, J. L., and Simpson, W. J. (1995). Measurement and prediction of the susceptibility of lager beer to spoilage by lactic acid bacteria. *J. Appl. Bacteriol.* 78, 419–425. doi: 10.1111/j.1365-2672.1995.tb03428.x
- Garcia-Betancur, J. C., Yepes, A., Schneider, J., and Lopez, D. (2012). Single-cell analysis of *Bacillus subtilis* biofilms using fluorescence microscopy and flow cytometry. *J. Vis. Exp.* 60, 3796. doi: 10.3791/3796
- Guldfeldt, L. U., and Arneborg, N. (1998). Measurement of the effects of acetic acid and extracellular pH on intracellular pH of nonfermenting, individual *Saccharomyces cerevisiae* cells by fluorescence microscopy. *Appl. Environ. Microbiol.* 64, 530–534.
- Haakensen, M., Schubert, A., and Ziola, B. (2009). Broth and agar hop-gradient plates used to evaluate the beer-spoilage potential of *Lactobacillus* and *Pediococcus* isolates. *Int. J. Food Microbiol.* 130, 56–60. doi: 10.1016/j.ijfoodmicro.2009.01.001
- Hutkins, R. W., and Nannen, N. L. (1993). pH homeostasis in lactic acid bacteria. *J. Dairy Sci.* 76, 2354–2365. doi: 10.3168/jds.S0022-0302(93)77573-77576
- Léonard, L., Bouarab Chibane, L., Ouled Bouhedda, B., Degraeve, P., and Oulahal, N. (2016). Recent advances on multi-parameter flow cytometry to characterize antimicrobial treatments. *Front. Microbiol.* 7:1225. doi: 10.3389/fmicb.2016.01225
- Lidstrom, M. E., and Konopka, M. C. (2010). The role of physiological heterogeneity in microbial population behavior. *Nat. Chem. Biol.* 6, 705–712. doi: 10.1038/nchembio.436
- Ryssel, M., Duan, Z., and Siegmundt, H. (2013). In situ examination of cell growth and death of *Lactococcus lactis*. *FEMS Microbiol. Lett.* 343, 82–88. doi: 10.1111/1574-6968.12134
- Sakamoto, K., and Konings, W. N. (2003). Beer spoilage bacteria and hop resistance. *Int. J. Food Microbiol.* 89, 105–124. doi: 10.1016/S0168-1605(03)00153-153
- Sakamoto, K., Van Veen, H. W., Saito, H., Kobayashi, H., and Konings, W. N. (2002). Membrane-bound ATPase contributes to hop resistance of *Lactobacillus brevis*. *Appl. Environ. Microbiol.* 68, 5374–5378. doi: 10.1128/AEM.68.11.5374-5378.2002
- Schurr, B. C., Behr, J., and Vogel, R. F. (2015a). Detection of acid and hop shock induced responses in beer spoiling *Lactobacillus brevis* by MALDI-TOF MS. *Food Microbiol.* 46, 501–506. doi: 10.1016/j.fm.2014.09.018
- Schurr, B. C., Hahne, H., Kuster, B., Behr, J., and Vogel, R. F. (2015b). Molecular mechanisms behind the antimicrobial activity of hop iso-alpha-acids in *Lactobacillus brevis*. *Food Microbiol.* 46, 553–563. doi: 10.1016/j.fm.2014.09.017
- Shabala, L., McMeekin, T., Budde, B. B., and Siegmundt, H. (2006). *Listeria innocua* and *Lactobacillus delbrueckii* subsp. *bulgaricus* employ different strategies to cope with acid stress. *Int. J. Food Microbiol.* 110, 1–7. doi: 10.1016/j.ijfoodmicro.2006.01.026
- Simpson, W. J. (1993). Cambridge prize lecture – studies on the sensitivity of lactic acid bacteria to hop bitter acids. *J. Inst. Brew.* 99, 405–411. doi: 10.1002/j.2050-0416.1993.tb01180.x
- Simpson, W. J., and Hughes, P. S. (1993). Cooperative binding of potassium ions to trans-isohumulone in the presence of divalent and trivalent cations. *Bioorg. Med. Chem. Lett.* 3, 769–772. doi: 10.1016/S0960-894X(01)81272-81275
- Smigic, N., Rajkovic, A., Nielsen, D. S., Siegmundt, H., Uyttendaele, M., Devlieghere, F., et al. (2009). Intracellular pH as an indicator of viability and resuscitation of *Campylobacter jejuni* after decontamination with lactic acid. *Int. J. Food Microbiol.* 135, 136–143. doi: 10.1016/j.ijfoodmicro.2009.07.023
- Stiefel, P., Schmidt-Emrich, S., Maniura-Weber, K., and Ren, Q. (2015). Critical aspects of using bacterial cell viability assays with the fluorophores SYTO9 and propidium iodide. *BMC Microbiol.* 15, 1–9. doi: 10.1186/s12866-015-0376-x
- Strovas, T. J., Sauter, L. M., Guo, X., and Lidstrom, M. E. (2007). Cell-to-cell heterogeneity in growth rate and gene expression in *Methylobacterium extorquens* AM1. *J. Bacteriol.* 189, 7127–7133. doi: 10.1128/jb.00746-747
- Suzuki, K. (2011). 125th anniversary review: microbiological instability of beer caused by spoilage bacteria. *J. Inst. Brew.* 117, 131–155. doi: 10.1002/j.2050-0416.2011.tb00454.x
- Suzuki, K., Asano, S., Iijima, K., Kuriyama, H., and Kitagawa, Y. (2008). Development of detection medium for hard-to-culture beer-spoilage lactic acid bacteria. *J. Appl. Microbiol.* 104, 1458–1470. doi: 10.1111/j.1365-2672.2007.03669.x
- Vindeløv, J., and Arneborg, N. (2002). *Saccharomyces cerevisiae* and *Zygosaccharomyces mellis* exhibit different hyperosmotic shock responses. *Yeast* 19, 429–439. doi: 10.1002/yea.844
- Yansanjav, A., Siegmundt, H., Jespersen, L., Vancanneyt, M., Swings, J., Hollerova, I., et al. (2004). Detection of resistance of lactic acid bacteria to a mixture of the hop analogue compounds tetrahydroiso-alpha-acids by noninvasive measurement of intracellular pH. *J. Appl. Microbiol.* 96, 1324–1332. doi: 10.1111/j.1365-2672.2004.02261.x
- Zhao, Y., Knöchel, S., and Siegmundt, H. (2014). In situ examination of *Lactobacillus brevis* after exposure to an oxidizing disinfectant. *Front. Microbiol.* 5:623. doi: 10.3389/fmicb.2014.00623

Conflict of Interest Statement: The authors declare that the research was conducted in the absence of any commercial or financial relationships that could be construed as a potential conflict of interest.

Copyright © 2017 Zhao, Knöchel and Siegmundt. This is an open-access article distributed under the terms of the Creative Commons Attribution License (CC BY). The use, distribution or reproduction in other forums is permitted, provided the original author(s) or licensor are credited and that the original publication in this journal is cited, in accordance with accepted academic practice. No use, distribution or reproduction is permitted which does not comply with these terms.



Repetitive Short-Term Stimuli Imposed in Poor Mixing Zones Induce Long-Term Adaptation of *E. coli* Cultures in Large-Scale Bioreactors: Experimental Evidence and Mathematical Model

Alexander Nieß, Michael Löffler, Joana D. Simen and Ralf Takors *

Institute of Biochemical Engineering, University of Stuttgart, Stuttgart, Germany

OPEN ACCESS

Edited by:

Jan-Ulrich Kreft,
University of Birmingham,
United Kingdom

Reviewed by:

Peter Neubauer,
Technische Universität Berlin,
Germany

Frank Delvigne,
University of Liège, Belgium

*Correspondence:

Ralf Takors
takors@ibvt.uni-stuttgart.de

Specialty section:

This article was submitted to
Systems Microbiology,
a section of the journal
Frontiers in Microbiology

Received: 29 April 2017

Accepted: 12 June 2017

Published: 28 June 2017

Citation:

Nieß A, Löffler M, Simen JD and
Takors R (2017) Repetitive Short-Term
Stimuli Imposed in Poor Mixing Zones
Induce Long-Term Adaptation of
E. coli Cultures in Large-Scale
Bioreactors: Experimental Evidence
and Mathematical Model.
Front. Microbiol. 8:1195.
doi: 10.3389/fmicb.2017.01195

Rapidly changing concentrations of substrates frequently occur during large-scale microbial cultivations. These changing conditions, caused by large mixing times, result in a heterogeneous population distribution. Here, we present a powerful and efficient modeling approach to predict the influence of varying substrate levels on the transcriptional and translational response of the cell. This approach consists of two parts, a single-cell model to describe transcription and translation for an exemplary operon (*trp* operon) and a second part to characterize cell distribution during the experimental setup. Combination of both models enables prediction of transcriptional patterns for the whole population. In summary, the resulting model is not only able to anticipate the experimentally observed short-term and long-term transcriptional response, it further allows envision of altered protein levels. Our model shows that locally induced stress responses propagate throughout the bioreactor, resulting in temporal, and spatial population heterogeneity. Stress induced transcriptional response leads to a new population steady-state shortly after imposing fluctuating substrate conditions. In contrast, the protein levels take more than 10 h to achieve steady-state conditions.

Keywords: scale-down, hybrid modeling, population heterogeneity, adaptation times, *Escherichia coli*

INTRODUCTION

Large-scale industrial bioprocesses make use of reactors ranging from 100 to 800 m³ reaction volume. For aerobic processes, stirred tank reactors are still preferred, albeit alternative setups such as airlift reactors may be attractive if reactor sizes exceed the volume of about 500 m³. All reactors have in common that gradients of substrates, dissolved gases and pH occur, which are the consequence of poor mixing conditions (Nienow et al., 1997). Cells are circulating in these reactors, thereby frequently passing through zones of different substrate availability. Accordingly, cellular interactions are repeatedly triggered (Oldiges and Takors, 2005; Lara et al., 2006; Neubauer and Junne, 2010; Takors, 2012). Noteworthy, related regulatory responses are not limited to changes of metabolism but also comprise transcriptional and translational programs (Löffler et al., 2016, 2017; Simen et al., 2017).

Often, microbial processes are controlled by limited substrate feeding to avoid non-wanted overflow metabolism and to prevent too high metabolic activity that may exceed the technical capacities of aeration and cooling. Industrial examples are the implementation of glucose or ammonia limitations (Neubauer et al., 1995). Recently, Chubukov et al. (2014) outlined that proper nitrogen (or phosphate) limitation may even increase biomass specific substrate uptake during production phases when cell growth is strongly limited. Michalowski et al. (2017) further succeeded to engineer the *E. coli* HGT host for likewise conditions.

Löffler et al. (2016) and Simen et al. (2017) studied the scenario of frequently occurring glucose or ammonia limitations by using a conventional STR-PFR (stirred tank reactor—plug flow reactor) setup as described by George et al. (1993). Unlike previous investigations, these studies installed steady-state growth conditions before large-scale gradients were repeatedly imposed on the cells by connecting the PFR to the STR. As such, a distinct reference steady-state was created that enabled quantitative and highly accurate analysis of the metabolic and transcriptional responses of the cells on the installed glucose or ammonia gradients.

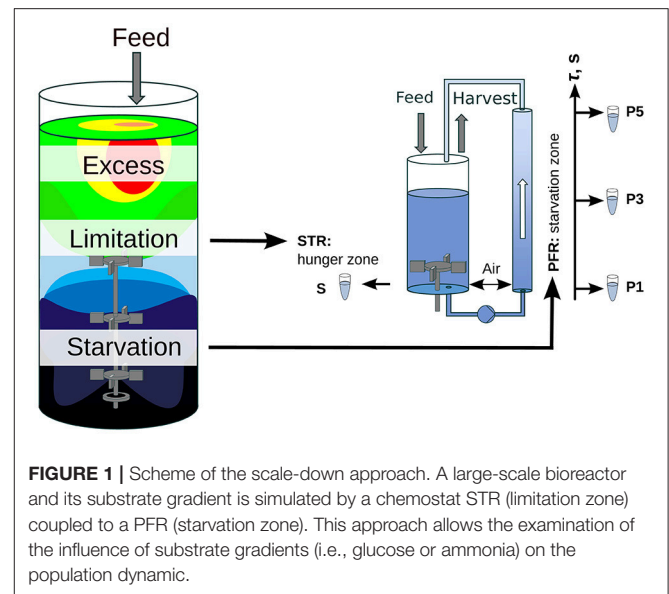
These data sets are the experimental basis for the modeling approaches presented in this study. By exploiting the metabolic and transcriptional time series it will be investigated whether and how similar dynamics can be modeled to predict short- and long-term regulatory responses of *E. coli*. Related data-driven models can serve as the core for ensemble modeling (Henson, 2003) to predict large scale cellular performance *in silico* and *ab initio*.

For the sake of simplicity, transcriptional dynamics of the tryptophan operon were chosen as an illustrative example. It has been shown by Simen et al. (2017) that the repetitive exposure to nitrogen starvation induced the frequent transcription of the *trp* operon. Considering the well-known attenuation control (Yanofsky, 2004, 2007), the expression of downstream genes *trpEDCBA*, consequently, indicates not only the ongoing transcriptional response on environmental triggers but also the start of protein translation. Accordingly, modeling *trp* expression dynamics needs to fulfill several challenges: (i) Short-term transcript dynamics observed in the PFR must be predicted, (ii) long-term transcript responses of the whole population should be mirrored, and (iii) the different time-scales of transcriptional and translational dynamics have to be reflected, too. This study will outline that every constraint is properly met by a simple mechanistic model.

MATERIALS AND METHODS

Experimental Setup

Oscillating substrate availability was simulated in a stirred-tank-reactor (STR) plug-flow-reactor (PFR) scale-down approach. **Figure 1** shows the schematic setup of the system. As Simen et al. (2017), the STR system was operated as nitrogen limited chemostat cultivation with a dilution rate of 0.2 h^{-1} (5 mL min^{-1}). The well-mixed bioreactor was simulated by using the steady-state condition in STR without the PFR (SS_0). After characterization of SS_0 the PFR was connected and a fraction



of cells cycled through the PFR loop. No additional feed was added into the PFR. Therefore, the cells shift from nitrogen limitation to starvation along the PFR. The experimental design allows the observation of the transcriptional responses along the PFR (short-term) and over the process time in the STR (long-term). The system characteristics and cultivation conditions were published in Löffler et al. (2016). Residence times τ of STR and PFR were estimated to be 6.2 min and 125 s, respectively. Samples for transcriptome analysis were taken at sampling ports P1, P3, and P5 in the PFR with corresponding residence times of 31, 70, and 110 s. Volumes in STR and PFR were 1.12 and 0.38 L, respectively. Biosuspension was continuously pumped through the PFR (180 mL min^{-1}).

Compared to SS_0 with a growth rate of 0.2 h^{-1} in the STR, the STR-PFR setup splits growth rates individually in the two compartments. Whereas, the total growth rate of the STR-PFR system is still 0.2 h^{-1} , no growth can be expected inside PFR when the nutrient is completely consumed. Accordingly, PFR can be subdivided into a first part considering still growing cells and a subsequent part characterized by no growth. Because the total system runs with the dilution rate of 0.2 h^{-1} , STR growth rates must be increased accordingly to compensate missing cell growth in the PFR. Calculation of growth rates in the STR can be performed based on the residence time distributed average growth rate that is set equal to the dilution rate. For the sake of simplicity and because nutrient starvation occurred very rapid in PFR, no growth was assumed to be existent in the total PFR compartment. Therefore, the average growth rate can be split into two different growth rates for each compartment (Equation 1).

$$\frac{\mu_{STR} \tau_{STR} + \mu_{PFR} \tau_{PFR}}{\tau_{STR} + \tau_{PFR}} = D \quad (1)$$

Samples for transcriptome analysis were taken at 25 and 120 min as well as at 28 h after installing the substrate gradient.

Transcript measurements are published in Simen et al. (2017) and are available under GEO Accession GSE90743.

Single-Cell Model

For the agent based transcription-translation model, DNA and mRNA templates are discretized in nucleotides, defining a 1D lattice. Movement of RNA polymerases (RNAPs) is treated according to Equation (2). Here, x describes the relative position of nucleotides inside the operon starting with the first mRNA encoding nucleotide of the operon sequence. RNAP movement is based on the elongation rate v_{elo}^{RNAP} and the distance Δx between two subsequent polymerases. The following criteria were considered for RNAP motion:

- The first elongation step is treated as the initiation step and can only occur if t is in the interval of possible induction (t_{ind}).
- The minimum distance Δx between two subsequent RNAPs is fulfilled.

$$\frac{dx_i}{dt} = \begin{cases} 0 & \text{if } x_i = 0 \wedge t \notin t_{ind} \\ 0 & \text{if } x_{i-1} - x_i < \Delta x \wedge i > 1 \\ v_{elo}^{RNAP} & \text{otherwise} \end{cases} \quad (2)$$

For each passed nucleotide on the DNA sequence, the respective nucleotide in the mRNA sequence is transcribed. The resulting mRNA strand i with length L_i^{mRNA} can be directly derived from x_i .

$$L_i^{mRNA}(t) = x_i(t) \quad (3)$$

For simplification, we neglected the modeling of the attenuation process considering terminator/antiterminator interactions and assumed ongoing translation only during nitrogen starvation instead. Position $y_{i,j}$ of a ribosome j on mRNA strand i is a function of L_i^{mRNA} and the position of the previous ribosome y_{j-1} . The number of ribosomes that translate a gene g ($N_g^{TL,max}$) can vary and depends on the gene itself. Ribosomal motion on a gene g starts at C_g^{start} (first coding nucleotide) and stops at C_g^{end} (third nucleotide of the terminating codon). The necessary criteria for translation are stated as follows:

- At least Δy nucleotides downstream are already synthesized.
- The previous ribosome is more than Δy nucleotides further downstream.
- The maximum number of translations for the given gene is not exceeded.

$$\frac{dy_{i,j}}{dt} = \begin{cases} 0 & \text{if } L_i - y_{i,j} \leq \Delta y \\ 0 & \text{if } y_{i,j-1} - y_{i,j} < \Delta y \wedge j > 1 \\ 0 & N_{i,g}^{TL}(t) \geq N_g^{TL,max} \\ v_{elo}^{Ribosome} & \text{otherwise} \end{cases} \quad (4)$$

The number of ribosomes acting on a single mRNA i is calculated following the Iverson brackets (Equation 5). These brackets return 1 if the term inside is true and 0 if the term is false.

$$N_{i,g}^{TL}(t) = \sum_j [y_{i,j}(t) \geq C_g^{start}] \quad (5)$$

The amount of synthesized proteins per cell from the single-cell model ($N_{g,SC}^{Protein}$) encoded by gene g can be calculated as the sum of all ribosomes acting on all mRNA strands that have passed the final nucleotide C_g^{end} .

$$N_{g,SC}^{Protein}(t) = \sum_i \sum_j [y_{i,j} > C_g^{end}] \quad (6)$$

Each mRNA strand is expected to be degraded by RNases. Initiation of mRNA breakdown begins at the start codon of transcription. Movement along mRNA is encoded by position z_i on strand i and depends on the degradation elongation rate v_{elo}^{RNase} . The following constraints define the motion of RNases:

- The number of active ribosomes per gene g $N_g^{TL,max}$ is estimated as the turnover ratio of mRNAs and proteins (see below)
- Δz encodes the closest nucleotide distance to the next ribosome downstream of z_i

$$\frac{dz_i}{dt} = \begin{cases} 0 & \text{if } N_{i,g}^{TL}(t) < N_g^{TL,max} \\ 0 & \text{if } y_{i,N_g^{TL,max}} - z_i \leq \Delta z \\ v_{elo}^{RNase} & \text{otherwise} \end{cases} \quad (7)$$

Accordingly, the current amount of mRNA per gene is calculated as the difference of already synthesized mRNAs and the amount of degraded mRNAs. The first is modeled from the number of complete mRNA strands synthesized. The second mirrors the amount of RNases that have passed the first codon.

$$N_{g,SC}^{mRNA}(t) = \sum_i [L_i^{mRNA}(t) > C_g^{end}] - \sum_i [z_i \geq C_g^{start}] \quad (8)$$

$N_g^{TL,max}$ is calculated as the turnover ratio of mRNAs per protein for a given gene g . Protein turnover $r_{turnover}^{Protein}$ was calculated based on protein levels at a growth rate of 0.2 h^{-1} ($k_{deg}^{Protein} = \mu$) (Valgepea et al., 2013). Active protein degradation was neglected and only growth based dilution was considered. mRNA turnover $r_{turnover}^{mRNA}$ was calculated based on the levels measured by Valgepea et al. (2013) with average half-lives of 2 min ($k_{deg}^{mRNA} = 20.79 \text{ h}^{-1}$) (Chen et al., 2015). However, no mRNA measurements of *trpA* were given in this data set. We thus assumed the translations per mRNA for *trpA* to be the same as for *trpB*, due to the fact that the resulting protein complex is a tetramer consisting of two *trpA* and two *trpB* (Hyde et al., 1988). *TrpL*, the leader peptide, was neglected in this calculation. **Table 1** shows the resulting translations per mRNA.

$$N_g^{TL,max} = \frac{r_{turnover}^{Protein}}{r_{turnover}^{mRNA}} = \frac{c_g^{Protein} k_{deg}^{Protein}}{c_g^{mRNA} k_{deg}^{mRNA}} \quad (9)$$

We used the *trp* operon as an example for several reasons: (i) The *trp* operon leads to a polycistronic mRNA (Yanofsky

TABLE 1 | Calculated translations per mRNA for the *trp* operon.

Gene	<i>trpE</i>	<i>trpD</i>	<i>trpC</i>	<i>trpB</i>	<i>trpA</i>
Translations per mRNA	4	4	5	10	10

The value for *trpA* was extrapolated from *trpB*.

et al., 1981), (ii) the attenuation sequence in the *trpL* leader peptide allows the coupled investigation of transcription and translation (see **Figure 2**), and (iii) the published data by Simen et al. shows that the *trp* operon is upregulated during STR-PFR cultivations. Accordingly, translation must have happened if transcripts of genes downstream of *trpL* are measured, as it is the case in the data sets used for this study. Simplification was made by treating the structural genes *trpGD* and *trpCF* and their corresponding proteins as single genes (*trpG* and *trpC*, respectively) and proteins.

All three actively moving species (RNAP, ribosomes and RNase) are treated as equally fast and their elongation rate was taken from the RNAP elongation rate reported by Chen et al. (2015) and set to 21 nucleotides s^{-1} (see **Table 2**). Minimum distances Δx , Δy , and Δz were set to 100 nucleotides each [which is larger than (Bremer and Dennis, 1987) estimated for a growth rate of 0.5 h^{-1}].

Each PFR passage induced transcription, however, with a delay of 30 s based on experimental observations. Once induction has started and RNAP has passed the attenuation sequence, transcription was assumed to continue until the terminator sequence after *trpA* was reached (see **Figure 2**).

Cell Distribution Model

The ensemble cell model needs to be embedded in a process model for describing the flow wiring and residence times of the cells in the compartments. The PFR is considered as a plug flow reactor showing almost equally distributed residence times for all cells. The STR is assumed to be ideally mixed, thus, having a residence time distribution constrained by the reaction volume and the throughput. Dilution and growth rate additionally influence the population.

For population balancing, the following events were considered to track the fate of each individual cell:

Cells may

1. leave the STR for entering the PFR and cycle back into STR after τ_{PFR} , the residence time in the PFR
2. be drained off by the efflux (harvest)
3. divide, setting all transcriptional and translational programs on default (no initiation of transcription or translation in the corresponding daughter cell)

The following probability functions α_i were defined

$$\alpha_1 = N_{STR} \frac{\dot{V}_{PFR}}{\dot{V}_{STR}} \quad (10)$$

$$\alpha_2 = N_{STR} \frac{\dot{V}_{Feed}}{\dot{V}_{STR}} \quad (11)$$

$$\alpha_3 = N_{STR}^0 D \quad (12)$$

For modeling event (1), the rate α_1 is used, indicating that a cell leaves the STR and enters the PFR again. Washout of cells (event 2) was treated equally with the dilution rate as flux value (α_2). The probability for cell division (α_3) is based on the set dilution rate D and the cell number N_{STR}^0 during SS_0 . Return of cells from the PFR compartment was fixed to occur after τ_{PFR} passed. Cells that are washed out by event (2) are deleted from the system and newly born cells from event (3) are treated as default daughter cells without any transcriptional deflection.

The reaction system was numerically solved by applying Gillespie's stochastic simulation algorithm (Gillespie, 1977). Time increment τ was solved based on the sum of the three reaction events considering the probabilities as indicated in Equation (13). The chosen reaction i is calculated, based on Equation (14). r_1 and r_2 are uniformly distributed random variables in the interval (0, 1).

$$\tau = \frac{1}{\sum \alpha_i} \ln \left(\frac{1}{r_1} \right) \quad (13)$$

$$\sum_{j=1}^{i-1} \alpha_j \leq r_2 \sum_{j=1}^3 \alpha_j \leq \sum_{j=1}^i \alpha_j \quad (14)$$

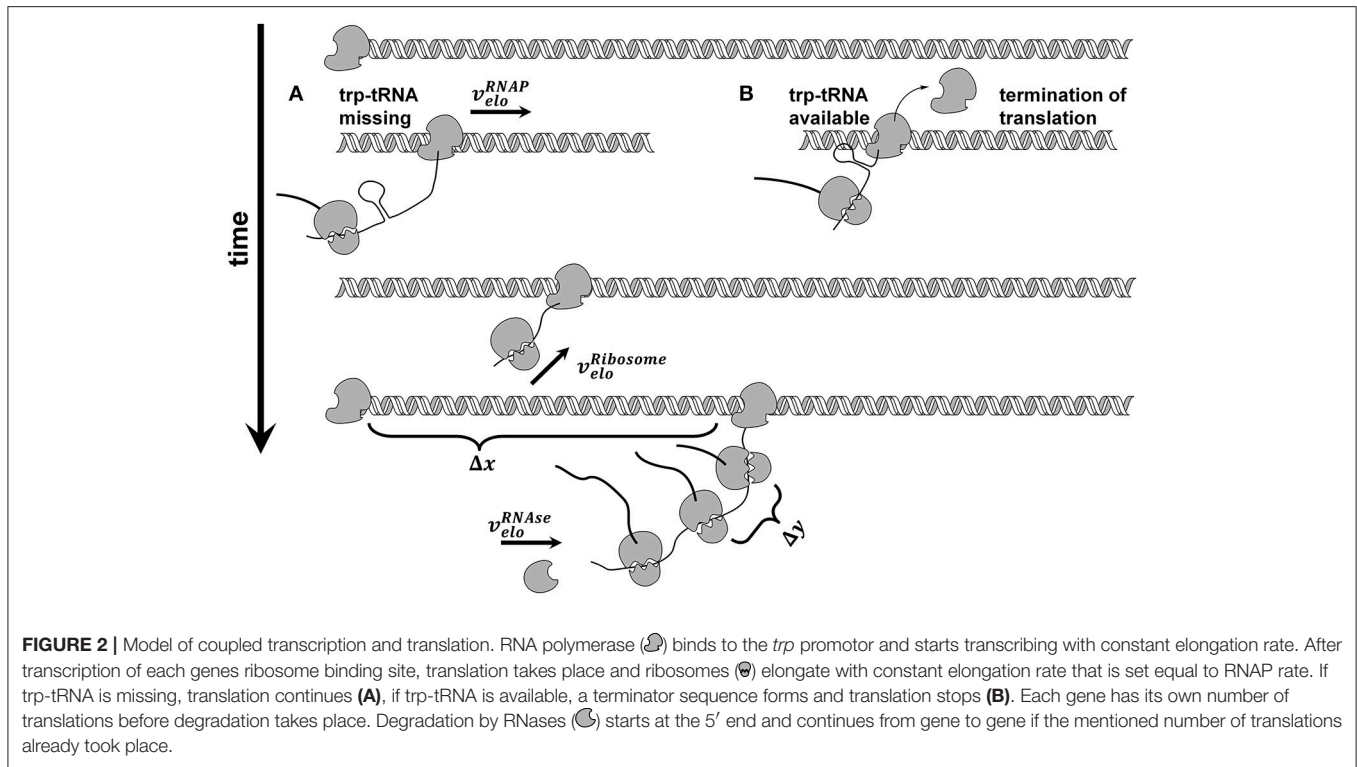
Simulations were performed using 10,000 cells, assuming uniform distribution in the STR (N_{STR}^0) before it is connected to the PFR. Simulations tracked cell numbers in the STR and the PFR as well as each transition of a cell from STR to PFR.

Coupling of Single-Cell and Cell Distribution Model

To minimize computational efforts, the impact of single-cell metabolic activities on the local environment was ignored. In essence, cells were considered to travel through a "frozen" bioreactor background that triggers transcriptional and translational responses as reflected in the single-cell model. For balancing the population distribution properly, the history of every cell was tracked. As the trigger "PFR" is of outstanding importance, the entrance of each cell into the PFR was logged.

The resulting in a set of time flags (t_i^{flag}) for each cell that was stored for the total simulation period, which allows detailed tracking of the cells motion in the STR-PFR setup. Additionally, the events (2) and (3) were tracked for each cell allowing the calculation of the population distribution in the STR and the PFR at each time step of simulation.

The simulation approach allowed the independent solution of the single-cell and cell distribution model. Simulations of the single-cell model resulted in distinct mRNA ($N_{g,SC}^{mRNA}(t)$) and protein ($N_{g,SC}^{Protein}(t)$) patterns for every cell entering and leaving the PFR and this constant sequence can be stored as look-up table. In the distribution model, each flag indicates start of induction, whose sequence is stored in the look-up table. Duration of an induction phase is defined from entering the PFR at t^{flag} until the last mRNA is degraded at $t^{flag} + \Delta t$. Superposition of all transcriptional and translational patterns over the cells lifetime results in a continuous description of transcriptional and translational patterns in the STR-PFR system.



Cellular growth by event (3) is treated as generation of a new default cell without any additional mRNA and protein content without altering the mother cell.

$$N_g^{mRNA}(t) = \sum_i \begin{cases} N_{g,SC}^{mRNA}(t - t_i^{flag}) & \text{if } t - t_i^{flag} \leq \Delta t \\ 0 & \text{otherwise} \end{cases} \quad (15)$$

$$N_g^{Protein}(t) = \sum_i \begin{cases} N_{g,SC}^{Protein}(t - t_i^{flag}) & \text{if } t - t_i^{flag} \leq \Delta t \\ N_{g,SC}^{Protein}(\Delta t) & \text{otherwise} \end{cases} \quad (16)$$

RESULTS

Key assumptions

Löffler et al. (2016) and Simen et al. (2017) showed that the repeated oscillation of the substrate availability of *E. coli*, simulated with a STR-PFR system, induce repeated on/off switching of several hundred genes. Among them, the frequent activation of the tryptophan operon could be observed (Simen et al., 2017). The mathematical model comprising the (Equations 2–16) was used to describe not only short- and long-term transcriptional dynamics but also to estimate the impact on protein formation by linking the transcription with the translation machinery. The following key assumptions were made: (i) Once transcription of mRNA has started, it continued until the stop signal was achieved at the end of the operon, namely on the relative position 6726 nt after *trpEDCBA* (Stoltzfus et al., 1988), (ii) mRNA was assumed to be immediately translated into proteins. The number of active ribosomes per

TABLE 2 | Model parameters used for simulation of both single-cell and cell distribution model.

Parameter	Value	Unit
v_{elo}^{RNAP}	21	Nucleotides per second
$v_{elo}^{Ribosome}$	21	Nucleotides per second
v_{elo}^{RNase}	21	Nucleotides per second
Δx	100	Nucleotides
Δy	100	Nucleotides
Δz	100	Nucleotides
t_{ind}	[30 125]	Seconds
\dot{V}_{PFR}	180	mL min ⁻¹
\dot{V}_{Feed}	5	mL min ⁻¹
V_{STR}	1,120	mL
D	0.2	h ⁻¹
N_{STR}^0	10,000	cells

gene (encoding mRNA) was calculated based on the experimental findings of Valgepea et al. (2013).

Modeling Short-Term Transcriptional Dynamics

The simulation of transcriptional dynamics during a single PFR passage was achieved using the single-cell model with the parameters listed in Table 1. Figure 3A depicts mRNA courses of two subsequent PFR-STR passages. At $t = 0$, the PFR entering cell is induced and initiates transcription after the experimentally observed delay time of 30 s. Then, transcription

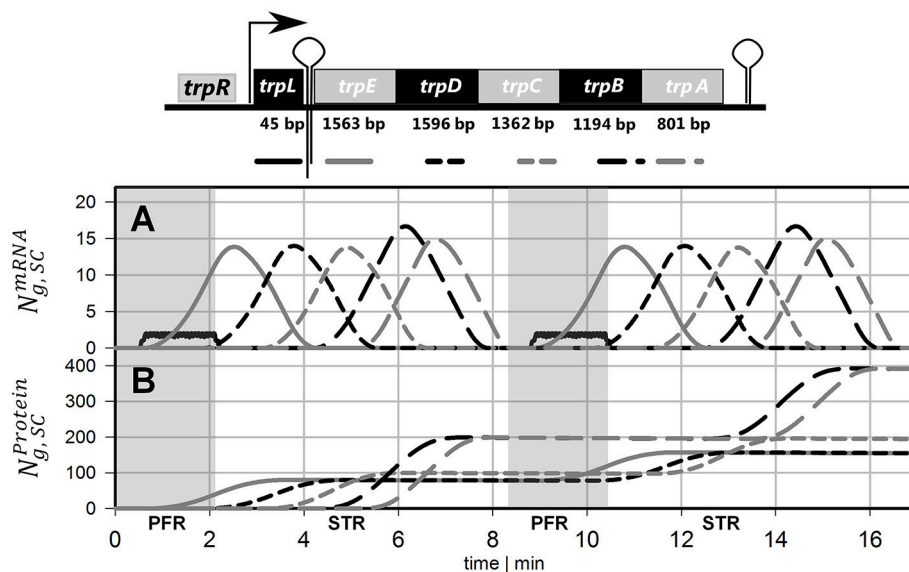


FIGURE 3 | Time courses of two subsequent cell cycles comprising PFR and STR passage. **(A)** mRNA and **(B)** protein profiles are shown, both simulated using the single-cell model. The genes and their gene products are encoded as follows: Black solid line = *trpL*, gray solid line = *trpE*, black short dashed line = *trpD*, gray short dashed line = *trpC*, black long dashed line = *trpB*, gray long dashed line = *trpA*. Gray shaded areas indicate that the cell currently passes the PFR.

of the *trp* operon starts with *trpL*. As shown, *trpL* is fully and *trpE* partially transcribed before the cell leaves the PFR. Accordingly, the remaining genes downstream of the operon were transcribed after the cell reenters the STR. Shortly after initiation, degradation of *trpL* mRNA has started, as indicated by the constant mRNA levels. After leaving the PFR, the cell stops further RNAP initiation and RNases immediately degrade the remaining transcripts. Noteworthy, all gene transcripts were fully degraded (except for a small residual of *trpA*) before the cells again reentered the PFR.

Modeling Protein Formation

Based on the single-cell model, translation of mRNA was simulated as depicted in **Figure 3B**. It was assumed that protein formation started as soon as the ribosomal binding site was transcribed. Because *trpL* encodes the leader peptide, translation modeling was simply focused on *trpEDCBA*. First, TrpE proteins were produced while the cells passed the PFR compartment. Downstream proteins were translated after the cells reentered the STR. Consequently, the majority of translation happened in STR. Protein formation is delayed and multiplexed compared to mRNA production. Accordingly, dynamics of protein courses are less steep than those of transcript levels. The latter are characterized by fast transcription and fast mRNA degradation that finally lead to sharp peaks of transcript contents. Protein degradation is slower by orders of magnitude. Consequently, only moderate pool dynamics and even protein accumulation was observed after PFR-STR transits.

Each PFR-STR cycle lasted for about 500 s. During this period, cells managed to produce 20 mRNA copies of the complete *trp* operon. Subsequent translation enabled the formation of 80 TrpED, 100 TrpC, and 200 TrpBA copies (considering

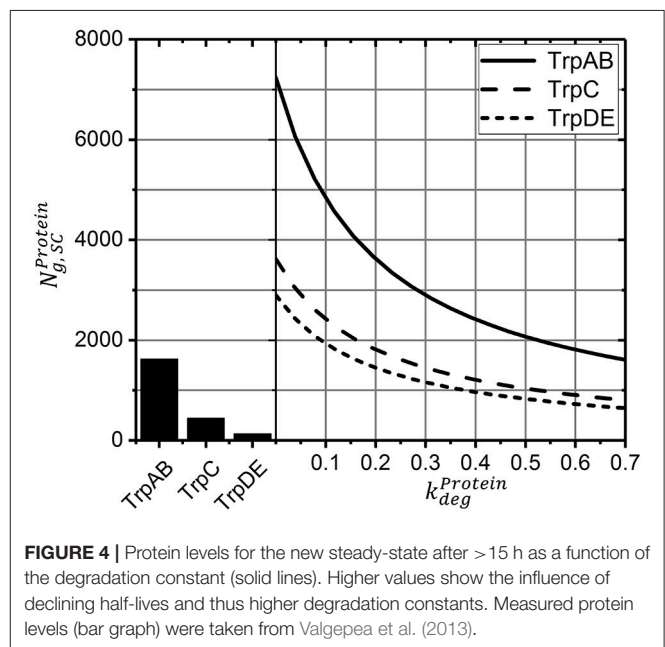


FIGURE 4 | Protein levels for the new steady-state after >15 h as a function of the degradation constant (solid lines). Higher values show the influence of declining half-lives and thus higher degradation constants. Measured protein levels (bar graph) were taken from Valgepea et al. (2013).

the ribosomal stoichiometry of **Table 1**) with corresponding translation rates of 9.6, 12 and 24 proteins per cell per minute.

As outlined above, protein degradation is known to be much slower than mRNA decay which enabled the simplified simulation of protein dynamics shown in **Figure 3B**. However, the scenario may change if steady-states are analyzed. As outlined in equation 17, steady-state protein levels will be dependent on

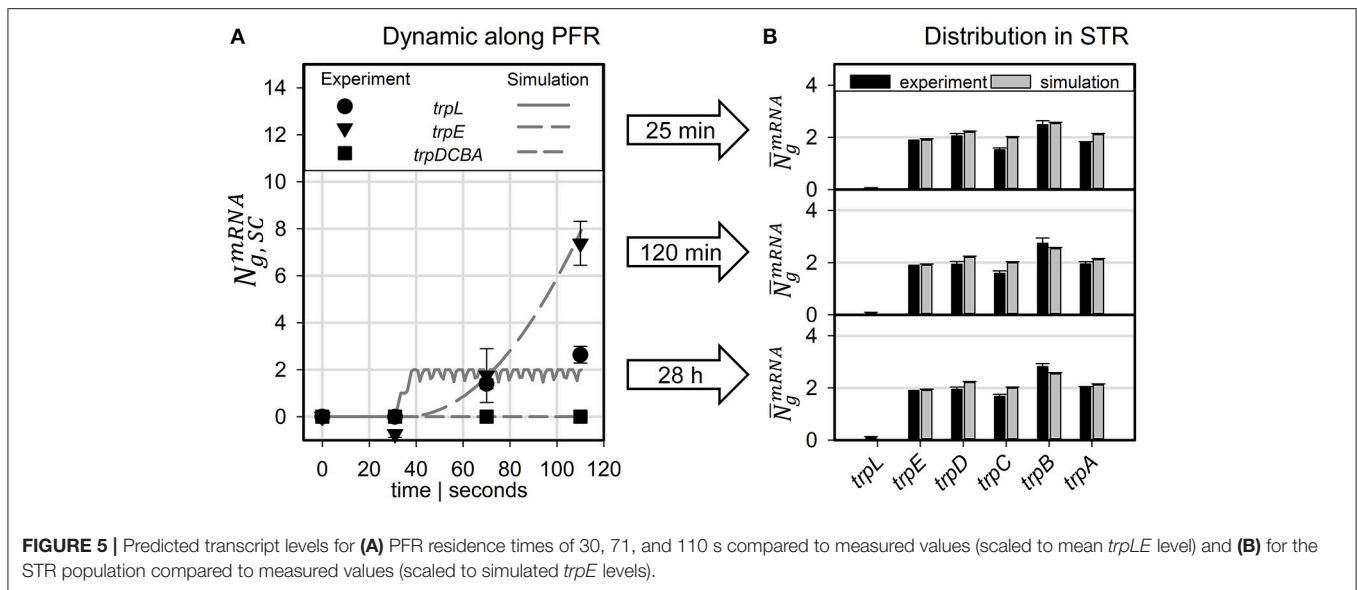


FIGURE 5 | Predicted transcript levels for (A) PFR residence times of 30, 71, and 110 s compared to measured values (scaled to mean *trpLE* level) and (B) for the STR population compared to measured values (scaled to simulated *trpE* levels).

the degradation constant.

$$\frac{dc_{Protein}}{dt} = r_{Translation} - r_{deg} = r_{Translation} - c_{Protein} k_{deg}^{Protein} = 0 \quad (17)$$

$$c_{Protein} = \frac{r_{Translation}}{k_{deg}^{Protein}} \quad (18)$$

Because the individual degradation constants for the *trp* gene products are unknown, simulation studies were performed and summarized in **Figure 4**. In essence, results for $k_{deg}^{Protein} = 0$ indicate protein loss simply based on cell drain under continuous operating conditions whereas results with $k_{deg}^{Protein} > 0$ consider additional protein degradation with the given rates. For comparison, experimental results are indicated, too. As shown, when $k_{deg}^{Protein}$ exceeds 0.6 h^{-1} (which corresponds to half-lives lower than 1.1 h) simulated protein levels are smaller than those reported for the given growth rate of 0.2 h^{-1} . Accordingly, the simplifying assumption to neglect protein degradation for simulating STR-PFR dynamics is validated as half-lives of 1.1 h fairly exceed cycling times of about 500 s (about 0.12 h).

Simulating Long-Term Adaptation

As indicated in Löffler et al. (2016) and Simen et al. (2017), the STR-PFR experiments were performed as a continuous cultivation. First, glucose- or ammonia limited steady-states were installed cultivating the cells in STR only. Then, the PFR was connected while retaining the total system dilution rate of 0.2 h^{-1} . As such, not only short-term transcript dynamics could be elucidated by sampling the PFR but also long-term adaptation of the whole population by studying transcript patterns in STR during the adaptation period of 28 h after PFR connection.

For simulation studies, the cell and the process model were linked predicting a stable distribution of 7526 ± 68 tracked cells

in the STR ($75.0 \pm 0.68\%$) and 2513 ± 47 simulated cells in the PFR ($25.0 \pm 0.47\%$). Accordingly, the simulated cell population matched well with the volumetric setup comprising 74.7 vol% in the STR and 25.3 vol% in the PFR.

Neglecting the residence time distribution in the STR indicates that cells in the STR are always induced as shown in **Figure 3**. Therefore, population heterogeneity is not observable. Including residence time distribution for a perfectly mixed reactor reveals the existence of several subpopulations. Whilst 34% of the cells are currently not induced, 48% of the cells are currently induced once and 18% of the population are induced multiple times. Multiple inductions in this context indicate that the cell reenters the PFR while still being induced from a previous PFR passage, resulting in multiple transcription events (time dependency is shown in Supplementary Material).

Figure 5A compares measured and simulated transcript dynamics of the *trp* operon while passing through the PFR. Notably, measured transcript dynamics were very similar so that measurements taken after 25, 120 min and 28 h were cumulated and indicated by a common variance. According to the modeling constraints, mRNA production started after 30 s which is in good agreement with experimental observations for *trpL* and for *trpE*. Synthesis of further downstream genes *trpDCBA* was neither predicted nor measured.

The long-term adaptation of the population was simulated for the exemplary time points of 25 and 120 min as well as for 28 h (see **Figure 5B**). Again, experiments and simulation results show a high agreement for all conditions. This also holds true for the short *trpL* mRNA which was hardly detected in the PFR, confirming the simulation.

To compare the dynamics of transcript and protein adaptation toward new steady-states, both species were simulated. For transcript studies, the average *trpA* transcription was considered. Protein formation of TrpA disregarded putative degradation and simply considered continuous cell drain under steady-state

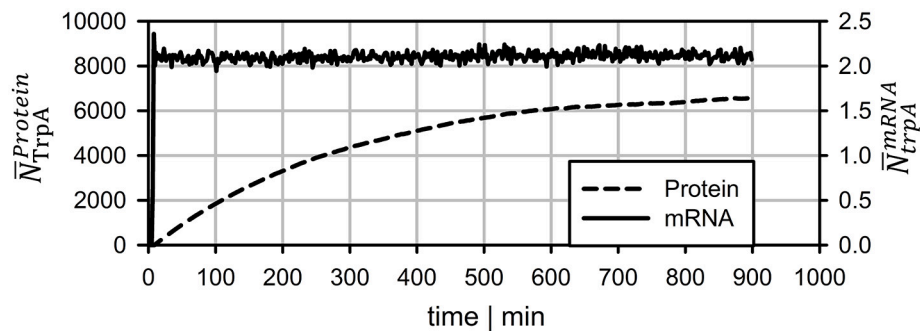


FIGURE 6 | Long-term prediction of transcript and protein levels neglecting protein degradation. mRNA levels reach stable levels after ~7 min whereas protein leveling takes more than 15 h.

conditions. **Figure 6** clearly outlines the different speeds. Whereas, transcript levels converge to a new steady-state within 10 min (slightly more than a PFR-STR cycle), proteins need about 15 h.

DISCUSSION

The transcriptional dynamics observed in the STR-PFR experiments of Löffler et al. (2016) and in particular Simen et al. (2017) were modeled using a combined cell and process model. By focusing on details of transcription and translation in the cell model, a set of 10,000 individual cells was created and tracked during their repeated passages through the STR-PFR system. Inherently, the modeling approach mirrors a mechanistic understanding linking external stimuli with cellular transcriptional responses thereby excluding putative stochastic events (Elowitz et al., 2002; Avery, 2006). Accordingly, the modeling approach showed fundamental characteristics of an ensemble model, as outlined by (Henson, 2003). Here, we used the *trp* operon as an example because its polycistronic mRNA consisting of five structural genes and a leader peptide was repeatedly transcribed envisaging ammonia limitation (Simen et al., 2017) and, most importantly, its induction was followed by attenuation which directly linked transcription and translation of the gene products. Only by using the approach of ensemble modeling, individual cell fates could be tracked which finally explain the occurrence of population heterogeneity.

Comparing the experimental observations of transcript dynamics with modeling predictions, high agreement between simulations and experimental data can be observed (**Figure 5**). The qualification holds true not only for the prediction of short-term transcript dynamics in the PFR but also for the long-term adaptations in the STR, visualized by analyzing samples up to 28 h after initial connection of the PFR with the STR. Notably, the high precision of transcript prediction was achieved without any parameter regression. Only literature documented parameters were chosen to fix the setting of the ensemble model. Again, this finding is qualified as a confirmation of the basic approach.

Protein formation was assumed to start immediately after mRNA transcription. Unlike mRNA degradation, no distinct decay kinetics for the *trp* genes were known. Simulation studies of

Figure 4 revealed that realistic protein half-lives should be about 1.1 h, which is in the range of experimental observations for other proteins (Nath and Koch, 1970; Lahtvee et al., 2014). Accordingly, impacts of protein degradation on short-term kinetics can be ruled out. However, the long-term adaptations indicated in **Figure 6** are likely to be affected. The additional consideration of decay kinetics will likewise reduce steady-state levels.

One of the key findings of the STR-PFR studies of Löffler et al. (2016) and Simen et al. (2017) was the observation that PFR induced regulatory responses are propagated into STR finally causing the adaptation of the whole population. Exactly this phenomenon could be modeled as well. **Figures 3, 5** document that only *trpL* and *trpE* are fully transcribed in PFR whereas the transcription of the rest of the operon continued in the STR. Subsequently, most of the stress induced cellular burden occurred after a time-delay in the well-mixed STR compartment and not immediately in the PFR, the origin of the trigger. As a consequence, the population in the STR is very heterogeneous, consisting of cells in different transcription and translation states. Some cells should be still propagating the PFR induced stress response, whereas others may have completed the same. Moreover, given that the STR and the PFR compartments do not physically exist in large-scale bioreactors, cells are expected to co-exist next to each other while circulating around. Similar studies have already been performed investigating the lifelines of fluctuating cells (Haringa et al., 2016; Kuschel et al., 2017).

CONCLUSION

The ensemble model used in this study succeeded to predict experimental observations of long- and short-term transcriptional dynamics with high precision and without parameter adjustments. As such, the approach demonstrated its fundamental suitability for predicting large-scale population heterogeneity as a consequence of local stress triggers. Accordingly, likewise modeling approaches open the door for an *in silico* scale-up design, simulating large-scale performance of the cells *ab initio*.

This study illustrates that locally induced stress responses are propagated into different regions of the bioreactor thereby creating temporal and spatial inhomogeneity of the population. Notably, cellular reactions do happen on different time

scales: Whereas transcriptional responses require <10 min, translational changes may continue for more than 10 h to reach new steady-states. Additionally, metabolic responses may occur which are likely to precede the transcriptional reaction. The hierarchical sequence of regulatory responses is overlaid with dynamics of mass transfer, mixing and process control which make it necessary to track individual cell responses properly for predicting large-scale performance of the total culture.

AUTHOR CONTRIBUTIONS

AN performed the modeling, designed the study, and prepared the manuscript. ML and JS performed the experiments and

prepared the manuscript. RT designed the study and prepared the manuscript.

FUNDING

The authors gratefully acknowledge the funding by the Bundesministerium für Bildung und Forschung (BMBF, Grant FKZ0316178A).

SUPPLEMENTARY MATERIAL

The Supplementary Material for this article can be found online at: <http://journal.frontiersin.org/article/10.3389/fmicb.2017.01195/full#supplementary-material>

REFERENCES

- Avery, S. V. (2006). Microbial cell individuality and the underlying sources of heterogeneity. *Nat. Rev. Microbiol.* 4, 577–587. doi: 10.1038/nrmicro1460
- Bremer, H., and Dennis, P. P. (1987). "Modulation of chemical composition and other parameters of the cell by growth rate," in *Escherichia coli and Salmonella typhimurium: Cellular and Molecular Biology*, Vol. 2, ed F. C. Neidhardt (Washington, DC: American Society for Microbiology), 1553–1569.
- Chen, H., Shiroguchi, K., Ge, H., and Xie, X. S. (2015). Genome-wide study of mRNA degradation and transcript elongation in *Escherichia coli*. *Mol. Syst. Biol.* 11:808. doi: 10.15252/msb.20159000
- Chubukov, V., Gerosa, L., Kochanowski, K., and Sauer, U. (2014). Coordination of microbial metabolism. *Nat. Rev. Microbiol.* 12, 327–340. doi: 10.1038/nrmicro3238
- Elowitz, M. B., Levine, A. J., Siggia, E. D., and Swain, P. S. (2002). Stochastic gene expression in a single cell. *Science* 297, 1183–1186. doi: 10.1126/science.1070919
- George, S., Larsson, G., and Enfors, S.-O. (1993). A scale-down two-compartment reactor with controlled substrate oscillations: metabolic response of *Saccharomyces cerevisiae*. *Bioprocess Eng.* 9, 249–257. doi: 10.1007/BF01061530
- Gillespie, D. T. (1977). Exact stochastic simulation of coupled chemical reactions. *J. Phys. Chem.* 81, 2340–2361. doi: 10.1021/j100540a008
- Haringa, C., Tang, W., Deshmukh, A. T., Xia, J., Reuss, M., Heijnen, J. J., et al. (2016). Euler-Lagrange computational fluid dynamics for (bio)reactor scale-down: an analysis of organism life-lines. *Eng. Life Sci.* 16, 652–663. doi: 10.1002/elsc.201600061
- Henson, M. A. (2003). Dynamic modeling of microbial cell populations. *Curr. Opin. Biotechnol.* 14, 460–467. doi: 10.1016/S0958-1669(03)00104-6
- Hyde, C. C., Ahmed, S. A., Padlan, E. A., Miles, E. W., and Davies, D. R. (1988). Three-dimensional structure of the tryptophan synthase alpha 2 beta 2 multienzyme complex from *Salmonella typhimurium*. *J. Biol. Chem.* 263, 17857–17871.
- Kuschel, M., Siebler, F., and Takors, R. (2017). Lagrangian trajectories to predict the formation of population heterogeneity in large-scale bioreactors. *Bioengineering* 4:27. doi: 10.3390/bioengineering4020027
- Lahtvee, P.-J., Seiman, A., Arike, L., Adamberg, K., and Vilu, R. (2014). Protein turnover forms one of the highest maintenance costs in *Lactococcus lactis*. *Microbiology* 160, 1501–1512. doi: 10.1099/mic.0.078089-0
- Lara, A. R., Galindo, E., Ramírez, O. T., and Palomares, L. A. (2006). Living with heterogeneities in bioreactors: understanding the effects of environmental gradients on cells. *Mol. Biotechnol.* 34, 355–382. doi: 10.1385/MB:34:3:355
- Löffler, M., Simen, J. D., Jäger, G., Schäferhoff, K., Freund, A., and Takors, R. (2016). Engineering *E. coli* for large-scale production - Strategies considering ATP expenses and transcriptional responses. *Metab. Eng.* 38, 73–85. doi: 10.1016/j.ymben.2016.06.008
- Löffler, M., Simen, J. D., Müller, J., Jäger, G., Laghrami, S., Schäferhoff, K., et al. (2017). Switching between nitrogen and glucose limitation: unraveling transcriptional dynamics in *Escherichia coli*. *J. Biotechnol.* doi: 10.1016/j.jbiotec.2017.04.011. [Epub ahead of print].
- Michalowski, A., Siemann-Herzberg, M., and Takors, R. (2017). *Escherichia coli* HGT: engineered for high glucose throughput even under slowly growing or resting conditions. *Metab. Eng.* 40, 93–103. doi: 10.1016/j.ymben.2017.01.005
- Nath, K., and Koch, A. L. (1970). Protein degradation in *Escherichia coli*. I. Measurement of rapidly and slowly decaying components. *J. Biol. Chem.* 245, 2889–2900.
- Neubauer, P., and Junne, S. (2010). Scale-down simulators for metabolic analysis of large-scale bioprocesses. *Curr. Opin. Biotechnol.* 21, 114–121. doi: 10.1016/j.copbio.2010.02.001
- Neubauer, P., Haggstrom, L., and Enfors, S. O. (1995). Influence of substrate oscillations on acetate formation and growth yield in *Escherichia coli* glucose limited fed-batch cultivations. *Biotechnol. Bioeng.* 47, 139–146. doi: 10.1002/bit.260470204
- Nienow, A. W., Edwards, M. F., and Harnby, N. (eds.). (1997). *Mixing in the Process Industries, 2nd Edn.* Oxford; Boston, MA: Butterworth-Heinemann.
- Oldiges, M., and Takors, R. (2005). Applying metabolic profiling techniques for stimulus-response experiments: chances and pitfalls. *Adv. Biochem. Eng. Biotechnol.* 92, 173–196. doi: 10.1007/b98913
- Simen, J. D., Löffler, M., Jäger, G., Schäferhoff, K., Freund, A., Müller, J., et al. (2017). Transcriptional response of *Escherichia coli* to ammonia and glucose fluctuations. *Microb. Biotechnol.* doi: 10.1111/1751-7915.12713. [Epub ahead of print].
- Stoltzfus, A., Leslie, J. F., and Milkman, R. (1988). Molecular evolution of the *Escherichia coli* chromosome. I. Analysis of structure and natural variation in a previously uncharacterized region between trp and tonB. *Genetics* 120, 345–358.
- Takors, R. (2012). Scale-up of microbial processes: impacts, tools and open questions. *J. Biotechnol.* 160, 3–9. doi: 10.1016/j.jbiotec.2011.12.010
- Valgepea, K., Adamberg, K., Seiman, A., and Vilu, R. (2013). *Escherichia coli* achieves faster growth by increasing catalytic and translation rates of proteins. *Mol. Biosyst.* 9, 2344–2358. doi: 10.1039/c3mb70119k
- Yanofsky, C. (2004). The different roles of tryptophan transfer RNA in regulating trp operon expression in *E. coli* versus *B. subtilis*. *Trends Genet.* 20, 367–374. doi: 10.1016/j.tig.2004.06.007
- Yanofsky, C. (2007). RNA-based regulation of genes of tryptophan synthesis and degradation, in bacteria. *RNA* 13, 1141–1154. doi: 10.1261/rna.620507
- Yanofsky, C., Platt, T., Crawford, I. P., Nichols, B. P., Christie, G. E., Horowitz, H., et al. (1981). The complete nucleotide sequence of the tryptophan operon of *Escherichia coli*. *Nucleic Acids Res.* 9, 6647–6668. doi: 10.1093/nar/9.24.6647

Conflict of Interest Statement: The authors declare that the research was conducted in the absence of any commercial or financial relationships that could be construed as a potential conflict of interest.

Copyright © 2017 Nieß, Löffler, Simen and Takors. This is an open-access article distributed under the terms of the Creative Commons Attribution License (CC BY). The use, distribution or reproduction in other forums is permitted, provided the original author(s) or licensor are credited and that the original publication in this journal is cited, in accordance with accepted academic practice. No use, distribution or reproduction is permitted which does not comply with these terms.



Simulation of *Escherichia coli* Dynamics in Biofilms and Submerged Colonies with an Individual-Based Model Including Metabolic Network Information

Ignace L. M. M. Tack, Philippe Nimmegeers, Simen Akkermans, Ihab Hashem and Jan F. M. Van Impe*

BioTeC+, Department of Chemical Engineering, KU Leuven, Ghent, Belgium

OPEN ACCESS

Edited by:

Jan-Ulrich Kreft,
University of Birmingham,
United Kingdom

Reviewed by:

Pablo Ivan Nikel,
The Novo Nordisk Foundation Center
for Biosustainability (DTU Biosustain),
Denmark

Eugen Bauer,
University of Luxembourg,
Luxembourg

*Correspondence:

Jan F. M. Van Impe
jan.vanimpe@kuleuven.be

Specialty section:

This article was submitted to
Systems Microbiology,
a section of the journal
Frontiers in Microbiology

Received: 30 August 2017

Accepted: 01 December 2017

Published: 13 December 2017

Citation:

Tack ILM, Nimmegeers P,
Akkermans S, Hashem I and
Van Impe JFM (2017) Simulation of
Escherichia coli Dynamics in Biofilms
and Submerged Colonies with an
Individual-Based Model Including
Metabolic Network Information.
Front. Microbiol. 8:2509.
doi: 10.3389/fmicb.2017.02509

Clustered microbial communities are omnipresent in the food industry, e.g., as colonies of microbial pathogens in/on food media or as biofilms on food processing surfaces. These clustered communities are often characterized by metabolic differentiation among their constituting cells as a result of heterogeneous environmental conditions in the cellular surroundings. This paper focuses on the role of metabolic differentiation due to oxygen gradients in the development of *Escherichia coli* cell communities, whereby low local oxygen concentrations lead to cellular secretion of weak acid products. For this reason, a metabolic model has been developed for the facultative anaerobe *E. coli* covering the range of aerobic, microaerobic, and anaerobic environmental conditions. This metabolic model is expressed as a multiparametric programming problem, in which the influence of low extracellular pH values and the presence of undissociated acid cell products in the environment has been taken into account. Furthermore, the developed metabolic model is incorporated in MICRოდIMS, an in-house developed individual-based modeling framework to simulate microbial colony and biofilm dynamics. Two case studies have been elaborated using the MICRოდIMS simulator: (i) biofilm growth on a substratum surface and (ii) submerged colony growth in a semi-solid mixed food product. In the first case study, the acidification of the biofilm environment and the emergence of typical biofilm morphologies have been observed, such as the mushroom-shaped structure of mature biofilms and the formation of cellular chains at the exterior surface of the biofilm. The simulations show that these morphological phenomena are respectively dependent on the initial affinity of pioneer cells for the substratum surface and the cell detachment process at the outer surface of the biofilm. In the second case study, a no-growth zone emerges in the colony center due to a local decline of the environmental pH. As a result, cellular growth in the submerged colony is limited to the colony periphery, implying a linear increase of the colony radius over time. MICRოდIMS has been successfully used to reproduce complex dynamics of clustered microbial communities.

Keywords: multiscale modeling, individual-based modeling, metabolomics, *E. coli*, biofilm dynamics

INTRODUCTION

In their natural or industrial settings, many bacterial species form clustered communities, such as biofilms or colonies, rather than living in a free-swimming planktonic state. Living as a community often confers specific advantages, such as antibiotic resistance and immune evasion due to horizontal gene transfer, resistance against flow shear forces and persistence in dynamic and stressing environments due to metabolic differentiation (Costerton, 1995; Costerton et al., 1999). This metabolic differentiation is the result of diffusion limitations and concomitant gradients in the nutrient, oxygen and metabolic waste product concentrations. These concentration gradients are induced by nutrient/oxygen consumption and the secretion of metabolic waste products such as acetic, formic, and lactic acid by the relatively densely packed cells (Stewart and Franklin, 2008).

Microbial colony and biofilm development is a significant issue in food industry. Biofilm formation on food equipment surfaces constitutes a major contamination source of the food products. Surface colony growth occurs when food surfaces are exposed to these microbial contamination sources of spoiling or pathogenic organisms. In mixed or coagulated food products, such as minced meat or cheese, these microbial contaminants can penetrate the food interior during the production process, resulting in submerged colony growth (Wimpenny et al., 1995). Cellular growth in clustered communities may also be used intentionally to obtain specific beneficial effects, such as biodegradation or synthesis by the use of catalytic biofilms (Benedetti et al., 2016).

This article focuses on the simulation of *Escherichia coli* biofilm and colony growth dynamics. *E. coli* is a particularly dangerous food pathogen for young, elderly and immunocompromised people causing gastrointestinal disorders, renal failure or even death (Rowe, 2009). An increasing trend of *E. coli* infections has been observed in the EU from 2009 to 2013, possibly due to an increased awareness after the large outbreak of EHEC O104:H4 in 2011 (EFSA and ECDC, 2015). In addition, as a facultative anaerobe, *E. coli* is able to survive both in the presence and absence of oxygen, increasing the risk of food contamination. Therefore, accurate quantitative microbial risk assessment is indispensable to guarantee microbial food safety in the whole food production and distribution chain. For this purpose, mathematical models are developed in predictive microbiology to describe and predict microbial dynamics in food products as a function of environmental conditions resembling food processing and storage (Buchanan, 1993).

Traditionally, predictive models are (semi-)empirically based on data of microbial dynamics in well-mixed liquids and only consider the average microbial population dynamics at a macroscopic scale. However, as a result of the heterogeneous environmental conditions in mature biofilms and colonies, and due to the concomitant metabolic differentiation among the constituting cells, the individual microbial cell is the most intuitive modeling level. In individual-based models (IbM), the individuals/agents of a population are described as discrete, unique, and autonomous entities (Grimm and Railsback, 2005; Railsback and Grimm, 2012). This enables the modeler to include

individual variability, directed or local interactions of agents with the surrounding medium or other agents, and adaptive physiological behavior. Population dynamics are not modeled explicitly, but emerge from the behavior of the individuals and their interactions with the environment and each other. As suggested above, in predictive microbiological IbMs, the microbial cell is taken as the individual modeling unit (Ginovart et al., 2002; Standaert et al., 2004; Dens et al., 2005; Prats et al., 2006; Verhulst et al., 2011; Ferrier et al., 2013; Tack et al., 2014, 2015).

Despite the specific advantages of IbMs, this kind of models is notorious for its complex structure (Grimm, 1999; Grimm et al., 1999). While traditional predictive models only consist of a limited set of equations, IbMs contain a multitude of mathematical and logical rules grouped in submodels, each representing a major and more or less independent process of the real-life system. This complexity can make IbMs computationally intensive and slow to run, hard to comprehend and communicate, data hungry, prone to overfitting, difficult to calibrate, and laborious to test. In the microbial systems considered in this work, the most complex process is the metabolism of the *E. coli* cells, which is determined by a myriad of possible intracellular reaction pathways. Therefore, it is necessary to develop a non-complex, yet accurate metabolic model, valid under the environmental conditions in our case studies.

Information on the individual cell metabolism could be included in IbMs by metabolic flux balance analysis (FBA) with genome-scale models (Palsson, 2006). To represent the specific microbial growth rate or the secretion rates of major cell products as a function of nutrient and oxygen consumption, phenotypic phase planes (PhPPs) can be constructed by performing FBAs at varying specific cellular nutrient and oxygen uptake rates. However, this would result in long run times due to the thousands/millions of cells in IbMs and the myriad of intracellular pathways in FBA. In addition, FBAs determine metabolic flux distributions by optimizing a certain cellular objective (e.g., maximization of biomass or metabolite production) which is often unknown, especially when the cell is exposed to stressing environmental conditions (Feist and Palsson, 2010). Therefore, the PhPPs are approximated in this article with a low-complexity linear model that contains the intracellular information from the FBAs without explicitly incorporating it. However, the PhPPs to which the linear model is calibrated are only valid when cells aim to maximize their growth. To account for deviations from growth-optimal conditions in the culture environment, growth inhibition and metabolic shifts due to low pH values and the presence of weak acid cell products in the environment are incorporated in the linear model.

Finally, the linear metabolic model is incorporated in MICRODIMS, an in-house developed IbM (Verhulst et al., 2011; Tack et al., 2015). In this way, MICRODIMS is applicable as a virtual laboratory to explore the behavior of *E. coli* cells on/in food products under various combinations of heterogeneous environmental conditions. Two case studies are elaborated in detail: (i) two-dimensional biofilm growth on abiotic food equipment surfaces, and (ii) three-dimensional submerged colony growth occurring in mixed or coagulated semi-solid food

products. In both case studies, oxygen limitations emerge in mature microbial structures due to diffusion limitations, leading to local pH drops as a result of the cellular secretion and accumulation of weak acid substances. The resulting metabolic differentiation among the cells influences the global population dynamics: low pH values and cell lysis at the substratum surface lead to biofilm detachment, while submerged colonies are characterized by the emergence of a central no-growth zone influencing the colony radius growth.

MATERIALS AND METHODS

In the first part of this section, the basic concepts of developing a non-complex metabolic model for *E. coli* are explained. These concepts have already been partly described in Tack et al. (2014). Secondly, the structure of the IbM in which the metabolic model is incorporated is described according to the ODD (Overview, Design concepts, and Details) protocol of Grimm et al. (2006, 2010).

Development of a Non-complex Metabolic Model for *E. coli*

The non-complex metabolic model that is incorporated in the IbM is based on systems biology concepts. These concepts and the derivation of the developed metabolic model will be explained in the following subsections. Furthermore, the dependency of the metabolic model outputs (i.e., the specific cellular growth rate and the secretion rates of the main cell products) on the environmental pH and concentrations of weak acid cell products is explained.

Flux Balance Analysis

In mathematical terms, the intracellular metabolic pathways and the exchange reactions with the extracellular environment are contained within the exchange stoichiometric matrix S_{exch} (Palsson, 2006):

$$\frac{dx}{dt} = S_{\text{exch}} \begin{pmatrix} \mathbf{v} \\ \mathbf{q} \end{pmatrix}, \quad (1)$$

with \mathbf{x} the concentrations of the involved metabolites, and \mathbf{v} and \mathbf{q} the metabolic fluxes through respectively the intracellular and exchange reactions.

Flux balance analysis (FBA) determines a steady-state solution of Equation (1) by optimizing a specific cellular objective function J , leading to the following optimization problem (Palsson, 2006):

$$\min_{\mathbf{v}, \mathbf{q}} \left[J = \mathbf{w} \cdot \begin{pmatrix} \mathbf{v} \\ \mathbf{q} \end{pmatrix} \right], \quad (2)$$

subject to

$$S_{\text{exch}} \begin{pmatrix} \mathbf{v} \\ \mathbf{q} \end{pmatrix} = 0, \quad (3)$$

$$v_{i,\min} \leq v_i \leq v_{i,\max}, \quad (4)$$

$$q_{i,\min} \leq q_i \leq q_{i,\max}. \quad (5)$$

In Equation (2), the weights \mathbf{w} are defined by the intended cellular objective. The constraints on the kinetic rates of the intracellular reactions ($v_{i,\min}$ and $v_{i,\max}$) and the physicochemical constraints on the external fluxes due to environmental conditions ($q_{i,\min}$ and $q_{i,\max}$) are taken into account in Equations (4, 5) respectively.

Phenotypic Phase Plane Analysis

Flux balance analysis is an accurate tool to determine the specific cellular growth rate and secretion rates of the main weak acid cell products for a known specific glucose and oxygen uptake rate. To examine the metabolic regimes of *E. coli* under different glucose and oxygen availability conditions, a phenotype phase plane (PhPP) analysis can be carried out by executing multiple FBAs for a range of specific glucose and oxygen uptake rates (Edwards et al., 2001), as illustrated in Figure 1. For these FBAs, the genome-scale model iAF1260 of Feist et al. (2007) has been used, and it has been assumed that the cell aims to maximize its biomass. The metabolic operation of the cell is retrieved from the PhPP by maximizing the specific cellular growth rate as a function of the specific glucose and oxygen uptake rate:

$$\max_{q_G, q_O} [J = \mu(q_G, q_O)] \quad (6)$$

subject to

$$0 \leq q_G \leq q_{G,\max} \cdot \frac{C_G}{K_G + C_G}, \quad (7)$$

$$0 \leq q_O \leq q_{O,\max} \cdot \frac{C_O}{K_O + C_O}. \quad (8)$$

The upper constraints for the glucose and oxygen uptake rate are determined according to the Monod kinetic law (Monod, 1942). In these constraints, $q_{G,\max}$ $\left[\frac{\text{mol}}{\text{gDW} \cdot \text{h}} \right]$ and $q_{O,\max}$ $\left[\frac{\text{mol}}{\text{gDW} \cdot \text{h}} \right]$ are kinetically the maximal specific uptake rates for glucose and oxygen (where DW is the abbreviation of dry weight, mol the indication of mole, and h the abbreviation of hour), C_G [mol/L] and C_O [mol/L] the extracellular glucose and oxygen concentrations (with L the abbreviation of liter), while K_G [mol/L] and K_O [mol/L] are the Monod half-saturation constants for respectively glucose and oxygen. The optimization problem in Equation (6) is straightforward to solve as the PhPP in Figure 1 is a monotonically increasing function of both the glucose and oxygen uptake rate, implying that the specific glucose and oxygen uptake rates are equal to the upper boundaries in Equations (7, 8). Values for the above-mentioned parameters can be found in Table 1.

A Linear Metabolic Model for *E. coli* under Reference Environmental Conditions

As the PhPP contains much information about intracellular metabolic fluxes from its constituting FBAs, it is not appropriate to incorporate it in its original form into an IbM. Multiple evaluations of the whole intracellular reaction network would result in an excessive increase of the required IbM simulation run time. For this reason, the planes in the PhPP at a specific oxygen

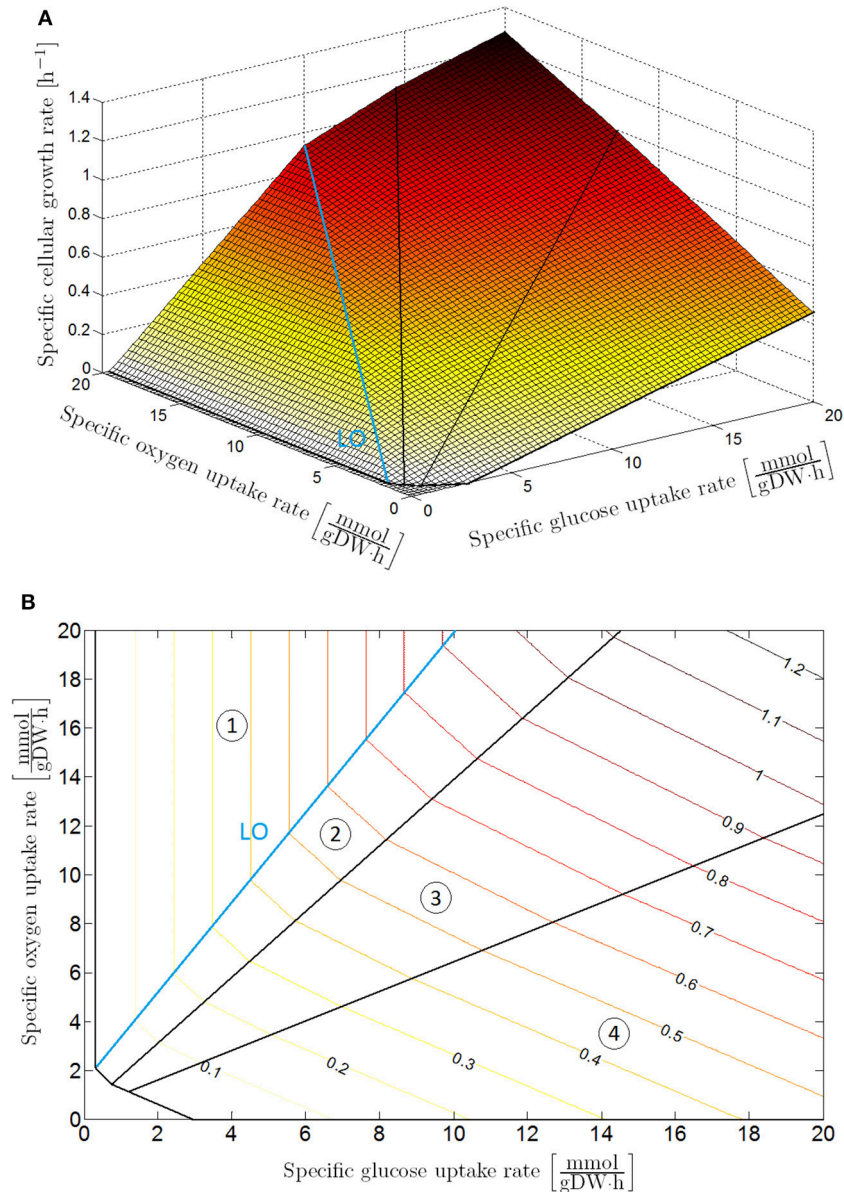


FIGURE 1 | Phenotypic phase plane analysis: specific cellular growth rate as a function of specific glucose and oxygen uptake rates with maximization of biomass growth as cellular objective, presented as **(A)** 3D plot and **(B)** contour plot. The phenotypic phase plane consists of four phases, each representing a different metabolic regime. In Sector 1 glucose is completely converted to CO_2 through the tricarboxylic (TCA) cycle. The other sectors are characterized by the secretion of weak acid cell products in the cellular environment: acetic acid in Sector 2; acetic and formic acid in Sector 3; acetic acid, formic acid and ethanol in Sector 4. On the boundary between Sector 1 and 2, glucose is converted to biomass at a maximal observed yield. For this reason, this boundary is indicated as the line of optimality (LO).

uptake rate are described by means of the linear growth law of Pirt (Schulze and Lipe, 1964; Pirt, 1965):

$$\mu = (q_G - m_G) \cdot Y_{X/G}, \quad (9)$$

with $q_G \left[\frac{\text{mol}}{\text{gDW} \cdot \text{h}} \right]$ the specific glucose uptake rate, $m_G \left[\frac{\text{mol}}{\text{gDW} \cdot \text{h}} \right]$ the maintenance coefficient, and $Y_{X/G} [\text{gDW/mol}]$ the biomass yield coefficient on glucose. The secretion rates of the main

acid metabolites (acetic, formic, and lactic acid) are expressed similarly:

$$q_i = Y_{i/G} \cdot q_G + q_i^0, \quad (10)$$

where $q_i \left[\frac{\text{mol}}{\text{gDW} \cdot \text{h}} \right]$ is the specific secretion rate of metabolite i , q_i^0 is the specific secretion rate at a zero glucose uptake rate and $Y_{i/G} [\text{mol/mol}]$ the production yield of metabolite i on glucose.

TABLE 1 | Parameter values.

Parameter	Value	Reference
$q_{G,max}$	$9.02 \cdot 10^{-3}$ mol/(gDW·h)	Portnoy et al., 2010
$q_{O,max}$	$16.49 \cdot 10^{-3}$ mol/(gDW·h)	Portnoy et al., 2010
K_G	$2.994 \cdot 10^{-6}$ mol/L	Ihssen et al., 2007
K_O	$0.121 \cdot 10^{-6}$ mol/L	Stolper et al., 2010

The Influence of pH and Weak Acids on the *E. coli* Metabolism

In the optimization problem in Equations (6–8), it is assumed that the cell aims to maximize its growth. This assumption is only valid for a non-stressing reference environment, i.e., a neutral M9 minimal medium enriched with glucose at 37°C. However, the cellular secretion of weak acid metabolites under oxygen-limited conditions in microbial biofilms and colonies constitutes an inhibiting factor for cellular growth and survival. The inhibiting effect of weak acid cell products on cellular growth is 2 fold: (i) dissociation of acid metabolites in the food environment leads to a decrease of the extracellular pH, and (ii) reintrusion of the lipophilic undissociated cell products into the cell results in an intracellular pH drop.

Under the stressing conditions of low extracellular pH values and the presence of undissociated acid cell products, the cellular objective changes to maximize survival chances. As a matter of fact, the cellular objective needs to be modified as

$$\max_{q_G, q_O} J(q_G, q_O, pH, [U_i]), \quad (11)$$

restating the optimization problem in Equations (6–8) as a multiparametric programming problem. However, the exact mathematical formulation of the cellular objective is unfortunately not known. For this reason, a more pragmatic approach is required.

Synergistic effects of low extracellular acidity and undissociated acid cell products in the environment can be taken into account in the maintenance coefficient in Equation (9):

$$m_G = m_{G,ref} + A \cdot \frac{[H^+] - 10^{-7}}{[H^+]_{min} - 10^{-7}} + B \cdot \sum_i \frac{[U_i]}{[U_i]_{min}}. \quad (12)$$

In this expression, the maintenance coefficient consists of three terms: (i) the reference maintenance coefficient $m_{G,ref}$ that can be derived from the reference PhPP in **Figure 1**, (ii) additional maintenance requirements due to an increase of the extracellular proton concentration $[H^+]$, and (iii) a supplementary effect of weak acid cell products in their undissociated form $[U_i]$. Microbial growth stops when the proton concentration reaches a critical value $[H^+]_{min}$. Analogous minimum inhibitory concentrations $[U_i]_{min}$ exist for the undissociated acid cell products. The mathematical constants A and B are calculated by replacing this expression for the maintenance coefficient in Equation (9).

The increase of the maintenance coefficient due to low extracellular pH values and the presence of undissociated acid cell

products does not only affect the microbial biomass growth, but also the secretion of metabolic products in Equation (10):

$$q_i = Y_{i/G} \cdot q_G + \frac{m_G}{m_{G,ref}} \cdot q_i^0, \quad (13)$$

ODD Description of the Developed IbM

The developed metabolic model is incorporated in the MICRODIMS IbM (Verhulst et al., 2011; Tack et al., 2015). This in-house developed IbM is adapted and extended to simulate the dynamics of microbial biofilms and submerged colonies. In this section, a general overview of the MICRODIMS simulator is described according to the first part of the standard ODD protocol of Grimm et al. (2006, 2010). Details about the specific MICRODIMS versions for the two considered case studies are included in the next section.

Model Purpose

The purpose of the new MICRODIMS versions is the simulation of chemical gradients and the resulting metabolic differentiation in *E. coli* biofilms and submerged colonies. The influence of this metabolic differentiation on the development of mature biofilms and colonies is investigated as well.

Entities, State Variables, and Scales

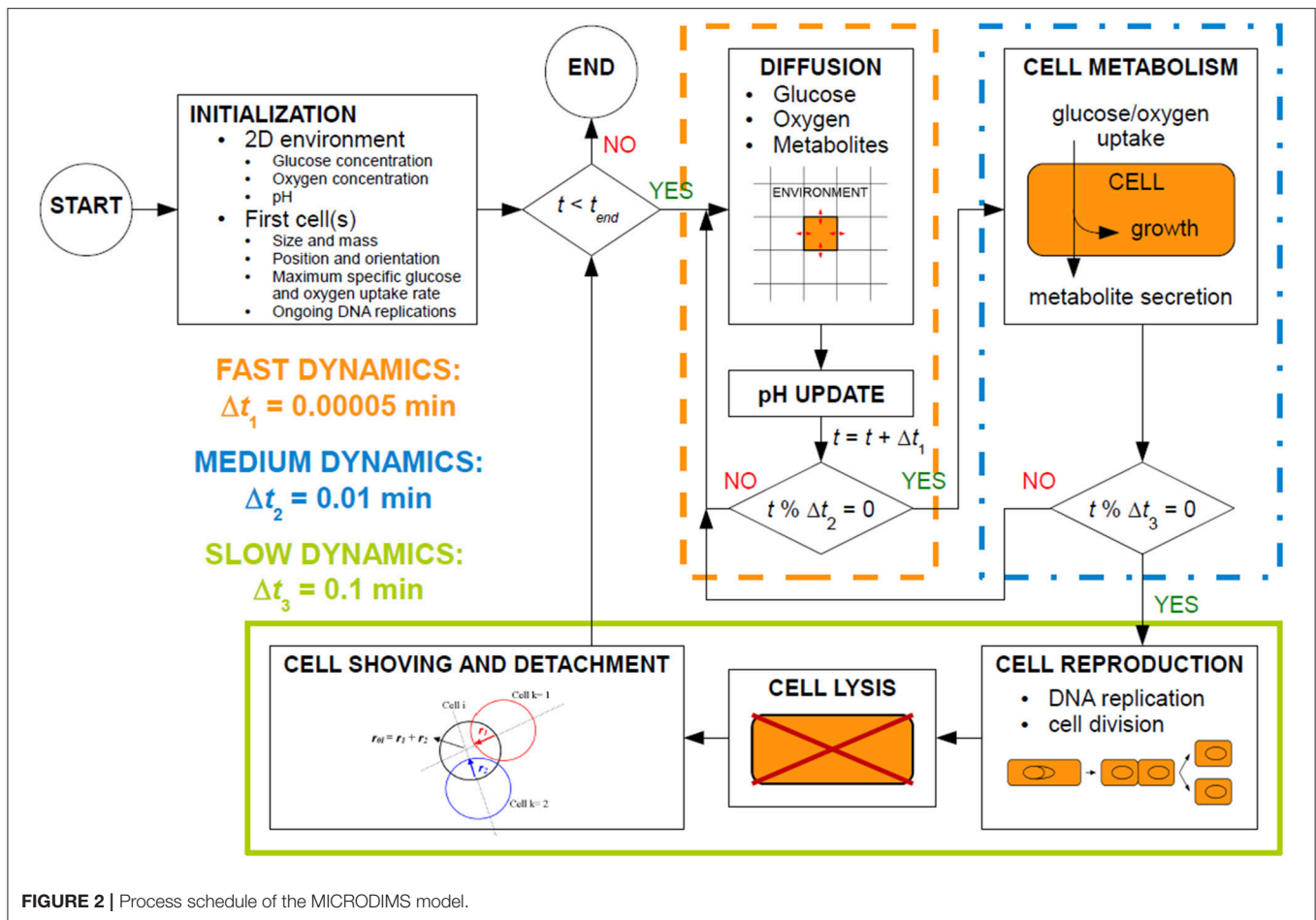
Microbial systems consist of two kinds of agents: the microbial cells and their surrounding environment.

The microbial cells contain the same state variables as in the previous MICRODIMS versions (Tack et al., 2015): cell mass and radius, spatial coordinates, maximum specific glucose and oxygen uptake rates and a list variable with information about the ongoing DNA replication cycles. In addition, an inclination vector is introduced to take the rod shape and orientation of *E. coli* into account.

The liquid environment is modeled as a two-dimensional space for the biofilm simulations, while the submerged colonies are simulated in a three-dimensional food environment. In both cases, the environment is discretized as a spatial grid. Each of the grid units is associated with a glucose, oxygen, acetic acid and formic acid concentration. To simulate chemical gradients at a microscopic level, the size of a grid unit needs to be in the same order of magnitude as a microbial cell, viz., 6 μm. The whole space has a dimension of 300 μm.

Process Overview and Scheduling

MICRODIMS consists of several interlinked subprocesses, as illustrated in **Figure 2**. These subprocesses exhibit different time dynamics (Picioreanu et al., 1999) and are executed at different time steps. In MICRODIMS, three time steps are used: (i) $\Delta t_1 = 0.00005$ min, a very short time step for the fast diffusion processes and the update of local pH values, (ii) $\Delta t_2 = 0.01$ min, an intermediate time interval for the metabolic processes of nutrient and oxygen uptake, biomass growth and metabolite secretion, and (iii) $\Delta t_3 = 0.1$ min, the long time step for slow processes such as cell reproduction, cell lysis, and cell movement. This cell movement consists of a shoving mechanism to avoid spatial overlap between the cells, and a detachment process for loosely bound biofilm cells. After the initiation of the simulation,



all the subprocesses are executed consecutively as presented in the simulation scheme in **Figure 2**.

Software

The MICRODIMS IbM has been implemented in the MASON multiagent simulation toolkit in Java (Luke et al., 2003, 2004, 2005). The strict separation between the execution of the model and graphical output increases the simulation speed in comparison to other IbM simulation toolkits, such as Repast Simphony.

RESULTS

Case Study I: Biofilm Growth

Over the last years, several models have been developed for the description of single species biofilm structures using information of genome-scale metabolic models (Biggs and Papin, 2013; Chen et al., 2016; Bauer et al., 2017). However, these models basically rely on one determining factor to explain the simulated biofilm morphologies at a mesoscopic level, namely the diffusion of nutrients/oxygen into and the diffusion of metabolic waste products out of the biofilm. In addition, the modeling unit in these cellular automaton models is the local microbial concentration in a small square of the environment. This spatial

resolution that is used to model the microbial cells, is too coarse to simulate morphological phenomena at a finer microscopic scale, such as the formation of cellular chains at the outer biofilm surface. To take these microscopic events into account, each cell needs to be modeled as a separate discrete entity in a realistic individual-based model, where the modeling unit is the microbial cell itself and direct microscopic interactions between the microbial cells (such as intercellular adhesion) can be taken into account. The emergence of these microscopic morphological phenomena in *E. coli* biofilms is described in this case study.

Model Details

Besides the incorporation of the developed metabolic model, other submodels in the basic MICRODIMS module of Verhulst et al. (2011) needed to be slightly adapted or included to simulate the characteristic dynamics of biofilms on food processing surfaces. In this subsection, these adaptations, and extensions are described in more detail.

Initialization and boundary conditions

The initial environment is neutral and does not contain any initial weak acid cell products. Initially, the oxygen concentration is taken to be the saturated oxygen concentration in water (6.73 mg/L) in order to clearly demonstrate the transition from

aerobic to anaerobic environmental conditions in the biofilm. Furthermore, the environment has a glucose concentration of 0.1 g/L in order to ensure that the simulation starts with a metabolic regime in region 1 of the PhPP (see **Figure 1**). In reality, the initial glucose concentration is typically higher (1 g/L) implying that the simulation would start in metabolic regime 2, 3, or 4 with a very high production of weak acid cell products already in the initial stages of the simulation. Consequently, the simulation would not demonstrate the full transition from aerobic to anaerobic conditions. In the environment, biofilm growth starts from three cells randomly situated at the substratum surface. This substratum is situated at the lower environmental boundary. It is modeled by means of a Neumann boundary condition, i.e., any chemical gradients or fluxes are absent at this insulating surface. In contrast, the opposite upper boundary of the environment is in contact with the bulk medium and is characterized by a Dirichlet boundary condition with constant concentrations. In this way, the bulk medium is represented as an infinite reservoir of nutrients and oxygen, and an infinite sink for metabolic waste products. The remaining two side boundaries are wrapped toward each other, creating periodic boundary conditions.

Diffusion

Diffusion is modeled according to the second law of Fick:

$$\frac{\partial C_i}{\partial t} = D_i \cdot \left(\frac{\partial^2 C_i}{\partial x^2} + \frac{\partial^2 C_i}{\partial y^2} \right), \quad (14)$$

with C_i [mol/L] the concentration of substance i in the liquid phase, D_i [$\mu\text{m}^2/\text{min}$] the diffusion coefficient of substance i , x [μm] and y [μm] the spatial dimensions, and t [min] the temporal dimension. This equation has no analytical solution in combination with the initial and boundary conditions defined in the previous paragraph. For this reason, it is discretized according to an explicit Forward-Time Central-Space (FTCS) numerical scheme (Roache, 1972). To incorporate the restrictive effect of EPS and surrounding microbial cells on the diffusion processes, the diffusivity D_i is deliberately decreased by a factor of 50 in the biofilm to provide a good match between the simulated biofilm morphologies and experimentally observed biofilm structures, as there are unfortunately no direct experimental data available for this decrease in diffusivity.

pH update

Local pH values are calculated from the acid cell product concentrations and their dissociation constants. This procedure has been explained in Tack et al. (2014).

Glucose and oxygen uptake

Glucose and oxygen uptake are modeled according to the Monod kinetic model (Monod, 1942). A normally distributed stochastic element with a coefficient of variation of 0.10 has been superposed on this kinetic model, to incorporate biological variability and growth asynchrony (Schaechter et al., 1962; Koch, 1993).

Cell reproduction

The DNA replication and cell division processes are simulated according to an adapted version of the model of Donachie (1968), that has been developed in Tack et al. (2014, 2015). Daughter cells are placed along the orientation of their mother cell, upon which a uniformly-distributed random deviation angle of maximally $\pi/8$ radians is superposed.

Cell movement

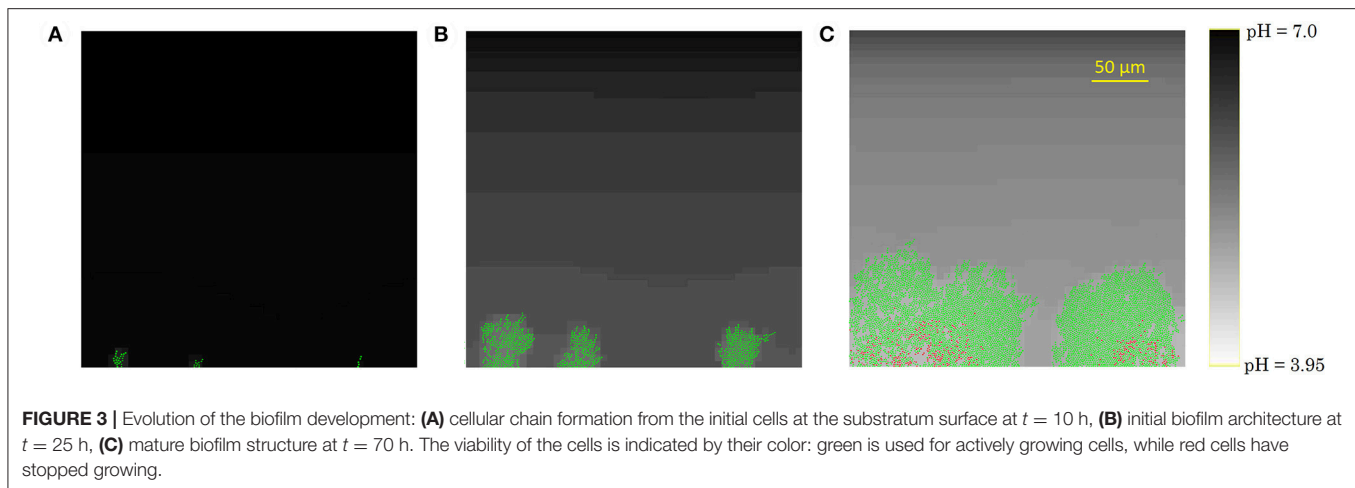
Spatial overlap between neighboring cells is avoided by means of a cell shoving mechanism (Kreft et al., 1998). Detachment of cells from the biofilm's outer surface occurs when these cells are not properly aligned with their neighbors. Cell adhesion factors on the cell surface, such as Antigen 43 (Ag43) are mainly concentrated around the cell poles, implying that only the cell poles take part in intercellular adhesion interactions (Vejborg and Klemm, 2009). If a cell has less than four neighbors and is not attached to the substratum surface, it is assumed that this cell is situated at the biofilm exterior. To stay attached to the biofilm, the orientation vectors of this cell and one of its neighbors need to be aligned within a maximal detachment angle θ_{\max} of $\pi/6$ with the line between the centers of these two cells.

Simulation Results

Biofilm development

The development of the biofilm structure in the IbM simulation is presented in **Figure 3**. Initially, cellular chains form from the initial cells at the substratum surface, which has been experimentally observed (Vejborg and Klemm, 2009). After this initial stage, the biofilm environment gets oxygen-depleted and acidified at the substratum surface, mainly due to acetic acid production and to a lesser extent due to the formic acid secretion. Lactic acid production was not observed in the simulations as the oxygen concentration never dropped to a completely anaerobic level, which is a necessary condition for lactic acid secretion by the microbial cells. This acidification inhibits cellular growth and survival at the substratum, leading to a mature biofilm structure with mushroom-shaped pillars separated by water-filled channels. These channels are more acidified than the bulk medium, inhibiting cell growth. The mushroom-shaped architecture of mature biofilms has also been observed experimentally (Reisner et al., 2003).

Finally, due to the acidic cellular stress, cells stop growing at the substratum, indicated by the red cell color in **Figure 3C**. Ultimately, these growth-compromised cells die, resulting in biofilm detachment. Experimental studies of *E. coli* biofilm growth have demonstrated the failure of biofilm formation and the detachment of already existing biofilms under anaerobic conditions (Colón-González et al., 2004). The absence of biofilm formation under anaerobic conditions has been explained by a reduced production of type 1 pili, inhibiting cell-substratum and cell-cell adhesion interactions. However, this explanation is not suitable for the detachment of already existing biofilms in which type 1 pili are abundantly available. This IbM simulation shows that acidification of the biofilm environment at the substratum surface can play a significant role in the biofilm detachment process as well.



Cell detachment

As the cell-cell adhesion factors on the cell surface are mainly concentrated around the cell poles, cells at the biofilm outer surface need to be well-aligned with their neighbors to avoid detachment from the biofilm due to flow shear forces. This results in the formation of cellular chains at the biofilm exterior surface (Vejborg and Klemm, 2009). To investigate the influence of the cell detachment process on the biofilm development and morphology, the maximal detachment angle θ_{max} is varied over a range of values. The results of this analysis are summarized in **Figure 4**. At higher values of θ_{max} , i.e., less restrictive detachment conditions, a thicker biofilm structure with more densely packed cells emerges, causing more severe acidification and cell death at the substratum surface. Less cellular chains protrude from the exterior biofilm surface. For lower values of θ_{max} , the opposite trend is observed as more cells detach from the biofilm and disperse into the bulk medium: the biofilm structure is thin and more open with many cellular chains. The biofilm structure at a maximal detachment angle of approximately $\pi/6$ corresponds best with experimental observations of *E. coli* biofilms (see e.g., Danese et al., 2000; Reisner et al., 2003; Veborg and Klemm, 2009).

Initial cell affinity for the substratum surface

For the initial attachment of planktonic cells to the substratum, these cells need to overcome electrostatic repulsive forces from the substratum, that is often conditioned by the adsorption of various solutes to avoid biofilm growth. High affinities of dispersed cells in the bulk medium for the substratum lead to high densities of initial cells at the substratum surface. Increasing the number of initial cells at the substratum in the simulation leads to more continuous and flat biofilm structures, as illustrated in **Figure 5**. Both mushroom-shaped pillar structures for low initial cell numbers and more continuous structures at higher cell-surface affinities have been experimentally observed (see respectively, Reisner et al., 2003; Veborg and Klemm, 2009). As a consequence, the substratum surface conditioning treatment plays a determining role in the formation of specific biofilm structures.

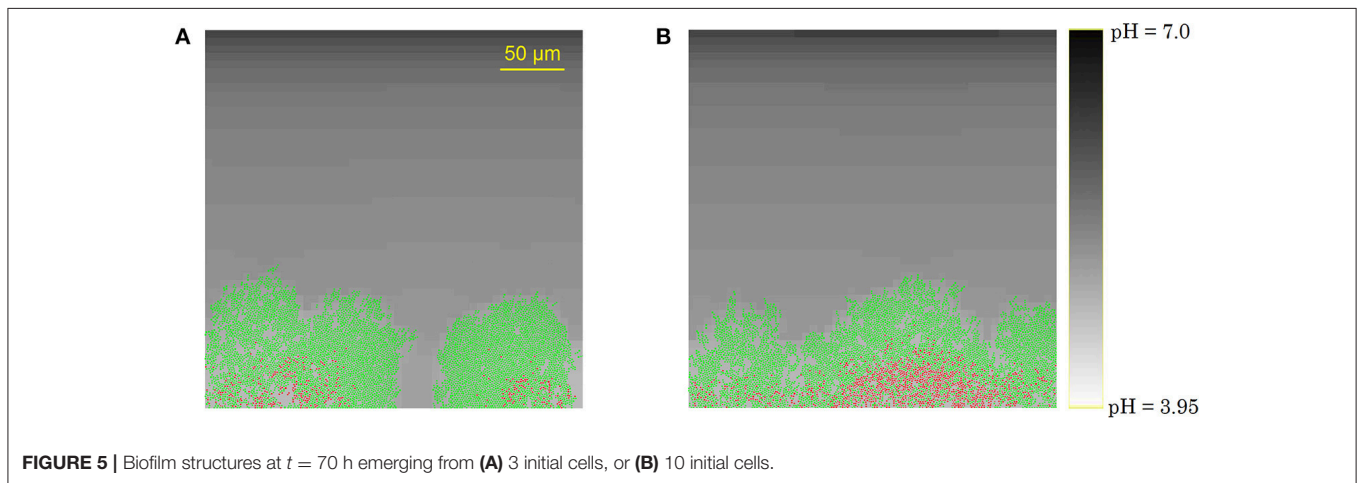
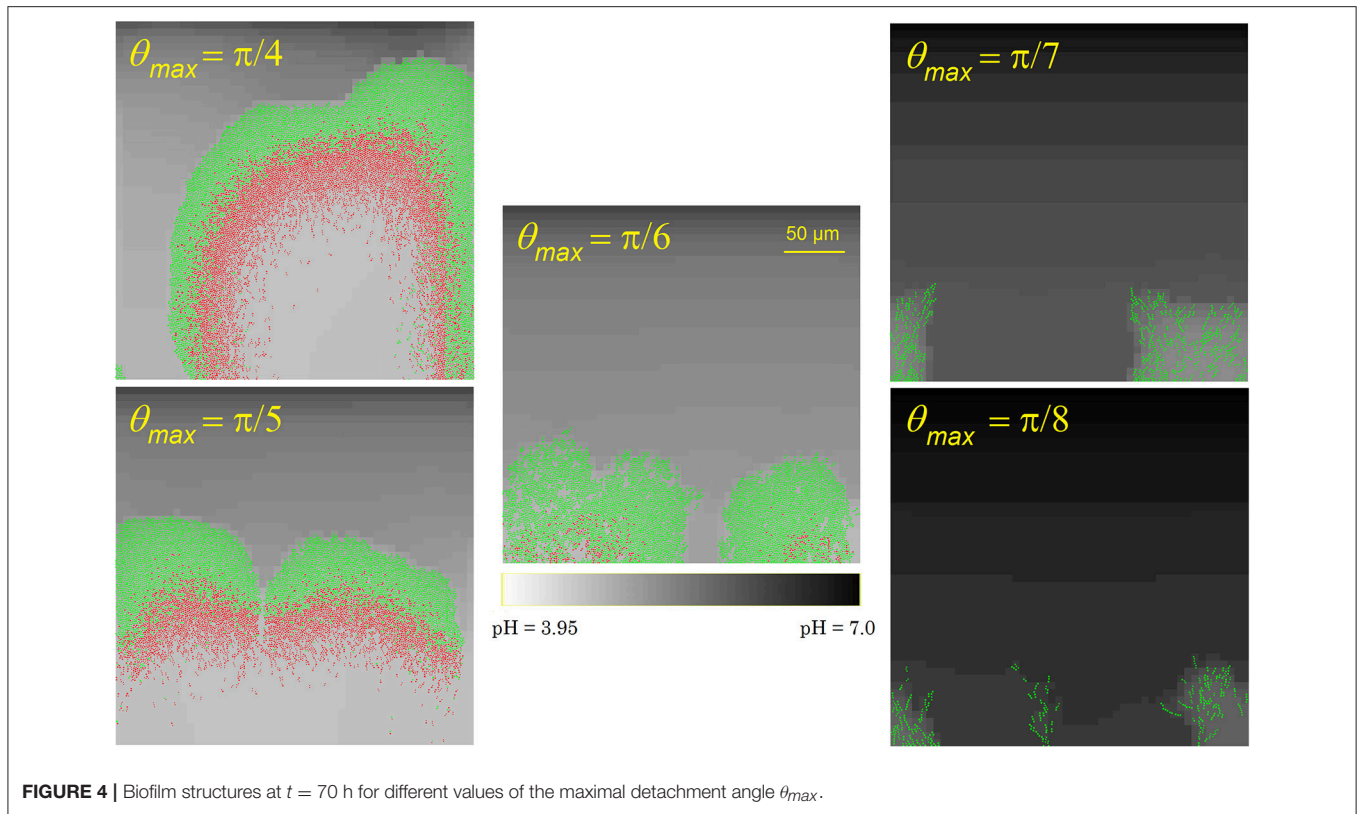
Case Study II: Submerged Colony Growth

Most individual-based models for colony behavior are developed to describe phenomena that are experimentally observed for colonies on the surface of semi-solid food media. It is however much more difficult to experimentally observe dynamics of submerged colonies that are growing in mixed food products (Boons et al., 2001). For this reason, this case study focuses on submerged colony growth behavior and its connection to surface colony dynamics.

Model Details

For the simulation of a submerged colony in semi-solid food products, the food system is modeled in principle as a three-dimensional environment to account for complex geometry as well, with the initial cell in the center. Note that the simulation of the growth of one submerged colony can be reduced to a two-dimensional problem in case of non-complex geometry. In such case, the two horizontal dimensions are equivalent, so only one horizontal dimension and the vertical dimension are needed if appropriate scaling of the spatial density of colonies from 3D to 2D is applied.

The simulation of the diffusion processes in the environment cannot be reduced to a two-dimensional problem, as substances diffuse from or to the colony in the three spatial dimensions. However, updating the local concentrations in a complete 3D environment would be too computationally expensive. Therefore, only a central layer of the environment has been simulated, indicated in blue in **Figure 6**. Nevertheless, diffusion interactions in the perpendicular direction on this layer have been taken into account. For these interactions, the concentrations of environmental substances in the layers above and below the central layer, indicated in yellow in **Figure 6**, need to be determined. Under the assumption that the isoconcentration planes of chemical substances around the submerged colony can be locally approximated by concentric spheres around the environmental origin, the concentrations in the environmental units in the yellow layers are deducible from goniometric principles and interpolation between concentrations in the central layer. More specifically, the concentration of substance



i in the yellow layers is expressed by means of the following expressions:

$$\begin{aligned}
 C_i(j, k, l-1) &= C_i(j, k, l+1) = \\
 &(1 - \text{sign}(\Delta_y) \cdot \Delta_y) \cdot \\
 &((1 - \text{sign}(\Delta_x) \cdot \Delta_x) \cdot C_i(j, k, l) + \\
 &\text{sign}(\Delta_x) \cdot \Delta_x \cdot C_i(j + \text{sign}(\Delta_x), k, l)) + \\
 &\text{sign}(\Delta_y) \cdot \Delta_y \cdot \\
 &((1 - \text{sign}(\Delta_x) \cdot \Delta_x) \cdot C_i(j, k + \text{sign}(\Delta_y), l) + \\
 &\text{sign}(\Delta_x) \cdot \Delta_x \cdot C_i(j + \text{sign}(\Delta_x), k + \text{sign}(\Delta_y), l)), \quad (15)
 \end{aligned}$$

where $C_i(j, k, l)$ is the concentration of substance i in the environmental unit with the coordinates (j, k, l) , and

$$\Delta_x = \Delta \cdot \frac{j}{\sqrt{j^2 + k^2}}, \quad (16)$$

$$\Delta_y = \Delta \cdot \frac{k}{\sqrt{j^2 + k^2}} \quad (17)$$

$$\Delta = \sqrt{j^2 + k^2 + 1} - \sqrt{j^2 + k^2}, \quad (18)$$

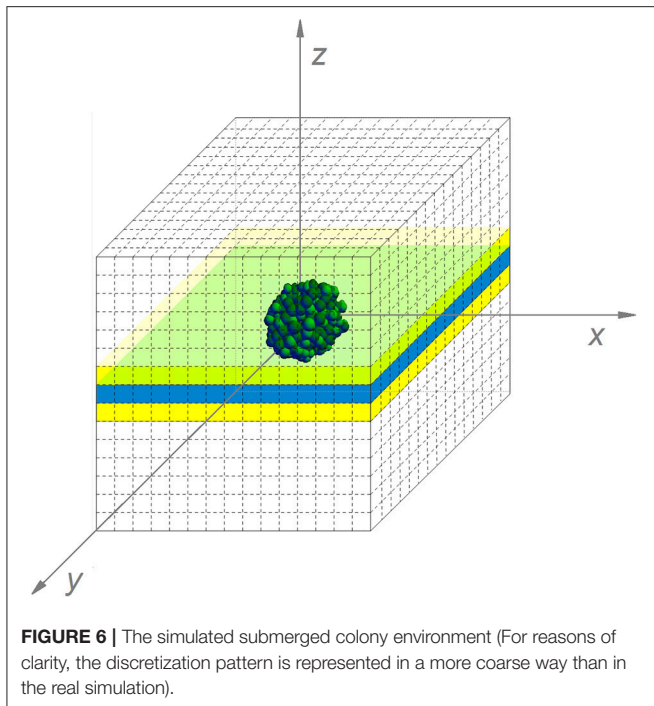


FIGURE 6 | The simulated submerged colony environment (For reasons of clarity, the discretization pattern is represented in a more coarse way than in the real simulation).

Initialization and boundary conditions

The simulation starts with one initial cell which is located in the origin of the environment. The environmental boundaries are characterized by constant chemical concentrations.

Diffusion

In the central environmental layer, diffusion processes are modeled according to the second law of Fick in three dimensions, discretized by means of the FTCS numerical scheme. For numerical stability reasons, a smaller time step $\Delta t_1 = 0.00002$ min is required in this explicit scheme for three-dimensional diffusion. For glucose and chemical compounds of the same molecular size as glucose, the diffusion coefficients in a 5% (w/v) agarose gel environment are approximately 75% of their normal diffusivities in water (Hooijmans et al., 1990; Andersson and Öste, 1994; Azevedo and Oliveira, 1995). The oxygen diffusivity is hardly effected by the agarose concentration (Guaccio et al., 2008).

Cell movement

As the cells cannot detach from the colony due to motility limitations, the spatial organization of the colony cells is only determined by cell shoving to avoid spatial overlap between neighboring cells.

Simulation Results

Figure 7 illustrates the growth of a submerged colony, starting from one initial cell in the origin of the environment. The colony remains more or less circular over its whole evolution, confirming the assumption that has been used to obtain the expressions in Equations (15–18). In the colony center, diffusion limitations lead to the accumulation of weak acid cell products,

mainly acetic acid. The resulting pH drop causes cell lysis, indicated by the emergence of a no-growth zone and the disappearance of cells in the colony center. Due to the emergence of these no-growth conditions in the colony center, the initially superlinear growth of the colony radius slows down, resulting in a linear colony radius increase, as presented in **Figure 8**. This linear radius increase has been observed for quasi-two-dimensional surface colonies as well (Kamath and Bungay, 1988; Wimpenny et al., 1995; Mitchell and Wimpenny, 1997), indicating that easily-observable qualitative trends in two-dimensional surface colony dynamics can be representative for the behavior of three-dimensional submerged colonies that require much more advanced monitoring techniques.

DISCUSSION

An in-house developed simulator for individual based modeling of microbial dynamics has been extended with a metabolic model for *E. coli* expressing specific cellular growth rate and metabolic secretion rates as a function of the local extracellular pH and the concentration of undissociated cell products, covering all metabolic regimes from anaerobic respiration to anaerobic fermentation.

From the simulations, it is observed that *E. coli* biofilm dynamics are mainly determined by metabolic differentiation due to concentration gradients of weak acid cell products, cell detachment leading to persistent cell chains, and the affinity of planktonic cells for the substratum surface. Experimental studies also suggest a role for quorum sensing by the production or addition of autoinducer 2 (AI-2) signaling molecules, or through the production of *N*-acyl-L-homoserine lactones (AHL) by other species (DeLisa et al., 2001; Sperandio et al., 2001; González Barrios et al., 2006; Beloin et al., 2008). The effect of quorum sensing mechanisms on biofilm and microbial colony behavior has been investigated in other IBM simulations (see e.g., Tang et al., 2007; Nadell et al., 2008; Melke et al., 2010; Jang et al., 2012). In addition, cross-feeding interactions between the *E. coli* cells, such as the consumption of the produced acetate by cells at the substratum surface (Oh et al., 2002), has not been taken into account as this acetate uptake only occurs under low environmental concentrations of glucose. In the performed simulations, there is no local glucose depletion at the substratum surface. Furthermore, cells under stressing conditions may exhibit additional complex behavior and resilience by going into a dormant state (Agafonov et al., 2001). This transition to dormancy has not been taken into account in the simulations. The scope of this case study is in fact limited to the simulation of mature biofilm morphologies and the emergence of these morphologies is solely dependent on cellular events at the outer biofilm surface where the cells are not hibernated. Finally, it should be noted that the formation of cellular chains is a typical phenomenon in *E. coli* biofilms, which has not been observed for other species such as *Pseudomonas aeruginosa*. It is therefore not recommended to extrapolate the applied cell adhesion model to other species than *E. coli*.

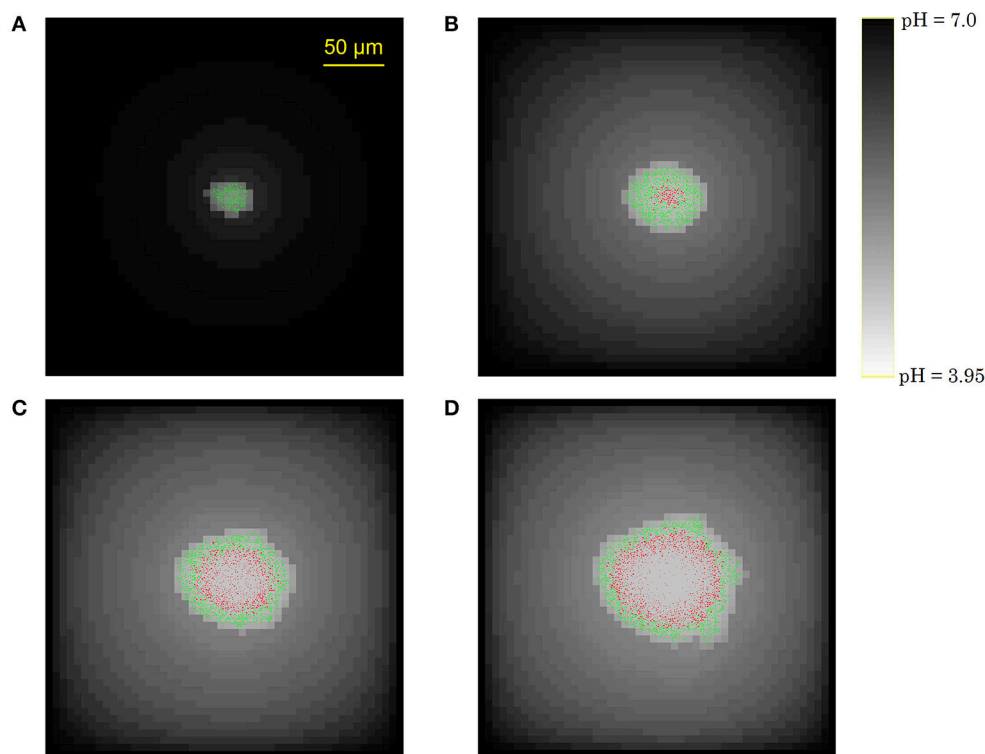


FIGURE 7 | Evolution of the submerged colony development: **(A)** initial phase without severe growth-inhibiting conditions, **(B)** emergence of a central no-growth zone, **(C,D)** cell lysis in the colony center.

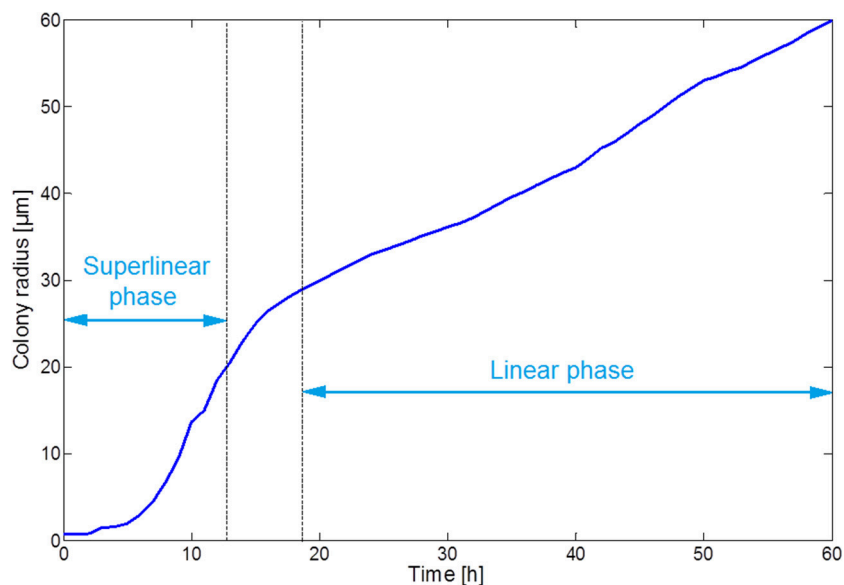


FIGURE 8 | Evolution of the colony radius.

The submerged colony simulations demonstrate that the initially homogeneous concentration of oxygen at saturation level decreases sharply over time in the colony center, while the oxygen concentration at the boundaries remains constant. However, it

should be noted that these constant boundary conditions are a strong simplification of the conditions in real food systems, as the overall oxygen availability in food products strongly depends on the distance from the food surface (Noriega et al., 2008).

The model may probably also be used for other food pathogens which are similar to *E. coli*, such as the gram-negative rod-shaped *Salmonella Typhimurium*. However, not enough microscopic data are available about this food pathogen to validate this assertion.

CONCLUSIONS

Mature microbial communities of clustered cells, such as biofilms or colonies, are of paramount industrial and medical importance. Such microbial communities are characterized by metabolic differentiation among the constituting microorganisms due to diffusion limitations and chemical gradients in their environment. Due to the metabolic differences between the cells according to their position in the community, it is most appropriate to simulate these biosystems by means of an IbM with the microbial cell as basic modeling unit.

In this article, an in-house developed IbM platform for microbial dynamics, MICRODIMS, has been extended with a new metabolic model for the simulation of two-dimensional biofilm dynamics on abiotic food processing surfaces and three-dimensional submerged colony behavior in semi-solid food products. This metabolic model covers all metabolic regimes from aerobic respiration to anaerobic fermentation and expresses the specific cellular growth rate and metabolic secretion rates as a function of the local extracellular pH and the concentration of undissociated cell products. This model allows to study metabolic differentiation due to oxygen gradients in the development of *E. coli* cell communities, whereby low local oxygen concentrations lead to cellular secretion of weak acid products.

This metabolic model is expressed as a multiparametric programming problem, in which the influence of low extracellular pH values and the presence of undissociated acid cell products in the environment has been taken into account.

Two case studies have been elaborated in this article, using the MICRODIMS simulator: (i) biofilm growth on a substratum surface and (ii) submerged colony growth in a semi-solid mixed food product.

In the biofilm case study, accumulation of weak acid cell products and a concomitant pH drop occur at the substratum

surface. This leads to cell lysis and biofilm detachment from the substratum. Apart from the metabolic cellular differentiation, biofilm dynamics are mainly determined by the cell detachment process at the biofilm outer surface, inducing the formation of protruding cell chains. The acidification of the biofilm environment and the emergence of typical mushroom-shaped morphologies of mature biofilms and the formation of cellular chains at the exterior surface of the biofilm are observed. In addition, high affinity of planktonic cells in the bulk medium for the substratum surface results in a high density of initial cells at the substratum and a more continuous and flat biofilm structure. The simulations show that these morphological phenomena are respectively dependent on the initial affinity of pioneer cells for the substratum surface and the cell detachment process at the outer surface of the biofilm.

The submerged colony case study demonstrates the development of a central no-growth zone with a sharp decline of the local pH, comparable to the pH drop at the substratum surface in the biofilm simulations. Cellular growth is limited to a thin band of cells at the colony periphery, resulting in a linear increase of the colony radius over time.

AUTHOR CONTRIBUTIONS

Authors jointly designed the study and wrote the manuscript. IT implemented the algorithms and performed the computations. JV supervised the study. All authors have read and approved the final manuscript.

FUNDING

The research of IT is funded by Ph.D. grant IWT SB-111565 of the Agency for Innovation by Science and Technology (IWT). IH is supported by FWO-SB grant 1S54217N of the Research Foundation-Flanders. In addition, this work is supported by project FWO-G.0930.13 of the Research Foundation-Flanders (FWO), project PFV/10/002 (Center of Excellence OPTEC-Optimization in Engineering) of the KU Leuven Research Fund, and the Belgian Program on Interuniversity Poles of Attraction, initiated by the Belgian Federal Science Policy Office (IAP Phase VII-19 DYSCO).

REFERENCES

- Agafonov, D., Vyacheslav, A., and Spirin, A. (2001). Ribosome-associated protein that inhibits translation at the aminoacyl-tRNA binding stage. *EMBO Rep.* 2, 399–402. doi: 10.1093/embo-reports/kve091
- Andersson, A. P., and Öste, R. E. (1994). Diffusivity data of an artificial food system. *J. Food Eng.* 23, 631–639. doi: 10.1016/0260-8774(94)90117-1
- Azevedo, I. C. A., and Oliveira, F. A. R. (1995). A model food system for mass transfer in the acidification of cut root vegetables. *Int. J. Food Sci. Technol.* 30, 473–483. doi: 10.1111/j.1365-2621.1995.tb01394.x
- Bauer, E., Zimmermann, J., Baldini, F., Thiele, I., and Kaleta, C. (2017). Individual-based metabolic modeling of heterogeneous microbes in complex communities. *PLoS Comput. Biol.* 13:e1005544. doi: 10.1371/journal.pcbi.1005544
- Beloin, C., Roux, A., and Ghigo, J.-M. (2008). “*Escherichia coli* biofilms,” in *Bacterial Biofilms*, Vol. 322 of *Current Topics in Microbiology and Immunology*, ed T. Romeo, (Berlin; Heidelberg: Springer-Verlag), 249–289.
- Benedetti, I., de Lorenzo, V., and Nikel, P. (2016). Genetic programming of catalytic *Pseudomonas putida* biofilms for boosting biodegradation of haloalkanes. *Metab. Eng.* 33, 109–118. doi: 10.1016/j.ymben.2015.11.004
- Biggs, M. B., and Papin, J. A. (2013). Novel multiscale modeling tool applied to *Pseudomonas aeruginosa* biofilm formation. *PLoS ONE* 8:e78011. doi: 10.1371/journal.pone.0078011
- Boons, K., Noriega, E., David, C., Hofkens, J., and Van Impe, J. (2001). “Effect of heterogeneous microstructure on the distribution and morphology of *Escherichia coli* colonies,” in *Proceedings of InterM 2013*, 10–13 October 2013 (Antalya).

- Buchanan, R. L. (1993). Predictive food microbiology. *Trends Food Sci. Technol.* 4, 6–11. doi: 10.1016/S0924-2244(05)80004-4
- Chen, J., Gomez, J. A., Hffner, K., Phalak, P., Barton, P. I., and Henson, M. A. (2016). Spatiotemporal modeling of microbial metabolism. *BMC Syst. Biol.* 10:21. doi: 10.1186/s12918-016-0259-2
- Colón-González, M., Méndez-Ortiz, M. M., and Membrillo-Hernández, J. (2004). Anaerobic growth does not support biofilm formation in *Escherichia coli* K-12. *Res. Microbiol.* 155, 514–521. doi: 10.1016/j.resmic.2004.03.004
- Costerton, J. W. (1995). Overview of microbial biofilms. *J. Ind. Microbiol.* 15, 137–140. doi: 10.1007/BF01569816
- Costerton, J. W., Stewart, P. S., and Greenberg, E. P. (1999). Bacterial biofilms: a common cause of persistent infections. *Science* 284, 1318–1322. doi: 10.1126/science.284.5418.1318
- Danese, P. N., Pratt, L. A., and Koller, R. (2000). Exopolysaccharide production is required for development of *Escherichia coli* K-12 biofilm architecture. *J. Bacteriol.* 182, 3593–3596. doi: 10.1128/JB.182.12.3593-3596.2000
- DeLisa, M. P., Wu, C. F., Wang, L., Valdes, J. J., and Bentley, W. E. (2001). DNA microarray-based identification of genes controlled by autoinducer 2-stimulated quorum sensing in *Escherichia coli*. *J. Bacteriol.* 183, 5239–5247. doi: 10.1128/JB.183.18.5239-5247.2001
- Dens, E. J., Bernaerts, K., Standaert, A. R., Kreft, J.-U., and Van Impe, J. F. (2005). Cell division theory and individual-based modeling of microbial lag: Part II. Modeling lag phenomena induced by temperature shifts. *Int. J. Food Microbiol.* 101, 319–332. doi: 10.1016/j.jfoodmicro.2004.11.017
- Donachie, W. D. (1968). Relationship between cell size and time of initiation of DNA replication. *Nature* 219, 1077–1079. doi: 10.1038/2191077a0
- Edwards, J. S., Ibarra, R., and Palsson, B. Ø. (2001). *In silico* predictions of *Escherichia coli* metabolic capabilities are consistent with experimental data. *Nat. Biotechnol.* 19, 125–130. doi: 10.1038/84379
- EFSA and ECDC (2015). The European Union summary report on trends and sources of zoonoses, zoonotic agents and food-borne outbreaks in 2013. *EFSA J.* 13:3991. doi: 10.2903/j.efsa.2015.3991
- Feist, A. M., Henry, C. S., Reed, J. L., Krummenacker, M., Joyce, A. R., Karp, P. D., et al. (2007). A genome-scale metabolic reconstruction for *Escherichia coli* K-12 MG1655 that accounts for 1260 ORFs and thermodynamic information. *Mol. Syst. Biol.* 3:121. doi: 10.1038/msb4100155
- Feist, A. M., and Palsson, B. Ø. (2010). The biomass objective function. *Curr. Opin. Microbiol.* 13, 344–349. doi: 10.1016/j.mib.2010.03.003
- Ferrier, R., Hezard, B., Lintz, A., Stahl, V., and Augustin, J.-C. (2013). Combining individual-based modeling and food microenvironment descriptions to predict the growth of *Listeria monocytogenes* on smear soft cheese. *Appl. Environ. Microbiol.* 79, 5870–5881. doi: 10.1128/AEM.01311-13
- Ginovart, M., López, D., and Valls, J. (2002). INDISIM, an individual-based discrete simulation model to study bacterial cultures. *J. Theor. Biol.* 214, 305–319. doi: 10.1006/jtbi.2001.2466
- González Barrios, A. F., Zuo, R., Hashimoto, Y., Yang, L., Bentley, W. E., and Wood, T. K. (2006). Autoinducer 2 controls biofilm formation in *Escherichia coli* through a novel motility quorum-sensing regulator (MqsR, B3022). *J. Bacteriol.* 188, 305–316. doi: 10.1128/JB.188.1.305-316.2006
- Grimm, V. (1999). Ten years of individual-based modelling in ecology: what have we learned and what could we learn in the future? *Ecol. Model.* 115, 129–148. doi: 10.1016/S0304-3800(98)00188-4
- Grimm, V., Berger, U., Bastiansen, F., Eliassen, S., Ginot, V., Giske, J., et al. (2006). A standard protocol for describing individual-based and agent-based models. *Ecol. Model.* 198, 115–126. doi: 10.1016/j.ecolmodel.2006.04.023
- Grimm, V., Berger, U., DeAngelis, D. L., Polhill, J. G., Giske, J., and Railsback, S. F. (2010). The ODD protocol: a review and first update. *Ecol. Model.* 221, 2760–2768. doi: 10.1016/j.ecolmodel.2010.08.019
- Grimm, V., and Railsback, S. F. (2005). *Individual-Based Modeling and Ecology*. Princeton Series in Theoretical and Computational Biology (Princeton, NJ: Princeton University Press).
- Grimm, V., Wyszomirski, T., Aikman, D., and Uchmański, J. (1999). Individual-based modelling and ecological theory: synthesis of a workshop. *Ecol. Model.* 115, 129–148. doi: 10.1016/S0304-3800(98)00186-0
- Guaccio, A., Borselli, C., abd Oliviero, O., and Netti, P. A. (2008). Oxygen consumption of chondrocytes in agarose and collagen gels: a comparative analysis. *Biomaterials* 29, 1484–1493. doi: 10.1016/j.biomaterials.2007.12.020
- Hooijmans, C. M., Geraats, S. G. M., van Neil, E. W. J., Robertson, L. A., and Heijnen, J. (1990). Determination of growth and coupled nitrification/denitrification by immobilized thiosphaera pantotropha using measurements and modeling of oxygen profiles. *Biotechnol. Bioeng.* 36, 931–939. doi: 10.1002/bit.260360908
- Ihssen, J., Grasselli, E., Bassin, C., François, P., Piffaretti, J.-C., Köster, W., et al. (2007). Comparative genomic hybridization and physiological characterization of environmental isolates indicate that significant (eco-)physiological properties are highly conserved in the species *Escherichia coli*. *Microbiology* 153, 2052–2066. doi: 10.1099/mic.0.2006/002006-0
- Jang, S. S., Oishi, K. T., Egbert, R. G., and Klavins, E. (2012). Specification and simulation of synthetic multicelled behaviors. *ACS Synth. Biol.* 1, 365–374. doi: 10.1021/sb300034m
- Kamath, R. S., and Bungay, H. R. (1988). Growth of yeast colonies on solid media. *J. Gen. Microbiol.* 134, 3061–3069. doi: 10.1099/00221287-134-11-3061
- Koch, A. L. (1993). Biomass growth rate during the prokaryote cell cycle. *Crit. Rev. Microbiol.* 19, 17–42. doi: 10.3109/10408419309113521
- Kreft, J.-U., G., B., and Wimpenny, J. W. T. (1998). BacSim, a simulator for individual-based modelling of bacterial colony growth. *Microbiology* 144, 3275–3287. doi: 10.1099/00221287-144-12-3275
- Luke, S., Balan, G., Panait, L., Cioffi-Revilla, C., and Paus, S. (2003). “MASON: A Java multi-agent simulation library,” in *Proceedings of the Agent 2003 Conference on Challenges in Social Simulation*, ed M. Clemmons (Chicago, IL: Argonne National Laboratory), 49–64.
- Luke, S., Cioffi-Revilla, C., Panait, L., and Sullivan, K. (2004). “MASON: A new multi-agent simulation toolkit,” in *Proceedings of Eight Annual Users/Researchers Meeting (SwarmFest 2004)* (Ann Arbor, MI: Center for the Study of Complex Systems, University of Michigan).
- Luke, S., Cioffi-Revilla, C., Panait, L., Sullivan, K., and Balan, G. (2005). MASON: A multiagent simulation environment. *Simulation* 82, 517–527. doi: 10.1177/0037549705058073
- Melke, P., Sahlin, P., Levchenko, A., and Jönsson, H. (2010). A cell-based model for quorum sensing in heterogeneous bacterial colonies. *PLoS Comput. Biol.* 6:e1000819. doi: 10.1371/journal.pcbi.1000819
- Mitchell, A. J., and Wimpenny, J. W. T. (1997). The effects of agar concentration on the growth and morphology of submerged colonies of motile and non-motile bacteria. *J. Appl. Microbiol.* 83, 76–84. doi: 10.1046/j.1365-2672.1997.00192.x
- Monod, J. (1942). *Recherches sur la Croissance des Cultures bactériennes*. Paris: Hermann.
- Nadell, C. D., Xavier, J. B., Levin, S. A., and Foster, K. R. (2008). The evolution of quorum sensing in bacterial biofilms. *PLoS Biol.* 6:e14. doi: 10.1371/journal.pbio.0060014
- Noriega, E., Laca, A., and Díaz, M. (2008). Modelling of diffusion-limited growth for food safety in simulated cheeses. *Food Bioprod. Process.* 86, 122–129. doi: 10.1016/j.fbp.2008.03.005
- Oh, M., Rohlin, L., Kao, K., and Liao, J. (2002). Global expression profiling of acetate-grown *Escherichia coli*. *J. Biol. Chem.* 277, 13175–13183. doi: 10.1074/jbc.M110809200
- Palsson, B. Ø. (2006). *Systems Biology: Properties of Reconstructed Networks*. New York, NY: Cambridge University Press.
- Picioreanu, C., van Loosdrecht, M. C. M., and Heijnen, J. J. (1999). Discrete-differential modelling of biofilm structure. *Water Sci. Technol.* 39, 115–122.
- Pirt, S. J. (1965). The maintenance energy of bacteria in growing cultures. *Proc. R. Soc. B Biol. Sci.* 163, 224–231. doi: 10.1098/rspb.1965.0069
- Portnoy, V. A., Scott, D. A., Lewis, N. E., Tarasova, Y., Osterman, A. L., and Palsson, B. Ø. (2010). Deletion of genes encoding cytochrome oxidases and quinol monooxygenase blocks the aerobic-anaerobic shift in *Escherichia coli* K-12 MG1655. *Appl. Environ. Microbiol.* 76, 6529–6540. doi: 10.1128/AEM.01178-10
- Prats, C., López, D., Giró, A., Ferrer, J., and Valls, J. (2006). Individual-based modelling of bacterial cultures to study the microscopic causes of the lag phase. *J. Theor. Biol.* 241, 939–953. doi: 10.1016/j.jtbi.2006.01.029
- Railsback, S. F., and Grimm, V. (2012). *Agent-Based and Individual-Based Modeling*. Princeton, NJ: Princeton University Press.
- Reisner, A., Haagensen, J. A. J., Schembri, M. A., Zechner, E. L., and Molin, S. (2003). Development and maturation of *Escherichia coli* k-12 biofilms. *Mol. Microbiol.* 48, 933–946. doi: 10.1046/j.1365-2958.2003.03490.x

- Roache, P. J. (1972). *Computational Fluid Dynamics*. Albuquerque, NM: Hermosa Publishers.
- Rowe, P. (2009). *Escherichia coli* O157:h7, other verotoxin-producing *E. coli* and the hemolytic uremic syndrome in childhood. *Can. J. Infect. Dis.* 6, 105–110. doi: 10.1155/1995/803560
- Schaechter, M., Williamson, J. P., Hood, J. R., and Koch, A. L. (1962). Growth, cell and nuclear divisions in some bacteria. *J. Gen. Microbiol.* 29, 421–434. doi: 10.1099/00221287-29-3-421
- Schulze, K. L., and Lipe, R. S. (1964). Relationship between substrate concentration, growth rate, and respiration rate of *Escherichia coli* in continuous culture. *Arch. Mikrobiol.* 48, 1–20. doi: 10.1007/BF00406595
- Sperandio, V., Torres, A. G., Giron, J. A., and Kaper, J. B. (2001). Quorum sensing is a global regulatory mechanism in enterohemorrhagic *Escherichia coli* O157:H7. *J. Bacteriol.* 183, 5187–5197. doi: 10.1128/JB.183.17.5187-5197.2001
- Standaert, A. R., Poschet, F., Geeraerd, A. H., Uylbak, F. V., Kreft, J.-U., and Van Impe, J. F. (2004). “A novel class of predictive microbial growth models: Implementation in an individual-based framework,” in *9th IFAC Symposium on Computer Applications in Biotechnology (CAB 2004)*, Vol. 9, eds M.-N. Pons and J. F. M. Van Impe, (Nancy: International Federation of Automatic Control), 183–188.
- Stewart, P. S., and Franklin, M. J. (2008). Physiological heterogeneity in biofilms. *Nat. Rev. Microbiol.* 6, 199–210. doi: 10.1038/nrmicro1838
- Stolper, D., Revsbech, N., and Canfield, D. (2010). Aerobic growth at nanomolar oxygen concentrations. *Proc. Natl. Acad. Sci. U.S.A.* 107, 18755–18760. doi: 10.1073/pnas.1013435107
- Tack, I., Logist, F., Noriega Fernández, E., and Van Impe, J. (2014). “An individual-based model for anaerobic dynamics of *Escherichia coli* colonies,” in *FOODSIM'2014*, ed A. Roudot (Brest: EUROSIS), 18–25.
- Tack, I. L. M. M., Logist, F., Noriega Fernández, E., and Van Impe, J. F. (2015). An individual-based modeling approach to simulate the effects of cellular nutrient competition on *Escherichia coli* K-12 MG1655 colony behavior and interactions in aerobic structured food systems. *Food Microbiol.* 4(Pt B), 179–188. doi: 10.1016/j.fm.2014.05.003
- Tang, W. J., Wu, Q. H., and Saunders, J. R. (2007). “Individual-based modeling of bacterial foraging with quorum sensing in a time-varying environment,” in *Evolutionary Computation, Machine Learning and Data Mining in Bioinformatics: 5th European Conference, EvoBIO 2007*, Vol. 4447, *Lecture Notes in Computer Science (LNCS)*, eds E. Marchiori, J. H. Moore and J. C. Rajapakse (Valencia; Berlin; Heidelberg: Springer-Verlag), 280–290.
- Vejborg, R. M., and Klemm, P. (2009). Cellular chain formation in *Escherichia coli* biofilms. *Microbiology* 155, 1407–1417. doi: 10.1099/mic.0.026419-0
- Verhulst, A., Cappuyns, A. M., Van Derlinden, E., Bernaerts, K., and Van Impe, J. F. (2011). Analysis of the lag phase to exponential growth transition by incorporating inoculum characteristics. *Food Microbiol.* 28, 656–666. doi: 10.1016/j.fm.2010.07.014
- Wimpenny, J. W. T., Leistner, L., Thomas, L. V., Mitchell, A. J., Katsaras, K., and Peetz, P. (1995). Submerged bacterial colonies within food and model systems: their growth, distribution and interactions. *Int. J. Food Microbiol.* 28, 299–315. doi: 10.1016/0168-1605(95)00065-8

Conflict of Interest Statement: The authors declare that the research was conducted in the absence of any commercial or financial relationships that could be construed as a potential conflict of interest.

Copyright © 2017 Tack, Nimmegeers, Akkermans, Hashem and Van Impe. This is an open-access article distributed under the terms of the Creative Commons Attribution License (CC BY). The use, distribution or reproduction in other forums is permitted, provided the original author(s) or licensor are credited and that the original publication in this journal is cited, in accordance with accepted academic practice. No use, distribution or reproduction is permitted which does not comply with these terms.



Analysis of *abrB* Expression during the Infectious Cycle of *Bacillus thuringiensis* Reveals Population Heterogeneity

Samia Ben Rejeb, Didier Lereclus and Leyla Slamti*

Micalis Institute, Institut National de la Recherche Agronomique, AgroParisTech, Université Paris-Saclay, Jouy-en-Josas, France

OPEN ACCESS

Edited by:

Weiwen Zhang,
Tianjin University, China

Reviewed by:

Mario Soberón,
Universidad Nacional Autónoma
de México, Mexico
Akos T. Kovacs,
Technical University of Denmark,
Denmark

*Correspondence:

Leyla Slamti
leyla.slamti@inra.fr

Specialty section:

This article was submitted to
Systems Microbiology,
a section of the journal
Frontiers in Microbiology

Received: 31 August 2017

Accepted: 28 November 2017

Published: 12 December 2017

Citation:

Ben Rejeb S, Lereclus D and
Slamti L (2017) Analysis of *abrB*
Expression during the Infectious Cycle
of *Bacillus thuringiensis* Reveals
Population Heterogeneity.
Front. Microbiol. 8:2471.
doi: 10.3389/fmicb.2017.02471

Using the model host/pathogen pair *Galleria mellonella*/*Bacillus thuringiensis*, we have shown that these bacteria could kill their insect host, survive in its cadaver and form spores by sequentially activating virulence, necrotrophism and sporulation genes. However, the population isolated from the cadavers was heterogeneous, including non-sporulating cells in an unknown physiological state. To characterize these bacteria, we used a transcriptional fusion between the promoter of a gene expressed during early exponential growth (*abrB*) and a reporter gene encoding a destabilized version of GFP, in combination with a fluorescent reporter of the necrotrophic state. The composition of the bacterial population during infection was then analyzed by flow cytometry. We showed that the *PabrB* promoter was activated in the population that had turned on the necrotrophic reporter, suggesting a re-entry into vegetative growth. Strikingly, the cells that did not go through the necrotrophic state did not activate the *PabrB* promoter and appear as a dormant subpopulation. We propose a new model describing the *B. thuringiensis* cell types during infection.

Keywords: population heterogeneity, single cell analysis, *Bacillus thuringiensis*, infectious cycle, dormancy

INTRODUCTION

Bacteria are often exposed to changes in their environment. Pathogenic bacteria in particular have to face an array of environments that change with the progression of the disease. They adapt most of the time by modifying their gene expression profile in response to the signals they receive. And interestingly, a clonal population will not always behave as a whole. Genetically identical bacteria can differentiate into specialized cell-types that will provide different answers to the signal received (Lopez and Kolter, 2010; Verplaetse et al., 2015; Mouammime et al., 2017).

Our model bacteria belong to the *Bacillus cereus* group. This group is composed of 8 Gram-positive and sporulating species including *B. anthracis*, *B. thuringiensis* and *B. cereus sensu stricto*. These pathogens are responsible for infections in humans and in animals. *B. anthracis* is the agent of anthrax (Mock and Fouet, 2001). *B. cereus* mainly causes food-borne toxin-infections and is also an opportunistic pathogen responsible of endocarditis, meningitis and endophthalmitis (Stenfors Arnesen et al., 2008; Bottone, 2010). *B. thuringiensis* is an insect pathogen whose host specificity depends on the production of insecticidal toxins (Deng et al., 2014). The entomopathogenic properties of this bacterium are widely used in the world for pest control (Sanahuja et al., 2011; Sanchis, 2011).

To understand the mechanisms involved in the pathogenicity of these bacteria we work with the insect model *Galleria mellonella*. This infection model has been successfully used to characterize numerous genes involved in the pathogenic properties of *B. cereus* and *B. thuringiensis* (Salamitou et al., 2000; Fedhila et al., 2006; Raymond et al., 2010). These bacteria are capable of carrying out a full infectious cycle in the larva of this insect. We have shown that this process is composed of three major phases (for a review Slamti et al., 2014). At the beginning of the infection, virulence factors are expressed under the control of the quorum sensor PlcR. These factors, which include proteases, phospholipases and cytotoxins, allow the bacteria to invade its host and to kill it (Salamitou et al., 2000). After the death of the insect, NprR, another quorum sensor, will trigger a necrotrophic lifestyle permitting the bacteria to survive in the cadaver (Dubois et al., 2016). Finally, the cells will sporulate and will be able to disseminate and withstand hostile environmental conditions.

A recent study reported the differentiation process of cells in insect cadavers, using fluorescent reporters under the control of promoters reflecting the activity of the regulators responsible for virulence, necrotrophism and sporulation at the cell level (Verplaetse et al., 2015). Although these physiological states take place in a sequential manner in a cell, the necrotrophic phase is only triggered in a part of the population in the insect cadaver, suggesting an activation specificity linked to the environment. It was also shown that sporulation only occurs in the sub-population that has activated the necrotrophic regulon. This is in agreement with the fact that the apo form of NprR inhibits sporulation, whereas NprR in complex with its signaling peptide NprX, activates the necrotrophic genes (Perchat et al., 2016). We also identified a category of cells that did not express any of the previously described reporters in biofilm and in the host (Verplaetse et al., 2015, 2016). This category represented about 20% of the population throughout the infectious process.

Here we investigated the physiological state of the cells that did not enter the necrotrophic state, since the necrotrophic sub-population is the most inclusive. We sought to determine if these cells were actively growing bacteria. To monitor the vegetative state of these bacteria we chose to assay the activity of the promoter of the *abrB* gene during insect infection using a fluorescent reporter. This gene encodes the AbrB transition state regulator and is transcribed during the transition from lag to exponential phase and during early exponential phase (O'Reilly and Devine, 1997; Lucking et al., 2009). This central regulator has been shown to repress the expression of stationary phase genes in *B. subtilis* (Perego et al., 1988; Strauch and Hoch, 1993) as well as the synthesis of the cereulide toxin synthesis and the expression of the *inhA1* metalloprotease-encoding gene in *B. cereus* (Grandvalet et al., 2001; Lucking et al., 2009). We engineered a *B. thuringiensis*-improved allele of the bright and fast folding sfGFP (Pedelacq et al., 2006) and, in order to follow fluctuations in gene expression, we destabilized the resulting protein by using the *ssrA*-mediated peptide tagging system that addresses specifically tagged proteins to the Clp degradation machinery in *Escherichia coli* and in *B. subtilis* (Keiler et al., 1996; Gottesman et al., 1998; Wiegert and Schumann, 2001). Using this tool, we showed that the *abrB* gene is expressed at the beginning

of the infection and at a later stage of the process, only in cells that already went through the necrotrophic state. However, there is still a bacterial population in an unknown physiological state and we show that more than 60% of this population are living cells.

MATERIALS AND METHODS

Bacterial Strains and Growth Conditions

The acrySTALLIFEROUS *B. thuringiensis* 407 Cry[−] strain (Bt 407[−]) (Lereclus et al., 1989) was used as the parental strain to create all the strains used in this study. *E. coli* strain DH5 α (Taylor et al., 1993) was used as the host strain for plasmid construction. *E. coli* strain ET12567 (MacNeil et al., 1992) was used to prepare DNA prior to electroporation in *B. thuringiensis*. Cells were grown in LB medium (1% tryptone, 0.5% yeast extract, 1% NaCl) or HCT medium (0.7% casein hydrolysate, 0.5% tryptone, 0.68% KH₂PO₄, 0.012% MgSO₄ 7H₂O, 0.00022% MnSO₄ 4H₂O, 0.0014% ZnSO₄ 7H₂O, 0.008% ferric ammonium citrate, 0.018% CaCl₂ 4H₂O, 0.3% glucose, pH 7.2) (Lereclus et al., 1982) at 37°C and stored at −80°C in LB containing 15% glycerol.

For *B. thuringiensis* cultures, t0 corresponds to the beginning of the transition between the exponential and stationary phases of growth.

The antibiotic concentrations used for selection of *B. thuringiensis* and *E. coli* were as follows: erythromycin, 10 μ g/mL; ampicillin, 100 μ g/mL. Chloramphenicol was used at a concentration of 100 μ g/mL to block the synthesis of proteins (Periago et al., 2002) in *B. thuringiensis*.

When required, xylose was used at a concentration of 20 mM.

Plasmid and Strain Constructions

DNA manipulations are detailed in the Supplementary Experimental Procedures. All the plasmids and strains used in this study are indicated in Tables 1, 2. Oligonucleotides are listed in Supplementary Table S1.

In Vitro Growth of the Cells for Measurement of the GFP-Based Fluorescence

To assay the GFP-based fluorescence of cells harboring the *sfGFP* gene and its derivatives designed to improve fluorescence, overnight cultures incubated at 30°C in HCT medium supplemented with erythromycin were diluted 1000-fold in HCT and incubated at 37°C under agitation until an OD₆₀₀ of 0.5. Xylose was then added and growth was resumed. Cells were harvested at the time of xylose addition (T0) as well as at other time points after xylose addition (Tn). Cultures were carried out in the same way to assay the GFP-based fluorescence of cells harboring the *gfp_{Bte}* gene and its derivatives designed to destabilize the GFP, except that chloramphenicol was added to the cells 1 h after xylose addition.

In all cases, the cells were harvested and fixed as described in Verplaetse et al. (2015). Essentially, the cells were centrifuged, fixed for 7 min in PBS-formaldehyde 4% then washed in PBS. The

pellet was then resuspended in GTE buffer (Vlamakis et al., 2008) and kept at 4°C until flow cytometry analysis or microscopy.

In Vivo Experiments

Intrahemocoelic injection experiments with *G. mellonella* were carried out essentially as described previously (Salamitou et al., 2000; Verplaetse et al., 2015). For each strain, 20 larvae were injected each with 2.10^4 bacteria and kept at 30°C for 72 h. 18 h after injection, surviving insects were eliminated. At each

time point, *B. thuringiensis* cells were harvested from 2 or 3 dead insects as follows: the larva was cut open, transferred to a 1.5 mL Eppendorf tube containing 1 ml of PBS and vortexed. The suspension was pipetted into a new 1.5 mL Eppendorf tube (leaving behind most of the large insect debris). The sample was centrifuged and the pellet was resuspended in PBS-formaldehyde 4%, fixed for 7 min then washed in PBS. This suspension was filtered onto a cotton pad in a 1 mL syringe in order to retain the cadaver debris and recover the bacterial cells in the filtrate. These

TABLE 1 | Plasmids used in this study.

Name	Relevant information	Reference
pHT304	Replicative multicopy <i>E. coli/B. thuringiensis</i> shuttle vector.	Arantes and Lereclus, 1991
pHT304.18	Replicative multicopy <i>E. coli/B. thuringiensis</i> shuttle vector.	Agaisse and Lereclus, 1994
p304-Pxy/+	pHT304 harboring a modified version of the xylose-inducible promoter region of <i>xylA</i> to enhance translation efficiency (Stammen et al., 2010). The original sequence AGGGGGAATCACATG was changed to AGGAGGTGACACCATG where the RBS is in bold letters and the translation start site is underlined.	Slamti et al., 2015
pPx' <i>sfGFP</i>	<i>sfGFP</i> was amplified by PCR from pCM11 (Pedelacq et al., 2006) using primer pair sfgfp1/sfgfp2, digested with BglII and KpnI, and cloned between the BamHI and KpnI restriction sites of pHT304.18-Px (Slamti and Lereclus, 2002). This created a transcriptional fusion between the xylose-inducible promoter region of <i>xylA</i> and <i>sfGFP</i> .	This study
pPx' <i>gfpBt</i>	<i>B. thuringiensis</i> codon optimized <i>gfpBt</i> , synthesized and cloned in the pEX plasmid by Eurofins Genomics (France), was amplified by PCR from this vector using primer pair sfgfp1/sfgfpBt2, digested with BglII and KpnI, and cloned between the BamHI and KpnI restriction sites of pPx to create a transcriptional fusion between PxyA and <i>gfpBt</i> .	This study
pPx+' <i>gfpBt</i>	<i>B. thuringiensis</i> codon optimized <i>gfpBt</i> , synthesized and cloned in the pEX plasmid by Eurofins Genomics (France), was amplified by PCR from this vector using primer pair sfgfpBt1/sfgfpBt2, digested with BsaI and KpnI, and cloned between the NcoI and KpnI restriction sites of p304-Pxy/+ to create a transcriptional fusion between Pxy/+ and <i>gfpBt</i> .	This study
pPx' <i>gfpBte</i>	<i>B. thuringiensis</i> codon optimized <i>gfpBt</i> , synthesized and cloned in the pEX plasmid by Eurofins Genomics (France), was amplified by PCR from this vector using primer pair sfgfpBtcomGBt1/sfgfpBt2, digested with BsaI and KpnI, and cloned between the NcoI and KpnI restriction sites of p304-Pxy/+.	This study
pPx' <i>gfpBte</i> LAA/ LVA/AAV/ASV	The forward primer included 24 bp encoding the first eight amino acids of <i>comGA</i> . These have been shown to enhance the stability of fluorescent proteins (Veening et al., 2004). The resulting cassette comprising the modified RBS from Pxy/+ and the <i>comGA</i> ' <i>gfpBt</i> sequence was designated <i>gfpBte</i> . <i>gfpBte</i> was amplified by PCR from pPx' <i>gfpBte</i> using primer pairs sfgfpBtcomGBt1/gfpLAA-gfpLVA-gfpAAV-gfpASV, digested with BsaI and KpnI, and cloned between the NcoI and KpnI restriction sites of p304-Pxy/+. The reverse primers add an <i>ssrA</i> tag to the gene: GKQNNLLSLAA for <i>gfpBte</i> LAA, GKQNNLLSLVA for <i>gfpBte</i> LVA, GKQNNLLSAV for <i>gfpBte</i> AAV and GKQNNLLSASV for <i>gfpBte</i> ASV. These tags will address the protein to proteases that will degrade them with varying efficiencies (Keiler and Sauer, 1996; Keiler et al., 1996; Andersen et al., 1998).	This study
pHT- <i>gfpBte</i> AAV	<i>gfpBte</i> AAV was amplified by PCR from pPx' <i>gfpBte</i> AAV using primer pair Xyl10/PU, and cloned between the SmaI and EcoRI restriction sites of pHT304.18.	This study
pPabR' <i>gfpBte</i> AAV	The promoter region of the <i>abrB</i> gene was amplified by PCR from the chromosome of Bt 407 using primer pairs PabR-B-F-XbaI/PabR-B-R-AscI and cloned between the XbaI and AscI restriction sites of pHT- <i>gfpBte</i> AAV.	This study
pPnprA' <i>mcherry</i> _{LGC}	pHT304.18 harboring a transcriptional fusion between the promoter of <i>nprA</i> and the <i>B. thuringiensis</i> -adapted <i>mcherry</i> reporter gene.	Verplaetse et al., 2015
pPabR' <i>gfpBte</i> AAV- PnprA' <i>mcherry</i> _{LGC}	The transcriptional fusion between the promoter region of <i>abrB</i> and the promoterless <i>gfpBte</i> AAV reporter gene was amplified from pPabR' <i>gfpBte</i> AAV using primer pair PabR-B-F-NcoI/gfpBteAAV-in-BglII. pPspolID' <i>yfp</i> -PnprA' <i>mcherry</i> _{LGC} (Verplaetse et al., 2015) was used as a PCR template to amplify the plasmid without the <i>PspolID</i> ' <i>yfp</i> region using primer pair Term-R-BglII/NprA-F-NcoI. This fragment and PabR' <i>gfpBte</i> AAV were digested with BglII and NcoI and ligated together to generate pPabR' <i>gfpBte</i> AAV-PnprA' <i>mcherry</i> _{LGC} which harbors the two transcriptional fusions in divergent orientation and separated by about 100 bp.	This study
pPaphA3' <i>sfGFP</i>	<i>sfGFP</i> was amplified by PCR from pCM11 (Pedelacq et al., 2006) using primer pair sfgfp1/sfgfp2 and digested with BglII and EcoRI. <i>PaphA3</i> was amplified from pDG792 (Guerout-Fleury et al., 1995) using primer pair PkanHind1/PkanBam2 and digested with HindIII and BamHI. Both fragments were cloned between the HindIII and EcoRI restriction sites of pHT304.18 generating a transcriptional fusion between the constitutive <i>PaphA3</i> promoter and <i>sfGFP</i> .	This study

were then concentrated by centrifugation, resuspended in GTE buffer (Vlamakis et al., 2008) and kept at 4°C until flow cytometry analysis or microscopy.

For the assessment of the percentage of live cells in the bacterial population in insect cadavers, the experiments were carried out in the same manner except that the cells were not fixed with formaldehyde. After filtration on the cotton pad, the suspension was centrifuged, resuspended in saline, incubated with the SYTOX Green Dead Cell Stain (Molecular Probes) according to the manufacturer's instructions and analyzed immediately with the flow cytometer. Dead bacteria will present a bright green fluorescence compared to live cells.

Flow Cytometry Analysis

Fluorescence was measured on a CyFlow Space cytometer (Partec, France). Details about the parameters used to collect fluorescence and the softwares used to analyze the data are given in the Supplementary Experimental Procedures. The different populations were identified using histograms or bi-parametric cytograms. GFP- or mCherry-expressing cells were identified as cells giving a higher signal intensity than the reporterless cells used as controls.

Fluorescence Microscopy

Cells were observed with an AxioObserver.Z1 Zeiss inverted fluorescence microscope equipped with a Zeiss AxioCam MRm digital camera and with Zeiss fluorescence filters. GFP was imaged using the 38 HE filter (excitation: BP 470/40, beam splitter: FT 495, emission: 525/50). mCherry was imaged using the 45 HE filter (excitation: BP 590/20, beam splitter: FT 605, emission: 620/14). Images were processed using the ZEN software package.

Nucleotide Sequence Accession Numbers

The DNA sequence of the plasmid containing the *gfp_{Bte}* AAV sequence was submitted to GenBank and is available under the accession number MF673728.

RESULTS

Construction of a GFP Variant Highly Expressed in *B. thuringiensis*

To facilitate the analysis of gene expression in *B. thuringiensis*, we engineered a highly expressed version of the sfGFP. We used the reporterless *sfgfp* (Pedelacq et al., 2006) under the control of the xylose-inducible *PxylA* promoter as a template for our improvement procedure. *sfgfp* encodes a version of the *Aequorea victoria* GFP that has been shown to be four times brighter and that folds 4 times faster *in vivo* than GFPmut3 (Milde, 2008). We modified the *sfgfp* gene and the features required for its translation to adapt it to *B. thuringiensis*. Our first step was to change the codon usage to one that would correspond better to that of our strain, using the GENEius software and the associated *B. thuringiensis* serovar *thuringiensis* codon usage table (Eurofins Genomics). We designated this allele *gfp_{Bt}*. We then modified the RBS present in the promoter region of *PxylA* to the improved RBS+, that resulted in a twofold increase in protein production in *B. megaterium*, as described in Stammen et al. (2010). Finally, we added the first 24 bp of *comGA* to the 5' end of the *sfgfp* coding sequence. The corresponding eight amino acids have been shown to enhance the stability of fluorescent proteins (Veening et al., 2004). The resulting cassette comprising the modified RBS and the *comGA*'*gfp_{Bt}* sequence was designated *gfp_{Bte}*. Using

TABLE 2 | Strains used in this study.

Name	Relevant information	Reference
Bt (pHT304)	Bt 407 ⁻ carrying the empty pHT304 vector and used as a Fluorescence ⁻ control.	This study
Bt (pPx)	Bt 407 ⁻ carrying the empty pPx vector and used as a Fluorescence ⁻ control.	This study
Bt (pPx' <i>sfgfp</i>)	Bt 407 ⁻ used to measure the fluorescence generated by the transcriptional fusion between the xylose-inducible promoter of <i>xylA</i> and <i>sfgfp</i> .	This study
Bt (pPx' <i>gfp_{Bt}</i>)	Bt 407 ⁻ used to measure the fluorescence generated by the transcriptional fusion between the xylose-inducible promoter of <i>xylA</i> and the <i>B. thuringiensis</i> codon-optimized <i>gfp_{Bt}</i> .	This study
Bt (pPx+' <i>gfp_{Bt}</i>)	Bt 407 ⁻ used to measure the fluorescence generated by the transcriptional fusion between <i>Pxyl+</i> and the <i>B. thuringiensis</i> codon-optimized <i>gfp_{Bt}</i> .	This study
Bt (pPx' <i>gfp_{Bte}</i>)	Bt 407 ⁻ used to measure the fluorescence generated by the transcriptional fusion between <i>Pxyl+</i> and the <i>B. thuringiensis</i> codon-optimized <i>gfp_{Bt}</i> to which the sequence encoding the first eight amino acids of <i>comGA</i> have been added.	This study
Bt (pPx' <i>gfp_{Bte}</i> LAAV/LVA/AAV/ASV)	Bt 407 ⁻ used to measure the fluorescence generated by the transcriptional fusion between <i>Pxyl+</i> and <i>gfp_{Bte}</i> to which a degradation tag has been added.	This study
Bt (pPabrB' <i>gfp_{Bte}</i> AAV)	Bt 407 ⁻ in which we measure the activity of the promoter of <i>abrB</i> using a reporter gene encoding an unstable GFP.	This study
Bt (pPnprA' <i>mcherry_{LGC}</i>)	Bt 407 ⁻ in which we measure the activity of the promoter of <i>nprA</i> using the <i>mcherry</i> reporter gene.	Verplaetse et al., 2015
Bt (pPabrB' <i>gfp_{Bte}</i> AAV-PnprA' <i>mcherry_{LGC}</i>)	Bt 407 ⁻ in which we measure the activity of the promoter of <i>abrB</i> , using a reporter gene encoding an unstable GFP, as well as the activity of the promoter of <i>nprA</i> , using <i>mcherry</i> .	This study
Bt (pPaphA3' <i>sfgfp</i>)	Bt 407 ⁻ used to measure the fluorescence generated by the transcriptional fusion between the promoter of <i>aphA3</i> and <i>sfgfp</i> .	This study

flow cytometry, we showed that the *gfp_{Bte}*-expressing cells grown in HCT medium were about 20 times brighter than the *sfgfp*-expressing cells, 2 h after the addition of xylose (**Figure 1A**; median fluorescence of 34 and 1.6 AU and pink and orange lines, respectively). Codon adaptation resulted in the most efficient improvement compared to the RBS modification and the *comGA* sequence addition. Indeed, the *gfp_{Bte}*-expressing cells are fivefold brighter than the *sfgfp*-expressing cells, whereas each subsequent modification step increased the fluorescence of the cells by approximately twofold (**Figure 1A**; median fluorescence of 8, 1.6, 22, and 34 AU and blue, orange, green and pink lines, respectively). This increase in fluorescence intensity is visible on the microscopy pictures taken 2 h after xylose addition (**Figures 1B–F**).

Construction of Unstable GFP_{Bte} Variants

To monitor variations in gene expression, we decided to generate an unstable version of the GFP_{Bte}. We used a previously described method that takes advantage of the *ssrA*-mediated peptide tagging system (Andersen et al., 1998). The principle of the method is to tag a protein for specific degradation by a protease. We added 10 amino acids at the N-terminal end of GFP_{Bte} with a variation in the last 3 amino acids of the sequence (GKQNNLSLAA/-LVA/-AAV/-ASV), generating GFP_{Bte}LAA, GFP_{Bte}LVA, GFP_{Bte}AAV, and GFP_{Bte}ASV. Amino acids GKQNNLSLAA correspond to the putative proteolytic tag added by the *ssrA* tmRNA we identified in the genome of strain *B. thuringiensis* 407. These amino acids have been shown to address the tagged protein to the Clp degradation machinery in *E. coli* and in *B. subtilis* (Keiler et al., 1996; Gottesman et al., 1998; Wiegert and Schumann, 2001). Each tag variant should alter the stability of the protein (Keiler and Sauer, 1996; Andersen et al., 1998). We monitored the fluorescence of the cells harboring the GFP_{Bte} tagged variants during growth in HCT medium and the results are presented on **Figure 2**. At the time of inducer addition, all the cells present a fluorescence similar to that of the reporterless cells (**Figure 2A**, left panel). 30 min after xylose induction, there is a striking difference between the cells harboring the wild-type -LAA or the -LVA tag and the cells harboring the -AAV or the -ASV tag (**Figure 2A**, second panel from the left). The latter present a fluorescence closer to that of the cells producing GFP_{Bte} whereas the fluorescence of the former is weaker. 1 h after xylose induction (**Figure 2A**, third panel from the left), the cells harboring the GFP_{Bte}LAA or the GFP_{Bte}LVA tag had a similar fluorescence (median fluorescence of 2 and 2.3 AU which is 33- and 28-fold lower than that of GfpBte-producing cells, respectively). The cells expressing *gfp_{Bte}*ASV were the most fluorescent (median fluorescence of 43AU, 1.5-fold lower than that of *gfp_{Bte}*-expressing cells), however, the histogram profile was not satisfying since it showed two peaks which indicate that *gfp* expression and/or GFP degradation in the population was highly heterogeneous. The cells harboring the GFP_{Bte}AAV presented a median fluorescence of 19 AU that was 3.5-fold lower than that of the GFP_{Bte}-producing cells (median fluorescence of 65 AU) and a histogram profile similar to that of the latter. Two hours after addition of the inducer (**Figure 2A**, right panel), all the histograms were similar to those observed 1 h after induction.

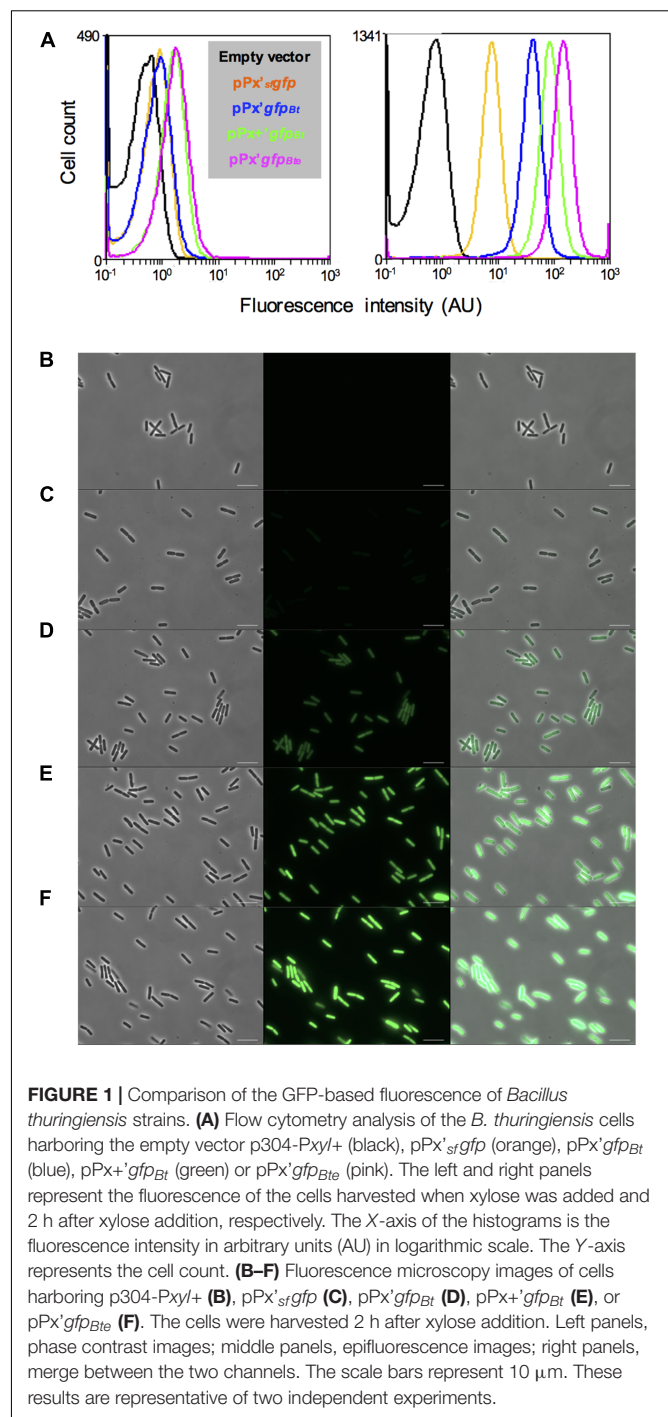


FIGURE 1 | Comparison of the GFP-based fluorescence of *Bacillus thuringiensis* strains. **(A)** Flow cytometry analysis of the *B. thuringiensis* cells harboring the empty vector p304-Pxyl+ (black), pPx'*sf*gfp (orange), pPx'*gfp_{Bte}* (blue), pPx'+*gfp_{Bte}* (green) or pPx'+*gfp_{Bte}* (pink). The left and right panels represent the fluorescence of the cells harvested when xylose was added and 2 h after xylose addition, respectively. The X-axis of the histograms is the fluorescence intensity in arbitrary units (AU) in logarithmic scale. The Y-axis represents the cell count. **(B–F)** Fluorescence microscopy images of cells harboring p304-Pxyl+ **(B)**, pPx'*sf*gfp **(C)**, pPx'*gfp_{Bte}* **(D)**, pPx'+*gfp_{Bte}* **(E)**, or pPx'+*gfp_{Bte}* **(F)**. The cells were harvested 2 h after xylose addition. Left panels, phase contrast images; middle panels, epifluorescence images; right panels, merge between the two channels. The scale bars represent 10 μm. These results are representative of two independent experiments.

gfp_{Bte}-expressing cells were more fluorescent than 1 h before (median fluorescence of 125 AU vs. 65 AU, respectively) whereas the fluorescence of *gfp_{Bte}*AAV-expressing cells was similar at both times (median fluorescence of 19 AU and 15 AU 1 and 2 h after addition of xylose, respectively). *gfp_{Bte}*AAV was thus chosen as a reporter of gene expression for the subsequent experiments.

The decrease in fluorescence of GFP_{Bte}AAV-producing cells was then monitored after the addition of chloramphenicol, an inhibitor of translation (Periago et al., 2002), to determine

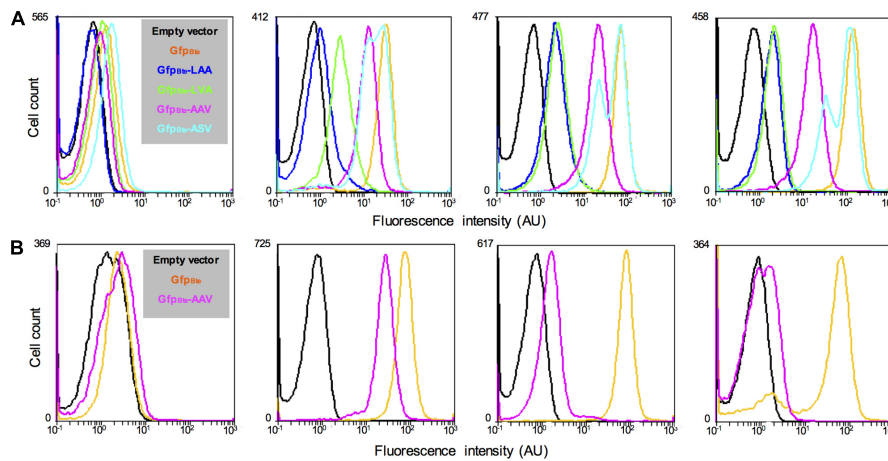


FIGURE 2 | Comparison of the fluorescence of *B. thuringiensis* strains harboring different alleles of *gfpBte*. **(A)** Flow cytometry analysis of the *B. thuringiensis* cells harboring the empty vector p304-PxyI+ (black), pPx'*gfpBte* (orange), pPx'*gfpBte*LAA (blue), pPx'*gfpBte*LVA (green), pPx'*gfpBte*AAV (pink), or pPx'*gfpBte*ASV (turquoise). The cells were harvested when xylose was added, 30 min, 1 h and 2 h after xylose addition (panels from left to right). **(B)** Flow cytometry analysis of the *B. thuringiensis* cells harboring the empty vector p304-PxyI+ (black), pPx'*gfpBte* (orange), and pPx'*gfpBte*AAV (pink). From left to right, the histograms show the fluorescence of cells harvested when xylose was added, 1 h after xylose addition (which also corresponds to the time when chloramphenicol was added), 1 and 22 h after chloramphenicol addition. The X-axis of the histograms is the fluorescence intensity in arbitrary units (AU) in logarithmic scale. The Y-axis represents the cell count. These results are representative of two independent experiments.

GFP stability (**Figure 2B**). The median fluorescence of *gfpBte*-expressing cells was similar at the time of and 1 h after chloramphenicol addition (median fluorescence of 73 AU and 77 AU, respectively) (**Figure 2B**, second and third panels from the left, respectively). In contrast, the median fluorescence of *gfpBte*AAV-expressing cells decreased by 17-fold between these two time-points (median fluorescence of 26 AU and 1.5 AU, respectively). 22 h after chloramphenicol addition, the majority of the *gfpBte*-expressing cells remained fluorescent whereas the *gfpBte*AAV-expressing cells presented a fluorescence close to that of the control cells (**Figure 2B**, right panel). These results indicate that, in these conditions, the GFP_{Bte}AAV-based fluorescence shows a half-life of approximately 15 min.

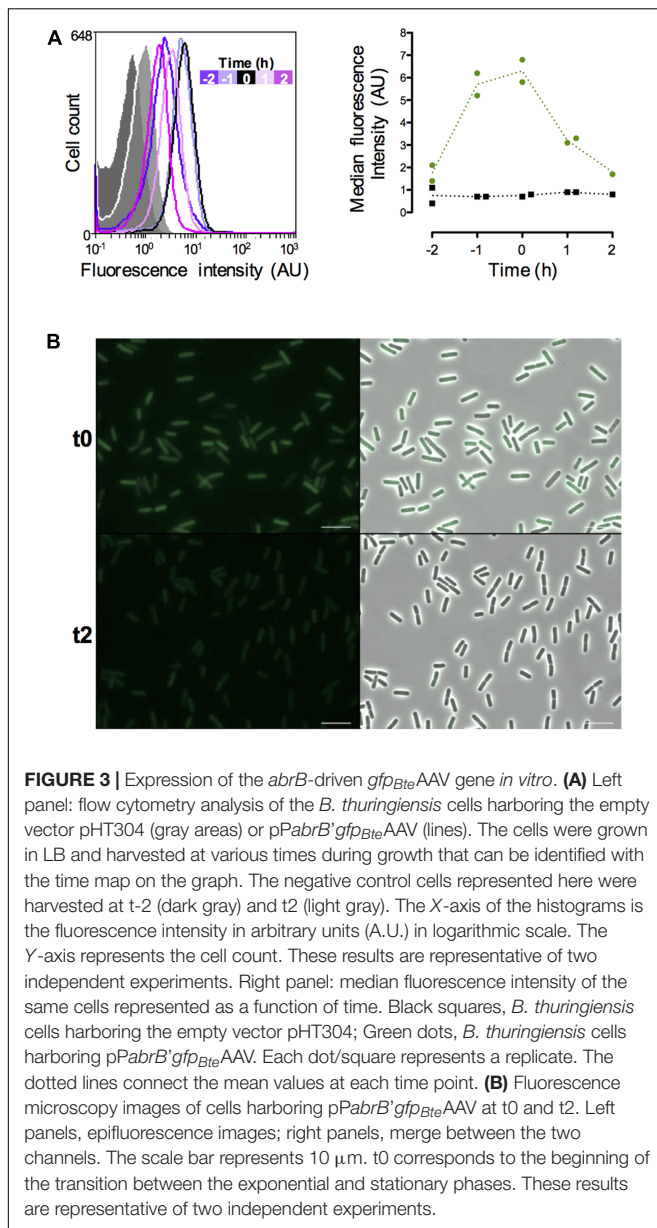
Monitoring the Expression of *abrB* in Vitro Using *gfpBte*AAV

In order to monitor the vegetative state of *B. thuringiensis* cells during the infectious cycle we chose to use the promoter of the *abrB* gene. This gene encodes a transition state regulator transcribed and active during the exponential phase (Perego et al., 1988; O'Reilly and Devine, 1997; Banse et al., 2008; Lucking et al., 2009). We monitored the fluorescence of the cells harboring a *PabrB'**gfpBte*AAV transcriptional fusion during growth in LB medium and the results are presented on **Figure 3**. The data are from two independent experiments. We represented 2 negative control samples on the graph to account for the difference between the auto-fluorescence of the reporter-less cells at t-2 and the cells harvested at the other time-points (**Figure 3A**, left panel). All the negative control histograms are shown in Supplementary Figure S1. The flow cytometry histograms show that the *PabrB'**gfpBte*AAV-expressing cells at t-2 are already fluorescent compared to the negative control

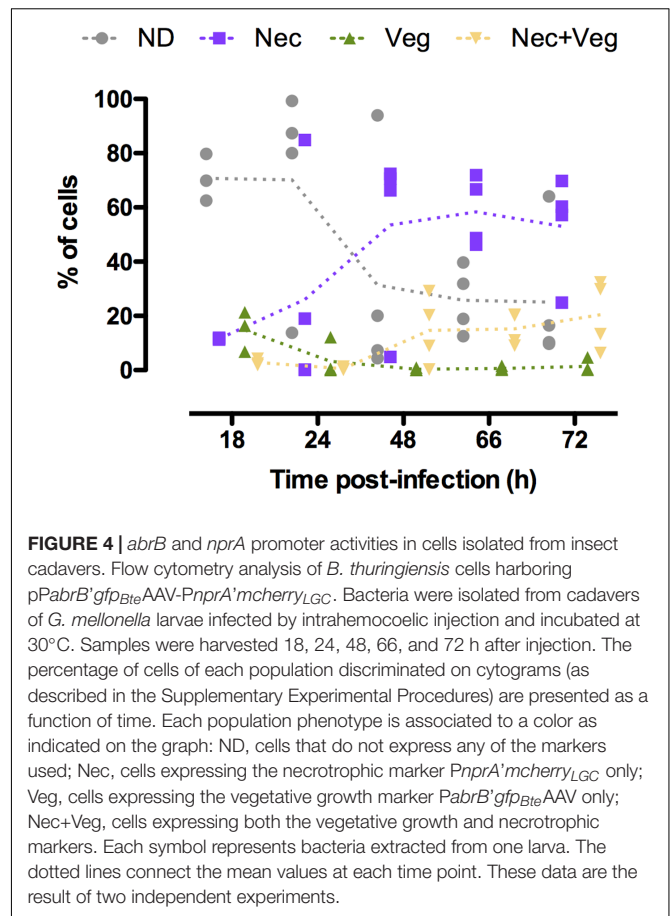
(median fluorescence of 2.1 vs. 0.4 AU, respectively) and their fluorescence increases until it reaches a maximum at t-1 and t0 before decreasing at t1 and t2 (median fluorescence of 5.2, 5.8, 3.1, and 2.7 AU, respectively, to be compared to the light gray negative control with a median fluorescence of 0.8 AU) (**Figure 3A**, left panel). At t24, the cells harboring *PabrB'**gfpBte*AAV do not present any fluorescence (Supplementary Figure S2). The shape of the histograms suggests that the *PabrB'**gfpBte*AAV fusion is expressed in a homogeneous fashion in the population (only 1 peak is visible). The right panel of **Figure 3A** recapitulates the data for both experiments as kinetics of median fluorescence intensity and shows that the peak of *PabrB'**gfpBte*AAV expression was reached between t-1 and t0. Microscopy pictures of *PabrB'**gfpBte*AAV-expressing cells harvested at t0 and at t2 support the flow cytometry data (**Figure 3B**). These results show that the *PabrB'**gfpBte*AAV transcriptional fusion is expressed during exponential phase and that we can visualize a decrease in its expression when the cells enter the transition phase.

abrB Expression Is Activated in Cells That Have Entered the Necrotrophic Pathway

We investigated the physiological state of *B. thuringiensis* cells during infection in order to characterize in more detail the composition of the population during this cycle. To achieve this objective we examined the state of the cells that did not activate the promoters previously used, in particular the necrotrophic reporter (Verplaetse et al., 2015). We infected *G. mellonella* larvae with *B. thuringiensis* cells harboring the *PnprA'**mCherry*_{LGC} transcriptional fusion as well as the *PabrB'**gfpBte*AAV transcriptional fusion on the same vector. *nprA* is under the control of NprR, the regulator of the necrotrophic



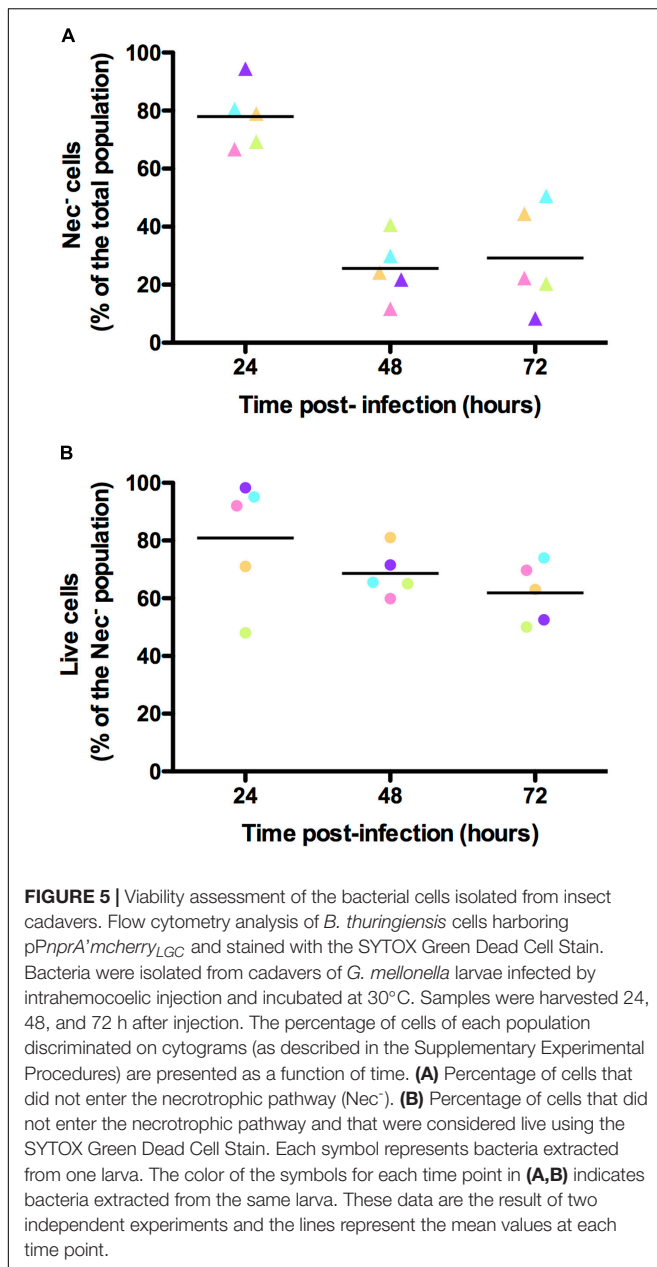
state, and reflects its activity (Perchat et al., 2011). We monitored the fluorescence of the cells harvested from the insect cadavers at various times following infection. The results are presented in **Figure 4**. The kinetics profile of the Nec+ population (i.e., cells expressing *nprA*) is similar to what has been published before (Verplaetse et al., 2015) with a low percentage of the population expressing *nprA* 18 h post-infection (pi) (mean value of 11%) that increases between 24 and 48 h pi (mean values of 27 and 68%, respectively) to reach a maximum 72 h pi (mean value of 74%). We observed that the vegetative *PabrB'gfp_{Bte}*AAV reporter is expressed at 18 h pi in 13% of the population. Interestingly, less cells expressed it at 24 h pi (mean value of 4%). The percentage of cells in which *PabrB* is expressed increased at 48 and 72 h pi (mean value of 15 and 22%, respectively). The expression of *PabrB'gfp_{Bte}*AAV is almost exclusively restricted



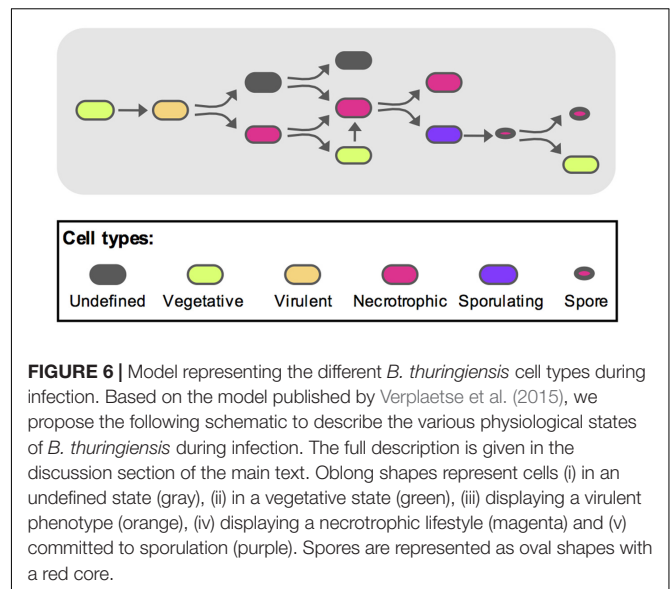
to cells that have activated the *nprA* gene promoter from 48 to 72 h pi. **Figure 4** also shows that the proportion of cells that did not express the necrotrophic or the vegetative reporters changed from 71% at 18 h pi to 25% 72 h pi. In order to verify that the expression patterns observed were not due to loss or copy number heterogeneity of the plasmid during the infectious process, we infected *G. mellonella* larvae with *B. thuringiensis* cells harboring the pPaphA3'sfGFP vector carrying a transcriptional fusion between the promoter of a constitutive gene in *B. thuringiensis*, and the reporter gene encoding sfGFP. The results show that the fusion is expressed in a homogeneous fashion in the population 24 and 72 h pi (only 1 peak is visible) (Supplementary Figure S3). Furthermore, a previous study has reported that 100 and 99.3% of the bacteria harvested from insect cadavers still carried a vector with the same backbone 48 and 96 h post-infection, respectively (Verplaetse et al., 2015). This indicates that the phenotypic heterogeneity observed for the reporters mentioned above is not due to plasmid instability or copy number heterogeneity in *B. thuringiensis* during infection.

Cells That Did Not Enter the Necrotrophic Pathway Are Viable

In order to verify that the bacteria that did not express any of the reporters used were alive, we infected *G. mellonella* larvae with *B. thuringiensis* cells harboring the PnprA'mcherry_{LGC}



transcriptional fusion and incubated the samples harvested from the insect cadavers at various times following infection with the SYTOX Green Dead Cell Stain. We then immediately monitored the mCherry- and SYTOX Green-based fluorescence of the bacteria. The cells recovered at each time-point were mostly alive. Indeed 89, 79, and 84% of the bacteria were not stained by the SYTOX Green Dead Cell dye at 24, 48, and 72 h pi, respectively (Supplementary Figure S4). **Figure 5A** shows that in these conditions we recovered 78, 26, and 29% of Nec⁻ cells at 24, 48, and 72 h pi, respectively. In these samples, the SYTOX Green stain shows that 81, 69, and 62% of the Nec⁻ bacteria were live cells, respectively (**Figure 5B**). This indicates that the majority of the cells that did not express any of the reporters used were not dead.



DISCUSSION

Our initial goal was to characterize in more detail the composition of the *B. thuringiensis* population during the infectious process. We were interested in particular by the cells that did not express any of the reporters we used in a previous study, especially the necrotrophic state reporter (Verplaetse et al., 2015).

To begin to answer this question we constructed a genetic tool to enable us to follow gene expression fluctuations using a fluorescent reporter. We used the *ssrA*-mediated peptide tagging system (for a review Karzai et al., 2000) that was published for the first time by Andersen et al. (1998) as a tool to destabilize GFP in order to follow transient gene expression in bacteria. Destabilizing the GFP would reduce the fluorescence of the cells harboring this construct. Thus, it was also necessary to improve its fluorescence in *B. thuringiensis* cells. GFP improvement has been described for other bacterial species (Veening et al., 2004; Overkamp et al., 2013) and even bacteria of the *B. cereus* group (using *gfpmut1* as the original template) (Sastalla et al., 2009). We designed a new construct *-gfp_{Bte}-* based on the *sfgfp* allele mainly because of its fast-folding properties (Pedelacq et al., 2006; Milde, 2008). The *B. thuringiensis* cells expressing *gfp_{Bte}* were 20-fold brighter than the ones harboring the initial construct. The best improvement resulted from the codon optimization. Destabilization of the protein was then accomplished by adding a degradation tag to the GFP_{Bte}. The resulting GFP_{Bte}AAV rendered the cells almost as fluorescent as the ones without the tag, but with a half-life of approximately 15 min compared to at least 7.5 h for the original construct. This destabilization method has been adapted by various laboratories to different bacterial species (for example Blokpoel et al., 2003; Hentschel et al., 2013; Mouammime et al., 2017). However, to our knowledge, this system has been only used in very few and elegant studies to monitor fluctuations in gene activity in an infection model (Nielsen et al., 2010; Laughlin et al., 2014).

We fused the *gfp_{Bte}* AAV reporter gene to the promoter of *abrB* and associated it to the *PnprA'mcherry_{LGC}* transcriptional fusion to determine if the bacteria that did not go through the necrotrophic state during the course of infection were vegetative cells. We saw that the promoter of the *abrB* gene was active throughout the infection cycle, at least from 18 h pi to 72 h pi. At 18 h pi a large number of bacteria did not express either reporter. We cannot exclude that these cells expressed the *PabrB'gfp_{Bte}* AAV fusion during the early stage of the infection, considering the unstable nature of the fluorescent protein and the fact that at this time point, the bacteria have reached a growth plateau after a period of active multiplication (Dubois et al., 2016). The proportion of vegetative cells and of undetermined cells then diminished as the proportion of necrotrophic cells increased. This was expected as the necrotrophic marker is a stationary phase marker. However, we did not expect the cells that went through the necrotrophic state to activate the *PabrB* promoter. The stability of the mCherry protein [half-life of more than 50 h (Verplaetse et al., 2015)] is a double-edged property. It allows us to follow the cells that went through the necrotrophic state but we do not know when -or if- they stopped expressing the necrotrophism genes. Using a fluorescent protein whose spectral properties change with time could help solve this issue (Tersikh et al., 2000). We hypothesize that the cells that activated *PabrB* were no longer in a necrotrophic state and that they resumed vegetative growth following a signal that they sensed. It was shown that the sporulating cells arose almost exclusively from necrotrophic cells in the host cadaver (Verplaetse et al., 2015). It is possible that re-activation of the vegetative state is a way of delaying sporulation in some cells. Sporulation is a costly and, at some point, irreversible process (Piggot and Hilbert, 2004). In *B. subtilis*, bacteria that have engaged in sporulation use toxins to kill non-sporulating cells (for a review Gonzalez-Pastor, 2011). This allows the non-committed sporulating cells to arrest sporulation and resume growth by using nutrients provided by the lysis of neighboring cells. Sporulation delay might be why the cells re-enter a vegetative state in this *PabrB'gfp_{Bte}* AAV-expressing sub-population. The mechanism by which this could occur remains to be elucidated. Another hypothesis, which would not exclude the above mentioned one, would be that some of the spores germinated. Indeed, the spores, that originate from necrotrophic cells, retain an mCherry-based fluorescence (Verplaetse et al., 2015, 2016) and the *PabrB* promoter is activated while spores are in the process of germination (data not shown). It is likely that if nutrients become accessible, at least some of the spores will germinate.

To recapitulate these events and integrate them with the previously published data (Verplaetse et al., 2015), we propose the following model as schematized on **Figure 6**. During the early steps of infection, the bacteria activate the vegetative state marker while multiplying. After the virulence stage and death of the host, the bacterial number has reached a plateau and part of the population will turn on the necrotrophic genes. Among these bacteria, some will re-enter a vegetative state. These cells will subsequently have to activate the necrotrophic genes before sporulation can occur in part of this sub-population. Some

spores are then able to germinate and resume vegetative growth. During this infectious cycle, some bacteria do not fit in any of the categories mentioned above. Indeed, the cells that did not go through the necrotrophic state did not appear to activate the *PabrB* promoter. About 20% of the population are still in an undetermined state. However, we have shown that about 70% of these bacteria are viable. This suggests that these cells could be dormant. Dormancy has been studied in Gram-positive and Gram-negative bacteria as a successful survival strategy (Rittershaus et al., 2013; Verstraeten et al., 2016). However, these species were non-sporulating. In sporulating bacteria, the spore is the ultimate form of dormancy. Nevertheless, a quiescent physiological state would constitute an alternative to the complex process of sporulation. Indeed, once the cells are committed to sporulation, they would not be able to return quickly to a vegetative state if competing bacteria invaded their niche. And bacteria in such a quiescent state could rapidly return to exponential growth, compared to germination, if favorable conditions were encountered, or might respond to a different resuscitation signal than that of germination. Many questions remain to be answered, such as the ability of these cells to grow back from this state. Their infectious capacity as well as their gene expression profiles during infection should also be investigated to determine if they can reproduce the parental phenotypes. We are now in the process of pursuing this research further.

AUTHOR CONTRIBUTIONS

Conceived and designed the study: LS and DL. Designed the experiments: LS. Performed the experiments: SBR and LS. Analyzed the data: LS, SBR, and DL. Wrote the paper: LS.

FUNDING

The CyFlow space flow cytometer used in this study was funded by the DIM Astrea (French regional program: Ast11 0137). This work was supported by the INRA (the National Institute for Agronomical Research). SBR was financed by an INRA apprenticeship grant.

ACKNOWLEDGMENTS

The authors thank Morgane Girault for her help with the experiments related to the *gfp* modifications. They are grateful to Christophe Buisson, Agnès Réjasse, and Christina Nielsen-LeRoux for their involvement in the *in vivo* experiments and to Emilie Verplaetse for helpful discussions.

SUPPLEMENTARY MATERIAL

The Supplementary Material for this article can be found online at: <https://www.frontiersin.org/articles/10.3389/fmicb.2017.02471/full#supplementary-material>

REFERENCES

- Agaisse, H., and Lereclus, D. (1994). Structural and functional analysis of the promoter region involved in full expression of the *cryIIIA* toxin gene of *Bacillus thuringiensis*. *Mol. Microbiol.* 13, 97–107. doi: 10.1111/j.1365-2958.1994.tb00405.x
- Andersen, J. B., Sternberg, C., Poulsen, L. K., Bjorn, S. P., Givskov, M., and Molin, S. (1998). New unstable variants of green fluorescent protein for studies of transient gene expression in bacteria. *Appl. Environ. Microbiol.* 64, 2240–2246.
- Arantes, O., and Lereclus, D. (1991). Construction of cloning vectors for *Bacillus thuringiensis*. *Gene* 108, 115–119. doi: 10.1016/0378-1119(91)90495-W
- Banse, A. V., Chastanet, A., Rahn-Lee, L., Hobbs, E. C., and Losick, R. (2008). Parallel pathways of repression and antirepression governing the transition to stationary phase in *Bacillus subtilis*. *Proc. Natl. Acad. Sci. U.S.A.* 105, 15547–15552. doi: 10.1073/pnas.0805203105
- Blokpoel, M. C., O'toole, R., Smeulders, M. J., and Williams, H. D. (2003). Development and application of unstable GFP variants to kinetic studies of mycobacterial gene expression. *J. Microbiol. Methods* 54, 203–211. doi: 10.1016/S0167-7012(03)00044-7
- Bottone, E. J. (2010). *Bacillus cereus*, a volatile human pathogen. *Clin. Microbiol. Rev.* 23, 382–398. doi: 10.1128/CMR.00073-09
- Deng, C., Peng, Q., Song, F., and Lereclus, D. (2014). Regulation of *cry* gene expression in *Bacillus thuringiensis*. *Toxins* 6, 2194–2209. doi: 10.3390/toxins6072194
- Dubois, T., Faegri, K., Gelis-Jeanvoine, S., Perchat, S., Lemy, C., Buisson, C., et al. (2016). Correction: necrotrophism is a quorum-sensing-regulated lifestyle in *Bacillus thuringiensis*. *PLOS Pathog.* 12:e1006049. doi: 10.1371/journal.ppat.1006049
- Fedhila, S., Daou, N., Lereclus, D., and Nielsen-Leroux, C. (2006). Identification of *Bacillus cereus* internalin and other candidate virulence genes specifically induced during oral infection in insects. *Mol. Microbiol.* 62, 339–355. doi: 10.1111/j.1365-2958.2006.05362.x
- Gonzalez-Pastor, J. E. (2011). Cannibalism: a social behavior in sporulating *Bacillus subtilis*. *FEMS Microbiol. Rev.* 35, 415–424. doi: 10.1111/j.1574-6976.2010.00253.x
- Gottesman, S., Roche, E., Zhou, Y., and Sauer, R. T. (1998). The ClpXP and ClpAP proteases degrade proteins with carboxy-terminal peptide tails added by the SsrA-tagging system. *Genes Dev.* 12, 1338–1347. doi: 10.1101/gad.12.9.1338
- Grandvalet, C., Gominet, M., and Lereclus, D. (2001). Identification of genes involved in the activation of the *Bacillus thuringiensis inhA* metalloprotease gene at the onset of sporulation. *Microbiology* 147, 1805–1813. doi: 10.1099/00221287-147-7-1805
- Guerout-Fleury, A. M., Shazand, K., Frandsen, N., and Stragier, P. (1995). Antibiotic-resistance cassettes for *Bacillus subtilis*. *Gene* 167, 335–336. doi: 10.1016/0378-1119(95)00652-4
- Hentschel, E., Will, C., Mustafa, N., Burkovski, A., Rehm, N., and Frunzke, J. (2013). Destabilized eYFP variants for dynamic gene expression studies in *Corynebacterium glutamicum*. *Microb. Biotechnol.* 6, 196–201. doi: 10.1111/j.1751-7915.2012.00360.x
- Karzai, A. W., Roche, E. D., and Sauer, R. T. (2000). The SsrA-SmpB system for protein tagging, directed degradation and ribosome rescue. *Nat. Struct. Biol.* 7, 449–455. doi: 10.1038/75843
- Keiler, K. C., and Sauer, R. T. (1996). Sequence determinants of C-terminal substrate recognition by the Tsp protease. *J. Biol. Chem.* 271, 2589–2593. doi: 10.1074/jbc.271.5.2589
- Keiler, K. C., Waller, P. R., and Sauer, R. T. (1996). Role of a peptide tagging system in degradation of proteins synthesized from damaged messenger RNA. *Science* 271, 990–993. doi: 10.1126/science.271.5251.990
- Laughlin, R. C., Knodler, L. A., Barhoumi, R., Payne, H. R., Wu, J., Gomez, G., et al. (2014). Spatial segregation of virulence gene expression during acute enteric infection with *Salmonella enterica* serovar Typhimurium. *MBio* 5, e00946–13. doi: 10.1128/mBio.00946-13
- Lereclus, D., Arantes, O., Chauvaux, J., and Lecadet, M. (1989). Transformation and expression of a cloned delta-endotoxin gene in *Bacillus thuringiensis*. *FEMS Microbiol. Lett.* 51, 211–217.
- Lereclus, D., Lecadet, M. M., Ribier, J., and Dedonder, R. (1982). Molecular relationships among plasmids of *Bacillus thuringiensis*: conserved sequences through 11 crystalliferous strains. *Mol. Gen. Genet.* 186, 391–398. doi: 10.1007/BF00729459
- Lopez, D., and Kolter, R. (2010). Extracellular signals that define distinct and coexisting cell fates in *Bacillus subtilis*. *FEMS Microbiol. Rev.* 34, 134–149. doi: 10.1111/j.1574-6976.2009.00199.x
- Lucking, G., Dommel, M. K., Scherer, S., Fouet, A., and Ehling-Schulz, M. (2009). Cereulide synthesis in emetic *Bacillus cereus* is controlled by the transition state regulator AbrB, but not by the virulence regulator PlcR. *Microbiology* 155, 922–931. doi: 10.1099/mic.0.024125-0
- MacNeil, D. J., Gewain, K. M., Ruby, C. L., Dezeny, G., Gibbons, P. H., and Macneil, T. (1992). Analysis of *Streptomyces avermitilis* genes required for avermectin biosynthesis utilizing a novel integration vector. *Gene* 111, 61–68. doi: 10.1016/0378-1119(92)90603-M
- Milde, S. (2008). *Improved Fluorescent Proteins for Synthetic Biology*. Available at: http://www.openwetware.org/wiki/IGEM:Cambridge/2008/Improved_GFP
- Mock, M., and Fouet, A. (2001). Anthrax. *Annu. Rev. Microbiol.* 55, 647–671. doi: 10.1146/annurev.micro.55.1.647
- Mouammine, A., Pages, S., Lanois, A., Gaudriault, S., Jubelin, G., Bonabaud, M., et al. (2017). An antimicrobial peptide-resistant minor subpopulation of *Photobacterium luminescens* is responsible for virulence. *Sci. Rep.* 7:43670. doi: 10.1038/srep43670
- Nielsen, A. T., Dolganov, N. A., Rasmussen, T., Otto, G., Miller, M. C., Felt, S. A., et al. (2010). A bistable switch and anatomical site control *Vibrio cholerae* virulence gene expression in the intestine. *PLOS Pathog.* 6:e1001102. doi: 10.1371/journal.ppat.1001102
- O'Reilly, M., and Devine, K. M. (1997). Expression of AbrB, a transition state regulator from *Bacillus subtilis*, is growth phase dependent in a manner resembling that of Fis, the nucleoid binding protein from *Escherichia coli*. *J. Bacteriol.* 179, 522–529. doi: 10.1128/jb.179.2.522-529.1997
- Overkamp, W., Beilharz, K., Detert Oude Weme, R., Solopova, A., Karsens, H., Kovacs, A., et al. (2013). Benchmarking various green fluorescent protein variants in *Bacillus subtilis*, *Streptococcus pneumoniae*, and *Lactococcus lactis* for live cell imaging. *Appl. Environ. Microbiol.* 79, 6481–6490. doi: 10.1128/AEM.02033-13
- Pedelacq, J. D., Cabantous, S., Tran, T., Terwilliger, T. C., and Waldo, G. S. (2006). Engineering and characterization of a superfolder green fluorescent protein. *Nat. Biotechnol.* 24, 79–88. doi: 10.1038/nbt1172
- Perchat, S., Dubois, T., Zouhir, S., Gominet, M., Poncet, S., Lemy, C., et al. (2011). A cell-cell communication system regulates protease production during sporulation in bacteria of the *Bacillus cereus* group. *Mol. Microbiol.* 82, 619–633. doi: 10.1111/j.1365-2958.2011.07839.x
- Perchat, S., Talagas, A., Poncet, S., Lazar, N., Li De La Sierra-Gallay, I., Gohar, M., et al. (2016). How quorum sensing connects sporulation to necrotrophism in *Bacillus thuringiensis*. *PLOS Pathog.* 12:e1005779. doi: 10.1371/journal.ppat.1005779
- Perego, M., Spiegelman, G. B., and Hoch, J. A. (1988). Structure of the gene for the transition state regulator, *abrB*: regulator synthesis is controlled by the *spo0A* sporulation gene in *Bacillus subtilis*. *Mol. Microbiol.* 2, 689–699. doi: 10.1111/j.1365-2958.1988.tb00079.x
- Periago, P. M., Van Schaik, W., Abee, T., and Wouters, J. A. (2002). Identification of proteins involved in the heat stress response of *Bacillus cereus* ATCC 14579. *Appl. Environ. Microbiol.* 68, 3486–3495. doi: 10.1128/AEM.68.7.3486-3495.2002
- Piggot, P. J., and Hilbert, D. W. (2004). Sporulation of *Bacillus subtilis*. *Curr. Opin. Microbiol.* 7, 579–586. doi: 10.1016/j.mib.2004.10.001
- Raymond, B., Johnston, P. R., Nielsen-Leroux, C., Lereclus, D., and Crickmore, N. (2010). *Bacillus thuringiensis*: an impotent pathogen? *Trends Microbiol.* 18, 189–194. doi: 10.1016/j.tim.2010.02.006
- Rittershaus, E. S., Baek, S. H., and Sasseti, C. M. (2013). The normalcy of dormancy: common themes in microbial quiescence. *Cell Host Microbe* 13, 643–651. doi: 10.1016/j.chom.2013.05.012
- Salamitov, S., Ramiés, F., Brehelin, M., Bourguet, D., Gilois, N., Gominet, M., et al. (2000). The PlcR regulon is involved in the opportunistic properties of *Bacillus thuringiensis* and *Bacillus cereus* in mice and insects. *Microbiology* 146(Pt 11), 2825–2832. doi: 10.1099/00221287-146-11-2825
- Sanahuja, G., Banakar, R., Twyman, R. M., Capell, T., and Christou, P. (2011). *Bacillus thuringiensis*: a century of research, development and commercial

- applications. *Plant Biotechnol. J.* 9, 283–300. doi: 10.1111/j.1467-7652.2011.00595.x
- Sanchis, V. (2011). From microbial sprays to insect-resistant transgenic plants: history of the biopesticide *Bacillus thuringiensis*. A review. *Agron. Sustain. Dev.* 31, 217–231. doi: 10.1051/agro/2010027
- Sastalla, I., Chim, K., Cheung, G. Y., Pomerantsev, A. P., and Leppla, S. H. (2009). Codon-optimized fluorescent proteins designed for expression in low-GC gram-positive bacteria. *Appl. Environ. Microbiol.* 75, 2099–2110. doi: 10.1128/AEM.02066-08
- Slamti, L., Lemy, C., Henry, C., Guillot, A., Huillet, E., and Lereclus, D. (2015). CodY regulates the activity of the virulence quorum sensor PlcR by controlling the import of the signaling peptide PapR in *Bacillus thuringiensis*. *Front. Microbiol.* 6:1501. doi: 10.3389/fmicb.2015.01501
- Slamti, L., and Lereclus, D. (2002). A cell-cell signaling peptide activates the PlcR virulence regulon in bacteria of the *Bacillus cereus* group. *EMBO J.* 21, 4550–4559. doi: 10.1093/emboj/cdf450
- Slamti, L., Perchat, S., Huillet, E., and Lereclus, D. (2014). Quorum sensing in *Bacillus thuringiensis* is required for completion of a full infectious cycle in the insect. *Toxins (Basel)* 6, 2239–2255. doi: 10.3390/toxins6082239
- Stammen, S., Muller, B. K., Korneli, C., Biedendieck, R., Gamer, M., Franco-Lara, E., et al. (2010). High-yield intra- and extracellular protein production using *Bacillus megaterium*. *Appl. Environ. Microbiol.* 76, 4037–4046. doi: 10.1128/AEM.00431-10
- Stenfors Arnesen, L. P., Fagerlund, A., and Granum, P. E. (2008). From soil to gut: *Bacillus cereus* and its food poisoning toxins. *FEMS Microbiol. Rev.* 32, 579–606. doi: 10.1111/j.1574-6976.2008.00112.x
- Strauch, M. A., and Hoch, J. A. (1993). Transition-state regulators: sentinels of *Bacillus subtilis* post-exponential gene expression. *Mol. Microbiol.* 7, 337–342. doi: 10.1111/j.1365-2958.1993.tb01125.x
- Taylor, R. G., Walker, D. C., and McInnes, R. R. (1993). *E. coli* host strains significantly affect the quality of small scale plasmid DNA preparations used for sequencing. *Nucleic Acids Res.* 21, 1677–1678. doi: 10.1093/nar/21.7.1677
- Tersikh, A., Fradkov, A., Ermakova, G., Zaraksky, A., Tan, P., Kajava, A. V., et al. (2000). “Fluorescent timer”: protein that changes color with time. *Science* 290, 1585–1588. doi: 10.1126/science.290.5496.1585
- Veening, J. W., Smits, W. K., Hamoen, L. W., Jongbloed, J. D., and Kuipers, O. P. (2004). Visualization of differential gene expression by improved cyan fluorescent protein and yellow fluorescent protein production in *Bacillus subtilis*. *Appl. Environ. Microbiol.* 70, 6809–6815. doi: 10.1128/AEM.70.11.6809-6815.2004
- Verplaetse, E., Slamti, L., Gohar, M., and Lereclus, D. (2015). Cell differentiation in a *Bacillus thuringiensis* population during planktonic growth, biofilm formation, and host infection. *MBio* 6, e00138–e00115. doi: 10.1128/mBio.00138-15
- Verplaetse, E., Slamti, L., Gohar, M., and Lereclus, D. (2016). Two distinct pathways lead *Bacillus thuringiensis* to commit to sporulation in biofilm. *Res. Microbiol.* 168, 388–393. doi: 10.1016/j.resmic.2016.03.006
- Verstraeten, N., Knapen, W., Fauvart, M., and Michiels, J. (2016). A historical perspective on bacterial persistence. *Methods Mol. Biol.* 1333, 3–13. doi: 10.1007/978-1-4939-2854-5_1
- Vlamakis, H., Aguilar, C., Losick, R., and Kolter, R. (2008). Control of cell fate by the formation of an architecturally complex bacterial community. *Genes Dev.* 22, 945–953. doi: 10.1101/gad.1645008
- Wiegert, T., and Schumann, W. (2001). SsrA-mediated tagging in *Bacillus subtilis*. *J. Bacteriol.* 183, 3885–3889. doi: 10.1128/JB.183.13.3885-3889.2001

Conflict of Interest Statement: The authors declare that the research was conducted in the absence of any commercial or financial relationships that could be construed as a potential conflict of interest.

Copyright © 2017 Ben Rejeb, Lereclus and Slamti. This is an open-access article distributed under the terms of the Creative Commons Attribution License (CC BY). The use, distribution or reproduction in other forums is permitted, provided the original author(s) or licensor are credited and that the original publication in this journal is cited, in accordance with accepted academic practice. No use, distribution or reproduction is permitted which does not comply with these terms.



Phenotypic Heterogeneity in Attachment of Marine Bacteria toward Antifouling Copolymers Unraveled by AFM

Sofiane El-Kirat-Chatel^{1,2}, Aurore Puymege³, The H. Duong^{3,4}, Perrine Van Overtvelt³, Christine Bressy³, L  na  k Belec³, Yves F. Dufr  ne² and Ma  lle Molmeret^{3*}

¹ CNRS and Universit   de Lorraine, Laboratoire de Chimie Physique et Microbiologie pour l'Environnement (LCPME), UMR 7564, Nancy, France, ² Institute of Life Sciences, Universit   catholique de Louvain, Louvain-la-Neuve, Belgium, ³ Laboratoire MAPIEM, EA4323, Universit   de Toulon, La Garde, France, ⁴ University of Science and Technology, The University of Danang, Danang, Vietnam

OPEN ACCESS

Edited by:

Weiwen Zhang,
Tianjin University, China

Reviewed by:

Musashi Takenaka,
Kobe University, Japan
Dimitris Tsaltas,
Cyprus University of Technology,
Cyprus

*Correspondence:

Ma  lle Molmeret
molmeret@univ-tln.fr;
maellemolmeret@hotmail.com

Specialty section:

This article was submitted to
Systems Microbiology,
a section of the journal
Frontiers in Microbiology

Received: 18 May 2017

Accepted: 11 July 2017

Published: 27 July 2017

Citation:

El-Kirat-Chatel S, Puymege A,
Duong TH, Van Overtvelt P,
Bressy C, Belec L, Dufr  ne YF and
Molmeret M (2017) Phenotypic
Heterogeneity in Attachment
of Marine Bacteria toward Antifouling
Copolymers Unraveled by AFM.
Front. Microbiol. 8:1399.
doi: 10.3389/fmicb.2017.01399

Up to recent years, bacterial adhesion has mostly been evaluated at the population level. Single cell level has improved in the past few years allowing a better comprehension of the implication of individual behaviors as compared to the one of a whole community. A new approach using atomic force microscopy (AFM) to measure adhesion forces between a live bacterium attached via a silica microbead to the AFM tipless cantilever and the surface has been recently developed. The objectives of this study is to examine the bacterial adhesion to a surface dedicated to ship hulls at the population and the cellular level to understand to what extent these two levels could be correlated. Adhesion of marine bacteria on inert surfaces are poorly studied in particular when substrata are dedicated to ship hulls. Studying these interactions in this context are worthwhile as they may involve different adhesion behaviors, taking place in salty conditions, using different surfaces than the ones usually utilized in the literacy. FRC (fouling release coatings)–SPC (self-polishing coatings) hybrids antifouling coatings have been used as substrata and are of particular interest for designing environmentally friendly surfaces, combining progressive surface erosion and low adhesion properties. In this study, a hybrid coating has been synthesized and used to study the adhesion of three marine bacteria, displaying different surface characteristics, using microplate assays associated with confocal scanning laser microscopy (CSLM) and AFM. This study shows that the bacterial strain that appeared to have the weakest adhesion and biofilm formation abilities when evaluated at the population level using microplates assays and CSLM, displayed stronger adhesion forces on the same surfaces at the single cell level using AFM. In addition, one of the strains tested which presented a strong ability to adhere and to form biofilm at the population level, displayed a

heterogeneous phenotypic behavior at the single cell level. Therefore, these results suggest that the evaluation of adhesion at the population level cannot always be correlated with adhesion forces measured individually by AFM and that some bacteria are prone to phenotypic heterogeneity among their population.

Keywords: marine bacteria, adhesion, heterogeneity, AFM, copolymers surfaces

INTRODUCTION

Little is known on adhesion of marine bacteria on surfaces in particular when they are dedicated to ship hulls. The comprehension of bacterial adhesion on these surfaces should help finding potential environmentally less toxic anti-adhesion or anti-fouling strategies. The specific intrinsic nature of marine bacteria, that are poorly studied and characterized, may modify the type of interactions that can be observed between a cell and its surface, particularly when the interactions take place in marine conditions, making them worthwhile studying. Overall, molecular or cellular mechanisms of bacterial adhesion have been in fact mostly evaluated at the population level but very rarely at the single cell level. Indeed, very few information are factually available on individual behaviors of bacteria regarding adhesion. Due to the development of new single cell level approaches, individual cells can be studied with the purpose of understanding how a single cell behaves as compared to its population of origin and if bacterial cells behave all similarly within a supposedly clonal population, after synchronization in growth culture, or if important behavioral differences exist between them. Recently, the idea that bacterial population could be composed of heterogeneous individuals has emerged, even when coming from a single cell or a group of clonal or genetically identical individuals (Grote et al., 2015; Martins and Locke, 2015). Differential gene expression could explain these phenotypic fluctuations. Some bacterial strains are also more prone to allelic variations than others (Davis and Isberg, 2016). In adhesion studies, atomic force microscopy (AFM) approaches have been used to study adhesion forces at the single cell level between a cell and a surface. They have been improved during the past few years, making it possible to study these interactions with alive bacteria (Kang and Elimelech, 2009; Loskill et al., 2012; Beaussart et al., 2013, 2014; El-Kirat-Chatel et al., 2014a). Indeed, a new approach using a silica microbead fixed on the tipless cantilever allows the attachment of a single cell that can stay alive during the time of the measurement. These approaches have been proven very useful to decipher adhesion of bacteria such as *Staphylococcus aureus*, *Escherichia coli* toward glass and functionalized surfaces.

In the marine context, all artificial surfaces immersed in seawater are subjected to the accumulation of marine organisms such as microorganisms and macrofoulers, known as marine biofouling. Current antifouling strategies rely on the wide use of self-polishing coatings (SPC), which release toxic biocides with a constant rate controlled by the coating erosion process (Yebra et al., 2004). The erosion of the coating is achieved through the hydrolysis of the polymeric binder in seawater making the polymer water-soluble. Fouling release coatings (FRC) represent

a second type of antifouling coatings, which are able to release organisms settled on the surface while boats are navigating (Lejars et al., 2012). Their efficacy relies on hydrophobicity, low surface energy and low elastic modulus of its poly(dimethylsiloxane) (PDMS) cross-linked matrix, which decreases the adhesion strength of marine organisms and enhance their removal. Despite, the clear environmentally friendly advantage of this antifouling solution, FRCs are inefficient when vessels are docked. During navigation, the coating is able to release the macrofouling but retains a microfouling film (composed mainly of bacteria and diatoms), which is still responsible for 10% of drag resistance (Schultz, 2007). An attractive option in developing such coatings is the synthesis of new polymers which are both hydrolyzable and hydrophobic/low-surface energy materials. Poly(dimethylsiloxane) blocks could be inserted in silylated-based polymers to provide access to a wide variety of materials with tunable hydrophobicity, water resistance and mechanical properties. Bressy and Margailan (2009), Bressy et al. (2010, 2014), Lejars et al. (2014) have synthesized tri-alkylsilyl ester-based statistical copolymers by conventional radical polymerization and several diblock copolymers using the reversible addition-fragmentation chain transfer (RAFT) polymerization for developing erodible binders for marine antifouling coatings. Hybrid copolymers with PDMS blocks or side-chains and silylated side groups have been reported to exhibit surface erosion and hydrophobic surfaces depending on the relative content of the two components (Lejars et al., 2013). These hybrid surfaces displaying SPC and FRC properties have been characterized including for their antifouling efficacy (Duong et al., 2014, 2015).

In this study, three strains isolated from the Mediterranean sea, presenting different phenotypical traits, have been used to evaluate their ability to adhere on a new antifouling coating dedicated to ship hulls at the population and the cellular level (Brian-Jaisson et al., 2014). TC5 belonging to the *Polaribacter* genus, a non-motile marine bacteria, is the most hydrophobic of the three strains according to Microbial Adhesion to Solvents (MATS) assays and has a poor ability to form biofilm on polystyrene when studied in microplates (Brian-Jaisson et al., 2014). TC10 and TC11 are two different strains of *Shewanella*, which are overall more hydrophilic and are motile. TC11 is able of a stronger adhesion and a faster capacity to form a biofilm on polystyrene while for TC10, it takes more time to form its biofilm. In this context, adhesion have been tested on an hybrid block copolymer SPC-FRC coating called MC3MB6 [PDMS-*b*-p(SiMA-*stat*-BMA)]. The results have been compared to its SPC block alone called MB6 (SiMA-*stat*-BMA). In contrast with conventional SPC, MB6 has no biocide but retaining the ability of self-hydrolysis. Both surfaces have been synthesized

and their properties characterized similarly as previously done (Duong et al., 2014, 2015). The adhesion assays of these three marine strains on the hybrid coatings have been performed through a microplate assay associated with CLSM and AFM, in order to verify if the adhesion forces measured at the single cell level could be correlated with the evaluation of the population adhesion. Bacterial adhesion has been very rarely evaluated at the same time, at the population and the cellular level to understand to what extent these two levels could be correlated for each of the strain.

MATERIALS AND METHODS

Substrates

Two copolymers based on *Tert*-butyldimethylsilyl methacrylate (SiMA) were synthesized as previously reported (Duong et al., 2014). Butyl methacrylate was used as co-monomer of SiMA to prepare films without cracking (Table 1). Each copolymer was dissolved in toluene, at a 40–50 wt% solid content, and applied on abraded poly(vinyl chloride) (PVC) substrates with a bar-coater resulting in about 100 μm dried thickness coatings. The surfaces of the samples for the contact angle measurement and for AFM measurements were 25 mm \times 45 mm and 10 mm \times 10 mm, respectively. The coated plates were left to dry in the open air for 15 days.

Characterization Methods

The number-average molar mass (M_n) and dispersity (\mathcal{D}) of polymers were determined by triple detection size exclusion chromatography (TD-SEC). Analyses were performed on a Viscotek apparatus, composed of a GPC Max (comprising a degasser, a pump and an autosampler) with a TDA-302 (RI refractive index detector, right and low angle light scattering detector at 670 nm and viscometer) and an UV detector ($\lambda = 298 \text{ nm}$). The following columns were used: a Viscotek HHR-H precolumn and two Viscotek ViscoGel GMHHR-H columns. THF was used as the eluent with a flow rate of 1.0 mL min^{-1} at 30°C. For each precipitated polymer, the refractive index increment (dn/dc) was determined using the OmniSec software, from a solution of known concentration (ca. 10 mg mL^{-1}) filtered through a 0.2 mm PTFE filter.

Differential scanning calorimetric (DSC) measurements were performed on a DSC Q10 apparatus from TA Instruments calibrated with indium. Polymer samples weighing 15–20 mg were run at equal heating and cooling rates, 10°C min^{-1} , under a constant stream of nitrogen. The MC3MB6 sample was first scanned from room temperature to 100°C

[PDMS-*block*-P(SiMA-*stat*-BMA)]. The sample was then cooled to -165°C . This temperature was held for 5 min to allow the system to attain thermal equilibrium before the second heating scan. The first heating ramp of each sample was discarded for this work. The glass transition temperature (T_g) values were determined as the midpoint between the onset and the end of a step transition using the TA Instruments Universal Analysis 2000 software.

Static contact angle measurements were carried out at room temperature using a sessile drop method with a DIGIDROP contact angle meter from GBX Instruments. Two test liquids: deionized water and diiodomethane (Sigma–Aldrich) were used. The liquid drop volume was 1 and 0.5 μL for water and diiodomethane, respectively. A picture of the liquid drop on the surface was taken 4 s after its formation for contact angle measurement. The reported contact angles were an average of five individual measurements in different regions of the same coating ($\pm\sigma$). Surface free energies of the coatings (γ_s) and their dispersive (γ_s^D) and polar components (γ_s^P) were calculated using the Owens–Wendt method. Dynamic contact angle measurements were carried out under ambient conditions by using the dynamic sessile drop technique. A water drop with a volume of around 1 μL is growing on a syringe tip and picked up by the surface. The syringe tip never leaves the liquid drop. The water was inflated and sucked up from the surface and the advancing and receding angles were obtained.

AFM Characterization of the Surface

Atomic force microscopy measurements were performed on a Nanoscope V controller equipped with a Multimode V Atomic Force Microscope, with a 8610 JVL type scanner. Tapping mode cantilever probes (RTESP model from BRUKER) were used to show the topography of the supported polymer films and to evaluate their Young modulus values. The system sensitivity and cantilever spring constant k_c are successively determined from force measurements on a rigid sample and from the thermal tune method (Butt et al., 2005), implemented in Bruker Nanoscope (V7.3) software. The topography was initially scanned in tapping mode with a cantilever spring constant around 48 N/m and a resonance frequency of $\sim 380 \text{ kHz}$. AFM force curves were performed with maximum forces lower than 1.5 μN (The slope of the force–displacement approach curve in the linear elastic range gives an apparent stiffness k_{eff} which is directly linked to the sample stiffness k_s knowing the cantilever stiffness (Butt et al., 2005). In the case of a perfectly elastic tip with a spherical end and a homogeneous sample, with no adhesive effects, the Hertz model can give an estimation of Young's modulus from k_s measurement (Butt et al., 2005; Belec et al., 2015). The slope

TABLE 1 | Characteristics of diblock and statistical copolymers prepared by reversible addition-fragmentation chain transfer (RAFT) polymerization of SiMA and BMA from PDMS-macro RAFT agent at 70°C in toluene.

Polymer	% _{mol} (DMS/SiMA/BMA)	% _{mass} (DMS/SiMA/BMA)	% <i>vol</i> _{PDMS}	M_n (g.mol ⁻¹)*	\mathcal{D}^*
MC3MB6	31/10/59	18/16/66	19	59,700	1.1
MB6	0/14/86	0/18/82	0	49,500	1.1

*Assessed by triple detection size exclusion chromatography (TD-SEC).

was calculated on the approach curves (between 400 and 450 nm of deflection). The standard deviation is calculated on seven measurements.

Microorganisms and Growth Conditions

Bacterial strains used in this study (TC for Toulon Collection) are listed in Supplementary Table S1. They were isolated from biofilms formed on inert surfaces immersed in the Mediterranean Sea (bay of Toulon, France, 43°06'23''N-5°57'17''E) (Camps et al., 2011; Briand et al., 2012). TC strains were grown in Vaatanen nine salt solution (VNSS) at 20°C in a rotary shaker (120 rpm) (Mardén et al., 1985) up to post-exponential phase prior to analysis.

Adhesion Assays on Polystyrene

Post-exponential phase grown cells were centrifuged and resuspended in artificial sea water (ASW). Then 200 μ L of cells were inoculated at OD_{600 nm} 0.3 in triplicate in black microplates (sterile black PS; Nunc, Fisher Scientific, Illkirch, France). After 24 h of incubation at 20°C, the non-adhered bacteria were eliminated by three successive washes (36g.L⁻¹ sterile NaCl solution). The adhered bacteria were stained by both Syto 61 Red and Syto 9 Green fluorescent markers (5 μ M) targeting bacterial DNA (Life technology). After 10 min, the excess stain was eliminated by one wash. Fluorescence intensity (FI) was measured using an Infinite 200 microplate fluorescence reader (Tecan, Lyon, France). A fluorescent intensity was calculated per well: Fluorescent intensity (FI) = FI average assay/FI average negative control. Three independent assays were done for each strain tested. Same results were found with both stains (data not shown).

Adhesion Assays on Copolymers

Adhesion assay on copolymers were performed as described for the adhesion assays on polystyrene excepted for the following points. PVC coverslips of 13 mm of diameter were coated with the MB6 and MC3MB6 polymers. Each copolymer previously dissolved in toluene, at a 40–50 wt% solid content, were applied on PVC coverslips with a bar-coater resulting in about 100 μ m dried thickness coatings. Coverslips were inserted in 24 well microplates (sterile transparent PS; VWR) and sterilized 15 min with UV. Post-exponential bacterial strains were resuspended in ASW and inoculated at OD_{600 nm} 1 in the microplates. After 24 h of incubation at 20°C strains were labeled with 5 μ M of Syto 9 Green fluorescent nucleic acid stain (Life technology). After 10 min, the excess stain was eliminated by three washes. FI was measured using an Infinite 200 microplate fluorescence reader (Tecan, Lyon, France). A fluorescent intensity was calculated per well: FI = FI average assay/FI average negative control. Three independent assays were done for each strain tested.

CSLM Observation

The same coverslips were used for the observation of the bacteria on the surfaces using confocal scanning laser microscopy (CSLM) Zeiss LSM 510. Briefly, the coated coverslips were glued onto a

glass slide and covered with prolong antifade (Life technology) and a new glass coverslips. After 48 h drying, the samples were stored at 4°C until use for CSLM observation.

Statistical Analysis

GraphPad Prism 5 (GraphPad Software, San Diego, CA, United States) was used for statistical analysis of the adhesion assays. Data were analyzed using one-way ANOVA and treatment effects were separated using Turkey's multiple comparison *post hoc* tests. Statistical significance was accepted at $p < 0.05$.

Atomic Force Microscopy Imaging

Atomic force microscopy contact mode images were obtained in air, at room temperature, using a Nanoscope VIII Multimode AFM (Nano Surfaces Business, Bruker Corporation, Santa Barbara, CA, United States), MSCCT cantilevers with a nominal spring constant of ~ 0.01 N/m (calculated with the thermal noise method), and a scanning rate of 2 Hz. One hundred μ L of cell suspension from post-exponential growth phase was put in contact with freshly cleaved mica supports mounted on steel pucks. The samples were incubated for 2 h at 30°C, gently rinsed in three successive baths of ultrapure water (Elga, purelab), and allowed to dry at 30°C overnight.

Cell Probes

For single-bacterial cell force spectroscopy, cell probes were prepared using a recently developed protocol that combines colloidal probe cantilevers and bioinspired polydopamine wet adhesives (Beaussart et al., 2013). Briefly, silica microspheres (6.1 μ m diameter, bangs laboratories) were attached on triangular shaped tipless cantilevers (NP-O10, Microlevers, Bruker Corporation) using UV-curable glue (NOA 63, Norland Edmund Optics). The cantilevers were then immersed for 1 h in a 10 mM Tris Buffer solution (pH 8.5) containing 4 mg ml⁻¹ dopamine hydrochloride (99%, Sigma), and dried with N₂ flow. Single bacteria were then attached onto polydopamine-coated colloidal probes using a Bioscope Catalyst AFM (Bruker corporation, Santa Barbara, CA, United States). To this end, 2 μ L of a cell suspension were added to 4 ml of ASW solution (pH 8, Sea salts, Sigma) in a glass Petri dish containing MB6 and MC3MB6 substrates. A single probe was brought into contact with an isolated cell for 3 min, and the obtained cell probe was then transferred over a solid substrate for further force measurements. Viability of the attached bacteria was checked using a Live-dead BacLight viability kit (Invitrogen, kit L7012) following the manufacturer instructions.

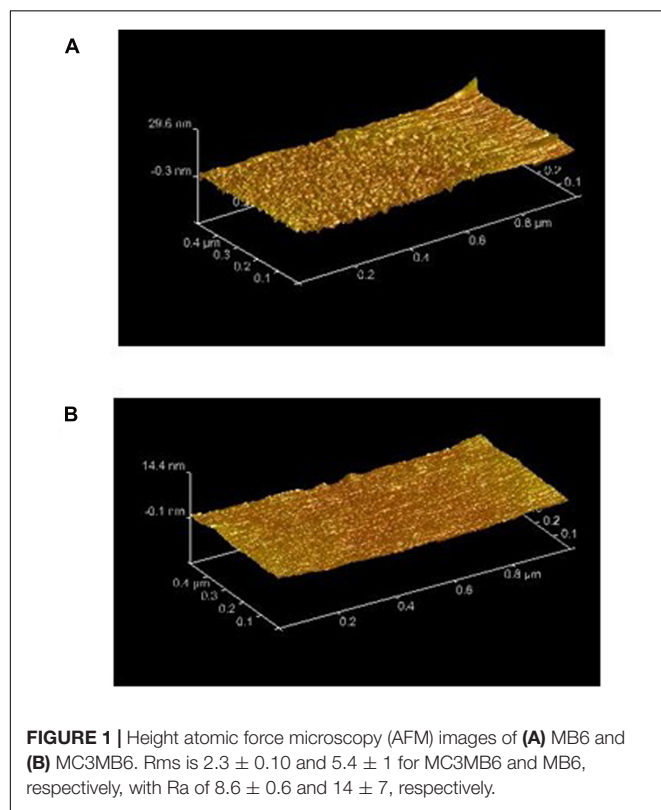
Single-Cell Force Spectroscopy Measurements

Single-cell force spectroscopy (SCFS) measurements were performed at room temperature (20°C) in ASW solution pH 8 and using a Bioscope Catalyst AFM (Bruker AXS Corporation, Santa Barbara, CA, United States). The nominal spring constant of the colloidal probe cantilever was ~ 0.06 N m⁻¹, as determined

TABLE 2 | Wetting properties of the coating surfaces.

Polymer	Contact angle (°)				Surface energies (mJ.m ⁻²)*		
	θ_{H_2O}	σ	$\theta_{CH_2I_2}$	σ	γ_s	γ_s^D	γ_s^P
MC3MB6	101.9	1	71.5	0.6	22	20.9	1.1
MB6	91.3	0.5	64.3	4.6	26.7	23.3	3.3

*Using Owens–Wendt's method (Owen and Wendt, 1969).



by the thermal noise method. Multiple force-distance curves were recorded on various spots of MB6 and MC3MB6 substrates using a maximum applied force of 250 pN, a contact time of 100 ms or 1 s, and constant approach and retraction speeds of 1000 nm s^{-1} . For each condition, the interaction forces of three bacterial cells from independent cultures were measured and $n > 400$ force curves were recorded for each bacteria.

RESULTS AND DISCUSSION

Polymers Synthesis and Characterization of Copolymer Surfaces

Well-defined diblock copolymers combining a tert-butyl-dimethylsilyl methacrylate (SiMA)-based block, as hydrolyzable “SPC-type” monomer, with a poly(dimethylsiloxane) (PDMS) block, as hydrophobic, “FRC-type” monomer have been investigated. The synthesis of the PDMS-*b*-p(SiMA-*stat*-BMA) block copolymer called MC3MB6 was achieved from copolymerizations of tert-butyl-dimethylsilyl methacrylate

TABLE 3 | Young's modulus at the coating surfaces measured by AFM.

Polymer	E (MPa)	Indentation (nm)
MC3MB6	73 ± 4	207 ± 4
MB6	88 ± 7	145 ± 5

(SiMA) and butyl methacrylate on PDMS macro-RAFT agents. The methodology relies on the synthesis of PDMS monofunctional chain transfer agents easily available in one synthetic step from commercially available hydroxylated PDMSs (Duong et al., 2014). A statistical copolymer P(SiMA-*stat*-BMA) called MB6, with a composition similar to the second block of MC3MB6, has also been prepared (Table 1). As these copolymers might be used in marine environment as coatings, their ability to form films without cracking is required. Good film properties have been displayed for MB6 and MC3MB6 due to their low glass transition temperature of $45\text{--}46^\circ\text{C}$ corresponding to P(SiMA-*stat*-BMA) block. In the case of MC3MB6, the T_g of the PDMS block (from -127 to -124°C) was not visible because of a low amount of DMS monomer units within the copolymer (Duong et al., 2014). Surface properties including wetting properties and smoothness have been investigated. Table 2 shows that the water contact angle values increased and the polar component of the surface free energy (γ_s^P) decreased when the PDMS block was added within the copolymer. Taken together these results show that MC3MB6 is more hydrophobic than its MB6 counterpart which could suggest according to the literature a close packing of the pendant methyl groups of the flexible siloxane chain at the film/air interface (Lejars et al., 2012). Tapping-mode AFM analysis shows the topography of the PDMS-based films to be smoother than the MB6 PDMS-free coating (Figure 1 and Supplementary Figure S1). In addition, the flexibility of the PDMS block coming from its low T_g value and the flexibility of the methacrylic block coming from the presence of BMA monomer units provided soft samples. A lower Young's modulus value and a higher indentation were found for the PDMS-based sample (Table 3). Taken together these results show that MC3MB6 surface is softer than MB6 one.

When immersing these silylester-based polymers in artificial seawater, the hydrophilic character of the two coating surfaces increased with time as the water contact angle θ_{H_2O} decreases with immersion time (Figure 2). This result is in agreement with the well-known hydrolysis reaction of the hydrophobic silyl ester groups of SiMA units into hydrophilic sodium carboxylate groups in artificial seawater (Bressy and Margaillan, 2009). Nevertheless, the surface of the PDMS-based coating MC3MB6 remains more hydrophobic than the MB6 one.

Adhesion Tests of Marine Bacteria on Polystyrene

Biofilm formation has been previously evaluated in different rich marine media for a number of marine bacteria isolated from the Mediterranean sea (Camps et al., 2011; Brian-Jaisson et al., 2014). Five of these marine bacterial strains (Supplementary Table S1), which were all isolated from biofilms formed on immersed supports in the bay of Toulon (France), were analyzed for their

adhesion ability in ASW on polystyrene (**Figure 3**). Three of them (TC9–TC10 and TC11) belong to *Shewanella* genus. TC5 and TC8 belong, respectively, to *Polaribacter* and *Pseudoalteromonas* genus (Supplementary Table S1). All strains except TC5, were able to form a biofilm in laboratory conditions (Brian-Jaisson et al., 2014). In this study, strains exhibited different adhesion patterns on polystyrene after 24 h (**Figure 3**) in a poor medium, ASW. Bacterial adhesion of TC11 was the strongest. TC8 adhered to polystyrene but fluorescence intensity was 1.6 times less than for TC11. Adhesion on polystyrene was weak for TC5 and very weak for the TC10 and TC9 strains. Three profiles based on adhesion on polystyrene and biofilm formation pattern can be identified: (i) a weak adhesion profile in ASW with an incapacity to form biofilm in rich media (Brian-Jaisson et al., 2014) for TC5; (ii) a strong adhesion on polystyrene with a strong ability to form biofilm in rich media for TC8 and TC11; (iii) a weaker ability to adhere on polystyrene in ASW and a slower capacity to form a biofilm in rich media for TC9 and TC10, corresponding thus to an intermediary phenotypic between the two first groups. For the following approaches, we therefore chose to work with one strain of each group. TC5 belonging to the *Polaribacter* genus, a non-motile marine bacteria, is the most hydrophobic of the three strains according to Microbial Adhesion to Solvents (MATS) assays, has a weak adhesion profile and has a poor ability to form biofilm (Brian-Jaisson et al., 2014). TC10 and TC11 are two different strains of *Shewanella*, which are overall more hydrophilic and are motile. TC11 is able of a stronger adhesion and a faster capacity to form a biofilm on polystyrene while for TC10, it takes more time to form its biofilm (Brian-Jaisson et al., 2014).

AFM Imaging to Unravel Morphological Features of Bacteria Species

We used AFM contact mode imaging in air to visualize the general cell topography of TC5, TC10, and TC11. For all strains, bacteria were small rod-shaped, which agree well with observations performed previously (Brian-Jaisson et al., 2014).

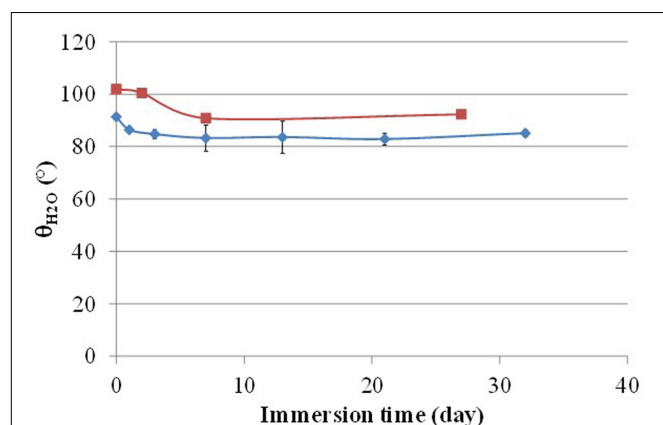


FIGURE 2 | Evolution of the static water contact angle of MC3MB6 (■) and (◆) MB6-based coatings with ASW immersion time.

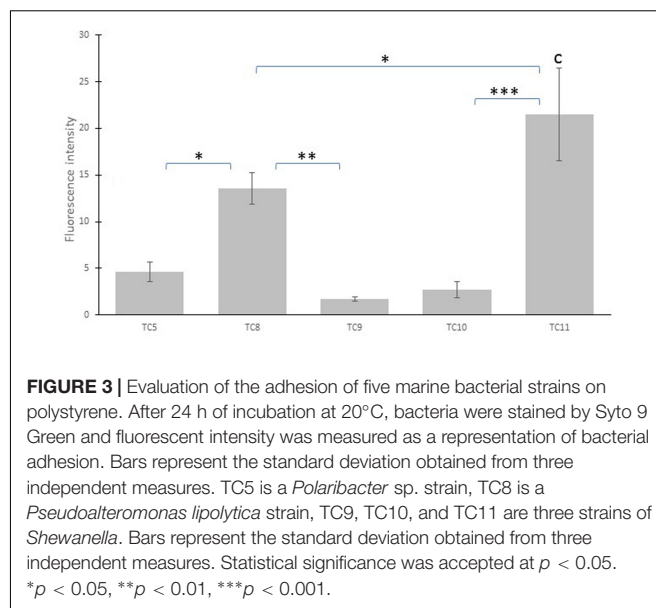


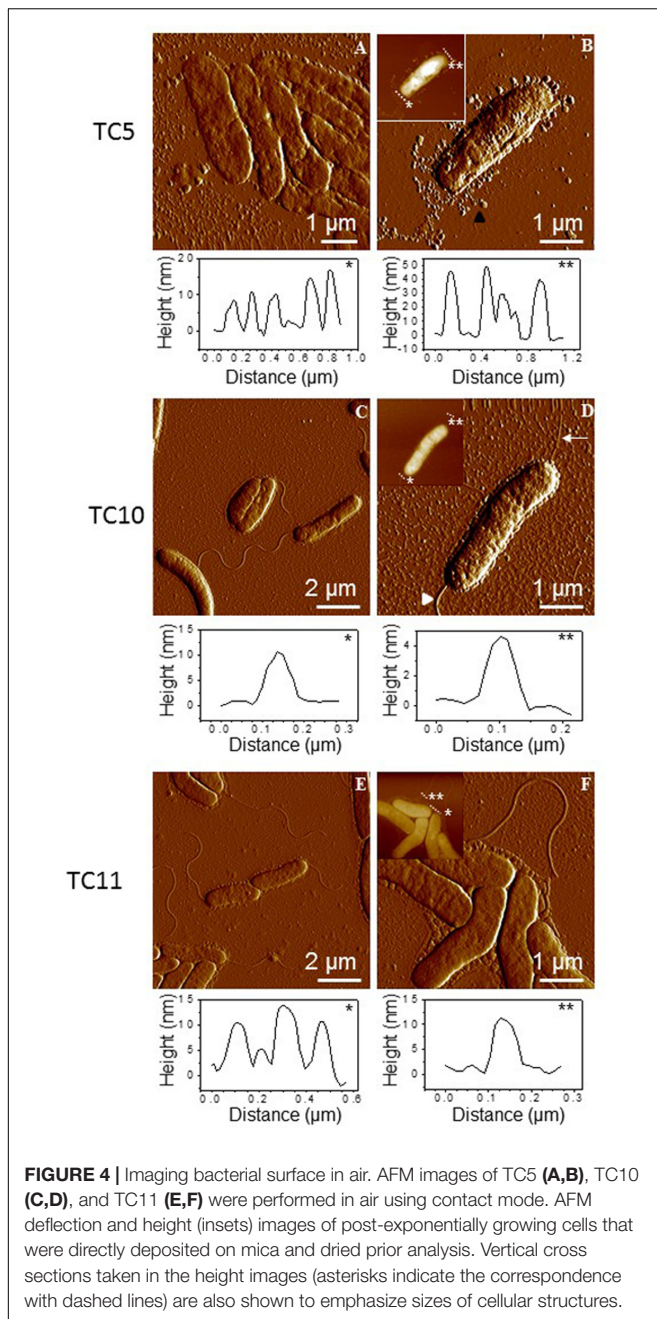
FIGURE 3 | Evaluation of the adhesion of five marine bacterial strains on polystyrene. After 24 h of incubation at 20°C, bacteria were stained by Syto 9 Green and fluorescent intensity was measured as a representation of bacterial adhesion. Bars represent the standard deviation obtained from three independent measures. TC5 is a *Polaribacter* sp. strain, TC8 is a *Pseudoalteromonas lipolytica* strain, TC9, TC10, and TC11 are three strains of *Shewanella*. Bars represent the standard deviation obtained from three independent measures. Statistical significance was accepted at $p < 0.05$. * $p < 0.05$, ** $p < 0.01$, *** $p < 0.001$.

TC5 and TC10 were about 3.4 μm long. TC11 seemed to be smaller and was about 2.6 μm long (**Figure 4**).

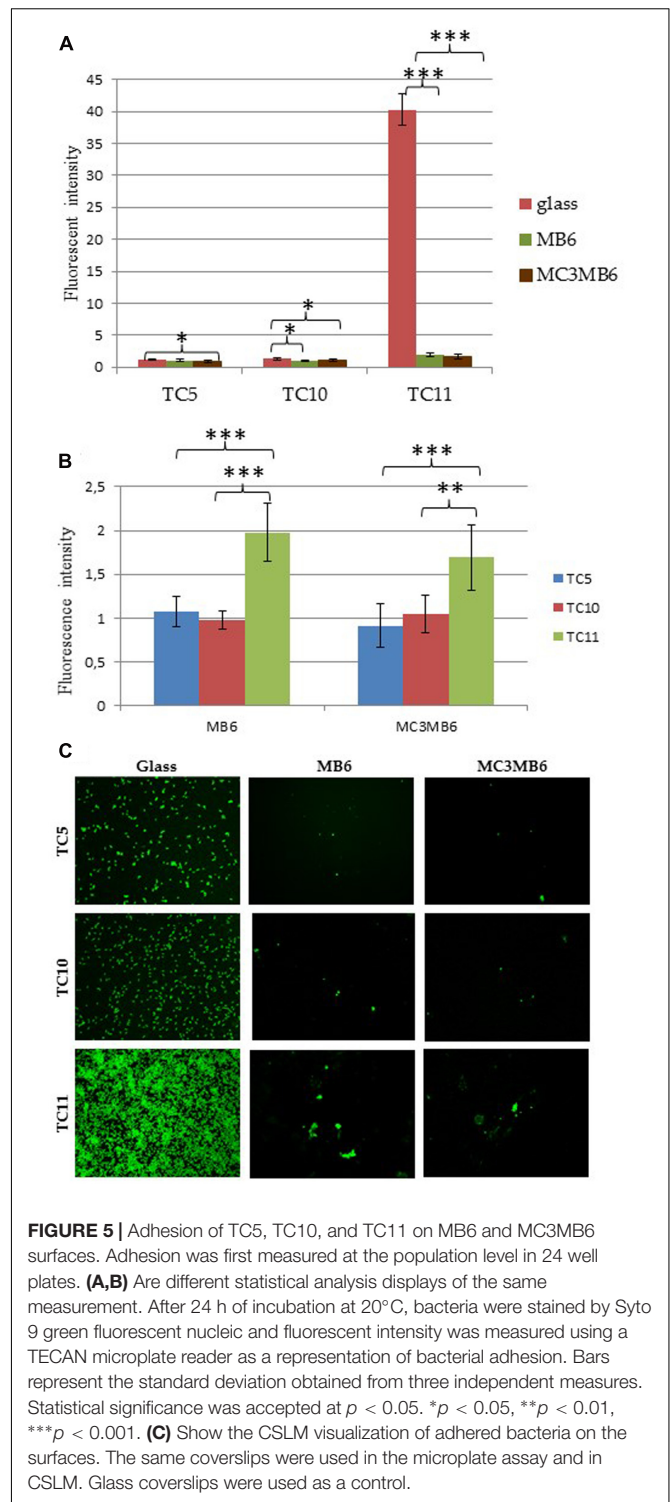
Pili and flagella are major contributors to mobility, adhesion and biofilm formation (Mattick, 2002; Telford et al., 2006; Pelicic, 2008; Belas, 2014; Laverty et al., 2014). As suspected flagella were clearly present on the surface of TC10 and TC11, while they were not seen for TC5 (**Figure 4**), previously described as non-motile (Brian-Jaisson et al., 2014). Furthermore, in few images of TC10, we observed a smaller and thinner structure, which could be pili, on the surface of this strain (**Figure 4D**, white thin arrow). Overall, pili were more difficult to observe than flagella. It is possible that pili were broken during the preparation of the cells for the AFM observation. Despite the presence of small residues particles most likely coming from the culture medium, spherical particles, which surround TC5 strain seem to be of different nature (**Figure 4B**, black triangle). We hypothesized that this strain produces outer membrane vesicles (OMV). A wide variety of Gram-negative bacteria secrete OMV including marine bacteria such as *Prochlorococcus* or *Shewanella vesiculosa* (Beveridge, 1999; Perez-Cruz et al., 2013; Biller et al., 2014). OMV are implicated in many functions such as bacterial survival, pathogenicity, enzyme delivery and biofilm formation (Beveridge, 1999; Schooling and Beveridge, 2006; Lee et al., 2008; Yonezawa et al., 2009; Baumgarten et al., 2012; van Hoek, 2013; Altindis et al., 2014; Murphy et al., 2014; Orench-Rivera and Kuehn, 2016). Taken together, these observations show that the *Polaribacter* TC5 strain presents different features from the 2 *Shewanella* strains as it has no flagella and seems to present OMV at its surface.

Evaluation of Adhesion on Copolymers at the Population Level

In order to evaluate bacterial adhesion on the hybrid MC3MB6 and its control MB6, these polymers were coated onto round PVC coverslips (as they did not stick well on glass) and



inserted in 24 well plates. Glass coverslips, widely used in fluorescence or CLSM microscopy experiments, served as a reference. Bacteria were then left to seed onto the surface for 24 h, washed off to remove non-adherent bacteria and then stained using the fluorescent marker Syto9. Because some polymers can present an autofluorescence, a direct observation of the same samples was performed using CLSM. This double approach is rarely undergone when such coatings are used. **Figures 5A,B** show that for each coating tested, TC11 was the strain displaying stronger adhesive properties, in particular with glass alone. TC11 adhered 2 and 1.5 times more than TC5 or TC10 on MB6 or MC3MB6, respectively (**Figure 5B**).



All three strains adhered better on glass coverslips than on the polymers (**Figures 5A,C**), with no significant difference in adhesion between MB6 and MC3MB6 (**Figure 5A**). These results have been corroborated with the CSLM observation as very few bacteria can be seen on either MC3MB6 or MB6 surfaces in sharp contrast with the glass surface (**Figure 5C**).

Taken together, these results suggest that copolymers MB6 and MC3MB6 prevent bacterial adhesion. While the adhesion was overall very weak, TC11 appears to adhere slightly better on these two surfaces. MB6 alone, composed of SiMA-*stat*-BMA with self-hydrolysis properties (with no biocide) is self-sufficient for the inhibition of bacterial adhesion in these conditions. The hydrophobic PDMS blocks, do not add in efficacy whichever bacteria studied despite their different hydrophilic surface properties (Brian-Jaisson et al., 2014). As previously described, hydrophobic/hydrophilic interactions can be easily overcome by the presence of extracellular appendages and covalent bindings, in particular in the stage of the “irreversible adhesion” (Garrett et al., 2008). Bacteria can adapt to their environment, i.e., the presence of a surface, very rapidly by, temporarily and in coordinated manner, specifically expressing numbers of proteins anchored in the membrane or being part of the extracellular appendages that can modify and overcome such interactions.

Single-Cell Adhesion Force Analysis

The results of the previous experiments reflect the behavior of the bacteria at the population level. In order to understand how each bacterium behaves on these surfaces at the single cell level, AFM was used in SCFS mode (Helenius et al., 2008; Muller et al., 2009) to quantify the adhesive properties of individual TC5, TC10, and TC11 bacterial cells toward surfaces MB6 and MC3MB6 (Beaussart et al., 2013). Briefly, a colloidal probe cantilever coated with polydopamine bioadhesive was used to pick up single cells without altering their viability (assessed using the Live-dead BacLight viability kit) and to measure force-distance curves between the bacterium and the surfaces MB6 and MC3MB6 (Figure 6). The three bacteria tested stayed alive during the course of the experiment.

We first used SCFS to investigate the adhesion force of single cells toward MB6 surfaces and the effect of contact time between cells and substrates. Figure 7 shows the adhesion force and rupture length histograms, together with representative force curves, obtained between TC5 (Figures 7A,B), TC10 (Figures 7C,D), and TC11 (Figures 7E,F) cells and MB6 surfaces at short (Figures 7A,C,E) and prolonged (Figures 7B,D,F) contact times. Consecutive force curves were recorded on different spots of the substrate and no changes were observed regarding the general features of the curves, indicating the cells were not damaged and cell surface properties were not altered by force measurements. Cell from independent cultures were analyzed and generally yielded similar behavior although sometimes one cell showed differences (Figures 7C,D,F) that we attribute to heterogeneity of the bacterial population. This phenotypic heterogeneity was less pronounced for TC5, whereas it was more obvious for TC11 whether at a short or long contact time. At short contact time, the adhesion frequency of TC5 cells on MB6 surfaces was ~30–35% with adhesive force curves presenting force of 50–400 pN and rupture distances of 100–900 nm (Figure 7A). Prolonged contact time (1 s) led to increased adhesion frequencies (75–90%), increased adhesion forces (from 300 to 2400 pN) and rupture lengths in the same range as at short contact time, yet with higher frequencies of short rupture distances (Figure 7B). At short contact time, most force

distance curves presented multiple well-defined individual peaks of 50–100 pN (Figure 7A, right histogram inset). According to previous observations, we attribute those multiple peaks signatures with flat regions preceding each peak to type IV pili interaction with MB6 surfaces (Touhami et al., 2006; Biais et al., 2010). The absence of such structures on bacterial images (Figures 4A,B) suggest that TC5 pili are fragile, short or could be retracted during sample drying. On 1 s contact time force curves, similar peaks were sometimes observed but the short distances interaction at higher forces (>300 pN) seemed to govern the adhesion of cell on MB6 surfaces. Such first large force and short distance adhesive events phenomenon could be attributed to the outer membrane surface property itself that needs longer contact time for interaction rather than appendages or adhesives molecules that would lead to longer rupture lengths. Analysis of TC10 cells led to similar results, still with few differences. Increasing the contact time did not significantly increases the adhesion frequency or the range of forces. As for TC5, force curves signatures obtained for TC10 suggested type IV pili interaction and this conclusion was confirmed by AFM images (Figure 4D). For TC11 cells, the adhesion frequency did not increase with contact time. However, adhesion forces of some cells significantly increased up to 10 nN (Figure 7F). These high forces corresponded to short rupture distances peak suggesting strong hydrophobic interactions between the cell surface and the MB6 substrate. At short contact time, force curves frequently showed a first adhesive event with sometimes a sawtooth pattern (Figure 7E, inset in right histogram, upper curve). This first peak may correspond to cell surface proteins interacting with MB6 surface and strengthened in force and number under prolonged contact time. On short contact time curves, although no pili were detected on bacterial images (Figures 4E,F), peaks following the initial adhesive event presented signatures that could be attributed to pili and as for TC5, we hypothesize that those pili were fragile, short or could be retracted on image samples. Force curves obtained after prolonged contact time revealed sawtooth pattern with regular peaks and long rupture distances. Based on previous observations, these signatures could correspond to proteins interacting with the surface and containing multiple repeats that are unfolded upon bacterial pulling from the substrate (Alsteens et al., 2009; Beaussart et al., 2014; El-Kirat-Chatel et al., 2014b).

The MC3MB6 surface was used similarly to evaluate the impact of the surface chemistry change on bacterial adhesion of TC5, TC10, and TC11 cells. Figure 8 shows the adhesion force and rupture length histograms, together with representative force curves, obtained between TC5 (Figures 8A,B), TC10 (Figures 8C,D), and TC11 (Figures 8E,F) cells and surfaces MC3MB6 at short (Figures 8A,C,E) and prolonged (Figures 8B,D,F) contact times. TC5 cells presented high frequency adhesion toward surface MC3MB6 (more than 70% at short contact times and about 100% at prolonged contact times). Increasing contact time resulted in higher adhesion forces (from 300–2000 pN to 1200–4800 pN). Force curves recorded for TC5 on surface MC3MB6 presented large initial force peaks followed by smaller forces that may correspond to stretching of cell surface molecules. Compared to results

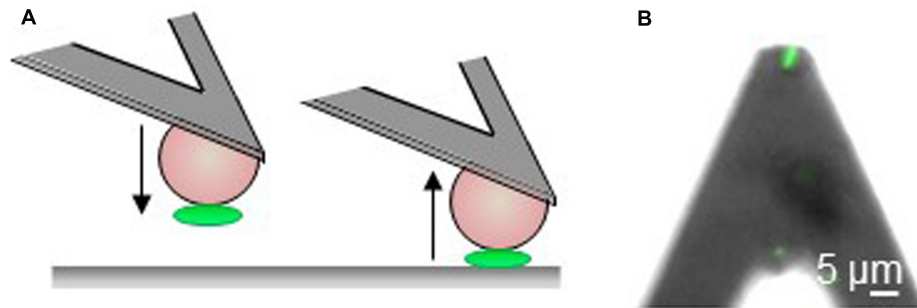


FIGURE 6 | The use of a microbead for single-cell force spectroscopy analysis. **(A)** Principle of single cell force spectroscopy with tip less cantilevers modified with colloidal beads and coated with polydopamine to attach a single bacteria (green) and probe it toward surfaces. **(B)** Optical microscope image of a single bacterium attached to the colloidal cantilever probes documenting that the cell is properly located and alive (green fluorescence).

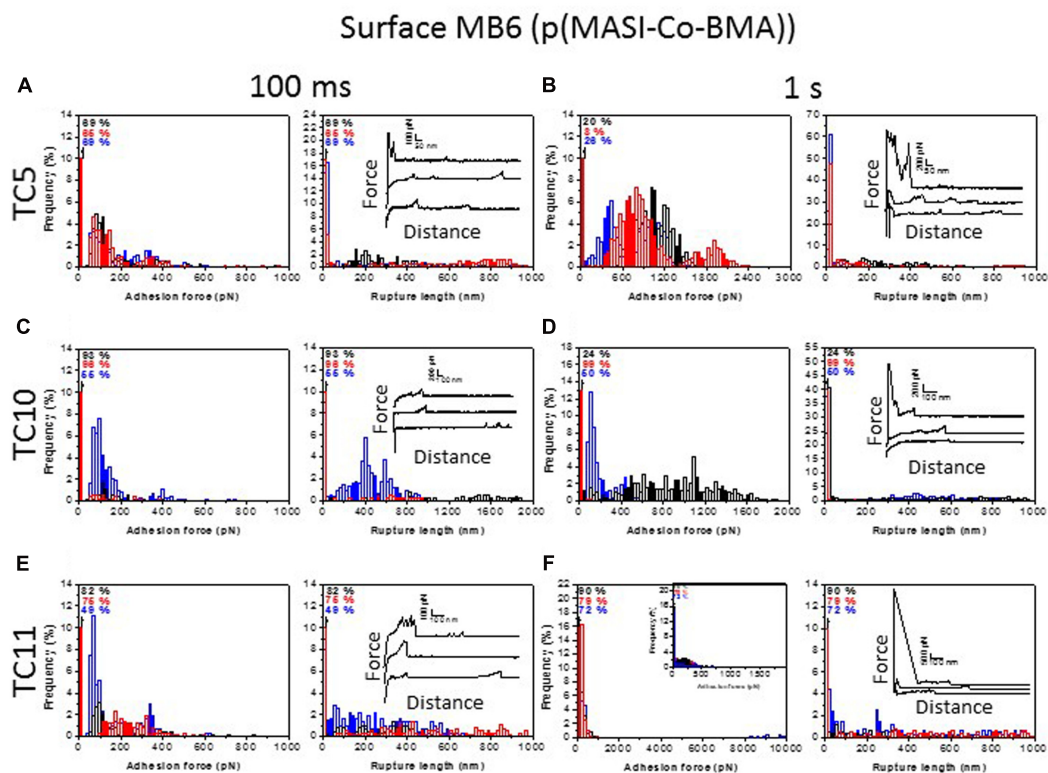
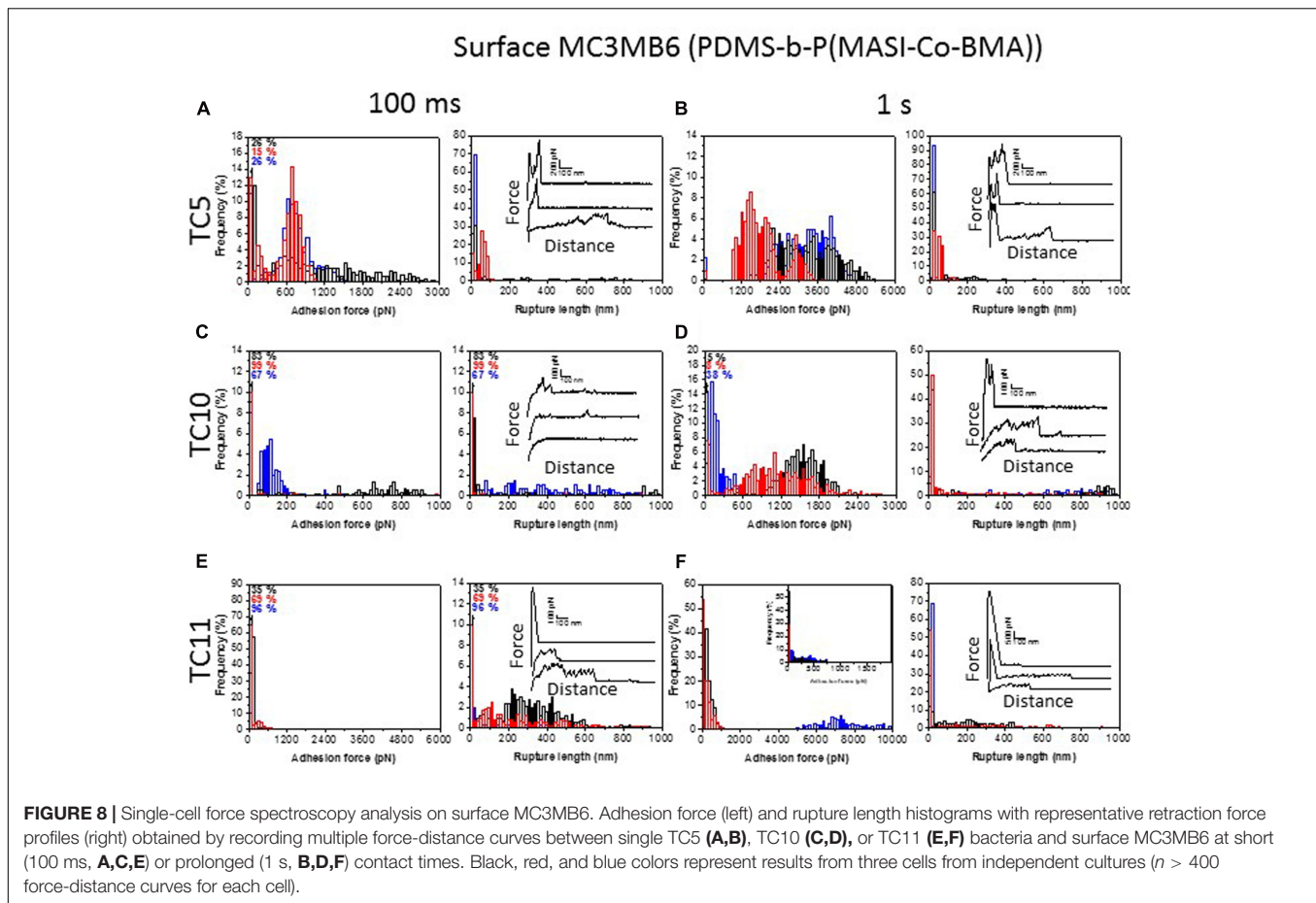


FIGURE 7 | Single-cell force spectroscopy analysis on surface MB6. Adhesion force (left) and rupture length histograms with representative retraction force profiles (right) obtained by recording multiple force-distance curves between single TC5 **(A,B)**, TC10 **(C,D)**, or TC11 **(E,F)** bacteria and surface MB6 at short (100 ms, **A,C,E**) or prolonged (1 s, **B,D,F**) contact times. Black, red, and blue colors represent results from three cells from independent cultures ($n > 400$ force-distance curves for each cell).

obtained on surfaces MB6, force curves recorded on surface MC3MB6 rarely presented pili signature, suggesting that TC5 pili are mostly involved in interaction with surface MB6 and that the interaction with surface MC3MB6 is governed by the cell wall itself together with surface adhesive molecules. TC10 cells presented slightly similar adhesive profile on surface MC3MB6 and surface MB6. Its adhesion to both surfaces is lower in term of frequency and force than the adhesion of

TC5. Based on force curves shape, this adhesion seems to be mainly controlled by pili at short contact time (small peaks at long distance and visualization of pili on image **Figure 4**) and at longer contact time, the cell adhesion through pili seems to be reinforced by cell wall and surface molecule (large initial peak and sawtooth pattern of molecules unfolding). TC11 cells were slightly more adhesive to surface MC3MB6 than what was observed for surfaces MB6. Still, the interaction looks similar



with almost no pili signature but rather protein unfolding and large initial peaks suggesting that TC11 adhere mainly through cell wall hydrophobicity and adhesive macromolecules containing repeated domains unfolded upon pulling. Phenotypic heterogeneity in adhesion was also more obvious on MC3MB6 for TC11 than for the two other strains, whether on short or long contact time.

To validate the specificity of the measured adhesion forces and rule out the possibility of artifact associated with the cell probe preparation, a control experiment was performed using a 1 s contact time (Supplementary Figure S2). Use of polydopamine-coated probes instead of bacterial probes led to a major reduction of adhesion frequency and no signatures similar to what we observed for cells were present. This control indicates that the adhesive events measured above reflect the interactions between bacteria and coatings.

Taken together, these results show first that TC5 was the most adhesive of the three strains on both surfaces in terms of frequency and presented large adhesion forces, in particular on the hydrophobic surface, MC3MB6, while TC10 showed a weaker adhesion on both surfaces with adhesion forces averaging 1000 or 1200 pN. The influence of surface chemistry is mostly observed for TC5. This comes in contrast with the results found at the population level, as TC11 was the bacteria that adhered the most

efficiently on polystyrene, glass as well as on MB6 and MC3MB6, even though adhesion on the antifouling surfaces was overall very low (Figure 4). Second, different extracellular components seem to be involved in the three strains adhesion on the surfaces. Short distance interactions at higher forces govern adhesion of TC5 and TC10 on the surfaces (Dufrene, 2015). Adhesion seems to be controlled by pili, cell wall on MB6 (and MC3MB6 for TC10) and by cell wall and stretching of surface molecules on MC3MB6. TC11 adheres mainly through cell wall hydrophobicity and adhesive macromolecules containing repeated domains unfolded upon pulling. Third, some TC11 cells were slightly more adhesive to both surfaces (with long rupture distances) than others. While TC5 and in a lesser extent TC10 showed a more homogenous response toward the surfaces, TC11 presented heterogeneous adhesion profiles toward both surfaces, with some bacterial cells presenting weak adhesion forces and some of them presenting very strong ones. Phenotypic heterogeneity within a population, which corresponds to the expression of substantial phenotypical differences by individuals when they are in a similar context, is thought to allow better chance of survival for the population as a whole entity. A subpopulation may be then better equipped to face stressful situations and settle in new environmental niches. This heterogeneity can come from variations of gene expression at the single cell level but also from allelic variations

(Davis and Isberg, 2016). Some bacteria are more susceptible to genetic variations than others (for instance the ones undergoing phase variation). These phenomena have been described for instance in biofilm with the apparition of persisters as well as in relation with QS dependent mechanisms due to highly heterogeneous gene expression at a single cell level (Grote et al., 2015). This is most likely a widespread phenomenon, which just started to be highlighted in the literature with the development of single cell approaches, even though this variability may differs from a bacterium to another. This emerging evidence of phenotypical variability need to be studied more precisely at the molecular and cellular level in order to understand how these variations can make a subpopulation adapt and survive in an environmental niche. It is possible that TC11 fits to this description and can present at the population level a better fitness when facing a new environment than TC5 or TC10. Phenotypic heterogeneity, and differential bacterial-bacterial collaborative interactions involved in biofilm formation could explain the reason why, despite a weaker adhesion at the single cell level, TC11 is able to form more biofilm than TC5 including in ASW (data not shown). Further studies would be required using, for instance, other single cell techniques, such as the newly developed single cell RNA-seq, allowing a broader vision of the variability to confirm these results (Davis and Isberg, 2016).

REFERENCES

- Alsteens, D., Dupres, V., Klotz, S. A., Gaur, N. K., Lipke, P. N., and Dufrene, Y. F. (2009). Unfolding individual *als5p* adhesion proteins on live cells. *ACS Nano* 3, 1677–1682. doi: 10.1021/nn900078p
- Altindis, E., Fu, Y., and Mekalanos, J. J. (2014). Proteomic analysis of *Vibrio cholerae* outer membrane vesicles. *Proc. Natl. Acad. Sci. U.S.A.* 111, E1548–E1556. doi: 10.1073/pnas.1403683111
- Baumgarten, T., Sperling, S., Seifert, J., von Bergen, M., Steiniger, F., Wick, L. Y., et al. (2012). Membrane vesicle formation as a multiple-stress response mechanism enhances *Pseudomonas putida* DOT-T1E cell surface hydrophobicity and biofilm formation. *Appl. Environ. Microbiol.* 78, 6217–6224. doi: 10.1128/AEM.01525-12
- Beaussart, A., El-Kirat-Chatel, S., Herman, P., Alsteens, D., Mahillon, J., Hols, P., et al. (2013). Single-cell force spectroscopy of probiotic bacteria. *Biophys. J.* 104, 1886–1892. doi: 10.1016/j.bpj.2013.03.046
- Beaussart, A., El-Kirat-Chatel, S., Sullan, R. M. A., Alsteens, D., Herman, P., Derclaye, S., et al. (2014). Quantifying the forces guiding microbial cell adhesion using single-cell force spectroscopy. *Nat. Protoc.* 9, 1049–1055. doi: 10.1038/nprot.2014.066
- Belas, R. (2014). Biofilms, flagella, and mechanosensing of surfaces by bacteria. *Trends Microbiol.* 22, 517–527. doi: 10.1016/j.tim.2014.05.002
- Belec, L., Nguyen, T., Nguyen, D., and Chailan, J. (2015). Comparative effects of humid tropical weathering and artificial ageing on a model composite properties from nano-to macro-scale. *Compos. Part A Appl. Sci. Manuf.* 68, 235–241. doi: 10.1016/j.compositesa.2014.09.028
- Beveridge, T. J. (1999). Structures of gram-negative cell walls and their derived membrane vesicles. *J. Bacteriol.* 181, 4725–4733.
- Biais, N., Higashi, D. L., Bruijck, J., So, M., and Sheetz, M. P. (2010). Force-dependent polymorphism in type IV pili reveals hidden epitopes. *Proc. Natl. Acad. Sci. U.S.A.* 107, 11358–11363. doi: 10.1073/pnas.0911328107
- Biller, S. J., Schubotz, F., Roggensack, S. E., Thompson, A. W., Summons, R. E., and Chisholm, S. W. (2014). Bacterial vesicles in marine ecosystems. *Science* 343, 183–186. doi: 10.1126/science.1243457
- Bressy, C., Hellio, C., Nguyen, M. N., Tanguy, B., Maréchal, J.-P., and Margaillan, A. (2014). Optimized silyl ester diblock methacrylic copolymers: a new class of binders for chemically active antifouling coatings. *Prog. Organ. Coat.* 77, 665–673. doi: 10.1016/j.porgcoat.2013.12.004
- Bressy, C., and Margaillan, A. (2009). Erosion study of poly (trialkylsilyl methacrylate)-based antifouling coatings. *Prog. Organ. Coat.* 66, 400–405. doi: 10.1016/j.porgcoat.2009.09.003
- Bressy, C., NGuyen, M. N., Tanguy, B., Ngo, V. G., and Margaillan, A. (2010). Poly (trialkylsilyl methacrylate) s: a family of hydrolysable polymers with tuneable erosion profiles. *Polym. Degrad. Stab.* 95, 1260–1268. doi: 10.1016/j.polymdegradstab.2010.03.017
- Briand, J. F., Djeridi, I., Jamet, D., Coupe, S., Bressy, C., Molmeret, M., et al. (2012). Pioneer marine biofilms on artificial surfaces including antifouling coatings immersed in two contrasting French Mediterranean coast sites. *Biofouling* 28, 453–463. doi: 10.1080/08927014.2012.688957
- Brian-Jaisson, F., Ortalo-Magne, A., Guentas-Dombrowsky, L., Armougom, F., Blache, Y., and Molmeret, M. (2014). Identification of bacterial strains isolated from the Mediterranean Sea exhibiting different abilities of biofilm formation. *Microb. Ecol.* 68, 94–110. doi: 10.1007/s00248-013-0342-9
- Butt, H.-J., Cappella, B., and Kappl, M. (2005). Force measurements with the atomic force microscope: Technique, interpretation and applications. *Surf. Sci. Rep.* 59, 1–152. doi: 10.1016/j.surfrep.2005.08.003
- Camps, M., Briand, J. F., Guentas-Dombrowsky, L., Culioli, G., Bazire, A., and Blache, Y. (2011). Antifouling activity of commercial biocides vs. natural and natural-derived products assessed by marine bacteria adhesion bioassay. *Mar. Pollut. Bull.* 62, 1032–1040. doi: 10.1016/j.marpolbul.2011.02.031
- Davis, K. M., and Isberg, R. R. (2016). Defining heterogeneity within bacterial populations via single cell approaches. *Bioessays* 38, 782–790. doi: 10.1002/bies.201500121
- Dufrene, Y. F. (2015). Sticky microbes: forces in microbial cell adhesion. *Trends Microbiol.* 23, 376–382. doi: 10.1016/j.tim.2015.01.011
- Duong, T. H., Bressy, C., and Margaillan, A. (2014). Well-defined diblock copolymers of poly (tert-butyl dimethylsilyl methacrylate) and poly (dimethylsiloxane) synthesized by RAFT polymerization. *Polymer* 55, 39–47. doi: 10.1016/j.polymer.2013.11.034
- Duong, T. H., Briand, J.-F., Margaillan, A., and Bressy, C. (2015). Polysiloxane-based block copolymers with marine bacterial anti-adhesion properties. *ACS Appl. Mater. Interfaces* 7, 15578–15586. doi: 10.1021/acsami.5b04234

AUTHOR CONTRIBUTIONS

SE-K-C has performed the AFM/SCFS experiments to measure adhesion forces between live bacteria and the surfaces under the supervision of YD. AP and PVO have performed the microbiology adhesion assays and CLSM experiments under the supervision of MM. TD has synthesized and characterized the copolymers under the supervision of CB and LB.

FUNDING

This work was supported by MAPIEM laboratory of the Université de Toulon, France and by the institute of Life Sciences of the Université catholique de Louvain, Belgium. PVO is the recipient of a French PACA Region doctoral fellowship.

SUPPLEMENTARY MATERIAL

The Supplementary Material for this article can be found online at: <http://journal.frontiersin.org/article/10.3389/fmicb.2017.01399/full#supplementary-material>

- El-Kirat-Chatel, S., Beaussart, A., Boyd, C. D., O'Toole, G. A., and Dufrène, Y. F. (2014a). Single-cell and single-molecule analysis deciphers the localization, adhesion, and mechanics of the biofilm adhesin LapA. *ACS Chem. Biol.* 9, 485–494. doi: 10.1021/cb400794e
- El-Kirat-Chatel, S., Boyd, C. D., O'Toole, G. A., and Dufrène, Y. F. (2014b). Single-molecule analysis of *Pseudomonas fluorescens* footprints. *ACS Nano* 8, 1690–1698. doi: 10.1021/nn4060489
- Garrett, T. R., Bhakoo, M., and Zhang, Z. (2008). Bacterial adhesion and biofilms on surfaces. *Prog. Nat. Sci.* 18, 1049–1056. doi: 10.1016/j.pnsc.2008.04.001
- Grote, J., Krysiak, D., and Streit, W. R. (2015). Phenotypic heterogeneity, a phenomenon that may explain why quorum sensing does not always result in truly homogenous cell behavior. *Appl. Environ. Microbiol.* 81, 5280–5289. doi: 10.1128/AEM.00900-15
- Helenius, J., Heisenberg, C. P., Gaub, H. E., and Muller, D. J. (2008). Single-cell force spectroscopy. *J. Cell Sci.* 121, 1785–1791. doi: 10.1242/jcs.030999
- Kang, S., and Elimelech, M. (2009). Bioinspired single bacterial cell force spectroscopy. *Langmuir* 25, 9656–9659. doi: 10.1021/la902247w
- Laverty, G., Gorman, S. P., and Gilmore, B. F. (2014). Biomolecular mechanisms of *Pseudomonas aeruginosa* and *Escherichia coli* Biofilm Formation. *Pathogens* 3, 596–632. doi: 10.3390/pathogens3030596
- Lee, E. Y., Choi, D. S., Kim, K. P., and Ghoo, Y. S. (2008). Proteomics in gram-negative bacterial outer membrane vesicles. *Mass Spectrom. Rev.* 27, 535–555. doi: 10.1002/mas.20175
- Lejars, M., Margaillan, A., and Bressy, C. (2012). Fouling release coatings: a nontoxic alternative to biocidal antifouling coatings. *Chem. Rev.* 112, 4347–4390. doi: 10.1021/cr200350v
- Lejars, M., Margaillan, A., and Bressy, C. (2013). Well-defined graft copolymers of tert-butyltrimethylsilyl methacrylate and poly (dimethylsiloxane) macromonomers synthesized by RAFT polymerization. *Polym. Chem.* 4, 3282–3292. doi: 10.1039/c3py00196b
- Lejars, M., Margaillan, A., and Bressy, C. (2014). Synthesis and characterization of diblock and statistical copolymers based on hydrolyzable siloxy silylester methacrylate monomers. *Polym. Chem.* 5, 2109–2117. doi: 10.1039/c3py01603j
- Loskill, P., Hahl, H., Thewes, N., Kreis, C. T., Bischoff, M., Herrmann, M., et al. (2012). Influence of the subsurface composition of a material on the adhesion of staphylococci. *Langmuir* 28, 7242–7248. doi: 10.1021/la3004323
- Mardén, P. T. A., Malmcrona-Friberg, K., Odham, G., and Kjelleberg, S. (1985). Physiological and morphological changes during short term starvation of marine bacterial isolates. *Arch. Microbiol.* 142, 326–332. doi: 10.1007/BF00491898
- Martins, B. M., and Locke, J. C. (2015). Microbial individuality: how single-cell heterogeneity enables population level strategies. *Curr. Opin. Microbiol.* 24, 104–112. doi: 10.1016/j.mib.2015.01.003
- Mattick, J. S. (2002). Type IV pili and twitching motility. *Annu. Rev. Microbiol.* 56, 289–314. doi: 10.1146/annurev.micro.56.012302.160938
- Muller, D. J., Helenius, J., Alsteens, D., and Dufrène, Y. F. (2009). Force probing surfaces of living cells to molecular resolution. *Nat. Chem. Biol.* 5, 383–390. doi: 10.1038/nchembio.181
- Murphy, K., Park, A. J., Hao, Y., Brewer, D., Lam, J. S., and Khursigara, C. M. (2014). Influence of O polysaccharides on biofilm development and outer membrane vesicle biogenesis in *Pseudomonas aeruginosa* PAO1. *J. Bacteriol.* 196, 1306–1317. doi: 10.1128/JB.01463-13
- Orench-Rivera, N., and Kuehn, M. J. (2016). Environmentally controlled bacterial vesicle-mediated export. *Cell Microbiol.* 18, 1525–1536. doi: 10.1111/cmi.12676
- Owen, D., and Wendt, R. (1969). Estimation of the surface free energy of polymer. *J. Appl. Polym. Sci.* 13, 1741–1747. doi: 10.1002/app.1969.070130815
- Pellic, V. (2008). Type IV pili: e pluribus unum? *Mol. Microbiol.* 68, 827–837. doi: 10.1111/j.1365-2958.2008.06197.x
- Perez-Cruz, C., Carrion, O., Delgado, L., Martinez, G., Lopez-Iglesias, C., and Mercade, E. (2013). New type of outer membrane vesicle produced by the Gram-negative bacterium *Shewanella vesiculosa* M7T: implications for DNA content. *Appl. Environ. Microbiol.* 79, 1874–1881. doi: 10.1128/AEM.03657-12
- Schooling, S. R., and Beveridge, T. J. (2006). Membrane vesicles: an overlooked component of the matrices of biofilms. *J. Bacteriol.* 188, 5945–5957. doi: 10.1128/JB.00257-06
- Schultz, M. P. (2007). Effects of coating roughness and biofouling on ship resistance and powering. *Biofouling* 23, 331–341. doi: 10.1080/08927010701461974
- Telford, J. L., Barocchi, M. A., Margarit, I., Rappuoli, R., and Grandi, G. (2006). Pili in gram-positive pathogens. *Nat. Rev. Microbiol.* 4, 509–519. doi: 10.1038/nrmicro1443
- Touhami, A., Jericho, M. H., Boyd, J. M., and Beveridge, T. J. (2006). Nanoscale characterization and determination of adhesion forces of *Pseudomonas aeruginosa* pili by using atomic force microscopy. *J. Bacteriol.* 188, 370–377. doi: 10.1128/JB.188.2.370-377.2006
- van Hoek, M. L. (2013). Biofilms: an advancement in our understanding of *Francisella* species. *Virulence* 4, 833–846. doi: 10.4161/viru.27023
- Yebra, D. M., Kiil, S., and Dam-Johansen, K. (2004). Antifouling technology—past, present and future steps towards efficient and environmentally friendly antifouling coatings. *Prog. Organ. Coat.* 50, 75–104. doi: 10.1016/j.porgcoat.2003.06.001
- Yonezawa, H., Osaki, T., Kurata, S., Fukuda, M., Kawakami, H., Ochiai, K., et al. (2009). Outer membrane vesicles of *Helicobacter pylori* TK1402 are involved in biofilm formation. *BMC Microbiol.* 9:197. doi: 10.1186/1471-2180-9-197

Conflict of Interest Statement: The authors declare that the research was conducted in the absence of any commercial or financial relationships that could be construed as a potential conflict of interest.

Copyright © 2017 El-Kirat-Chatel, Puymège, Duong, Van Overtvelt, Bressy, Belec, Dufrène and Molmeret. This is an open-access article distributed under the terms of the Creative Commons Attribution License (CC BY). The use, distribution or reproduction in other forums is permitted, provided the original author(s) or licensor are credited and that the original publication in this journal is cited, in accordance with accepted academic practice. No use, distribution or reproduction is permitted which does not comply with these terms.



Extracellular Polymeric Substance Production and Aggregated Bacteria Colonization Influence the Competition of Microbes in Biofilms

Pahala G. Jayathilake^{1*}, Saikat Jana¹, Steve Rushton^{2*}, David Swailes³, Ben Bridgens¹, Tom Curtis^{4*} and Jinju Chen^{1*}

¹ School of Engineering, Newcastle University, Newcastle upon Tyne, United Kingdom, ² School of Natural and Environmental Sciences, Newcastle University, Newcastle upon Tyne, United Kingdom, ³ School of Mathematics, Statistics and Physics, Newcastle University, Newcastle upon Tyne, United Kingdom, ⁴ Centre for Synthetic Biology and the Bioeconomy, Newcastle University, Newcastle upon Tyne, United Kingdom

OPEN ACCESS

Edited by:

Jan-Ulrich Kreft,
University of Birmingham,
United Kingdom

Reviewed by:

Sara Mitri,
University of Lausanne, Switzerland
Knut Drescher,
Max Planck Institute for Terrestrial
Microbiology, Germany

*Correspondence:

Pahala G. Jayathilake
jayathilake.pahala-gedara@ncl.ac.uk
Steve Rushton
steven.rushton@newcastle.ac.uk
Tom Curtis
tom.curtis@newcastle.ac.uk
Jinju Chen
jinju.chen@newcastle.ac.uk

Specialty section:

This article was submitted to
Systems Microbiology,
a section of the journal
Frontiers in Microbiology

Received: 28 April 2017

Accepted: 12 September 2017

Published: 27 September 2017

Citation:

Jayathilake PG, Jana S, Rushton S, Swailes D, Bridgens B, Curtis T and Chen J (2017) Extracellular Polymeric Substance Production and Aggregated Bacteria Colonization Influence the Competition of Microbes in Biofilms. *Front. Microbiol.* 8:1865. doi: 10.3389/fmicb.2017.01865

The production of extracellular polymeric substance (EPS) is important for the survival of biofilms. However, EPS production is costly for bacteria and the bacterial strains that produce EPS (EPS+) grow in the same environment as non-producers (EPS-) leading to competition between these strains for nutrients and space. The outcome of this competition is likely to be dependent on factors such as initial attachment, EPS production rate, ambient nutrient levels and quorum sensing. We use an Individual-based Model (IbM) to study the competition between EPS+ and EPS- strains by varying the nature of initial colonizers which can either be in the form of single cells or multicellular aggregates. The microbes with EPS+ characteristics obtain a competitive advantage if they initially colonize the surface as smaller aggregates and are widely spread-out between the cells of EPS-, when both are deposited on the substratum. Furthermore, the results show that quorum sensing-regulated EPS production may significantly reduce the fitness of EPS producers when they initially deposit as aggregates. The results provide insights into how the distribution of bacterial aggregates during initial colonization could be a deciding factor in the competition among different strains in biofilms.

Keywords: individual-based model, biofilm, competition, EPS, aggregates, quorum sensing

INTRODUCTION

Biofilms are surface associated communities of bacteria that are surrounded by adhesive extracellular polymeric substance (EPS) (Davey and O'toole, 2000) which not only provides them with mechanical integrity but also allows resistance against attack from foreign entities. Understanding the dynamics of growth and competition between several microbial species in a biofilm is crucial for our understanding of chronic diseases such as cystic fibrosis, infection in medical devices, biofouling and various processes used in wastewater treatment. Mathematical models such as Cellular Automaton (CA) and Individual-based Models (IbMs) (Kreft et al., 2001; Picioreanu et al., 2004; Xavier et al., 2005; Nadell et al., 2008; Lardon et al., 2011; Jayathilake et al., 2017) have been instrumental in providing insights into the spatiotemporal growth and competition of microbes under varying conditions. Kreft et al. (1998) proposed the use of IbM as a bottom-up approach

which attempts to predict community behavior based on the actions and characteristics of the constituent individuals. The IbM was introduced to cope with artifacts which occurred due to the discrete displacement of biomass in CA (Picioreanu et al., 2004; Tang and Valocchi, 2013). As Ib modeling leads to more realistic biofilm structures (Kreft et al., 2001), it has been widely used to study social evolution in biofilms (Kreft, 2004; Xavier and Foster, 2007; Nadell et al., 2008; Mitri et al., 2011).

Kreft (2004) used IbM to study competition between the rate and yield strategists in biofilms and concluded that certain spatial structures are needed for maintenance of yield strategists. The rate strategists are found to dominate the biofilm in the short-term due to their high growth rates, while in the long run the yield strategists dominate since they consume nutrients more economically. Nadell et al. (2010) studied competition between enzyme secreting and non-secreting bacteria under different ratios between nutrient provision and nutrient consumption, and found that if the ratio is small, cell (bacteria) lineage segregation occurs and consequently the cooperative cells (i.e., enzyme-secreting cells) dominate within the biofilm. The cell lineage segregation confers an advantage to the cooperative cells because they are not exploited by non-cooperative ones. Mitri et al. (2011) found that addition of new species in a multispecies biofilm especially in resource limited scenarios would reduce the fitness of existing cooperative cells that secrete public goods. In addition, the ecological advantages of quorum sensing (QS) -regulated enzyme production (Schluter et al., 2016), QS inhibition (Wei et al., 2016) and evolution of bacteriocin production (Bucci et al., 2011) in biofilms have also been investigated using IbM.

EPS mediated adhesion is known to be very important for bacterial biofilm development as it affects both the initial attachment to surfaces and the subsequent resistance to shear flows. However, bacterial adhesion to surfaces ought to be costly because it restricts bacteria mobility and hinders movement to nutrient rich environments. Schluter et al. (2015) studied the effect of EPS mediated adhesion and found that cells with greater adhesive capabilities gained a competitive advantage when nutrients are abundant. Xavier and Foster (2007) showed that cells that constitutively produce EPS (EPS+) outcompete non-producers (EPS-) in the presence of significant nutrient gradients. When the EPS+ and EPS- strains are co-cultured in a biofilm, the EPS+ cells initially grow slower than EPS- cells because the EPS+ cells spend a fraction of energy on EPS production, and therefore the EPS- bacteria would initially dominate in the biofilm. However, eventually the production of EPS would help the EPS+ cells to push their descendants into nutrient rich top layers and hence the progeny of EPS+ bacteria would get more access to nutrients and would dominate in the biofilm in long run. Quorum sensing (QS) is a cell-cell communication mechanism used to regulate gene expression and production of public goods in biofilms (Fuqua and Greenberg, 2002). Nadell et al. (2008) investigated the competitive advantage of quorum sensing-mediated down regulation of EPS production. They found that EPS producers under negative quorum sensing control (i.e., EPS production by bacteria stops at high cell densities, referred to as the QS- strain), would dominate when competing with EPS+ strain. However, this effect only lasts for

a limited time and the EPS+ cells dominate in the long-term because EPS+ cells suffocate the QS- cells by continuously secreting polymeric substance thereby separating QS- cells from nutrients.

These studies demonstrate that spatial distribution of microbes influences the microbial competition in biofilms. In addition nutrient gradients have been known to cause cell lineage segregation in biofilms and the effect has been addressed in many papers (Xavier and Foster, 2007; Nadell et al., 2010). Generally, low nutrient conditions favor cooperative strains (or species) that produce public goods such as EPS and enzymes. The biofilm structure is also influenced by other factors including microbial mobility, adhesion, initial attachment frequency and bacteria re-attachment to the biofilm (van Gestel et al., 2014); however, the effect of these factors on microbial competition in biofilms has not been extensively investigated. For example, when a biofilm grows in a reactor, it can experience erosion and sloughing due to hydrodynamic shearing and the detached biofilm clusters can re-colonize new surfaces and develop into biofilms. Similarly, the aerobic granular sludge aggregates found in sequencing batch reactors can be transported to new locations and have the ability to colonize new surfaces (McSwain et al., 2005). It is therefore very likely that bacterial aggregates deposit on new surfaces, hence biofilms originate from both individual cells (single cells) and cell clusters (aggregates). Only recently, Melaugh et al. (2016) and Kragh et al. (2016) addressed a similar problem by performing IbM simulations to understand the trade-off between aggregate surface area and relative height compared to single cell colonizers. The findings suggest that single cells perform better when competition is low (i.e., at low single cell densities) and multicellular rounded aggregates perform better when competition is high (i.e., at high single cell densities). In more competitive environments the aggregates perform better because they have access to nutrient rich areas due to their initial height advantage compared to single cells. This trade-off is likely to be influenced by EPS production characteristics of cells because EPS provides cells with sufficient structure to reach high nutrient layers. Moreover, multispecies biofilms may contain strains of bacteria that can either be EPS+ or EPS-. Therefore, EPS production characteristics of cells might offset the competitive advantage gained by bacterial aggregates due to their height.

In the present study, we develop a two-dimensional biofilm model based on IbM principles to understand competition between cells and aggregates which express a combination of characteristics (EPS+, EPS-, QS+ and QS-, described under "Methods" below). We simulate the spatiotemporal dynamics of competition under various scenarios of attachment (i.e., as single cells or multiple aggregates) and for different values of energy invested in EPS production by the microbes. The maximum competitive advantage is obtained when the EPS+ cells are initially deposited on the substratum as smaller aggregates and are randomly distributed among individual cells of the EPS-. We also study the effect of quorum sensing-regulated EPS production on competition between single cells and aggregates for different values of QS signal threshold. Overall, the work demonstrates the role of EPS production in conferring an

advantage to either single cells or aggregates as they form biofilms under differing conditions.

METHODS

Individual-Based Model

The components of the two-dimensional Ib model are similar to that used in Nadell et al. (2008). The bacteria are represented as hard spheres, each having variable mass/volume and a set of growth parameters. Each bacterium grows by consuming substrate (S) which is supplied from the bulk liquid. Four strains are considered: (i) EPS producer with no quorum sensing (EPS+), (ii) no EPS production, with no quorum sensing (EPS−), (iii) EPS producer under negative quorum sensing in which EPS secretion stops at high cell densities (QS−), and (iv) EPS producer under positive quorum sensing in which polymer secretion starts at high cell densities (QS+). The growth rate of a bacterium of any strain (EPS+, EPS−, QS+, QS−) having a mass of m is calculated as:

$$\frac{dm}{dt} = \left((1 - f Q(AI)) \mu_{\max} \frac{S}{K_S + S} - \frac{\sigma}{Y_{AX}} \right) m \quad (1)$$

where μ_{\max} , K_S , and S are the maximum specific growth rate, half saturation coefficient and local substrate concentration, respectively. σ and Y_{AX} are the production rate and corresponding yield of the quorum sensing signal (auto-inducer, AI). The EPS producing bacteria spend a fraction of the energy (f) gained from nutrients on EPS production and the remaining fraction ($1-f$) on growth and division. The value of the switching function $Q(AI)$ is calculated as explained below. As shown in **Table 1**, all strains except EPS− can produce EPS and all strains produce AI . Over time EPS accumulates within the shells around the EPS producing cells and is subsequently excreted as EPS particles. Once a bacterium reaches a pre-determined cellular mass, it divides into two cells. The pressure build-up due to biomass growth is released by biofilm expansion (Kreft et al., 1998). The concentrations of substrate (S) and auto-inducer (AI) are calculated as:

$$\frac{\partial S}{\partial t} = D_S \nabla^2 S - \frac{\mu_{\max}}{Y_{XS}} \frac{S}{K_S + S} X \quad (2)$$

$$\frac{\partial AI}{\partial t} = D_{AI} \nabla^2 AI + \sigma X \quad (3)$$

where X is the local biomass concentration and D represents the diffusion coefficient of the respective solute. For the non-quorum sensing strains EPS+ and EPS− the function $Q(AI)$ given in Equation (1) is independent of the AI signal and is always equal to 1 and 0, respectively. For the negative quorum sensing strain (QS−), $Q(AI) = 1$ if the quorum sensing signal concentration is less than the quorum sensing threshold τ and $Q(AI) = 0$ otherwise. For the positive quorum sensing strain (QS+), $Q(AI) = 1$ if the quorum sensing signal concentration is greater than the quorum sensing threshold τ and otherwise $Q(AI) = 0$.

The physical space in which the biofilm grows is represented by a rectangular space of $400 \mu\text{m} \times 200 \mu\text{m}$ divided into a

200×100 computational grid. The x direction has periodic boundaries which means that a bacterium that is pushed beyond the boundary plane re-enters the domain through the opposite boundary plane. The y direction has the no-flux boundary condition at the substratum and Dirichlet boundary condition at the opposite end, which is the bulk liquid. Bacteria can spread toward the bulk liquid but not into the substratum (Kreft and Wimpenny, 2001). Equations (2) and (3) are solved for the steady state solution, as the rate of diffusion of solutes is very fast compared to the bacterial growth rate. Additional details about the model can be found in Xavier and Foster (2007) and Nadell et al. (2008).

Numerical Simulations and Data Analysis

At the beginning of any simulation the bacteria are placed on the inert, impermeable substratum located at $y = 0$ and are considered to be attached. Initially, 50 cells of each bacterial strain (EPS producing and non-producing) are placed on the substratum. The simulations are performed for a maximum of 12-days as the simulation box ($400 \mu\text{m} \times 200 \mu\text{m}$) cannot accommodate larger biofilms. Similar to others (Xavier and Foster, 2007), the fitness of EPS+ is calculated as $w_{EPS+} = \log_2 \left(\frac{N_{EPS+,t}}{N_{EPS+,0}} \right)$, where $N_{EPS+,0}$ is the initial number of bacterial cells and $N_{EPS+,t}$ represents the number of bacterial cells at a chosen time t . The fitness of EPS− is defined in the same manner and the relative fitness of EPS+ compared to EPS− is calculated as $w_r = \frac{w_{EPS+}}{w_{EPS-}}$. The fitness of QS+ and QS− strains relative to EPS− are defined in the same manner. The parameters used for the numerical simulations are listed in **Table 2**. Each simulation is replicated 10 times and the average is taken for the analysis. We also analyse the relationships between relative fitness of EPS+/QS+/QS− and various input variables discussed below by using generalized linear modeling (GLM) in the R statistical programming language.

RESULTS AND DISCUSSION

In the following sections, the competition between various strains of bacteria (EPS+/QS+/QS−/EPS−) are investigated for a period of 12 days given that they initially attach on the surfaces as either cells or aggregates.

Competition between EPS Producing (EPS+) and EPS Non-producing (EPS−) Strains

Competition between EPS+ strain and EPS− strain when they initially deposit on the substratum as individual cells has been studied by Xavier and Foster (2007). A similar case is reproduced here as a control. The bacteria (50 EPS+ and 50 EPS−) are randomly inoculated on the substratum and all of the cells have equal access to substrate (at $t = 0$ s). **Figure 1** shows the biofilm formation for different values of investment in EPS production (different f -values). It is seen that if there is no investment in EPS ($f = 0$, **Figure 1B**) both species grow identically and there is no competitive advantage for either. However, if energy investment in EPS production is relatively high ($f = 0.6$, **Figure 1D**),

TABLE 1 | Stoichiometric table.

Reaction	Soluble components		Particulate components			Rate expression
	S	AI	$X_{EPS+,QS+,QS-}$	X_{EPS-}	EPS	
EPS+/QS+/QS- growth	$-\frac{1}{Y_{XS}}$		$1 - fQ(AI)$		$fQ(AI)$	$\mu_{\max} \frac{S}{K_S + S} X_{EPS+,QS+,QS-}$
EPS- growth	$-\frac{1}{Y_{XS}}$			1		$\mu_{\max} \frac{S}{K_S + S} X_{EPS-}$
AI production by EPS+/QS+/QS-		1	$-\frac{1}{Y_{AX}}$			$\sigma X_{EPS+,QS+,QS-}$
AI production by EPS-		1		$-\frac{1}{Y_{AX}}$		σX_{EPS-}

The substrate and auto inducer are considered as soluble components, while the bacteria and EPS are considered are particulate components. EPS+ cells invest a fraction (f) of energy on EPS production and the remaining $1-f$ goes for biomass production. $Q = 1$ for EPS+. For QS- strain, the function Q is equal to zero if auto inducer concentration AI is greater than a certain threshold value (τ) and otherwise Q is equal to 1 and it is other way around for QS+.

TABLE 2 | Parameters used for the simulations.

Symbol	Description	Value	Reference
τ	Quorum sensing threshold	$5-10 \times 10^{-7} \text{ kg/m}^3$	Frederick et al., 2011
σ	AI production rate	$1.7 \times 10^{-8} \text{ s}^{-1}$	Vaughan et al., 2010
f	Fraction of energy investment in EPS	0–0.6	Nadell et al., 2008
μ_{\max}	Maximum bacteria growth rate	1 h^{-1}	Nadell et al., 2008
ρ	Biomass density	220 kg/m^3	Kreft, 2004
ρ_{EPS}	EPS density	33 kg/m^3	Nadell et al., 2008
D_S	Diffusivity of substrate	$1.6 \times 10^{-9} \text{ m}^2/\text{s}$	Nadell et al., 2008
D_{AI}	Diffusivity of AI	$1.6 \times 10^{-9} \text{ m}^2/\text{s}$	Vaughan et al., 2010
K_S	Half-saturation constant	$3.5 \times 10^{-5} \text{ kg/m}^3$	Nadell et al., 2008
Y_{XS}	Yield of biomass on substrate	0.5	Nadell et al., 2008
Y_{AX}	Yield of auto-inducer on biomass	20	Nadell et al., 2008
S_b	Bulk substrate concentration	$5 \times 10^{-4} \text{ kg/m}^3$	Nadell et al., 2010
L	Boundary layer thickness	$100 \text{ }\mu\text{m}$	–

EPS+ strain is outcompeted by EPS- strain. At an intermediate fraction of energy investment ($f = 0.2$, **Figure 1C**), EPS+ cells dominate in the biofilm. The variation of relative fitness of EPS+ cells as a function of investment in EPS (f) and EPS material density ρ_{EPS} is shown in **Figure 2A**. If the density of EPS decreases compared to the density of bacteria (i.e., ratio ρ/ρ_{EPS} increases) it is advantageous for EPS+ cells since the volume of polymeric substances expands faster. This results in the EPS+ strain being pushed into substrate rich environments while EPS- cells are starved. Xavier and Foster (2007) also briefly demonstrated that the amount of substrate plays a vital role in the competition between EPS+ and EPS- strains. We find that the relationship between the ratio of the fitness of EPS producers to non-producers for different values of EPS investment ($0 < f < 0.6$) is unimodal for density ratio $\rho/\rho_{EPS} > 2.2$ ($t = 6.745$, $P = 0$ and $t = -9.809$, $P = 0$ respectively for the linear and quadratic terms for investment in EPS, f , more details about GLM are in Supporting information), indicating that above a certain threshold of investment in EPS the relative fitness of EPS producers declines. For low density ratio conditions ($\rho/\rho_{EPS} < 2.2$), the relative fitness of the EPS+ strain declines with increased investment in EPS.

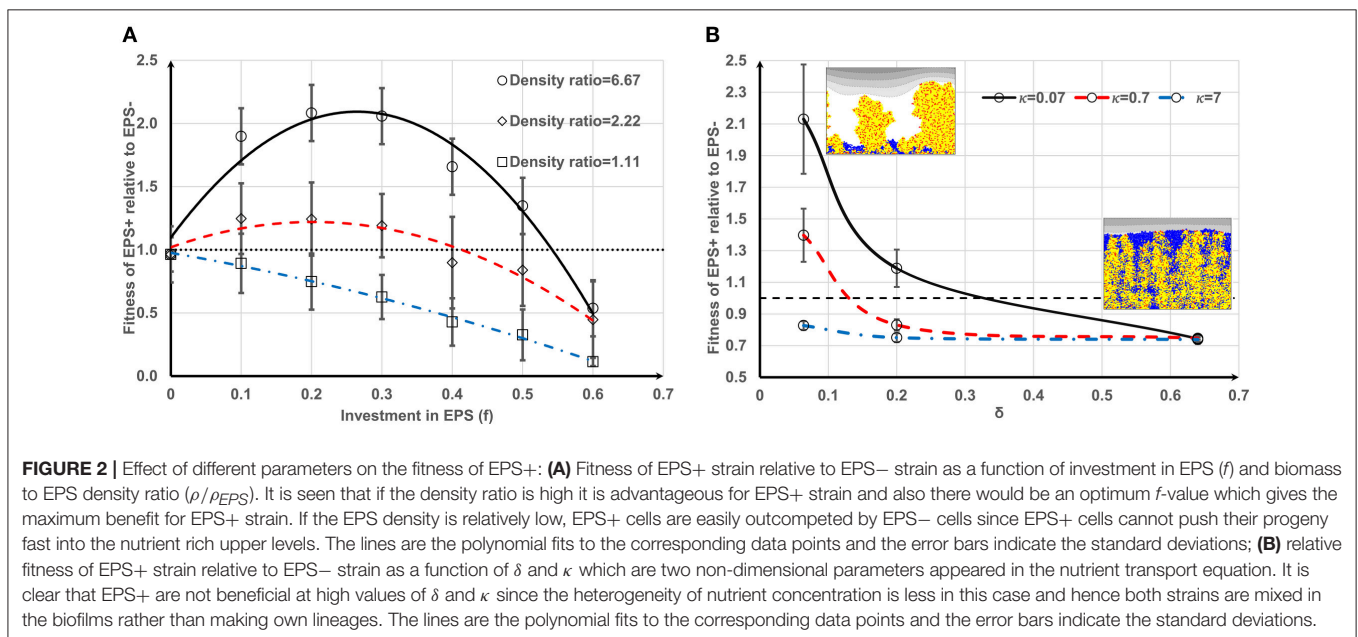
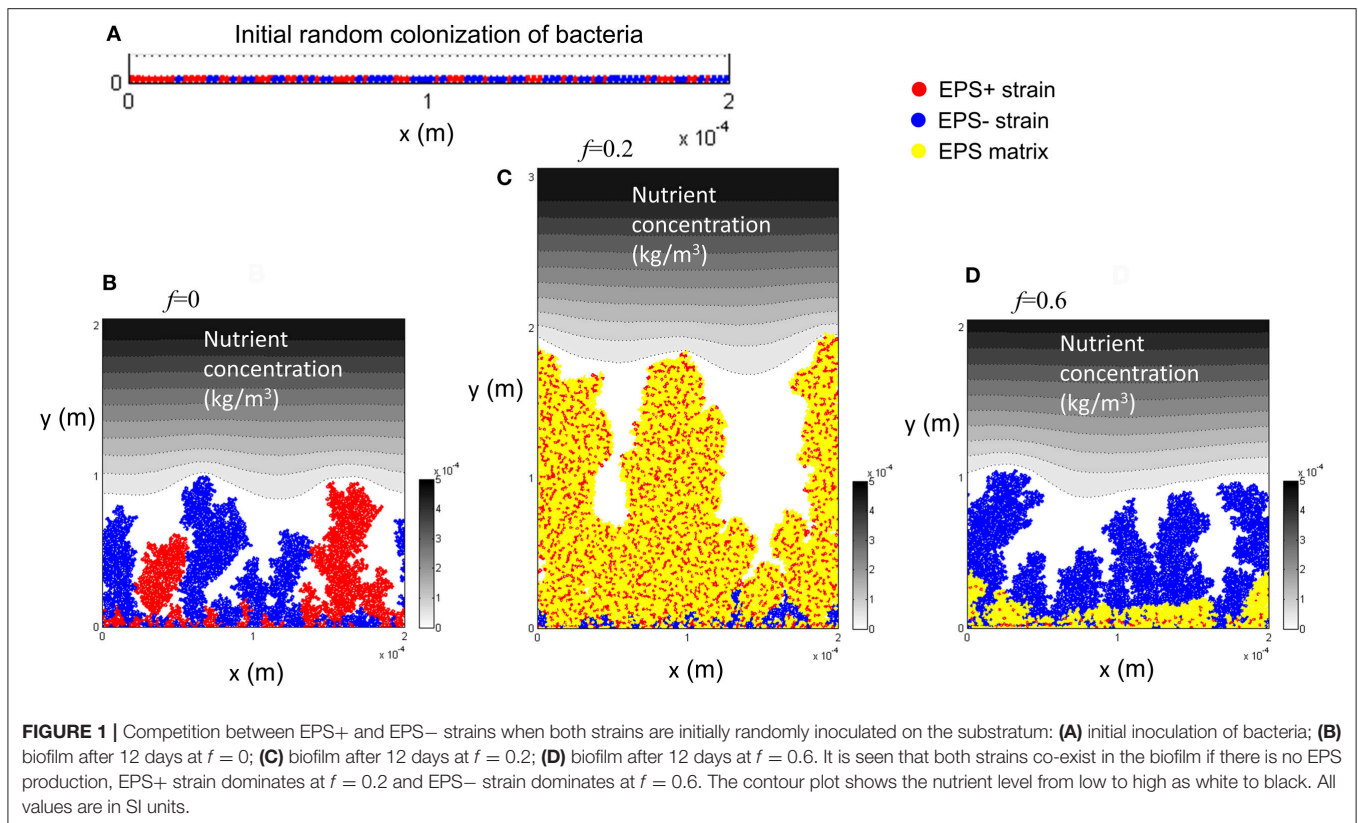
To better understand the trade-off due to substrate limitation and bacteria growth, we direct our attention to the nutrient

transport equation. (The density ratio for the following simulations is $\rho/\rho_{EPS} = 6.67$ which is estimated from the parameters in **Table 2**). For our model, the substrate gradients are determined by Equation (2), which can be re-written in non-dimensional form as:

$$\frac{\partial S^*}{\partial t^*} = \delta^2 \nabla^2 S^* - \frac{S^*}{\kappa + S^*} X^* \quad (4)$$

where $S^* = S/S_b$ is the non-dimensional concentration and S_b denotes the bulk substrate concentration. $\delta = \sqrt{\frac{D_S Y_{XS} S_b}{\mu_{\max} \rho L^2}}$ and $\kappa = \frac{K_S}{S_b}$ are non-dimensional parameters, and ρ and L are biomass density and substrate concentration boundary layer thickness, respectively. The dimensionless parameter δ (Nadell et al., 2010) represents the ratio between the maximum rate of substrate transport and maximum rate at which substrate is consumed by bacteria. The biological meaning of κ is subtle: it expresses the affinity of the bacteria for a substrate in the context of given bulk substrate concentration.

It can be deduced from Equation (4) (if we only consider the y direction) that the steady state substrate transport is given by $\frac{d^2 S^*}{dy^{*2}} = \frac{1}{\delta^2} \frac{S^*}{\kappa + S^*} X^*$, and thus the substrate gradient across the biofilm is $\frac{dS^*}{dy^*} = \frac{1}{\delta} \sqrt{2X^*(S^* - \kappa \ln(S^* + \kappa) + C)}$,



where C is a constant. It is obvious that the substrate gradients are negatively correlated with κ and δ . Increasing the value of either parameter would decrease substrate gradients and therefore result in substrate rich conditions throughout the biofilm. **Figure 2B** shows that when κ and δ increase, the

EPS- strain easily outcompetes the EPS+ strain due to smaller substrate gradients across the biofilm. If κ is very high ($\kappa = 7$), the EPS- strain outcompetes the EPS+ strain regardless of δ . Increasing either parameter results in substrate rich conditions throughout the biofilm and results in a lack of lineage segregation

in the biofilm. Since the EPS+ and EPS− strains are well mixed in the biofilm network the EPS+ cells can be exploited by EPS− cells. We were inspired by Nadell et al. (2013) to derive a simple relationship analogous to Hamilton's rule for the competition between EPS producers and non-producers to show that our model predictions (Figures 1, 2) are consistent with this rule. According to Hamilton's rule (Hamilton, 1964), a cooperative strategy, such as EPS production, will evolve if $rB > C$, where r , B and C are relatedness (measure of genetic similarity of the neighboring cells to the focal cell), fitness benefit, and fitness cost, respectively. The growth rate of a EPS+ cell can be written as $\frac{dm_{EPS+}}{dt} = [\mu_0(1 + B) - f]m_{EPS+}$, where B is the additional benefit gained by the cell because the cell is advected to high nutrient layers by the polymeric substances and μ_0 is the specific growth rate of the cell. A nearby EPS− cell will also be benefited by EPS production depending on how far that cell resides from the EPS+ cell. If we assume this EPS-mediated benefit is inversely proportional to the distance from the EPS+ cell (d), the growth rate of EPS− cell can be written as $\frac{dm_{EPS-}}{dt} = [\mu_0(1 + Br_{EPS+}/d)]m_{EPS-}$, where r_{EPS+} is the radius of EPS+ cell. The EPS+ cell will outcompete EPS− cell if EPS+ cell has higher fitness and therefore:

$$\frac{1}{m_{EPS+}} \frac{dm_{EPS+}}{dt} > \frac{1}{m_{EPS-}} \frac{dm_{EPS-}}{dt} \quad (5)$$

which gives that if $[\mu_0(1+B)-f] > [\mu_0(1+Br_{EPS+}/d)]$. Therefore, the cooperative strategy will evolve if:

$$(1 - r_{EPS+}/d)B > f/\mu_0 \quad (6)$$

The condition given in Equation (6) is analogous to Hamilton's rule, $rB > C$, with $r = 1 - r_{EPS+}/d$ and $C = f/\mu_0$. According to Equation (6), when f increases the relationship will fail at a point where the EPS− strain would outcompete the EPS+ strain. Figures 1, 2 clearly show this behavior. Equation (6) also indicates that EPS+ cells will dominate if EPS− cells are far away from the growing EPS+ cells ($d \gg r_{EPS+}$, meaning that relatedness is high). Figure 2B shows similar behavior; the EPS+ strain dominates when there is lineage segregation (for low κ and δ) and EPS− strain dominates when the two strains are mixed (for high κ and δ). Despite the simplicity of the current 1b model, it can predict the competition between polymer producers and non-producers in biofilms which is akin to Hamilton's rule.

Competition between Aggregates and Cells (with EPS+/EPS− Characteristics)

In reality, biofilms can be initiated by a mixture of single cells and aggregates. If there is a steep nutrient gradient across the biofilm (i.e., small κ and δ values), the initial colonization pattern (i.e., excess of aggregates or single cells) could have a profound effect on the fate of the biofilm inhabitants. Two recent studies (Kragh et al., 2016; Melaugh et al., 2016) that did not consider EPS production, found that bacteria attaching as aggregates would have a competitive advantage over single cells; as the height of the former gives better access to resources. This competition can be directly influenced by over expression of EPS in the aggregates

which can provide them with even greater access to resources and thereby an even greater advantage. To investigate such scenarios we modeled the competition between EPS+ and EPS− bacteria when they attach on the substratum as either circular aggregates or individual cells.

We start the investigation by considering two different scenarios for the initial cell and aggregate attachment on the substratum:

- (i) Case 1: EPS+ bacteria are deposited as aggregates and EPS− bacteria are distributed as single cells.

We consider the case in which EPS+ and EPS− cells deposit on the substratum as aggregates and single cells, respectively. The initial number of aggregates is varied between 1, 2, and 5 such that the cell number ratio between two strains is always 1:1. Therefore, as the number of aggregates increases, the size of each aggregate decreases accordingly (Figure S1). Given the pattern of initial colonization, EPS+ aggregates should have two distinct advantages: as the aggregates produce EPS they can suffocate EPS−, and they can use their height advantage to obtain improved access to substrate.

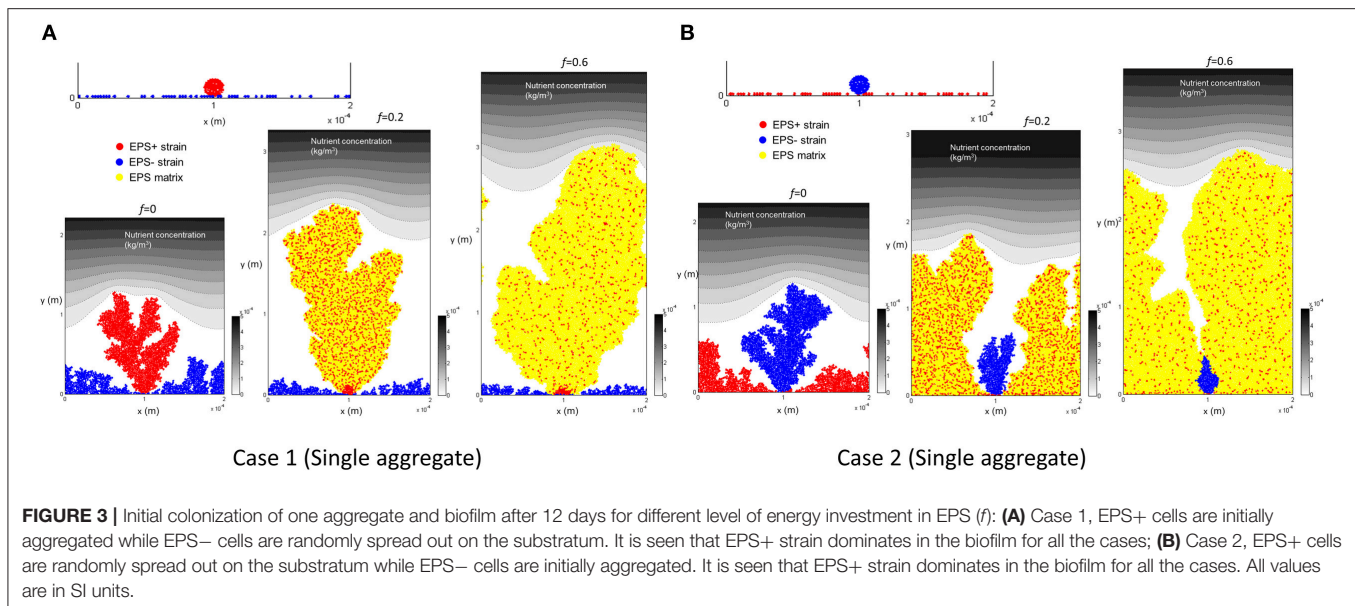
Figure 3A shows biofilm growth when EPS+ strain deposits as a single aggregate. We find that EPS+ strain grows as a single tower and the growth of EPS− cells is inhibited. The population density of EPS+ cells in the EPS matrix decreases as f (the fraction of energy devoted to EPS production) increases.

- (ii) Case 2: EPS+ bacteria are spread out as single cells and EPS− bacteria are deposited as aggregates.

We consider the situation in which the EPS− and EPS+ cells deposit on the substratum as aggregates and single cells, respectively. Similar to Case 1, the number of aggregates is varied as 1, 2, and 5 while maintaining the 1:1 ratio between the strains. Even though EPS− cells do not produce EPS, they are still likely to aggregate due to pili-pili interactions between bacterial cells (Ponisch et al., 2017). Aggregates of EPS− may have a competitive advantage over EPS+ cells due their height and better access to nutrients, however the EPS+ cells may gain a competitive advantage by producing EPS.

Figure 3B shows the results when EPS− strain deposits as a single aggregate. We find that, although EPS− cells are initially aggregated and have some competitive advantage due to height, EPS+ cells always dominate in the biofilm. As the energy invested in EPS production is relatively high ($f = 0.6$), the EPS− tower is surrounded by the polymeric matrix due to rapid EPS production and hence EPS− aggregate is not able to access nutrients.

The variation in the relative fitness of EPS+ cells for both cases (i and ii) is shown in Figure 4. At relatively low values of EPS investment ($f < 0.25$), starting as a single aggregate (EPS+ or EPS−) decreases the relative fitness of EPS+ bacteria when compared to both strains starting as single cells (Figure 4A). However, with greater EPS investment ($f > 0.45$), the relative fitness of EPS+ strain is significantly enhanced even though EPS− cells gain a height advantage by starting out as an aggregate. An increase in the number of aggregates results in the relative fitness curves moving upward and downward for Case 1 or Case 2, respectively (Figure S2), indicating that the number of



aggregates have a significant effect on the competition between these two strains. As the number of aggregates increases (i.e., size of each aggregate decreases), the initially aggregated strain receives competitive advantage over the other strain.

EPS production ($f > 0$), no matter how modest, is better than no EPS production in nearly all situations as it allows better access to nutrients, suggesting that, if bacteria can produce EPS, they should. Our results show that the EPS+ strain obtains the maximum competitive advantage (**Figures 4A,B**) at $f = 0.5 \pm 0.1$ ($P = 0.0131$) when EPS- strain is initially deposited as one/two aggregates and EPS+ strain is deposited as single cells. However, as the number of aggregates increases to five (**Figure 4C**) the EPS+ strain obtains the maximum competitive advantage at around $f = 0.3 \pm 0.2$ ($P = 0.0146$) when EPS+ cells are initially deposited as aggregates and EPS- strain as single cells.

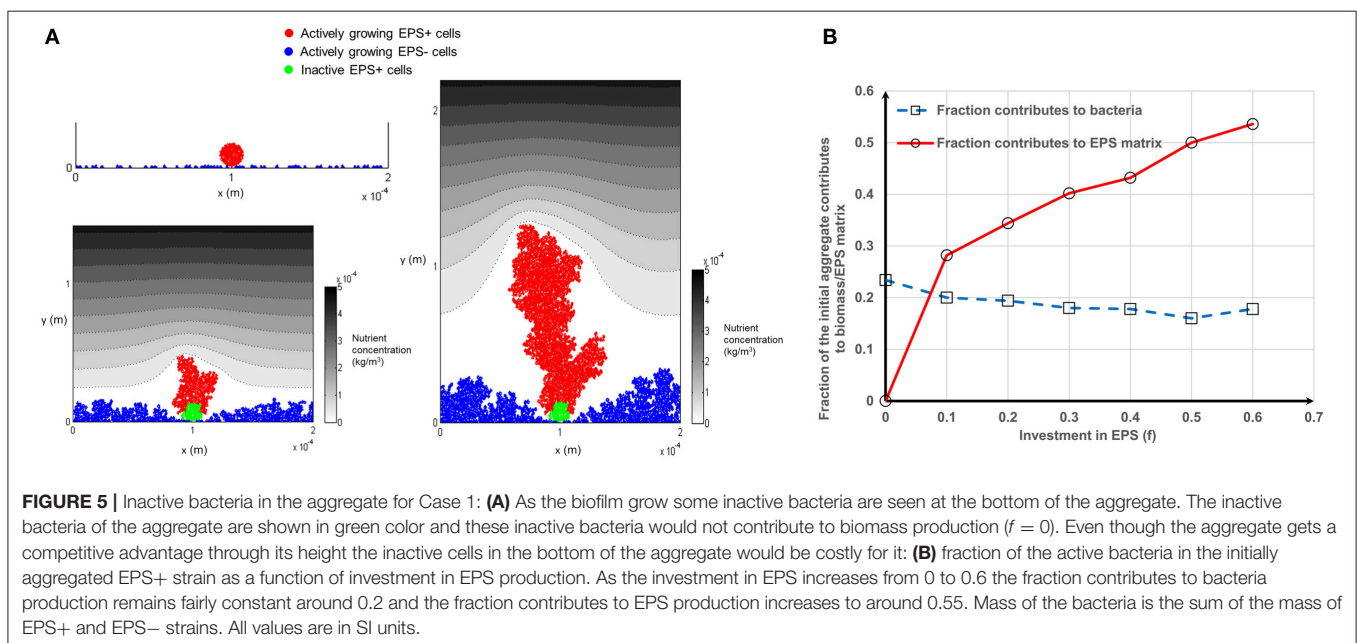
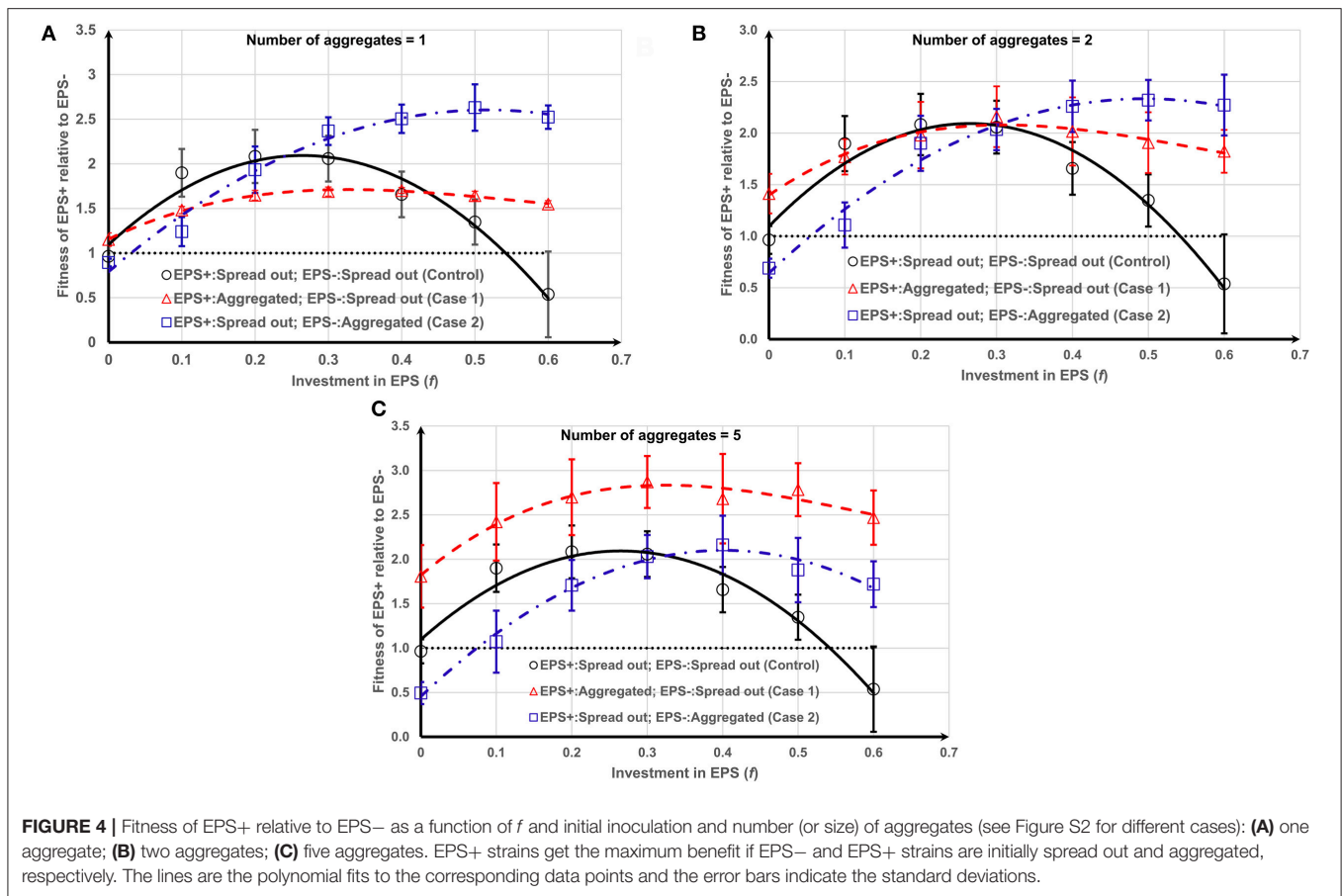
Generalized linear modeling for the data shown in **Figure 4** was also performed to test the statistical significance of the results as detailed in the Supporting information. Case 1 with higher numbers of aggregates has higher relative fitness for EPS+ strain than either control or Case 2 ($t = 9.737$, $P < 2 \times 10^{-16}$). This indicates that EPS+ aggregates that are spread out more widely across the substratum relative to the non-EPS producers have a fitness advantage compared to when they are clumped into one colony, relative to non-EPS producers or when they are both distributed as single cells on the surface. The optimum EPS investment to maximize the relative fitness of EPS producers is clearly dependent on the spread and size of aggregates in the initial population.

The variation in fitness curves seen for Case 1 and Case 2 (**Figure 4**) for different numbers of aggregates can be further explained by scrutinizing the contribution of the initial aggregate to the biomass (mass of EPS+/EPS- cells) and EPS production over time. Bacteria at the bottom of the aggregate do not contribute to biomass production, irrespective of their status (EPS+ or EPS-) because they do not get sufficient substrate

(**Figure 5A**). This limits the ability of a tall aggregate to compete with the singleton cells that surround it. When EPS investment increases from $f = 0$ – 0.6 , the fraction of aggregate which contributes to EPS production increases from zero to around 0.55 ; while the fraction of aggregate which contributes to bacteria production hovers around a value of 0.2 (**Figure 5B**). Since the production of a unit volume of EPS is less expensive than the production of biomass (EPS+ strain) (material density of EPS is smaller than that of biomass, **Table 2**); it is easier for cells to directly invest in EPS production rather than creating new EPS+ cells. Separately, **Figure 4** shows that the initially aggregated strain can obtain a fitness advantage by a greater margin if that strain deposits as smaller aggregates (**Figures 4B,C**). When the aggregate size decreases, the inactive bacteria seen in the initial aggregate (**Figure 5**) also decreases and hence a greater number of cells of the aggregated strain are available to actively compete with the other strain.

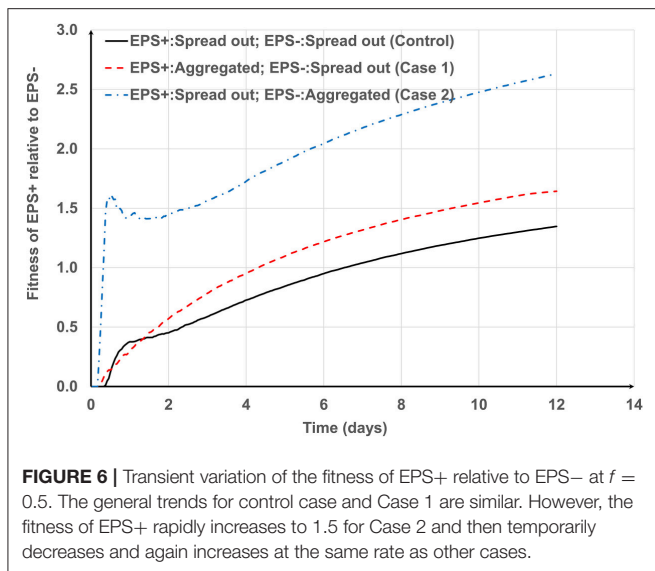
For Case 1, when EPS+ and EPS- strains are deposited as aggregates and single cells respectively, the EPS- cells are outcompeted by EPS+ cells over the whole range of f values ($0 < f < 0.6$). However, in Case 2, the distributed EPS+ cells can be outcompeted by EPS- aggregates if they do not produce enough EPS ($f < 0.1$, **Figure 4C**). This is in contrast to the control case (single cell attachment) where the EPS- cells can “catch a ride” on the polymeric material only when EPS+ cells heavily invest on EPS (when $f > 0.5$) and get lifted toward the nutrient rich surface (see **Figures 1, 4**), thereby gaining an advantage over the EPS+ cells. The segregation of the EPS+ and EPS- strains, as observed in Case 1 and Case 2, prevents the non-producers from being pushed to the top by the EPS+ neighbors investing heavily ($f > 0.5$) in production of polymeric material.

For smaller aggregates (**Figure 4C**) the greatest relative fitness for EPS+ is observed when EPS+ cells (around $f = 0.3$) are initially deposited as aggregates and EPS- strains are deposited as single cells (Case 1). This is expected because the EPS+ strain



gains competitive advantage owing to its moderate height (even though they have a fraction of inactive bacteria) and ability to produce EPS. However, for larger aggregates (**Figures 4A,B**), the

greatest relative advantage is observed when the EPS producers (around $f = 0.5$) are single cells and the non-producers are aggregated (Case 2) and this seems counter-intuitive. On closer



inspection of time dependent relative fitness of EPS+ ($f = 0.5$, Case2, one aggregate) we find that it increases rapidly to around 1.5 at time < 1 day, and then decreases transiently, before increasing again at the same rate as the other two scenarios (Figure 6). Therefore, the overall superior fitness of the EPS+ strain at $f = 0.5$ (Figures 4A,B) at day 12 can be attributed to the initial boost in fitness for the cells as seen in Figure 6. The reason for this initial fitness boost for EPS+ cells is two-fold: larger EPS- aggregates can have many inactive cells, and all EPS+ cells initially have good access to nutrients, hence they grow well. The initial fitness boost increases as f decreases since the EPS+ strain can invest more energy on production of EPS+ cells than polymeric substance. However, at low f -values, the EPS+ strain cannot maintain this initial boost for long since the EPS+ colonies cannot expand quickly due to lack of EPS.

Overall, the microbes with EPS+ characteristics gain a better competitive advantage if they initially colonize the surface as smaller aggregates and are widely spaced between the cells of EPS-. As the aggregate size decreases the EPS producing strain dominates in the biofilm even with lower levels of EPS production.

Competition between QS+/QS- and EPS- Strains

While EPS production is advantageous it is also metabolically expensive, and therefore it should be beneficial for its production in bacteria to be regulated through a feedback control mechanism such as quorum sensing. Two quorum sensing settings are considered in this work. In the first setting, QS- cells compete with EPS- cells and in the second setting QS+ cells compete with EPS- cells. For the sake of simplicity, the study is carried out at $f = 0.5$ which gives better fitness for EPS producers for a single aggregate deposition (Figure 4A). We examine the effects of different QS threshold values on the relative fitness of QS- and QS+ strains for the three scenarios mentioned above (control,

Case1 and Case 2) but focus only on the case of a single aggregate (Figure S1).

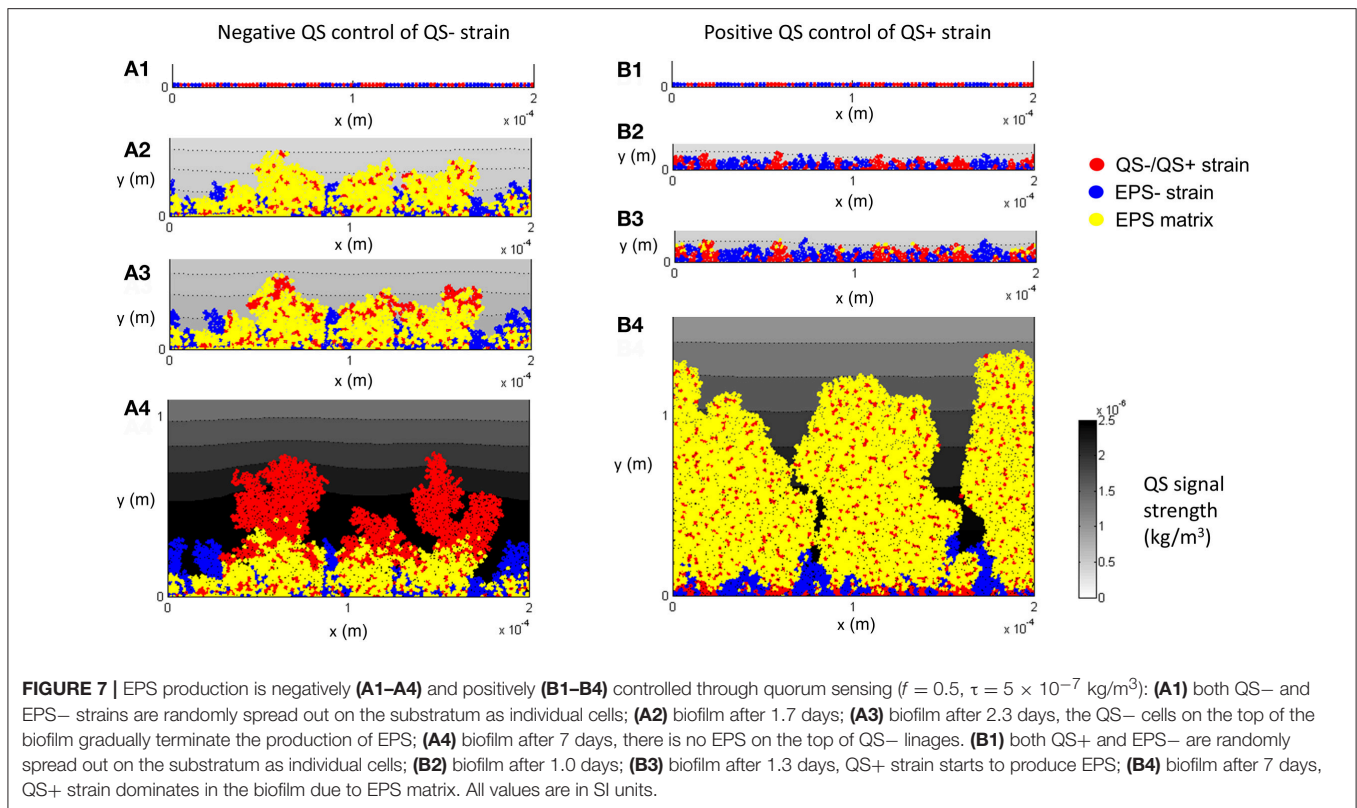
Figure 7 shows the diffusion of AI from the biofilm to the surrounding liquid and the resulting QS-regulation for the control case. Starting with single cells being deposited on the substratum (Figure 7A1), the population of QS- increases (Figure 7A2) and reaches the threshold for AI, $\tau = 5 \times 10^{-7} \text{ kg/m}^3$ (Figure 7A3), then EPS production is terminated but the QS- cells (colored red in Figure 7A4) continue to proliferate under the negative QS control. For the positive QS control, starting from single cells (Figure 7B1), initial growth (duration < 1.3 days) of both strains is similar because their characteristics are identical when there is no EPS production (Figure 7B2). The QS+ strain then starts to produce EPS when AI reaches its threshold of $\tau = 5 \times 10^{-7} \text{ kg/m}^3$ (Figure 7B3) and subsequently the QS+ strain dominates in the biofilm because they gain a competitive advantage due to formation of EPS matrix (Figure 7B4).

We compare three cell deposition scenarios (control, Case 1 and Case 2) when EPS production is regulated through QS, and examined the effect of threshold concentration of the auto-inducer ($\tau = 1 \times 10^{-7}$, 5×10^{-7} , 8×10^{-7} , and $10 \times 10^{-7} \text{ kg/m}^3$) on the fitness of different strains.

Figure 8 shows how the negative QS control affects the relative fitness of QS- strains for three cell deposition scenarios. The relationship between the fitness of EPS producers relative to non-producers under different initial deposition scenarios is significantly related to the threshold value of the auto-inducer concentration ($t = 12.141$, $P = 0$).

For the control case (Figure 8A), at the lowest threshold ($\tau = 1 \times 10^{-7} \text{ kg/m}^3$) the relative fitness is around 1 over time. This is because the QS- strain quickly reaches the QS threshold and terminates EPS production. Both QS- and EPS- strains become biologically identical and hence the relative fitness is around 1. At moderate thresholds ($\tau = 5 \times 10^{-7} \text{ kg/m}^3$) the fitness of QS- is only enhanced in the early stages of biofilm growth. However, higher thresholds ($\tau = 8 \times 10^{-7}$ and $10 \times 10^{-7} \text{ kg/m}^3$) consistently improve QS- strain fitness. Low thresholds confer an initial short-term advantage followed by consistent reduction in fitness; higher thresholds confer a long-term advantage which is consistent with the findings of Nadell et al. (2008). The QS influence for Case 1 (QS- aggregate vs. EPS- single cells, Figure 8B) is analogous to the control case, except at the lowest threshold. At the lowest threshold the QS- strain stops production at the onset of growth; they only have the height advantage (Case 1) and therefore take longer to dominate the biofilm.

The benefit of QS in Case 2 (EPS- aggregate vs. QS- single cells, Figure 8C) is either negative or marginally positive. Quorum sensing is only of long-term value at the highest threshold ($\tau = 10 \times 10^{-7} \text{ kg/m}^3$). At the lowest threshold ($\tau = 1 \times 10^{-7} \text{ kg/m}^3$) the relative fitness of QS- strain rapidly increases to 8.5 and then gradually decreases and finally becomes negative. QS- cells stop producing polymeric substance in the beginning, and then the growth of the QS- strain is boosted ($\tau = 1 \times 10^{-7} \text{ kg/m}^3$). The reason behind this initial fitness boost for the QS- strain has already been explained in Figure 6.

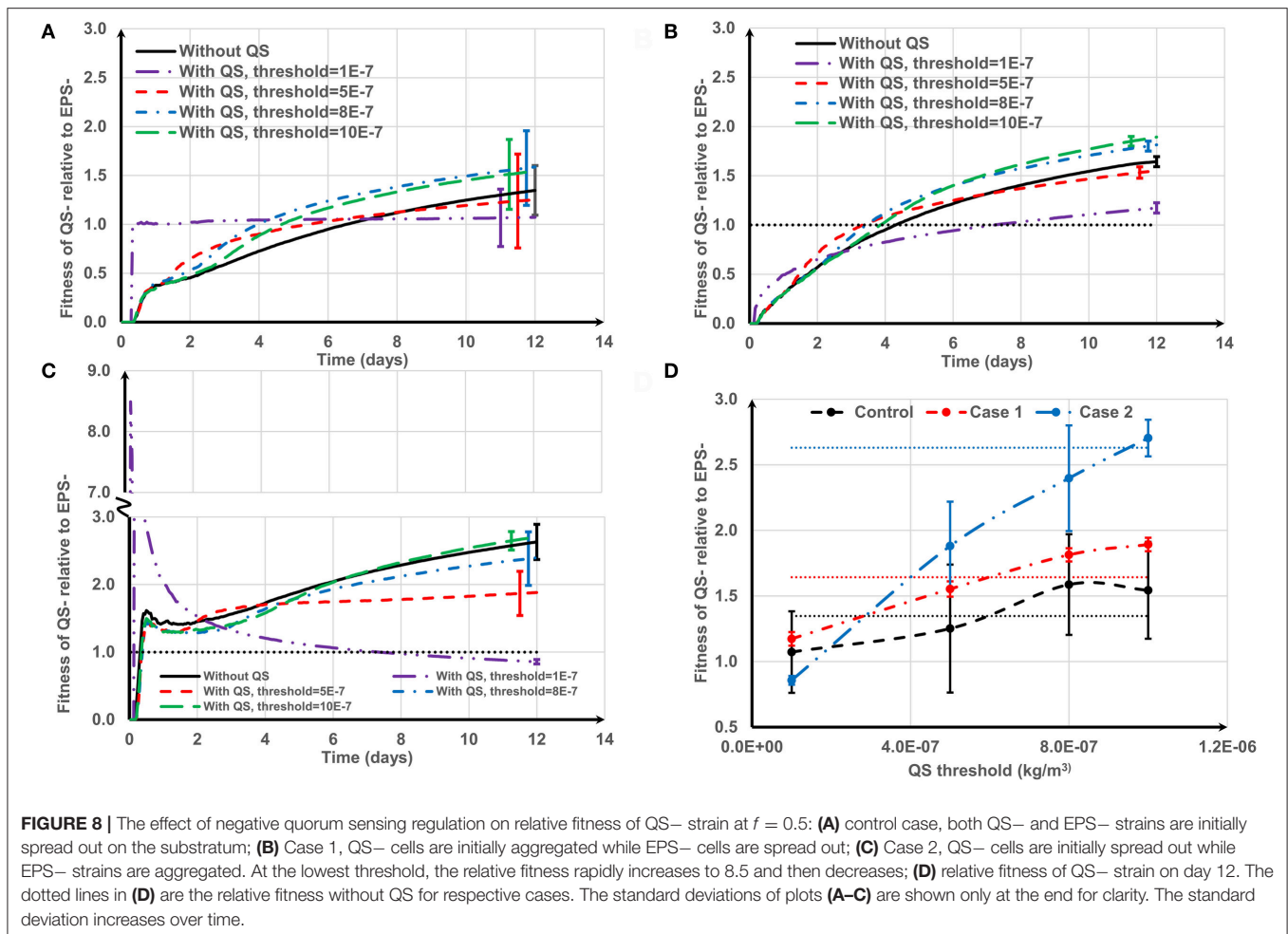


At the lowest threshold, EPS– cells dominate in the long run because they have a competitive advantage due to their initial height.

Figure 8D indicates that the long-term fitness of the QS– strain is more sensitive to the QS threshold for Case 2, but less sensitive for the other two cases. Moreover, for all the cell deposition scenarios, the relative fitness of the QS– strain is positively correlated with the QS threshold (the Pearson's correlation coefficients are 0.9512, 0.9921, and 0.9927 for control, Case 1 and Case 2, respectively). QS– cells are not outcompeted for the whole range of QS thresholds for the control and Case 1. Since QS– cells terminate EPS production at the onset of growth at the lowest threshold, both strains are identical for the control case and QS– cells have the height advantage for Case 1 (see **Figure 4**, control and Case 1 at $f = 0$). However, in Case 2, when QS– cells stop EPS production at the onset of growth, the QS– strain is easily outcompeted by EPS– due to the height advantage of the EPS– (see **Figure 4**, Case 2 at $f = 0$). At the highest QS threshold ($\tau = 10 \times 10^{-7} \text{ kg/m}^3$), although the relative fitness of QS– strain is at least slightly enhanced compared to the strains without QS for all attachment scenarios, only for Case 1 can we guarantee that QS– benefits from quorum sensing ($P = 2.38\text{E-}9$). This is because at higher thresholds, the QS– strain terminates EPS production after they dominate the biofilm, hence stopping EPS production may give a definite advantage to QS– strain for Case 1 because this strain also has the height advantage due to its initial aggregate nature.

Figure 9 shows how the positive QS control affects the relative fitness of EPS producing strains for the three cell deposition scenarios. For the control (**Figure 9A**), the quorum sensing-regulated EPS production marginally enhances the relative fitness of QS+ strain for the whole range of QS thresholds ($10^{-7} < \tau < 10^{-6} \text{ kg/m}^3$). At higher thresholds ($\tau > 1 \times 10^{-7} \text{ kg/m}^3$), the QS+ strain does not produce EPS for a long time and thus the relative fitness of QS+ strain is around 1 until they start to produce EPS, and subsequently their fitness increases once EPS production commences. However, at the lowest threshold ($\tau = 1 \times 10^{-7} \text{ kg/m}^3$), EPS production starts quickly and so the QS+ strain needs time (about 6 days, **Figure 9A**) to dominate in the biofilm because it invests energy on both EPS matrix and QS+ cells, which is analogous to biofilm growth without quorum sensing regulation. There is an optimum QS threshold value for the control case at around $\tau = 5 \times 10^{-7} \text{ kg/m}^3$ ($P = 0.006$) (**Figure 9D**). However, for Case 1 and Case 2 (either strain initially deposited as an aggregate), the positive QS regulation of EPS is advantageous only at the beginning of biofilm growth (**Figures 9B,C**). The long-term relative fitness of the QS+ strain decreases as the QS threshold increases ($P < 0.005$) (**Figure 9D**). Therefore, the relative fitness of the QS+ strain is negatively correlated with QS threshold for Case 1 and Case 2 (the respective Pearson's correlation coefficients are -0.9867 and -0.9644).

Generalized linear modeling was used to investigate the collective effects of aggregate type, quorum sensing threshold and the occurrence of positive or negative regulation on the



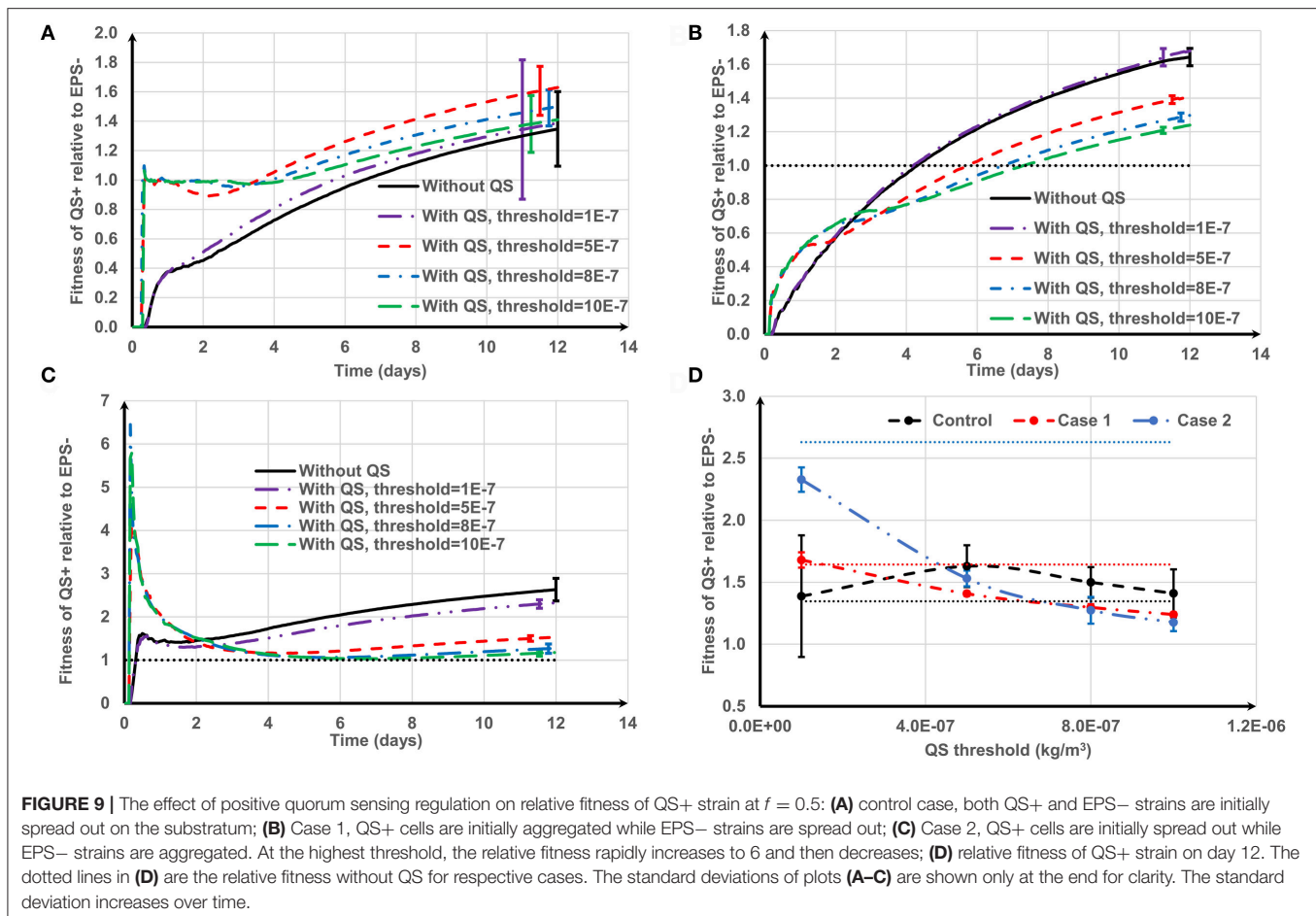
relative fitness of EPS producers compared to non-producers as detailed in the Supporting information. The detrimental effect of the quorum sensing threshold ($t = -6.540$, $P = 3.83 \times 10^{-10}$) and the occurrence of positive vs. negative control of EPS production ($t = -10.248$, $P < 2 \times 10^{-16}$) on relative fitness is very significant. There is a significant correlation between the quorum sensing threshold and whether the EPS is positively or negatively regulated ($t = 13.868$, $P < 2 \times 10^{-16}$) indicating a synergy between the two variables in their effects on fitness. The relative fitness of EPS producers is also dependent on the nature of cell deposition, with aggregated EPS producers (Case 2) resulting in higher fitness than the other two deposition scenarios ($t = 6.660$, $P = 1.94 \times 10^{-10}$).

Overall, we conclude that quorum sensing-regulated EPS production would enhance the fitness of EPS producers only marginally, or even reduces their competitive advantage, under the investigated conditions. This analysis shows that quorum sensing-mediated gene regulation in bacteria may be detrimental at times depending on the nature of the competition. Zhao and Wang (2017) argued that depending on the conditions there would be a “right time” and “right place” in which QS-regulated EPS production can favor biofilm growth; otherwise it would have unfavorable consequences for the EPS

producers. Numerical experiments of Frederick et al. (2011) also show that QS-regulated EPS production rarely facilitates a biofilm to achieve a high cell population. However, maximizing offspring generation is not the only strategy bacteria may have, and sometimes production of EPS is beneficial if the objective is to produce a thick EPS protective layer. Therefore, further studies are needed to understand the role of QS-regulated EPS production for the cell deposition scenarios investigated here, taking into account the multiple functional roles of EPS in bacterial biofilms.

CONCLUSIONS

Microbial competition between two bacterial strains with differing EPS producing characteristics (EPS+/QS+/QS- vs. EPS-), has been studied using an IBM, with one strain initially deposited on the substratum as aggregate(s) and the other as individual cells. The results show that when there is no quorum sensing and if EPS- cells attach as relatively large aggregates; then the EPS+ cells gain the maximum competitive advantage if they attach on the substratum as single cells (under the condition that the EPS+ strain invests about half of their energy in EPS production). Xavier and Foster (2007) and Nadell et al. (2008)



also showed that the optimum investment in EPS is around 0.5, when EPS+ compete with others that invest either more or less in EPS production (in these studies, both strains are initially deposited as single cells on the surface, similar to the control case in this paper). However, when the EPS+ strain is deposited in relatively small clusters and the EPS- strain is deposited as single cells, then the EPS+ bacteria always benefit from producing EPS regardless of the level of energy invested in EPS. According to this simulation, as the EPS+ aggregate size decreases they need to expend less energy on EPS production ($f < 0.5$) to gain the maximum fitness advantage.

Quorum sensing-regulated EPS production is found to provide no significant advantage over continuous EPS production for all of the cell deposition scenarios, for the range of parameters chosen for the present study. Our numerical results indicate that quorum sensing-regulated EPS production significantly reduces the competitive advantage gained by matrix producers when they deposit as aggregates and compete with single cells of EPS- or vice-versa.

Laser-diffraction particle-size scanning tests have shown that 90% of the total planktonic biomass of *Pseudomonas aeruginosa* consist of cellular aggregates in the size range of 10–400 μm (Schleheck et al., 2009). Therefore, it is inevitable that single cells deposited on a surface will compete with different sizes of

bacterial aggregates of *P. aeruginosa* which are deposited on the same surface. Our simulation results may give an insight into this competition because the present results indicate that the aggregate size plays a significant role in the competition with single cells. *In vitro* experiments of Kragh et al. (2016) have shown that aggregates of *P. aeruginosa* gain a competitive advantage over their single cells when competing in the same environment. These experiments could be extended to investigate the effects of different EPS production characteristics and different aggregate sizes on microbial competitions in biofilms, and then our predictions could be tested.

Wessel et al. (2014) used a gelatin based three-dimensional printing strategy to make different sizes of *P. aeruginosa* aggregate and showed that when the aggregate size exceeds a critical size, localized oxygen depletion regions were found inside the aggregate. These *in vitro* experimental results show that the growth rate decreases as the aggregate size increases which is consistent with our findings. Although the experimental and simulation results based on continuous model have general agreements, there was some discrepancy due to simplifying assumptions including uniform oxygen consumption throughout the aggregate. However, an Individual-based modeling technique similar to the present study should give more comparable results to these experiments because the IbM can capture heterogeneities

inside aggregates more accurately. The present simulation techniques can also be adapted to study the interaction of bacteria such as *Sinorhizobium meliloti* that forms aggregates (Dorken et al., 2012) with other species during the wastewater treatment process (Ben Rebah et al., 2002).

Even though it is widely believed that public goods producing bacteria are benefited by quorum sensing-regulated gene modulations, our numerical results show that quorum sensing can also have detrimental effects on public good producers. However, these numerical simulations need to be extended to cover a wider range of parameters and be experimentally tested to draw a solid conclusion about these findings.

In the present Individual-based Model, factors such as bacteria motility, founder cell density, detachment and attachment etc. are not considered and these developments can form the basis for future work. Moreover, for biofilms growing in a flow environment, the mechanical strength of the biofilm mediated by the EPS composition can provide insights into the biological evolution of polymer producing strains. The flow can also advect quorum sensing signals which can cause the bacteria to misread their local cell density, thereby influencing bacterial competition in constricted geometries, for example in the pores of the soil.

REFERENCES

- Ben Rebah, F., Tyagi, R. D., and Prevost, D. (2002). Production of S-meliloti using wastewater sludge as a raw material: effect of nutrient addition and pH control. *Environ. Technol.* 23, 623–629. doi: 10.1080/09593332308618378
- Bucci, V., Nadell, C. D., and Xavier, J. B. (2011). The evolution of bacteriocin production in bacterial biofilms. *Am. Nat.* 178, E162–E173. doi: 10.1086/662668
- Davey, M. E., and O'toole, G. A. (2000). Microbial biofilms: from ecology to molecular genetics. *Microbiol. Mol. Biol. Rev.* 64, 847. doi: 10.1128/MMBR.64.4.847-867.2000
- Dorken, G., Ferguson, G. P., French, C. E., and Poon, W. C. K. (2012). Aggregation by depletion attraction in cultures of bacteria producing exopolysaccharide. *J. R. Soc. Interf.* 9, 3490–3502. doi: 10.1098/rsif.2012.0498
- Frederick, M. R., Kuttler, C., Hense, B. A., and Eberl, H. J. (2011). A mathematical model of quorum sensing regulated EPS production in biofilm communities. *Theor. Biol. Med. Model.* 8:8. doi: 10.1186/1742-4682-8-8
- Fuqua, C., and Greenberg, E. P. (2002). Listening in on bacteria: acyl-homoserine lactone signalling. *Nat. Rev. Mol. Cell Biol.* 3, 685–695. doi: 10.1038/nrm907
- Hamilton, W. D. (1964). The genetical evolution of social behaviour I. *J. Theor. Biol.* 7, 1–16. doi: 10.1016/0022-5193(64)90038-4
- Jayathilake, P. G., Gupta, P., Li, B., Madsen, C., Oyebamiji, O., Gonzalez-Cabaleiro, R., et al. (2017). A mechanistic individual-based model of microbial communities. *PLoS ONE* 12:e0181965. doi: 10.1371/journal.pone.0181965
- Kragh, K. N., Hutchison, J. B., Melaugh, G., Rodesney, C., Roberts, A. E. L., Irie, Y., et al. (2016). Role of multicellular aggregates in biofilm formation. *Mbio* 7:e00237-16. doi: 10.1128/mBio.00237-16
- Kreft, J. U. (2004). Biofilms promote altruism. *Microbiology* 150, 2751–2760. doi: 10.1099/mic.0.26829-0
- Kreft, J. U., and Wimpenny, J. W. T. (2001). Effect of EPS on biofilm structure and function as revealed by an individual-based model of biofilm growth. *Water Sci. Technol.* 43, 135–141. doi: 10.3410/f.1002556.27556
- Kreft, J. U., Booth, G., and Wimpenny, J. W. T. (1998). BacSim, a simulator for individual-based modelling of bacterial colony growth. *Microbiology* 144, 3275–3287. doi: 10.1099/00221287-144-12-3275
- Kreft, J. U., Picioreanu, C., Wimpenny, J. W. T., and van Loosdrecht, M. C. M. (2001). Individual-based modelling of biofilms. *Microbiology* 147, 2897–2912. doi: 10.1099/00221287-147-11-2897
- Lardon, L. A., Merkey, B. V., Martins, S., Dotsch, A., Picioreanu, C., Kreft, J. U., et al. (2011). iDynoMiCS: next-generation individual-based modelling of biofilms. *Environ. Microbiol.* 13, 2416–2434. doi: 10.1111/j.1462-2920.2011.02414.x
- McSwain, B. S., Irvine, R. L., Hausner, M., and Wilderer, P. A. (2005). Composition and distribution of extracellular polymeric substances in aerobic flocs and granular sludge. *Appl. Environ. Microbiol.* 71, 1051–1057. doi: 10.1128/AEM.71.2.1051-1057.2005
- Melaugh, G., Hutchison, J., Kragh, K. N., Irie, Y., Roberts, A., and Bjarnsholt, T. (2016). Shaping the growth behaviour of biofilms initiated from bacterial aggregates. *PLoS ONE* 11:e0149683. doi: 10.1371/journal.pone.0149683
- Mitri, S., Xavier, J. B., and Foster, K. R. (2011). Social evolution in multispecies biofilms. *Proc. Natl. Acad. Sci. U.S.A.* 108, 10839–10846. doi: 10.1073/pnas.1100292108
- Nadell, C. D., Bucci, V., Drescher, K., Levin, S. A., Bassler, B. L., and Xavier, J. B. (2013). Cutting through the complexity of cell collectives. *Proc. R. Soc. B Biol. Sci.* 280:20122770. doi: 10.1098/rspb.2012.2770
- Nadell, C. D., Foster, K. R., and Xavier, J. B. (2010). Emergence of spatial structure in cell groups and the evolution of cooperation. *PLoS Comput. Biol.* 6:e1000716. doi: 10.1371/journal.pcbi.1000716
- Nadell, C. D., Xavier, J. B., Levin, S. A., and Foster, K. R. (2008). The evolution of quorum sensing in bacterial biofilms. *PLoS Biol.* 6:e14. doi: 10.1371/journal.pbio.0060014
- Picioreanu, C., Kreft, J. U., and van Loosdrecht, M. C. M. (2004). Particle-based multidimensional multispecies Biofilm model. *Appl. Environ. Microbiol.* 70, 3024–3040. doi: 10.1128/AEM.70.5.3024-3040.2004
- Ponisch, W., Weber, C. A., Juckeland, G., Biais, N., and Zaboradaev, V. (2017). Multiscale modeling of bacterial colonies: how pili mediate the dynamics of single cells and cellular aggregates. *New J. Phys.* 19:015003. doi: 10.1088/1367-2630/aa5483
- Schleheck, D., Barraud, N., Klebensberger, J., Webb, J. S., McDougald, D., Rice, S. A., et al. (2009). *Pseudomonas aeruginosa* PAO1 preferentially grows as aggregates in liquid batch cultures and disperses upon starvation. *PLoS ONE* 4:e5513. doi: 10.1371/journal.pone.0005513
- Schluter, J., Nadell, C. D., Bassler, B. L., and Foster, K. R. (2015). Adhesion as a weapon in microbial competition. *ISME J.* 9, 139–149. doi: 10.1038/ismej.2014.174

AUTHOR CONTRIBUTIONS

All authors listed, have made substantial, direct and intellectual contribution to the work, and approved it for publication.

ACKNOWLEDGMENTS

The authors would like to thank the UK Engineering and Physical Sciences Research Council (EPSRC) for funding this work as part of the Newcastle University Frontiers in Engineering Biology (NUFEB) project (EP/K039083/1). This work would not have been possible without the multi-disciplinary collaboration that has been enabled by this award.

SUPPLEMENTARY MATERIAL

The Supplementary Material for this article can be found online at: <http://journal.frontiersin.org/article/10.3389/fmicb.2017.01865/full#supplementary-material>

Data supporting this publication is openly available under an 'Open Data Commons Open Database License'. Additional metadata are available at: <https://doi.org/10.17634/123172-2>. Please contact Newcastle Research Data Service at rdm@ncl.ac.uk for access instructions.

- Schluter, J., Schoech, A. P., Foster, K. R., and Mitri, S. (2016). The evolution of quorum sensing as a mechanism to infer kinship. *PLoS Comput. Biol.* 12:e1004848. doi: 10.1371/journal.pcbi.1004848
- Tang, Y. N., and Valocchi, A. J. (2013). An improved cellular automaton method to model multispecies biofilms. *Water Res.* 47, 5729–5742. doi: 10.1016/j.watres.2013.06.055
- van Gestel, J., Weissing, F. J., Kuipers, O. P., and Kovacs, A. T. (2014). Density of founder cells affects spatial pattern formation and cooperation in *Bacillus subtilis* biofilms. *ISME J.* 8, 2069–2079. doi:10.1038/ismej.2014.52
- Vaughan, B. L., Smith, B. G., and Chopp, D. L. (2010). The influence of fluid flow on modeling quorum sensing in bacterial biofilms. *Bull. Mathemat. Biol.* 72, 1143–1165. doi: 10.1007/s11538-009-9485-8
- Wei, G. P., Lo, C., Walsh, C., Hiller, N. L., Marculescu, R. (2016). *In Silico* Evaluation of the Impacts of Quorum Sensing Inhibition (QSI) on strain competition and development of QSI resistance. *Sci. Rep.* 6:35136. doi:10.1038/srep35136
- Wessel, A. K., Arshad, T. A., Fitzpatrick, M., Connell, J. L., Bonnecaze, R. T., Shear, J. B., et al. (2014). Oxygen limitation within a bacterial aggregate. *Mbio* 5:e00992-14. doi: 10.1128/mBio.00992-14
- Xavier, J. B., and Foster, K. R. (2007). Cooperation and conflict in microbial biofilms. *Proc. Natl. Acad. Sci. U.S.A.* 104, 876–881. doi: 10.1073/pnas.0607651104
- Xavier, J. B., Picioreanu, C., and van Loosdrecht, M. C. M. (2005). A framework for multidimensional modelling of activity and structure of multispecies biofilms. *Environ. Microbiol.* 7, 1085–1103. doi: 10.1111/j.1462-2920.2005.00787.x
- Zhao, J., and Wang, Q. (2017). Three-dimensional numerical simulations of biofilm dynamics with quorum sensing in a flow cell. *Bull. Mathemat. Biol.* 79, 884–919. doi: 10.1007/s11538-017-0259-4

Conflict of Interest Statement: The authors declare that the research was conducted in the absence of any commercial or financial relationships that could be construed as a potential conflict of interest.

Copyright © 2017 Jayathilake, Jana, Rushton, Swailes, Bridgens, Curtis and Chen. This is an open-access article distributed under the terms of the Creative Commons Attribution License (CC BY). The use, distribution or reproduction in other forums is permitted, provided the original author(s) or licensor are credited and that the original publication in this journal is cited, in accordance with accepted academic practice. No use, distribution or reproduction is permitted which does not comply with these terms.



From Genes to Ecosystems in Microbiology: Modeling Approaches and the Importance of Individuality

Jan-Ulrich Kreft¹, Caroline M. Plugge², Clara Prats³, Johan H. J. Leveau⁴, Weiwen Zhang⁵ and Ferdi L. Hellweger^{6*}

¹ Centre for Computational Biology, Institute for Microbiology and Infection, School of Biosciences, University of Birmingham, Birmingham, United Kingdom, ² Laboratory of Microbiology, Wageningen University and Research, Wageningen, Netherlands, ³ Department of Physics, School of Agricultural Engineering of Barcelona, Universitat Politècnica de Catalunya–BarcelonaTech, Castelldefels, Spain, ⁴ Department of Plant Pathology, University of California, Davis, Davis, CA, United States, ⁵ Laboratory of Synthetic Microbiology, Key Laboratory of Systems Bioengineering (Ministry of Education), School of Chemical Engineering and Technology, Tianjin University, Tianjin, China, ⁶ Civil and Environmental Engineering Department, Marine and Environmental Sciences Department, Bioengineering Department, Northeastern University, Boston, MA, United States

OPEN ACCESS

Edited by:

Steve Lindemann,
Purdue University, United States

Reviewed by:

Christopher Scott Henry,
Argonne National Laboratory (DOE),
United States

Matthew B. Sullivan,
Ohio State University, United States

*Correspondence:

Ferdi L. Hellweger
ferdi@coe.neu.edu

Specialty section:

This article was submitted to
Systems Microbiology,
a section of the journal
Frontiers in Microbiology

Received: 25 July 2017

Accepted: 07 November 2017

Published: 27 November 2017

Citation:

Kreft JU, Plugge CM, Prats C,
Leveau JHJ, Zhang W and
Hellweger FL (2017) From Genes to
Ecosystems in Microbiology: Modeling
Approaches and the Importance of
Individuality. *Front. Microbiol.* 8:2299.
doi: 10.3389/fmicb.2017.02299

Models are important tools in microbial ecology. They can be used to advance understanding by helping to interpret observations and test hypotheses, and to predict the effects of ecosystem management actions or a different climate. Over the past decades, biological knowledge and ecosystem observations have advanced to the molecular and in particular gene level. However, microbial ecology models have changed less and a current challenge is to make them utilize the knowledge and observations at the genetic level. We review published models that explicitly consider genes and make predictions at the population or ecosystem level. The models can be grouped into three general approaches, i.e., metabolic flux, gene-centric and agent-based. We describe and contrast these approaches by applying them to a hypothetical ecosystem and discuss their strengths and weaknesses. An important distinguishing feature is how variation between individual cells (individuality) is handled. In microbial ecosystems, individual heterogeneity is generated by a number of mechanisms including stochastic interactions of molecules (e.g., gene expression), stochastic and deterministic cell division asymmetry, small-scale environmental heterogeneity, and differential transport in a heterogeneous environment. This heterogeneity can then be amplified and transferred to other cell properties by several mechanisms, including nutrient uptake, metabolism and growth, cell cycle asynchronicity and the effects of age and damage. For example, stochastic gene expression may lead to heterogeneity in nutrient uptake enzyme levels, which in turn results in heterogeneity in intracellular nutrient levels. Individuality can have important ecological consequences, including division of labor, bet hedging, aging and sub-optimality. Understanding the importance of individuality and the mechanism(s) underlying it for the specific microbial system and question investigated is essential for selecting the optimal modeling strategy.

Keywords: microbial ecology, gene-centric modeling, metabolic flux modeling, agent-based modeling, individuality, heterogeneity, single cell

INTRODUCTION

Microbes are important drivers of biogeochemical cycles in all ecosystems and impact their environments in a plethora of ways. For example, in lakes, the harmful cyanobacterium *Microcystis aeruginosa* can bloom and produce toxins that make the water unsafe to drink (Paerl et al., 2011). The common gut bacterium *Bacteroides fragilis* produces a chemical that helps the host develop its immune system (Atarashi et al., 2013).

Models are important tools for understanding and managing ecosystems. They can be used to advance scientific understanding by interpreting field observations and aid in hypothesis testing. For example, Jöhnk et al. (2008) used a model to quantify the roles of temperature range and buoyancy regulation in the fitness of the toxic cyanobacterium *Microcystis* during heat waves. Buffie et al. (2015) applied the model of Stein et al. (2013) to infer an antagonistic interaction in the gut between the pathogen *Clostridium difficile* and another species of that genus, *Clostridium scindens*. For ecosystem management, models can be used to answer “what if” questions and make predictions about the effects of future environmental conditions. For example, Blumberg and Di Toro (1990) used a model to predict the effects of climate warming on phytoplankton and dissolved oxygen in a lake. Bucci et al. (2016) predicted the composition of the mouse gut microbiota following infection with *C. difficile*.

In the past decades, microbiology has experienced rapid advances in observational and experimental technologies, resulting in substantial progress in the understanding of microbes at the molecular level. For example, nitrogen (N) fixation by the cyanobacterium *Anabaena* involves a division of labor among N-fixing heterocysts and photosynthesizing vegetative cells. The nitrogen-containing β -aspartyl-arginine is produced by cyanophycinase in heterocysts, transferred intercellularly to vegetative cells where it is converted to aspartate and arginine by isoaspartyl dipeptidase (Burnat et al., 2014). Another example involves transcription of genes to messenger RNA (mRNA) and translation to proteins, which is performed by RNA polymerase (RNAP) and the ribosome complex, respectively. In bacteria, those can form a single transcribing and translating “expressome” complex, with known 3D structure and functional consequences on transcriptional pausing, backtracking and termination (Kohler et al., 2017). Characterization of ecosystems is following the same trend. For example, lakes used to be characterized using bulk measures, like Chlorophyll *a* and total phosphorus concentrations, but observations are now often at the molecular level, including gene expression (transcript levels) (Vila-Costa et al., 2013). Animal and human microbiota are now routinely characterized using multiple omics technologies, such as community characterization using bacterial 16S ribosomal RNA (rRNA) polymerase chain reaction (Costello et al., 2009), and increasingly meta-genomics, transcriptomics and proteomics (Wang et al., 2015).

The development of models is lagging behind as most models still do not make use of molecular level understanding or observations. It is recognized that there is a substantial gap between our microbial ecology models and current microbiology knowledge and environmental observations (Fuhrman et al.,

2013; Trivedi et al., 2013; Hellweger, 2015; Dick, 2017; Stec et al., 2017). For example, lake phytoplankton models still simulate phytoplankton biomass concentrations (e.g., μg Chlorophyll *a* L^{-1}) and the effect of a nutrient on the growth rate using an equation developed 75 years ago (Monod model). Likewise, most models of the gut aggregate species into functional groups based on metabolic pathways (Kettle et al., 2015). Models are now being developed that explicitly resolve genes and make predictions at the population and ecosystem level.

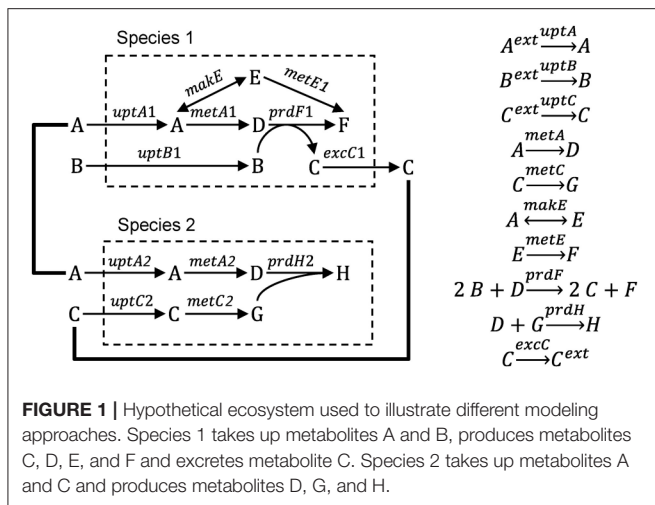
This paper has two parts. First, we review existing modeling approaches. Here, we focus on mechanistic models that explicitly include genes and simulate population-level properties (e.g., microbe concentration, nutrient uptake) rather than empirical models. One aspect in which the existing approaches differ is their representation of microbial individuality. The second part of our review will use examples to explain why including individuality is important.

PART 1: REVIEW OF EXISTING MODELING APPROACHES

In this section we describe three modeling approaches that have been used to bridge the gap between genes and ecosystems, including metabolic flux, gene-centric and agent-based modeling (ABM). We illustrate each approach using a hypothetical ecosystem, where two microbial species grow and interact via three metabolites (**Figure 1**). We then discuss a number of examples from the literature, focusing mostly on the modeling aspects of the studies. Then we highlight the weaknesses and strengths of each approach. Finally, we characterize the models along a number of dimensions, including space, time, function, heterogeneity, species diversity and genes.

Literature Selection Criteria

The review is focused on the use of gene-level models for advancing understanding and making predictions of microbial ecosystems. To keep the scope of the review manageable, we included only quantitative models, which are required for predictions, although qualitative models may be sufficient to advance understanding. We applied the following selection criteria: (1) model uses a mechanistic (vs. empirical) approach; (2) model explicitly considers at least one actual gene or protein; (3) model includes some form of direct or indirect interaction among microbes; (4) model includes multiple microbial species (or strains) or phenotypes in different locations; and (5) model makes predictions at the population level. We therefore exclude empirical models that correlate observed gene distributions to environmental factors and function (e.g., carbon export in the ocean, Guidi et al., 2016), models that use hypothetical genes or digital genomes describing behavioral traits (e.g., Lenski et al., 1999; Clark et al., 2011), scale up single-cell models using multiple independent simulations where the cells do not interact (e.g., Emonet and Cluzel, 2008; Labhsetwar et al., 2013) and studies that infer interactions from comparison of metabolic networks and do not make quantitative predictions (e.g., Levy and Borenstein, 2013; Zelezniak et al., 2015).



Metabolic Flux Modeling

Definition

This approach builds on the genome-scale, constraint-based modeling approach most commonly applied to single species (Feist et al., 2008). In this approach, the genome sequence is used to derive a network of potential metabolic reactions by a combination of automated and manual (curation) steps. Then, a flux distribution is predicted, typically by optimizing the flux distribution to maximize an objective function, like maximization of biomass production (Schuster et al., 2008). The extension of this approach to multiple species builds on efforts to extend it to multiple compartments of higher eukaryotic organisms. There are three approaches to multi-species metabolic flux modeling, which we will refer to as environmentally coupled, directly linked and aggregated approaches. The environmentally coupled approach builds on the dynamic flux balance analysis (FBA) approach (Varma and Palsson, 1994), where the microbes and extracellular metabolites are represented using concentration state variables. The growth rate and metabolite fluxes are computed from FBA assuming a common pool for extracellular metabolites and that the system is in a steady state during each time step. The directly linked approach explicitly links the metabolic networks of the species using exchange reactions. This is conceptually the same way in which multi-compartment organisms are modeled. The aggregated approach (also referred to as pooled, supra-organism or enzyme soup approach) involves constructing one network by combining the individual networks and removing duplicates. This ignores cellular boundaries and is most applicable to metagenomic datasets. **Box 1** illustrates these three approaches for the hypothetical ecosystem shown in **Figure 1**. This approach has also been referred to as Ecosystems Biology (Klitgord and Segrè, 2011) or Community Systems Biology (Zengler and Palsson, 2012).

Examples

There have been several applications of metabolic flux models to communities of microbes. For recent reviews see Zengler and Palsson (2012), Biggs et al. (2015), Tan et al. (2015), Zomorodi

and Segrè (2016), Perez-Garcia et al. (2016), and Gottstein et al. (2016).

Environmentally coupled models

Scheibe et al. (2009) applied FBA to learn about the growth of *Geobacter* and uranium bioremediation in a contaminated groundwater site where *Geobacter* dominates the community. They coupled a genome-scale FBA model to a two-dimensional reactive transport model. The FBA model computes growth rate and fluxes based on ambient acetate, Fe(III) and ammonia concentrations in each grid element. Those growth rates and fluxes are then used by the reactive transport model to compute the *Geobacter* biomass, acetate, Fe(III) and ammonia concentrations, as well as other processes like U(VI) reduction. The new ambient concentrations are then again used by the FBA model to compute the growth rate and fluxes at the next time step and so on. Due to computational constraints, the FBA calculations were done *a priori* for 1,000 combinations of metabolite concentrations and stored in a look-up table, rather than a dynamic coupling between the models. One of the main advantages of the FBA-based approach is that it allows for variable substrate utilization and growth yields, which is not supported by conventional models. The model was able to make predictions of similar quality as the previous reactive transport model (i.e., without FBA component), but it did so without the need to calibrate rate parameters (**Figure 2**).

Tzamali et al. (2009) and Tzamali et al. (2011) used the dynamic FBA approach to simulate the interaction among various *E. coli* strains, including wild type and single gene knockouts. For various substrates, they identified potential communities of co-existing strains. For example, growth on pyruvate supported communities with up to 6 strains. The most efficient community of 4 mutants produced 2.2% more biomass than a pure culture of the wild type.

Zhuang et al. (2011) developed a dynamic, genome-scale FBA model of two species in competition in a uranium-contaminated aquifer. *Rhodospirillum rubrum* and *Geobacter* both oxidize acetate and reduce Fe(III), but only *Geobacter* can reduce U(VI), rendering it less soluble and therefore contributing to the clean-up of the site. The FBA models of the two species calculate growth and metabolite production/consumption rates, which are used to integrate biomass and metabolite concentration state variables. The model predicted that, under low-ammonia conditions, *Rhodospirillum rubrum* is outcompeted by *Geobacter*, which can fix nitrogen, and that this promotes respiration (vs. biomass production) and associated U(VI) reduction, which are patterns consistent with observations.

Zhuang et al. (2012) expanded the model by Zhuang et al. (2011) and applied it to design remediation scenarios. In particular, they used two separate FBA models for attached and planktonic *Geobacter* to differentiate their functions: planktonic cells reduce U(VI) and attached cells reduce Fe(III). Attachment and detachment rates were used to transfer biomass among these two fractions. This illustrates one approach by which heterogeneity can be simulated in these types of models.

Harcombe et al. (2014) developed dynamic FBA models of two and three species on a two-dimensional grid, where biomass

BOX 1 | From genes to ecosystems using metabolic flux modeling.*Single species*

The starting point for a metabolic flux model is a set of mass balance equations:

$$\frac{dx}{dt} = \mathbf{S} \cdot \mathbf{v} \quad (\text{B1.1})$$

where \mathbf{x} (mmol gDW⁻¹, i.e., per gram biomass dry weight) is a vector of metabolite concentrations, \mathbf{S} is the stoichiometric matrix and \mathbf{v} (mmol gDW⁻¹ h⁻¹) is a vector of reaction rates for uptake, excretion, internal metabolism and growth. Typically, a steady-state is assumed so the derivatives are zero. The stoichiometric matrix (\mathbf{S}) for species 1 of the hypothetical ecosystem is presented in **Table B1**, where columns are reactions and rows are metabolites. Lower and upper bounds for the reaction rates, determined based on thermodynamics, enzyme kinetics or measurements, can be included in the optimization procedure.

There are typically infinitely many solutions that satisfy the equation. For example, in species 1 (**Figure B1.1**), biomass (metabolite F) can be produced by any combination of two pathways (A → E → F or A → D → F). Computational methods are available that decompose the stoichiometric matrix into unique sets of functional units (pathways) such as elementary modes or extreme pathways (Papin et al., 2004). A more common approach, flux-balance analysis (FBA), involves optimizing reaction rates to maximize the value of some objective function using linear programming (LP). Several objective functions have been used, such as minimizing ATP production and maximizing production of some metabolite, but maximizing biomass production yield or rate is often considered to be the most appropriate in an ecological context. When biomass production is maximized, it is assumed that the cell regulates fluxes through its metabolic network in a way that maximizes biomass production. The corresponding objective function for the species 1 of our example system is to maximize the production of metabolite F ($V_{MetE1} + V_{PrdF1}$ or $V_{Growth1}$ in **Table B1**). This is relatively simple and real models typically use a more complex biomass growth function, e.g., a genome-scale model may include various precursors (e.g., G6P, F6P) and cofactors (e.g., ATP, NADH). Algorithms that integrate gene expression data are also available (Becker and Palsson, 2008). FBA is fundamentally a steady-state approach, but a pseudo-time-variable model can be constructed (Varma and Palsson, 1994; Mahadevan et al., 2002).

Multiple species—environmentally coupled models

Figure B1.1 illustrates the dynamic, multi-species metabolic flux modeling methodology. The model includes state variables for microbial biomass (X) and extracellular metabolites (C). The microbes grow according to a growth rate (μ) and consume/produce metabolites according to specific consumption/production rates (V). Those values are calculated from the metabolic flux models, which are optimized to maximize the growth yield subject to a number of constraints, including a maximum consumption rate for each metabolite based on its concentration. A simulation will proceed in a step-wise manner: (1) Calculate the constraints based on all C . (2) Optimize the metabolic model of each species, which yields μ and V . (3) Calculate the new X for both species based on μ . (4) Calculate the new C for both metabolites based on V from both species. Repeat. When the metabolic model does not lead to a viable solution, a simple death routine can be invoked (Zhuang et al., 2011). It is conceptually straightforward to include other reactions (e.g., between extracellular compounds) and transport (Scheibe et al., 2009).

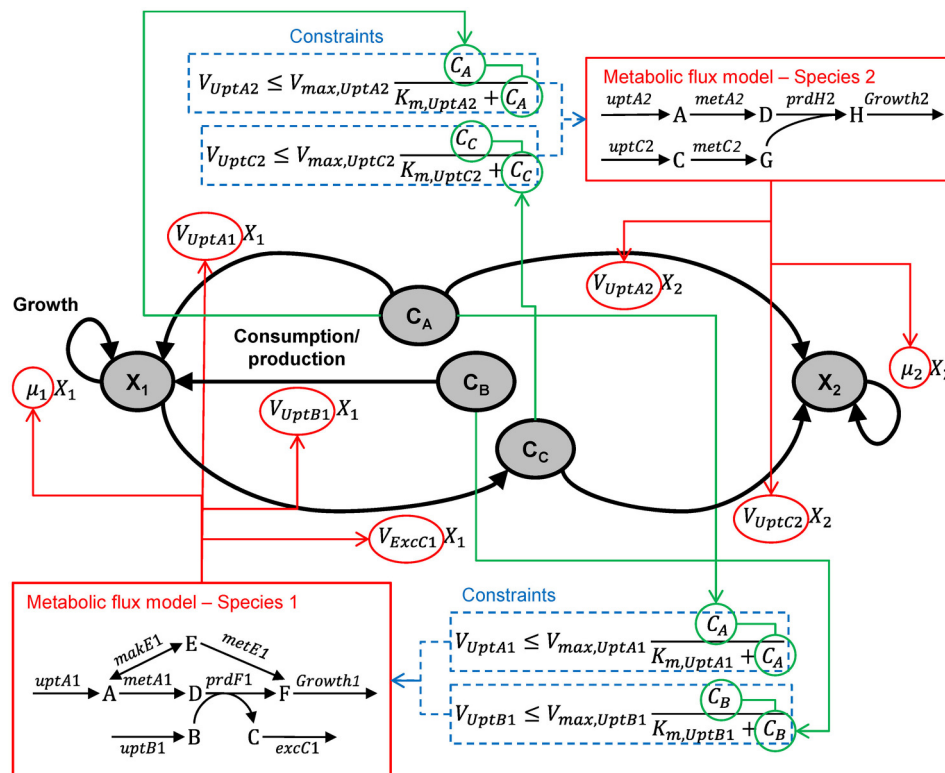


FIGURE B1.1 | Multi-species metabolic flux modeling—environmentally coupled models. After Figure 2 in Zhuang et al. (2011). X (gDW L⁻¹) = microbial biomass concentration, C (mmol L⁻¹) = extracellular metabolite concentrations, μ (h⁻¹) = specific growth rates, V (mmol gDW⁻¹ h⁻¹) = specific flux velocities.

(Continued)

BOX 1 | Continued*Multiple species—directly linked model*

Figure B1.2 illustrates the multi-species metabolic flux modeling approach developed by Stolýar et al. (2007). The metabolic models for each species (**Figure B1.1**) are combined into a single model. Exchange of metabolites among the species occurs by directly linking their reactions, which constrains them to be the same. This is equivalent to assuming there is no change in the extracellular metabolite concentrations. The model is optimized to maximize a weighted combination of the biomasses.

Multiple species—aggregated model

Figure B1.3 illustrates the multi-species metabolic flux modeling approach developed by Taffs et al. (2009). The reactions and metabolites for the two species (as shown in **Figure B1.1**) are merged into a single model and a single objective function is used to determine the flux distribution.

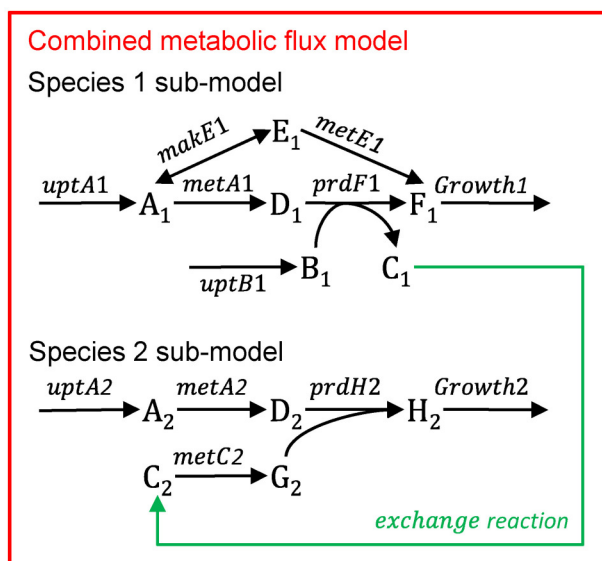


FIGURE B1.2 | Multi-species metabolic flux modeling—directly linked model. After Figure 2 in Stolýar et al. (2007). The metabolic models for each species (**Figure B1.1**) are combined into one model, with exchange reactions linking their metabolisms.

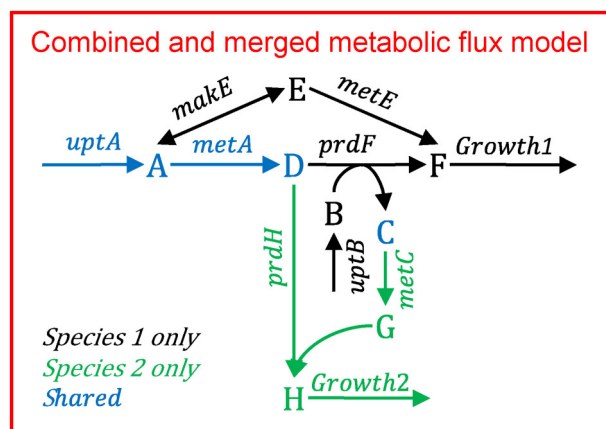


FIGURE B1.3 | Multi-species metabolic flux modeling—aggregated model. After Figure S2 in Taffs et al. (2009). The metabolic models for each species (as shown in **Figure B1.2**) are merged into one model.

(Continued)

BOX 1 | Continued

TABLE B1 | Stoichiometric Matrix (S) and lower and upper bounds for the FBA of species 1.

	V_{MetA1}	V_{MakE1}	V_{MetE1}	V_{PrdF1}	V_{UptA1}	V_{UptB1}	V_{ExcC1}	$V_{Growth1}$
A	-1	-1	0	0	1	0	0	0
B	0	0	0	-2	0	1	0	0
C	0	0	0	2	0	0	-1	0
D	1	0	0	-1	0	0	0	0
E	0	1	-1	0	0	0	0	0
F	0	0	1	1	0	0	0	-1
Lower	0	$-\infty$	0	0	0	0	0	0
Upper	∞	∞	∞	∞	MM*	MM*	∞	∞

Rows are metabolites and columns are reactions. *Calculated from extracellular substrate concentration using the Michaelis-Menten function (see Figure B1.1).

grows and dies, extracellular metabolites are consumed and produced, and biomass and metabolites move by diffusion. Cole et al. (2015) extended the dynamic FBA approach further to three dimensions and used it to simulate growth of *E. coli* in colonies on agar. The model was able to simulate the small-scale environmental heterogeneity in dissolved oxygen and nutrient concentrations, and the resulting phenotypic differentiation of the bacteria (i.e., fermenting cells in the interior). Other multi-species, environmentally coupled metabolic flux models were presented by Salimi et al. (2010), Hanly and Henson (2011), Hanly and Henson (2013), Biggs and Papin (2013), Chiu et al. (2014) and Louca and Doebeli (2015). Zomorodi et al. (2014) presented a dynamic version of the multi-level optimization routine presented previously (Zomorodi and Maranas, 2012, see below).

Directly linked models

Stolyar et al. (2007) developed an FBA model of two microbes that are mutualistic in the absence of sulfate, *Desulfovibrio vulgaris* and *Methanococcus maripaludis*. In the scenario evaluated, *D. vulgaris* grows on lactate, producing H_2 , formate, CO_2 and acetate, which support the growth of *M. maripaludis*. The model consists of three compartments, representing the metabolism of the two species and the exchange between them. The metabolite fluxes in the central metabolism of each species and exchange reactions are represented using 89 and 82 equations, respectively. The third compartment represents the exchange flux of H_2 , formate, CO_2 and acetate, where H_2 and formate were not allowed to accumulate in the medium, so that their rates of production by *D. vulgaris* and consumption by *M. maripaludis* are the same. The combined model was optimized to maximize biomass production of both species, with a larger weight for *D. vulgaris*, based on observations. However, the biomass ratio of the two species is constrained by the exchange reaction, so it was relatively invariant to the weights used. The model suggested that the H_2 was essential, but that formate could be eliminated.

Wintermute and Silver (2010) applied the FBA modeling approach at the genome scale to 46 *E. coli* mutants, each incapable

to synthesize an essential metabolite. Growth experiments were conducted with 1,035 binary strain combinations. A joint FBA of each pair allowing for exchange of all shared metabolites between the strains was developed. The models were optimized to minimize the difference between the flux distributions of the wildtype and mutant (minimization of metabolic adjustment, MOMA, Segrè et al., 2002). The idea behind this objective function is that the regulatory system is still based on the wildtype and has not yet adjusted to the mutation. The joint FBA models were consistent with the finding that pairings of mutants blocked in the same biosynthetic pathway rarely show synergistic growth (4% of the cases) while pairings of mutants in separate pathways did so in 18% of cases. The model correctly predicted that strains grow best when they require small amounts of metabolites that are cheap to produce by the other strain. The ability of simple stoichiometric models to predict fitness costs and benefits of metabolic cross-feeding is encouraging.

Klitgord and Segrè (2010) applied the FBA modeling approach to binary pairs of seven species and identified the media composition that would support symbiosis. They developed genome-scale FBA models of all possible binary pairs and did a systematic search for media compositions that would support growth of the pair but not the individual species.

Huthmacher et al. (2010) generated an FBA model of the metabolism of the malaria causing *Plasmodium falciparum* and its host, the erythrocyte (red blood cell). By constraining the metabolic network with gene expression data of *P. falciparum*, they were able to predict metabolic fluxes for different life cycle stages of the pathogen.

Zomorodi and Maranas (2012) developed a community FBA modeling framework and applied it to a number of systems, including those of Stolyar et al. (2007) and Taffs et al. (2009). A novel aspect in this work is the consideration of multiple objective functions, including maximization of growth of each species as well as biomass production at the community level, which can be used to explore tradeoffs between selfish and altruistic driving forces.

Other multi-species, directly linked metabolic flux models were produced by Taffs et al. (2009), Bizukojc et al. (2010),

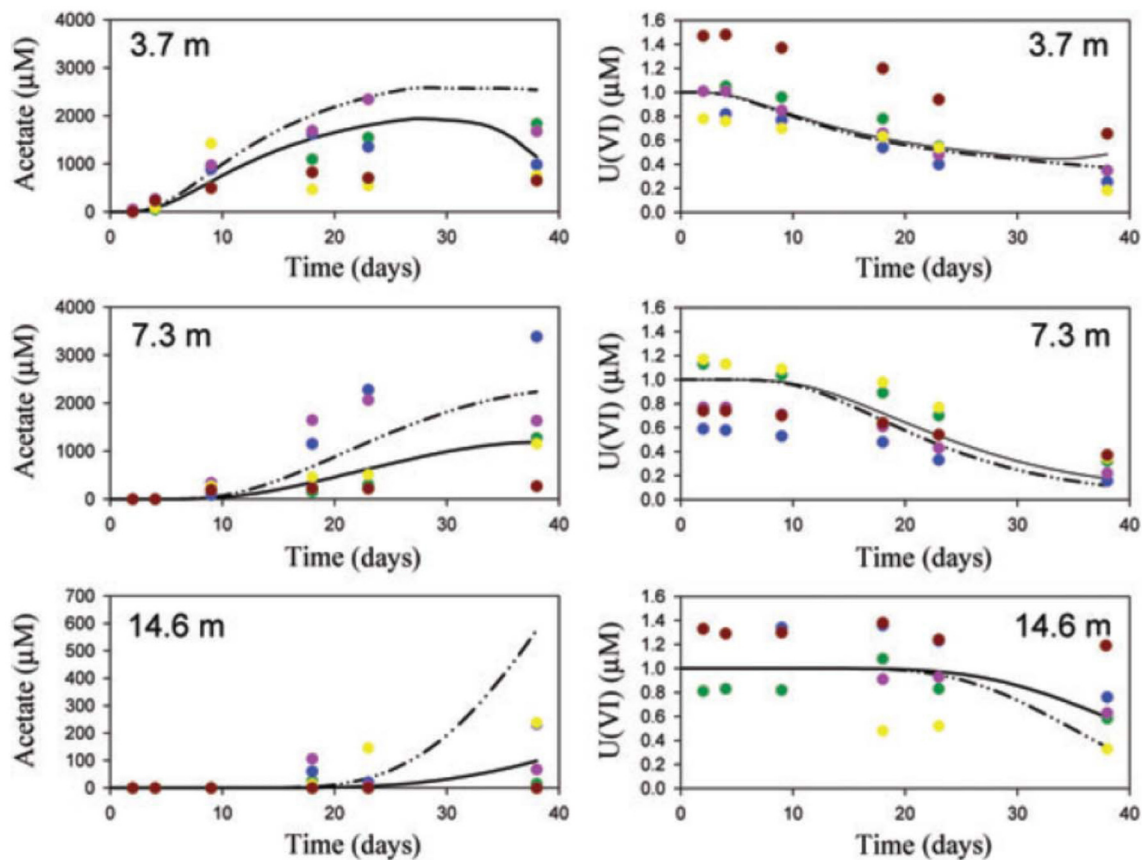


FIGURE 2 | Comparison of observations (symbols), traditional model (solid lines) and FBA-based model (dashed lines). Reproduced from Scheibe et al. (2009) with permission. The figure shows acetate and U(VI) concentrations at a groundwater bioremediation site. Concentration time series are presented at 3.7, 7.3, and 14.6 m distance from the acetate injection gallery. Acetate increases at progressively later times as the distance from the injection gallery increases. Consistent with this, U(VI) decreases at progressively later times. Colors identify single wells.

Bordbar et al. (2010), Freilich et al. (2011), Khandelwal et al. (2013), Nagarajan et al. (2013), Shoaie et al. (2013), Ye et al. (2014), El-Semman et al. (2014), Merino et al. (2015) and Heinken and Thiele (2015).

Aggregated models

Taffs et al. (2009) applied different approaches to model three species (oxygenic phototrophs, filamentous anoxygenic phototrophs and sulfate-reducing bacteria) in the thermophilic, phototrophic mat communities from Octopus and Mushroom Springs in Yellowstone National Park (USA). One of their approaches does not consider compartments, but lumps all reactions into one species (see **Box 1**). This approach ignores compartmentalization and the fact that intermediate intracellular metabolites from one species may not be available to another. However, it does not require assigning individual enzymes or reactions to species, functional groups or guilds and is well suited for data from metagenomics. A unique aspect of this study is the use of elementary mode analysis (EMA), which is an alternative to FBA and characterizes the set of all possible flux distributions, rather than just the optimal one.

Tobalina et al. (2015) applied the aggregated approach to naphthalene-contaminated soil communities. An interesting aspect of that study was that the model was based on metaproteomics data, which implicitly accounts for regulation.

Cerqueda-García and Falcón (2016) applied the aggregated approach to study the metabolism of communities in microbial mats and microbialites (living carbonate rock structures similar to corals and stromatolites). Starting with metagenomic datasets, they reconstructed a metabolic network, and then used EMA to identify feasible pathways through this network for C and N assimilation. They identified a number of alternative CO_2 fixation pathways, which were not identified for these systems previously.

Strengths

- The FBA approach can directly utilize molecular data, genomics, transcriptomics, proteomics and metabolomics, from pure laboratory cultures and the environment (e.g., metagenomics) as long as annotations are available, which is increasingly the case.
- The approach is comprehensive in terms of functions and metabolites. This is likely to be increasingly useful, as

recent observations from a number of environments suggest that bacteria have a high substrate specificity (Kindaichi et al., 2013; Salcher et al., 2013). For example, when a freshwater community was presented with 14 radiolabeled low-molecular weight (LMW) organic substrates, the two most abundant microbes belonging to the *Actinobacteria* ac1 and *Alphaproteobacteria* LD12 tribes had no overlap in their substrate acquisition spectra. The concept of dissolved organic carbon (DOC) as a common currency for heterotrophic microbes is too simplistic. One of the main applications of FBA has been to understand complex substrate uptake patterns.

Weaknesses

- The directly linked and aggregated approaches assume the system to be in a steady-state. The environmentally coupled approach also assumes steady-state flux distributions during each time step, but flux distributions can change from time to time. For many cases this assumption will be sensible, but for others not. For example, planktonic bacteria experience a very heterogeneous nutrient regime and may experience nutrient patches with short durations (~60 s, Taylor and Stocker, 2012), comparable to the time required for gene expression, protein translation and maturation. Genome-scale models are being developed that go beyond steady-state metabolite fluxes (e.g., include dynamic transcript, protein and metabolite pools, Karr et al., 2012) and this technology will eventually be applied at the ecosystem scale.
- It is not always clear what objective function should be used to optimize the flux distribution (Schuster et al., 2008). Maximization of biomass production seems like a good choice from a biotechnological perspective. However, there are cases where it is advantageous to divert production away from biomass, including to storage products, toxins or EPS (Merino et al., 2015), which may conflict with the biomass objective. Moreover, in a well-mixed, stable environment, specific growth rate will likely be maximized by natural selection while in a spatially structured environment such as a biofilm, the biomass yield is likely to be maximized by natural selection (Kreft, 2004).
- The approach typically entails specifying a biomass composition, and commonly this is applied across different conditions. However, the biomass composition is known to change (Benyamini et al., 2010).
- Growth dilution of metabolites, other than the ones used in the growth equation (see above), is typically ignored (Benyamini et al., 2010). Specifically, there should be a “ $-\mu x$ ” on the right-hand side of Equation B1.1. Accounting for growth dilution is conceptually straightforward but it requires specifying the metabolite concentrations, which are not typically available at the genome scale. Metabolomics data can help to fill this gap, but this would be difficult for all metabolites, times and locations in the model and impossible for prediction simulations. Another hurdle is the computational cost. The metabolite dilution FBA (MD-FBA) model of Benyamini et al. (2010) uses mixed-integer linear programming (MILP, vs. LP used by FBA), which is computationally more demanding than LP. This limitation may be especially important for

applications that require solutions for multiple species, times and locations.

- The approach does not account for individual heterogeneity (see Part 2).

Gene-Centric Modeling

Definition

In the gene-centric or functional gene approach, the model is built based on genetic information, as in metabolic flux modeling, but focused on capturing the dynamic behavior of specific genes or gene activities in the system. Thus, the biogeochemical fluxes are based on the genetic composition of the microbial community. Microbes are grouped based on specific functional or proxy genes and tracked using corresponding concentration state variables. This is similar in spirit to modeling functional groups (e.g., N-fixers, lactate producers, Le Quéré et al., 2005; Kettle et al., 2015). The concentrations of genes (e.g., number of gene copies per liter) are simulated using mass balance differential equations, which is how typical microbial ecology models simulate species. The rate of gene production (or growth) can be tied to the Gibbs free energy released by the reaction catalyzed by the corresponding enzyme. The approach is illustrated in **Box 2**.

Examples

Reed et al. (2014) presented the gene-centric approach and applied it to study nitrogen cycling in the Arabian Sea oxygen minimum zone (OMZ). The model includes eight functional genes, including those for denitrification (nitrate reductase, *narG*, nitrite reductase, *nirK*), aerobic ammonia oxidation (ammonia monooxygenase, *amoA*) and anaerobic ammonium oxidation (anammox, hydrazine oxidoreductase, *hzo*), as well as relevant metabolites, including dissolved oxygen (O_2), ammonium (NH_4^+), nitrate (NO_3^-), and nitrite (NO_2^-). The model-predicted gene abundances were compared directly to observations from qPCR (gene copies L^{-1} , **Figure 3**). The authors also compared model-predicted changes in gene abundances over time to observed mRNA concentrations in a qualitative manner (gene copies $L^{-1} s^{-1}$ vs. mRNA copies L^{-1} , **Figure 3**). An interesting problem addressed by this model is the dual role of nitrogen as an energy source and biomass component, where the latter is not considered by the gene-centric approach. This was handled by calculating the total biomass increase/decrease and removing/adding corresponding amounts of N from/to the extracellular metabolite pools. The model was used to show that denitrification is the dominant nitrogen loss process in this area, which is different from many other OMZs, where anammox dominates.

Reed et al. (2015) applied the gene-centric approach to simulate functional genes for sulfur, nitrite, ammonia, methane and hydrogen oxidation and associated metabolites in a submarine hydrothermal vent plume. The pathways for oxidation of a number of reduced sulfur species (e.g., hydrogen sulfide, thiosulphate) co-occur in one species (SUP05), so the pathways were combined into one functional gene in the model. The authors compared their model-predicted relative abundance (%) of functional genes to observations. The hydrogen concentration

BOX 2 | From genes to ecosystems using gene centric modeling.

The following description is based on Reed et al. (2014), but adapted to the hypothetical ecosystem considered here and some of the nomenclature is altered to facilitate comparison with the other approaches. The first step in the development of the model is to identify the functional genes. For the hypothetical example, we will use *prdF* and *metC* and ignore the others (**Figure B2**). Thus, state variables $prdF_g$ and $metC_g$ (no. L^{-1}) represent species 1 and 2, respectively. The reactions mediated by these gene products are assumed to be the limiting reactions along the pathway, but exchange with extracellular metabolites requires accounting for the input and output of the entire pathway. For *prdF*, the overall reaction is:



The production rate of *metC* genes as a result of metabolism associated with the *metC* gene (R_{metC} , no. $L^{-1} d^{-1}$) is:

$$R_{metC} = metC_g F_{T,metC} \mu_{max,metC} \frac{C_C}{K_{m,metC,C} + C_C} \quad (B2.2)$$

$metC_g$ (no. L^{-1}) is the *metC* gene concentration. $F_{T,metC}$ is a thermodynamic potential factor, which accounts for the chemical energy available to drive the metabolism, and can be estimated from the energy yield of the associated reaction. $\mu_{max,metC}$ (d^{-1}) is the maximum specific growth rate. C_C (molC L^{-1}) and $K_{m,metC,C}$ (molC L^{-1}) are the extracellular concentration and half-saturation constant for metabolite C. The production rate of *prdF* genes (R_{prdF}) is:

$$R_{prdF} = prdF_g F_{T,prdF} \mu_{max,prdF} \frac{C_A}{K_{m,prdF,A} + C_A} \frac{C_B}{K_{m,prdF,B} + C_B} \frac{K_{i,prdF,C}}{K_{i,prdF,C} + C_C} \quad (B2.3)$$

The last fraction accounts for inhibition by metabolite C. The mass balance equation for extracellular metabolite B is (transport and other reactions are omitted for clarity):

$$\frac{dC_B}{dt} = -\frac{\gamma_{prdF,B}}{\gamma_{prdF,A}} \frac{R_{prdF}}{q_{prdF} Y_{prdF}} \quad (B2.4)$$

$\gamma_{prdF,B}$ and $\gamma_{prdF,A}$ are stoichiometric coefficients. Here, 2 mol B are consumed for every 1 mol A, so $\gamma_{prdF,B} = 2$ and $\gamma_{prdF,A} = 1$. q_{prdF} (no. gDW $^{-1}$, i.e., per gram biomass dry weight) is the intracellular concentration of *prdF* genes, which depends on the number of gene copies in the genome. Y_{prdF} (gDW molA $^{-1}$) is the yield, which depends on the energy yield of the associated reaction. For metabolite A, we have to consider consumption by both species:

$$\frac{dC_A}{dt} = -\frac{R_{prdF}}{q_{prdF} Y_{prdF}} - \frac{\gamma_{metC,A}}{\gamma_{metC,C}} \frac{R_{metC}}{q_{metC} Y_{metC}} \quad (B2.5)$$

Here, A and C are consumed in equal amounts, so $\gamma_{metC,A} = \gamma_{metC,C} = 1$. Metabolite C is consumed by the reaction associated with *metC* and produced by the reaction associated with *prdF*:

$$\frac{dC_C}{dt} = -\frac{R_{metC}}{q_{metC} Y_{metC}} + \frac{\gamma_{prdF,C}}{\gamma_{prdF,A}} \frac{R_{prdF}}{q_{prdF} Y_{prdF}} \quad (B2.6)$$

Here, 2 mol C are produced for every 1 mol A consumed, so $\gamma_{prdF,C} = 2$ and $\gamma_{prdF,A} = 1$. The mass balance for gene *prdF* is:

$$\frac{dprdF_g}{dt} = R_{prdF} - k_d prdF_g \quad (B2.7)$$

where k_d (d^{-1}) is the death rate. The first term in the gene mass balance equation accounts for the production of the gene due to the growth associated with its reaction and the second term accounts for mortality.

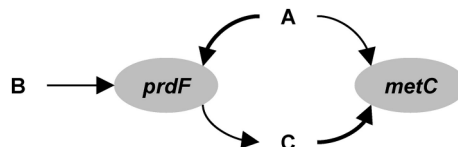


FIGURE B2 | Gene centric modeling.

is relatively low in this system and their model predicted no significant increase in hydrogenase gene abundance due to aerobic hydrogen oxidation. However, substantial quantities of hydrogenase genes were observed suggesting that they may be produced because they co-occur with a gene that does experience substantial growth as observed (SUP05 may have genes for sulfur

and hydrogen oxidation, Anantharaman et al., 2013). When this coupling is included in the model, it was able to reproduce the observations.

Louca et al. (2016) presented a gene-centric model of six functional genes and eight metabolites for a number of dissimilatory redox pathways involved in nitrogen and sulfur

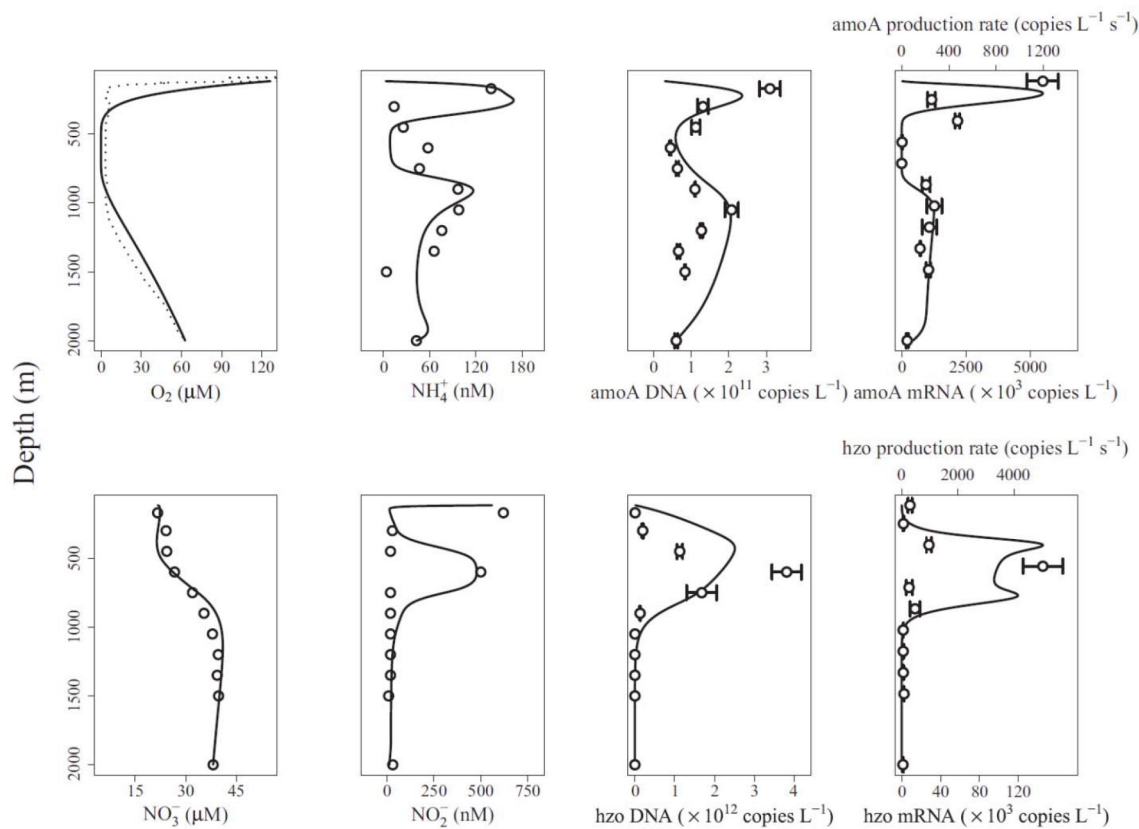


FIGURE 3 | Comparison of gene-centric model predictions (solid lines) to observations (dotted line in top left and symbols in other panels) of metabolites, gene and mRNA levels in the Arabian Sea oxygen minimum zone. From Reed et al. (2014). Copyright © (2014) by the National Academy of Sciences. The figure shows an oxygen low from about 400 to 900 m and a coincident low in ammonia monooxygenase (*amoA*) DNA and mRNA, and an increase in anaerobic ammonium oxidation (anammox, hydrazine oxidoreductase, *hzo*) DNA and mRNA.

cycling in a seasonally anoxic fjord (Saanich Inlet, Vancouver Island, Canada). That model extends the gene-centric modeling approach by explicitly simulating mRNA and proteins, assuming their production rates are proportional to the corresponding reaction rates and subjecting them to transport and decay processes. Model predictions for mRNA and proteins were compared to observations on a qualitative basis. The model was used to gain insights into the sulfur and nitrogen pathways in this system. For example, the model predicted incomplete denitrification by the SUP05 clade, which results in leakage of nitrite that supports anammox and loss of nitrogen.

Strengths

- The approach is readily integrated into existing models based on concentration state variables (Reed et al., 2014).
- The approach makes quantitative predictions of gene levels that can be compared directly to observations.

Weaknesses

- While this modeling approach is readily applied to chemotrophs where there is a direct link between the

rate of the reaction and the growth rate of the microbe, it is less clear how to apply it to a phytoplankton species that may be limited by nitrate, but uses the energy derived from sunlight to reduce it to ammonia for incorporation into amino acids. Heterotrophs growing on a complex mixture of dissolved organic matter (DOM) may also be difficult to model with this approach.

- The extension of the method to mRNA and proteins (Louca et al., 2016) includes simulating them as independent concentration variables. This does not account for their natural co-existence in the cell and may lead to some odd effects, like mRNA and protein appearing in locations where there are no corresponding genes.
- The method supports multiple co-occurring genes (see Reed et al., 2014 for equations), but that is based on constant fractions within a community, which may change dynamically and spatially in a natural community (e.g., species succession in phytoplankton). This method is also more difficult to implement. The reader is invited to rework the example in **Box 2** for a model that uses *metA* and *metC* (which co-occur in species 1) as functional genes.

- The approach does not account for individual heterogeneity (see Part 2).

Agent-Based Modeling (ABM)

Definition

ABM or individual-based modeling (IBM) involves simulating microbes as individuals. This is in contrast to the traditional population-level approach, where microbes are simulated as concentration state variables. ABM is already an established modeling technology in microbial ecology (Hellweger et al., 2016a). Microbial ABMs increasingly resolve intracellular mechanisms and the extension to genes is a natural progression and already well on the way. The approach is illustrated in **Box 3**. This approach has also been referred to as Systems BioEcology (Hellweger, 2009).

Examples

ABM was used by Hellweger (2009) to explore the role of photosynthesis genes (*psbA*, *hli*) carried by viruses that infect the marine cyanobacterium *Prochlorococcus*. The idea is that these genes help to maintain the host photosynthesis apparatus during the latent period, increasing energy to support the replication of the virus. The model simulates individual viruses and host cells and explicitly resolves mechanisms of gene expression, protein synthesis, photosynthesis and events associated with infection at the molecular level. The model was calibrated to observations of virus and host gene transcript and protein levels and then used to simulate population dynamics in the water column of the Sargasso Sea. Modeled populations were diverse, including multiple virus types (different combinations of *psbA* and *hli* copies) and cells with different light histories, cell cycle phases and infection stages. Using competition experiments between virus strains that have different combinations of *psbA* and *hli*, and evolution experiments (i.e., gene packaging error), the model predicted an optimal gene content that matched that of the wild-type.

An ABM of the cyanobacterium *Synechococcus* and its circadian clock was constructed by Hellweger (2010). The model structure is similar to the *Prochlorococcus* model described above. A new feature was the explicit simulation of the concentration of proteins with different phosphorylation states and their interaction. The modeled population includes cells at different phases in their cell and circadian cycles and gene expression levels (*psbAI* luminescence) were compared to observations at the individual level.

Mina et al. (2013) used an ABM of genetically-engineered quorum sensing *E. coli* cells in a three-dimensional microfluidics chamber. The model simulates a heterogeneous population of individual, motile cells, each with a number of genes (*luxI*, *aiiA*, and *yemGFP*) and associated proteins, which communicate via a diffusible substance. They showed that autoinducer oscillations on the population level do not follow simply from synchronizing single cell oscillations. Single cells can switch between a state of constant signal concentration and oscillations, depending on the parameters of the positive and negative feedback loops in the gene regulatory network. Yet in a population of these cells, only the oscillatory state is stable—once cell density exceeds a threshold.

Hellweger et al. (2014) built an ABM of the yeast *Saccharomyces cerevisiae* and used it to explore the fitness effect of age-correlated stress resistance. The model explicitly simulates the regulation of the proteins Tsl1 and Tps3, which synthesize the stress protectant trehalose. Their expression is modeled using constant, age-dependent and stochastic terms. The population is diverse consisting of cells in different phases of their cell cycles as well as different ages, damage and Tsl1/Tsl3 expression levels. The modeled heterogeneity was compared to observations obtained using flow cytometry. Comparison of the various expression strategies showed that age-correlated stress resistance can be beneficial under some conditions.

A model of *Anabaena*—nitrogen interactions was developed by Hellweger et al. (2016b). This model simulates the uptake of various forms of nitrogen and early intracellular assimilation pathways. Uptake and intracellular reactions are mediated by enzymes (e.g., GlnA) and their expression is controlled by a number of regulatory proteins (e.g., NtcA). A novel feature of this model is the explicit simulation of cell differentiation and division of labor. When fixed nitrogen is depleted, the cells become nitrogen-stressed and some differentiate into heterocysts, which are anoxic cells that fix nitrogen and pass the fixed nitrogen to their neighboring vegetative cells (**Figure 4C**). The model was informed by observations from 269 laboratory experiments from 55 papers published from 1942 to 2014, including transcript levels and enzyme activities (**Figures 4A,B**). Hellweger et al. (2016b) also applied the model to a hypothetical lake, but validation by comparison to field observations was not performed.

Another gene-level ABM was developed by Hellweger (2013) to explore the mechanisms underlying adaptation of *E. coli* to tetracycline resistance.

Strengths

- The main advantage of ABM is the ability to resolve intra-population heterogeneity. We will discuss the importance of individuality in the second part of this review.
- In ABM, the description of the system is very flexible and not constrained by having to use one specific mathematical formalism (e.g., the stoichiometric matrix of the FBA approach). For example, on/off control of a gene by light can be modeled simply using an “if” statement (if light is on, then turn on gene, otherwise turn it off). It is much more difficult to incorporate this into a stoichiometric matrix or differential mass balance equation.

Weaknesses

- This approach is relatively complex and difficult to apply. Although it can theoretically be extended to the whole-genome scale, past models have focused on a handful of genes, transcripts, proteins and metabolites. This is due to the limited availability of rate formulations and parameters, and the difficulty of calibrating a model with numerous non-linear feedbacks.

Summary of Examples

The models reviewed above are characterized along six different dimensions, including space, time, function, heterogeneity,

BOX 3 | From genes to ecosystems using agent-based modeling.

Here the approach for dynamic, molecular-level, mechanistic modeling is illustrated by application to the hypothetical ecosystem (**Figure 1**). The model explicitly resolves genes, transcripts, proteins and metabolites (**Figure B3**). Following the central dogma of biology, genes are transcribed by the RNA polymerase to yield transcripts (mRNA), which are translated by the ribosomes to yield proteins, which then carry out various functions. Once a biomass (in the case of strain 1 the metabolite E, Q_E) threshold is reached, the DNA polymerase is induced, which synthesizes DNA. Once that is complete, cell division is induced and the cell divides, which involves division of all intracellular components. The approach entails explicitly modeling genes, transcripts and proteins. However, typically only a handful of representative genes are simulated using a coarse-grained approach (Castellanos et al., 2004; Hellweger, 2013).

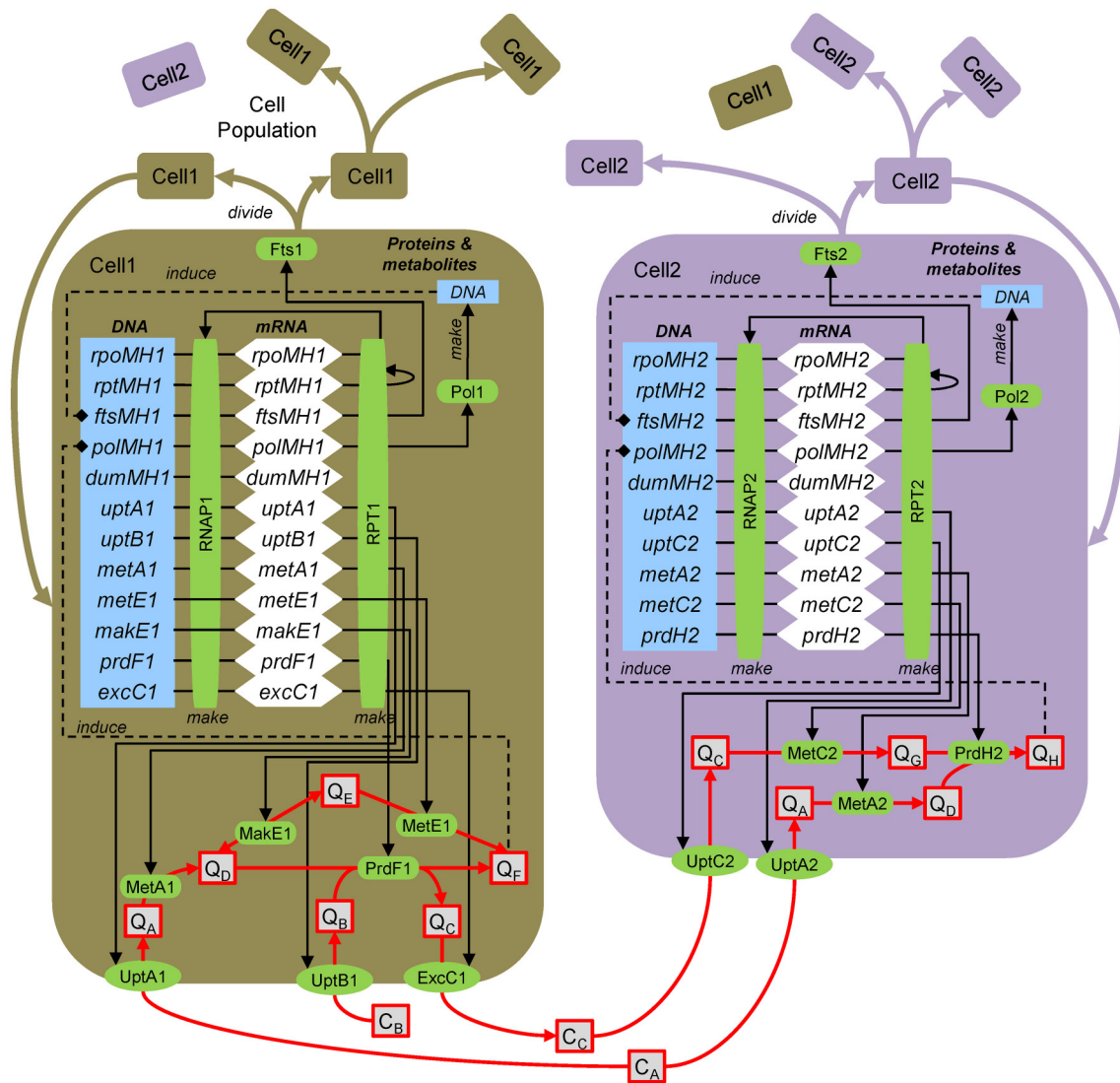


FIGURE B3 | Agent-based modeling of microbes. Gene/protein: *rpoMH*/RNAP, RNA polymerase; *rptMH*/RPT, ribosome; *ftsMH*/Fts, cell division; *polMH*/Pol, DNA polymerase; *dumMH*, dummy (accounts for genes not explicitly considered); *uptA*/UptA, uptake A; *metA*/MetA, metabolism A; *excC*/ExcC, excretion C. Substrates and metabolites (extracellular, concentration C; intracellular, quota Q): C_A , substrate A; Q_H , metabolite H, etc. After Figure 1 of Hellweger (2009).

To illustrate the approach, we present the equations for *uptB1* transcription, UptB1 synthesis, UptB1 rate and Q_B mass balance. Here, intracellular concentrations are defined on a per biomass dry weight (DW) basis, but carbon and volume can also be used. The *uptB1* transcript ($uptB1_t$, mol mRNA gDW⁻¹, i.e., per gram biomass dry weight) mass balance equation is:

$$\frac{duptB1_t}{dt} = \frac{k_{s,T}}{L_{DNA}} RNAP1 \gamma_{uptB1} uptB1_g - k_{d,T} uptB1_t - \mu_g uptB1_t \quad (B3.1)$$

(Continued)

BOX 3 | Continued

where $k_{S,T}$ (bp RNAP⁻¹ s⁻¹) is the transcription rate, L_{DNA} (bp) is the total DNA length, $RNAP1$ (mol protein gDW⁻¹) is the RNA polymerase level, y_{uptB1} is the *uptB1* expression level (may depend on various factors), $uptB1_g$ is the number of *uptB1* gene copies, $k_{d,T}$ (s⁻¹) is the mRNA decay rate and μ_g (s⁻¹) is the specific growth rate. The UptB1 (mol gDW⁻¹) protein mass balance is:

$$\frac{dUptB1}{dt} = k_{S,P} \frac{uptB1_t}{TxL} RPT1 - k_{d,P,UptB1} UptB1 - \mu_G UptB1 \quad (B3.2)$$

where $k_{S,P}$ (nt RPT⁻¹ s⁻¹) is the translation rate, TxL (mol mRNA gDW⁻¹) is the total mRNA, $RPT1$ (nmol protein gDW⁻¹) is the ribosome level and $k_{d,P,UptB1}$ (s⁻¹) is the UptB1 decay rate. The UptB1 rate (V_{UptB1} , mol gDW⁻¹ s⁻¹) is:

$$V_{UptB1} = UptB1 \frac{k_{UptB1} C_B}{K_{m,UptB1} + C_B} \frac{K_{i,UptB1}}{K_{i,UptB1} + Q_B} \quad (B3.3)$$

where k_{UptB1} (molB molUptB1⁻¹ s⁻¹) is the UptB1 catalytic rate constant, $K_{m,UptB1}$ (molB L⁻¹) is the half-saturation constant and $K_{i,UptB1}$ (molB gDW⁻¹) is the inhibition constant. The intracellular metabolite B (Q_B , mol gDW⁻¹) mass balance is:

$$\frac{dQ_B}{dt} = V_{UptB1} - 2 V_{SynF1} - \mu_G Q_B \quad (B3.4)$$

where V_{PrdF1} (molF gDW⁻¹ s⁻¹) is the PrdF1 reaction rate (the factor 2 accounts for 2 mol B per 1 mol F, see **Figure 1**).

species diversity, and genes (**Figure 5**). These dimensions were selected as they highlight differences between the reviewed models, nevertheless, the list is not exhaustive and other dimensions can be used, like types of interactions. The figure illustrates that, together, the population of past models covers the entire space. However, no single model or approach has covered the entire space by itself. The gene centric approach is amenable to space, time and species diversity and those dimensions have been explored in past models. Function and genes dimensions are linked in this approach, and limited because each species is typically associated with only one function. Simulating individual heterogeneity is difficult with the population-level gene centric approach and has not been explored in past models. Metabolic flux models are routinely genome-scale, and past models have pushed the boundaries along other dimensions, including space, time (although only quasi-time-variable), and species diversity. Function is often limited to metabolism and heterogeneity to phenotypes. The agent-based approach is flexible along most dimensions, but limited in terms of gene coverage and models with more than a handful of genes have yet to be developed.

PART 2: THE IMPORTANCE OF INDIVIDUALITY

A key distinction between the modeling approaches reviewed above is their consideration of individuality and heterogeneity. It is now well established that microbial populations in the environment and laboratory exhibit substantial heterogeneity in properties and behaviors. There are probably cases where this individuality averages out and is of no consequence to the ecology or biogeochemistry of the system (e.g., steady-state growth of a single species on a single nutrient). However, there are also cases where individuality has been shown to critically affect the fitness of a population. A thorough understanding of individual

heterogeneity and its potential ecological consequences is critical for selecting the most appropriate modeling strategy.

In this part, we review the importance of individuality. There are a number of mechanisms that produce heterogeneity in a population, which we refer to as sources. Once heterogeneity is introduced, it can be maintained and amplified in a number of ways. Finally, there are a number of important ecological consequences of heterogeneity (**Figure 6**).

From a modeling perspective, the distinction of sources, amplifiers and consequences is important. Specifically, sources of heterogeneity are included in the design of the model. In other words, there are equations or parts of the model code that produce heterogeneity. For example, stochastic cell division asymmetry can be included in an agent-based model by randomly varying the daughter biomass from the perfect 50/50 split after division. Amplifiers are mechanisms that operate at the individual level and change the cell's properties. The resulting additional heterogeneity is not prescribed in the model design, but it emerges from running it (i.e., it is a model output). For example, heterogeneity in birth sizes may lead to heterogeneity in generation times without any added equation or code. Consequences are also not included in the design of a model, but they emerge as population- or ecosystem-level properties rather than individual-level properties.

Sources of Individuality

There are many mechanisms that can produce and maintain individual heterogeneity. Here we consider a mechanism that would lead a colony growing up from a single cell to become heterogeneous to be a “source of heterogeneity.” Of course these mechanisms can also operate and produce/modify heterogeneity in other scenarios.

Stochastic Interactions of Molecules

Intracellular “concentrations” of transcription factors and macromolecules (DNA, mRNA, proteins) are often low. For

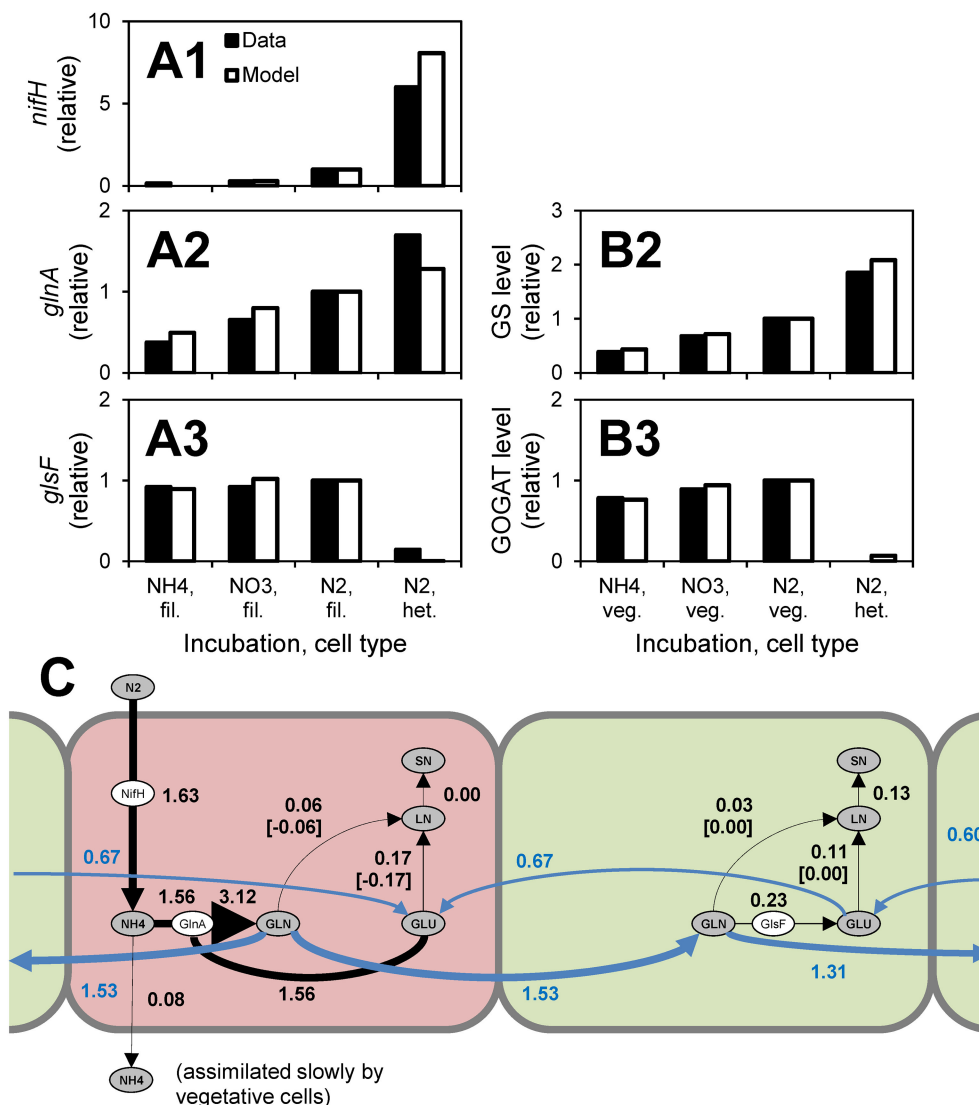
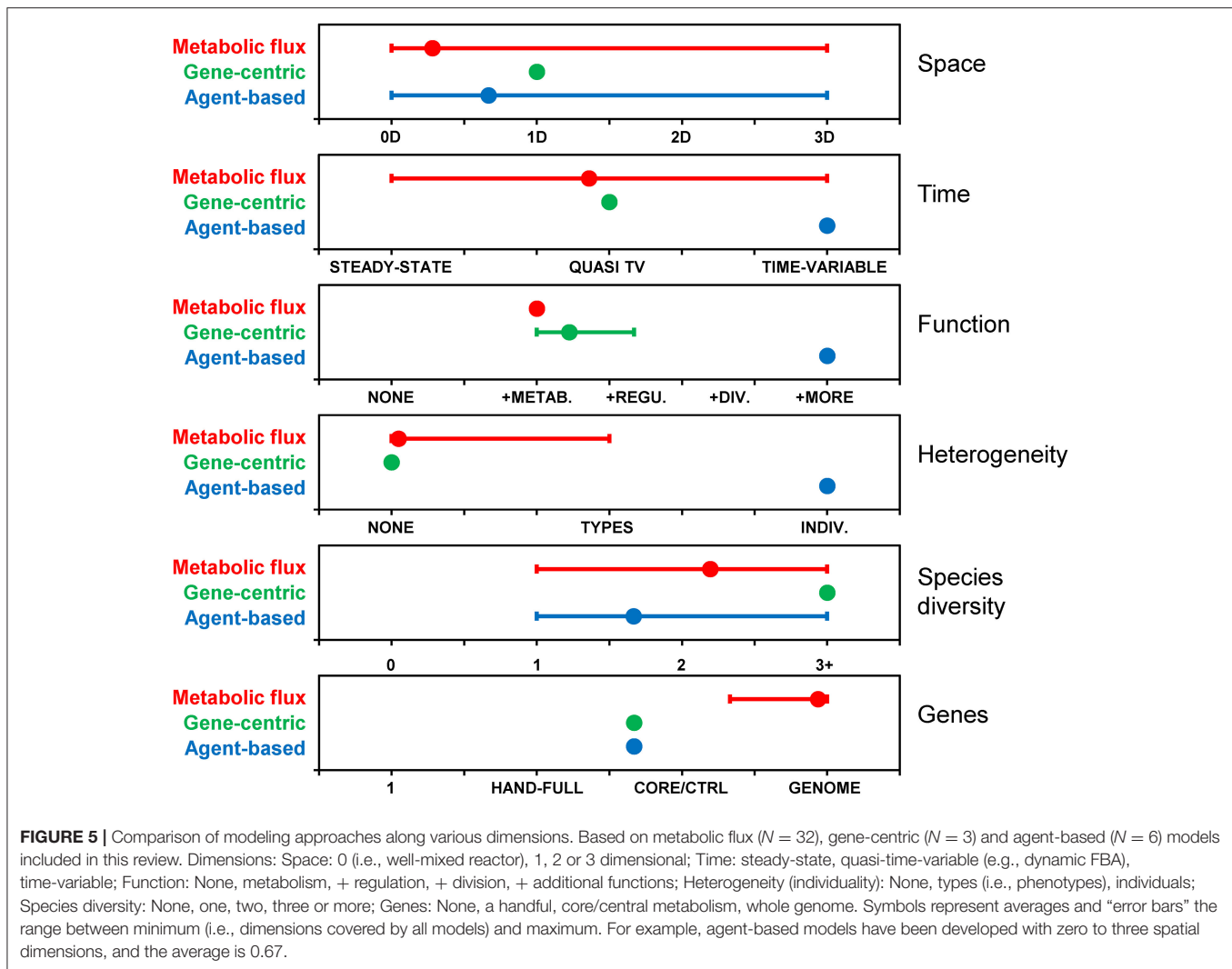


FIGURE 4 | *Anabaena*—nitrogen interaction model. (A,B) Comparison to observations of transcript levels in filaments (fil., i.e., all cells), vegetative cells (veg.) and heterocysts (het.) (A) and enzyme activities (B) of cells grown under different conditions (data are from Martin-Figueroa et al., 2000). (C) N fluxes for growth on N₂. Red, heterocysts; Green, vegetative cells. Numbers are fluxes in pmol N cell⁻¹ d⁻¹. From Hellweger et al. (2016b). The figure shows that heterocysts have higher levels of nitrogenase (*nifH*) transcripts, higher levels of glutamine synthetase (*glnA*, GS) transcripts and enzyme levels and lower levels of glutamate synthase (*glsF*, GOGAT) transcripts and enzyme activities. These observations support the model where N₂ is fixed in heterocysts and combined with glutamate (GLU) that is imported from adjacent vegetative cells to yield glutamine (GLN), which is then exported to vegetative cells and further incorporated into labile nitrogen (LN) and structural nitrogen (SN) pools.

example, natural populations have on average less than one transcript per gene (Cottrell and Kirchman, 2016). That means the continuum assumption underlying deterministic chemical reaction kinetics is not met and corresponding regulatory or signaling networks can exhibit substantial stochasticity. This leads to intra-population heterogeneity and when coupled with positive feedbacks can lead to bi-stability and phenotypic differentiation (Veening et al., 2008). For example, the expression level of heterodisulfide reductase subunit A (central for respiration in sulfate reducers) in *Desulfovibrio vulgaris* cells varied by as much as 50-fold in a sample of 30 individual cells (Qi et al., 2014). Another example is stochasticity in the

chemotaxis regulatory network. Low concentrations of signaling molecules, specifically phosphorylated CheY, lead to behavioral variability of individuals, and this can be reduced by increasing the concentration of this element in the network (Korobkova et al., 2004). However, stochastic gene expression may be more the exception than the rule as the expression of most genes in *E. coli* does not show any bursts (Silander et al., 2012). Metabolic pathways are usually considered to be unaffected by stochasticity because of the higher numbers of metabolic enzymes and metabolites in the cell, but the stochastic expression of catabolic enzymes has been found to lead to fluctuations in growth rate that can perturb the expression of other enzymes



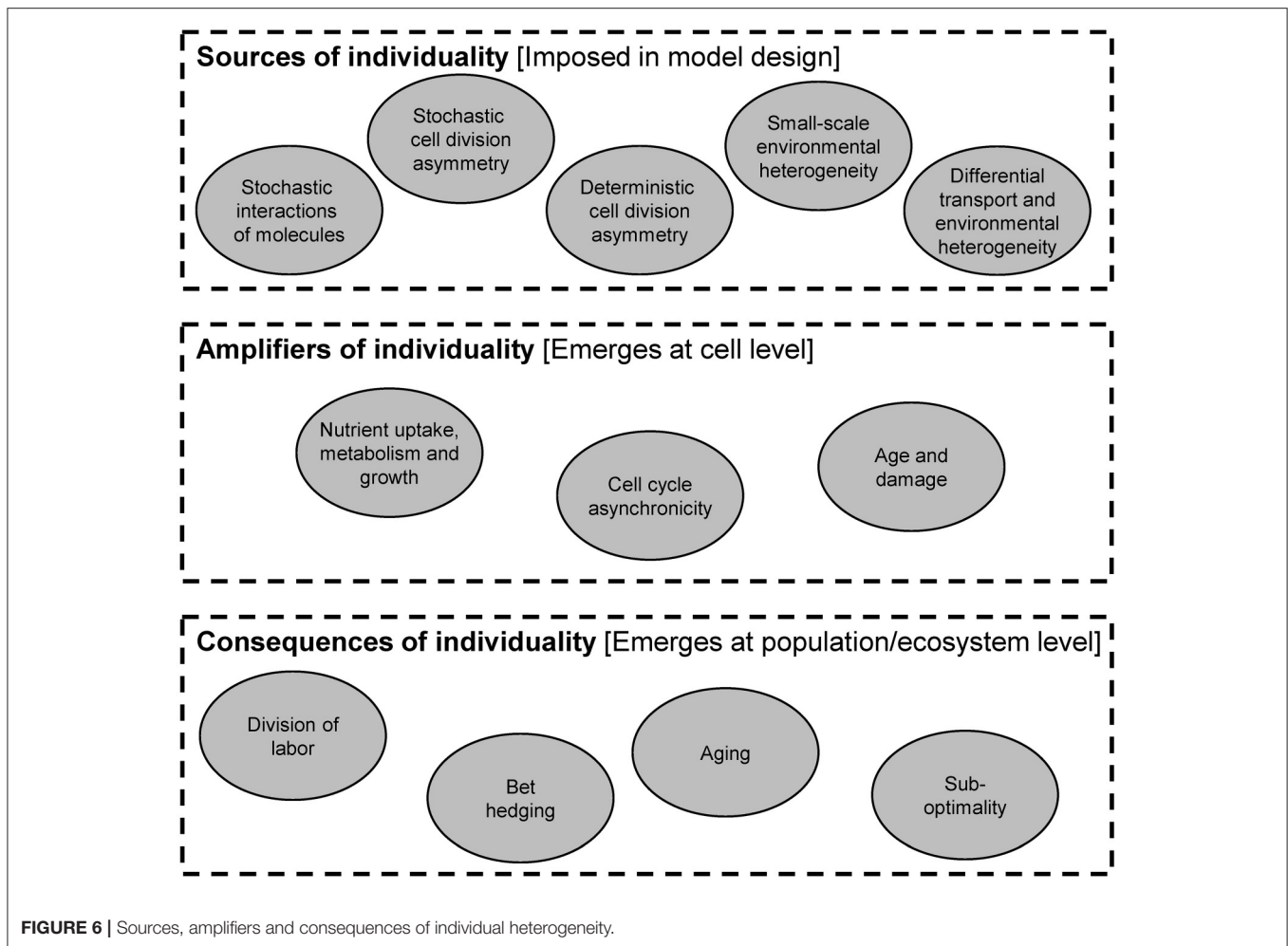
(Kiviet et al., 2014). Heterogeneity may also arise from changes to the DNA, including mutation, recombination and methylation (Avery, 2006; van der Woude, 2011).

Stochastic Cell Division Asymmetry

Another source of cell-to-cell variability is stochastic partitioning of cellular components during cell division. This may be due to low copy numbers of mRNAs, proteins, plasmids and genomes (Huh and Paulsson, 2011; Jahn et al., 2015), or imperfections in the cell division machinery leading to unequal daughter cell sizes and consequently asymmetry in all cellular components. Bacteria can control this heterogeneity by molecular mechanisms that are increasingly understood. For example, interactions of MinCDE proteins with themselves and the polar membranes set up a spatial gradient inside the cell that favors assembly of the FtsZ cell division ring in the middle of the cell (Kieser and Rubin, 2014). Missing components of this regulatory system have been implicated in the higher division asymmetry observed for *Mycobacterium smegmatis* compared to *E. coli* (Aldridge et al., 2012).

Deterministic Cell Division Asymmetry

In addition to stochastic processes, there are deterministic mechanisms that lead to cell division asymmetry. Replication in budding bacteria and yeast obviously produces two different individuals and population heterogeneity. In *Saccharomyces cerevisiae*, the mother cell is larger and accumulates damage, including bud scars, extrachromosomal DNA circles (ERCs) and carbonylated proteins, which are retained preferentially by the mother cell during division by binding to special cellular compartments (Unruh et al., 2013; **Figure 7**). Also, for cells that divide by apparently symmetric binary fission, one “daughter” inherits the old pole and one the new pole. The old pole may have accumulated more damage or other properties over its longer lifetime. For example, division in *E. coli* is associated with asymmetric segregation of damaged protein aggregates (Lindner et al., 2008). The aggregates diffuse by stochastic Brownian motion but they are too large to enter the nucleoid region and therefore get trapped at the poles (Coquel et al., 2013). The asymmetry goes beyond damage. For example, since the outer membrane (OM) is synthesized mostly along the cylindrical part



of the cell, old poles have older OM and may include proteins that were previously expressed and now repressed (Ursell et al., 2012). Bacteria with flagella at one pole will also generate two different daughter cells at division (Christen et al., 2010).

Small-Scale Environmental Heterogeneity

Spatially structured microenvironments constitute another driver of heterogeneity. For example, microbes in colonies, biofilms or granular sludge flocs experience gradients in dissolved oxygen and nutrient concentrations (Wimpenny and Coombs, 1983; Matsumoto et al., 2010). The response of the microbes to these different conditions, including growth and acclimation, leads to a microbial population with heterogeneous properties. For example, the growth rate of *Pseudomonas putida* cells in biofilms was monitored using a reporter consisting of the growth rate-regulated *rrnBP1* promoter and unstable GFP (Sternberg et al., 1999). Cells along the periphery of the biofilm were observed to grow rapidly, whereas those on the inside grew slower or not at all.

Differential Transport and Environmental Heterogeneity

Transport, whether passive (e.g., with water or air) or active (e.g., chemotaxis), can act differently on individuals within a

homogenous population. Water flow velocities tend to be larger near the center of conduits (e.g., pores, pipes, rivers). Even for a uniform flow field, advection is generally associated with diffusion causing individuals from one location to be transported to different locations. On leaf surfaces, cells can be dispersed to different locations and grow into microcolonies, followed by detachment and colonization elsewhere (van der Wal et al., 2013). Also, transport by active mechanisms, like chemotaxis, entails stochastic variability and can lead to different paths of individuals (due to stochastic signaling, see above) (Korobkova et al., 2004). Often the environment exhibits substantial heterogeneity at this scale. For example, the nutrient concentrations in surface waters are highly heterogeneous, with microscale patches created by lysing cells, phytoplankton exudates or marine snow (Stocker, 2012; Taylor and Stocker, 2012; Zehr et al., 2017). Similarly, nutrient availability on plant leaf surfaces varies greatly at a micrometer scale and often correlates with local topography (Remus-Emsermann et al., 2011). Even environments that are designed to be homogenous, like strongly agitated small-scale fermentors, can be heterogeneous (Dunlop and Ye, 1990). When differential transport occurs in a heterogeneous environment, it can lead to intra-population heterogeneity as microbes respond to their individual conditions (i.e., by gene expression, nutrient uptake, and growth). By the same argument, the population at

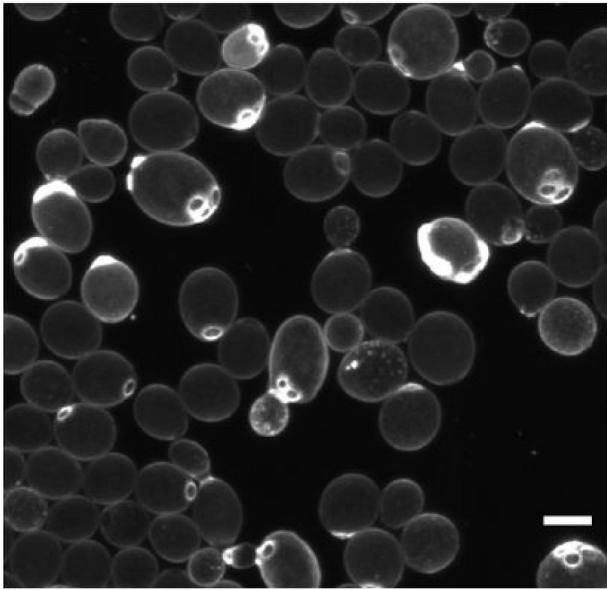


FIGURE 7 | Deterministic cell division asymmetry in the budding yeast *Saccharomyces cerevisiae* leads to heterogeneity in size and bud scars (stained bright). Scale bar is 5 μm . Reproduced from van Deventer et al. (2015) with permission.

any given location may be comprised of individuals with vastly different life histories (Bucci et al., 2012). For example, depending on how they were formed (by a mechanism of staying-together or coming-together), aggregates of bacteria on leaf surfaces may consist of cells that are either clonal with similar life histories or represent a variety of previous leaf surface experiences (Tecon and Leveau, 2012).

Amplifiers of Individuality

The heterogeneity produced by the above sources can manifest itself in a number of properties and behaviors, which can then feed forward and produce heterogeneity in other properties and behaviors, effectively amplifying the overall heterogeneity.

Nutrient Uptake, Metabolism, and Growth

Stochastic gene expression, or any of the other primary sources of heterogeneity discussed above, may result in different levels of some functional enzyme and behavior, such as nutrient uptake. For example, the assimilation of nitrate and urea is very heterogeneous when a cultured population of nitrate-acclimated, marine dinoflagellate *Prorocentrum minimum* cells is exposed to a sudden input of urea (a preferred N source) (Figure 8; Matantseva et al., 2016). This may in turn affect nutrient metabolism and growth. For example, single-cell observations for *Methylobacterium extorquens* AM1 showed high variability in cell size at division, division time (2.5-fold range) and growth rate (Strovas et al., 2007). Consequently, even some bulk housekeeping functions, like metabolism and growth, which are generally considered to be relatively homogenous, can be very heterogeneous, even in cultured populations.

Cell Cycle Asynchronicity

Asymmetric division can lead to an asynchronous population (i.e., where cells are in different phases in the cell cycle) because size can be a major checkpoint for various cell cycle phases. Since the cells perform different tasks at different phases in the cell cycle, this translates into a population with heterogeneous behavior. For example, in *Saccharomyces cerevisiae*, 800 genes are cell-cycle regulated (Spellman et al., 1998) and in *Caulobacter crescentus*, over 500 genes (Laub et al., 2000). In photosynthetic microorganisms, such as microalgae and cyanobacteria, gene expression is also tied to the light-dark cycle, often via a circadian clock (Ito et al., 2009). Unless the population grows at a generation time of 1 day, it will consist of cells with various phase differences between their cell and diel cycles. This effectively adds another dimension of variation and increases the number of phenotypes and population heterogeneity.

Age and Damage

Asymmetric segregation of damage during cell division produces younger and older cells and therefore an age distribution in the population. This affects the growth rates and other behaviors of cells. For instance, damaged protein aggregates are partitioned asymmetrically in *E. coli* and new-pole cells with less damage have a 4% higher specific growth rate (Lindner et al., 2008). In *S. cerevisiae*, older cells also grow slower and they synthesize more of the stress protectant trehalose (Levy et al., 2012).

Ecological Consequences of Individuality

In many cases the heterogeneity may simply average out and be of little consequence to the fitness of the population. However, there are a number of cases where heterogeneity has been shown to have important ecological consequences.

Division of Labor

Phenotypic differentiation forms the basis for a division of labor, where different cells carry out complementary tasks that benefit the population. For example, oxygenic photosynthesis and nitrogen fixation are incompatible processes. Specifically, the enzyme nitrogenase, encoded by genes *nifH*, *nifD* and *nifK* and responsible for reducing N_2 to NH_4^+ , breaks down in the presence of oxygen. To overcome this problem, the filamentous cyanobacterium *Anabaena* can differentiate into two types: photosynthesizing vegetative cells and nitrogen fixing heterocysts (Flores and Herrero, 2010). Another example includes evolved populations of *E. coli* where the labor of converting glucose to CO_2 is divided over two cell types: one that converts glucose to acetate while the other converts acetate to CO_2 (Harvey et al., 2014). There is also altruistic division of labor, which is the tasked sacrifice of some members of the group to benefit others. For example, *Salmonella* cells that invade the gut tissue get killed by the host immune system, but not before triggering a host response that kills other bacteria in the gut lumen but not the subpopulation of *Salmonella* cells that stayed behind and now have a competitive advantage in the gut lumen (Ackermann et al., 2008). The basis for this strategy lies in the stochastic expression of genes coding for a Type III Secretion System (T3SS) within the clonal *Salmonella* population: only a subset of cells within

this population express a T3SS and it is this subset of cells that is capable of invading the gut tissue. Another example is the split into motile and immotile subpopulations of *Pseudomonas aeruginosa* that only together can generate mushroom-shaped biofilms (Ghanbari et al., 2016). Division of labor does not have to involve a direct effect of one phenotype on the other, but it may simply involve growing on different nutrients, like nitrate and urea, allowing the population to maximize uptake (Matantseva et al., 2016).

Bet Hedging

The future is uncertain and may bring unpredictable changes in stresses or any other environmental factors. If cells could react instantly to changes in their environment, a good strategy may be to rely on sensing and responding, but if the response is too slow,

it is better to maintain a diversity of phenotypes (Kussell and Leibler, 2005), which is referred to as bet hedging. In the context of stress resistance, bet hedging is when a population contains some cells that are ill-adapted to the current environment but better adapted to potential future stresses. An important example are persister cells that are produced spontaneously, make up a small fraction of the population, are inhibited in growth (dormant) but can survive antibiotics (Balaban et al., 2004, 2013; **Figure 9**). Dormancy is widespread in microbes (Lennon and Jones, 2011), and when it involves a fraction of the cells and is not purely responsive to environmental conditions (i.e., at least partially spontaneous) it can also be considered a bet hedging strategy. For example, the cyanobacterium *Anabaena* forms akinetes that sink to the sediment bed and can serve as a seedbank for future blooms. This can be considered a bet hedging

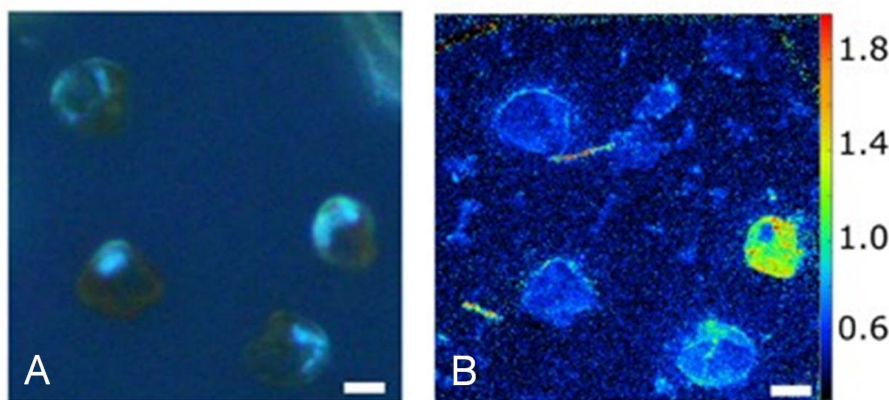


FIGURE 8 | Heterogeneity in urea uptake by *P. minimum* at the single-cell level. **(A)** *P. minimum* cells in UV light. **(B)** ^{15}N -urea uptake by *P. minimum* cells depicted as $^{12}\text{C}^{15}\text{N}^- / ^{12}\text{C}^{14}\text{N}^-$ ratio. Scale bar is 5 μm . Reproduced from Matantseva et al. (2016) with permission.

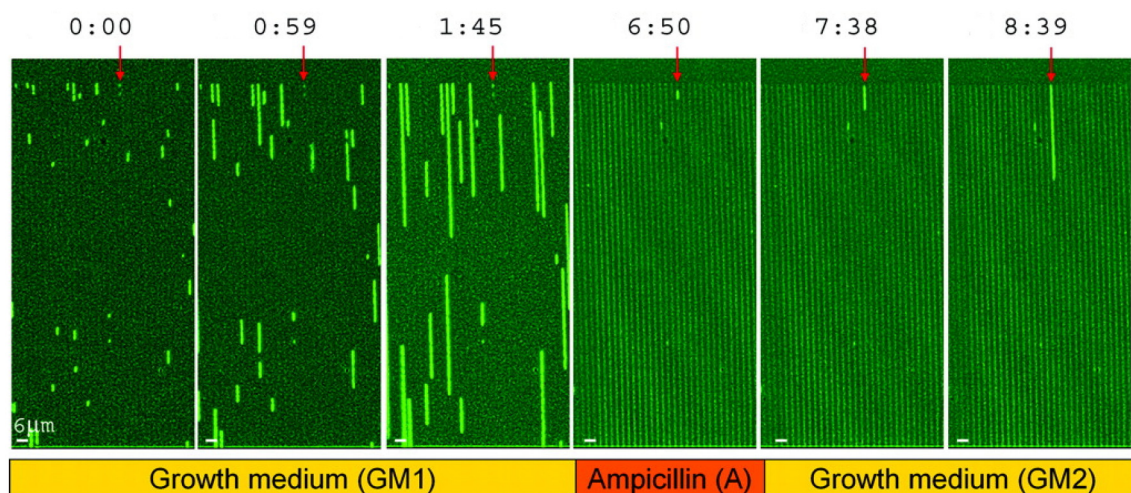


FIGURE 9 | Survival of persister cells under antibiotic treatment. Growth of a *hipA7* mutant, which produces a larger fraction of persisters, in microfluidic channels. Times are in hours:minutes. Bacteria are exposed to three phases, including growth medium (GM1), ampicillin (A) and then washing and again growth medium (GM2). Persister cells are marked with a red arrow. Reproduced from Balaban et al. (2004) with permission.

strategy to protect the population from being wiped out by some factor (washout, grazing), but it may also be a case of division of labor, as the migration to the sediment bed allows the cells to accumulate nutrients (Hellweger et al., 2008). Bet-hedging strategies do not have to involve an all-or-nothing differentiation, but can be gradual. For example, populations of the budding yeast have a gradual (and age-correlated) distribution of the stress-protectant trehalose (Levy et al., 2012). Finally, bet hedging is not restricted to stress resistance, but it may involve nutrient acquisition. For example, diversifying chemotactic behaviors in clonal populations could be an adaptation to foraging in variable environments (Frankel et al., 2014).

Aging

Aging is a strategy for eliminating damage from a population by concentrating it in a few cells that will eventually be discarded (i.e., die of old age). The alternative is to repair or eliminate the damage in some way. The evidence for aging to provide a significant ecological benefit in microbes is elusive, probably because the extent of damage segregation varies between species and environmental conditions. For example, for *E. coli*, one study showed asymmetric partitioning of damaged protein aggregates and decreased growth rates of older cells (Lindner et al., 2008), but in another study growth rates were not observed to decrease over many generations (Wang et al., 2010). Thus, there is an ongoing debate about the ecological benefits of aging in bacteria (Clegg et al., 2014; Koleva and Hellweger, 2015). Several recent studies suggest that aging does not increase fitness or does not occur under benign conditions but instead is a stress response at the population level (Coelho et al., 2013; Clegg et al., 2014; Iyer-Biswas et al., 2014; Vedel et al., 2016).

Sub-Optimality

In the absence of conditions that make heterogeneity advantageous (division of labor, bet hedging or aging), it is disadvantageous or sub-optimal. For any given set of (constant) conditions, there is only one optimal behavior that maximizes fitness (for one species). This has been explored in the context of nutrient assimilation and the effect on growth. Nutrient quotas of phytoplankton can be quite heterogeneous. This heterogeneity leads to a reduction in growth rate, compared to a hypothetical population with uniform quotas, due to the non-linearity of the underlying process (Bucci et al., 2012; Fredrick et al., 2013). When the cell's environment (and thus the heterogeneity) is controlled using microfluidic culturing technology, the growth rate increases compared to flask cultures (Dusny et al., 2012). Another case of sub-optimality stems from a mismatch between cell and environmental cycles. When a population of cells in

different phases of their cell cycle grows in a cyclically varying environment (i.e., diel cycle in light or temperature), the cells have different alignments between these two cycles. It is reasonable to expect that some of those alignments may be more optimal than others, leading to sub-optimality.

Consideration of Individuality in Models

From the above review, it is clear that individual heterogeneity can have important effects on the ecology of microbes and the ecosystems harboring them. Any model that is to capture these effects, whether for advancing understanding or making predictions, has to be able to simulate the production and amplification of this heterogeneity. Therefore, when selecting a modeling strategy it is important to understand upfront the role of heterogeneity in the system, and how it is produced and amplified. Then, a modeling approach can be selected. For example, the ecology of infectious bacteria is in many ways controlled by bet hedging, which builds on individual heterogeneity. In some cases, such as persisters that can survive antimicrobial or other stresses, there are only two phenotypes. This type of heterogeneity has been modeled with the metabolic flux approach (Zhuang et al., 2012). Other cases involve a more gradual differentiation, like age-correlated stress resistance. Resolving this type of heterogeneity has been modeled using the agent-based approach (Hellweger et al., 2014).

AUTHOR CONTRIBUTIONS

All authors listed have made a substantial, direct and intellectual contribution to the work, and approved it for publication.

ACKNOWLEDGMENTS

This review grew out of a recent @ASM conference entitled "The individual microbe: Single-cell analysis and agent-based modeling." We would like to thank the American Society of Microbiology (ASM) for support and the conference participants for the stimulating discussions. Two reviewers provided constructive criticism. J-UK thanks the UK National Centre for Replacement, Refinement and Reduction of Animals in Research (NC3Rs) for funding the development of eGUT (grant NC/K000683/1). JL acknowledges funding by USDA-NIFA-AFRI through grant #2013-02075. WZ acknowledges funding by the National Science Foundation of China through grants No. 21621004 and No. 31370115. FH acknowledges funding by NSF through grants DEB-1240894 and ENG/ECCS-1404163.

REFERENCES

- Ackermann, M., Stecher, B., Freed, N. E., Songhet, P., Hardt, W.-D., and Doebeli, M. (2008). Self-destructive cooperation mediated by phenotypic noise. *Nature* 454, 987–990. doi: 10.1038/nature07067
- Aldridge, B. B., Fernandez-Suarez, M., Heller, D., Ambravaneswaran, V., Irimia, D., Toner, M., et al. (2012). Asymmetry and aging of mycobacterial cells lead to variable growth and antibiotic susceptibility. *Science* 335, 100–104. doi: 10.1126/science.1216166
- Anantharaman, K., Breier, J. A., Sheik, C. S., and Dick, G. J. (2013). Evidence for hydrogen oxidation and metabolic plasticity in widespread deep-sea sulfur-oxidizing bacteria. *Proc. Natl. Acad. Sci. U.S.A.* 110, 330–335. doi: 10.1073/pnas.1215340110

- Atarashi, K., Tanoue, T., Oshima, K., Suda, W., Nagano, Y., Nishikawa, H., et al. (2013). Treg induction by a rationally selected mixture of Clostridia strains from the human microbiota. *Nature* 500, 232–236. doi: 10.1038/nature12331
- Avery, S. V. (2006). Microbial cell individuality and the underlying sources of heterogeneity. *Nat. Rev. Microbiol.* 4, 577–587. doi: 10.1038/nrmicro1460
- Balaban, N. Q., Gerdes, K., Lewis, K., and McKinney, J. D. (2013). A problem of persistence: still more questions than answers? *Nat. Rev. Microbiol.* 11, 587–591. doi: 10.1038/nrmicro3076
- Balaban, N. Q., Merrin, J., Chait, R., Kowalik, L., and Leibler, S. (2004). Bacterial persistence as a phenotypic switch. *Science* 305, 1622–1625. doi: 10.1126/science.1099390
- Becker, S. A., and Palsson, B. O. (2008). Context-specific metabolic networks are consistent with experiments. *PLoS Comput. Biol.* 4:e1000082. doi: 10.1371/journal.pcbi.1000082
- Benyamini, T., Folger, O., Rupp, E., and Shlomi, T. (2010). Flux balance analysis accounting for metabolite dilution. *Genome Biol.* 11:R43. doi: 10.1186/gb-2010-11-4-r43
- Biggs, M. B., Medlock, G. L., Kolling, G. L., and Papin, J. A. (2015). Metabolic network modeling of microbial communities. *Wiley Interdiscip. Rev. Syst. Biol. Med.* 7, 317–334. doi: 10.1002/wsbm.1308
- Biggs, M. B., and Papin, J. A. (2013). Novel multiscale modeling tool applied to *Pseudomonas aeruginosa* biofilm formation. *PLoS ONE* 8:e78011. doi: 10.1371/journal.pone.0078011
- Bizukojc, M., Dietz, D., Sun, J., and Zeng, A.-P. (2010). Metabolic modelling of syntrophic-like growth of a 1,3-propanediol producer, *Clostridium butyricum*, and a methanogenic archaeon, *Methanosarcina mazei*, under anaerobic conditions. *Bioprocess Biosyst. Eng.* 33, 507–523. doi: 10.1007/s00449-009-0359-0
- Blumberg, A. F., and Di Toro, D. M. (1990). Effects of climate warming on dissolved oxygen concentrations in lake Erie. *Trans. Am. Fish. Soc.* 119, 210–223.
- Bordbar, A., Lewis, N. E., Schellenberger, J., Palsson, B. Ø., and Jamshidi, N. (2010). Insight into human alveolar macrophage and *M. tuberculosis* interactions via metabolic reconstructions. *Mol. Syst. Biol.* 6:422. doi: 10.1038/msb.2010.68
- Bucci, V., Nunez-Milland, D., Twining, B., and Hellweger, F. (2012). Microscale patchiness leads to large and important intraspecific internal nutrient heterogeneity in phytoplankton. *Aquatic Ecol.* 46, 101–118. doi: 10.1007/s10452-011-9384-6
- Bucci, V., Tzen, B., Li, N., Simmons, M., Tanoue, T., Bogart, E., et al. (2016). MDSINE: microbial dynamical systems INference engine for microbiome time-series analyses. *Genome Biol.* 17:121. doi: 10.1186/s13059-016-0980-6
- Buffie, C. G., Bucci, V., Stein, R. R., McKenney, P. T., Ling, L., Gouberne, A., et al. (2015). Precision microbiome reconstitution restores bile acid mediated resistance to *Clostridium difficile*. *Nature* 517, 205–208. doi: 10.1038/nature13828
- Burnat, M., Herrero, A., and Flores, E. (2014). Compartmentalized cyanophycin metabolism in the diazotrophic filaments of a heterocyst-forming cyanobacterium. *Proc. Natl. Acad. Sci. U.S.A.* 111, 3823–3828. doi: 10.1073/pnas.1318564111
- Castellanos, M., Wilson, D. B., and Shuler, M. L. (2004). A modular minimal cell model: purine and pyrimidine transport and metabolism. *Proc. Natl. Acad. Sci. U.S.A.* 101, 6681–6686. doi: 10.1073/pnas.0400962101
- Cerqueda-García, D., and Falcón, L. I. (2016). Metabolic potential of microbial mats and microbialites: autotrophic capabilities described by an *in silico* stoichiometric approach from shared genomic resources. *J. Bioinform. Comput. Biol.* 14:1650020. doi: 10.1142/S0219720016500207
- Chiu, H.-C., Levy, R., and Borenstein, E. (2014). Emergent biosynthetic capacity in simple microbial communities. *PLoS Comput. Biol.* 10:e1003695. doi: 10.1371/journal.pcbi.1003695
- Christen, M., Kulasekara, H. D., Christen, B., Kulasekara, B. R., Hoffman, L. R., and Miller, S. I. (2010). Asymmetrical distribution of the second messenger c-di-GMP upon bacterial cell division. *Science* 328, 1295–1297. doi: 10.1126/science.1188658
- Clark, J. R., Daines, S. J., Lenton, T. M., Watson, A. J., and Williams, H. T. (2011). Individual-based modelling of adaptation in marine microbial populations using genetically defined physiological parameters. *Ecol. Modell.* 222, 3823–3837. doi: 10.1016/j.ecolmodel.2011.10.001
- Clegg, R. J., Dyson, R. J., and Kreft, J.-U. (2014). Repair rather than segregation of damage is the optimal unicellular aging strategy. *BMC Biol.* 12:52. doi: 10.1186/s12915-014-0052-x
- Coelho, M., Dereli, A., Haese, A., Kühn, S., Malinowska, L., DeSantis, M. E., et al. (2013). Fission yeast does not age under favorable conditions, but does so after stress. *Curr. Biol.* 23, 1844–1852. doi: 10.1016/j.cub.2013.07.084
- Cole, J. A., Kohler, L., Hedhli, J., and Luthy-Schulten, Z. (2015). Spatially-resolved metabolic cooperativity within dense bacterial colonies. *BMC Syst. Biol.* 9:15. doi: 10.1186/s12918-015-0155-1
- Coquel, A.-S., Jacob, J.-P., Primet, M., Demarez, A., Dimiccoli, M., Julou, T., et al. (2013). Localization of protein aggregation in *Escherichia coli* is governed by diffusion and nucleoid macromolecular crowding effect. *PLoS Comput. Biol.* 9:e1003038. doi: 10.1371/journal.pcbi.1003038
- Costello, E. K., Lauber, C. L., Hamady, M., Fierer, N., Gordon, J. I., and Knight, R. (2009). Bacterial community variation in human body habitats across space and time. *Science* 326, 1694–1697. doi: 10.1126/science.1177486
- Cottrell, M. T., and Kirchman, D. L. (2016). Transcriptional control in marine copiotrophic and oligotrophic bacteria with streamlined genomes. *Appl. Environ. Microbiol.* 82, 6010–6018. doi: 10.1128/AEM.01299-16
- Dick, G. J. (2017). Embracing the mantra of modellers and synthesizing omics, experiments and models. *Environ. Microbiol. Rep.* 9, 18–20. doi: 10.1111/1758-2229.12491
- Dunlop, E. H., and Ye, S. J. (1990). Micromixing in fermentors: metabolic changes in *Saccharomyces cerevisiae* and their relationship to fluid turbulence. *Biotechnol. Bioeng.* 36, 854–864. doi: 10.1002/bit.260360816
- Dusny, C., Fritzsche, F. S. O., Frick, O., and Schmid, A. (2012). Isolated microbial single cells and resulting micropopulations grow faster in controlled environments. *Appl. Environ. Microbiol.* 78, 7132–7136. doi: 10.1128/AEM.01624-12
- El-Semman, I. E., Karlsson, F. H., Shoaie, S., Nookaew, I., Soliman, T. H., and Nielsen, J. (2014). Genome-scale metabolic reconstructions of *Bifidobacterium adolescentis* L2-32 and *Faecalibacterium prausnitzii* A2-165 and their interaction. *BMC Syst. Biol.* 8:41. doi: 10.1186/1752-0509-8-41
- Emonet, T., and Cluzel, P. (2008). Relationship between cellular response and behavioral variability in bacterial chemotaxis. *Proc. Natl. Acad. Sci. U.S.A.* 105, 3304–3309. doi: 10.1073/pnas.0705463105
- Feist, A. M., Herrgård, M. J., Thiele, I., Reed, J. L., and Palsson, B. Ø. (2008). Reconstruction of biochemical networks in microorganisms. *Nat. Rev. Microbiol.* 7, 129–143. doi: 10.1038/nrmicro1949
- Flores, E., and Herrero, A. (2010). Compartmentalized function through cell differentiation in filamentous cyanobacteria. *Nat. Rev. Microbiol.* 8, 39–50. doi: 10.1038/nrmicro2242
- Frankel, N. W., Pontius, W., Dufour, Y. S., Long, J., Hernandez-Nunez, L., and Emonet, T. (2014). Adaptability of non-genetic diversity in bacterial chemotaxis. *Elife* 3:e03526. doi: 10.7554/eLife.03526
- Fredrick, N. D., Berges, J. A., Twining, B. S., Nuñez-Milland, D., and Hellweger, F. L. (2013). Use of agent-based modeling to explore the mechanisms of intracellular phosphorus heterogeneity in cultured phytoplankton. *Appl. Environ. Microbiol.* 79, 4359–4368. doi: 10.1128/AEM.00487-13
- Freilich, S., Zarecki, R., Eilam, O., Segal, E. S., Henry, C. S., Kupiec, M., et al. (2011). Competitive and cooperative metabolic interactions in bacterial communities. *Nat. Commun.* 2:589. doi: 10.1038/ncomms1597
- Fuhrman, J., Follows, M., and Forde, S. (2013). Applying “-omics” data in marine microbial oceanography. *Eos Trans. Am. Geophys. Union* 94, 241–241. doi: 10.1002/2013EO270006
- Ghanbari, A., Dehghany, J., Schwebbs, T., Müskens, M., Häussler, S., and Meyer-Hermann, M. (2016). Inoculation density and nutrient level determine the formation of mushroom-shaped structures in *Pseudomonas aeruginosa* biofilms. *Sci. Rep.* 6:32097. doi: 10.1038/srep32097
- Gottstein, W., Olivier, B. G., Bruggeman, F. J., and Teusink, B. (2016). Constraint-based stoichiometric modelling from single organisms to microbial communities. *J. R. Soc. Interface* 13:20160627. doi: 10.1098/rsif.2016.0627
- Guidi, L., Chaffron, S., Bittner, L., Eveillard, D., Larhlimi, A., Roux, S., et al. (2016). Plankton networks driving carbon export in the oligotrophic ocean. *Nature* 532, 465–470. doi: 10.1038/nature16942
- Hanly, T. J., and Henson, M. A. (2011). Dynamic flux balance modeling of microbial co-cultures for efficient batch fermentation of glucose and xylose mixtures. *Biotechnol. Bioeng.* 108, 376–385. doi: 10.1002/bit.22954

- Hanly, T. J., and Henson, M. A. (2013). Dynamic metabolic modeling of a microaerobic yeast co-culture: predicting and optimizing ethanol production from glucose/xylose mixtures. *Biotechnol. Biofuels* 6:44. doi: 10.1186/1754-6834-6-44
- Harcombe, W. R., Riehl, W. J., Dukovski, I., Granger, B. R., Betts, A., Lang, A. H., et al. (2014). Metabolic resource allocation in individual microbes determines ecosystem interactions and spatial dynamics. *Cell Rep.* 7, 1104–1115. doi: 10.1016/j.celrep.2014.03.070
- Harvey, E., Heys, J., and Gedeon, T. (2014). Quantifying the effects of the division of labor in metabolic pathways. *J. Theor. Biol.* 360, 222–242. doi: 10.1016/j.jtbi.2014.07.011
- Heinken, A., and Thiele, I. (2015). Anoxic conditions promote species-specific mutualism between gut microbes *in silico*. *Appl. Environ. Microbiol.* 81, 4049–4061. doi: 10.1128/AEM.00101-15
- Hellweger, F., Fredrick, N., and Berges, J. (2014). Age-correlated stress resistance improves fitness of yeast: support from agent-based simulations. *BMC Syst. Biol.* 8:18. doi: 10.1186/1752-0509-8-18
- Hellweger, F. L. (2009). Carrying photosynthesis genes increases ecological fitness of cyanophage *in silico*. *Environ. Microbiol.* 11, 1386–1394. doi: 10.1111/j.1462-2920.2009.01866.x
- Hellweger, F. L. (2010). Resonating circadian clocks enhance fitness in cyanobacteria *in silico*. *Ecol. Modell.* 221, 1620–1629. doi: 10.1016/j.ecolmodel.2010.03.015
- Hellweger, F. L. (2013). *Escherichia coli* adapts to tetracycline resistance plasmid (pBR322) by mutating endogenous potassium transport: *in silico* hypothesis testing. *FEMS Microbiol. Ecol.* 83, 622–631. doi: 10.1111/1574-6941.12019
- Hellweger, F. L. (2015). 100 Years since Streeter and Phelps: it is time to update the biology in our water quality models. *Environ. Sci. Technol.* 49, 6372–6373. doi: 10.1021/acs.est.5b02130
- Hellweger, F. L., Clegg, R. J., Clark, J. R., Plugge, C. M., and Kreft, J.-U. (2016a). Advancing microbial sciences by individual-based modelling. *Nat. Rev. Microbiol.* 14, 461–471. doi: 10.1038/nrmicro.2016.62
- Hellweger, F. L., Fredrick, N. D., McCarthy, M. J., Gardner, W. S., Wilhelm, S. W., and Paerl, H. W. (2016b). Dynamic, mechanistic, molecular-level modelling of cyanobacteria: *Anabaena* and nitrogen interaction. *Environ. Microbiol.* 18, 2721–2731. doi: 10.1111/1462-2920.13299
- Hellweger, F. L., Kravchuk, E. S., Novotny, V., and Gladyshev, M. I. (2008). Agent-based modeling of the complex life cycle of a cyanobacterium (*Anabaena*) in a shallow reservoir. *Limnol. Oceanogr.* 53, 1227–1241. doi: 10.4319/lo.2008.53.4.1227
- Huh, D., and Paulsson, J. (2011). Non-genetic heterogeneity from stochastic partitioning at cell division. *Nat. Genet.* 43, 95–100. doi: 10.1038/ng.729
- Huthmacher, C., Hoppe, A., Bulik, S., and Holzhütter, H.-G. (2010). Antimalarial drug targets in *Plasmodium falciparum* predicted by stage-specific metabolic network analysis. *BMC Syst. Biol.* 4:120. doi: 10.1186/1752-0509-4-120
- Ito, H., Mutsuda, M., Murayama, Y., Tomita, J., Hosokawa, N., Terauchi, K., et al. (2009). Cyanobacterial daily life with Kai-based circadian and diurnal genome-wide transcriptional control in *Synechococcus elongatus*. *Proc. Natl. Acad. Sci. U.S.A.* 106, 14168–14173. doi: 10.1073/pnas.0902587106
- Iyer-Biswas, S., Wright, C. S., Henry, J. T., Lo, K., Burov, S., Lin, Y., et al. (2014). Scaling laws governing stochastic growth and division of single bacterial cells. *Proc. Natl. Acad. Sci. U.S.A.* 111, 15912–15917. doi: 10.1073/pnas.1403232111
- Jahn, M., Günther, S., and Müller, S. (2015). Non-random distribution of macromolecules as driving forces for phenotypic variation. *Curr. Opin. Microbiol.* 25, 49–55. doi: 10.1016/j.mib.2015.04.005
- Jöhnk, K. D., Huisman, J. E. F., Sharples, J., Sommeijer, B. E. N., Visser, P. M., and Stroom, J. M. (2008). Summer heatwaves promote blooms of harmful cyanobacteria. *Glob. Chang. Biol.* 14, 495–512. doi: 10.1111/j.1365-2486.2007.01510.x
- Karr, J. R., Sanghvi, J. C., Macklin, D. N., Gutschow, M. V., Jacobs, J. M., Bolival, B., et al. (2012). A whole-cell computational model predicts phenotype from genotype. *Cell* 150, 389–401. doi: 10.1016/j.cell.2012.05.044
- Kettle, H., Louis, P., Holtrop, G., Duncan, S. H., and Flint, H. J. (2015). Modelling the emergent dynamics and major metabolites of the human colonic microbiota. *Environ. Microbiol.* 17, 1615–1630. doi: 10.1111/1462-2920.12599
- Khandelwal, R. A., Olivier, B. G., Röling, W. F. M., Teusink, B., and Bruggeman, F. J. (2013). Community flux balance analysis for microbial consortia at balanced growth. *PLoS ONE* 8:e64567. doi: 10.1371/journal.pone.0064567
- Kieser, K. J., and Rubin, E. J. (2014). How sisters grow apart: mycobacterial growth and division. *Nat. Rev. Microbiol.* 12, 550–562. doi: 10.1038/nrmicro3299
- Kindaichi, T., Nierychlo, M., Kragelund, C., Nielsen, J. L., and Nielsen, P. H. (2013). High and stable substrate specificities of microorganisms in enhanced biological phosphorus removal plants. *Environ. Microbiol.* 15, 1821–1831. doi: 10.1111/1462-2920.12074
- Kiviet, D. J., Nghe, P., Walker, N., Boulineau, S., Sunderlikova, V., and Tans, S. J. (2014). Stochasticity of metabolism and growth at the single-cell level. *Nature* 514, 376–379. doi: 10.1038/nature13582
- Klitgord, N., and Segrè, D. (2010). Environments that induce synthetic microbial ecosystems. *PLoS Comput. Biol.* 6:e1001002. doi: 10.1371/journal.pcbi.1001002
- Klitgord, N., and Segrè, D. (2011). Ecosystems biology of microbial metabolism. *Curr. Opin. Biotechnol.* 22, 541–546. doi: 10.1016/j.copbio.2011.04.018
- Kohler, R., Mooney, R. A., Mills, D. J., Landick, R., and Cramer, P. (2017). Architecture of a transcribing-translating expressome. *Science* 356, 194–197. doi: 10.1126/science.aal3059
- Koleva, K. Z., and Hellweger, F. L. (2015). From protein damage to cell aging to population fitness in *E. coli*: insights from a multi-level agent-based model. *Ecol. Modell.* 301, 62–71. doi: 10.1016/j.ecolmodel.2015.01.024
- Korobkova, E., Emonet, T., Vilar, J. M. G., Shimizu, T. S., and Cluzel, P. (2004). From molecular noise to behavioural variability in a single bacterium. *Nature* 428, 574–578. doi: 10.1038/nature02404
- Kreft, J.-U. (2004). Biofilms promote altruism. *Microbiology* 150, 2751–2760. doi: 10.1099/mic.0.26829-0
- Kussell, E., and Leibler, S. (2005). Phenotypic diversity, population growth, and information in fluctuating environments. *Science* 309, 2075–2078. doi: 10.1126/science.1114383
- Labhsetwar, P., Cole, J. A., Roberts, E., Price, N. D., and Luthey-Schulten, Z. A. (2013). Heterogeneity in protein expression induces metabolic variability in a modeled *Escherichia coli* population. *Proc. Natl. Acad. Sci. U.S.A.* 110, 14006–14011. doi: 10.1073/pnas.1222569110
- Laub, M. T., McAdams, H. H., Feldblyum, T., Fraser, C. M., and Shapiro, L. (2000). Global analysis of the genetic network controlling a bacterial cell cycle. *Science* 290, 2144–2148. doi: 10.1126/science.290.5499.2144
- Lennon, J. T., and Jones, S. E. (2011). Microbial seed banks: the ecological and evolutionary implications of dormancy. *Nat. Rev. Microbiol.* 9, 119–130. doi: 10.1038/nrmicro2504
- Lenski, R. E., Ofria, C., Collier, T. C., and Adami, C. (1999). Genome complexity, robustness and genetic interactions in digital organisms. *Nature* 400, 661–664. doi: 10.1038/23245
- Le Quéré, C., Harrison, S. P., Colin Prentice, I., Buitenhuis, E. T., Aumont, O., Bopp, L., et al. (2005). Ecosystem dynamics based on plankton functional types for global ocean biogeochemistry models. *Glob. Chang. Biol.* 11, 2016–2040. doi: 10.1111/j.1365-2486.2005.1004.x
- Levy, R., and Borenstein, E. (2013). Metabolic modeling of species interaction in the human microbiome elucidates community-level assembly rules. *Proc. Natl. Acad. Sci. U.S.A.* 110, 12804–12809. doi: 10.1073/pnas.1300926110
- Levy, S. F., Ziv, N., and Siegal, M. L. (2012). Bet hedging in yeast by heterogeneous, age-correlated expression of a stress protectant. *PLoS Biol.* 10:e1001325. doi: 10.1371/journal.pbio.1001325
- Lindner, A. B., Madden, R., Demarez, A., Stewart, E. J., and Taddei, F. (2008). Asymmetric segregation of protein aggregates is associated with cellular aging and rejuvenation. *Proc. Natl. Acad. Sci. U.S.A.* 105, 3076–3081. doi: 10.1073/pnas.0708931105
- Louca, S., and Doebeli, M. (2015). Calibration and analysis of genome-based models for microbial ecology. *Elife* 4:e08208. doi: 10.7554/eLife.08208
- Louca, S., Hawley, A. K., Katsev, S., Torres-Beltran, M., Bhatia, M. P., Kheirandish, S., et al. (2016). Integrating biogeochemistry with multiomic sequence information in a model oxygen minimum zone. *Proc. Natl. Acad. Sci. U.S.A.* 113, E5925–E5933. doi: 10.1073/pnas.1602897113
- Mahadevan, R., Edwards, J. S., and Doyle, F. J. (2002). Dynamic flux balance analysis of diauxic growth in *Escherichia coli*. *Biophys. J.* 83, 1331–1340. doi: 10.1016/S0006-3495(02)73903-9
- Martin-Figueroa, E., Navarro, F., and Florencio, F. J. (2000). The GS-GOGAT pathway is not operative in the heterocysts. Cloning and expression of glsF gene

- from the cyanobacterium *Anabaena* sp. PCC 7120. *FEBS Lett.* 476, 282–286. doi: 10.1016/S0014-5793(00)01722-1
- Matantseva, O., Skarlato, S., Vogts, A., Pozdnyakov, I., Liskow, I., Schubert, H., et al. (2016). Superposition of individual activities: urea-mediated suppression of nitrate uptake in the dinoflagellate *Prorocentrum minimum* revealed at the population and single-cell levels. *Front. Microbiol.* 7:1310. doi: 10.3389/fmicb.2016.01310
- Matsumoto, S., Katoku, M., Saeki, G., Terada, A., Aoi, Y., Tsuneda, S., et al. (2010). Microbial community structure in autotrophic nitrifying granules characterized by experimental and simulation analyses. *Environ. Microbiol.* 12, 192–206. doi: 10.1111/j.1462-2920.2009.02060.x
- Merino, M. P., Andrews, B. A., and Asenjo, J. A. (2015). Stoichiometric model and flux balance analysis for a mixed culture of *Leptospirillum ferriphilum* and *Ferropasma acidiphilum*. *Biotechnol. Prog.* 31, 307–315. doi: 10.1002/btpr.2028
- Mina, P., di Bernardo, M., Saverly, N. J., and Tsaneva-Atanasova, K. (2013). Modelling emergence of oscillations in communicating bacteria: a structured approach from one to many cells. *J. R. Soc. Interface* 10:20120612. doi: 10.1098/rsif.2012.0612
- Nagarajan, H., Embree, M., Rotaru, A.-E., Shrestha, P. M., Feist, A. M., Palsson, B. O., et al. (2013). Characterization and modelling of interspecies electron transfer mechanisms and microbial community dynamics of a syntrophic association. *Nat. Commun.* 4:2809. doi: 10.1038/ncomms3809
- Paerl, H. W., Hall, N. S., and Calandrino, E. S. (2011). Controlling harmful cyanobacterial blooms in a world experiencing anthropogenic and climatic-induced change. *Sci. Total Environ.* 409, 1739–1745. doi: 10.1016/j.scitotenv.2011.02.001
- Papin, J. A., Stelling, J., Price, N. D., Klamt, S., Schuster, S., and Palsson, B. O. (2004). Comparison of network-based pathway analysis methods. *Trends Biotechnol.* 22, 400–405. doi: 10.1016/j.tibtech.2004.06.010
- Perez-Garcia, O., Lear, G., and Singhal, N. (2016). Metabolic network modeling of microbial interactions in natural and engineered environmental systems. *Front. Microbiol.* 7:673. doi: 10.3389/fmicb.2016.00673
- Qi, Z., Pei, G., Chen, L., and Zhang, W. (2014). Single-cell analysis reveals gene-expression heterogeneity in syntrophic dual-culture of *Desulfovibrio vulgaris* with *Methanosarcina barkeri*. *Sci. Rep.* 4:7478. doi: 10.1038/srep07478
- Reed, D. C., Algar, C. K., Huber, J. A., and Dick, G. J. (2014). Gene-centric approach to integrating environmental genomics and biogeochemical models. *Proc. Natl. Acad. Sci. U.S.A.* 111, 1879–1884. doi: 10.1073/pnas.1313713111
- Reed, D. C., Breier, J. A., Jiang, H., Anantharaman, K., Klausmeier, C. A., Toner, B. M., et al. (2015). Predicting the response of the deep-ocean microbiome to geochemical perturbations by hydrothermal vents. *ISME J.* 9, 1857–1869. doi: 10.1038/ismej.2015.4
- Remus-Emsermann, M., de Oliveira, S., Schreiber, L., and Leveau, J. (2011). Quantification of lateral heterogeneity in carbohydrate permeability of isolated plant leaf cuticles. *Front. Microbiol.* 2:197. doi: 10.3389/fmicb.2011.00197
- Salcher, M. M., Posch, T., and Pernthaler, J. (2013). *In situ* substrate preferences of abundant bacterioplankton populations in a prealpine freshwater lake. *ISME J.* 7, 896–907. doi: 10.1038/ismej.2012.162
- Salimi, F., Zhuang, K., and Mahadevan, R. (2010). Genome-scale metabolic modeling of a clostridial co-culture for consolidated bioprocessing. *Biotechnol. J.* 5, 726–738. doi: 10.1002/biot.201000159
- Scheibe, T. D., Mahadevan, R., Fang, Y., Garg, S., Long, P. E., and Lovley, D. R. (2009). Coupling a genome-scale metabolic model with a reactive transport model to describe *in situ* uranium bioremediation. *Microb. Biotechnol.* 2, 274–286. doi: 10.1111/j.1751-7915.2009.00087.x
- Schuster, S., Pfeiffer, T., and Fell, D. A. (2008). Is maximization of molar yield in metabolic networks favoured by evolution? *J. Theor. Biol.* 252, 497–504. doi: 10.1016/j.jtbi.2007.12.008
- Segrè, D., Vitkup, D., and Church, G. M. (2002). Analysis of optimality in natural and perturbed metabolic networks. *Proc. Natl. Acad. Sci. U.S.A.* 99, 15112–15117. doi: 10.1073/pnas.232349399
- Shoaie, S., Karlsson, F., Mardinoglu, A., Nookaew, I., Bordel, S., and Nielsen, J. (2013). Understanding the interactions between bacteria in the human gut through metabolic modeling. *Sci. Rep.* 3:2532. doi: 10.1038/srep02532
- Silander, O. K., Nikolic, N., Naslaver, A., Bren, A., Kikoin, I., Alon, U., et al. (2012). A genome-wide analysis of promoter-mediated phenotypic noise in *Escherichia coli*. *PLoS Genet.* 8:e1002443. doi: 10.1371/journal.pgen.1002443
- Spellman, P. T., Sherlock, G., Zhang, M. Q., Iyer, V. R., Anders, K., Eisen, M. B., et al. (1998). Comprehensive identification of cell cycle-regulated genes of the yeast *Saccharomyces cerevisiae* by microarray hybridization. *Mol. Biol. Cell* 9, 3273–3297. doi: 10.1091/mbc.9.12.3273
- Stec, K. F., Caputi, L., Buttigieg, P. L., D'Alelio, D., Ibarbalz, F. M., Sullivan, M. B., et al. (2017). Modelling plankton ecosystems in the meta-omics era. Are we ready? *Mar. Genomics* 32, 1–17. doi: 10.1016/j.margen.2017.02.006
- Stein, R. R., Bucci, V., Toussaint, N. C., Buffie, C. G., Ratsch, G., Pamer, E. G., et al. (2013). Ecological modeling from time-series inference: insight into dynamics and stability of intestinal microbiota. *PLoS Comput. Biol.* 9:e1003388. doi: 10.1371/journal.pcbi.1003388
- Sternberg, C., Christensen, B. B., Johansen, T., Toftgaard Nielsen, A., Andersen, J. B., Givskov, M., et al. (1999). Distribution of bacterial growth activity in flow-chamber biofilms. *Appl. Environ. Microbiol.* 65, 4108–4117.
- Stocker, R. (2012). Marine microbes see a sea of gradients. *Science* 338, 628–633. doi: 10.1126/science.1208929
- Stolyar, S., Van Dien, S., Hillesland, K. L., Pinel, N., Lie, T. J., Leigh, J. A., et al. (2007). Metabolic modeling of a mutualistic microbial community. *Mol. Syst. Biol.* 3:92. doi: 10.1038/msb4100131
- Strovas, T. J., Sauter, L. M., Guo, X., and Lidstrom, M. E. (2007). Cell-to-cell heterogeneity in growth rate and gene expression in *Methylobacterium extorquens* AM1. *J. Bacteriol.* 189, 7127–7133. doi: 10.1128/JB.00746-07
- Taffs, R., Aston, J. E., Brileya, K., Jay, Z., Klatt, C. G., McGlynn, S., et al. (2009). *In silico* approaches to study mass and energy flows in microbial consortia: a syntrophic case study. *BMC Syst. Biol.* 3:114. doi: 10.1186/1752-0509-3-114
- Tan, J., Zuniga, C., and Zengler, K. (2015). Unraveling interactions in microbial communities - from co-cultures to microbiomes. *J. Microbiol.* 53, 295–305. doi: 10.1007/s12275-015-5060-1
- Taylor, J. R., and Stocker, R. (2012). Trade-offs of chemotactic foraging in turbulent water. *Science* 338, 675–679. doi: 10.1126/science.1219417
- Tecon, R., and Leveau, J. H. J. (2012). The mechanics of bacterial cluster formation on plant leaf surfaces as revealed by bioreporter technology. *Environ. Microbiol.* 14, 1325–1332. doi: 10.1111/j.1462-2920.2012.02715.x
- Tobalina, L., Bargiela, R., Pey, J., Herbst, F.-A., Lores, I., Rojo, D., et al. (2015). Context-specific metabolic network reconstruction of a naphthalene-degrading bacterial community guided by metaproteomic data. *Bioinformatics* 31, 1771–1779. doi: 10.1093/bioinformatics/btv036
- Trivedi, P., Anderson, I. C., and Singh, B. K. (2013). Microbial modulators of soil carbon storage: integrating genomic and metabolic knowledge for global prediction. *Trends Microbiol.* 21, 641–651. doi: 10.1016/j.tim.2013.09.005
- Tzamal, E., Poirazi, P., Tollis, G., and Reczko, M. (2009). Computational identification of bacterial communities. *Int. J. Biol. Life Sci.* 1, 185–191.
- Tzamal, E., Poirazi, P., Tollis, I. G., and Reczko, M. (2011). A computational exploration of bacterial metabolic diversity identifying metabolic interactions and growth-efficient strain communities. *BMC Syst. Biol.* 5:167. doi: 10.1186/1752-0509-5-167
- Unruh, J. R., Slaughter, B. D., and Li, R. (2013). Quality control: putting protein aggregates in a bind. *Curr. Biol.* 23, R74–R76. doi: 10.1016/j.cub.2012.12.005
- Ursell, T. S., Trepagnier, E. H., Huang, K. C., and Theriot, J. A. (2012). Analysis of surface protein expression reveals the growth pattern of the Gram-negative outer membrane. *PLoS Comput. Biol.* 8:e1002680. doi: 10.1371/journal.pcbi.1002680
- van der Wal, A., Tecon, R., Kreft, J.-U., Mooij, W. M., and Leveau, J. H. J. (2013). Explaining bacterial dispersion on leaf surfaces with an individual-based model (PHYLLOSIM). *PLoS ONE* 8:e75633. doi: 10.1371/journal.pone.0075633
- van der Woude, M. W. (2011). Phase variation: how to create and coordinate population diversity. *Curr. Opin. Microbiol.* 14, 205–211. doi: 10.1016/j.mib.2011.01.002
- van Deventer, S., Menendez-Benito, V., van Leeuwen, F., and Neefjes, J. (2015). N-terminal acetylation and replicative age affect proteasome localization and cell fitness during aging. *J. Cell Sci.* 128, 109–117. doi: 10.1242/jcs.157354
- Varma, A., and Palsson, B. O. (1994). Stoichiometric flux balance models quantitatively predict growth and metabolic by-product secretion in wild-type *Escherichia coli* W3110. *Appl. Environ. Microbiol.* 60, 3724–3731.
- Vedel, S., Nunns, H., Košmrlj, A., Semsey, S., and Trusina, A. (2016). Asymmetric damage segregation constitutes an emergent population-level stress response. *Cell Systems* 3, 187–198. doi: 10.1016/j.cels.2016.06.008

- Veening, J. W., Smits, W. K., and Kuipers, O. P. (2008). Bistability, epigenetics, and bet-hedging in bacteria. *Annu. Rev. Microbiol.* 62, 193–210. doi: 10.1146/annurev.micro.62.081307.163002
- Vila-Costa, M., Sharma, S., Moran, M. A., and Casamayor, E. O. (2013). Diel gene expression profiles of a phosphorus limited mountain lake using metatranscriptomics. *Environ. Microbiol.* 15, 1190–1203. doi: 10.1111/1462-2920.12033
- Wang, P., Robert, L., Pelletier, J., Dang, W. L., Taddei, F., Wright, A., et al. (2010). Robust growth of *Escherichia coli*. *Curr. Biol.* 20, 1099–1103. doi: 10.1016/j.cub.2010.04.045
- Wang, W.-L., Xu, S.-Y., Ren, Z.-G., Tao, L., Jiang, J.-W., and Zheng, S.-S. (2015). Application of metagenomics in the human gut microbiome. *World J. Gastroenterol.* 21, 803–814. doi: 10.3748/wjg.v21.i3.803
- Wimpenny, J. W. T., and Coombs, J. P. (1983). Penetration of oxygen into bacterial colonies. *Microbiology* 129, 1239–1242. doi: 10.1099/00221287-129-4-1239
- Wintermute, E. H., and Silver, P. A. (2010). Emergent cooperation in microbial metabolism. *Molecular Systems Biology* 6:407. doi: 10.1038/msb.2010.66
- Ye, C., Zou, W., Xu, N., and Liu, L. (2014). Metabolic model reconstruction and analysis of an artificial microbial ecosystem for vitamin C production. *J. Biotechnol.* 182, 61–67. doi: 10.1016/j.jbiotec.2014.04.027
- Zehr, J. P., Weitz, J. S., and Joint, I. (2017). How microbes survive in the open ocean. *Science* 357, 646–647. doi: 10.1126/science.aan5764
- Zelezniak, A., Andrejev, S., Ponomarova, O., Mende, D. R., Bork, P., and Patil, K. R. (2015). Metabolic dependencies drive species co-occurrence in diverse microbial communities. *Proc. Natl. Acad. Sci. U.S.A.* 112, 6449–6454. doi: 10.1073/pnas.1421834112
- Zengler, K., and Palsson, B. O. (2012). A road map for the development of community systems (CoSy) biology. *Nat. Rev. Microbiol.* 10, 366–372. doi: 10.1038/nrmicro2763
- Zhuang, K., Izallalen, M., Mouser, P., Richter, H., Risso, C., Mahadevan, R., et al. (2011). Genome-scale dynamic modeling of the competition between *Rhodospirillum rubrum* and *Geobacter* in anoxic subsurface environments. *ISME J.* 5, 305–316. doi: 10.1038/ismej.2010.117
- Zhuang, K., Ma, E., Lovley, D. R., and Mahadevan, R. (2012). The design of long-term effective uranium bioremediation strategy using a community metabolic model. *Biotechnol. Bioeng.* 109, 2475–2483. doi: 10.1002/bit.24528
- Zomorodi, A. R., Islam, M. M., and Maranas, C. D. (2014). d-OptCom: dynamic multi-level and multi-objective metabolic modeling of microbial communities. *ACS Synth. Biol.* 3, 247–257. doi: 10.1021/sb4001307
- Zomorodi, A. R., and Maranas, C. D. (2012). OptCom: a multi-level optimization framework for the metabolic modeling and analysis of microbial communities. *PLoS Comput. Biol.* 8:e1002363. doi: 10.1371/journal.pcbi.1002363
- Zomorodi, A. R., and Segrè, D. (2016). Synthetic ecology of microbes: mathematical models and applications. *J. Mol. Biol.* 428, 837–861. doi: 10.1016/j.jmb.2015.10.019

Conflict of Interest Statement: The authors declare that the research was conducted in the absence of any commercial or financial relationships that could be construed as a potential conflict of interest.

Copyright © 2017 Kreft, Plugge, Prats, Leveau, Zhang and Hellweger. This is an open-access article distributed under the terms of the Creative Commons Attribution License (CC BY). The use, distribution or reproduction in other forums is permitted, provided the original author(s) or licensor are credited and that the original publication in this journal is cited, in accordance with accepted academic practice. No use, distribution or reproduction is permitted which does not comply with these terms.

Advantages of publishing in Frontiers



OPEN ACCESS

Articles are free to read
for greatest visibility
and readership



FAST PUBLICATION

Around 90 days
from submission
to decision



HIGH QUALITY PEER-REVIEW

Rigorous, collaborative,
and constructive
peer-review



TRANSPARENT PEER-REVIEW

Editors and reviewers
acknowledged by name
on published articles

Frontiers

Avenue du Tribunal-Fédéral 34
1005 Lausanne | Switzerland

Visit us: www.frontiersin.org

Contact us: info@frontiersin.org | +41 21 510 17 00



REPRODUCIBILITY OF RESEARCH

Support open data
and methods to enhance
research reproducibility



DIGITAL PUBLISHING

Articles designed
for optimal readership
across devices



FOLLOW US

[@frontiersin](https://twitter.com/frontiersin)



IMPACT METRICS

Advanced article metrics
track visibility across
digital media



EXTENSIVE PROMOTION

Marketing
and promotion
of impactful research



LOOP RESEARCH NETWORK

Our network
increases your
article's readership